

Proceedings of the 2014 International Conference on

MATERIALS SCIENCE AND ENERGY ENGINEERING

(CMSEE 2014)

Shyan-Lung Chung • Xiaolong Li

editors

World Scientific

Proceedings of the 2014 International Conference on

MATERIALS SCIENCE AND ENERGY ENGINEERING

(CMSEE 2014)

This page intentionally left blank

Proceedings of the 2014 International Conference on

MATERIALS SCIENCE AND ENERGY ENGINEERING

(CMSEE 2014)

Sanya, China 12 – 14 Dec 2014

editors

Shyan-Lung Chung

National Cheng Kung University, Taiwan

Xiaolong Li

College of Technology, Indiana State University, USA

World Scientific

NEW JERSEY • LONDON • SINGAPORE • BEIJING • SHANGHAI • HONG KONG • TAIPEI • CHENNAI

Published by

World Scientific Publishing Co. Pte. Ltd.

5 Toh Tuck Link, Singapore 596224

USA office: 27 Warren Street, Suite 401-402, Hackensack, NJ 07601

UK office: 57 Shelton Street, Covent Garden, London WC2H 9HE

British Library Cataloguing-in-Publication Data

A catalogue record for this book is available from the British Library.

PROCEEDINGS OF THE 2014 INTERNATIONAL CONFERENCE ON MATERIALS SCIENCE AND ENERGY ENGINEERING (CMSEE 2014)

Copyright © 2015 by World Scientific Publishing Co. Pte. Ltd.

All rights reserved. This book, or parts thereof, may not be reproduced in any form or by any means, electronic or mechanical, including photocopying, recording or any information storage and retrieval system now known or to be invented, without written permission from the publisher.

For photocopying of material in this volume, please pay a copying fee through the Copyright Clearance Center, Inc., 222 Rosewood Drive, Danvers, MA 01923, USA. In this case permission to photocopy is not required from the publisher.

ISBN 978-981-4678-96-4

Printed in Singapore

Editorial

Recent Innovations in Material Science and Energy Engineering

This proceedings published by World Scientific consists of ninety-seven best papers presented at the 2014 International Conference on Materials Science and Energy Engineering (CMSEE2014), which was held in Sanya, Hainan, China during December 12-14, 2014. The CMSEE2014 was hosted by American Society of Science and Engineering (ASSE) and published by World Scientific.

CMSEE2014 covers a wide range of fundamental studies, technical innovations and industrial applications in material science and energy engineering. There are two main goals for the conference: First, to provide a comprehensive and global forum for the participants to exchange scientific research ideas; second, to stimulate the interests and ambition of participants for further researches in the future.

The conference consists of keynote speeches, oral sessions and poster sessions. We were pleased to have more than 130 participants from different countries and regions in the world including China, Canada, Japan, Korea, Taiwan, Turkey, Egypt and Russia.

All papers submitted to the conference were subject to a rigorous peer-review process by at least two independent reviewers. Acceptance was subject to a satisfactory review and on completion of the reviewers' recommended and mandatory changes and final examination by the guest editor. It is expected to be a key publication related to advances in materials science and technology for industrial engineers and academic researchers. The CMSEE2014 delegates will be sent information by email on how to access the issue.

On behalf of the CMSEE2014 organizing committee, I would like to take this opportunity to express my appreciation to all the authors who submitted

their manuscripts to this book. And, finally, I would like to express my deepest and sincere gratitude to Dr. Yan H. Ng from World Scientific for his elaborate support dedicated to the publication of this proceedings.

Shyan-Lung Chung
Professor
Department of Chemical Engineering,
National Cheng Kung University,
Tainan, Taiwan, ROC
Guest Editor

Contents

Chapter 1: Material Science and Material Processing Technology

Depth-Dependency of the Hardness of NiTi Shape Memory Alloys at Different Load Modes by Nanoindentation Experiments
W.P. Wu and W. Yang 1

Calculation Model of Turnover Steel Ladle Based on Gantt Chart
B.F. Huang, X.L. Zhou, G.F. Zhang and Z. Shi 8

The Research of the Property of the PEO Modified PBC Porous Membrane
X.H. Gu, X. Song, P. Zeng and X.W. Zhang 16

MCA Modeling of Nanostructuring Burnishing
A.I. Dmitriev and V.P. Kuznetsov 21

Fabrication and Electrical Properties Analysis of SWCNTs/PDMS Composites
F.J. Liu and J.T.W. Yeow 27

The Preparation and Photocatalytic Degradation Property of the Fe-octacarboxylic Acid Phthalocyanine/Attapulgite Nano-composite Catalyst
Z.C. Yuan and D.J. Chen 34

The Research on Dilational Viscoelasticity of the Interface between ASP Solution and Oil
H.F. Xia, X. Lai, H.Y. Qiao, X.X. Liu and Q. Fan 40

The High Renaissance Properties of Porous Three Dimensional Graphene Using One Step Reduction and Its Application in Flexible Conductor
C.F. Feng, Z.F. Yi, Z. Peng and L.X. Kong 47

Preparation and Effects of Mg&Zr-doping on the Electrochemical Properties of Spinel $Li_4Ti_5O_{12}$ as Anode Material for Lithium Ion Battery
Z. Wang, W.Q. Shao, S.O. Chen, H.L. Li, L.Y. Jing, Y.Q. Ban and X.J. Guo 53

Influence of Deposition Parameters on TiC_xN_{1-x} Composite Films by Multi-aRC Ion Plating
D.Q. Ke, Y.J. Pan, H. Zhang, B. Hong and X.F. Lu 59

Application of Dynamic Scaling to the Surface Properties of TiC_xN_{1-x} Nano Films
D.Q. Ke, Y.J. Pan, B. Hong, X.F. Lu and H. Zhang 65

Thermodynamics of Pb^{2+} Adsorption on Amino Ion Exchange Fiber
T.T. Zheng, Q. Gan, J.X. Qian and C.G. Feng 71

Supercritical CO_2 Extraction of Volatile Oil from Compound Recipe of Clove and Cinnamon
C. Li 79

Optimization of Ultrasonic-assisted Extraction of Polysaccharides from Imperatae Rhizoma Using Response Surface Methodology
X.B. Shang and C. Li 86

Effect of Electromagnetic Field Phase and Frequency on Efficiency of Mould Electromagnetic Stirrer for Continuous Casting Billet
J.C. Li and B.F. Wang 93

Microstructure Evolution of Mg-Zn-Zr-Nd Magnesium Alloy during Partial Remelting
Y.Y. Wan, Y.B. Wang, M.Q. Lu, X.S. Li and J.Q. Tao 99

Blood Compatibility of Oxidized Bacterial Cellulose/Silk Fibroin Composite Membrane
S.Y. Wang, T. Huang, L.Y. Sheng, C. Lai and T.F. Xi 107

Characterization and Properties of TEMPO-oxidized Bacterial Cellulose-Hydroxypatite for Osseous Regeneration
T. Huang, S.Y. Wang, L.Y. Sheng, C. Lai and T.F. Xi 113

Enhanced Crystallization Kinetics of Poly(lactic acid) with Carbon Nanotube (CNT) as the Nucleating Agent: An Evaluation Using In-situ Measurement
F.X. Lu, B. Yang, R. Xia, L. Hu, J.B. Miao and J.S. Qian 120

Investigation on Trace Dysprosium and Boron Doping NiAl-based Eutectic Alloy Fabricated by Injection Casting
L.Y. Sheng, F. Yang, C. Lai, Q.L. Wang and T.F. Xi 128

Conductive Polypyrrole Composited PET and Cotton Fabrics with Alkali Treatment
Y. Chen, J.T. Ju and J.T. Tang 135

Characterization of Structural Homogeneity of Type IV Silica Glass
Y.C. Sun, C.D. Rao, X.F. Song, X.R. Du, X.Q. Zhang and H. Wang 142

Improving Water Vapor Barrier of Green-Based Nanocellulose Film via Hydrophobic Coating
P. Lu, Y.F. Pan and H.N. Xiao 148

Synthesis, Characterization, and Catalytic Properties of MnO_x/SBA-16 for Toluene Oxidation
Y.J. Zhang, L. Zhang, J.G. Deng, S.H. Xie, H.G. Yang, Y. Jiang and H.X. Dai 154

The Preliminary Study on Polylactide/Polystyrene/Nanoclay Composites
W.L. Zhu, X.F. Peng and N.Q. Zhou 168

Preparation and Catalytic Performance of Cu-supported on Manganese Oxide for Catalytic Oxidation of CO
H.X. Zhao, L.N. Yan, Q. Ye, H. Lu and D. Wang 174

Research on Forming Process of Connecting Rod Formed by Squeeze Casting
H. Chen, S.X. Chai, T.Q. Deng and Y.Y. Wan 179

The Analysis of In-plane Uniaxial Anisotropy in Magnetic Thin Film Using Longitudinal MOKE and a Rotating Field (ROTMOKE)
F. Wang and H. Wang 187

Cast Nylon/Bentonite Nanofibers Prepared for UV Resistance
X.H. Liu, X. Yang and C.E. Wang 195

Research on Electrical Properties of Carbon Fiber-Steel Slag Cement Based Composites
W.G. Xing, X.S. Tian, L. Liu and R. Shen 202

Research on Mechanical Properties of Carbon Fiber-Steel Slag Cement Based Composites
X.S. Tian, L.M. Meng and J.J. Shen 208

Investigation of the Structure of the Electrodeposited Alloy CoNiW by Methods HAADF STEM and AFM
A. Kirillov, E. Modin, E. Pustovalov, A. Fedorets, A. Dubinets and V. Plotnikov 215

Effect of Cooling Rate on Microstructure and Transformation Temperature of GCr15 Bearing Steel
X.D. Huo, Z.Z. Tian, L.J. Li and N.F. Liu 220

Influence of Electrical Voltage on the Wear Resistance of TA2 Alloy
X.J. Guo, M.Q. Li, F.H. Wei and C. Ma 226

Simultaneous Imaging Polarimeter Using an Azo-polymer Orientation Array
P.Z. Yan, J.G. Gao, K.Y. Wang, X.Y. Zhang and P.C. Cui 232

Effect of Surface Grafting on the Dielectric Properties of Barium Titanate Nanoparticles with Controllable Polymer Shielding Layers
H.L. Tang, H.Y. Guo and X.B. Liu 238

Characterization of In situ Synthesized Nitrides Reinforced Fe Matrix Wear-resistant Coating by (Ar-N_2) TIG Arc/Cored-Wires Weld Overlaying Technology
M.R. Liu, H.C. Cheng and L. Li 247

Ultraviolet Light Sensing Using Gold-coated Prism Overlaid with Azo-polymer
X.Y. Zhang, J.J. Ma, K.Y. Wang and P.Z. Yan 255

Microstructure and Mechanical Properties of a Nickel-based Honeycomb Sandwich at High Temperature
Q.M. Zhang, X.D. He and Y. Li 261

Microstructure and Mechanical Properties of Spot Welding Joint of Dissimilar High Strength Steel
Y. *Wang, X.X. Qin, W.X. Jiang, M.Y. Li and J.W. Ren*..... 269

Effect of Cold-Rolling and Annealing on Microstructure and Texture of Interstitial Free Steel
J.H. Qu and J.Q. Liu 275

Crystallization Behavior of Biodegradable Poly (3-hydrobutyrate-co-3-hydroxyvalerate)/Hyperbranched Poly (Ester Amide) Blends
W.L. Zheng, L. Chen and Z.Y. Qin 281

Hydrothermal Conversion of Glucose to Lactic Acid with $Al(OH)_3$
Z.S. Zhang, G.D. Yao and F.M. Jin..... 289

Amphiphilic Conetworks Based on End-Group Cross-Linking of Polydimethylsiloxane Pentablock Copolymer and Polymethylhydrosiloxane
M. Qiu and C.J. He 296

The Effects of Surface Preparation on Growth of CuO Nanowires During Thermal Oxidation
C.H. Xu, X.L. Li, Y.L. Liu, Y. Li and J.Z. Wang 302

Preparation of Uniform PMMA-SiO_2 Particles with High Content of SiO_2 via In situ Suspension Polymerization
T. Chen, Y.X. Wang, Y.H. Zhang and C.J. Yan 308

Preparation, Characterization and Photocatalytic Activity of TiO_2/Fe Composite Coatings
L. Hao, Y. Lu and S.J. Guan..... 314

The Growth Control of $Zn_{1-x}Mg_xO$ Films and Photo-Electrical Property Research
X.H. Wang, X. Zhou and G. Zhang 320

Effects of Li Content on Microstructure and Corrosion Morphology of Mg-Li-Al-Ca Alloy in NaCl Solution
H.X. Yu 327

Effect of Low Content SiO_2 on the Crystallization Behaviour and Dynamic Mechanical Properties of Polyurethane/SiO Composites
Y.H. Yi 332

Spectral Extinction Coefficient Test of the Photoelectric Jamming Aerosol
T. Zhang, X.D. Dai, L. Chen, C.S. Chen, H.F. Liu, M.Y. Dai and L.N. Ren 338

Research on Tensile Properties for Low-Alloy Steel after Fire Damage
C. Wang, J. Chen and Y.P. Wang 345

Preparation of Nanoporous Nickel Phosphates with Surfactants and Application in Intumescent Flame Retardant Polypropylene Composites
S.B. Nie, X. Dong, L. Liu, D.Y. Wang and C. Peng 351

Precipitate Analysis of Nanoparticle-Reinforced Tin Bronze Using Atom Probe Tomography
K.X. Chen, Y.W. Niu, X.H. Chen, D. Ding and Z.D. Wang 357

The Complex Band Structure of $Hg_{1-x}Cd_xTe$ Material
X.B. Wang and T.S. Xia 365

Mechanical and Structural Evolution of SiC/Zr-Si-C Coated C/SiC Composites under Thermal Shock Tests
X. Yang and F. Cao 370

The Crystal Structure of the $PrAl_8Cu_3Ni$ Quaternary Compound
B. He, C.S. Qin, D.G. Li, L. Hu and M. Qin 380

Simulation of Melt Flow and Interface Shape of 450 mm Czochralski Grown Silicon Single Crystal
X.Y. Zhang, X.J. Guan, J. Wang, Q.K. Zeng and Z.B. Pan 384

Thermal Structural Analysis of Surface of Pulling-Straightening Roller Based on ANSYS
L.Y. Wang, B.S. Yu, L.P. Liu and H. Chen 392

Evaluation Method on Anti-Icing Effects of Hydrophobic Coating
C.H. Xiao 400

Characterization and Property of Mg-Doped Cu_2SnSe_3 Bulks with the Mg Substitution at the Sn Site
D.H. Kuo and W. Wubet 407

A Facile Synthesis of Mesoporous Silica Nanoparticle and its Morphology Manipulation by Varying pH Value
Z.F. Yi, C.F. Feng, D. Cahill and L.X. Kong 413

Investigation on Microstructure and Properties of X90 High-Strength Pipeline Steel Welded Joints
Z.Y. Bi 419

Chapter 2: Energy Material and Energy Processing Technology

Parameter Optimization Research of Oil Spill Tracking Buoy
R. Yang and Q. Gu 427

Mechanism of Pump Efficiency Promotion by Multi Traveling Valve Device
X.L. Li, W. Xiao, X.Q. Liu, L.P. Zhou and H.R. Xu 434

Characteristics and Advances of Graphene
L. Liu and C.C. Zhou 440

Radiation in a Thermal Analysis of a Power Box
B. Chen and N. Li 444

Design of the Charger with MPPT Function for Photovoltaic Power Generation
B. Zhang, Y.W. Wang and S. Zhang 449

Review and Prospects: Application and Research of Heat Pumps in China
Y.Y. Sun, R.H. Wu and C.J. Sun 456

Ab initio Molecular Dynamics Simulation on Carbothermal Reduction Mechanism of Fluorapatite in Vacuum
X.H. Zhu, Y.C. Liu, Q. Bai, B. Jing and Q.X. Li 464

Methods of Estimating VaR Based on Gray Peaks over Threshold Model
R.Q. Wang and Z.Q. Xiao 472

Effect of Nozzle on Performance of Swirl-Cooled Combustor
K. Li, Z.X. Zeng and Y.H. Xu 478

Experimental Study on the Pyrolysis Characteristics of Demineralized Phragmites
J.M. Shi, M. Lin, Y.S. Xie, X.P. Xi, H.L. Wang and Y.Y. Gong 488

Application of Array Sonic Logging in the Study of Regional Geostress in Nanpu Sag
J.M. Yao, X.X. Tao, W.H. Zhang and S. Wang 498

Monitoring for Transmission Line Galloping Based on Monocular Vision
K. Xie, Z.B. Lv, W. Yang, Y.B. Shao and G.L. Song 506

Energy Flow Modeling and Analysis of Electrical Hydraulic Power Steering System for Electric Bus
Z.L. Jiang and G.B. Shi 513

Experimental Research on Coal Water Slurries Prepared by Single and Blended Coals
Y.X. Hu, J.Z. Liu, J.Y. Lin, J.H. Zhou and K.F. Cen 524

Feasibility Study and Development of Eolic Energy in the Ponza
C. Andrea, M. Giuseppina, C. Filippo and S. Vincenzo 534

Study on Piezoelectric Harvesting Mechanism of Nonlinear Cantilever Harvester
C.H. Sun, J. Liu, H.B. Wang and G.Q. Shang 544

Analysis on the Response Time of the Battery Energy Storage System
S. Li, Z.M. Wang and W.H. Luo 553

A Rapid Calculation Method of Wind Farm Collector Lines Maximum Length Applied to Planning and Design
G.D. Liao, L.Y. Li, X.T. Xie, P. Ai, Y. Lu and M.J. Li 561

Study on Anti-Clogging Performance of Large Diameter Fluidized Bed Sewage Heat Exchanger
H.Y. Bi, Y.M. Shang and X.H. Gu 573

A Discussion on the Feasibility of Large Consumers Direct Power Purchasing
Y. Gao, H.Y. Zhong, A.R. Xu, L. Zhang, X.P. Wang and C.Y. Qu 578

Research on Distributed Generation and Its Application in Oil Field Distribution Power Network
J. Xu, H.W. Li and W. Fang 585

Graphene Decorated TiO_2 Nanorods Photo-Anode for Solar Hydrogen Production
H. Kim, S.J. An and B.L. Yang 595

Failure Analysis of a Pipeline in Sour Gas Field
J. Yan, T. Gu, H.G. Chang, Q. Zhang, N.G. Zhang, Z.D. Liu, H. Wu, G.Y. Wu, M.W. Yang and L. Mo 601

The Diurnal Change Model of the Instantaneous Amount of Solar Radiation Incident on the Horizontal Surface Near the Ground
Z.S. Guo and X.P. Zhang 608

Synthesis Preparation and Properties Study on Phase Change Material of $Na_2SO_4 \cdot 10H_2O@SiO_2$
H.M. Wang, Z.F. Lu and D.W. Huang 617

Chapter 3: Environmental Material and Environmental Processing Technology

Study of Pore Sites Introduced by Mechanochemical Milling in Saponite Nanoparticles by Positronium Spectroscopy
K. Numata and K. Sato 621

The Study on Photocatalytic Degradation Performance to Musk Ketone with TiO_2/C Hybrid Aerogel in Aqueous Solution
F. Pan, D.H. Chen, X. Shao, R. Zhang and L.L. Zhu 626

Study on Excess Sludge Disintegration by Fenton Oxidation
J. Yin, W.Y. Wang and Y. Hu 634

Investigation on Environment Benefit and Problem of Solar Power Generation Technology
L.Q. Qi, Z.X. Li and Y.J. Zhang 641

Qualitative and Quantitative Analysis of Bu-Gong Saponin
S.L. Cui 648

Compressive Strength of Paper Fruit-Shipping Box and its Optimization
Y.P. E, L.H. Zhang, T.T. Zhu and L.P. Li 655

Production of Low Carbon Dioxide Emission Geopolymer Green Cement
T.W. Cheng, Y.C. Ding and C.W. Jhong 661

Study on the Efficiency of Microbial Mutagenesis Experiments and Degradation of Methane
W.J. Nie, S.Q. Wang and C.T. Hou 667

The Influence of Ammonia Regeneration for CuO/γ-Al_2O_3 Catalyst of Desulfurization Performance
W.J. Nie, L. Zhang and N. Zhang 672

Author Index 677

Depth-Dependency of the Hardness of NiTi Shape Memory Alloys at Different Load Modes by Nanoindentation Experiments

Yang Wei

Department of Engineering mechanics, School of Civil Engineering, Wuhan University, Wuhan, China
E-mail: 2009301890033@whu.edu.cn

Wen-Ping Wu†

State Key Laboratory of Water Resources & Hydropower Engineering Science, Wuhan University, Wuhan, China
†*E-mail: wpwu@whu.edu.cn*

The depth-dependency of the hardness in phase transition NiTi shape memory alloys (SMAs) at different indentation load modes are examined by nanoindentation experiment using a Berkovich indenter tip. The results indicated that different indentation load modes have a very slight effect on the indentation depth and hardness for a same maximum load. Moreover, the depth-dependency of hardness of NiTi SMAs is independent of indentation load modes, the hardness mainly come from the resistance to the phase transition and follows a reciprocal relationship with the indentation depth for a Berkovich indenter.

Keywords: Nanoindentation; Hardness; Phase Transition; Niti Shape Memory Alloys.

1. Introduction

NiTi shape memory alloys (SMAs) are a typical phase transition materials and are well known for their extraordinary shape memory and superelastic properties. In order to optimally design the future SMAs-based devices and to improve the performance of small-scale systems, a further study on micro- and nano-scale behavior of the material is necessary. In such very small length scales, the hardness of the material has attracted great interest and become an important factor in evaluating the wear, fatigue and friction behavior of these devices [1].

It is well known that the hardness of many metallic material exhibits the depth dependence during nanoindentation [2-4]. For SMAs, Amini et al. [5] conducted the measurement of the hardness-depth relationship of NiTi SMAs at different temperatures. Liu et al. [6] studied depth dependence of nanohardness of a CuAlNi using different indenter tips. Huang et al. [7] and Laplanche et al. [8]

investigated crystal orientation effects on the onset of plasticity in single-crystal NiTi and orientation dependence of stress-induced martensite formation during nanoindentation in NiTi SMAs, respectively. Moreover, hardness-depth relationship of NiTi SMAs in spherical nanoindentation [9], temperature dependence of indentation profile [10, 11], pseudoelastic behavior [12, 13], and loading rate dependency of maximum indentation depth have been investigated [14]. However, a little attention had been paid to the study of the depth dependence of hardness at different load modes, a further study of the microscopic mechanisms responsible for the depth dependence of hardness is necessary.

In this paper, the nanoindentation tests on phase transition NiTi SMAs were performed. The effect of indentation load modes on the indentation depth and hardness were examined. The objective is to examine the depth dependence of hardness at different indentation load modes, and to offer a theoretical explanation for the observed depth dependence.

2. Materials and Experimental Set Up

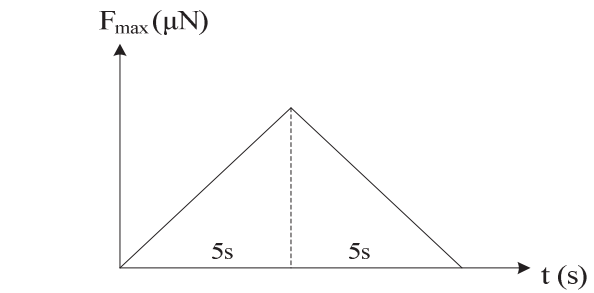
Nanoindentation tests were performed on the NiTi (Ni-56.4wt% and Ti-43.6wt%) with shape memory effect (SME) polycrystalline sheets using Hysitron TriboIndenter TI950 Nanohardness tester at the room temperature. The NiTi sheets with [100] orientation were cut (5 mm × 5 mm) into pieces and the size of the grain was 100 nm. Three different nanoindentation load modes were applied to conduct nanoindetation test in a quasi-static mode at room temperature using a diamond Berkovich tip (100 nm radius) with a face angle of 142.3°. Three types of nanoindentation loads (mode I 5-0-5: loading 5s, unloading 5s; mode II 5-2-5: loading 5s, maintain 2s, unloading 5s; mode III cycle: loading 0.5s, maintain 1s, unloading 0.5s, then performing 10 cycles by increasing load amplitude) are shown in Fig. 1. These three nanoindentation loads have the same loading rate (loading and unloading) though the load modes are different.

3. Experimental Results and Discussion

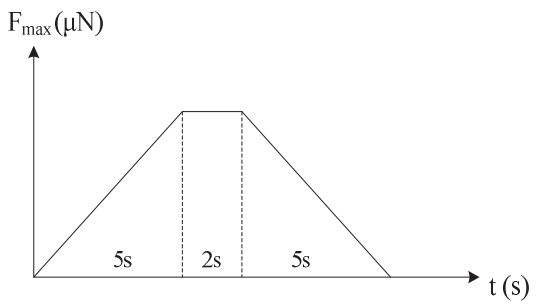
3.1. Load-Displacement Curves at Different Load Modes

Fig. 2a shows the typical loading unloading curves for three different load modes at the same maximum load of 5000μN by the Berkovich tip indented on NiTi SMAs. It can be seen that the load-displacement curves have features of plasticity-like response with residual depths, which are mainly due to the

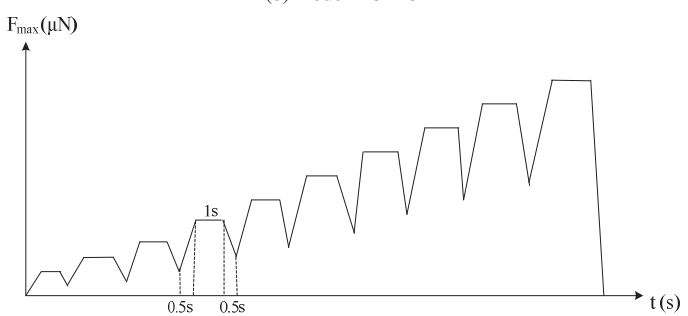
retained phase transition strain after unloading. The curves revealed that the inelastic deformation via dislocation motion and a stress-induced martensitic transformation during indentation [6]. Moreover, the load-displacement curves are different for the different indentation load modes, but indentation depth has only slight difference at the same maximum load of 5000uN, the indentation depth at load mode II (maintain 2s) is slightly larger than that of load modes I and III, which is related to the creep of materials at the maintain time.



(a) mode I: 5-0-5



(b) mode II: 5-2-5



(c) mode III: cycle

Fig. 1. Three load modes for nanoindentation: (a) mode I 5-0-5, (b) mode II 5-2-5, (c) mode III cycle.

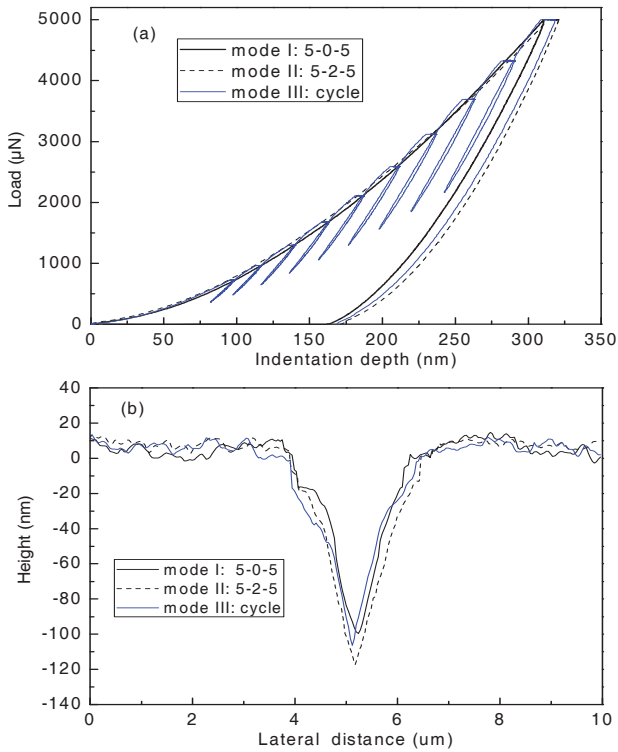


Fig. 2. (a) Load-displacement curves and (b) cross-section of surface profiles measured nanoindent for three different load modes at the maximum load of 5000μN.

Cross-section of surface profiles measured nanoindent at the maximum load of 5000 μN is shown in Fig. 2b, which presents a more quantitative impression of indentation depth at different load modes. It is noted that the remnant indentation depth after complete unloading is about 160 nm in Fig. 2a; however, the remnant indentation depth measured by a scan line profile is about 120nm in Fig. 2b. This is mainly caused by the surface tilt of the NiTi samples, if the scan line profile in the vertex of surface tilt, the remnant indentation depth measured by a scan line profile is smaller than the remnant indentation depth after complete unloading in the load-displacement curves.

3.2. Nanohardness versus Indentation Depth

Fig. 3a shows the depth dependence of hardness on NiTi SMAs at different indentation load modes using the Berkovich indenter. To test the depth dependence of hardness, the applied maximum indentation loads ranged from

10000μN to 200μN, the hardness was computed by applying Oliver-Pharr method [15]. It is found that the nanohardness increases with decreasing indentation depth at different indentation load modes, that is to say, the smaller the depth, the larger the hardness, and the depth dependence of hardness is independent of load modes. The hardness decreases from about 9.5 GPa to the saturated amount of nearly 3 GPa, and three different load modes have similar trend.

Fig. 3b shows the measurement and fitting of the hardness-depth relationship of NiTi SMAs at different indentation load modes. It can be seen from Fig. 3b that the hardness manifests a reciprocal relationship with the indentation depth. Moreover, the fitting curves of hardness-depth relationship are very similar at different indentation load modes, namely, the hardness-depth relationship is independent of load modes.

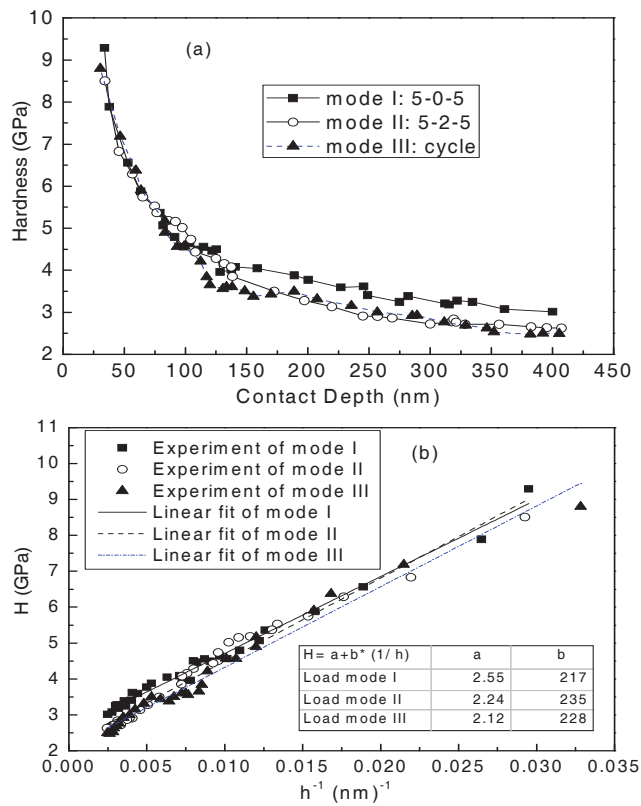


Fig. 3. (a) Hardness versus indentation depth and (b) the measurement and fitting of the hardness-depth relationship for three different indentation load modes.

The fitting curves in Fig. 3b shows the linear relationship between the hardness H and the inverse of indentation depth (1/h) under three load modes, which well captured the test data and confirmed the depth dependence of the hardness reported by Amini et al. [5], and Amini et al. [5] expressed the relationship between the hardness H and depth h: $H=\frac{F}{A}=\beta_1 l(\frac{1}{h})+\beta_2$. The first term here reflects hardness level due to the interfacial energy of the Martensite transformed zone created during phase transition and the second term is due to the bulk energy induced during indentation. However, it is noted that the slope of fitting line in Fig. 3b is about 7 times lower than that reported by Amini et al. [5]. This is because that Amini et al. [5] performed nanoindentation test using the maximum load was about 450000μN, resulting in a much larger of the interfacial energy of the Martensite transformed zone. Accordingly, the slop of fitting line reported by Amini et al. is much larger than that in Fig. 3b.

The above results and analysis by nanoindentation experiment using a Berkovich indenter revealed that different load modes have no effect on the depth dependence of hardness of NiTi SMAs, the hardness has a reciprocal relationship with the indentation depth.

4. Conclusions

(1) The different indentation load modes induce the different load-displacement curves. Load modes have only slight effect on the indentation depth and hardness for the same maximum load.

(2) The hardness-depth relationship of NiTi is independent of load modes, the hardness mainly come from the resistance to the phase transition and follows a reciprocal relationship with the indentation depth for a Berkovich indenter.

Acknowledgements

The work was supported by National Natural Science Foundation of China (Grant No. 11102139), and China Postdoctoral Science Foundation (Grant Nos. 20110491205 and 2012T50665).

References

1. L. Qian, Q. P. Sun, X. Xiao, Role of Phase Transition in the Unusual Microwear Behavior of Superelastic NiTi Shape Memory Alloy, *Wear*. 260(2006) 509-522.
2. Y. Liu, A. H. W. Ngan, Depth dependence of Hardness in copper single crystals measured by nanoindentation, *Script Mater*. 44(2001) 237-241.

3. W. D. Nix, H. Gao, Indentation size effects in crystalline materials: a law for strain gradient plasticity, *J. Mech. Phys. Solids*. 46(1998) 411-425.
4. N. A. Fleck, J. W. Hutchinson, A phenomenological theory for strain grainent effect in plasticity, *J. Mech. Phys. Solids*. 41(1993)1825-1857.
5. Amini, W. Yan, Q. P. Sun, Depth dependency of indentation hardness during solid-state phase transition of shape memory alloys, *Appl. Phys. Lett.* 99(2011)021901.
6. Liu, Q. P. Sun, Y. P. Zhao, T. X. Yu, Depth dependence of nanohardness in a CuAlNi single crystal shape memory alloy, *Int. J. Nonlinear Sci. Numer. Simul.* 3(2002)535-538.
7. X. Huang, A. G. Ramirez, Crystal orientation effects on the onset of plasticity in single-crystal NiTi, *Scripta Mater.* 65(2011)879-882.
8. G. Laplanche, J. Pfetzing-Micklich, G. Eggeler, Orientation dependence of stress-induced martensite formation during nanoindentation in NiTi shape memory alloys, *Acta Mater*, 68(2014) 19-31.
9. W. Yan, A. Amini, Q. P. Sun, on anomalous depth-dependency of the hardness of NiTi shape memory alloys in spherical nanoindentation, J. *Mater. Res.* 28(2013) 2031-2039.
10. W. M. Huang, J. F. Su, M. H. Hong, B. Yang, Pile-up and sink-in in micro-indentation of a NiTi shape-memory alloy, *Script Mater.* 53(2005)1055–1057.
11. C. Liu, Y. P. Zhao, Q. P. Sun, T. X. Yu, Z. X. Cao, Characteristic of microscropic shape memory effect in a CuAlNi alloy by nanoindentation, *J. Mater. Sci.* 40(2005), 1501-1504.
12. X. G. Ma, K. Komvopoulos, Nanoscale pseudoelastic behavior of indented titanium-nickel films, *Appl. Phys. Lett.* 83(2003)3773-3775.
13. X. G. Ma, K. Komvopoulos, Pseudoelasticity of shape-memory titanium–nickel films subjected to dynamic nanoindentation, *Appl. Phys. Lett.* 84(2004)4274-4276.
14. Amini, Y. He, Q. P. Sun, Loading rate dependency of maximum nanoindentation depth in nano-grained NiTi shape memory alloy, *Mater. Lett.* 65(2011)464-466.
15. W. C. Oliver, G. M. Pharr, An improved technique for mining hardness and elastic modulus using load and displacement sensing indentation experiments, *J. Mater. Res.*7 (1992)1564-1583.

Calculation Model of Turnover Steel Ladle Based on Gantt Chart

Huang Bang-fu[1, 2, a*], Zhou Xiao-lei[1, 2, b], Zhang Gui-fang[1, 2, c], Shi Zhe[1, 2, d]

[1]*Faculty of Metallurgical and Energy Engineering, Kunming University of Science and Technology, Yunnan Kunming 650093*

[2]*Clean Metallurgy Key Laboratory of Complex Iron Resources, University of Yunnan Province, Kunming 650093, China*

E-mail: [a]kmusthbf@163.com, [b]Zheshi5@hotmail.com, [c]970319108@qq.com, [d]Zheshi5@hotmail.com*

In order to realize production organization optimization and put forward scientific and reasonable number calculation model of steel ladle, turnover behaviors was analyzed with steel ladle of Q steelworks as the object of study. Steel ladle turnover cycle of various refining process was measured. Steel ladle Gantt charts of 1 continuous caster and 2 continuous casters were drawn out. Calculation model of turnover number and rotation ratio were put forward by analyzing cast overlap time, which includes greater than, less than, and in between the turnover cycle of steel ladle. Researches show that steel ladle turnover number can be decreased through optimizing turnover cycle and decreasing cast overlap time.

Keywords: Steelworks; Gantt chart; Steel Ladle; Turnover Number; Rotation Ratio.

1. Introduction

Steel ladle has many functions between basic oxygen furnace (BOF) and continuous caster (CC), such as cohesion-matching and coordination-buffer and liquid steel transportation carrier and secondary refining vessel, its operation status represents operation efficiency of steelmaking and continuous casting interface system. In the process of practical production, the less turnover number means the higher rotation ratio of steel ladle and the hotter tapping ratio of liquid steel [1], which has important significance for reducing BOF tapping temperature and keeping CC constant speed. The existing ladle researches focused on scheduling management area by using numerical modeling [2, 3] and simulation analysis [4, 5]. The existing operation control of steel ladle includes use management [6] and establishment of turnover model [7] and turnover rate [8], but

* Corresponding author.

there were few researches that estimates scientific and reasonable turnover number of steel ladle. The studies of steel ladle turnover number mainly focused on calculation method that based on 1 BOF or 1 CC, such as production method and time calculation method and turnover period matching method [9, 10]. However, the existing calculation methods of steel ladle turnover number were just considered the factors, such as steel output in a certain period of time and smelting cycle of BOF and casting cycle of CC. Those existing calculation methods were not considered the influencing factors of different cast overlap time and casting time. Therefore, calculation results are often greater than actual requirement turnover number. It can be seen that existing studies cannot provide guidance for production.

In this work, the behaviors and cycle of steel ladle in Q steelworks were analyzed in order to put forward scientific and reasonable calculation model. Gantt charts of steel ladle under 1 CC and 2 CCs were drawn out. Through optimizing operation time and adjusting cast plan, turnover number will be reduced, and rotation ratio will be raised. The research achievement will realize efficient control of steel ladle and production organization optimization of steelworks.

2. Behaviors And Cycle Of Steel Ladle

There have 3 BOFs, 3 LFs, 1 RH and 2 CCs in Q steelworks. The nominal capacity of each BOF is 100 t. Besides, it has 3 online baking positions, 2 offline baking positions, 1 hot repair position and 1 cold repair position.

The layout of Q steelworks decides the turnover behaviors of steel ladle. In order to research turnover cycle and rule of steel ladle, turnover behaviors of steel ladle need be analyzed firstly. As shown in follows.

Liquid steel of No.1 CC and No.2 CC can be supplied through the route of BOF-LF-CC, but the route of BOF-LF-RH-CC is only supplied liquid steel for No.2 CC. Empty steel ladle has 2 turnover routes, which includes pouring slag→hot repair→online baking→tapping and pouring slag→cold repair→offline baking→tapping.

After analyzing operation paths of heavy ladle and empty ladle, each section time of turnover cycle has been classified and measured [11]. Such as, turnover cycle of No.1 CC steel ladle is calculated and equals 173 min, which includes heavy ladle operation time (78 min) and casting time (32 min) and empty ladle operation time (63 min). Turnover cycle of No.2 CC steel ladle can be calculated and equals 164 min, which includes heavy ladle operation time (74 min) and casting time (27 min) and empty ladle operation time (63 min). When the liquid steel of No.2 CC is refined by the route of BOF-LF-RH-CC, turnover cycle equals 205 min, which includes heavy ladle operation time (115 min) and casting time (27 min) and empty ladle operation time (63 min).

3. Calculation Model Of Steel Ladle

Gantt chart is a set of lines chart, horizontal axis represents time, vertical axis represents activities, and lines represents project performance [12].

In order to research the Gantt charts of 1 cast and 2 casts, the refining routes of liquid steel were set as BOF-LF-CC. The Gantt charts are shown in the fellows.

(1) Calculation model of 1 cast

Based on turnover rule and each section time of steel ladle, the 1 cast Gantt chart of No.1 CC is drawn out. As shown in Fig. 1, lines represent turnover behaviors of steel ladle, and the same color line represents 1 steel ladle.

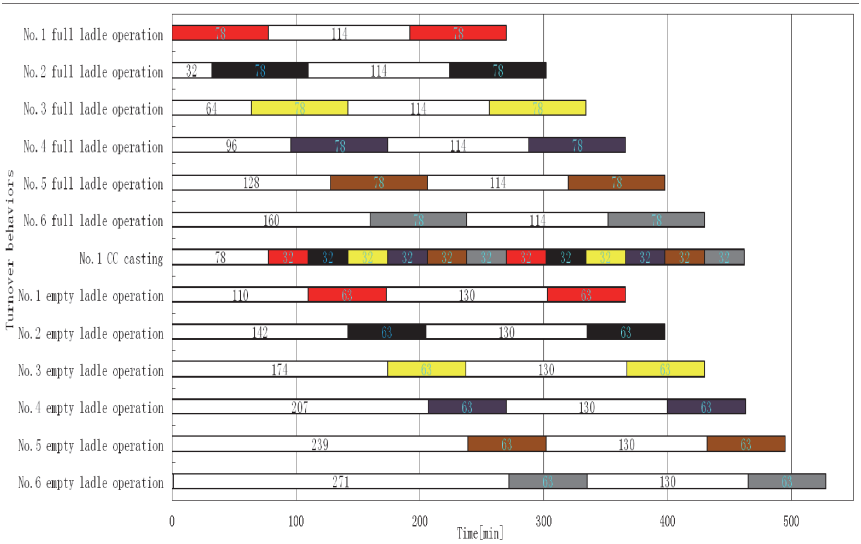


Fig. 1 Gantt chart of single cast.

It can be vivid saw that turnover rule of steel ladle in each section time form the Fig. 1. Through analyzing the turnover rule of steel ladle, it can be observed that No.1 steel ladle marked by red can transport the liquid steel of 7th heat when it has finished the first turnaround task. Therefore, No.1 CC needs 6 steel ladles for satisfying casting requirement. Besides, there have some relationships between turnover number and casting time and turnover cycle. After researching the relationships, calculation model of turnover number is put forward, as shown in Eq. (2).

$$T_{\text{ladle}} = T_{heavy} + T_{empty} + T_{cc} . \tag{1}$$

$$n = \frac{T_{\text{ladle}}}{T_{cc}} . \tag{2}$$

where T_{ladle} represents turnover cycle of steel ladle, min; T_{heavy} represents operation time of heavy steel ladle, min; T_{empty} represents operation time of empty steel ladle, min; T_{cc} represents 1 heat casting time of CC, min; n represents turnover number of steel ladle. Based on casting time of 1 heat equals 32 min and turnover cycle of steel ladle equals 173 min, the n_{1cc} is calculated and equals 5.4, which means No.1 CC need 6 steel ladles for satisfying continuous casting. Based on casting time of 1 heat equals 27 min and turnover cycle of steel ladle equals 164 min, the n_{2cc} is calculated and equals 6.1, which means No.2 CC need 7 steel ladles for satisfy continuous casting.

Studies have shown that all above calculation results is consistent with turnover number of steel ladle in actual production process of Q steelworks.

(2) Calculation model of casts overlap

There has mixed using phenomenon of steel ladle when the 2 CCs are producing at the same time. If the cast end time of No.1 CC is earlier than No.2 CC, some steel ladles of No.1 CC may be supplied for turnover ladle of No.2 CC when they have finished primary turnaround task. Consequently, the total number, which equals turnover ladle number of No.1 CC direct plus turnover ladle number of No.2 CC, is often greater than actual need turnover number.

Based on No.1 CC needs 6 steel ladles and 1 cast has 21 heats, the 6 steel ladles need turnover 3 times and first 3 steel ladles need turnover once more during 1 cast. Based on No.2 CC needs 7 steel ladles and 1 cast has 25 heats, the 7 steel ladles need turnover 3 times and first 4 steel ladles need turnover once more during 1 cast. Therefore, it is only need to draw out the last 9 heats Gantt chart of No.1 CC and first 11 heats of No.2 CC for researching calculation model under casts overlap. The casts overlap includes $T > T_{ladle}^{cc1} > T_{ladle}^{cc2}$ and $T_{ladle}^{cc1} \geq T \geq T_{ladle}^{cc2}$ and $T_{ladle}^{cc1} > T_{ladle}^{cc2} > T$. Besides, the rotation ratio of steel ladle will also be put forward by analyzing Gantt chart under various cast overlap time.

1) $T > T_{ladle}^{cc1} > T_{ladle}^{cc2}$

As shown in Fig. 2: the cast overlap time equals 256 min, which is greater than 173 min and 164 min. After analyzing the Gantt chart of steel ladle under the condition of $T > T_{ladle}^{cc1} > T_{ladle}^{cc2}$, there has no steel ladle of No.1 CC supplied for transporting liquid steel of No.2 CC. Calculation model of total number is shown in Eq. (3).

$$N_{total} = n_1 + n_2 = \frac{T_{ladle}^{cc1}}{T_{cc1}} + \frac{T_{ladle}^{cc2}}{T_{cc2}} . \tag{3}$$

where N_{total} represents total number of steel ladle, n_1 represents the number of steel ladle turnover around No.1 CC, n_2 represents number of steel ladle turnover around No.2 CC.

Rotation ratio is the utilization coefficient of steel ladle, the value of rotation ratio equals casting heat number of CC divided by turnover number of steel ladle in a certain period of time. Therefore, the calculation model of rotation ratio is put forward according to its definition. As shown in Eq. (4).

$$f = \frac{N_1 + N_2}{n_1 + n_2}. \tag{4}$$

where f represents rotation ratio of steel ladle, N_1 represents the number of 1 cast heat of No.1 CC, N_2 represents the number of 1 cast heat of No.2 CC.

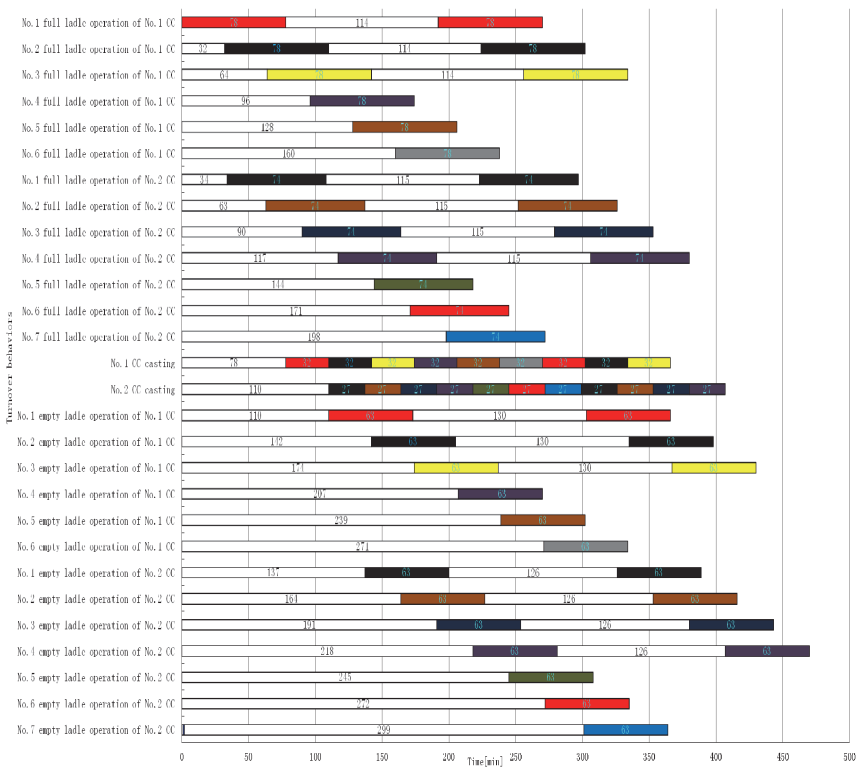


Fig. 2 Gantt chart of steel ladle under the condition of $T > T_{ladle}^{cc1} > T_{ladle}^{cc2}$.

According to Eq. (3) and Eq. (4), the total number of steel ladle used by 2 CCs is calculated and equals 13, the rotation ratio is calculated and equals 3.54.

2) $T_{ladle}^{cc1} \geq T \geq T_{ladle}^{cc2}$

If the cast overlap time equals 170 min which is less than 173 min and greater than 164 min. There has some steel ladles of No.1 CC supplied for transporting liquid steel of No.2 CC. Further analysis, there has 2 cases under the condition of $T_{ladle}^{cc1} \geq T \geq T_{ladle}^{cc2}$, which include the cast end time of No.1 CC is earlier than No.2 CC and the cast end time of No.2 CC is earlier than No.1 CC. The 2 cases are analyzed in the following specificly.

The end casting time of No.1 CC is earlier than No.2 CC:

1) $(n_1\text{-}T / T_{CC1}) < 1$: according to n_1 equals 6 and T equals 170 min and T_{CC1} equals 32 min, it can be worked out that (6-170/32) = 0.7<1, which means that all of steel ladle used by No.1 CC can't supply for transporting the liquid steel of No.2 CC. Calculation model of turnover number is the same as the Eq. (3). The rotation ratio is shown in Eq. (4).

2) $(n_1\text{-}T / T_{CC1}) \geq 1$: it means casting heat number during the overlap time is less than turnover number of steel ladle for No.1 CC. There has steel ladles of No.1 CC supplied for transporting the liquid steel of No.2 CC. In other words, the number of new input steel ladle for No.2 CC can be reduced, which compared with 7. Calculation model of turnover number is shown in Eq. (5).

$$n = n_1 + \frac{T}{T_{cc2}}. \tag{5}$$

Calculation model of rotation ratio is shown in Eq. (6).

$$f = \frac{N_1 + N_2}{n_1 + T/T_{cc2}}. \tag{6}$$

3) $T_{ladle}^{cc1} > T_{ladle}^{cc2} > T$

If the cast end time of No.1 CC is earlier than No.2 CC. The cast overlap time of 2 CCs equals 128 min, which is less than both turnover cycles of steel ladle turnover around No.1 CC and No.2 CC respectively. According to n_1 equals 6 and T equals 128 min and T_{CC1} equals 32 min, it can be worked out that (6-128/32) =2>1, which means that some steel ladles used by No.1 CC can supply for transporting the liquid steel of No.2 CC, such as the No.4 steel ladle marked by violet can transport the 6th heat liquid steel of No.2 CC. Studies have shown that calculation model of turnover number is the same as Eq. (5) and calculation model of rotation ratio is shown in Eq. (6).

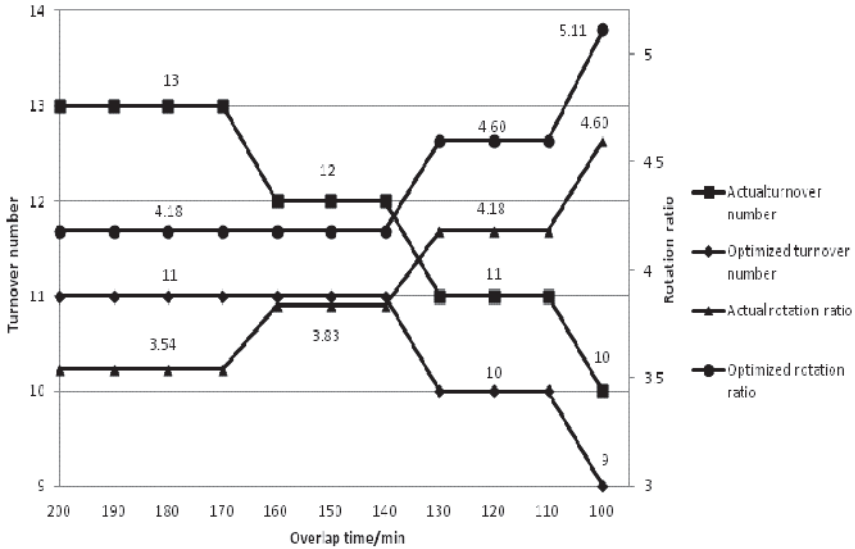


Fig. 3 Relationship between overlap time and turnover number and rotation ratio.

4. Optimization of Cast Plan

The chart of relationship between overlap time and turnover number and rotation ratio is drawn out by setting overlap time from 100 min to 200 min, the overlap time includes greater than, less than, and in between the turnover cycle of steel ladle turnover around No.1 CC and No.2 CC respectively. Besides, the cast end time of No.2 CC is set earlier than No.1 CC. The relationship is shown in Fig. 3.

As shown in Fig. 3: optimized number of steel ladle is less than actual turnover number at least 1. The shorter overlap time represents the less turnover number and the higher rotation ratio whether actual or optimized value.

To sum up, in order to reduce turnover number and raise rotation ratio, on the one hand, turnover cycle must be optimized. On the other hand, cast plan must be scheduled for reducing overlap time and intersecting cast start time of CC.

5. Conclusions

(1) The calculation model of steel ladle turnover number for single CC is proposed. The calculation models of turnover number and rotation ratio are obtained under cast overlap time is greater than, less than, and in between turnover cycle of steel ladle.

(2) Through applying calculation model, the steel ladle turnover number of No.1 CC and No.2 CC can be reduced.

(3) When the casting heat number is less than turnover number during the overlap time, the turnover number can be reduced, and the rotation ratio can be raised.

References

1. J. Hong, X.H. Li and Y.S. Li: submitted to *Journal of research on iron and steel* (2001)
2. P. P. Mohanty: submitted to *The International Journal of Advanced Manufacturing Technology* (2004)
3. A. Bellabdaoui, J. Teghem: submitted to *International Journal of Production Economics* (2006)
4. A. Atighehchian, M. Bijari and H. Tarkesh: submitted to *Journal of Computers and Operations Research* (2009)
5. D. F. Zhu, Z. Zheng and X. Q. Gao: submitted to *Journal of Iron and Steel Research, International* (2010)
6. M. Zou, J.H. Tang: submitted to *Journal of Gansu metallurgy* (2011)
7. X.D. Wu, D. Zhou and J.Z. Zhen: submitted to *Journal of Steelmaking* (2009)
8. J. Cai, H.B. Wang and D.F. He: submitted to *Journal of University of Science and Technology Beijing* (2013)
9. D.F. He, A.J. Xu and P.F. Wu: submitted to *Journal of University of Science and Technology Beijing* (2011)
10. Q. Liu, P. Zhao and X.D. Wu: submitted to *Journal of University of Science and Technology Beijing* (2005)
11. B.F. Huang, N.Y. Tian and G.S. Li: submitted to *Journal of Metallurgical Industry Automation* (2011)
12. D.F. He, G. Yu and A.J. Xu: submitted to *Journal of University of Science and Technology Beijing* (2010)

The Research of the Property of the PEO Modified PBC Porous Membrane

Xiaohua Gu[a], Xue Song[b] Peng Zeng[c], Xiwei Zhang[d]
College of Materials Science and Engineering,
Qiqihar University, Qiqihar, China
E-mail: [a]songxue19900404@163.com, [b]821849763@qq.com,
[c]zeng.peng.110@163.com, [d]862356783@qq.com

In this paper, the PBC and PCL porous membranes were fabricated through thermally induced phase separat ion (TIPS). PBC and PCL were modified by polyethylene glycol (PEO), then observed the morphology of cell culture and compared the proliferation of these two group porous membranes. The two groups both have the cell spreading and breeding, closely join and good morphology. PEO modified PBC have the obvious preponderance and good advantages for cell culture, proliferation and fission growth.

Keywords: Thermally Induced Phase Separat Ion(TIPS); PBC(poly(butylene carbonate)); Polyethylene Glycol(PEO); Porous Membrane.

1. Introduction

The backbone structure of PBC is similar to the polycaprolactone (PCL)[1]. PBC is the material which replace oxygen atom of the methylene beside ester bond of PCL. PBC is the fully biodegradable material. This product is made with cheap non-oil route, and made from monomer of CO_2 as a raw material through transesterification method [2]. This material is a new type of high melt strength and low cost of aliphatic polycarbonate. Its structural formula is as follow;

$$\left[O(CH_2)_4OOC\right]_n \quad (n=515\sim1295)$$

Aliphatic polyester is the best type of biodegradable material of good property of synthetic polymer, and the PBC is belong to this kind of biodegradable material [3]. The polymer was decomposed to low molecular glycol and water and CO_2 under the effect of microbes in nature through alcoholysis reaction or hydrolysis reaction [4]. As a kind of synthetic material, there exists gaps of hydrophilicity between PBC and natural materials. So, PEO (molecular weight 200,000) modified PBC porous membrane and compared with PEO modified PCL [5]. PEO modified PBC porous membrane were used in

cell culture and had many cells growth and spread. The tentacles of cells evenly spread and grow in good condition, they were more advantageous than the modified PCL in cell proliferation in this paper.

2. Experimental

2.1. *Main Materials*

PBC(molecular weight, Mn: 70,000) purchased from the Jiangsu Sanfangxiang Group (Jiangsu, China). PCL(molecular-weight, Mn: 80,000) provided by the Shanghai Tianqing Biological material Co., LTD. PEO (molecular weight, Mn:200,000, use PEO2 to expression) and analytically pure supplied by Sigma-Aldrich Company. The modified α-MEM culture medium and fetal calf serum obtained from Hyclone, USA. 0.25% pancreatic enzyme supplied by GBICO, USA. MTT provived by Sigma, USA. Dimethyl sulfoxide(DMSO) purchased from Guangzhou Chemical Reagent Factory(Guangzhou, China). Alkaline phosphatase kit provided by Zhongshengbeikong biotechnology company limited by shares. (Beijing, China).

2.2. *The Preparation of Modification Porous Membrane*

3% PEO2 was dissolved in the DMF(diluent of TIPS) solution, then based on double diffusion principle and replaced DMF using water as coagulation bath. It could promote the polymer material forming, at the same time water also had the effect of the cooling medium. Through this method obtained PEO modified PBC and PCL porous membrane.

2.3. *Cell Culture and Morphology Observation*

Pancreatic enzyme (0.25%) was used to deal with bone tissue, cut them into patches(area: 2mm^2). Then put them in the pancreatin which volume was 5~20 times. They need dissolve for 16~18h. After digestion, abandoned the pancreatic enzyme and put into the culture medium blow and beat. Finally split in different bottles and cultivated in CO_2 incubator. The PBC and PCL porous membrane which modified by PEO soaked 2h in ethanol solution(75%) and ultraviolet radiation irradiated 0.5h, PBS buffer solution rinsed 2~3 times with complete nutrient culture solution for the night. Selecting the rats skull ossification cell system MC3T3-E1 inoculated on these two kind of porous membrane respectively. The condition was 5%CO_2, 37ºC and humidness 100%. The modified porous membrane had to cell culture for 8h. After that, porous membrane were rinsed 3 times by PBS buffer solution and used glutaraldehyde

(2.5%) immobilization for 24h. They need to dehydrate for 10 minutes under the different alcohol gradient 30, 50, 70, 90%. Then using alcohol(100%) dehydrate for 3 times. The porous membrane were metal sprayed after freeze drying. After all of that, the cells morphology were observed under FESEM .

2.4. *Cell Proliferation Test Observation*

The cell culture condition described as above. During cultivating 1 day and 7 day cells were determined by MTT cell detection respectively. In selected detection time point, every hole added 20μL MTT solution and cultivated 4 h in incubator. Then sucked up nutrient solution in each hole and added 150μLDMSO to each hole. Low speed oscillation shaked beds for 10 min to make the crystal substance dissolved. The solution was sucked from each hole and added to 96-well plates. On the enzyme standard instrument wavelength of 490 nm tested absorbance value, and analyzed the results.

3. Results and Discussion

3.1. *Porous Membrane Cell Spreading and Breeding Experiment*

Figure 1 shows the SEM for cell spreading on PEO modified PBC and PCL porous membranes after 8 hours. From the figures we can find that these two porous membranes both have cell spreading and breeding, closely join and good morphology. Cell tentacles extend evenly and growt in good condition. PBC have more cells spreading.

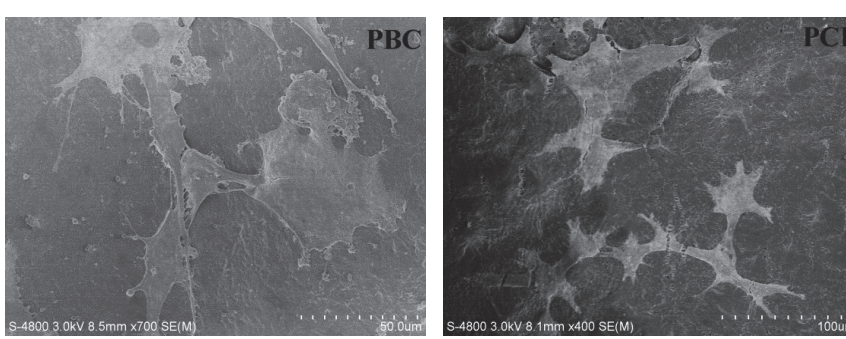


Figure. 1 SEM micrograph of PEO modified PCL and PBC porous membrane after culturing MC3T3-E1 cells for 8 hours.

As is shown in Table 1, it is the experiment results of cell breeding for 1 day and 7 day. From the Table 1, we can conclude that proliferation of modified

porous membrane are better than blank group. Especially, cultivating 7 day illustrate that porous membranes have huge advantage for cell proliferation. In addition, comparing with the modified PCL porous membrane, PEO modified PBC porous membrane have a better result than that. They have a good help for more cell proliferation and fission growth.

Table. 1 The MTT results of PEO modified and PCL porous membranes.

	1 day	7 days
PBC P-M	0.1503±0.01	0.5483±0.07
PCL P-M	0.1483±0.01	0.4363±0.03
Blank	0.0663±0.005	0.0663±0.005

4. Conclusions

By the two groups of experiments we can find that with the PCL this widely known as the safety of medical biological material, the PEO modified PBC also provide an ideal cell adhesion basement and get good cell proliferation. From the cell culture experiment results, PEO modified PBC and PCL porous membranes have more cell proliferation and fission growth. These two porous membranes both have cell spreading and breeding, joint closely and good morphology. Cell tentacles extend evenly and grow in good condition. PBC have more cells spreading. In addition, comparing with the modified PCL porous membrane, PEO modified PBC porous membrane have a better MMT result than that. They have a good help for more cell proliferation and fission growth. It illustrates that PBC porous membrane is more favorable for the growth of cells.

Acknowledgements

This work was financially supported by Natural Science Foundation of Heilongjiang Province (E201259).

References

1. Kweon HY, Yoo MK, Park IK, et al. *Biomaterials* 2003; 24: 801-808.
2. John J, Mani R, Bhattacharya M. *J Polym Sci A PolymChem.* 40(2002): 2003-2014.
3. Jin W, Liu ZC, Chun LC. Synthesis and Properties of Biodegradable Poly (ester-co-carbonate) Multiblock Copolymers Comprising of Poly(butylene Succinate) and Poly(butylene Carbonate) by Chain Extension*[J]. Industril & Engineering Chemistry Research*. 2012, 10785-10792.

4. Wen ZX, Xi H, Chun LC et al. High-molecular-weight aliphatic polycarbonates by melt polycaondensation of dimethyl carbonate and aliphatic diols: synthesis and characterization *[J]. Society of Chemical Intustry.* 2011, 60: 1060-1067.
5. Robert M, Noel-Hudson MS, *J. Font. Cell Biology and Toxicology*. 1994; 10: 361-365.

MCA Modeling of Nanostructuring Burnishing

Andrey I. Dmitriev[1,2†]

[1]*Institute of Strength Physics and Materials Science, SB RAS, 2/4 Akademicheskii Ave., Tomsk, 634055, Russia*
[2]*Tomsk State University, 36 Lenin Ave., Tomsk, 634050, Russia*
[†]*E-mail: dmitr@ispms.tsc.ru*

Viktor P. Kuznetsov

Kurgan State University, Gogol str. 25 640669, Kurgan, Russia
E-mail: wpkuzn@mail.ru

The operating characteristics of various machine parts are defined by the physical and mechanical properties of the surface layer. Unfortunately what parameters and mechanisms are responsible for certain surface modification are not well-understood till now. In this regards the methods of computer simulation can be a useful tool to investigate surface changing during contact interaction as well as burnishing. In the paper the method of movable cellular automata is used to study the details of burnishing process. By help of modeling we try to reproduce the conditions of burnishing for two scale levels. Results of our modeling are close to the experimental observation.

Keywords: Modeling; Movable Cellular Automata; Nanostructuring; Burnishing.

1. Introduction

Surface burnishing is highly efficient method of surface finish of high-precision parts. Thus, in [1] it is noted that the burnishing improves the wear resistance of machine parts by 20-40%, the fatigue by 30-70%, and the resistance to contact fatigue by 20-40%. The change of surface characteristics after burnishing is connected with the structure modification of a thin surface layer due to plastic deformation. The indenter motion causes changes in orientation and shape of grains, which are crushing, flattening and stretching and finally form the texture of a new surface layer [2]. Such modification of structure is confirmed by various authors. In particular, in [3] it is noted that there is the possibility of formation of nanostructured surface layer during friction, which is the result of an

† Corresponding author.

inhomogeneous distribution of deformation and shear instability of the material near the surface. In spite of the progress in experimental study of burnishing it is still not quite clear what parameters and mechanisms are responsible for the particular surface modification. In this context, methods of computer simulation can be a useful tool to investigate features of surface changing. A great interest is the ability to study the structural and phase transformations in a surface layer with thickness of up to hundred micrometers where processes responsible for tribological behavior of the material are taking place. Complexity of theoretical study is that this scale is too small for a physically correct description by the macroscopic approach and too big for the modeling methods of atomic scale. In this context, here there is an attempt to use the method of movable cellular automata, which permits modeling at different scales for the study of the material behavior under conditions of burnishing. Therefore, the objective of the paper was to investigate the behavior of surface layer under burnishing by help of MCA simulation and to verify the results of modeling by existing experimental data.

2. A General Formalism of the MCA Method

The MCA method [4 – 6] is based on conventional concept of cellular automata. It is an extension of cellular automaton approach achieved by incorporating some basic postulates and relations of particle-related methods. The movable cellular automaton is an object of finite size, possessing translational and rotational degrees of freedom. The key features of MCA method are the introduction of a new type of state, namely the state of a pair of automata (elements). In the considered case there are two types of pairs of automata: chemically bonded (named as “linked”) and “unlinked”. The transition from the first to second allows one to simulate the damage of the material. Interaction between automata is defined by normal (acting along the line connecting the mass centres) and tangential forces, each of which is the sum of the corresponding potential and the dissipative component. The principles of writing the equation of motion for a system of movable cellular automata and prescribing interactions between them are described in [4, 5]. In contrast, for example to the method of discrete elements, the MCA method uses the many-particle interaction where the force calculation is based on the spatial configuration of nearest neighbors.

3. Scale level I

3.1. *Numerical Model*

As shown in Fig. 1a, the model setup included two bodies in sliding contact. The upper block was an indenter (diamond tool), while the lower one played a role of

the steel to be burnished. The mechanical properties of the model materials were defined by their stress-strain curves taken from [7] and depicted in Fig. 1b. So, the input parameters to define the mechanical properties of each material are: Young modulus, Poisson ratio, elastic limit, yield strength, ultimate tensile strength, strain at yield strength and breaking strain. The automata size was adjusted to 10 μm. The loading was set in two stages. At the first stage the indenter was pressed into the sample at a constant force. The constant normal force corresponding to the contact pressures in the range between P = 1 MPa and P = 10 MPa for different calculations acted upon all the elements of the upper layer of the indenter. At the second stage of loading a motion of indenter with constant velocity in a tangential direction was simulated. A sliding velocity (V) was equal to 10 m/s. The positions of all automata of the lower layer of the sample were fixed. The substrate was generated form the same model steel as the bulk of the sample. The upper automata of the sample represent the free surface. To simulate the extended size of the modeled object in the direction OX the periodic boundary conditions was used. In order to imitate the extension of the sample in vertical direction an additional layer adjacent to the substrate was introduced, in which added dissipative forces was acting on each automaton. The sample with an initially defect-free surface was modeled.

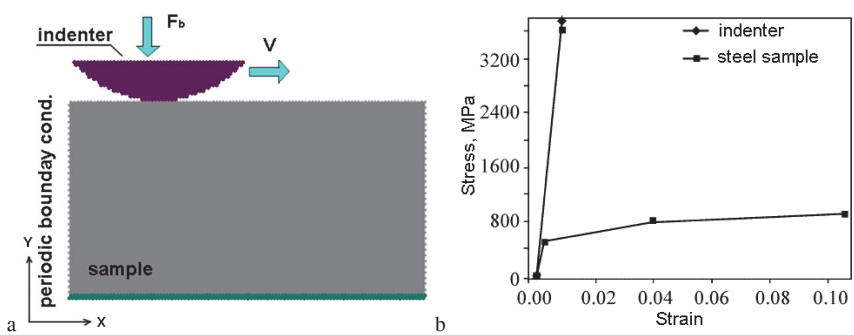


Fig. 1. (a) Initial structure and a loading scheme, (b) response functions of modeled materials.

3.2. *Results of Simulation*

For the analysis of the results, the distributions of tensor components of stress and strain, as well as various integral characteristics, such as the intensity of stresses and strains were used. Figure 2 shows the distributions of the intensities of stresses and strains obtained for the sample at the end of the first passage of the indenter ($t=1.1\cdot10^6\Delta t$). It was shown that, as expected, the maximum value of the intensity of deformation occur in the loaded area under of the indenter and, subsequently, stored after the passage of the indenter in a thin surface layer. At the same time, the

maximum values of the stress intensity remain localized in an area directly exposed to the indenter and decrease after its passage. This agrees well with the results obtained using the macroscopic modeling [8] where the distribution of the accumulated residual strain in the surface layer, as well as the character of the load when indenter is moving were shown.

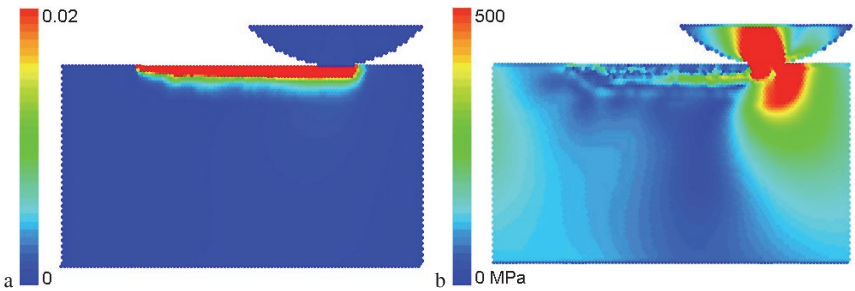


Fig. 2. (a) Strain intensity and (b) stress intensity distributions after the first pass of indenter.

4. Scale level II

4.1. *Numerical Model*

For nano-scale modeling we have chosen a contact zone spot between two bodies in sliding with relative velocity transversely directed with respect to compressive stress as shown in Fig. 3. The boundary conditions and a scheme of loading were the same as for above calculations. The automata size was equal to 1 μm. The value of applied external force was adjusted to the same normal pressure as in the previous case. An initial random roughness on the nanometre scale was created artificially at both surfaces by removing some single automata from the initially flat interface.

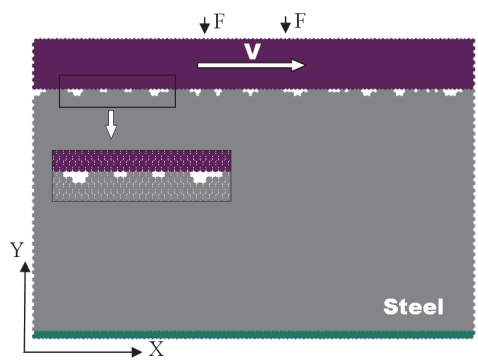


Fig. 3. Initial structure of the setup.

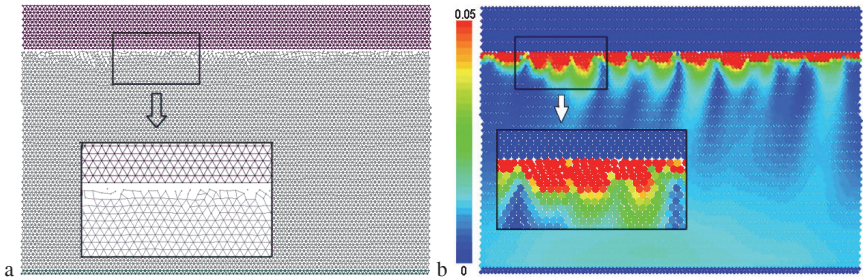


Fig. 4. (a) Structure of inter-automata ties and (b) strain intensity distribution for the time $t=1.2\cdot10^6\Delta t$.

4.2. *Results of Simulation*

Our computations demonstrate that on being brought in sliding contact, the asperities immediately start deforming and fracturing. Simultaneously, new linked pairs are created so that the result is the generation of a structurally modified subsurface layer under the loading. This structural modification penetrates only to 5 – 8 μm depth below the surface unless corresponding normal stress is higher than 5 MPa. The steady-state configurations of the inter-automaton pairs are shown in (Fig. 4a) where the linked pairs correspond to no-modification states and are marked by lines connecting the relevant automatons' center points. It can be seen that the zone where automata pair state switching occurs stays localized within the contact area for all time intervals. Similar conclusion is feasible from the analysis of the strain intensity fields (Fig. 4b) obtained for the same moment of time. The strain intensity is higher at the areas where the best mating conditions between the indenter and sample surfaces are provided.

Structural evolution of the inter-automaton ties as well as strain intensity field for compressive stress level at higher pressure (> 8 MPa) shows the thickness of the layer with broken inter-automaton ties is more than 10 μm. The interparticle relations are being switching in this layer in both directions between “linked” and “unlinked” type of states thus serving to develop processes of segmentation and intermixing. As before, the thickness of the layer is kept constant for the steady state motion.

5. Conclusion

The results of our computer simulation show that motion of the indenter along the burnished surface gives rise to a complex stress-strain state in the material region near the indenter. The behavior of material particles in this layer is very similar to that of observed during sliding with seizure when a plasticized metal layer flows like a quasi-viscous nanocrystalline material under condition of shear

instability [9]. In spite of the fact that such a treatment serves to produce nanosized subgrain structure and thus increase the hardness, the quasi-viscous flow would strongly affect the surface quality. Therefore, it is favorable decision to avoid applying loading condition that lead to establishing such a mode.

The basic consistency between the results of numerical modeling and experimental observation gives us the confirmation about ability to use the methods of computer simulation in order to optimize the conditions of technological process.

Acknowledgments

The work was supported by the Russian Science Foundation, Grant No. 14-19-00718. Preliminary experimental study was done within the State reference of the R&D 01201461774 by V.P.K.

References

1. Odintsov V.G. Finishing treatment of parts by diamond burnishing and vibroburnishing. Moscow, *Mashinostroenie*, 1981.
2. Pshibylskii V. Technology of surface plastic treatment, Moscow, *Metallurgya*, 1991.
3. Kuznetsov V.P., Makarov A.V., Kiryakov A.E. “Experimental study of formation of surface layer of parts under finishing treatment”, Proc. V Conf. Modern probl. of machine-building Tomsk, 2010.
4. Psakhie S.G., Shilko E.V., Smolin A.Yu., et al. Approach to simulation of deformation and fracture of hierarchically organized heterogeneous media, including contrast media1 // Phys. Mesomech. 14(5-6) (2011) 224.
5. Österle W., Dmitriev A.I., Kloß H. Does ultra-mild wear play any role in dry friction applications, such as automotive braking? // Faraday Discussions, 156, (2012) 159-171.
6. Dmitriev A.I., Österle W. Modelling the sliding behaviour of tribofilms forming during automotive braking: Impact of loading parameters and property range of constituents // Tribology Let. 53 (2014) 337–351.
7. Grigoryev I.S., Meylikhov E.Z. Physical parameters. Handbook, Moscow, Energoatomizdat, 1991.
8. V.P. Kuznetsov, I.Yu. Smolin, A.I. Dmitriev, et al., Finite element simulation of nanostructuring burnishing // Phys. Mesomech. 16(1) (2013) 62-72.
9. Tarasov S.Yu., Rubtsov V.E. Shear instability in the subsurface layer of a material in friction // Physics of the Solid State 53(2) (2011) 358-362.

Fabrication and Electrical Properties Analysis of SWCNTs/PDMS Composites

Fangjun Liu

School of Automation Science and Engineering, South China University of Technology, Guangzhou, China, 510641
E-mail: lfj816@gmail.com

John T. W. Yeow†

Department of Systems Design Engineering and Waterloo Institute for Nanotechnology, University of Waterloo, Ontario, Canada, N2L 3G1
†E-mail: jyeow@uwaterloo.ca

In this study, a simple and cost effective fabrication method is presented to disperse single-walled carbon nanotubes (SWCNTs) in polydimethylsiloxane (PDMS). Chloroform is used to disperse SWCNTs and dissolve PDMS. Ultrasonication was applied to evaporate chloroform to minimize agglomerates during conventional evaporate process that involves solvent evaporation with heat. Experiment results show that the long term mild ultrasonication process does not affect the electrical properties of PDMS nanocomposites. Furthermore, the percolation behaviour of SWCNTs/PDMS composite was found to be at 0.5 weight percentage (wt.%) loading of SWCNTs and a fairly linear resistance was observed when different bias voltages were applied.

Keywords: PDMS; Fabrication; Electrical Conductivity; Single Wall Carbon Nanotube; Nanocomposite.

1. Introduction

Dispersing carbon nanotubes (CNTs) into polymer to obtain high-performance materials in mechanical or electrical properties has attracted much attention in recent years. Since low atomic-number composite materials show better performance for shielding space radiation, CNTs filled polymer can also apply in radiation shielding field[1, 2]. Using a small amount of CNTs loading in polymer to achieve high-performance materials in mechanical or electrical properties has been applied in diverse applications due to excellent mechanical and electrical properties of CNTs[3].

Polydimethylsiloxane (PDMS) has superior mechanical elasticity, excellent flexibility and biocompatibility, which makes it an ideal host matrix for nanocomposite applied in many application[4]. Combined with electrical conductivity, PDMS could be used for many other applications in micro-electro-mechanical systems, microfluidics and biomedical area[5]. CNTs are considered as potential conductive fillers for PDMS based composite. As reported by Ashaket et al., strain sensor made in CNTs/PDMS composite with small CNTs loading, has much large range than conventional metallic strain gauges[6].

The performance of CNTs based composite strongly depends on the dispersion quality of CNTs in polymer. Since CNTs are easily entangled requiring external force to break the CNT bundles[7]. Shear mixing, mechanical stirring and ultrasonication are three main physical dispersion methods. Composites containing high loading of CNTs can be realized through shear mixing, but this process tends to damage the CNTs, thereby significantly reducing its conductivity. Furthermore, the dispersion of CNTs in PDMS and chloroform solution almost immediately form agglomerates after mechanical stirring[7]. Ultrasonic agitation process with high frequency could also cause damage to CNTs which could significantly decrease the conductivity of CNTs[4].

Our purpose is to find a better way to obtain higher conductive SWCNTs/PDMS composite with smaller SWCNTs loading. Since the dispersion quality is critical to final performance of the composite, our aim is to improve the dispersion quality of the CNTs in PDMS. In this study, we use mild ultrasonication to evaporate solvent (chloroform), instead of applying heat for solvent removal, to obtain a stable solution and minimize the amount of CNTs agglomerates. SWCNTs/PDMS composite samples with small SWCNTs loading was obtained using this simplified fabrication method. The electrical properties of these samples have been characterized at room temperature. The percolation threshold was observed at 0.5 wt.% SWCNTs loading in our experiment and results shown the electrical conductivity of PDMS enhanced dramatically even at a small SWCNTs loading.

2. Experiment Methods

2.1. *Materials*

PDMS (Sylgard 184 Elastomer) was purchased from Dow Corning. Single-walled carbon nanotubes (SWCNTs) of sizes 1 to 2 nm in diameter and 5-30 μm of length, with 90% purity were obtained from Cheaptubes.com. Chloroform, an

organic solvent used to help CNTs dispersion, was bought from Sigma-Aldrich. All materials were used as purchased.

2.2. *PDMS/ SWCNTs Composites Fabrication*

The SWCNTs/PDMS composites were fabricated by carefully weighing (via digital balance) the desired quantity of SWCNTs and PDMS elastomer e.g. 0.05g of SWCNT in 4.5g of PDMS pre-polymer (PDMS pre-polymer and curing agent in the ratio of 10:1). Branson 3800 Ultrasonic Cleaners was used to disperse SWCNTs in pre-polymer. Chloroform was used as dispersion agent during the whole ultrasonic process. Ultrasonicaiton time depends on the amount chloroform been added. After all chloroform was evaporated by ultrasonication, add curing agent to the pre-polymer and SWCNT mixture, pour SWCNT and PDMS solution in petridishes, put these samples into a vacuum oven to remove air bubbles for 1 hour and then heat them at 80ºC until fully cured.

3. Results and Discussion

3.1. *Electrical Properties*

The current-voltage characteristics of each sample were measured using an Keithley 6487 Picoammeter, which was interfaced to a laptop for data collection and analysis. The data was stored in excel sheets. The Picoammeter was programmed to operate with a sweep voltage of 0-50 V in steps of 1 V under room temperature. The corresponding resistance values were recorded for 4 groups of samples by different percentages of SWCNT (0, 0.1, 0.4 and 0.5 wt.%) mixed in PDMS. All samples were in the same dimension. Copper electrodes were employed to make contact to samples.

To fully study the electrical conductivity around percolation threshold, the percentages of SWCNTs loading we choose is relative small. Fig.1 shows the resulting resistance versus the voltage applied between samples. It can be clearly seen that the resistance decreases as the SWCNTs loading (wt.%) increases; resistance drops dramatically when PDMS filled in with 0.5 wt.% SWCNTs, which denotes percolation threshold can be achieved within 0.5 wt.%.

Pure PDMS under long time ultrasonic process would not influence its electrical conductivity, as shown in Fig.1, the difference of resistance between plain PDMS with (plain PDMS(b)) and without chloroform (plain PDMS(a)) under long time ultrasonic process can be ignored, which means all changes observed on electrical conductivity of SWCNTs/PDMS samples are affected by SWCNTs fillers.

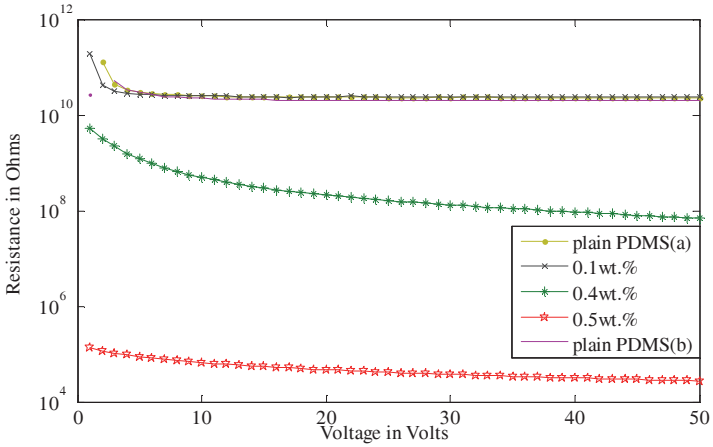


Fig.1 Resistance vs voltage with different SWCNTs weight percentage.

Fig.1 also shows a fairly linear resistance when voltages are beyond 5 V. We chose the samples with percentage at percolation threshold, transferred the resistance into electrical conductivity, using equation below:

$$\sigma = L/RS. \tag{1}$$

where R is resistance ohm, S is the cross sectional area of contact electrode in m^2, and L is the thickness of samples in m.

The variation of conductivity of 4 group composites with varying SWCNT loading at voltage 5 V is shown in Fig.2. It can be clearly seen that the conductivity increases with SWCNTs loading increases. Though samples with smaller percentage (0.1 and 0.4 wt.%) are not electrical conductive, the conductivity still enhanced obviously. The one has CNTs loading closer to percolation threshold, the bigger magnitude of conductivity had achieved. As shown in Table 1, the conductivity of samples at 0.5 wt.% SWCNTs loading is 3.3663e+05 times that of plain PDMS.

Table 1 Conductivity versus SWCNTs loading when applied voltage is 5 V.

Percentage(wt.%)	0	0.1	0.4	0.5
σ (S/m)	6.6432e-11	7.2946e-11	8.9899e-08	2.2363e-05
$(\sigma-\sigma_0)/\sigma_0$	0	0.0981	1.3522e+03	3.3663e+05

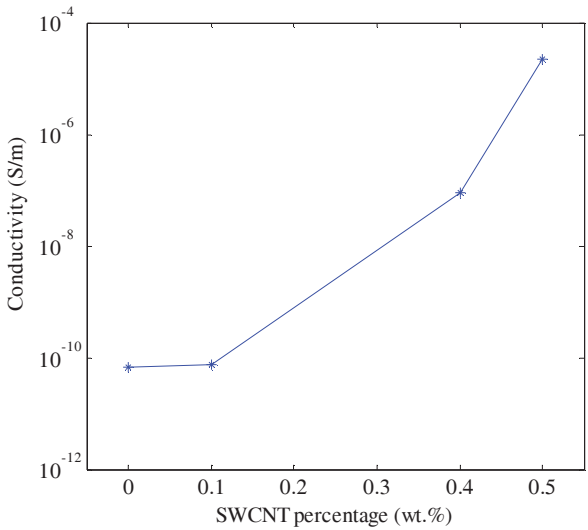


Fig.2 Conductivity vs SWCNTs loading.

3.2. *Future Work*

For application need a small CNTs fillers but require electrical conductivity around 10^{-2}S/M, as described in introduction, can achieve easily by this simple fabrication method. For applications desire higher electrical conductivity, larger percentage of CNTs loading or higher purity SWCNTs should be considered. Two more groups of samples with larger percentage, 0.8 wt.% and 2 wt.%, were obtained by the same fabrication method. However, the conductivity decreased as CNTs loading increased, as depicted in Fig.3. The possible reason is the different proportion of CNTs disperse in chloroform applied. Four groups samples with small CNTs percentage discussed before (0, 0.1, 0.4, 0.5 wt.%) used the same proportion, per 10mg CNTs disperse in 30ml chloroform, but samples with 2 wt.% SWCNTs loading was, per 10mg CNTs disperse in 12ml chloroform. It seem lower density of CNTs in chloroform is required at initial stage of ultrasonication to obtain a better conductive composites. These deduction need to be verified next step and the optical proportion should be found to fully use the advantage of fabrication method proposed in this work. The one with 0.8 wt.% CNTs has the same proportion with former smaller percentage CNTs loading and used the same simplified fabrication process, but the 125ml glass bottle used to hold solution in ultrasonic water bath at the beginning did not change into 25ml-bottle to continue ultrasonic when the solution left inside as chloroform evaporating is less than

20ml. The fluid surface had not change for hours, which might because the ultrasonic is not powerful enough to disperse liquid at this surface-volume ratio. Also, this reduction in conductivity needs to be verified by more detailed tests.

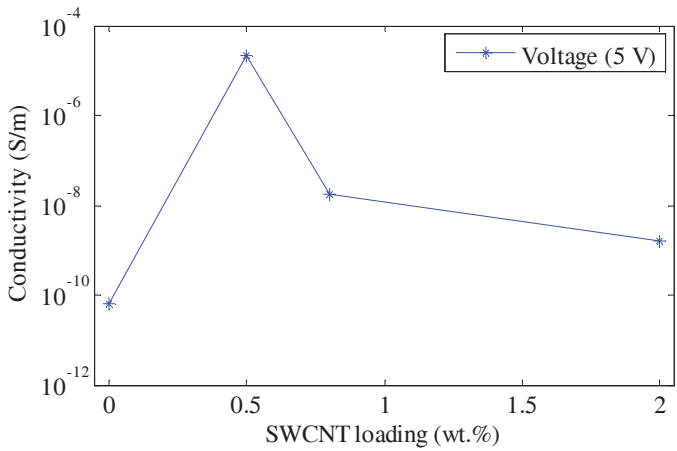


Fig.3 Conductivity change vs SWCNT loading.

4. Conclusion

The dispersion quality of CNTs in polymer matrix is critical to the performance of composite. CNTs are trend to agglomerates due to its high-aspect ratio and unstable when physical dispersion method. We presented a fabrication method, using ultrasonic process, instead heat process in conventional method, to evaporate Chloroform. Evaporate was done by mild ultrasonic to minimize the size and amount of agglomerates. Furthermore, chloroform is a solvent helpful to uniformly disperse CNTs and dissolve PDMS, and the amount used to disperse per 10mg CNTs might also cause the change of conductivity of final products. Percolation threshold of composite made by this fabrication method was observed under 0.5 wt.% SWCNTs loading. The electrical conductivity enhance greatly even with a small SWCNTs loading.

Acknowledgment

This work is founded by Chinese Scholarship Council.

References

1. Nambiar S, Yeow JT. Polymer-composite materials for radiation protection. *ACS applied materials & interfaces*. 2012;4:5717-26.

2. Li Z, Nambiar S, Zheng W, Yeow J. PDMS/single-walled carbon nanotube composite for proton radiation shielding in space applications. *Materials Letters*. 2013;108:79-83.
3. Lee JH, Nam YW, Jung H-C, Baek D-H, Lee S-H, Hong JS. Shear induced CNT/PDMS conducting thin film for electrode cardiogram (ECG) electrode. *BioChip Journal.* 2012;6:91-8.
4. Zhu J, Kim J, Peng H, Margrave JL, Khabashesku VN, Barrera EV. Improving the dispersion and integration of single-walled carbon nanotubes in epoxy composites through functionalization. *Nano letters.* 2003;3:1107-13.
5. Kang I, Schulz MJ, Kim JH, Shanov V, Shi D. A carbon nanotube strain sensor for structural health monitoring. *Smart Materials and Structures*. 2006;15:737-48.
6. Arshak K, Perrem R. Fabricaition of a thin-film strain-gauge transducer using Bi_2O_3-V_2O_3. Sensors and Actuators A: *Physical*. 1993;36:73-6.
7. Chu K, Kim D, Sohn Y, Lee S, Moon C, Park S. Electrical and Thermal Properties of Carbon-Nanotube Composite for Flexible Electric Heating-Unit Applications. *Electron Device Letters, IEEE.* 2013;34:668-70.

The Preparation and Photocatalytic Degradation Property of the Fe-octacarboxylic Acid Phthalocyanine/Attapulgite Nano-composite Catalyst

Zhicheng Yuan, Dajun Chen†

State Key Laboratory for Modification of Chemical Fibers and Polymer Materials, College of Materials Science and Engineering, Donghua University, Shanghai 201620, People's Republic of China
E-mail: williamyuan@mail.dhu.edu.cn, †cdj@dhu.edu.cn

A novel nano-composite catalyst was prepared from immobilization of Fe-octacarboxylic acid phthalocyanine onto the matrix material attapulgite. The structure of the catalyst was analyzed by Fourier transform infrared. The photocatalytic degradation property was investigated by using Rhodamine B (RhB) as model, and the results showed that the nano-composite exhibited higher activity for degradation of RhB than that of the pure attapulgite.

Keywords: Photocatalysis; Fe-octacarboxylic Acid Phthalocyanine; Attapulgite; RhB.

1. Introduction

With the development of the industry, the pollution from dye wastewater is becoming overwhelming problem all over the world due to the growing use of a variety of dyes in the textile, polymers, food, plastic and pharmaceutics industries [1, 2]. Generally, Most of the dyes used in textile industries are toxic and carcinogenic to human beings [3]. Therefore, removal of dyes from industrial wastewater gradually becomes an important issue.

To solve this problem, advanced oxidation processes (AOPs) have been developed and become emerging technologies due to their effectiveness in degradation reactions for organic wastes [4]. Among this, photocatalysis, which has recently concentrated on the degradation of the pollutants of all kinds of residual organics in the aquatic environment, is the most efficient and consistent method dyes due to their simplicity, fast degradation and non generation of toxic materials [5].

Phthalocyanines (Pcs), derivatives of the aromatic tetraazaporphyrins, have a variety of applications in materials and biology [6]. Metallophthalocyanine (MPcs) complexes are attractive because of their extraordinary molecular

stability, especially for their excellent photocatalytic degradation property. However, this application is restricted by the difficulty in recovery and high tendency for aggregation of planar macrocycles which impair the catalytic activity [7].

In this paper, Fe-octacarboxylic acid phthalocyanine (FeOCAP) was immobilized onto solid supports-attapulgite (AT) to obtain the optimal catalytic activity, which can be used in the photocatalytic degradation of Rhodamine B (RhB).

2. Experimental

2.1. *Materials*

The AT clay powder was supplied by Jiangsu Junda Attapulgite Material Co., Ltd. RhB and other regents were purchased from Sinopharm Chemical Reagent Co., Ltd. All these reagents were used as received. FeOCAP was prepared by our research group.

2.2. *Preparation of FeOCAP/AT*

1g AT was dispersed in 50 mL deionized water with continuous ultrasonification and stirring in 1 h. Then 10 mL FeOCAP (0.001 mol/L) was added dropwise into the AT dispersion under ultrasonification and stirring. After stirring overnight, the blue FeOCAP/AT powder was washed with water, alcohol, and acetone successively, and dried in vacuum oven.

2.3. *Characterizations*

The FeOCAP/AT and AT samples were tested by a Nicolet Impact NEXUS-8700 Fourier transform infrared spectroscopy (FT-IR) in the range of 500-4000 cm^{-1}. The sample powder was mixed with KBr powder and then was compressed into a transparent sheet. Thirty two scans were conducted to achieve an adequate signal to noise ratio.

Photocatalytic degradation of RhB was carried out in the aqueous solution at room temperature with continuously stirring and UV-lamp irradiated. The intensity of UV-lamp is 20 W and the maximum wavelength is 295 nm. The UV-lamp was held on 5 cm above the sample. The initial concentration of RhB was 5 mg/L and the volume was 20 mL. After the catalyst (0.05 g) was added into RhB, at given time intervals, the samples (3 mL) were centrifuged to remove photocatalyst and then analyzed immediately on a UV-vis spectrometer

(T6, Purkinge General) in the range of 400-800 nm. The percentage dye removal (R) has been calculated using the following equation:

$$R \text{ (percentage removal)} = (C_0 - C_t) / C_0 \times 100\% \quad (1)$$

where, C_0 is the initial concentrations of RhB (mg/L), t refers to the time of treatment.

3. Results and Discussion

3.1. *Preparation of FeOCAP/AT*

In the preparation process, AT is ultrasonic dispersed in the deionized water to obtain nanoscale dispersion. Then FeOCAP is added dropwise into AT dispersion solution. As the surface of AT is abundant of -OH and FeOCAP has a lot of -COOH, those reactive groups will be attractive by hydrogen bond and macromolecular interaction. Therefore, the surface of AT will be covered with FeOCAP particles to form nano-composite materials. AT will act as matrix materials to help the dispersion of FeOCAP, which can overcome the high tendency for aggregation of planar macrocycles.

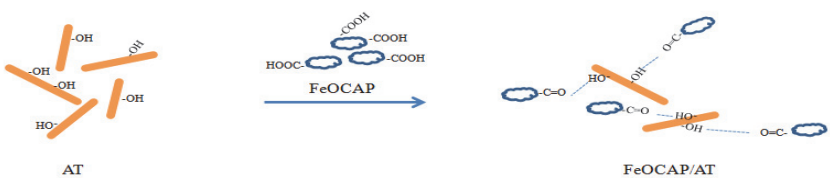
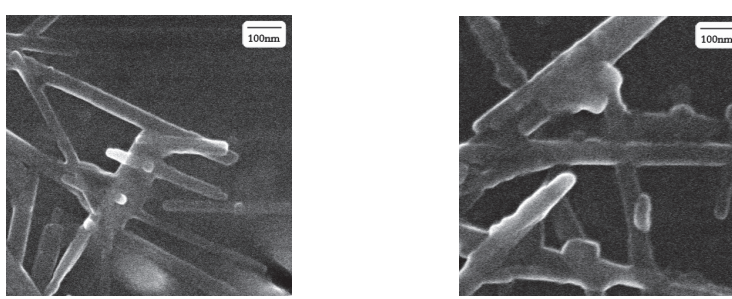


Fig. 1. The illustration of FeOCAP/AT nano-composite catalyst.



(a) (b)

Fig. 2. FESEM images of blank AT (a) and FeOCAP-AT (b).

The SEM result, as can been seen in Fig. 2, shows that the pure AT exhibits a fibrous structure and the size of a single fiber is about 50 nm in width and 0.5-1 μm in length. After introduction of FeOCAP (Fig. 2(b)), the width increases to 150 nm and the FeOCAP can be clearly seen covered on the surface of AT.

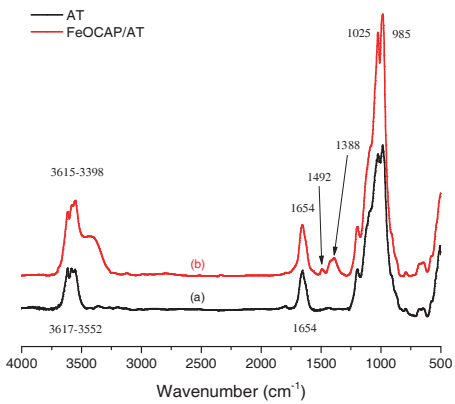


Fig. 3. FT-IR spectrum of AT (a) and FeOCAP/AT (b).

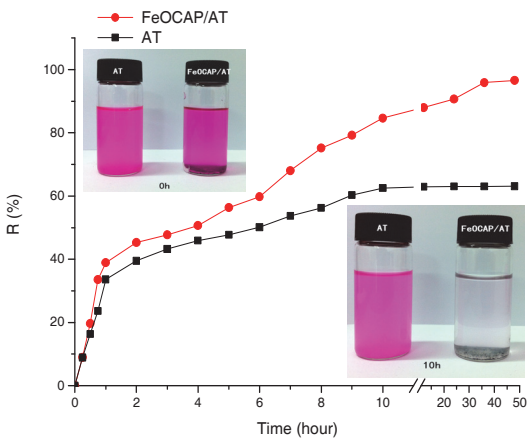


Fig. 4. Plot of R vs the time of treatment.

The result of Fourier transform infrared spectroscopy analysis is further to prove this conclusion. AT is a kind of hydrated octahedral layered magnesium

aluminum silicate absorbent mineral. As shown in the FT-IR spectra (Fig. 3), the absorbance bands at 1025 cm^{-1} and 985 cm^{-1} are caused by the stretching vibration of Si-O and the stretching vibration peak caused by the Si-O-Si, respectively, which are the characteristic peaks of AT. The stretching vibrations -OH are the peaks at around 3500 cm^{-1}, while the bending vibration absorbance peak exists at 1654 cm^{-1}. Those characteristic peaks can be seen in both two samples, which show that both samples contain AT. Compared with the pure AT, the spectra of FeOCAP/AT complex appears new peaks. The peaks at 1492, 1388 cm^{-1} are assignable to the skeleton stretching of phthalocyanine [8], which can prove FeOCAP are successful introduced to the AT matrix.

3.2. *Photocatalytic Degradation Property*

In order to investigate the photocatalytic performance of FeOCAP/AT, RhB, a kind of commercial non-biodegradable toxic dye with aromatic structure, is selected as the model. The percentage removal of AT and FeOCAP/AT for RhB are showed in Fig. 4. The R values are both increase with time and the values of FeOCAP/AT are always higher than that of AT. After 10h, the R values of AT is tend to steady, while this of FeOCAP/AT can still increase. This can be attributed to the fact that the pure AT can't possess catalytic degradation property and the removal of RhB is more tend to physical adsorption. As this adsorption mainly depends on high porosity and large specific surface area, it is inevitable to have the limited adsorption capacity. This suggests that the pure AT could not catalyze the degradation process of RhB. Compared with the pure AT, the removal of RhB in the FeOCAP/AT system involves two processes: adsorption of RhB onto the FeOCAP/AT and photocatalytic degradation of the adsorbate. RhB can be absorbed by AT, which is similar to the pure AT. After that, under the irradiation of UV-lamp, FeOCAP will generate excited-state singlet oxygen which possesses high oxidative capability. Because of this high activity singlet oxygen, RhB will be oxidative degradation. Therefore, FeOCAP/AT nano-composite catalytic can not only adsorb RhB though AT but also make RhB degradation by the catalytic effect of FeOCAP.

4. Summary

In this paper, the FeOCAP is successful introduced into the AT matrix. In the photocatalytic degradation of RhB study, this nano-composite shows a high efficiency in generation singlet oxygen and an excellent photocatalytic degradation property. The percentage removal of RhB can get nearly 98%, which is much higher than the pure AT. The results indicate that the

FeOCAP/AT nano-composite is a promising materials applied in photocatalytic degradation of pollution, which will be benefit for the global environment.

References

1. S. Akhtar, A.A. Khan, Q. Husain, Potential of immobilized bitter gourd (Momordica charantia) preoxidases in the decolourization and removal of textile dyes from polluted wastewater and dyeing effluent, *Chemosphere* 60 (2005) 291-301.
2. V.K. Gupta, A. Mittal, V. Gajbe, J. Mittal, Removal and recovery of the hazardous azo dye acid orange 7 through adsorption over waste materials: bottom ash and de-oil soya, *Ind. Eng. Chem. Res.* 45 (2006) 1446-1453.
3. S. Kant, D. Pathania, P. Singh, P. Dhiman, A. Kumar, Removal of malachite green and methylene blue by $Fe_{0.01}Ni_{0.01}Zn_{0.98}O$/polyacrylamide nanocomposite using coupled adsorption and photocatalysis, *Appl. Catal. B: Environ.* 147 (2014) 340-352.
4. T. Eylem, K. Mehmet, Y.H. Cengiz, O. Koray, Pure ZnO and composite ZnO/TiO_2 catalyst plates: A comparative study for the degradation of azo dye, pesticide and antibiotic in aqueous solutions, *J. Colloid and Interface Sci.* 430 (2014) 6-11.
5. E.N. El Qada, S.J. Allen, G.A. Walker, Adsorption of basic dyes from aqueous solution onto activated carbons, *Chem. Eng. J.* 135 (2008) 174-184.
6. W.S. Li, T. Aida, Dendrimer Porphyrins and Phthalocyanines, *Chem. Rev.* 109 (2009) 6047-6076.
7. M.Q. Hu, Y.M. Xu, J.C. Zhao, Efficient photosensitized degradation of 4-chlorophenol over immobilized aluminum tetrasulfophthalocyanine in the presence of hydrogen peroxide, *Langmuir* 20 (2004) 6302-6307.
8. J. Mack, M.J. Stillman, Assignment of the optical spectra of metal phthalocyanines through spectral band deconvolution analysis and ZINDO calculations, *Coordination Chemistry Reviews* 219 (2001) 993-1032.

The Research on Dilational Viscoelasticity of the Interface between ASP Solution and Oil

Xia Hui Fen[a], Lai Xu[b†], Qiao Hong Yu[c], Liu Xiao Xiao[d], Fan Qi[e]

Northeast Petroleum University, China

E-mail: [a]757581676@qq.com, [b†]398842582@qq.com, [c]172352015 @qq.com, [d]474073203@qq.com, [e]1285143872@qq.com

Dilational viscoelasticity of the interface between the ASP solution with different weak alkali concentrations and oil is measured by the tracker fully automatic droplet interfacial tension meter. In this paper, the rules of interfacial dilational viscoelasticity with different dilational frequency and alkali concentrations are stated. The results show that with the increase of frequency, interfacial dilational viscous and elastic modulus of the ASP solution with alkali concentration of 0.4% will decline. Meanwhile, the data of other solutions remain unchanged. Elastic modulus has the trend to become greater than viscous modulus.

Keywords: Interfacial Dilational Elastic Modulus; Interfacial Dilational Viscous Modulus; Dilational Frequency; Alkali Concentration.

1. Introduction

ASP solution is composed by Na_2CO_3, heavy alkyl benzene sulfonate (HABS) and hydrolyzed polyacryamide (HPAM). The solution is also called ternary solution. In ASP compound system, the capillary number can be increased by raising viscosity of ASP and lowering interfacial tension. Macroscopic sweep efficiency and microcosmic displacement efficiency can both be increased. But for a long time, the researches on ASP system concentrate on the field of ultra-low interfacial tension and lack the exploration of interfacial rheology. Thus, the interfacial viscoelasticity show its significant value in the tertiary oil recovery fundamental researches.

Interfacial dilational viscoelasticity is an important dynamic nature of interface and also a parameter to evaluate the membrane resistance [1]. The reason why interfaces show their viscoelasticity is the micro relaxation process appearing on the interface or near the interface. So the parameter of interfacial

† Corresponding author.

dilational viscoelasticity can reflect the information of micro process [2]. The interfacial dilation method is developed in recent years [3]. By using the pendant drop method, molecules' interfacial information is got by studying the reflection of the interface balance tension under different disturbance conditions [4]. The intensity and structure of the oil-water interface membrane play a decisive role for the stability of crude emulsion. Therefore, basing on previous theory and experiment results, the paper focuses on the interfacial dilational modulus to study viscoelasticity of the interface between oil and ASP system with different concentrations alkali.

2. Theory

When periodic compressions and expansions occur on the liquid-liquid interface, interfacial tension will cyclical change accordingly. Interfacial dilational modulus is defined as the ratio of the variation of interfacial tension to the variation of relative interfacial area, which is:

$$\varepsilon = \frac{d\gamma}{d\ln A} \tag{1}$$

In the formula: ε — interfacial dilational modulus.

Dilational modulus can be also written as imaginary form:

$$\varepsilon = \varepsilon_d + i\omega\eta_d \tag{2}$$

In the formula, ε_d — interfacial elastic modulus; η_d — interfacial viscous modulus; ω — the sine function frequency of interface area. The real number and imaginary number are the elastic modulus and viscous modulus respectively[5].

3. Experiment

3.1. *Equipment and Reagent*

Tracker full-automatic droplet interfacial tension meter produced by The French I. T. Concept Company, ZC-18Q super constant temperature water bath, and KX-1 control box are used. And the ASP solution used in the experiment is composed of Na_2CO_3, heavy alkyl benzene sulfonate (HABS) and hydrolyzed polyacryamide (HPAM)

3.2. *Experimental Procedures*

When the constant temperature bath up to 45ºC, we put the light source, the glass sample pool with n-hexane solution and CCD camera into a row on the machine

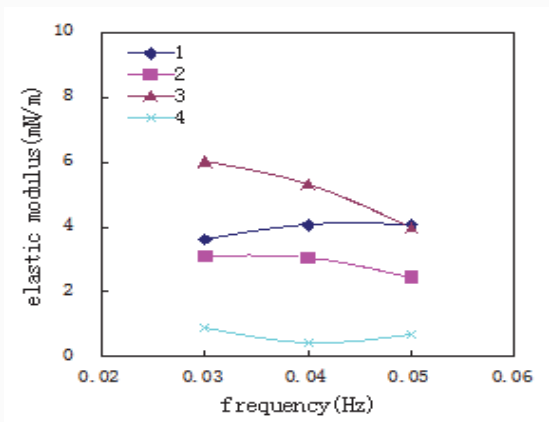
base. Then we adjust the injector with ASP solution, and control motor to form droplets, and set different working frequency (0.02-0.05 Hz) to measure the change of droplet interface area. Software will send a message to electric motor shaft to get photos of each droplet by the CCD camera, and finally transform photos into data. Then the software can calculate and record any time of area, volume, interfacial tension of the droplets.

4. Experimental Results and Analysis

In the ASP solutions prepared in the experiment, mass concentration of HABS is 0.3%, concentration of HPAM is 1500 mg/l and concentrations of Na_2CO_3 are different. The molecular weight of polymer is between 1200×10^4 and 1600×10^4.

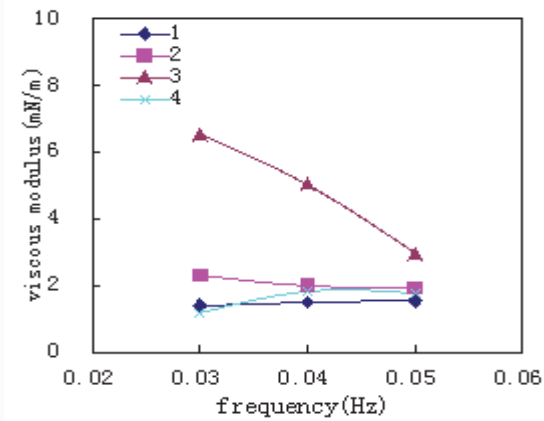
4.1. *The Influence of Frequency on Viscoelasticity of the Interface between Weak Alkali ASP System and Oil*

Figure 1 shows the influence of frequency on interfacial viscoelasticity modulus of four kinds of solutions which are binary solution and ASP solutions of alkali concentrations of 0.4%, 0.8% and 1%, respectively. From the figure, we can know that the interfacial dilational viscous and elastic modulus are minimum when the solution is without alkali, those in ASP solution are all greater than in binary solution. With the increase of frequency, interfacial viscous and elastic modulus of the ASP solution with alkali content of 0.4% will decline. In addition, viscous and elastic modulus of other solutions used in the experiment is slightly increased. That is to say, viscous and elastic modulus of ASP solutions has less dependence on frequency.



(a)

Figure 1 The influence of frequency on interfacial elastic modulus and viscous modulus



(b)

Figure 1 (*Continued*)

In the figure, line 1 represents the solution whose alkali concentration is 1%, line 2 represents the solution whose alkali concentration is 0.8%, line 3 represents the solution whose alkali concentration is 0.4%, and line 4 represents the binary solution.

After Na_2CO_3 is added into the solution, interfacial elastic modulus is increased. Then it can be speculated that when the surface is periodically disturbed, the addition of Na_2CO_3 makes the surfactant micelle fall apart which absorb on the polymer. Thus, more HABS ions gathering on the interface by diffusion increase HABS monomer concentration. On one hand, it reduces the interfacial tension; On the other hand, the strength of interfacial membrane is increased due to arranging more surfactant ions on the interface [6].

Relaxation process has its own characteristic frequency. When the working frequency is consistent with the characteristic frequency, the largest contribution to the dilational viscous modulus will be made by the relaxation process [7,8]. In ASP solution, the working frequency is the same as characteristic frequency in the relaxation process when the alkali content is 0.4% and the frequency is 0.03Hz. So in this situation, the largest contribution to the dilational viscous modulus is appeared. The other viscous modulus with different alkali concentrations is very small.

4.2. *The Influence of Weak Alkali Concentration on Viscous and Elastic Modulus of the Interface between ASP System and Oil*

Figure 2 shows the influence of weak alkali concentration on dilational viscous modulus and elastic modulus of the interface between ASP system and oil with

the frequency of 0.4. From the figure, it can be concluded that when there is no alkali in the solution, viscous modulus is bigger than elastic modulus. When the concentration of alkali is 0.2% or 0.4%, viscous modulus and elastic modulus are almost the same. When the concentration of alkali is bigger 0.6%, viscous modulus is smaller than elastic modulus.

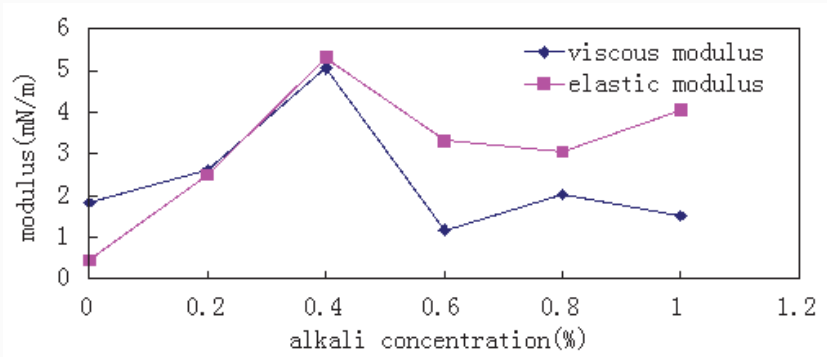


Figure 2 The influence of weak alkali concentration on dilational viscous modulus and elastic modulus

When the concentration of Na_2CO_3 is 0.4%, the adsorption of surfactant has close to saturated. Elasticity of membrane reached the maximum. When the concentration of Na_2CO_3 is between 0.4% and 0.6%, the concentration of Na^+ is very high, that is to say salinity of the solution is very high. HBAS is anionic surfactant, and polyacrylamide is anionic polymer, the surfactant and polymer can make a shielding effect with a large amount of Na^+. It leads to the decrease of interfacial elastic modulus due to the untight arrangement of the surfactant [9,10]. When the alkali concentration is between from 0.6% and 1%, ion concentration is too high in the solution; and the concentrations of surfactant and polymer in the solution are all constant; and the arrangement of molecules, ions, groups are stable. So the interfacial elastic modulus basically remains unchanged.

Viscosity part is related to the relaxation process including the exchange of the interface molecules between interface and the bulk phase, and the change of interface molecular arrangement. On one hand, with the increase of weak alkali concentration, it will lead to an increase in the number of relaxation process and more contribution the relaxation process making to the viscous part; on the other hand, with the increase of the concentration of weak alkali, the exchange between solution and interface molecules becomes faster, it leads to the decrease of interfacial tension gradient when the interface deforms. Then the viscous modulus reduces. Thus the viscous modulus will have a maximum value with the increase of concentration of weak alkali [11,12]. When the concentration of Na_2CO_3 is 0.4%,

the relaxation process on the interface or near the interface makes the largest contribution to the viscous modulus. When the concentration of Na_2CO_3 is higher than 0.4%, the high ion concentration compels the relaxation process to occur slowly. Therefore, the viscous modulus decreases.

To conclude, both elastic modulus and viscous modulus will reach the maximum when the alkali concentration is 0.4%. And then they will decrease. But after the decrease, elastic modulus tends to stable while viscous modulus will decrease continually. Thus, the elastic modulus will be greater than viscous modulus gradually.

5. Conclusions

(1) The viscous modulus and elastic modulus of ternary solution are greater than those of binary solution. With the increase of frequency, viscous modulus and elastic modulus of interfacial dilational of the ASP solution with alkali content of 0.4% will decline. These of the other solution used in the experiment remain unchanged. The dependence of viscous modulus and elastic modulus on frequency is less.

(2) When there is no alkali in the solution, viscous modulus is greater than elastic modulus. When the concentration of alkali is between 0.2% and 0.4%, viscous modulus and elastic modulus are almost the same. When the concentration of alkali is greater than 0.6%, viscous modulus is less than elastic modulus.

Acknowledgment

The project was supported by National Science and Technology Major Project of the Ministry of Science and Technology of China (Grant No:2011ZX05009) and the National Natural Science Foundation of China (Grant No:51374076).

References

1. Tong Haiying. The research of interfacial dilational viscoelasticity of interface active material. 2007
2. Luo Lan, Zhang Lu, Fang Hongbo. The effect of compound flooding chemical on interfacial dilational viscoelasticity of oil active material. *Oil Exploration and Development*, 2003, 24(11): 21-25.
3. Dou Lixia, Cao Xulong, Jiang Xiaofang, etc. The research of interface characteristic of polyacrylamide solution. *Colloid and Polymer*, 2004, 22(2): 1 4-16.

4. Song Xinwang, Wang Yiyang, Cao Xulong, etc. oil-water interfacial dilational viscoelasticity with alkyl benzene sulfonate of different structure. *Journal of Physical Chemistry*, 2006, 22(12): 1441-1444.
5. Zhang Lei, Wang Xiaochuan, Gong Qing, etc. Dilational rheological properties of air/water interface and 2, 5 - dipropyl - 4-11 alkyl benzene sulfonic acid sodium surface. *Journal of Physical Chemistry*, 2007, 23(10): 1652-1656.
6. Ma Li, Hou Jiru, Zhao Fenglan, etc. The effect of alkali on the formation of ultralow interfacial tension and dilational rheological property of interface film. *Daqing Petroleum Geology and Development*, 2010, 29(6): 149-154.
7. Cao Xulong, Zhang Lei, Cheng Jianbo. The effect of Gemini surfactant on the adsorption film dilational rheological property of hydrophobically associating polyacrylamide interface. *Daqing Petroleum Geology and Development*, 2010, (31): 998-1002.
8. Wang Dongxian, Luo Lan, Zhang Lu, etc. The interface interaction of hydrophobic associated copolymer and surfactant. *Journal of Chemical Physics*, 2005, 21(11): 1205-1210.
9. Wu Wenxiang, Zhang Hongliang, Hu Jingbang, etc. The research of rheological property of Alkali-surfactant-polymer ternary solution. J*ournal of Daqing Petroleum Institute*, 1994, 18(4).
10. Jing Bo, Zhang Jian, Lv Xin, etc. The study of the interaction of partially hydrolyzed polyacrylamide and surfactant with interfacial dilational rheology. *Oilfield Chemistry*, 2011, 28(4): 431-434.
11. Liu Xuepeng, Feng Jie, Zhang Lu, etc. Different electrical Gemini surfactant interfacial dilational properties *[J]. Journal of Physical Chemistry*, 2010, 26(5): 1277-1283.
12. Xia Huifen, Lv Jiangyan, Feng Haichao,etc. The research of weak alkali on the Viscoelasticity of the interface between ASP solution and Oil. *Experimental Technology and Management*, 2013, 10: 34-37.

The High Renaissance Properties of Porous Three Dimensional Graphene Using One Step Reduction and Its Application in Flexible Conductor

Feng Chunfang[a†], Yi Zhifeng[b], and Kong Lingxue[c†]

Institute for Frontier Materials, Deakin University, Pigdons Road, Waurn Ponds, Victoria 3216, Australia
E-mail: [a †]chunfang@deakin.edu.au, [b] yzhi@deakin.edu.au, [c†]lingxue.kong@deakin.edu.au

Peng Zheng

Agricultural Product Processing Research Institute, Chinese Academy of Tropical Agricultural Sciences, Zhanjiang, Guangdong 524001, China
E-mail: zpengcatas@126.com

A super conductive graphene with continuous three dimensional (3D) porous structures that can potentially be used as flexible conductors has been produced by one step reduction of graphene oxide (GO) film. The high renaissance properties have been demonstrated by mechanical and electrical results where a noticeable increase in the electrical conductivity to 3850 S/cm has been demonstrated after embedding the 3D graphene foam into nearly insulated polydimethylsiloxane (PDMS). The graphene integrated PDMS film has a higher strain up to 100% elongation compared with the strain of only 60% for PDMS. Fourier transform infrared (FTIR) and x-ray photoemission spectroscopy (XPS) results reveal that most oxidized groups have been removed, which contributes to the renaissance of most outstanding properties of graphene because of the recovery of sp2 carbon structures.

Keywords: Porous 3D Graphene; High Renaissance Properties; One Step Reduction; Flexible Conductor.

1. Introduction

Graphene, a two dimensional (2D) sp2-bonded hexagonal carbons, has attracted much attention for its outstanding electric and thermal conductivities, and high mechanical properties [1]. For example, the electron mobility of the graphene is faster than any known conductors at room temperature, and it has found many

† Corresponding authors.

applications in the fields of electrodes, super-capacitors and energy storage devices [2,3,4,5]. However, 2D graphene restricts many potential applications, such as flexible conductors, due to its structural limit. Therefore, in order to expand graphene application into other technological frontiers, continuous three dimensional (3D) graphene structures have to be synthesized. Methods to synthesize graphene have been comprehensively studied, such as mechanical cleave, chemical vapour deposition and reduction of graphene oxide (GO) [6]. Among these methods, preparing graphene from reduction of GO is the only way to mass produce graphene [7].

Herein, we developed a one-step reduction route to fabricate a porous 3D graphene foam with high renaissance properties and explore its applications in flexible conductors. This freestanding 3D graphene was developed by the reduction of GO film which was produced from cheap graphite. The method we reported provides a simple way to produce large amount of graphene that can be applied into other materials of any shape and size.

2. Experimental Section

2.1. *Materials*

Natural flake graphite (particle size <45μm) was purchased from Sigma Aldrich (United States). Polydimethylsiloxane (PDMS) was ordered from Dow Corning (United States). Sulfuric acid (98%) (H_2SO_4), sodium nitrate ($NaNO_3$), potassium permanganate ($KMnO_4$), hydrogen peroxide (H_2O_2) and hydrazine hydrate (35 wt %) of AR grade were all obtained from Chem-Supply Pty Ltd (Australia).

2.2. *Synthesis of GO Solution*

Well dispersed GO suspension was synthesized from natural flake graphite according to modified Hummers method and detailed experimental steps can be found in the previous paper [8,9].

2.3. *Formation of Freestanding GO Film*

50 mL of aqueous GO (0.5 mg/mL) was sonicated for 15 mins before vacuum filtration. GO film was formed by filtration, vacuum drying and separation from filter membrane. A freestanding GO film is quite important to the formation of 3D porous graphene which can be post processed to any shape with desired polymers.

2.4. *One Step Reduction of GO Film to 3D Porous Graphene*

One freestanding GO film was put into a stainless steel autoclave prefilled with 50 μL hydrazine hydrate and heated to 100 ℃ for 12h. The obtaind freestanding reduced graphene film was imbedded into PDMS and cured under 70ºC for 2 hours.

2.5. *Characterization Techniques*

X-ray powder diffraction (XRD) patterns were recorded in the range of 2θ=5–65° (by steps of 0.05°) using a Phillips PW-1729 diffractometer (35 kV, 28 mA) (Amsterdam, the Netherlands) with CuKα radiation (λ=0.154 nm). Attenuated total reflectance Fourier transform infrared (FTIR) spectra of GO film and reduced 3D porous graphene were measured on a Bruker Vetex-70 FTIR spectrometer and recorded in the range of 600–4,000 cm^{-1} at a resolution of 4 cm^{-1}. Scanning electron microscopy images were captured on a Supra 55VP (Zeiss, Germany). All samples were coated with carbon using an BAL-TEC SCD 050 sputter coater (Leica Microsystems, Australia). X-ray photoemission spectroscopy (XPS) spectra were acquired at pass energy of 160 eV and 1 eV/step and a pressure in the analysis chamber of 5×10^{-9} torr by the instrument of Kratos AXIS Nova (Kratos Analytical Ltd, UK). The electrical conductivity data were collected on a Keithley Model 2400 combined with a four-point probing system (KeithLink Technology Co., Ltd. Taiwan). The mechanical properties were proformed by an universal tension tester model TCD-200 and the load cell is 10 N.

3. Results and Discussion

3D porous reduced graphene oxide (RGO) foam was prepared by a simple filtration process followed with one step reduction (Figure 1). After reduction, the distance between GO layers increased and porous structure created, which is demonstrated by cross-section SEM images of GO film and RGO foam. The gas produced during the chemical reduction of GO contributes to form porous graphene foam structures because gas can permeate into tight GO layers and enhance the distance of GO layers. One intuitive effect of the reduction is the increased hydrophobicity with the contact angle changed from 30.76º to 104.05º.

The change in hydrophilic performance is due to the change of chemical components. FTIR and XPS are important surface analysis techniques which can reveal the chemical structure on the surface of samples. As seen from the FTIR results (Figure 2 left), the strong peaks at around 1720, and 1100 cm^{-1} in the FTIR spectrum of GO corresponding to carbonyl (C=O) and epoxy (C–O–C) stretching

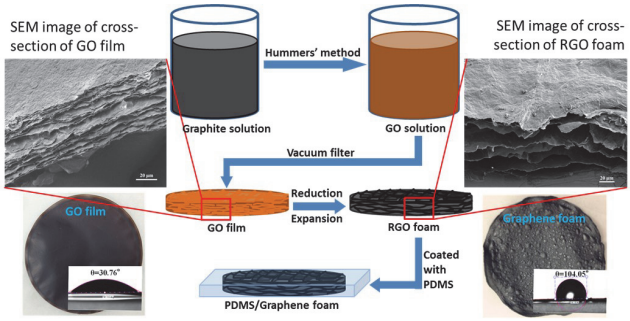


Figure 1. Schematic diagram of formation of 3D porous RGO foam.

vibrations [10,11], respectively have been weakened in the FTIR spectrum of RGO. This illustrates that most hydrophilic groups have been removed after the reduction, which has also been proved by XPS results (Figure 2 right) where two obvious peaks are shown in low resolution XPS spectra of GO and RGO samples relating to C 1s and O 1s [12]. There is a noticeable increase in the C 1s peak and decrease in the O 1s peak for the RGO foam sample compared with GO film. The removal of oxygen elements on the surface of GO sheet would recover the most properties of graphene such as high electrical conductivity because the oxygen functional groups on the surface of graphene sheet are the main obstacle to restrict the speed of electron mobility.

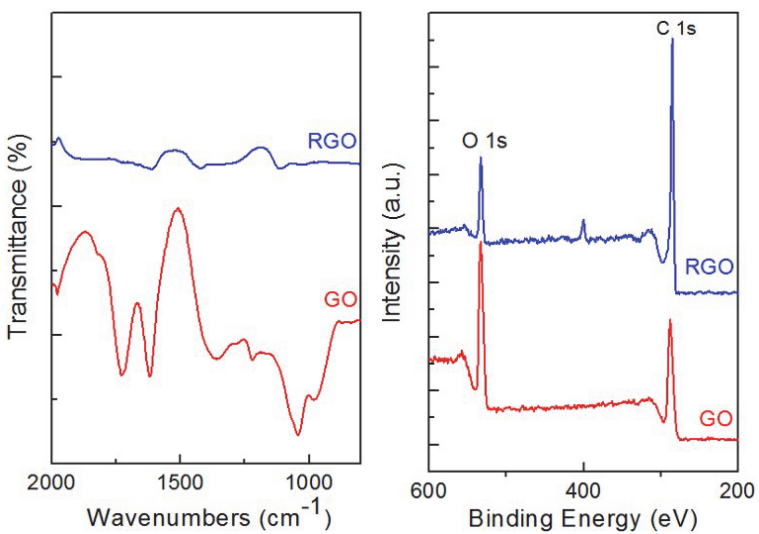


Figure 2. The FTIR spectra (left) and the low resolution XPS spectra (right) of GO and RGO.

The high renaissance electrical properties were measured with a four-point probing system. Pure PDMS is a super flexible film but poor conductivity. After embedding RGO foam into PDMS, a very high electrical conductivity of 3850 S/cm is obtained (Figure 3 insert table). This is in good agreement with the chemical structure changes in the FTIR and XPS results. Another interesting phenomenon is that with the incorporation of RGO into PDMS the elasticity of PDMS increased. Pure PDMS can only achieve an elongation of around 60% and PDMS/RGO sample can go up to 100% deformation, which is probably because the RGO foam inside the PDMS film contributes to the extra 40% deformation due to the 3D porous structure (Figure 3). This flexible flim with high electrical conductivity has broad applications as flexible conductors.

4. Summary

In summary, a continuous 3D graphene foam with a greatly improved performance in electrical and mechanical properties has been developed. It has potential applications as electrodes in flexible and stretchable materials.

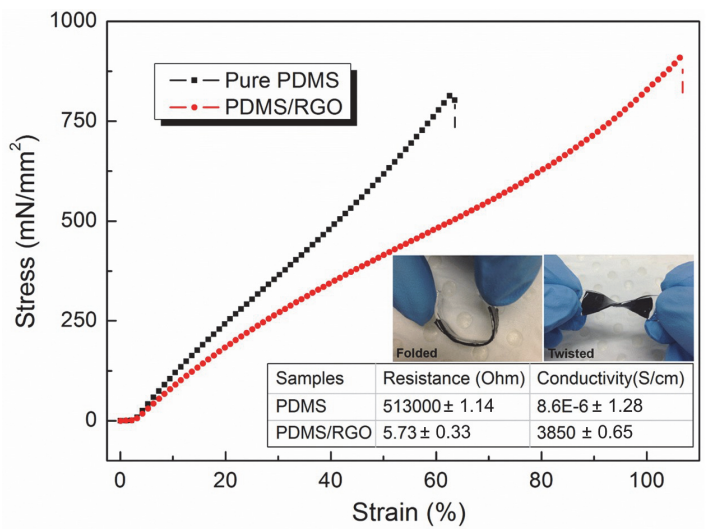


Figure 3. The stress to strain curve for PDMS and PDMS/RGO samples. Insert: a table of electrical properties for PDMS and PDMS/RGO samples and photos of folded and twisted PDMS/RGO samples.

References

1. A.Y.W. Sham, S.M. Notley, A review of fundamental properties and applications of polymer-graphene hybrid materials, *Soft Matter* (2013).
2. Z.-S. Wu, G. Zhou, L.-C. Yin, W. Ren, F. Li, H.-M. Cheng, Graphene/metal oxide composite electrode materials for energy storage, *Nano Energy* 1 (2012) 107-131.
3. H. Bai, K. Sheng, P. Zhang, C. Li, G. Shi, Graphene oxide/conducting polymer composite hydrogels, *Journal of Materials Chemistry* 21 (2011) 18653-18658.
4. C. Biswas, Y.H. Lee, Graphene versus carbon nanotubes in electronic devices, *Advanced Functional Materials* 21 (2011) 3806-3826.
5. M.F. Craciun, I. Khrapach, M.D. Barnes, S. Russo, Properties and applications of chemically functionalized graphene, *Journal of Physics: Condensed Matter* 25 (2013) 423201.
6. W. Choi, I. Lahiri, R. Seelaboyina, Y.S. Kang, Synthesis of Graphene and Its Applications: A Review, Critical Reviews in Solid State and Materials Sciences 35 (2010) 52-71.
7. S. Pei, H.M. Cheng, The reduction of graphene oxide, Carbon 50 (2012) 3210-3228.
8. L.F. Dumée, C. Feng, L. He, Z. Yi, F. She, Z. Peng, W. Gao, C. Banos, J.B. Davies, C. Huynh, S. Hawkins, M.C. Duke, S. Gray, P.D. Hodgson, L. Kong, Single step preparation of meso-porous and reduced graphene oxide by gamma-ray irradiation in gaseous phase, *Carbon* 70 (2014) 313-318.
9. L.F. Dumée, C. Feng, L. He, F.-M. Allioux, Z. Yi, W. Gao, C. Banos, J.B. Davies, L. Kong, Tuning the grade of graphene: Gamma ray irradiation of free-standing graphene oxide films in gaseous phase, *Applied Surface Science* 322 (2014) 126-135.
10. D.W. Lee, L. De Los Santos V, J.W. Seo, L.L. Felix, A. Bustamante D, J.M. Cole, C.H.W. Barnes, The Structure of Graphite Oxide: Investigation of Its Surface Chemical Groups, *The Journal of Physical Chemistry* B 114 (2010) 5723-5728.
11. J.I. Paredes, S. Villar-Rodil, A. Martínez-Alonso, J.M.D. Tascón, Graphene Oxide Dispersions in Organic Solvents, *Langmuir* 24 (2008) 10560-10564.
12. X. Dong, C.-Y. Su, W. Zhang, J. Zhao, Q. Ling, W. Huang, P. Chen, L.-J. Li, Ultra-large single-layer graphene obtained from solution chemical reduction and its electrical properties, *Physical Chemistry Chemical Physics* 12 (2010) 2164-2169.

Preparation and Effects of Mg&Zr-doping on the Electrochemical Properties of Spinel $Li_4Ti_5O_{12}$ as Anode Material for Lithium Ion Battery

Zhen Wang[a], Weiquan Shao[b†]

Physics Science College of Qingdao University, Qingdao, 266071, P. R. China
E-mail: [a]wangzhen198901@126.com, [b†]qduswq@163.com

Shaou Chen[†], Yueqin Ban, Xiaojie Guo

Key Laboratory of Photonics Materials and Technology in University of Shandong, Qingdao University, Qingdao 266071, China
[†]E-mail: shaouchen@126.com

Hongliang Li, Laiying Jing

Laboratory of New Fiber Materials and Modern Textile, Growing Basis for State Key, Laboratory, College of Chemistry, Chemical Engineering and Environment, Qingdao University, Qingdao 266071, China
E-mail: lhl@qdu.edu.cn

The anode materials $Li_4Ti_5O_{12}$ was successfully prepared through solid-state reaction using Li_2CO_3 and TiO_2. The phase purity and microstructure of the synthesized powders were studied by X-ray diffraction, scanning electron microscopy (SEM). The particles are well dispersed with diameters distributed in the range of 200–250 nm. $Li_4Ti_5O_{12}$ was doped with different mole fractions of Mg\Zr to improve the electrochemical performance of the sample at a high current rate. The better charge and discharge capacities, 123mAh/g and 130mAh/g, were obtained when the current density was 1C. The rate performance of $Li_4Ti_5O_{12}$ could also be enhanced by doping Mg\Zr.

Keywords: $Li_{3.9}Mg_{0.1}Ti_{4.9}Zr_{0.1}O_{12;}$ Lithium Ion Battery; Anode Material; Solid-phase Method.

1. Introduction

The applications of mobile power sources have increased dramatically in the past several years[1]. Spinel lithium titanate ($Li_4Ti_5O_{12}$) has attracted increasing attention as a superior anode material for energy storage cells, because it has excellent Li-ion insertion and extraction reversibility, and is almost structurally unchanged during the charge/discharge process[2,3]. It has a potential flat

† Corresponding authors.

of 1.55V (versus Li+\Li) for the Li insertion, above the reduction potential of common electrolyte solvents. On one hand, upon Li insertion, the distortion of the crystal lattice of $Li_4Ti_5O_{12}$ is almost negligible, which may enable a stable cycle property[4]. On the other hand, $Li_4Ti_5O_{12}$ also has excellent lithium ion mobility, hence promising the realization of high battery rate. To develop high rate lithium storage devices, well dispersed active materials and large contact area between the active materials and electrolyte are usually the two fundamental requirements. However, the low electric conductivity (10^{-9} Scm^{-1}) does lead to initial capacity loss and poor rate capability. Nanotechnology and substituting Li or Ti by other metals have been proposed to overcome the obstacle. Generally, nanostructured $Li_4Ti_5O_{12}$ with various morphologies such as nanowires and nanotubes have shown high rate capability and excellent cycling reversibility[5-8]. Another method to obtain a high rate capability is to modify $Li_4Ti_5O_{12}$ with some other metal ions[9-11]. Such as Mg^{2+}, replaces Li^+, the redundant electrons will improve the electron conductance of $Li_4Ti_5O_{12}$ as active material, resulting in the increase of the electrochemical performance at high current[12]. In this paper, the author doped $Li_4Ti_5O_{12}$with different mole ratios of Mg\Zr to substitute for Li\Ti, and investigated the effect of Mg\Zr-doping on the electrochemical properties.

2. Experimental

$Li_4Ti_5O_{12}$ was synthesized by using Li_2CO_3 and TiO_2 as starting materials. In the first process, a certain amount of Li_2CO_3 and TiO_3 were mixed thoroughly with the mole ratio of 4:5, followed by adding ethyl alcohol and ball-milling for half an hour. In order to obtain the original $Li_4Ti_5O_{12}$, the powder obtained in the first stage were fully dried and grinded, followed by sintering at 800ºC in the air for 10h. The preparation process of $Li_{3.9}Mg_{0.1}Ti_{4.9}Zr_{0.1}O_{12}$ was the same with $Li_4Ti_5O_{12}$, besides the addition of MgO and ZrO_2 in the solution of the first process.

3. Results and Discussion

To investigate the influence of Mg\Zr doped on $Li_4Ti_5O_{12}$, X-ray diffraction analysis was carried out on the material, the results as shown in Figure.1. According to the X-ray diffraction pattern, it is apparent that the XRD pattern of $Li_{3.9}Mg_{0.1}Ti_{4.9}Zr_{0.1}O_{12}$ coincides with that of the standard $Li_4Ti_5O_{12}$ PDF card(No.0207), and no other characteristic peaks appeared. This indicated that Mg^{2+} and Zr^{4+} had entered into the lattice of single-phase spinel compounds. However, the characteristic peaks of TiO_2 has emerged obviously in $Li_{3.9}Mg_{0.1}Ti_5O_{12}$ samples. Moreover, a large number of characteristic peaks

appeared in the $Li_4Ti_{4.9}Zr_{0.1}O_{12}$ samples, suggesting that the samples contained TiO_2 phase and parts of ZrO_2 and Li_2TiO_3.

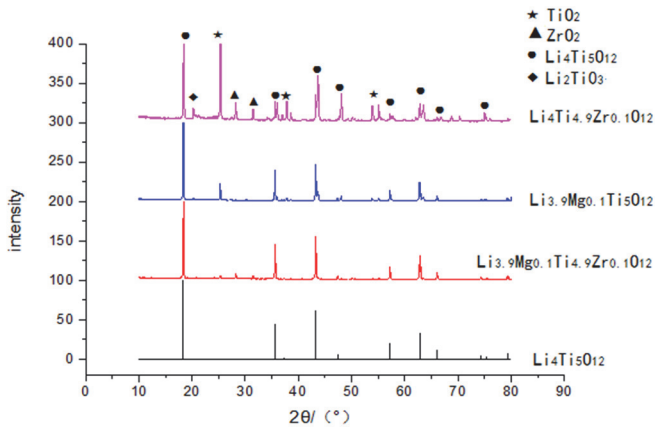


Figure.1 X-ray diffraction patterns of synthesized doped $Li_4Ti_5O_{12}$ samples.

The particle size of $Li_4Ti_5O_{12}$ and $Li_{3.9}Mg_{0.1}Ti_{4.9}Zr_{0.1}O_{12}$ samples was investigated by the SEM, as shown in Figure.2. It can be seen from the Figure.2(a), the particle size of $Li_4Ti_5O_{12}$ is 2.5μm as well as the $Li_{3.9}Mg_{0.1}Ti_{4.9}Zr_{0.1}O_{12}$ is 0.5μm, and the $Li_4Ti_5O_{12}$ samples present porous structure. And the $Li_{3.9}Mg_{0.1}Ti_{4.9}Zr_{0.1}O_{12}$ samples exhibits block-shaped particles and is well crystallized with a uniform and narrow size distribution shown in Figure.2(b). The larger surface area will increase the contact areas between active material and electrolyte which help to facilitate Li^+ coming through the material during the cycling process[13].

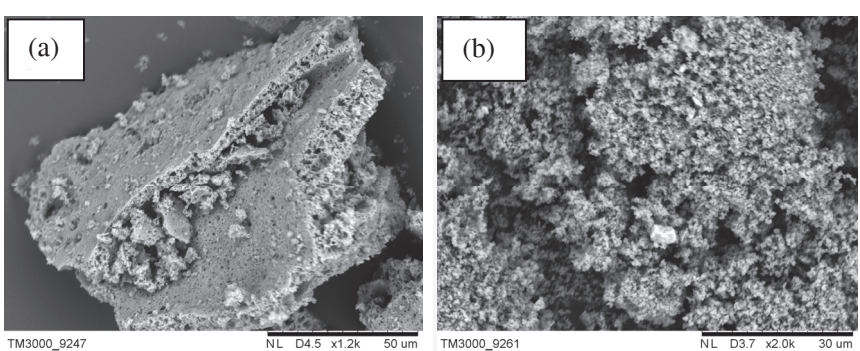


Figure.2 SEM images of $Li_4Ti_5O_{12}$(a) and $Li_{3.9}Mg_{0.1}Ti_{4.9}Zr_{0.1}O_{12}$(b) samples.

The electrochemical properties of the powders are determined by charge\discharge test at constant current density using $Li_{3.9}Mg_{0.1}Ti_{4.9}Zr_{0.1}O_{12}$/Li half cells. The electrochemical performances in terms of discharge and charge capacities of $Li_{3.9}Mg_{0.1}Ti_{4.9}Zr_{0.1}O_{12}$ were compared with $Li_4Ti_5O_{12}$ under a current density 1C in the voltage range of 1.0-2.5V. From the Figure.3(a), it can be seen that both the pure and doped samples with similar type of charge/discharge profiles exhibit a flat charge and discharge potential plateau at around 1.5-1.6 V (versus Li/Li^+), which correspond to the reversible phase transition between $Li_4Ti_5O_{12}$ and $Li_7Ti_5O_{12}$, revealing that the Mg\Zr doping does not change the electrochemical reaction process of $Li_4Ti_5O_{12}$. It is obvious that $Li_{3.9}Mg_{0.1}Ti_{4.9}Zr_{0.1}O_{12}$ has better performance than those of $Li_4Ti_5O_{12}$ by delivering higher charge and discharge capacity at the same current densities of 1C. The discharge capacities is 130mAh/g for $Li_{3.9}Mg_{0.1}Ti_{4.9}Zr_{0.1}O_{12}$ as well as 82mAh/g for $Li_4Ti_5O_{12}$ at 1C.

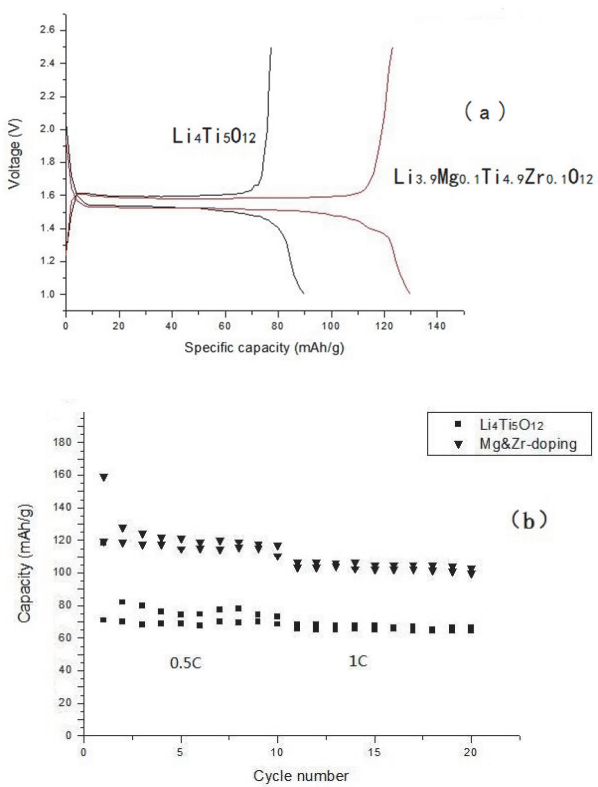


Figure.3 (a) The charge/discharge curves of the $Li_4Ti_5O_{12}$ and doped powders (current rate, 0.5C); (b) Cycling performance of the $Li_4Ti_5O_{12}$ and doped powders (current rate, 0.5-1C).

The capacities of the $Li_{3.9}Mg_{0.1}Ti_{4.9}Zr_{0.1}O_{12}$ electrodes were measured at different current rates, as shown in Figure.3(b). It can be seen that the doped sample possess better rate performance than the pristine $Li_4Ti_5O_{12}$ within the tested rate range. At a low current density of 0.5C, the doped sample presents a higher first discharge capacity between the two samples. The two doping elements contribute to improvement of the electrochemical property of $Li_4Ti_5O_{12}$ by the following mechanism: the substitution of Mg^{2+} into Li^+ sites increases the amount of Ti^{3+}\$Ti^{4+}$ mixing as charge compensation and the substitution of Ti^{4+} in $Li_4Ti_5O_{12}$with larger size Zr^{4+} improves the conductivity and lithium-ion diffusion of $Li_{3.9}Mg_{0.1}Ti_{4.9}Zr_{0.1}O_{12}$ at the same time[14].

4. Conclusions

The cubic spinel $Li_{3.9}Mg_{0.1}Ti_{4.9}Zr_{0.1}O_{12}$ samples was successfully synthesized by means of Solid-phase method. The structure and electrochemical performance of $Li_{3.9}Mg_{0.1}Ti_{4.9}Zr_{0.1}O_{12}$ were investigated. Mg\Zr doping does not change the XRD phase composition of $Li_4Ti_5O_{12}$. A certain amount of Mg\Zr doping increases the specific capacity significantly, as well as the rate capability of $Li_4Ti_5O_{12}$.

Acknowledgements

This work was supported by the Project of Shandong Province Higher Educational Science and Technology Program (Grant No. J14LJ08, J13LJ07 and J10LD12), the Natural Science Foundation of Shandong Province, China for Distinguished Young Scholars (Grant No. JQ201103), the Taishan Scholars Program of Shandong Province, China, the financial support from the Natural Science Foundation of Shandong Province under grant no. 2009 ZRA02012, ZR2012FZ006.

References

1. V. Etacheri, R. Marom, R. Elazari, G. Salitra, D. Aurbach, *Energy Environ. Sci.* 4(2011) 3243.
2. T. Ohzuku, K. Ariyoshi, S. Yamamoto, Y. Makimura, Chem. Lett. 5(2001) 1270.
3. Agung Nugrohoa, Dohyeon Yoonb, Oh-Shim Joo. *Chemical Engineering Journal* 258(2014) 357.
4. W. Wang, J.G. Tu, S.B. Wang, J.G. Hou, H.M. Zhu, S.Q. Jiao, *Electrochim. Acta* 68(2012) 254.
5. C. Lai, Y.Y. Dou, X. Li, X.P. Gao, *J. Power Sources* 195 (2010) 3676.

6. S.L. Chou, J.Z. Wang, H.K. Liu, S.X. Dou, *J. Phys. Chem. C* 115 (2011) 16220.
7. J. Haetge, P. Hartmann, K. Brezesinski, J. Janek, T. Brezesinski, *Chem. Mater*. 23(2011) 4384.
8. Yaoyao Zhang et al., *J Power Sources*, 250(2014)50
9. Jiaqing Wang, Zhenzhong Yang, Weihan Li, Xiongwu Zhong, Lin Gu, Yan Yu. *Journal of Power Sources* 266(2014) 323.
10. Zhenwei Zhang, Liyun Cao, Jianfeng Huang, Sen Zhou, Yicheng Huang, Yingjun Cai 39(2013) 6139.
11. Wei Wang, Bo Jiang, Weiyi Xiong, Zhen Wang, Shuqiang Jiao. *Electrochimica Acta* 114(2013) 198.
12. Zhiguo Wang, Zhixing Wang, Wenjie Peng, Huajun Guo, Xinhai Li. *Ceramics International* 40(2014) 10053.
13. Chih-Yuan Lin, Yi-Ruei Jhan, Jenq-Gong Duh. *Journal of Alloys and Compounds* 509(2011) 6965.
14. Seul-Ki Kim, Eun-Seok Kwon, Tae-Heui Kim, Jooho Moon, Joosun Kim *Ceramics International* 40(2014) 8869.

Influence of Deposition Parameters on TiC_xN_{1-x} Composite Films by Multi-aRC Ion Plating

Deqing Ke[a], Yingjun Pan[b], Heng Zhang[c], Bo Hong[d], Xufeng Lu[e]

School of Materials and Metallurgy, State Key Laboratory of Refractories and Metallurgy, Wu Han University of Science and technology, Wu Han 430081, China
E-mail: [a]kedeqing@wust.edu.cn, [b]hbwhpyj@163.com, [c]493838630@qq.com, [d]1215391580@qq.com, [e]576454998@qq.com

The TiC_xN_{1-x} composite films were synthesized at various substrate bias voltages, the deposition time and the flux ratio of N_2 and C_2H_2 by multi-arc ion plating (MAIP). The relationship between deposition parameters and specific capacitance of aluminum foil were investigated. The specific capacitance and microstructure of TiC_xN_{1-x} composite films were analyzed by means of capacitor tester (CT), field scanning electron microscopy (FSEM) and X-ray diffraction (XRD). The results indicated that specimen reached a high specific capacitance at 1920μF/cm^2 when bias voltage is 150 V, deposition time is 20 min and the flux ratio of N_2 and C_2H_2 is 1:1. In addition, the morphology analysis showed that TiC_xN_{1-x} composite films grew outwardly with small island-like or columnar aggregates of small and uniform particles.

Keywords: TiC_xN_{1-x} Composite Films; Deposition Parameters; Specific Capacitance; Multi-arc Ion Plating.

1. Introduction

Capacitors are a class of basic electronic components used widely as telecom, computer, civil and military electronic products. At present, etching is the main manufacturing technique for improving the specific capacitance of aluminum foil for capacitors. However, there have been some disadvantages with the etch process such as low specific capacitance, complex etching processing procedures and serious environmental pollution, etc [1-3].

TiC_xN_{1-x} composite films have been widely studied due to their superior properties, such as high hardness, high temperature oxidation resistance, excellent wear resistance and anticorrosion [4-7]. It is a very broad research field for the various deposition methods, sophisticated microstructural design and the muti-element nanocomposites. But few studies have researched the electronic properties of these films. A. Zaoui [8] predicted that the formation of an optimized TiCN films would have considerable potential in specific capacitance.

The purpose of this study is to solve the disadvantages above, and to proposed a new method for preparation of high capacitance TiC_xN_{1-x}/Al composite foil by multi-arc ion plating. The TiC_xN_{1-x} composite films were fabricated and the specific capacitance and microstructure of TiC_xN_{1-x} composite films were analyzed by means of capacitor tester (CT), field scanning electron microscopy (FSEM) and X-ray diffraction (XRD).

2. Experimental

2.1. *Films Deposition*

The TiC_xN_{1-x} composite films were deposited on pure aluminum foil (99.9% purity) substrates using multi-arc ion plating. Cathode Ti target (99.99% purity) was installed on the opposite side of the barrel-shaped vacuum chamber wall. The substrates, with the identical substrate-target distance of 290 mm, were held by the star-like rotation bracket and rotated around the central axis at a speed of 4 rpm. The pure aluminum foil substrates were polished to an average surface roughness Ra≤0.05 μm by emery paper and diamond spray ultrasonically cleaned ordinal in acetone and alcohol for 20 min before placed into the deposition chamber.

In the beginning, the chamber was evacuated down to a base pressure of less then 5.0×10^{-3} Pa meanwhile the chamber and the substrates were rapid heated and kept at the temperature of 150ºC to eliminate tiny liquid contaminants and solid pollutants. For the 15 min plasma cleaning, high purity argon (Ar, 99.99% purity) was introduced and the substrate negative bias voltage was fixed at 900 V. The argon flow rate (in the range of 40-50 sccm) was determined by the total pressure. To study the effect of deposition parameters on TiC_xN_{1-x} composite films, deposition time ranging from 10 min, 15 min, 20 min, 25 min and 30 min were applied while negative bias voltage was fixed at 150 V and the flux ratio of N_2 and C_2H_2 was fixed at 1:1, and negative bias voltages changed ranging from 50 V, 100 V, 150 V, 200 V and 250 V while deposition time fixed at 20 min and the flux ratio of N_2 and C_2H_2 was fixed at 1:1, and the flux ratio of N_2 and C_2H_2 ranging from 1:1, 1:2, 2:3, 3:2 and 2:1 while deposition time fixed at 20 min and negative bias voltage was fixed at 150 V.

2.2. *Characterization Methods*

The specific capacitance of the specimens were measured by capacitor tester (CT, Chroma LCR METER MODEL-100). The surface morphologies of the specimens were observed using field scanning electron microscopy (FSEM,

NOVA NAND-400). The crystallographic phases of the composite films were analyzed by a X-ray diffractometer (XRD, XPert PRO MPD) using Cu-Kα (wavelength λ=0.15406 nm) radiation operated at 40 KV and 40 mA, the scans recorded in a range from 10º to 90º with the step size of 0.02º and a 0.5 s dwell time.

Table 1 The detailed deposition parameters and specific capacitance

samples	deposition time / min	bias voltage/V	flux ratio of N_2 and C_2H_2	specific capacitance μF/cm^2
1	10	150	1:1	1040
2	15	150	1:1	1597
3	20	150	1:1	1920
4	25	150	1:1	1643
5	30	150	1:1	1207
6	20	50	1:1	1235
7	20	100	1:1	1578
8	20	200	1:1	1482
9	20	250	1:1	1095
10	20	150	1:2	1027
11	20	150	2:3	1523
12	20	150	3:2	1598
13	20	150	2:1	1595

3. Results and Discussions

3.1. *Specific Capacitance of Composition Films*

The detailed deposition parameters and specific capacitance were summarized in Table 1. The relationship between specific capacitance and deposition parameters (Fig.1) can be concluded from Table 1.

Fig.1(a) shows the relationship between specific capacitance and deposition time. As show in Fig.1(a), when deposition time increased from 10 min to 20 min the specific capacitance increased sharply from 1040 μF/cm^2 to 1920 μF/cm^2, but decreased sharply to1207 μF/cm^2 corresponding to the deposition time of 30 min.

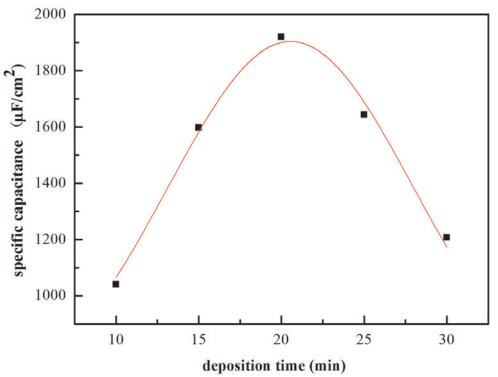
Fig.1(b) shows the relationship between specific capacitance and bias voltage. As show in Fig.1(b), when bias voltage increased from 50 V to 150 V the specific capacitance increased sharply from 1235 μF/cm^2 to 1920 μF/cm^2, but decreased sharply to 1095 μF/cm^2 corresponding to the bias voltage of 250 V.

Fig.1(c) shows the relationship between specific capacitance and the flux ratio of N_2 and C_2H_2. As show in Fig.1(c), when flux ratio of N_2 and C_2H_2 increased from 1:2 to 1:1 the specific capacitance increased sharply from 1027 μF/cm^2 to 1920 μF/cm^2, but stayed the same at 1595 μF/cm^2 in spite of the increasing of the flux ratio of N_2 and C_2H_2.

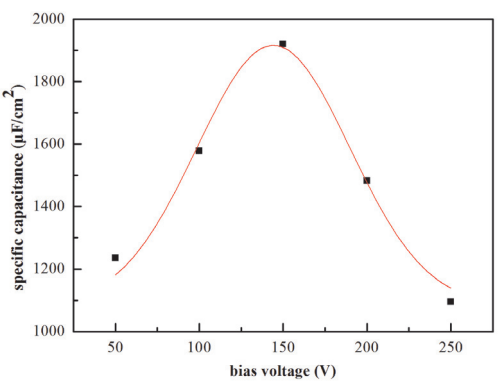
3.2. *Surface Morphology and Compositions*

Fig.2 shows the surface morphology of specimen with the highest specific capacitance. As show in Fig.2, film grew outwardly along the vertical cylindrical aluminum foil surface. TiC_xN_{1-x} grain with small and uniform particles has the diameter between 10 to 20 nm. The particle clearance is commonly a few nanometers, and the largest is below 100 nm.

Fig.3 shows the XRD spectra of TiC_xN_{1-x} composite films with the highest specific capacitance. As show in Fig.3, TiC_xN_{1-x} composite films possess typical amorphous structure. It is this special amorphous cellular growth makes TiC_xN_{1-x}/Al composite foil covering coefficient increases significantly, specific capacitance of 1920 μF/cm^2, more than 2 times higher than that of traditional etching method.

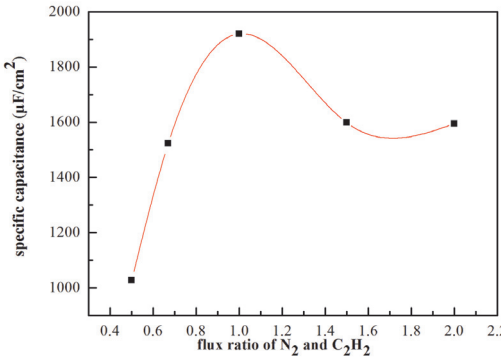


(a)



(b)

Fig.1 The relationship between specific capacitance and deposition parameters (a) deposition time, (b) bias voltage, (c) flux ratio of N_2 and C_2H_2



(c)

Fig.1 (*Continued*)

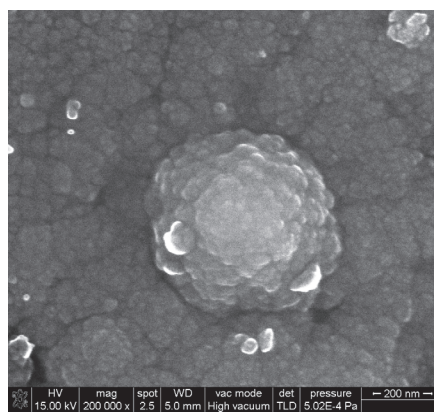


Fig.2 The surface morphology of specimen with the highest specific capacitance

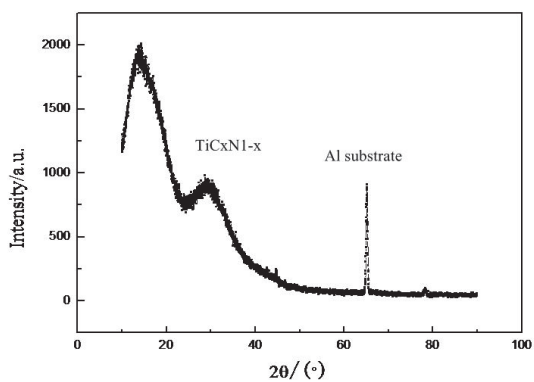


Fig.3 The XRD spectra of TiC_xN_{1-x} composite films with the highest specific capacitance

4. Conclusions

When negative bias voltage is 150V, deposition time is 20min and the flux ratio of N_2 and C_2H_2 is 1:1, TiC_xN_{1-x}/Al composite foil reaches a high specific capacitance at 1920μF/cm^2.

The morphology of TiC_xN_{1-x} film grew outwardly with small island-like or columnar aggregates of small and uniform particles.

Acknowledgements

We thank M. Tan for experiments and assistance in information preparation.

References

1. Q.C. Zhou, Y.J. Pan: *Electronic Components and Materials*, Vol. 27 (2008) No.3, p.32-34. (In Chinese)
2. J.H. Huang, Y.J. Pan: *Electronic Components and Materials*, Vol. 28 (2009) No.9, p.15-19. (In Chinese)
3. J.H. Huang, Y.J. Pan and Y.Y. Tan: *Journal of Wuhan University of Science and Technology*, Vol. 32 (2009) No.3, p.251-254. (In Chinese)
4. C. Harry, D.J. Carlos and S.R. *Gregory: Surface and Coatings Technology*, Vol. 215 (2013), p. 119-126.
5. Y. Manabu, P.P. Wang and M. Ri-ichi: *Surface and Coatings Technology,* Vol. 206 (2012) No.8 , p. 2168-2172.
6. X.D. Wang, X. Pan and W.T. Ye: *Surface and Coatings Technology*, Vol. 228 (2013) No.1, p. 194-197.
7. C. Czettl, C. Mitterer and U. Mühle: *Surface and Coatings Technology*, Vol. 206 (2011) No.7, p. 1691-1697.
8. A. Zaoui, B. Bouhafs, P. Ruterana: *Materials Chemistry and Physics*, Vol. 91 (2005) No.1, p. 108-115.

Application of Dynamic Scaling to the Surface Properties of TiC_xN_{1-x} Nano Films

Deqing Ke[a], Yingjun Pan[b], Bo Hong[c], Xufeng Lu[d], Heng Zhang[e]

School of Materials and Metallurgy, The State Key Laboratory of Refractories and Metallurgy, Wu Han University of Science and Technology, Wu Han 430081, China

E-mail: [a]kedeqing@wust.edu.cn, [b]hbwhpyj@163.com, [c]1215391580@qq.com, [d]576454998@qq.com,[e]493838630@qq.com

The surface evolution of TiC_xN_{1-x} nano films, formed by multi-arc ion plating (MAIP) on pure aluminum foil substrates, has been investigated using atomic force microscopy (AFM). Results are analyzed using dynamic scaling theory. TiC_xN_{1-x} nano film had a smooth-rough-smooth period and two distinct stages. In stages I, high values are obtained for dynamic scaling coefficients α=0.65±0.04, β=0.50±0.05, $\alpha+\alpha/\beta\approx2$, where α is the roughness exponent and β is the growth exponent, it was KPZ universality type. In stage Ⅱ, the roughness exponent α was 0.35 and the surface roughening rate slowed down.

Keywords: TiC_xN_{1-x} nano films, dynamic scaling, roughness exponent, growth exponent.

1. Introduction

The growth mode of thin films is governed by the surface energy of the film and the interface energy between the film and substrate, along with kinetic factors such as surface diffusion, presence of step-edge barriers, and shadowing effects [1,2]. Detailed measurements are needed to address how the surface morphology evolves at different stages of growth. These studies must be coupled with theory to better understand the underlying factors driving surface feature formation [3-5]. It is generally believed that the surface morphology development, during film growth, is affected by competition between surface roughening and smoothing effects. Dynamic surface growth models, such as scaling theory [6], a universal concept of diffusion-mediated growth that interrelates island density, average island size and coverage, have been successfully applied to interpret the surface morphology evolution of thin-film layers including metals[7,8]. However, kinetics of growth was hardly any addressed on TiC_xN_{1-x} nano films.

This work aims at studying dynamic phenomena occurring during multi-arc ion plating of TiC_xN_{1-x} nano films and elucidation of the mechanisms of the film growth. The surface evolution of TiC_xN_{1-x} nano films on pure aluminum foil is

quantitatively analyzed by AFM. By means of AFM, we evaluate the thickness-dependent evolution of the overall surface roughness, as well as the mound shapes. We present a systematic study of the growth mechanisms governing the surface morphology of this material based on detailed AFM characterization combined with an examination of the dynamic scaling properties obtained from analysis of the data.

2. Experimental

2.1. *Films Deposition*

The TiC_xN_{1-x} nano films were deposited on pure aluminum foil (99.9% purity) substrates using multi-arc ion plating. Cathode Ti target (99.99% purity) was installed on the opposite side of the barrel-shaped vacuum chamber wall. The substrates, with the identical substrate-target distance of 290 mm, were held by the star-like rotation bracket and rotated around the central axis at a speed of 4 rpm. The pure aluminum foil substrates were polished to an average surface roughness $Ra \leq 0.05$ μm by emery paper and diamond spray ultrasonically cleaned ordinal in acetone and alcohol for 20 min before placed into the deposition chamber.

In the beginning, the chamber was evacuated down to a base pressure of less then 5.0×10^{-3} Pa meanwhile the chamber and the substrates were rapid heated and kept at the temperature of 150ºC to eliminate tiny liquid contaminants and solid pollutants. For the 15 min plasma cleaning, high purity argon (Ar, 99.99% purity) was introduced and the substrate negative bias voltage was fixed at 900 V. The argon flow rate (in the range of 40-50 sccm) was determined by the total pressure. To study the surface evolution of TiC_xN_{1-x} nano films, deposition time ranging from 10 min, 15 min, 20 min, 25 min, 30 min were applied while negative bias voltage was fixed at 150 V and the flux ratio of N_2 and C_2H_2 was fixed at 1:1.

2.2. *Characterization Methods*

By means of atomic force microscopy (AFM, NanoScope IIIa MultiMode), we evaluate the thickness-dependent evolution of the overall surface roughness, as well as the mound Shapes.

3. Results and Discussions

Fig. 1 shows three-dimensional morphology of TiC_xN_{1-x} film with different deposition time, sampling range is 10 μm ×10 μm. As show in Fig. 1, when

deposition time t < 20 min, with the increasing of deposition time, the scope of the TiC_xN_{1-x} surface island is obviously observable, the number of the island on the surface of the flat area disappeared and replaced by high density island on the surface. When deposition time t > 20 min, surface islands approach each other and merge each other subsequently due to the gap between each other decreases, then the difference between the height of each surface island decreases, and gradually flattening, forming a flat area. It is clearly that with the increasing of deposition time, the thin film on the surface undergo a process from smooth to rough and to smooth.

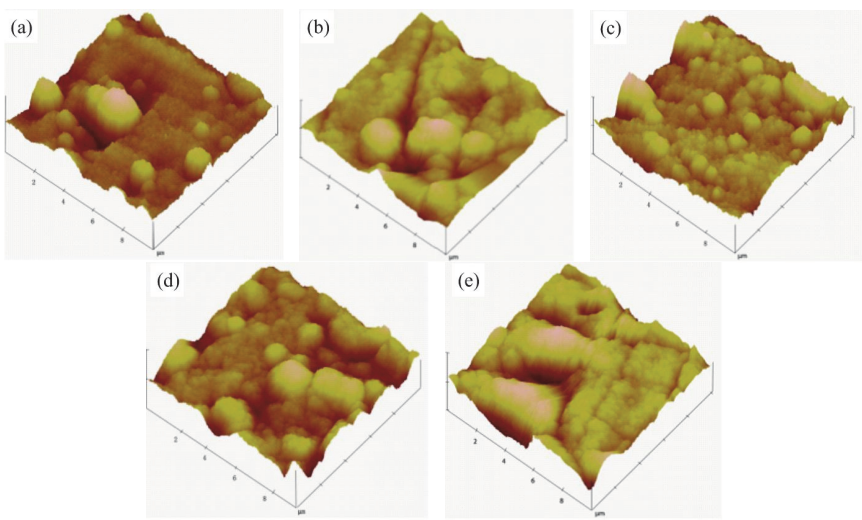


Fig. 1 The representative AFM image of TiC_xN_{1-x} film surface with deposition time: (a) 10min; (b) 15min; (c) 20min; (d) 25min; (e) 30min.

Fig. 2 shows the relationship between the surface roughness (R) and deposition time (t). Logarithmic coordinate (lnR-lnt) was used. As show in Fig. 2, the surface roughness of the dynamics of evolution is obviously different from the two stages. Defined as I and II respectively. In stages III, namely the deposition time t < 20 min, with the increase of deposition time, TiC_xN_{1-x} film roughness increased from 98.74 nm to 119.28 nm. when deposition time is 20 min, the roughness of TiC_xN_{1-x} film reached a maximum of 144.63 nm. TiC_xN_{1-x} film growth exponent was 0.50±0.05, a slightly larger than the pure diffusion effect of growth exponent 0.33, this indicated that TiC_xN_{1-x} film growth is mainly controlled by the diffusion process. β=0.50±0.05 is according with the unstable growth pattern due to the additional energy barrier in the steps of

forming, so the adsorption of atoms in the vertical and horizontal movement is not symmetrical.

In stage II, when deposition time t > 20 min, the surface roughness reduced to 108.11 nm from 130.05 nm and the growth pattern changed, in later growth stage, roughness exponent was used to describe scaling behavior.

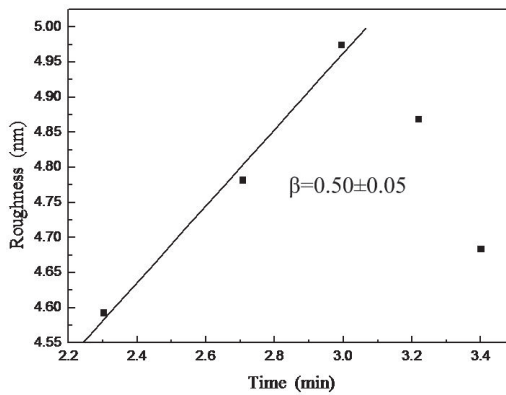


Fig. 2 Relationship between the surface roughness and deposition time.

In order to quantitatively describe TiC_xN_{1-x} film surface morphology change, logarithmic coordinate was used to analyze the surface topography of AFM one-dimensional power spectral density analysis (1DPSD), as shown in Fig. 3. The surface roughness of dynamic evolution is obviously different from the two stages.

In stage I, 1DPSD linear approximation, fitting based on high-frequency linear area, high frequency line value γ was 2.23±0.04, and the corresponding roughness exponent α was 0.65±0.04. In stage II, the roughness exponent α dropped to 0.35, which further illustrates the growth mode change. Smaller roughness exponent reflects the actual height differences between neighboring grain is not obvious, roughness decreased and surface coarsening rate slowed down, which according to the results from the previous growth index analysis is identical.

In stage I, the scaling exponent α=0.65±0.04，β=0.50±0.05，α+α/β≈2, is well follow the theoretical Kardar-Parisi-Zhang (KPZ) universal type. The KPZ equation is a non-linear stochastic partial differential equation. It describes the temporal change of the height (h) at place (x) and time (t). In stage II, roughness exponent α=0.35, surface coarsening rate slowed down. The reason why there are two stages in growth process can be interpreted as: when the deposition time is too short, Al had a greater influence on the substrate of the thin film surface

coarsening. In the early film surface roughness increases with the increase of deposition time due to the increasing of substrate surface atoms on per unit area. When the deposition time is long enough, the surface roughness of the film decreased with the increasing of deposition time, because of the influence of the Al substrate effect is abated, the ability to enhance proliferation and migration of the atom, leading to its growth mechanism changed.

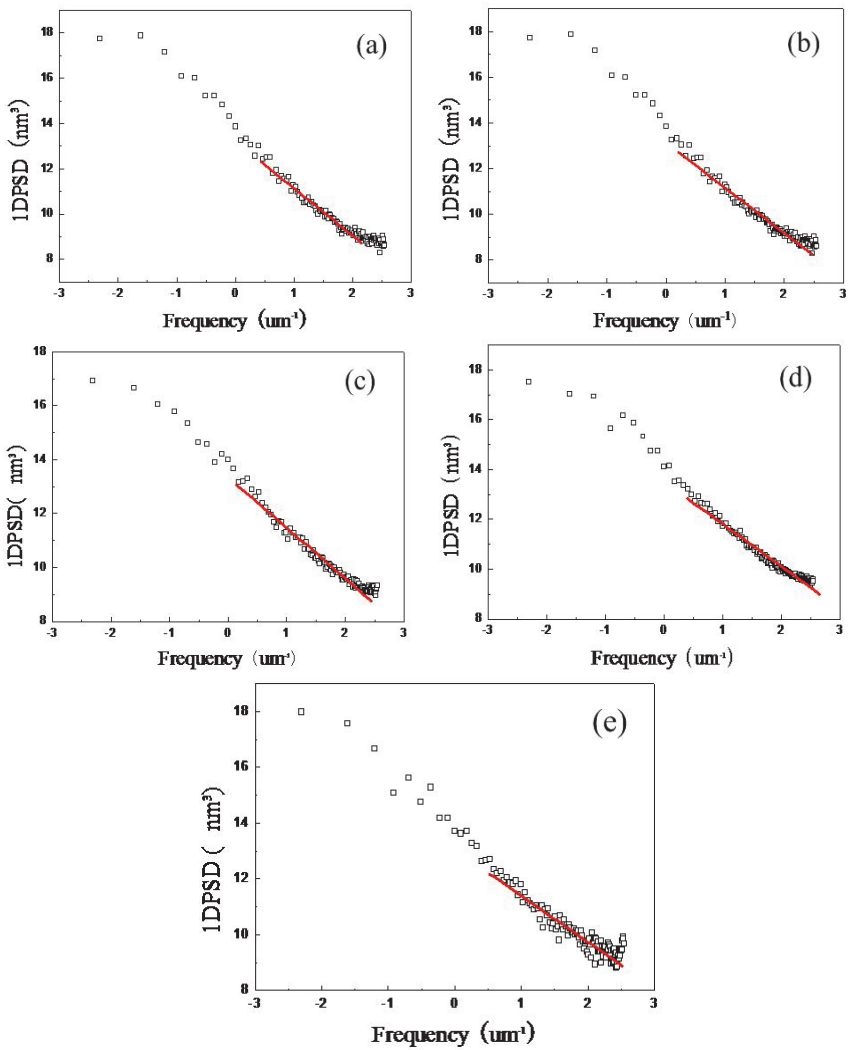


Fig. 3 The surface topography of AFM 1DPSD with deposition time: (a) 10min; (b) 15min; (c) 20min; (d) 25min; (e) 30min.

4. Conclusions

TiC_xN_{1-x} film growth shows a smooth-rough-smooth period.

TiC_xN_{1-x} film had two distinct stages. In stage I, the scaling exponents were $\alpha = 0.65 \pm 0.04$, $\beta = 0.50 \pm 0.05$ and $\alpha+\alpha/\beta \approx 2$, it was KPZ universality class. In stage II, the roughness exponent α was 0.35 and the surface roughening rate slowed down.

Acknowledgements

We thank M. Tan for experiments and assistance in information preparation.

References

1. H.J. Gao, Li Gao: *Progress in Surface Science*, Vol. 85 (2010) No.1, p. 28-91.
2. A. Choukourov, I. Melnichuk and I. Gordeev: *Thin Solid Films*, Vol. 565 (2014), p. 249-260.
3. G.X. Zhang, L.W. Brandon and M. Holtz: *Surface Science*, Vol. 605 (2011) No.3, p. 463-467.
4. J.W. Evans, P.A. Thiel and M.C. Bartelt: *Surface Science Reports*, Vol. 61 (2010) No.1, p. 1-128.
5. Y.L. Li, B.W. Muir, C.D. Easton: *Applied Surface Science*, Vol. 288 (2014), p. 288-294.
6. P. Luff, M. White: Thin Solid Films, Vol. 6 (1970) No.3, p. 175-195.
7. N. Boonthanom, M. White: *Thin Solid Films*, Vol. 24 (1974) No.2, p. 295-306.
8. X.N. Xie, H.J. Chung and C.H. Sow: *Materials Science and Engineering*: R: Reports, Vol. 54 (2006) No.1, p.1-48.

Thermodynamics of Pb^{2+} Adsorption on Amino Ion Exchange Fiber

Tingting Zheng[a], Qiang Gan[b], Jinxin Qian[c], Changgen Feng[d*]
State key Laboratory of Explosion Science and Technology, Beijing institute of Technology, Beijing 100081, P R China
[a]zhengtingting9011@126.com, [b]ganqiang@bit.edu.cn,
[c]qianjinxin1989@163.com, [d]cgfeng@cast.org.cn*

Thermodynamics of Pb^{2+} adsorption on amino ion exchange fiber (AIEF) were tested by batch adsorption experiments, in order to study the Pb2+ adsorption effect of AIEF. The results show that, the maximum adsorption capacity of 0.001mol/L Pb^{2+} could be obtained at pH5.26, with the adsorption capacity of 150.2 mg/g. Adsorption isotherms at different temperatures were obtained, and Langmuir model was found to fit well with the experiment data. The thermodynamic parameters indicated that the adsorption of Pb^{2+} on AIEF was an entropy-driven, endothermic and spontaneous process.

Keywords: Amino ion exchange fiber; lead ion; adsorption; thermodynamics.

1. Introduction

Lead is one of the major pollutants of heavy metal ions, causing a serious damage on human's lungs, kidneys, reproductive and cardiovascular system[1]. Currently, many methods, including ion exchange method, adsorption method, precipitation and electrolytic, were used to treat heavy metals wastewater. Among these treatment processes, ion exchange method is proved to be effective, which can realize the recycling of heavy metals and avoid secondary pollution[2]. In 1995, Yang[3] firstly used epoxy weak alkaline ion exchange resin to remove lead at the level of 0.2 mg/L, since than ion exchange resin has been used to treat heavy mental wastewater. But resin is easy to be oxidized and polluted, as well as low repetition rate, which limit its application[4]. In 1996, Zhang[5] synthesized amphiprotic chelating ion exchange fibers, which can adsorb lead completely at the condition of 1:10 liquid-solid effects, with the adsorption capacity of 1.6mmol/g. Compared with the ion exchange resin, fibrous material have a higher adsorption and desorption rate, small resistance filter, and can be used in a variety of sharps[4].

* Corresponding author.

Recently, polyamine type ion exchange fiber as a new type of fibers was widely used to adsorb heavy metal ions, such as Cr, Cd, Cu, etc.[6-8]. 2004, Deng[9, 10] synthesized the styrene type strongly basic anion exchange fiber, which is applied in the adsorption of Cd, Cr heavy metal ions. In this study, in order to study Pb^{2+} adsorption property of AIEF, adsorption isotherms at different temperatures were obtained, suitability of Langmuir equilibrium isotherm model was investigated, and thermodynamic parameters were also tested.

2. **Experimental Apparatus and Materials**

AIEF has been prepared form chloramethylated styrene grafted polypropylene fiber reacted with amido, which made by my own laboratory.

Aqueous solution of 0.001mol/L Pb^{2+} was prepared by dissolving lead nitrate (Pb2NO3) (AR, Aladdin) in distilled water, nitric acid (63%, AR, Sinopharm), xylenol orange(AR, Sinopharm), sodium acetate(CH3CHOONa) (AR, Sinopharm), acetic acid (>99.5%)(AR, Sinopharm). Apparatus included electronic analytical (AR2140 Ohaus), precision acidity meter (PHS-25 Jingke), mechanical pipetters (20-200μL Biohit), UV-visible spectrophotometer (725P Apl), electrothermal contant-temperature dry box (DHP-9032, Blue Pard), water batch oscillator (SHA-B, Blue Pard).

3. **Analytical Method**

The concentration of Pb^{2+} was measured by UV-visible spectroscopy using xylenol orange as the color agent at the wavelength of 575 nm, while adding buffered solution (pH 5.50). The linear equation of standard curve could be described as

$$A=0.10786+0.12866c \tag{1}$$

where A is the absorbance of the purple colored solution, and c is the concentration of Pb^{2+}. The correlation coefficient R^2 is 0.99911.

4. **Adsorption Experiment**

Adsorption experiments were carried out under batch mode. 25mL of Pb^{2+} aqueous solution with particular initial concentration and pH value was placed in a set of 50 mL glass conical flasks, respectively. A certain quality of AIEF was added to the adsorbent solutions. In a water batch oscillator, the mixture of Pb^{2+} and AIEF was agitated at a speed of 110 rpm under a constant temperature for a regular time. The aqueous solution was sampled at predetermined time intervals. Adsorption capacities at time t, Qt, and equilibrium, Qe, are expressed respectively as

$$Qt=\frac{(C_0-C_t)V}{m} \quad (2)$$

$$Qe=\frac{(C_0-C_e)V}{m} \quad (3)$$

where C_0, C_t, and C_e are Pb^{2+} the concentrations of original, residual and equilibrium Pb^{2+} solution, respectively; V is the volume of solution; m is the mass of AIEF.

5. Results and Discussion

5.1. *Effect of pH on Adsorption*

The pH value of solution has an important effect on adsorption of metal, especially for the metals whose speciation is governed by the solution acidity. Experiments were performed to examine the influence of initial pH on the adsorption of Pb2+, by using 207.2 mg/mL solutions and 0.0250g (±0.0005g) AIEF at 298K, 120 rpm agitation for 12h. The original pH value of solution was adjusted from 1.32 to 6.30 with HNO_3 and NaOH.

Figure 1 shows the influence of pH on the Pb^{2+} adsorption. AIEF reached a maximum value of adsorption capacity at pH value increases from 1.32 to 5.29, while the adsorption capacity of Pb^{2+} grows from 9.110 mg/g to 150.2 mg/g. When the pH value is higher than 5.29, the adsorption capacity decreases to 90.57 mg/g at pH 6.30.

Figure 1 shows that pH makes a big difference to adsorption capacity. The surface of AIEF is preferentially adsorbed by H^+ instead of Pb^{2+}. When the pH value is higher than 5.00, the adsorption capacity of Pb^{2+} is enhanced by the lower concentration of H^+ [11].

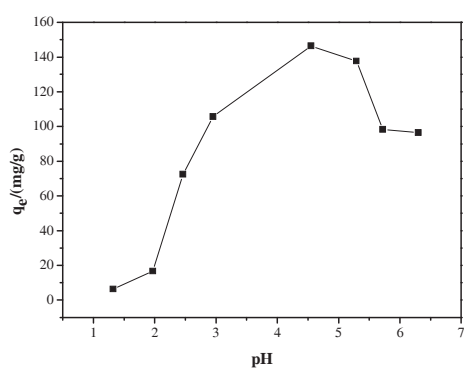


Fig.1 Effect of pH on adsorption

5.2. *Adsorption Isotherms*

Equilibrium isotherms at different temperatures for Pb^{2+} adsorption were conducted at pH5.00 (25mL different ion concentration from 89.88mg/L to 471.0mg/L and 0.0250g AIEF). Figure 2 shows the equilibrium isotherms for Pb^{2+} adsorption on AIEF.

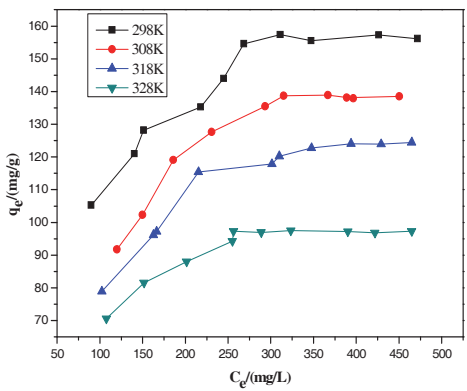


Fig.2 Adsorption isotherms of Pb^{2+}

It can be seen that the isotherm rises in the initial stage until the plateau appears at 250mg/L~300mg/L, and the Pb^{2+}untake decreased with temperature, which implies an exothermic process of Pb^{2+} adsorption on AIEF in temperature range of 298-328K.

Several adsorption isotherm models, such as Langmuir, Freundlich have been applied to describe the adsorption process[12], Langmuir model was applied in this experiment.

Langmuir model[13] could be described as

$$Q_e=\frac{q_m k_L C_e}{k_L C_e+1} \tag{4}$$

where Ce is the equilibrium concentration of Pb^{2+} (mg/L); qe and qm are the equilibrium adsorption amount of Pb^{2+} and the saturated monolayer adsorption capacity of Pb^{2+} (mg/g), respectively; kL is an adsorption equilibrium constant related to the affinity of binding sites. Equation (3) is transformed to the linear form of the Langmuir equation:

$$\frac{C_e}{q_e}=\frac{1}{q_m k_L}+\frac{C_e}{q_m} \tag{5}$$

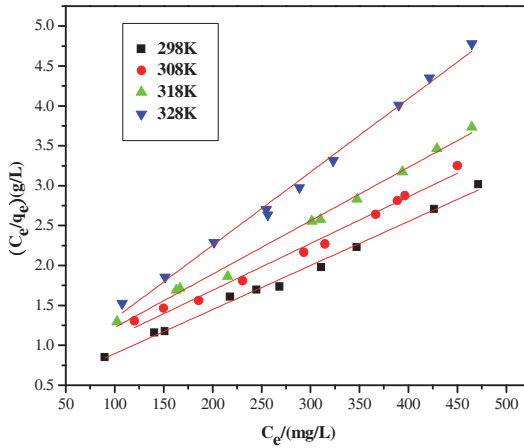


Fig.3 Langmuir plot for adsorption of Pb2+ on AIEF

Figure 3 indicates the fitting lines of the Langmuir linear equation at different temperature. Table 1 including some adsorption parameters is derived from the linear regression method. As seen from Table 1, the high correlation coefficients (R^2>0.99) demonstrate Langmuir equation could be used as the thermodynamic model of Pb^{2+} adsorption process. Therefore, it could be concluded that Pb^{2+} adsorption is a monolayer adsorption process and the chemisorptions property between Pb^{2+} and the active sites on AIEF.

Table 1 Adsorption equilibrium constants obtained from Langmuir isotherms

T/K	Langmuir constant		
	q_m/(mg/g)	k_L	R^2
298	181.2	0.0160	0.9968
308	170.6	0.0113	0.9946
318	149.7	0.0120	0.9971
328	108.9	0.0219	0.9969

5.3. *Thermodynamic Study*

In order to study the thermodynamic properties of the fiber, some thermodynamic parameters, including enthalpy change ΔH, Gibbs free energy change ΔG, Entropy change ΔS.

ΔH can be obtained by the Clausius-Claoeyron equation represented as[14]

$$\ln c=\frac{\Delta H}{RT}+k \tag{6}$$

ΔG is usually got by the Gibbs equation: [15]

$$\Delta G=-RT\int_0^x q\frac{dx}{x} \tag{7}$$

Finally, simplied equation is obtained:

$$\Delta G=-RT\ln(1+kL) \tag{8}$$

ΔS can be calculated by the Gibbs-Helmholtz equation: [16]

$$\Delta S=\frac{(\Delta H-\Delta G)}{T} \tag{9}$$

where *c* is the equilibrium concentration; T is the thermodynamic temperature; R is the mole gas constant (8.314J/(mol·K)); k is a constant. *x* is the molar fraction of absorbate; q is the adsorption capacity; k_L is obtained in Table 1.

The values of ΔH, ΔG, ΔS are shown in the Table 2.The negative of ΔH indicates the exothermic nature of the adsorption. The negative values of ΔG reflect that the adsorption of Pb^{2+} on AIEF was a spontaneous process. The values of ΔS are positive, demonstrating an increase in the randomness at the solid/liquid interface.

Table 2 Thermodynamic parameters for adsorption of Pb2+ on AIEF

q_e/	ΔH/	ΔG/(kJ·mol^{-1})				ΔS/(J·mol^{-1}·K^{-1})			
(mg·g)	(kJ·mol^{-1})	298K	308K	318K	328K	298K	308K	318K	328K
100	-24.49	-39.33	-28.77	-31.54	-59.08	49.80	13.90	22.17	105.5
110	-27.20	-39.33	-28.77	-31.54	-59.08	40.70	5.097	13.65	97.20
120	-31.07	-39.33	-28.77	-31.54	-59.08	27.72	7.468	1.478	85.40

Function groups of the AIEF contain N atom, which exists in the form of a pair of unpaired electron to form a stable structure, play an important role on the high adsorption capacity of heavy metals. This study focus on the thermodynamic properties AIEF, which have a good effect on treatment of Pb2+, with the adsorption capacity of 150mg/g. Compared with other reported fibers, such as polypropylene amine oxime chelate fiber[17], loading-polyamide resin[18], etc., the adsorption capacity of AIEF increases significantly. Further researches will pay attention to the adsorption kinetics, mixed adsorption of two or three heavy metal ions and so on, in order to have deeper insight toward AIEF, which would benefit for the improvement of its mechanical strength, thermal stability, and application for other heavy metal ions.

6. Conclusions

AIEF is effective in the removal of Pb^{2+} from aqueous solution. The maximum adsorption capacity of Pb^{2+} could be obtained at pH 5.26, and the effect of temperature on the adsorption is also studied. The experiment results show that the Langmuir model is in good agreement with reasonable calculated parameters. The thermodynamic parameters indicate that the adsorption of Pb^{2+} on AIEF is a spontaneous, entropy-driven and endothermic process.

References

1. Z. J. Zhang, D. H. Li, Z. G. Xu. *Environmental Protection Science*, 2005, 31:41-47.
2. Q. S. Chen, Z. F. Meng, *Studies of Trace Elements and Health*, 2008, 25:66-68.
3. M. D. Yang, F. Y. Bao, G. Y. Dang, etc. *Non-ferrous Metals*, 1995, 47:49-52.
4. L. Y. Tang, N. Liu, R. W. Fu, Environmental Technology, 2001, 4:42-46.
5. B. W. Zhang, Q. B. Liu, X. J. Zhang, etc. *Metallurgical Analysis,* 1996, 16:1-5.
6. Deng, Q. X. Zeng, C. G. Feng, etc. *Journal of Radiation Research and Radiation Technology*, 2004, 22:276-280.
7. C. L. Song, Z. W. Chen, H. M. Fan. *Journal of Ship Science and Technology*, 2009, 4:125-128.
8. M. Y. Li, X. Liu, J. J. Lv. *Journal of Functional Materials*, 2012, 43:779-782.
9. Q. Deng, Q. X. Zeng, C. G. Feng. *Journal of Materials Engineering*, 2006, 11:22-26.
10. Q. Deng, Q. X. Zeng, C. G. Feng. *Polymer Materials Science and Engineering*, 2006, 22:157-160.
11. C. B. Xia, H. W. Shi. *Multipurpose Utilization of Mineral Resources*. 2001, 3:15-17.
12. C. G. Feng, Q. Deng, Q. X. Zeng, *Journal of Functional Materials*, 2005, 36:142.
13. I. Langmuir. *Journal of the American Chemical Society*, 1916, 38:2221-2295.
14. X. C. Fu, W. X. Shen, T. Y. Yao, etc. *Beijing: Higher Education Press*, 2006. (in Chinese)
15. W. S. W. Ngah, S. Fatinathan. *Chemical Engineering Journal*, 2008, 14:62-72.

16. A. K. Meena, K. Kadirvelu, G. K. Mishra, etc. *Journal of Hazardous Material*, 2008, 150:604-611.
17. C.G. Feng, Y.R. Sun, M. Y. Li, *Spectroscopy and Spectral Analysis*, 2012, 32:3188-3192.
18. Ramazan Coşkun, Yasin Dilci, *Journal of Macromolecular Science*, 2014, 51:767-782.

Supercritical CO_2 Extraction of Volatile Oil from Compound Recipe of Clove and Cinnamon

Chao Li

College of Food Engineering, Xuzhou Institute of Technology, Xuzhou 221000, China
E-mail: chaoge002@163.com

The optimal parameters of supercritical CO_2 extraction (SCE) of volatile oil from the compound recipe of clove and cinnamon (same mass of clove and cinnamon) was studied using response surface methodology. The optimized extraction conditions were temperature 49.7ºC pressure 25MPa, time 4.0h, CO_2 flow rate 3.0L/h. The extraction yield (EY) of volatile oil from the compound recipe of clove and cinnamon was 11.20% and the contents of Cinnamaldehyde, Eugenol, β-Caryophyllene and Eugenol acetate were 15.39%, 60.30%, 7.45% and 12.90%, respectively. A dynamic model was established basing on the partial differential mathematical model of mass balance and the Fick's first law. The results of numerical simulation agreed well with the experimental data.

Keywords: Supercritical CO_2 Extraction; Volatile Oil; Components Analysis; Dynamic Model.

1. Introduction

Clove (*Eugenia caryophyllata* Thunb) is widely cultivated in Madagascar, Sri Lanka, Indonesia and the south of China. The volatile oil extracted from clove has been recognized since antiquity to possess biological activities, including antibacterial[1], insecticidal[2] and antioxidant[3] properties. Cinnamon (*Cinnamomum cassia* Presl) is native to South-West Asia, e.g. Sri Lanka and the south of China. Volatile oil extracted from cinnamon has antibacterial[4], antifungal[5] and insecticidal[6] activities. The same mass of clove and cinnamon can compose a compound recipe called "clove and cinnamon Power", which has analgesic and antispastic activities, especially in cure and erase stomach and abdomen pains, and its volatile compounds are responsible for the activities displayed. The volatile oil was often extracted by steam distillation, reflux extraction, ultrasonic-assisted extraction and microwave-assisted extraction. But steam distillation is time-consuming, and the other three methods are not green and environmentally friendly. SCE is non-toxic, non-explosive, cost-efficient, readily available, and easy to remove from the extracted materials. It has been documented as an effective method for preparing volatile oil from plant

materials. However, few publications on extraction of volatile oil from compound recipe by SCE are available till now. The aim of the paper is to optimize the SCE process of volatile oil from the compound recipe of clove and cinnamon by simultaneous extraction, analyse the composition of the volatile oil extracted by GC-MS and establish the dynamic model of the extraction process.

2. Materials and Methods

2.1. *Materials*

Clove and Cinnamon were purchased from Guangzhou Nanbeihang Traditional Chinese Medicine Co., Ltd, China. They were dried at 30ºC in a ventilated drying oven for 24h and stored in plastic bags at ambient temperature and protected from light, and ground by Mini-plant Sample Mill (Taisete CO., Tianjin, China) to make particle size 60~80 mesh. Cinnamaldehyde and Eugenol were purchased from China Pharmaceutical Biological Products Analysis Institute. β-Caryophyllene and Eugenol acetate were purchased from TCI (Shanghai) Development Co., Ltd. *N*-hexane of analytical reagent grade was supplied by Sichuan United Chemical Industry Institute, China. The SCE equipment with a capacity of 1L was designed by Guangzhou Light Engineering Institute. CO_2 gas(>99.5 vol%) was obtained from Guangzhou Yuegang Gas Company, China; 6890N/5975 GC-MS instrument (Agilent Technologies, USA).

2.2. *Methods*

2.2.1. *Experimental design*

The effects of some factors, such as temperature, pressure, time and CO_2 flow rate, on the extraction yield (EY) of volatile oil were firstly considered in preliminary studies, and then on the basis of results above, the Box-Behnken design was applied to optimize the extraction process of volatile oil from the compound recipe of clove and cinnamon. The effects of independent variables x_1 (temperature), x_2 (pressure), x_3 (time) and x_4 (CO_2 flow rate) at three levels in the extraction process was shown in Table 1.

Table 1. Codes and levels of factors used in Box-Behnken design.

Independent variable	Symbol	Levels		
		-1	0	1
Temperature(ºC)	x_1	45	50	55
Pressure(mpa)	x_2	17	21	25
Time(h)	x_3	3.0	3.5	4.0
CO_2 flow rate (L/h)	x_4	2.0	2.5	3.0

The generalized second-order polynomial model used in the response surface analysis was as follows:

$$EY(\%) = \beta_0 + \sum_{i=1}^{4} \beta_i x_i + + \sum_{j \le i}^{4} \beta_{ij} x_i x_j + \sum_{i=1}^{4} \beta_{ii} x_i^2$$

where EY(%) is the predicted response value, β_0, β_i, β_{ij} and β_{ii} are the regression coefficients for intercept, linear, interaction and quadratic terms, respectively, and x_i and x_j are the independent variables. The factor number (n) here is 4 in this experiment. The software Design-Expert V 7.0.0 was used to generate response surfaces and contour plots while holding a variable constant in the second-order polynomial model. And according to the Box-Behnken Design, 27 tests are required for the regression and fit of regression coefficients in the equation above.

2.2.2. *Calculation of EY of volatile oil*

EY of volatile oil was calculated using the following formula:

$$EY = \frac{m_t}{m_0} \times 100\%$$

where m_t is the mass of extracted volatile oil, g; m_0 is the initial mass of raw material put into the extractor, g; *EY* is the initial volatile oil content of raw power, %.

2.2.3. *GC-MS analysis*

GC-MS analysis were performed using a 6890N/5975 gas chromatography-mass spectrometer instrument (Agilent Technologies, USA) equipped with a fused-silica capillary column (HP-5MS, 30m×0.25mm×0.25μm). The oven was started at 100ºC, then temperature programmed at 4ºC/min to a final temperature of 180ºC. The inlet temperature was kept at 250ºC all the time. The carrier gas, helium, was at a constant flow-rate of 1.0mL/min and a 50:1 split ratio were used. Ion source temperature was 230ºC. The ionization energy was 70eV. The interface temperature was 280ºC. In the range of *m/z* 33 to 450 aum, mass spectra were recorded with 3.52 scans/s velocity. Samples were run in *N*-hexane with a dilution of 0.1% (V/V). The identification was performed through GC-MS with the help of NIST05 Mass Spectra Library and papers reported. The percentage of content was calculated by peak area normalization.

3. Results and Discussion

3.1. *Optimization of SCE*

3.1.1. *Fitting the model*

Table 2. The experiment results of Box-Behnken.

No.	x_1	x_2	x_3	x_4	EY (%)	No.	x_1	x_2	x_3	x_4	EY (%)
1	-1	-1	0	0	6.30	15	0	-1	1	0	7.36
2	1	-1	0	0	6.18	16	0	1	1	0	9.66
3	-1	1	0	0	8.73	17	-1	0	-1	0	6.77
4	1	1	0	0	8.59	18	1	0	-1	0	6.72
5	0	0	-1	-1	5.82	19	-1	0	1	0	8.12
6	0	0	1	-1	7.15	20	1	0	1	0	8.04
7	0	0	-1	1	8.67	21	0	-1	0	-1	5.27
8	0	0	1	1	10.0	22	0	1	0	-1	7.66
9	-1	0	0	-1	6.09	23	0	-1	0	1	8.12
10	1	0	0	-1	5.97	24	0	1	0	1	10.51
11	-1	0	0	1	8.94	25	0	0	0	0	8.03
12	1	0	0	1	8.82	26	0	0	0	0	7.72
13	0	-1	-1	0	5.92	27	0	0	0	0	7.91
14	0	1	-1	0	8.35						

The predicted model can be described by the following equation in terms of actual values:

$$EY(\%) = -56.99 + 1.77x_1 + 0.42x_2 + 2.61x_3 + 2.3x_4 - 2.5\times10^{-4}x_1x_2 - 3\times10^{-3}x_1x_3 + 0x_1x_4 - 1.625\times10^{-2}x_2x_3 + 0x_2x_4 + 0x_3x_4 - 1.765\times10^{-2}x_1^2 - 1.17\times10^{-3}x_2^2 - 0.11x_3^2 + 0.11x_4^2$$

The significance of each coefficient was determined using the *F*-test and *P*-value in Table 3. As shown in Table 3, the model was of great significance ($P<0.0001$), the Lack of Fit ($P=0.9997>0.05$) was not significant, the adjusted coefficient of determination (R^2_{Adj}) of the predicted model was 0.9973 and the Adeq. Precision was 98.467 (much larger than 4). Thus, the predicted model seemed to represent the observed values. And the response was sufficiently explained by the model. The corresponding variables would be more significant if the absolute *F*-value becomes greater and the *P*-value becomes smaller. It could be seen that the linear terms of temperature (x_1) was significant, and the linear terms of pressure (x_2), time (x_3) and CO_2 flow rate (x_4) and the quadratic term of temperature (x_1^2) was very significant.

Table 3. ANOVA results of quadratic regression model.

Source	SS	Df	MS	*F*-value	*P*-value	
Model	48.30	14	3.45	676.33	<0.0001	**
x_1 (temperature)	0.033	1	0.033	6.48	0.0256	*
x_2 (pressure)	17.16	1	17.16	3364.29	<0.0001	**
x_3 (time)	5.44	1	5.44	1066.63	<0.0001	**
x_4 (CO_2 flow rate)	24.37	1	24.37	4777.29	<0.0001	**
x_1x_2	1×10^{-4}	1	1×10^{-4}	0.02	0.8910	
x_1x_3	2.25×10^{-4}	1	2.25×10^{-4}	0.044	0.8372	
x_1x_4	0	1	0	0	1.0000	
x_2x_3	4.22×10^{-3}	1	4.22×10^{-3}	0.83	0.3807	
x_2x_4	0	1	0	0	1.0000	
x_3x_4	0	1	0	0	1.0000	
x_1^2	1.04	1	1.04	203.58	<0.0001	**
x_2^2	1.875×10^{-3}	1	1.875×10^{-3}	0.37	0.5556	
x_3^2	4.033×10^{-3}	1	4.033×10^{-3}	0.79	0.3914	
x_4^2	4.033×10^{-3}	1	4.033×10^{-3}	0.79	0.3914	
Residual	0.061	12	0.0051			
Lack of Fit	0.012	10	0.0012	0.051	0.9997	
Pure Error	0.049	2	0.0245			
Cor Total	48.36	26				
	R^2=0.9987		R^2_{Adj}=0.9973		Adeq.Precision=98.467	

* Significant at 0.05 level, ** Significant at 0.01 level.

3.1.2. *Verification of predicted model*

The best results of supercritical CO_2 extraction of volatile oil (Y =11.17%) were found at 49.7ºC, 25MPa, 4.0h and 3.0L/h. In order to verify this result, supercritical CO_2 extraction of volatile oil was carried out at these optimal conditions and EY of volatile oil extracted was obtained as 11.20% as experimental result.

3.2. *Components analysis of volatile oil*

The composition of volatile oil extracted at optimal conditions analyzed by GC-MS was as follows: the contents of Cinnamaldehyde 15.39%, Eugenol 60.30%, β-Caryophyllene 7.45%, Eugenol acetate 12.90% and other components 3.96%, respectivelly.

3.3. *Dynamic model*

The dynamic model as developed by Luo Denglin[7] was employed to describe the experimental data of this study.

$$E = E_{\infty}(1 - e^{-kt})$$

where E was the specific EY of volatile oil in time t, E_{∞} was the E value for infinite extraction time, and k was rate constant.

The specific dynamic equation was modeled by Origin 7.5. E=13.14×(1-$e^{-0.4212 \times t}$) described all the experimental data quite well (R^2=0.9941, AARD=3.467%), as it was shown in Fig. 2.

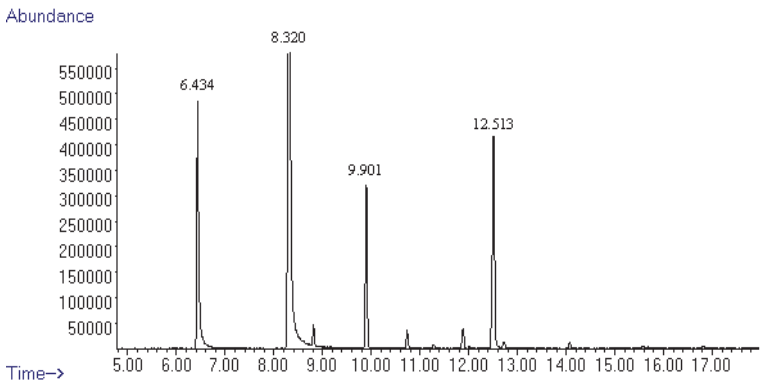


Fig. 1. Total ion current (TIC) chromatogram of volatile oil.

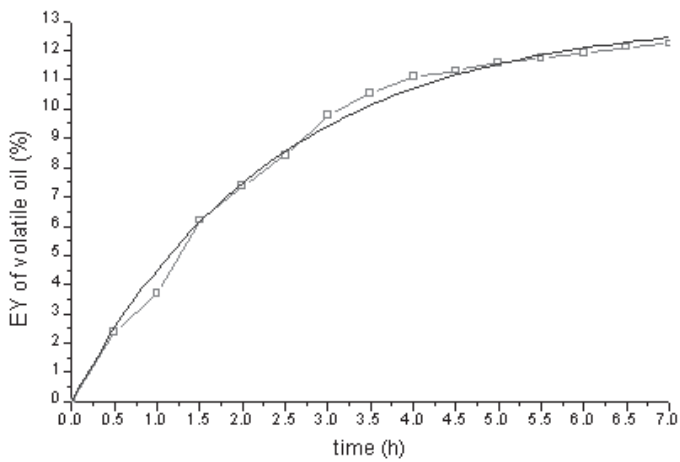


Fig. 2. Model fitting Curve.

4. Conclusions

(1) The paper discusses effects of temperature, pressure, time and CO_2 flow rate on EY of volatile oil from the compound recipe of clove and cinnamon. On

the basis of these, the paper optimized the extraction process of SCE by a Box Benken design. The optimal extraction condition was temperature 49.7°C, pressure 25MPa, time 4.0h and CO_2 flow rate 3.0L/h.

(2) Cinnamaldehyde, Eugenol, β-Caryophyllene and Eugenol acetate were the main componsition of volatile oil extracted at the optimal condition, the contents of them in extracted volatile oil were 15.39%, 60.30%, 7.45% and 12.90%, respectively.

(3) The dynamic model, $E=13.14\times(1-e^{-0.4212\times t})$, gave quite a good fit to EY versus extraction time data over the entire range of conditions studied (R^2=0.9941, AARD%=3.467%).

Acknowledgements

This work was financially supported by the national Spark Program project (No.2013GA690416).

References

1. Didry N, Dubreuil L, Pinkas M. Activity of thymol, carvacrol, cinnamaldehyde and eugenol on oral bacteria[J]. *Pharmaceutica Acta Helvetiae*, 1994, 69(1): 25–28.
2. Huang Y, Ho SH, Lee H C, et al. Insecticidal properties of eugenol, isoeugenol and methyleugenol and their effects on nutrition of Sitophilus zeamais Motsch. (Coleoptera: Curculionidae) and Tribolium castaneum (Herbst) (Coleoptera: Tenebrionidae)[J]. *Journal of Stored Products Research*, 2002, 38(5): 403–412.
3. Lee K G, Shibamoto T. Antioxidant property of aroma extract isolated from clove buds [Syzygium aromaticum (L.) Merr. Et Perry][J]. *Food Chemistry*, 2001, 74(4): 443–448.
4. Hili P, Evans C S, Veness R G. Antimicrobial action of essential oils: the effect of dimethylsulphoxide on the activity of cinnamon oil[J]. *Letters in Applied Microbiology*, 1997, 24(4): 269–275.
5. Chang S T, Chen P F, Chang S C. Antibacterial activity of leaf essential oils and their constituents from Cinnamomum osmophloeum[J]. *Journal of Ethnopharmacology*, 2001, 77(1): 123–127.
6. Lee H C, Cheng S S, Chang S T. Antifungal property of the essential oils and their constituents from Cinnamon osmophloeum leaf against tree pathogenic fungi[J]. *Journal of the Science of Food and Agriculture*, 2005, 85(12): 2047-2053.
7. Luo D L. Ultrasound-assisted extraction of ginsensides from ginseng in supercritical CO_2 reverse microemulsions[D]. Doctor Dissertation, South China University of Technology, Guangzhou, 2006.

Optimization of Ultrasonic-assisted Extraction of Polysaccharides from Imperatae Rhizoma Using Response Surface Methodology

Xue-bing Shang[a] and Chao Li[b†]

College of Food Engineering, Xuzhou Institute of Technology, Xuzhou 221000, China
E-mail: [a]shangxuebing63@sina.com, [b†]305786072@qq.com

The ultrasonic-assisted extraction process of polysaccharides from Imperatae Rhizoma by response surface methodology (RSM) was optimizated in the paper. Based on the Box-Behnken design principles, the RSM with three factors and three levels was adopted. The experimental data were analyzed by the RSM softwares of Design-Expert V 7.0.0. The results showed that the optimal extraction parameters were solvent to material ratio 12.6mL/g, extraction temperature 61.6ºC and extraction time 55.6min. Under the above-mentioned conditions, it can be included that the experimental extraction yield of polysaccharides was 0.402%, which was close to the predicted value 0.399%.

Keywords: Imperatae Rhizoma; Polysaccharides; Ultrasonic-assisted extraction.

1. Introduction

Imperatae Rhizoma is the dried rhizome of *Imperata cylindrica* Beauv. var. *major* (Nees) C. E. Hubb [1]. It can induce diursis, regulate the immunity, accelerate blood clotting and have anti-inflammatory activity et al [2-3]. The main active ingredients of Imperatae Rhizoma are polysaccharides and triterpenes. Ultrasonic-assisted is an inexpensive, simple and efficient alternative to conventional extraction techniques. The enhancement in extraction obtained by using ultrasonic is mainly attributed to the effects of acoustic cavitations produced in the solvent by the passage of an ultrasonic wave. Ultrasonic also exerts a mechanical effect, allowing greater penetration of solvent into the sample matrix, increasing the contact surface area between solid and liquid phase. As a result the solute quickly diffuses from solid phase to the solvent [4]. In the present study, ultrasonic-assisted extraction parameters, such as solvent to material ratio, extraction temperature and time, were optimized using a three-variable and three-level Box-Behnken design (BBD), in order to obtain the optimal conditions for the extraction of polysaccharides from Imperatae Rhizoma.

† Corresponding author.

2. Materials and Methods

2.1. *Materials*

Imperatae Rhizoma, purchased from a herb market in Bozhou, was grounded in a laboratory to a fine and homogeneous powder using mullers and then sieved through an 40 mesh sieve and were kept in sealed plastic bag at room temperature. All other chemicals were of analytical grade.

2.2. *Ultrasonic-assisted extraction (UAE)*

The UAE was performed in a KBS-250 ultrasonic-assisted system (20kHz, 250W, Kunshan Ultrasonic Instruments Co. Ltd., China). Samples were placed into a volumetric beaker (100mL), made up to volume with the extraction solvent and sonicated for different time at the required temperature. The temperature was controlled by circulating external water from a thermostatted water bath.

2.3. *Box-Behnken design*

On the basis of results of single factor experiments, a three-variable and three-level Box-Behnken design was devised in Table 1.

Table 1. Design table of codes and levels of factors.

Independent variable	Symbol	Levels		
		-1	0	1
Solvent to material ratio /(ml/g)	x_1	10	12	14
Extraction temperature /ºC	x_2	50	60	70
Extraction time /min	x_3	35	50	65

The generalized second-order polynomial model used in the response surface analysis was as follows:

$$EY = \beta_0 + \sum_{i=1}^{3} \beta_i x_i + \sum \sum_{j \le i}^{3} \beta_{ij} x_i x_j + \sum_{i=1}^{3} \beta_{ii} x_i^2$$

where EY is the predicted response value, β_0, β_i, β_{ij} and β_{ii} are the regression coefficients for intercept, linear, interaction and quadratic terms, respectively, and x_i and x_j are the independent variables.

2.4. *Preparation of standard curve*

0.0, 1.0, 2.0, 4.0, 6.0, 8.0, 10.0mL glucose standard solution (2.5mg/mL) were put into volumetric flask and diluted with water till 1.0mL for a final

concentration of 0, 0.10, 0.20, 0.40, 0.60, 0.80 and 1.0mg/mL, individually. Then 2.0mL above-mentioned solutions, 1.0mL 5% phenol and 5.0mL dense H_2SO_4 were mixed into each tube, individually. After fully reacting for 15min at 100ºC, absorbance value of each tube was examined in 490 nm. The regression equation between concentration (mg/mL) value of glucose and absorbance value were obtained as A=17.949C-0.017(R^2=0.9977).

2.5. *Extraction yield (EY)*

The extraction yield of polysaccharides was calculated using the following formula:

$$EY(\%) = \frac{W_0}{W_t} \times 100$$

where W_0, mass of polysaccharides extracted (g) and W_t, mass of Imperatae Rhizoma (g).

3. Results and Discussion

3.1. *Single factor experiments*

3.1.1. *Effects of ethanol volume fraction*

As shown in Fig. 1, several ethanol volume fractions were used to extract the polysaccharides from Imperatae Rhizoma. It was proved that ultrasonic-assisted extraction of polysaccharides had the highest extraction yield (0.305%) using ethanol volume fraction 20%. Therefore, it was used as the extraction solvent.

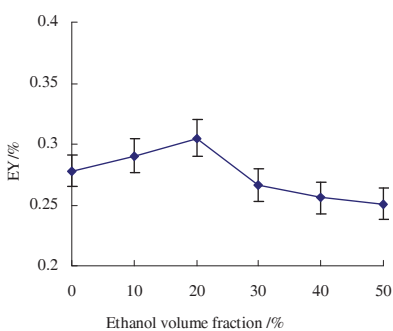


Fig. 1. Effects of ethanol volume fraction

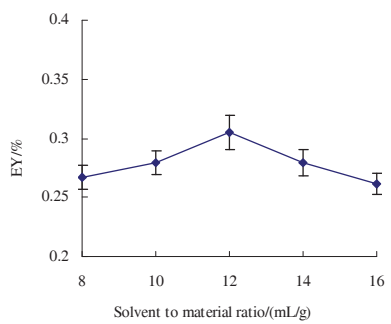


Fig. 2. Effects of solvent to material ratio.

3.1.2. *Effects of solvent to material ratio*

Fig. 2 showed the extraction yield of polysaccharides increased from 0.287% to 0.305%, when solvent to material ratio increased from 8mL/g to 12mL/g. After solvent to material ratio reached 12mL/g, the extraction yield decreased slowly. This suggested that the solvent to material ratio of 12mL/g was the optimal ratio.

3.1.3. *Effects of ultrasonic power*

Fig. 3 showed the effects of ultrasonic power on the extraction yield of polysaccharides. The extraction yield increased when ultrasonic power increased from 25W to 75W, but it declined slowly when the ultrasonic power further increased from 75W to 125W. This suggested that 75W was the optimal ultrasonic power.

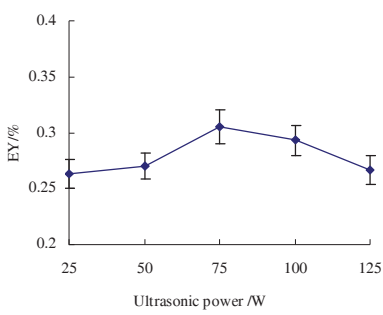


Fig. 3. Effects of ultrasonic power.

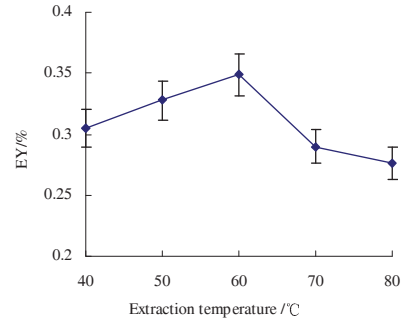


Fig. 4. Effects of extraction temperature.

3.1.4. *Effects of extraction temperature*

Fig. 4 showed the effects of extraction temperature under sonication on the extraction yield of polysaccharides. The extraction yield increased with the temperatures increasing from 40ºC to 60ºC, but declined when the temperatures were above 60ºC. This suggested that 60ºC was the optimal extraction temperature.

3.1.5. *Effects of extraction time*

As shown in Fig. 5, the extraction yield increased continuously with the prolonging of extraction time. After a certain extraction period, the extraction yield achieved a maximum. The optimal extraction time was 50min in respect to the maximum extraction yield of 0.392%. If prolonging the extraction time again, the extraction yield decreased obviously. This was because too longer

exposure in ultrasonic irradiation, resulting in the decomposition of certain active constituents. So 50min was chose for the extraction time.

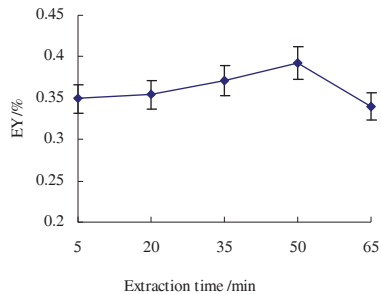


Fig. 5. Effects of extraction time.

3.2. *Optimization of UAE experiments*

3.2.1. *Fitting the model*

Table 2. Experimental design of a three-variable and three-level Box-Behnken design.

No.	x_1 /(mL/g)	x_2 /℃	x_3 /min	EY(%)	No.	x_1 /(mL/g)	x_2 /℃	x_3 /min	EY(%)
1	10	50	50	0.349	9	12	50	35	0.345
2	14	50	50	0.360	10	12	70	35	0.362
3	10	70	50	0.361	11	12	50	65	0.358
4	14	70	50	0.380	12	12	70	65	0.378
5	10	60	35	0.374	13	12	60	50	0.397
6	14	60	35	0.375	14	12	60	50	0.392
7	10	60	65	0.384	15	12	60	50	0.399
8	14	60	65	0.388					

The predicted model can be described by the following equation in terms of actual values:

$$EY(\%)=-0.905+0.0369x_1+0.0312x_2+3.72\times10^{-3}x_3+1\times10^{-4}x_1x_2+2.5\times10^{-5}x_1x_3+5\times10^{-6}x_2x_3-1.75\times10^{-3}x_1^2-2.65\times10^{-4}x_2^2-3.89\times10^{-5}x_3^2$$

As shown in Table 3 that the model was of great significance ($P=0.0022<0.01$), the Lack of Fit ($P=0.3278>0.05$) was not significant, the adjusted coefficient of determination (R^2_{Adj}) of the predicted model was 0.9228 and the Adeq.Precision was 12.856 (much larger than 4). So the predicted model seemed to represent the observed values and the responses were sufficiently explained by the model.

Table 3. ANOVA results of quadratic regression model for response surface.

Source	SS	DF	MS	F-value	P-value	
Model	3.94×10^{-3}	9	4.38×10^{-4}	19.60	0.0022	**
x_1	1.53×10^{-4}	1	1.53×10^{-4}	6.85	0.0472	*
x_2	5.95×10^{-4}	1	5.95×10^{-4}	26.63	0.0036	**
x_3	3.38×10^{-4}	1	3.38×10^{-4}	15.12	0.0115	*
x_1x_2	1.6×10^{-5}	1	1.6×10^{-5}	0.72	0.4361	
x_2x_3	2.25×10^{-6}	1	2.25×10^{-6}	0.10	0.7638	
x_1x_3	2.25×10^{-6}	1	2.25×10^{-6}	0.10	0.7638	
x_1^2	1.81×10^{-4}	1	1.81×10^{-4}	8.09	0.0360	*
x_2^2	2.59×10^{-3}	1	2.59×10^{-3}	116.01	0.0001	**
x_3^2	2.83×10^{-4}	1	2.83×10^{-4}	12.65	0.0163	*
Residual	1.12×10^{-4}	5	2.23×10^{-5}			
Lack of Fit	8.57×10^{-5}	3	2.86×10^{-5}	2.20	0.3278	
Pure Error	2.6×10^{-5}	2	1.3×10^{-5}			
Cor Total	4.05×10^{-3}	14				
		R^2_{Adj}=0.9228		Adeq.Precision =12.856		

* Significant at 0.05 level, ** Significant at 0.01 level.

3.2.2. *Verification of predicted model*

Table 4. Optimum parameters, predicted and experimental value.

Optimum parameters			EY	
Solvent to material ratio	extraction temperature	extraction time	Experimental[a]	Predicted
12.6ml/g	61.6℃	55.6min	0.402%	0.399%

[a] Means ± standard deviation (n=3).

Table 4 showed that the experimental extraction yield of polysaccharides was 0.402%, which was close to the predicted value 0.399%.

4. Conclusions

The optimal extraction parameters were solvent to material ratio 12.6mL/g, extraction temperature 61.6ºC and extraction time 55.6min. Under the above-mentioned conditions, it can be included that the experimental extraction yield of polysaccharides was 0.402%, which was close to the predicted value 0.399%.

Acknowledgments

We gratefully acknowledge the financial support received by the Xuzhou Institute of Technology Project (No. XKY2013323) and the national Spark Program Project (No. 2013GA690415).

References

1. Editorial Board of Pharmacopoeia of the People's Republic of China. *The Pharmacopoeia of the People's Republic of China*, Volume 1[S]. Beijing: Chemical Industry Press, 2010(1): 99.
2. The Editorial Board of Chinese Materia Medica. *Chinese Materia Medica*, Volume 23[M]. Shanghai: Shanghai Science & Technology Publishers, 1999: 357-361.
3. YUE X R, HOU Z X, LIU P, et al. Anti-inflammatory effect of imperata cylindrical[J]. *Chinese Journal of Clinical Rehabilitation*, 2006, 10(43): 85-87.
4. ROSTAGNO M A, PALMA M, BARROSO C G. Ultrasound-assisted extraction of soy isoflavones[J]. *Journal of Chromatography A*, 2003, 1012(2): 119-128.

Effect of Electromagnetic Field Phase and Frequency on Efficiency of Mould Electromagnetic Stirrer for Continuous Casting Billet

Jianchao Li†

School of Materials Science and Engineering, Inner Mongolia University of Technology, Inner Mongolia, Hohhot 010051, China
†E-mail: jchli2000@126.com

Baofeng Wang

School of Material and Metallurgy, Inner Mongolia University of Science and Technology, Inner Mongolia, Baotou 014010, China
E-mail: Baofeng_wang@126.com

Coupled analysis of magnetic field and fluid field of two and three phase's mould electromagnetic stirrer for square billet continuous casting was carried by the method of numerical simulation. The distribution of magnetic flux density and liquid steel velocity with same current value and frequency were obtained and compared. Calculated results showed that, two phase's mould electromagnetic stirrer, had higher stirring magnetic flux density, but stirring velocity and stirring efficiency were the almost same as those of three phase's mould electromagnetic stirrer. Based on it, coupled analysis of magnetic field and fluid field in two phase's M-EMS for square billet continuous casting was carried with same current value and frequency range from 2Hz to 8Hz. Calculated results showed that liquid steel stirring velocity along the mould reached maximum at the frequency value of 3Hz. The magnetic flux density in stirring zone was measured without load. Calculated results showed agreements with experimental data.

Keywords: Electromagnetic Stirring; Billet; Magnetic Flux Density; Phase Angle; Frequency

1. Introduction

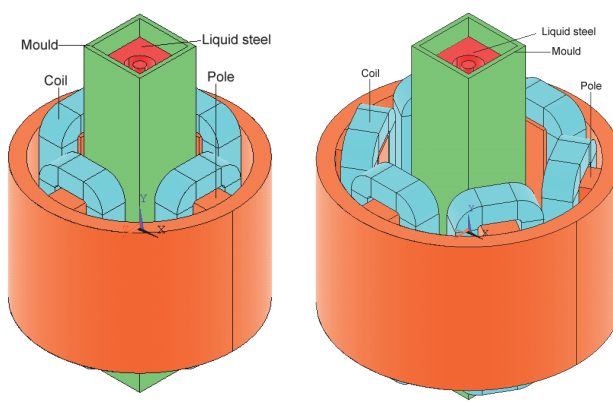
To obtain a better appreciation of M-EMS systems, understanding of the relations between the magnetic density and its distribution and operating parameters in the steel is necessary. Although there is a great deal of theoretical work [1-4] to date on stirring induced in a column of liquid metal by a rotary electromagnetic field, it relevance to the industrial electromagnetic stirring remains limited. Though many researchers had carried out long-term research on M-EMS, the research on different phase and frequency on the efficiency of M-EMS is seldom. Although the electromagnetic body force was calculated, but

it is unsuitable to assess the efficiency of M-EMS according to the magnetic body force along the mould because the distribution of magnetic body force is uneven. The different phase of M-EMS was researched in the literature [5], but the results were calculated according to two dimensional model.

In this paper, Coupled analysis of magnetic field and fluid field of two and three phase's mold electromagnetic stirrer for square billet continuous casting were carried by the method of numerical simulation. The distributions of magnetic flux density, magnetic volume force and liquid steel velocity with same current value and variable frequency were obtained and compared. The optimal phase of M-EMS was concluded. Based on the above, the research about different frequency on stirring efficiency was carried out and the optimal current frequency was discussed here deeply.

2. Model Description

At beginning, the section of coil is loaded with current density. Current density is determined by current, coil number and section area. For the two-phase and three-phase stirrer, current phase difference is 90 and 120 degrees respectively. Fig.1 shows the calculation model used in the electromagnetic field analysis. Owing to magnetic flux transmission in the air, the air around and inside the stirrer is included in the model. In order to show the details of the stirrer, the air is not drawn. In this calculation, the steel and coil, iron core and air were divided into respective finite elements. The element type of steel, coils and iron core is hexahedral. The element type of air, owing to its irregularity shape, is tetrahedral. Table 1 summarizes the process parameters of stirrer together with the dimensions of billet.



(a) (b)

Fig. 1. Geometry structure of the model with (a) two phase and (b) three phase M-EMS.

Table 1. Parameters for computation.

Item	Values
Mould thickness	0.012 (m)
Dimensions of billet	0.15×0.15 (m)
Current	130 (A)
Frequency	3 (Hz)
Casting speed	2.4 (m/min)
Mould length	0.8 (m)
Height of poles	0.38 (m)

3. Computational Results and Discussion

Fig. 2 shows the relation between time and magnetic flux density in the center of liquid steel in two periods. The magnetic flux density in the center of liquid steel arise from 0 to 0.0505T in the first period quickly and holds a constant in the following time when the two phase M-EMS is used. In contract, the magnetic flux density varied from 0 to 0.0468T using the three phase M-EMS. The magnetic flux density with two phase M-EMS is larger than that with three phase M-EMS. Computed velocity vector at center section of the stirring zone is showed in Fig. 3. As seen in this figure, the velocity in the center of liquid steel with two phase M-EMS is as same amostly as that with three phase M-EMS. But there are four dead zones in which liquid steel is stirred weakly in the corner of liquid steel. The dead zone area with two phase M-EMS is much more than that with three phase M-EMS.So stirring efficiency of two electromagnetic stirers are amostly same.Owing to requiring six coils with three phase M-EMS and four coils with two phase M-EMS, with same current and frequency, energy conservation is much obvious with two phase M-EMS. Owing to larger inner space, the coils is located easily and the stirrer life may be increased by means of increasing coil turns and decreasing coil current. The magnetic flux density in stirring zone center was measured using the 5080 Gauss meter, which is clear in Fig. 4. Comparison of calculated and experimental data are consistent.

Based on the above, stirring efficient of two phase M-EMS is as same mostly as that of three phase M-EMS. Coupling calculation of magnetic field and fluid field in two phase's M-EMS for 150mm billet continuous casting was carried with current of 130A and frequency range from 2Hz to 8Hz. A point calculated velocity, which is10mm away from the center of the edge, is defined as the stirring velocity. Optimal frequency was obtained according to the stirring velocity. Fig. 5 shows the relationship between the stirring velocity and frequency. As seen from the figure, the stirring velocity reaches maximum at frequency value of 3Hz.

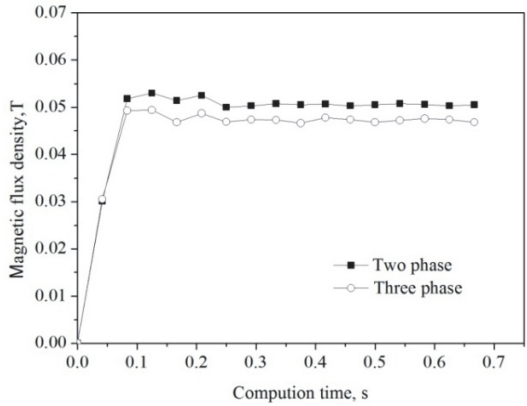
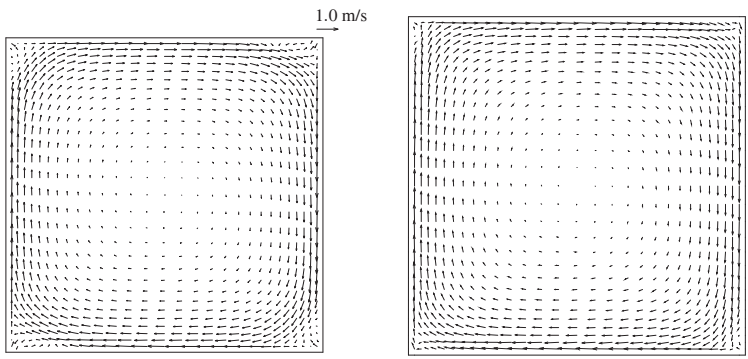


Fig. 2. Relation between time and magnetic flux density in the liquid steel center.



(a) (b)

Fig. 3. Distribution of liquid steel velocity at center section of the stirring zone with (a) two phase and (b) three phase M-EMS.

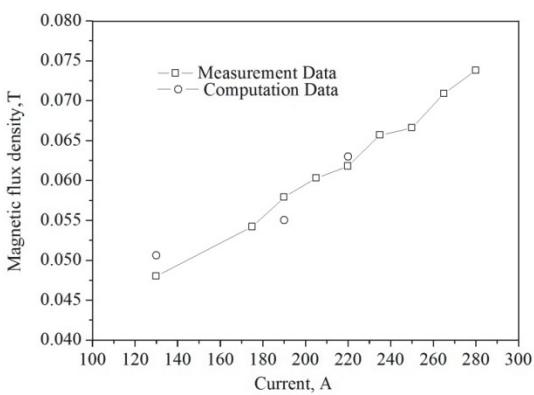


Fig. 4. Comparison of magnetic flux density calculated with that measured in stirring zone center.

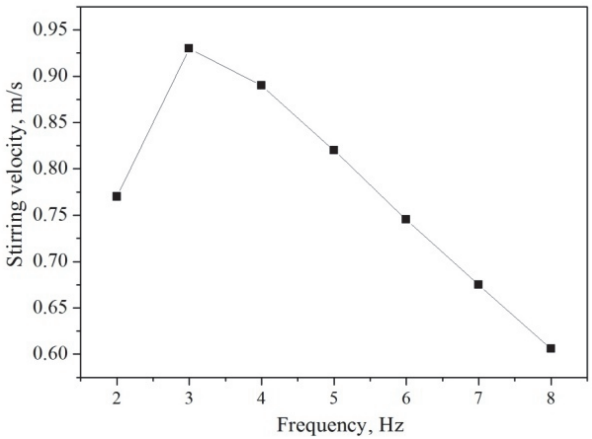


Fig. 5. The relation between stirring velocity and frequency in the liquid steel.

4. Conclusions

Calculated results show that, two-phase's mold electromagnetic stirrer, has higher stirring magnetic flux density. Stirring velocity and stirring efficiency are the almost same as those of three phase's mold electromagnetic stirrer, but energy conservation is much obvious with two phase M-EMS. The optimal magnetic field frequency is 3Hz when the two phase M-EMS is used for continuous casting 150 billet.

Acknowledgements

The authors would gratefully thank the financial support of Natural Science Foundation of Inner Mongolia (2014MS0545) and Inner Mongolia University of Technology Research Project (ZD201306).

References

1. Hideaki Yamamura, Takehiko Toh, Hiroshi Harada, etc. Optimum magnetic flux density in quality control of casts with level DC magnetic field in continuous casting mold, *ISIJ Int.* 41(2001) 1229-1235.
2. L. Bettelman. Effect of mold EMS design on billet casting productivity and product quality, *Can. Metall. Q.* 38(2000) 301-309.
3. Leonardo B. Trindade, Antonio C. F. Vilela. Numerical Model of Electromagnetic Stirring for Continuous Casting Billets, *IEEE Trans. Magn.* 38(2002) 3658-3660.

4. Yu Haiqi, Zhu Miaoyong. Influence of electromagnetic stirring on the transport phenomena in round billet continuous casting mold and macrostructure of high carbon steel billet, *Ironmaking Steelmaking*. 39(2012) 574-584.
5. Wang Xiao-dong, Li Ting-ju, Jin Jun-ze. Study of well balanced phase of harmonic electromagnetic field, *J. Dalian Univ. Tech.* 42(2002) 75-78.

Microstructure Evolution of Mg-Zn-Zr-Nd Magnesium Alloy during Partial Remelting

Yuanyuan Wan†, Yanbin Wang, Meiqi Lu, Xiaosong Li and Jianquan Tao
Southwest Technique and Engineering Institute, Chongqing, 400039, China
†E-mail: wyy789000@sina.com

In this paper, extrusion has been utilized to predeform ZK60 with Nd addition. Partial remelting was carried out at 589ºC for holding times in the range 0-90min. During partial remelting, extruded microstructure rapidly evolutes into recrystallised grains and liquid occurs initially at grain boundaries. With prolonging holding time, grains coarsen and liquid film gradually changes from continuous state into discontinuous state, resulting in the agglomeration between adjacent grains. Local melting was caused by non-uniform deformation in the alloys during extrusion.

Keywords: Semi-Solid Microstructure; Extrusion; Partial Remelting; Magnesium Alloy.

1. Introduction

Semi-solid processing is a relatively new technology directed to the production of structural components [1-2]. Compared with conventional casting and forging, semi-solid processing shows several potential advantages, such as the reduction of porosity, less entrapped air and low forging force [3-4]. The main disadvantage of the process is that the starting material must be treated in such away that the microstructure is spheroidal rather than dendritic when reheated to the semi-solid state. A number of methods, such as magnetohydrodynamic (MHD) stirring, spray casting (SC), semi-solid thermal transformation (SSTT), Strain induced melt activation (SIMA) and recrystallisation and partial remelting (RAP) have been reported to produce alloys with a spheroidal microstructure. These methods were summarized in Atkinson [1].

Among all these methods to produce semi-solid billets, SIMA and RAP have several potential advantages. They omit the procedure of molten metal treatment and are applicable for both low and high melting point alloys [5]. During SIMA the RAP, the oxidation and combustion problems of magnesium alloys can be effectively reduced to attain pure alloys and make the semi-solid processing easy [6]. The main similarity between the two routes is that a critical level of strain must be introduced into the material through deformation.

Several researchers have reported on the microstructural evolution of magnesium alloys during partial remelting [7-8]. Zhao et al. [7] had introduced equal channel angular extrusion (ECAE) into the SIMA process to replace conventional upset or extrusion. They found that as-cast ZK60-RE magnesium alloys are successfully extruded by ECAE. The semi-solid microstructure of ECAE-formed ZK60-RE consists of fine and spheroidal grains surrounded by grain boundary liquid films. Chen et al. [8] found that the eutectic melting activation energy of ECAE-formed alloy decreases with increasing numbers of extrusion passes.

The present paper aims to produce spheroidal microstructure of ZK60-Nd alloys by the RAP route. Furthermore, the model for the changes of shape factor during particle remelting is proposed on the basis of experiment results.

2. Experimental

A ZK60 alloy was chosen as the master alloy. The ZK60-Nd alloy was produced by melting the ZK60 alloy in an electric resistance furnace being flushed continuously with SF_6 and CO_2 gas (mixing ratio was 1:100) at 740ºC, then the Nd element in the form of interalloy were added into the melt. The melt was held at 740ºC for about 15min to ensure that the Nd element was completely dissolved. After that the melt was poured in a metal mold to form a rod with a diameter of 60mm and a length of 160mm. The chemical compositions of ZK60 and ZK60-Nd alloys, which were determined by an inductively coupled plasma analyzer respectively, are listed in Table 1. The liquidus and solidus of the ZK60-Nd alloy are 446ºC and 639ºC respectively, by differential scanning calorimetry (DSC) experiment at 4ºCmin^{-1}.

Table 1. The compositions of ZK60 and ZK60-Nd magnesium alloys (wt.%).

Alloy	Mg	Zn	Zr	Nd
ZK60	Balance	4.89	0.62	—
ZK60-Nd	Balance	5.17	0.54	0.89

The as-cast ZK60-Nd alloy was machined into a rod with a diameter of 52mm and a length of 80mm for extrusion. During extrusion, as-cast ZK60-Nd alloys were extruded into bars with a diameter of 13mm at 200ºC. The extrusion ratio was 16:1. During partial remelting experiments, the extruded samples with a diameter of 10mm and a length of 12mm were heated in a resistance furnace controlled by PID, with which the fluctuation of temperature was controlled within ±1ºC. Partial remelting experiments were set to 589ºC for different holding times, ranging from 0min to 90min at the heating rate of 0.5ºC/s. In this

work, the beginning time of isothermal holding was defined as 0 min. At the same time, to examine the effect of heating rate on microstructure evolution, partial remelting of samples at the heating rate of 2ºC/s was also studied. Samples were protected by an atmosphere of Ar gas during partial remelting. When a sample was held to the predetermined times, it was taken out immediately for water quenching. Partial remelted samples were grounded and polished by standard metallographic techniques. 4% HNO_3 aqueous solution was used to etch partial remelted samples. The microstructure observation was carried out in a metallurgical microscope. Grain size was measured using the equivalent diameter in this paper. The equivalent diameter is the diameter of a circle of which the area is equal to the area of the grain. For each sample, measurements were taken from the whole sectioned area excluding regions close to the edges, with 220–320 grains counted per sample. The solid fraction (f_s) was calculated by the Sheil equation. Size and globularity of solid particles were calculated in each case by using the equations (1) and (2) [9].

$$D_{eq} = \frac{\sum_{N=1}^{N} \sqrt{4A/\pi}}{N} \tag{1}$$

$$F = \frac{\sum_{N=1}^{N} \frac{4\pi A}{P^2}}{N} \tag{2}$$

where A and P are area and perimeter of solid particles respectively and N is the number of particles.

3. Results and Discussion

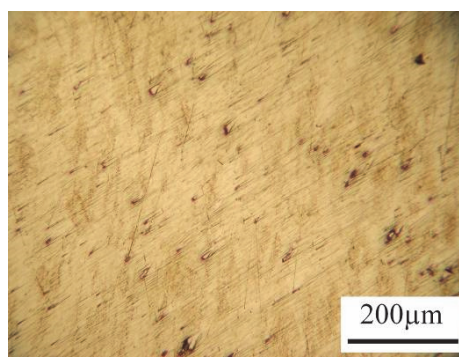


Fig. 1. Typical microstructure of the extruded ZK60-Nd alloy.

A typical starting material microstructure is shown in Fig. 1. The grains are unrecrystallised as shown by the contrast variations within the elongated grains. The material can therefore be classified as being consistent with the RAP route (see the section of Introduction).

Fig. 2 shows the semi-solid microstructures of the ZK60-Nd alloy after partial remelting at 589ºC for different holding times: 0min, 10min, 40min, 60min and 90min. As shown in Fig. 2 (a), the deformed structure rapidly evolutes into recrystallised grains at 589ºC for 0min. The average grain size is about 38μm. Optical image analysis indicates that the liquid fraction is about 0.19. It is obvious that recrystallisation leads to the disappearance of the deformed microstructure. After extrusion, a small portion of distortion energy remains stored in the ZK60-Nd alloy. The distortion energy is mainly in the form of elastic energy in the strain fields surrounding vacancies and dislocations and point defects generated during the extrusion process. Since dislocation, vacancies and point defects possess excess energy, there is a thermodynamic driving force for the elimination of dislocation to reduce the total free energy of the system [10]. During rise in temperature, recovery and recrystallisation progressively occur at the expense of consuming distortion energy. When heating temperature increases above the eutectic temperature, the liquid phase forms at grain boundaries. As shown in Fig. 2 (b), with the future increase of the holding time, the grain boundary liquid film was thicker and liquid fraction is about 0.22. Globular grains, with an average size of about 47 μm, were surrounded by liquid film. When the holding time was extended to 40min, the globular grains remarkably grew and then interconnected, which resulted in the agglomeration of solid particles, as shown in Fig. 2 (c). At this time, the fraction of liquid fraction is about 0.23. After 40 min, although solid particles still grew by agglomeration, the liquid fraction was almost not changed, which indicated that the liquid and solid phases had been in the state of dynamic equilibrium.

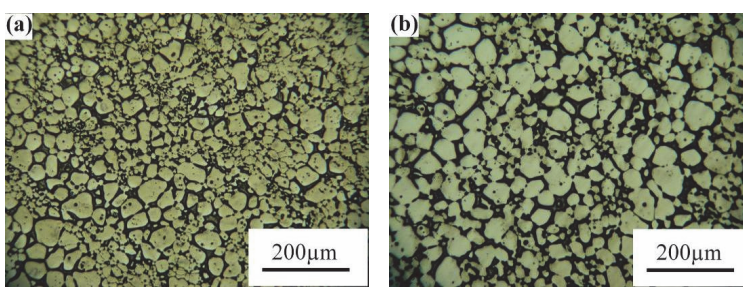


Fig. 2. Optical micrograph of extruded formed ZK60-Nd partial remelted at 589ºC at the rate of 0.5ºC/s for (a) 0min, (b) 10min, (c) 40min, (d) 60min and (e) 90min.

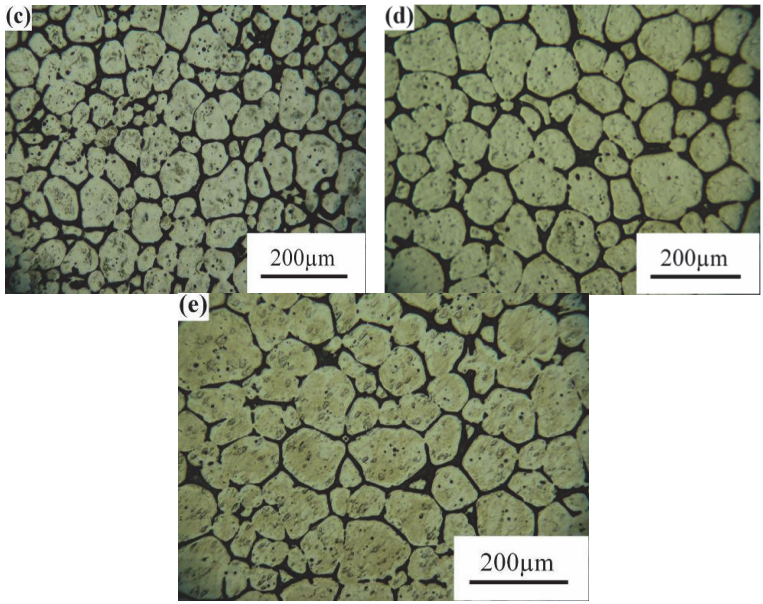


Fig. 2. (*Continued*)

Fig. 3 shows the microstructure of as-cast ZK60-Nd for 40min at 589ºC. As shown in Fig. 2, the microstructure of extruded sample had fully recrystallised grains with almost negligible contents of entrapped liquid phase. However, as shown in Fig. 3, the as-cast sample shows irregular shapes and a large amount of entrapped liquid phase. Comparing Fig. 2 with Fig. 3, it can be concluded that the microstructure spheroidization is indeed induced by the previous extrusion deformation. The extrusion ratio of 16:1 was adequate for producing ideal semi-solid microstructure.

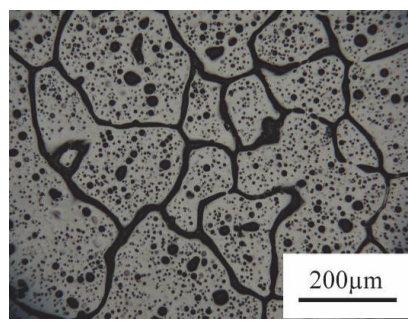


Fig. 3. Microstructure of as-cast ZK60-Nd alloy after partial remelting at the rate of 0.5ºC/s for 40min at 589ºC.

Fig. 4 shows the relationship between shape factor and holding time during partial remelting. According to Eq. 2, shape factor of perfectly globular particles is one. As shown in Fig. 4, increase of holding time from 0min to 60min increases the value of shape factor while the shape factor decreases as holding time increases from 60min to 90min. The change of shape factor was probably a result of change of liquid film thickness.

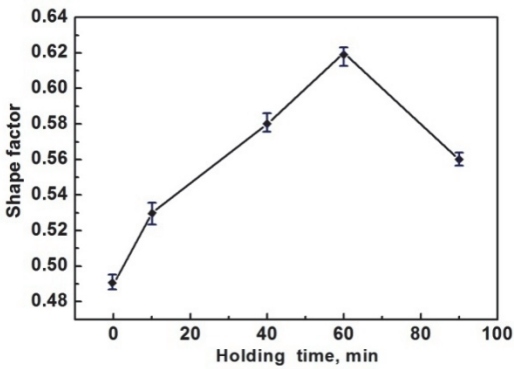


Fig. 4. The shape factor of solid particles vs. holding time.

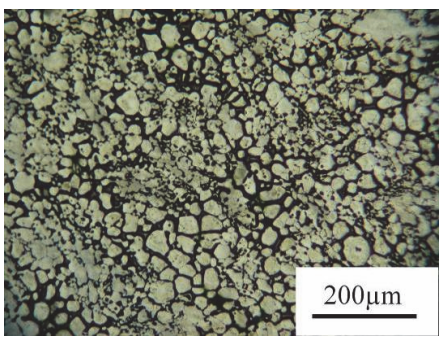


Fig. 5. Microstructure of the extruded ZK60+RE alloy partial remelting in the semi-solid state at the rate of 2ºC/s at 589ºC for 0 min.

Fig. 5 is the microstructure of the extruded ZK60-Nd alloy partial remelting in the semi-solid state at the rate of 2ºC/s at 589ºC for 0 min. As shown in Fig. 5, the liquid phase is distributed irregularly and appears in certain areas. Comparing Fig. 5 with Fig. 2(a), the phenomenon of local melting is more obvious at higher heating rate. Local melting is a special phenomenon of recrystallisation in the semi-solid state. The main reason of local remelting is the non-uniform deformation in the alloys during the extrusion process. Inhomogeneous deformation during extrusion inevitably results in

heterogeneous structure. After extrusion, some areas with higher dislocation density have higher distortion energy, which will supply higher melting energy. Under this condition, local melting firstly occurs at this higher dislocation density region during partial remelting. When heating rate is relative low, the liquid have enough time to occur and surround recrystallised grains. Therefore, local melting is not obvious at relative low heating rate, as shown in Fig. 2(a).

4. Conclusions

The initial extruded alloys have a predominantly unrecrystallised structure. During partial remelting at 589ºC without holding, recrystallised grains are surrounded by continuous liquid films. With prolonging holding time, recrystallised grains gradually become globular. After the completion of grain spheroidization, recrystallised grains remarkably coarsen and liquid film first become thinner and then changes from continuous state into discontinuous state, which results in agglomeration between adjacent grains. The agglomeration between adjacent grains leads to decrease in degree of sphericity. Moreover, local melting is mainly caused by inhomogeneous deformation during extrusion.

References

1. ATKINSON H V. Modelling the semisolid processing of metallic alloys [J]. *Progress Material Science*, 2005, 50: 346-352.
2. ATKINSON H V, BURKE K, VANEETVELD G. Recrystallisation in the semi-solid state in 7075 aluminium alloy [J]. *Materials Science Engineering A*, 2008, 490: 267-268.
3. LUO S, CHEN Q, ZHAO Z. Effects of processing parameters on the microstructure of ECAE-formed AZ91D magnesium alloy in the semi-solid state [J]. *Journal of Alloys and Compounds*, 2009, 477: 602-607.
4. ZHAO Z, CHEN Q, WANG Y, SHU D. Effect of predeformation on semi-solid microstructure of ZK60+RE magnesium alloy [J]. *Transactions of Nonferrous Metals Society of China*, 2009, 19: 535-539.
5. ZHAO Z, CHEN Q, KANG F, SHU D. Microstructural evolution and tensile mechanical properties of thixoformed AZ91D magnesium alloy with the addition of yttrium [J]. *Journal of Alloys and Compounds*, 2009, 482: 455-467.
6. ZHAO Z, CHEN Q, HU C, HUANG S. Near-liquidus forging, partial remelting and thixoforging of an AZ91D+Y magnesium alloy [J]. *Journal of Alloys and Compounds*, 2009, 485: 455-467.

7. ZHAO Z, CHEN Q, WANG Y, SHU D. Microstructural evolution of an ECAE-formed ZK60-RE magnesium alloy in the semi-solid state [J]. *Materials Science Engineering A*, 2009, 506: 8-15.
8. CHEN Q, LUO S, ZHAO Z. Microstructural evolution of previously deformed AZ91D magnesium alloy during partial remelting [J]. *Journal of Alloys and Compounds*, 2009, 477: 726-731.
9. LIN H Q, WANG J G, WANG H Y, JIANG Q C. Effect of predeformation on the globular grains in AZ91D alloy during strain induced melt activation (SIMA) process [J]. *Journal of Alloys and Compounds*, 2007, 431: 141-147.
10. MANSON-WHITTON E D, STONE I C, JONES J R, GRANT P S, CANTOR B. Isothermal grain coarsening of spray formed alloys in the semi-solid state [J]. *Acta Materialia*, 2002, 50: 2517-2535.

Blood Compatibility of Oxidized Bacterial Cellulose/Silk Fibroin Composite Membrane

Shuaiyan Wang[a], Tao Huang[b],
School of Laboratory Medicine and Life Science, Wenzhou Medical University, Wenzhou 325035, China
[a] E-mail: shuaiyanwang@126.com, [b] E-mail: htao1314179@163.com,

Liyuan Sheng[c], Chen Lai[d], Tingfei Xi[e] *
ShenZhen Key Laboratory of Human Tissue Regeneration and Repair, Shenzhen Institute of Peking University, Shenzhen 518057, China
[c] E-mail: lysheng@yeah.net, [d] E-mail:laichen1110@163.com,
*[*e] E-mail: xitingfei@pku.edu.cn*

In this work, the oxidized bacterial cellulose (BC) was modified by silk fibroin (SF) to improve its blood compatibility. The oxidized BC pellicles were added to the aqueous silk fibroin solution containing crosslinking agents at room temperature for different times to obtain the composite membranes. The structure of the new composites membranes were evaluated by X-ray photoelectron spectroscopy (XPS). The results showed that silk fibroins were successfully fabricated on the oxidized bacterial cellulose (OBC) membranes surfaces, and the analysis on the quantity of the elements exhibits that the atom percentage of nitrogen reaches its maximum value at 24 h. The platelet adhesion, hemolytic test and protein adsorption results exhibited that the OBC/SF had significantly excellent blood compatibility featured by lower platelet adhesion and protein adsorption without causing hemolysis. This work provides a simple approach to fabricate composite biomaterials which exhibit wide biomedical application prospects.

Keywords: Bacterial cellulose; Oxidation; Silk fibroin; Composite membrane.

1. Introduction

Bacterial cellulose (BC) is a form of cellulose secreted by organisms such as Acetobacter, Acanthamoeba, Achromobacter and Zoogloea. Similar with the molecular structure of plant cellulose, bacterial cellulose is a linear syndiotactic homopolymer composed of D-anhydroglucopyranose units (AGU), which are linked together by β-1,4-glycosidic bonds. However, different from the common plant cellulose, BC has higher purity, crystallinity, high thermal stability (250-300ºC), good biocompatibility, good water retention capacity and high

* Corresponding author.

mechanical properties. Malm[1] has proven that biosynthetic small caliber vascular grafts made from BC are effective for only up to 13 months in sheep carotid arteries. Due to its compact nanomesh structure may prevent cell migration into scaffolds or sponges composed of it, preventing it in certain applications. The C6 primary hydroxyls of bacterial cellulose are selectively oxidized to form carboxylate groups using the TEMPO/NaClO/$NaClO_2$ system[2]. In result, the hydrogen bonds between nanofibers are destroyed, the internal structure becomes less compact. But oxidized bacterial cellulose membranes could cause thrombus formation. To solve the problem, a kind of protein should be coated on the OBC membranes surfaces. Silk fibroin (SF) is a natural polymer fibrous protein extracted from silk and is biocompatible, biodegradable, non-toxic, and possesses a certain degree of brittleness. Presently, many researches have been carried out on SF using in artificial blood vessels[3]. OBC and SF, which are both naturally derived, possess a strong affinity for cells and can provide the approximate extracellular matrix scaffold conditions necessary for growth and development within the body.

2. Experimental Procedure

2.1. *The oxidized bacterial cellulose / silk fibroin composite membranes and characterization*

The pellicles were suspended in a 0.05 M phosphate buffer solution. TEMPO, $NaClO_2$ and NaClO were added to the solution. The suspension was stirred at approximately 60ºC for 12 h. The composite membranes were prepared by adding 25 ml of the aqueous 10% (w/v) silk fibroin solution containing crosslinking agents to the oxidized bacterial cellulose pellicles at room temperature for 12 h, 24h, 36h and 48h.

XPS were recorded with a Kratos AXIS 165 electron spectrometer (Japan) using monochromated Al Kα X-ray irradiation at 350 W. The standard take-off angle used for analysis was 45º.

2.2. *Hemolysis assay and Platelet adhesion[4] Protein adsorption*

The membranes were then immersed in 1 mL of a physiological buffered saline containing bovine serum albumin (BSA, 1 mg/mL) at 37ºC for 2 h. The concentration of the free of proteins was determined by using pierce™ BCA Protein Assay Reagent Kit at 562 nm. The adsorbed proteins amounts were the difference value between the total proteins (1mg) and measured proteins (the free of proteins).

3. Results and Discussion

The wide-scan XPS spectra of samples prepared under various conditions are shown in Fig.1. Due to the main composition of polysaccharides in BC, its XPS result exhibits strong peaks of oxygen and carbon. Though the peaks of OBC become weak, it is almost the similar as that of BC. The silk fibroin strengthening has introduced the peak of nitrogen in the composite membrane, which should be ascribed to the introducing of nitrogen during adsorption of SF. Such a result also indicates that the formation of peptide bond (–NH–CO–) in the composite. In general, the synthesis time could generate little effect on the composition. The analysis on the quantity of the elements exhibits that the atom percentage of nitrogen reaches its maximum value at 24 h, as shown in Table 1. However, the percentage of carbon (C1s) of the OBC/SF composite membrane exhibits an increases tendency, but the percentage of oxygen (O1s) decreases gradually, compared with that of OBC. The O/C ratio in OBC is little higher than that in BC. It is interesting that the OBC/SF composite membrane reacted for 24 h has the highest content of oxygen and nitrogen.

Hemolysis is defined as the release of hemoglobin into plasma due to damage of erythrocytes films, which is directly related to the blood compatibility of the implant materials. Results obtained from the hemolytic rate experiment are shown in Table 2. Hemolysis rates of the samples in vitro are all less than 5%, which indicates that they all have good blood compatibility, based on the requirements of ISO 10993. Generally, the observed hemolysis data are well consistent with the results of protein adhesion test displayed as following.

The amount of protein adsorbed on the surface of the implant material is one of the dominant factors in evaluating its blood compatibility of biomaterials. The results of the BSA adsorption tests are showed in Fig.2. It can be clearly seen that compared with the OBC, the OBC/SF composite membrane absorbs fewer proteins and moreover with the crosslinking time increasing, the absorbed protein of OBC/SF decreases further, especially OBC/SF with crosslinking time of 36 h. This reduction may be attributed to SF immobilized on the surface of OBC films, resulting in charge repulsion between silk fibroin and albumin, because both proteins show negative charge under the condition of pH 7.4. In other word, the carboxylate groups on OBC may have a strong interaction with proteins, so there are more proteins adsorbed on OBC, compared with the composite membrane. Therefore, the presence of SF in the composite membrane prevents the occurrence of such phenomenon. As expected, hydrogen bonding between bacterial cellulose generates a strong epulsive force to protein at specific separation distances[5]. Albumin, the concentration of which is the highest in plasma, transports many small molecules in the blood (for instance,

bilirubin, calcium, progesterone, and drugs), and it is prime importance in maintaining the osmotic pressure of the blood. A lower amount of protein absorbed indicated a lower amount of fibrinogen absorbed at the same time[4]. Then it can be concluded that OBC/SF crosslinking time for 36 h has a better blood compatibility, compared to others.

The observation on the composite membrane surface after platelet adhesion is shown in Fig.3. Clearly, the OBC exhibits higher platelet numbers and more platelet aggregation. Because platelet adhesion is thought to be the next step to protein adsorption with a link by link relationship in thrombosis. So the higher protein adsorption on the surface would result in the higher activation and adhesion of platelets. However, when the SF layer is coated on the surface of OBC, there is almost no platelet adhered on the surface (Fig.3c). Furthermore, almost no obvious difference could be observed on platelet adhesion among surfaces with different crosslinking times (Fig.3b-e), which implies that all SF surfaces have excellent resistance to platelet adhesion. This is incomplete in agreement with the tendency of the protein adsorption above. So perhaps it is the conformation of the adsorbed fibrinogen, more than its amount, takes the primary responsibility for platelet adhesion and activation[6].

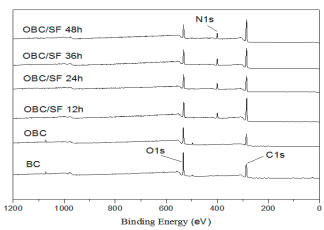


Fig.1 XPS spectra of samples prepared under different crosslinking time.

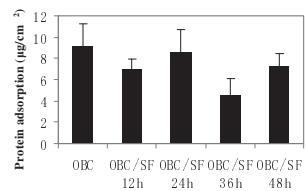


Fig.2 Amount of protein adsorbed on the OBC substrates. Data from three separate experiment are shown as mean±SD.

Table 1. Elemental surface composition of samples.

Sample	element （atom %）			atomic ratio
	C1s	O1s	N1s	O/C
BC	62.4	34.5	/	0.55
OBC	61.5	34.5	/	0.56
OBC/SF 12h	70.3	19.3	9.2	0.27
OBC/SF 24h	66.9	20.2	11.9	0.3
OBC/SF 36h	69.6	19	11	0.27
OBC/SF 48h	72.6	16.8	9.8	0.23

Table 2. Hemolysis rate and standard deviation of sample.

sample	hemolysis rate (%)	SD
OBC	1.22	0.0082
OBC/SF 12h	1.65	0.0072
OBC/SF 24h	0.93	0.0039
OBC/SF 36h	0.55	0.0058
OBC/SF 48h	0.55	0.0038

4. Conclusions

The bacterial cellulose was performed by chemical method, and then the oxidized bacterial cellulose was modified by silk fibroin with different crosslinking times. XPS element analysis made it sure that the SF was successfully fabricated on OBC, and the analysis on the quantity of the elements exhibits that the atom percentage of nitrogen reaches its maximum value at 24 h. Meanwhile, the results of platelet adhesion, hemolysis test and protein adsorption indicated the OBC/SF composite membranes had blood compatibility.

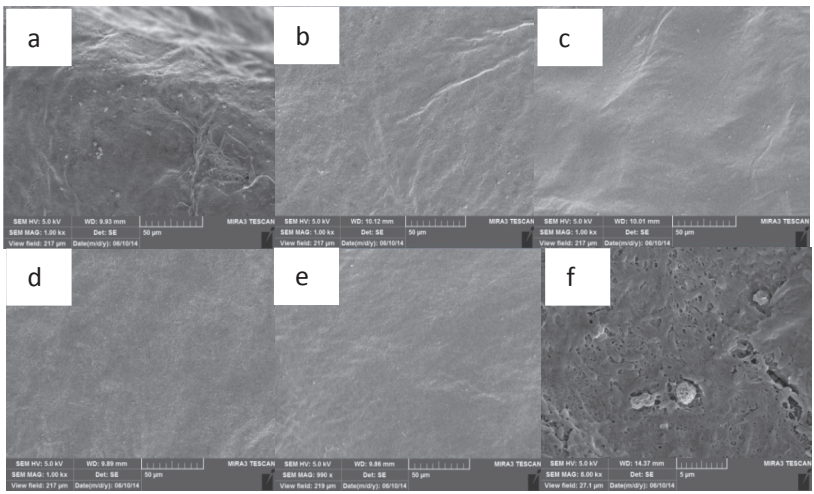


Fig.3 SEM photographs of OBC (a), OBC/SF 12h (b), OBC/SF 24h (c), OBC/SF 36h (d), OBC/SF 48h (e) and platelet adhesion with the magnification of ×8000 (f).

Acknowledgements

This study has been supported by the National "Twelfth Five-Year" Plan for Science & Technology Support, small diameter artificial blood vessels (NO.2012BAI18B06 and HZ20140419114), the Shenzhen International Cooperative Research Project (GJHZ20140419114548516) and the Strategic New Industry Development Special Foundation of Shenzhen (JCYJ20130402172114948 and JCYJ20130402164725011).

Reference

1. C.J. Malm, B. Risberg and A. Bodin, Small calibre biosynthetic bacterial cellulose blood vessels: 13-months patency in a sheep model, Scand. *Cardiovasc. J.*. 46 (2012) 57-62.
2. T. Saito, Y. Okita, T.T. Nge, J. Sugiyama and A. Isogai, TEMPO-mediated oxidation of native cellulose: microscopic analysis of fibrous fractions in the oxidized products, *Carbohydr. Polym*.. 65 (2006) 435-440.
3. I. Cattaneo, M. Figliuzzi, N. Azzollini, V. Catto and S. Farè, In vivo regeneration of elastic lamina on fibroin biodegradable vascular scaffold, *Int. J. Artif. Organs*. 36 (2013) 166-174.
4. M. Wang, J. Yuan, X.B. Huang, X.M. Cai, L. Li and J. Shen, Grafting of carboxybetaine brush onto cellulose membranes via surface-initiated ARGET-ATRP for improving blood compatibility, *Colloids and Surfaces B*: Biointerfaces. 103 (2013) 52-58.
5. P.S. Liu, Q. Chen, X. Liu, B. Yuan, S.S. Wu, J. Shen, and S.C. Lin, Grafting of Zwitterion from Cellulose Membranes via ATRP for Improving Blood Compatibility, *Biomacromolecules*. 10 (2009) 2809-2816.
6. S.N. Rodrigues, I.C. Goncalves, M.C.L. Martins, M.A. Barbosa and B.D. Ranter, Fibrinogen adsorption, platelet adhesion and activation on mixed hydroxyl-/methyl-terminated self-assembled monolayers', *Biomaterials*, 2006, 27, 5357-5367.

Characterization and Properties of TEMPO-oxidized Bacterial Cellulose-Hydroxypatite for Osseous Regeneration

Tao Huang[a], Shuaiyan Wang[b]

School of Laboratory Medicine and Life Science, Wenzhou Medical University, Wenzhou 325035, China

E-mail: [a]htao1314179@163.com; [b]wangshuaiyan_leng@163.com

Liyuan Sheng[c], Chen Lai[d], Tingfei Xi[e*]

ShenZhen Key Laboratory of Human Tissue Regeneration and Repair, Shenzhen Institute of Peking University, Shenzhen 518057, China

E-mail: [c]lysheng@yeah.net; [d]laichen1110@163.com; [e]xitingfei@pku.edu.cn*

TEMPO-oxidized bacterial cellulose (TBC)/ hydroxypatite (HA) composites prepared by physical synthesis was characterized. And the porosity and protein adsorption was measured to evaluate the properties of the composites. Fourier transform infrared (FTIR) spectroscopy and scanning electron microscopy (SEM) images demonstrated that HA formed with appearing the peak of PO_4^{3-}. The contact angles significantly decreased after oxidation and physical blending. Meanwhile the surface energy of TBC-HA increased clearly compared with TBC. After blending, the porosity increased and the maximum was 86.8% in the weight ratio of 1. The protein adsorption performed better after oxidation. And the protein entrapment efficiency (EE) of TBC was 22%. Base on this work, the TBC-HA composites would be demonstrated the potential application for osseous regeneration.

Keywords: Bacterial Cellulose; Hydroxypatite; Oxidation; Composite.

1. Introduction

Each year, 2 millions bone grafts are performed worldwide resulting in total health care costs of approximately $ 15 billions [1]. The bone repairing tissue engineering was the new treatment. While the approach lack of appropriate materials, its application was limited. In recent years, a new strategy to fabricate the scaffolds with more than two components with different physicochemical properties was proposed, when a one-component scaffold cannot suffice.

The biological bone was made up of collagen matrix reinforced with HA crystals [2]. BC was an attractive alternative to mimic collagen fibers because of

* Corresponding author.

its good biocompatibility, high tensile strength, fine fibril network, high crystallinity and moldability [3]. In addition, HA was a ceramic with chemical composition similar to the mineral component of bone that has received attention for its biocompatibility and osteoconductivety [4]. The HA was considered to promote bone formation in the defect, provide stiffness, and be replaced over time as new bone forms in its place.

In this study, based on TEMPO-oxidized modification of BC pulp, TBC-HA composites were fabricated by physical blending. The composites were characterized by FTIR, FE-SEM, contact angle and surface free energy. And its porosity and protein adsorption were analyzed.

2. Experimental Material

2 g dry BC pulp was suspended in 400ml sodium phosphate buffer (0.5 M/L, pH=6.8) using a homogenizer with the speed of 16000 rpm at room temperature. TEMPO (0.06 g), NaClO2 (3 g) were dissolved in the resulting suspension. The 0.1 M/L sodium hypochlorite was used as the oxidation medium, and was added to the flask at one step. Then the suspension was stirred at 60ºC for 6 h. At the end of a predetermined reaction time, the oxidation process was stopped by 10ml ethanol. Then the TBC was thoroughly washed four times with water by filtration and lyophilized.

Various weight rations of dry TBC and HA powder (0.25, 0.5, 1) were physical blending. The products were installed in a cylindrical mold. Then we frozen the mold at -25ºC for 10 h and lyophilized for further analysis.

2.1. *Characterizations*

FT-IR spectra of samples were recorded using a Nicolet 6700 spectrometer (Thermo USA) with the wave number range of 4000-650 cm-1. The morphologies of the samples were observed by using FE-SEM. Prior to analysis, the samples sputter-coated with platinum via sputtering debate.

The water and glycerin contact angles of the samples were measured with an OCA20 data physics instrument using the sessile drop technique. The polar and dispersive components of the samples surface energy were calculated using the Owens-Wendt approach.

2.2. *Properties*

The porosity were calculated from the mass of each cylindrical scaffold using the solvent displacement method by a solid density meter [5]. The dry scaffold sample was weighted (M1). M3 was the wet weight of the scaffold. It was

immersed in the dehydrated alcohol for 24h until it was saturated. Then we put the wet scaffold on suspension frame and weighted (M2). The porosity was calculated as follows:

$$\text{Porosity } (\%) = (M3\text{-}M1) / (M3\text{-}M2) \quad (1)$$

Entrapment efficiency (EE) which represented the amount of the protein adsorption of scaffold samples were weighted. It was calculated by the Eq. 2:

$$EE\ (\%) = (Wo\text{-}Wf) / Wo \quad (2)$$

where Wo was the amount of original protein content and Wf was the amount of protein content after adsorption. And the Wf was obtained according to the literature described [6].

3. Results and Discussion

The FTIR spectra of freeze-dried native BC, TBC and TBC-HA composites were shown in Fig. 1. After oxidation occurred, a band appeared at 1605 cm-1 which corresponded to C=O stretching vibrations in the COO– group [7], indicating the successful oxidation of the hydroxyl groups to carboxyls groups. The absorption bands at 1020cm-1 attributed to the stretching mode of PO43- appeared in Fig. 2 (c, d). Compared with the spectra of TBC, the bonds of O-H was shifted to low wavenumbers or disappeared, which may be attributed to a coordinate bond possibly formed between the HA and the hydroxyl bonds. The results showed that HA crystals deposited on the three dimensional fibrous network of TBC.

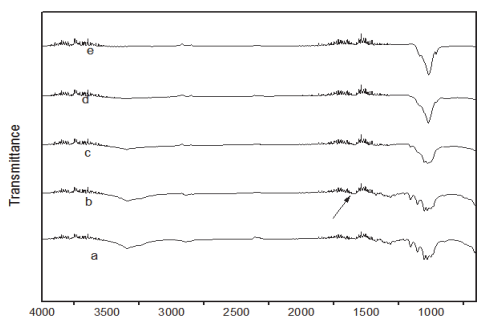


Fig. 1 FT-IR spectra of BC (a), TBC (b), TBC-HA 0.25 (c), TBC-HA 1 (d), HA (e)

SEM images of the samples were shown in Fig. 2. The BC and TBC had similar fibril morphology which demonstrated that oxidation did not disrupt the

integral structure of the polymer. And as shown in Fig. 3(a, b), BC and TBC had so ultrafine 3D nanoporous networks structure that they provided an excellent scaffold to deposit HA particles and facilitated cellular adherence for bone tissue engineering application. In the Fig. 3(c, d), it could be observed that the spiculate HA particles formed on the TBC matrix. And the amount of HA particles depositing on the TBC-HA 1 was more than that of TBC-HA 0.25. It had been claimed that the HA particles depositing on the fiber was favorable for adhesion and spreading of osteoblasts [8].

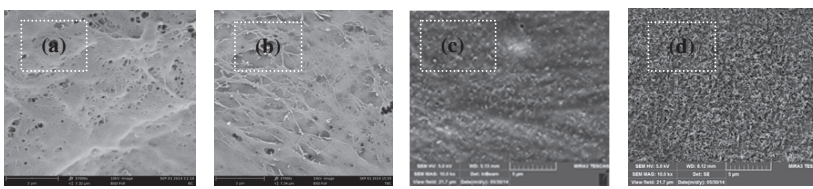


Fig. 2 SEM images of (a) pure BC, (b) TBC, (c) TBC-HA 0.25 and (d) TBC-HA 1

The contact angle significantly decreased for the TBC-HA composites discs (23.96°) than for BC discs (46.23) and TBC discs (62.30). This indicated that the hydrophilicity of TBC-HA was better than TBC and BC. Owing to HA particles arranging relatively loose, it had more lacuna with water molecules accessing easily. Rapid hydration of the material could facilitate the adhesion of biomolecules and enhance bone apposition in the early healing phase.

The surface energy of the various samples was shown in Fig. 3. The increase of the polar component of TBC was due to the substitution of the hydroxyl groups by more polar carboxylate groups. The polar components clearly increased with the adding of HA. Polar components included the interactions of the dipole and the hydrogen bonding. The introduction of inorganic which had the polar and hydrogen bonding resulted in the rise of the polar components.

The porosity of the scaffolds was an important factor that affected cellular activity and tissue regeneration, that was, sufficient porosity facilitated diffusion of nutrients and clearance of wastes. The porosity for different samples was reported in Fig. 4. After oxidation, the porosity was significantly lower. And accompanied by the adding of HA, the porosity of composites scaffold increased. This was due to the formation of the HA crystal which loosely arranged and had many lacunas [9]. Meanwhile the HA crystal was prone to reunite which produced more porous. In addition, the porosity of the scaffold was also high enough for the application in tissue engineering.

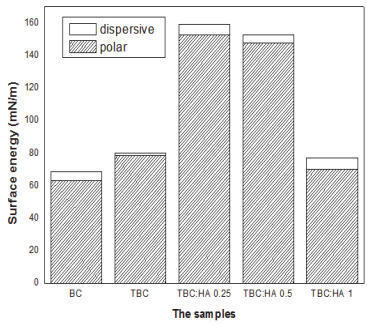


Fig. 3 The surface free energy of the samples

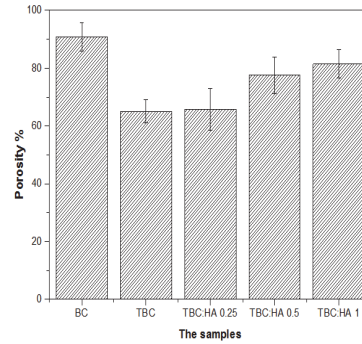


Fig. 4 Porosity of the scaffold (n=3)

The interaction between cells and materials was achieved by protein adsorption on the surface of materials. So cells adhesion strength was generally considered to have relation with protein adsorption. The results of the protein entrapment efficiency were shown in Fig. 5. It could be clearly seen that the entrapment efficiency drastically increased in TBC. To a certain extent, this increase was attributed to anionic carboxyl which can attract the protein. While the entrapment efficiency decreased with the increase of HA. This reduction may be attributed to the pore size decreasing with the addition of HA. The higher entrapment efficiency indicated cells adhesion strength was stronger. Hence, it could be concluded that TBC and TBC-HA (0.25) had a better protein adsorption.

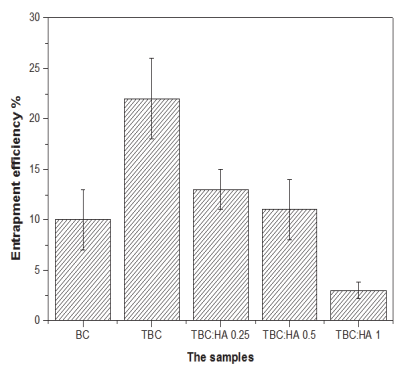


Fig. 5 The protein entrapment efficiency (EE) of scaffold samples

4. Conclusions

FTIR and SEM indicated that BC was oxidized and the HA deposited on TBC. The contact angle demonstrated the hydrophilicity increased with the oxidation

and physical blend occurring. It can be known that HA could increase the surface free energy. The amount of protein adsorption was most in TBC. And the porosity of composites had met the requirement of bone repair. In conclusion, the novel TBC-HA composite will have a good prospect as the bone biomaterial substitute.

Acknowledgements

This study has been supported by the National "Twelfth Five-Year" Plan for Science & Technology Support, small diameter artificial blood vessels (NO.2012BAI18B06 and 2012BAI18B05), the Shenzhen International Cooperative Research Project (GJHZ20140419114548516) and the Strategic New Industry Development Special Foundation of Shenzhen (JCYJ20130402172114948 and JCYJ20130402164725011).

References

1. J. Will, R. Melche, N. Travitzky, U. Kneser, E. Polykandriotis and P. Greil, Porous ceramic bone scaffolds for vascularized bone tissue regeneration, *J. Mater. Sci.*. 19 (2008) 2781-2791.
2. S.A. Hutchens, S.B. Roberto, R.E. Barbara and J.R. Claudia, Biomimetic synthesis of calcium-deficient hydroxyapatite in a natural hydroge, *Biomaterials*. 27 (2006) 4661-4670.
3. Y.Z. Wan, Y. Huang, C.D. Yuan, S. Raman, Y. Zhu, H.J. Jiang, F. He and C. Gao, Biomimetic synthesis of hydroxyapatite/bacterial cellulose nanocomposites for biomedical application, *Mater. Sci. Eng. C*. 27 (2007) 855-864.
4. R.W. Joseph, K.L. Sheeny and J.W.J. Amy, The mechanical properties and osteoconductivity of hydroxypatite bone scaffold with multi-scale porosity, *Biomaterial*. 28 (2007) 45-59.
5. R. Zhang and P.X. Ma, Poly(alpha-hydroxyl acids)/hydroxyapatite porous composites for bone-tissue engineering. I. Preparation and morphology, *J. Biomed. Mater.* Res. 44 (1999) 446-455.
6. P. Liu, S. Lin, Grafting of Zwitterion from cellulose membrance via ATRP for improving blood compatibility, *Biomacromodecules*. 10 (2009) 2809-2816.
7. H. Fukuzumi, T. Saito, Y. Okita and A. Isogai, Thermal stabilization of TEMPO-oxidized cellulose, *Polym Degrad Stab.* 95 (2010) 1502-1508.
8. R. Filmon, M.F. Basle, A. Barbier and D. Chappard, Adherence of osteoblast-like cells on calcospherites developed on abiomaterial

combining poly (2-hydroxyethyl) methacrylate and alkaline phosphatase, *Bone*. 20 (2002) 152-158.

9. Y. Wang, T. Wang, Y. Qi, Perparation and absorption mechanism of high water absorbing nano-hydroxyapatite, *Bulletin of the chinses ceramin society*. 33 (2014) 1146-1149.

Enhanced Crystallization Kinetics of Poly(lactic acid) with Carbon Nanotube (CNT) as the Nucleating Agent: An Evaluation using In-situ Measurement

Fei-Xue Lu[a], Bin Yang[b†], Ru Xia[c], Lei Hu, Ji-Bin Miao and Jia-Sheng Qian

College of Chemistry & Chemical Engineering, and Key Laboratory of Environment-Friendly Polymeric Materials of Anhui Province, Anhui University, Hefei 230601, Anhui, China

E-mail: [a]lufeixue26@163.com, [b†]yangbin@ahu.edu.cn, [c]xiarucn@sina.com

Poly (lactic acid) (PLA)/carbon nanotube (CNT) composites were prepared by melt blending method. The non-isothermal crystallization behavior of neat PLA and PLA/CNT cooled at different cooling medium temperatures were investigated and compared using density method in this study. Our results showed that the addition of CNT, even at a low concentration as 0.25 wt.%, could play a role as a heterogeneous nucleating agent during the non-isothermal crystallizing process of PLA and significantly enhance the crystallization of PLA/CNT composites. The *Avrami* model was employed to describe the non-isothermal crystallization process of PLA, indicating that CNT had a stronger effect to accelerate the overall cooling rate and crystallization rate, and increased the crystallinity of PLA composites.

Keywords: Poly (lactic acid); Crystallization Rate; Solidification; Carbon Nanotube.

1. Introduction

Poly lactic acid (PLA) has drawn increasing attentions in recent decades for its excellent mechanical properties, biodegradability and biocompatibility, and has been widely applied, including in biomedical and packaging area [1, 2]. However, there are still some shortcomings for PLA material, for instance, poor impact resistance, low toughness and inherent brittleness. In addition, owing to the relatively slow crystallization rate, the application of PLA in the industrial applications has been restricted, and the degradation rate of PLA also depends on the degree of crystallinity [3]. Therefore, to improve the crystallinity of PLA has become a research hotspot.

Adding nucleating agent (NA), an efficient way to promote the crystallization rate of PLA, can remarkably enhance crystallization temperature and the degree of crystallinity, which can further improve the heat resistance, mechanical properties

as well as the processability of the materials. *He*, et al [4] investigated the effect of phthalimide compound on the nonisothermal and isothermal crystallization behavior of PLA, and found that phthalimide can act as an efficient NA to promote the crystallization of PLA during the cooling stage from melt state. Cock et al[5]. argued that polycaprolactone (PCL) played an active role of nucleating agent for PLA in PLA/PCL blends. Su et al [6]. proposed that the modified carbon black (MCB) had a stronger effect on surface nucleation than on crystal growth of PLA.

In the present work, carbon nanotube (CNT) was used to act as NA for PLA. The paper mainly deals with the influence of different cooling temperature and 0.25 wt.% CNT on the crystallization rate and crystallinity of PLA. The results will be helpful for the processing and application of PLA.

2. Experimental

2.1. *Material*

The material PLA (Model: Nature Works 7032D) used in this study was provided by the Cargill Dow LLC, with a density of 1.252 g/cm^3, and a melt flow rate (MFR) of 8.0 g/10 min under 210°C/2 kg. Fig. 1 presents the P-V-T curves of the PLA resin, obtained using the 2d-Tait equation with the material parameters taken from the literature [7]. The CNT used are multi-walled (degree of purity >95%) were fabricated by *Shenzhen Harbor Nano Technology Co. Ltd*., with average diameter of 60~100 nm and length of 5~15 μm.

2.2. *Sample Preparation*

Firstly, soak the PLA resin and CNT powders within ethanol in an ultrasonic dispersion machine for 45 min. Subsequently, dry the mixture in an electric drying oven. After mixing the dried mixture in a high-speed mixer at the ambient temperature for 20 min, a twin screw extruder was used to prepare the polymer nano-composite (PLA with 0.25 wt % of CNT loading). The extruded composites were granulated for further study of solidification behaviors.

On the basis of our previous work [8], the experimental set-up in this study was illustrated in Fig. 2. The material was put at the bottom of a specially-designed metallic container, which was initially heated to 220°C and held for 15 min at 220°C. An armoring copper-constantan micro-thermocouple was fixed on the bracket with its tip inserted into the PLA melt at half the thickness. At the end of temperature holding stage, quickly move the metallic container into the reservoir full of cooling medium, and the water flows into the container through the holes on the metallic wall and flooded over the melt. The decay of temperature during the

whole cooling stage was recorded by Keithley-2700 Data Acquisition System (DAS) with a sampling time of 1s.

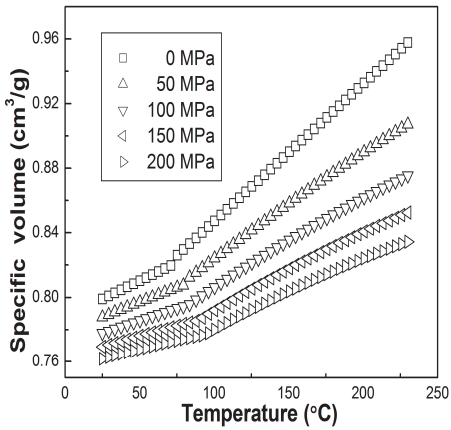


Fig. 1. The P-V-T curves of PLA (Nature Works 7032D).

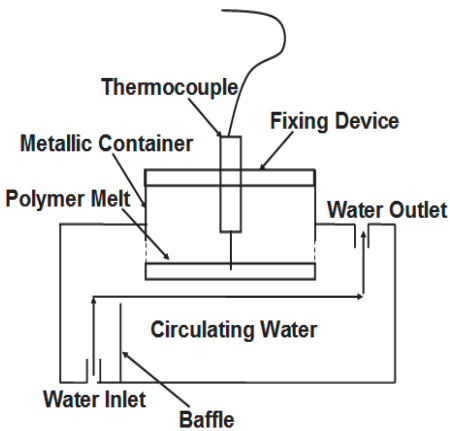


Fig. 2. Schematic of the experimental instrument for *in-situ* temperature measurement.

3. Result and Discussion

Fig. 3 illustrated the real-time temperature decay curves of PLA and PLA/0.25 wt.% CNT under different cooling medium temperature conditions. It can be seen that with the passage of time, the system temperature decreased rapidly and cooling rate also decreased gradually. In addition, the cooling rate of composites further increased with the addition of 0.25 wt.% CNT. The main reason was because the addition of 0.25 wt.% CNT could remarkably accelerate the

crystallization rate (as will be seen later). And higher crystallinity was favorable to the improvement of thermal conductivity of the material.

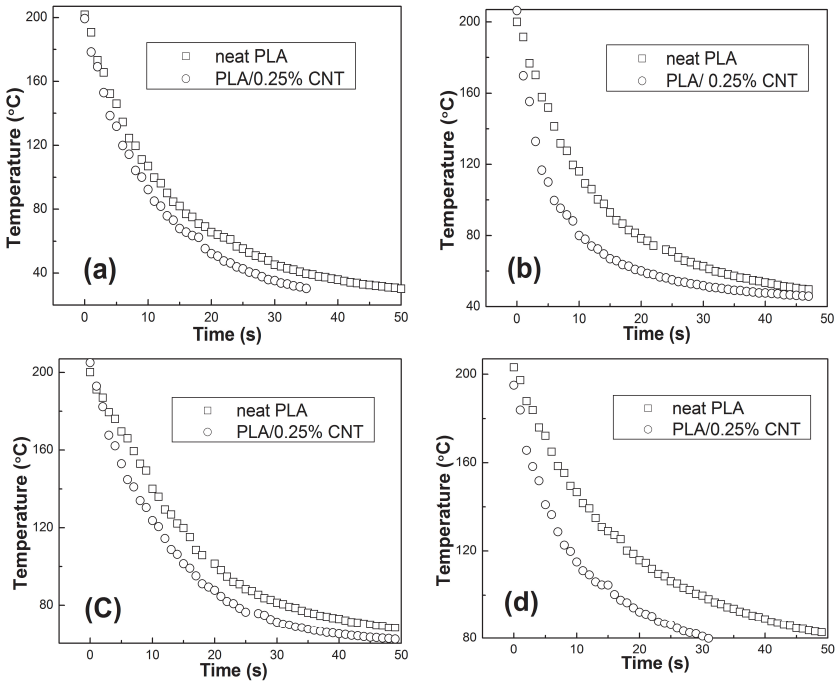


Fig. 3. Real-time temperature decay curves with cooling medium temperatures of 20°C (a), 40°C (b), 60°C (c) and 80°C (d).

Fig. 4 shows two double logarithmic curves of dimensionless temperature and time for neat PLA and PLA/0.25% CNT, obtained from Fig. 3. For better comparison, dimensionless temperature was adopted and defined in the following equation [9]:

$$\theta = (T\text{-}T_w)/(T_0\text{-}T_w) \quad (1)$$

where T_w and T_0 are the cooling medium temperature and the initial melt temperature, respectively. Fig. 4a displayed the change of $ln\ \theta$ with time ($ln\ t$) is relatively slow in the initial stage. In addition, the cooling curves at different cooling medium temperatures nearly coincide except for a later stage (i.e., the solid-state cooling period). The difference in cooling rates will lead to different crystallinities (will be discussed later), which further influence the latent heat released during crystallization. However, the released latent heat can slow down

the cooling rate to an extent. In consequence, the deviation of the cooling data in solid-state stage (cf. Fig. 4a) can be due to the degree that the cooling rate was slowed down during the crystallization process. In Fig. 4b, it can be seen that the cooling curves are separated from each other since the initial stage, which is totally different from Fig. 4a. The reason is that the addition of 0.25 wt.% CNT, which will alter the nucleating mechanism (from homogeneous to heterogeneous nucleation), and accelerate the crystallization rate (as will be illustrated later). The accelerating effects of the crystallization rate (due to heterogeneous nucleation) should also be subject to the cooling conditions (i.e., the different temperatures of cooling medium), which jointly resulted in the separation in cooling data of PLA/0.25 wt.% CNT throughout the cooling period.

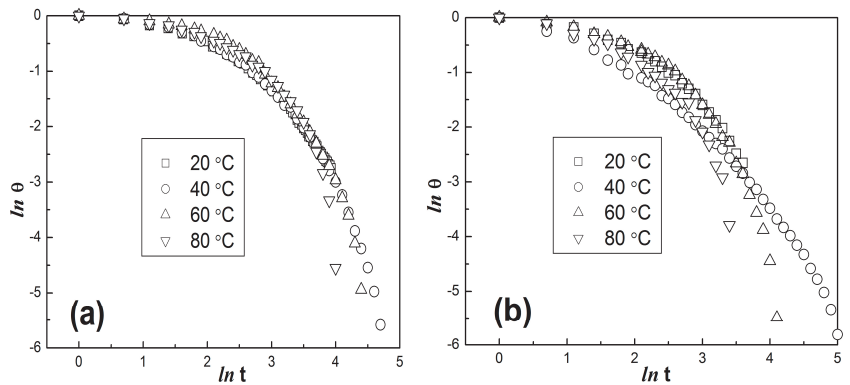


Fig. 4. The double logarithmic curves of neat PLA (a) and PLA/0.25% CNT (b), where θ is the dimensionless temperature.

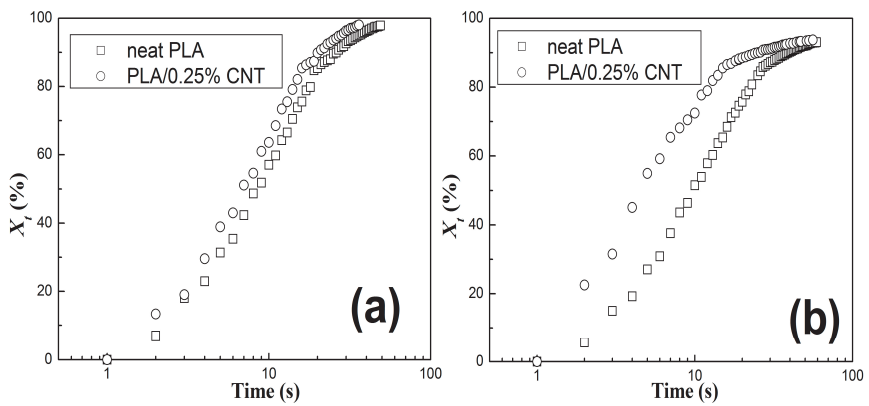


Fig. 5. Variation of relative crystallinity (Xt) as a function of time (t) under different cooling medium temperature condition. (a) Cooling medium temperature 20°C; (b) cooling medium temperature 40°C; (c) cooling medium temperature 60°C; (d) cooling medium temperature 80°C.

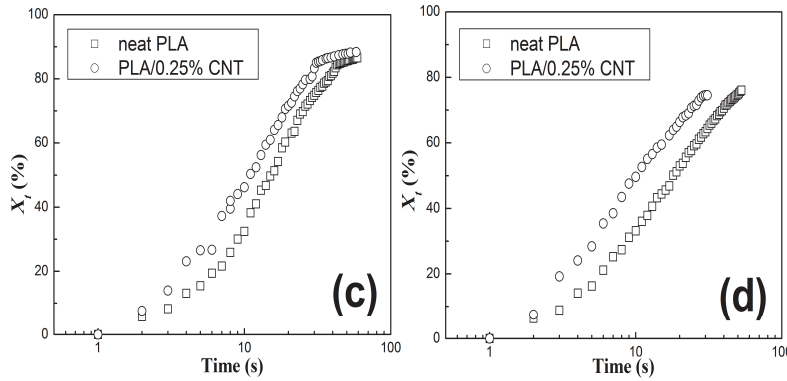


Fig. 5. (*Continued*)

The plots of relative crystallinity (X_t) as a function of time (t) under different cooling medium temperature conditions were shown in Fig. 5. The crystallinity was obtained by the following equation which was derived from the Avrami equation:

$$X_t = \frac{\rho_c}{\rho} \cdot \frac{\rho - \rho_a}{\rho_c - \rho_a} \times 100\% = \frac{V_a - V}{V_a - V_c} \times 100\% \quad (2)$$

where ρ_c = 1.252 g/cm^3 and ρ_a = 1.073 g/cm^3 are the densities of the 100% crystallized and amorphous zones of PLA, respectively. V_c and V_a are the specific volumes of the 100% crystallized and amorphous phases, respectively. When the temperature value is known under a specific pressure, the value of V can be thus determined (cf. Fig. 1). It can be seen in Fig. 5 that the crystallization rate of PLA was relatively high in the initial stage and remarkably slowed down with the elapsed time. When the crystallinity reached ~75%, the rate of crystallization tended to become smooth and steady. For a given time period, the higher the cooling medium temperature, the lower the crystallinity. This phenomenon is in accordance with earlier discussion (cf. Fig. 4). Furthermore, the addition of CNT considerably enhances the crystallization rate under various cooling conditions (whatever the cooling medium temperature), which indicates that CNT can play a role as a nucleating agent for the crystallization and increase the overall crystallization rate of PLA.

4. Conclusion

The influence of CNT on the non-isothermal crystallization behavior of PLA under different cooling medium temperatures were investigated and compared in this study. The results showed that the incorporation of a small amount of CNT

will significantly enhance the crystallization kinetics of PLA. The non-isothermal crystallizing data were analyzed using the Avrami model, which indicates that the addition of CNT alters the nucleating mechanism (from homogeneous to heterogeneous nucleation), and CNT can serve as an efficient nucleating agent for the crystallization to accelerate the overall cooling rate and crystallization rate, as well as increase the crystallinity of the PLA composites.

Acknowledgement

This work is supported by the National Natural Science Foundation of China (Grant No. 51203002, 51403001, 51273001), the Research Fund for the Doctoral Program of Higher Education of China (Grant No. 20113401110003), and the "211 Project" (J18520128) of Anhui University.

References

1. P.J. Pan, G.R. Shan, Y.Z. Bao. Enhanced nucleation and crystallization of poly (L-lactic acid) by lmmiscible blending with poly(vinylidene fluoride). *Industrial and Engineering Chemistry Research*, 2014, 53: 3148-3156.
2. R. Zhang, Y.M. Wang, K.J. Wang, G.Q. Zheng, Q. Li, C.Y. Shen. Crystallization of poly(lactic acid) accelerated by cyclodextrin complex as nucleating agent. *Polymer Bulletin*, 2013, 70: 195-206.
3. A. Auliawan, E.M. Woo. Nanocomposites based on vermiculite clay and ternary blend of poly(L-lactic acid), poly(methyl methacrylate), and poly(ethylene oxide). *Polymer Composites*, 2011, 32: 1916-1926.
4. D.R. He, Y.M. Wang, C.G. Shao, G.Q. Zheng, Q. Li, C.Y. Shen. Effect of phthalimide as an efficient nucleating agent on the crystallization kinetics of poly(lactic acid).*Polymer Testing*, 2013, 32: 1088-1093.
5. F. Cock, A.A. Cuadri, M. Garcia-Morales, P. Partal. Thermal, rheological and microstructural characterisation of commercial biodegradable polyesters. *Polymer Testing*, 2013, 32: 716-723.
6. Z.Z. Su, W.H. Guo, Y.J. Liu, Q.Y. Li, C.F. Wu. Non-isothermal crystallization kinetics of poly (lactic acid)/modified carbon black composite. *Polymer Bulletin*, 2009, 62: 629-642.
7. W.H. Guo, B. Yang, R. Xia, L.F. Su, J.B. Miao, J.S. Qian, P. Chen, X.K. Yu, Q.L. Zhang, S.Q. Deng. Three-dimensional simulation of the shrinkage behavior of injection-molded poly lactic acid (PLA): Effects of temperature, shear rate and part thickness. *Journal of Research Updates in Polymer Science*, 2013, 2: 168-173.

8. S.P. Liang, B. Yang, X.R. Fu, W. Yang, N. Sun, S. Hu, M.B. Yang. A simple method for forecast of cooling time of high density polyethylene during gas-assisted injection molding. *Journal of Applied Polymer Science*, 2010, 117: 729-735.
9. B. Yang, R. Xia, J.B. Miao, J.S. Qian, M.B. Yang, P. Chen. Probing solidification kinetics of high-density polyethylene during injection molding using an in-situ measurement technique. *Polymer Testing*, 2013, 32: 202-208.

Investigation on Trace Dysprosium and Boron Doping NiAl-based Eutectic Alloy Fabricated by Injection Casting

Liyuan Sheng[a†], Chen Lai[b], Qiaoli Wang[c] and Tingfei Xie[d]

Shenzhen Key Laboratory of Human Tissue Regeneration and Repair, Shenzhen Institute, Peking University, Shenzhen 518057, China

E-mail: [a†]lysheng@yeah.net, [b]laichen1110@163.com, [c]wangqiaoli@163.com, [d]w140933@pku.edu.cn

Fang Yang

Shenzhen Airlines, Shenzhen Bao'an International Airport, Shenzhen 518128, China

E-mail: fyang_sz@yeah.net

The NiAl-Cr(Mo) eutectic alloy doped with Dy and B was prepared by injection casting technique and its microstructure and mechanical properties have been investigated. The results exhibit that with the addition of Dy, the Ni_5Dy phase has been formed along the NiAl/Cr(Mo) phase boundaries in intercellular region. Microstructure of the injection-cast alloy gets well optimization, which can be characterized by the fine interlamellar spacing, high proportion of eutectic cell area and fine homogeneous distributed Ni_5Dy phase. Compared with the conventionally cast alloy, the room temperature mechanical properties of the injection-cast alloy get significant improvement, which can be attributed to the fine microstructure, the homogeneous distribution of the Dy elements and the extension of solid solution.

Keywords: Nial-Based Eutectic Alloy; Dysprosium; Microstructure; Mechanical Properties.

1. Introduction

As a kind of potential high temperature structural materials, NiAl owns many advantages such as high melting point, low density and excellent capacity of heat transmission [1-4]. However, poor room temperature ductility, toughness and elevated temperature strength hinder its application in aircraft engine. Former researches show that adding of refractory metal can improve its room temperature toughness and elevated temperature strength by forming quasi-binary or ternary eutectic systems [5-8]. Among them, NiAl-28Cr-6Mo (NiAl-Cr(Mo) for short) eutectic alloy had been regarded as most promising

† Corresponding author.

one, because of its relatively good combination of high and room temperature mechanical properties [9-11]. However, its room temperature ductility is still very low. It is well known that the B is a potential strengthener in NiAl, and trace addition of B will bring great increase in yield strength. In recent studies, Dy has been introduced into the NiAl-based alloy and improved its mechanical properties by strengthening the grain boundary [12]. But the segregation of Dy along eutectic cell boundary would result in the stiffness phase and decrease the mechanical properties. Injection casting is an excellent method for microstructure optimization, solubility extension and so on, which can improve the ductility and toughness without deteriorating the strength of material. So in the present work the microstructural evolution and mechanical properties of NiAl-Cr(Mo) eutectic alloy containing trace Dy and B prepared by injection casting were studied.

2. Experimental Procedure

The master alloy of 33Ni-33Al-28Cr-6Mo (at%) containing 0.1% Dy and 0.01% B (wt%) were prepared by induction melting from with starting materials of 99.99% Ni, 99.9% Al, 99.9% Cr, 99.9% Mo, 99.9% Dy and Ni-20%B respectively, and cast into rods with 50mm in diameter. Then, the rods were cut into slices, and some of them were investigated at as-cast state; the remaining were crushed for inject casting. The inject casting were conducted with water-cooled copper mold method, and the crushed master alloy were put into quartz tube for remelting, and then injected through a nozzle with a diameter of 0.5mm into copper mold with an inner cavity with 10 mm in diameter and 100 mm in length. Microstructural characterization was carried out by scanning electron microscope (SEM) with energy-dispersive X-ray spectroscopy (EDS) analysis. The foils for transmission electron microscope (TEM) observation were prepared by the conventional twin jet polishing technique using an electrolyte of 10% perchloric acid in methnol at –20 ^{o}C after mechanical polishing to 50μm and cutting into disc with a diameter of 3.0 mm . The samples were examined in a Philips TEM 420 analytical electron microscope operated at 150 kv. Due to the brittleness of the NiAl at room temperature, the compression test was employed to examine its mechanical properties. Compressive specimens with size 4×4×6 mm^3 were cut from conventionally-cast alloy and injected-cast alloy by electro-discharge machining (EDM) and all surfaces were mechanically ground with 600-grit SiC abrasive prior to compressive test. The compressive were conducted in Gleeble 1500 test machine at room temperature with an initial strain rate of 1×10^{-3} s^{-1}.

3. Results and Discussion

The microstructure morphology and the phase content were observed and analyzed by scanning electron microscopy (SEM). Fig. 1 shows the typical microstructure of the NiAl-Cr(Mo)-Dy-B alloy prepared by conventionally-cast process. The alloy is mainly composed of eutectic cell and intercellular zone with a small amount of white phases distributed along the cell boundaries, and the EDS test reveal that the white phases are rich of Dy as shown in Fig. 1(c). In the eutectic cells, black NiAl and gray Cr(Mo) plate phases exhibit the radially emanating pattern from the cell interior to the cell boundaries, while in the intercellular zone, coarser NiAl dendrites and Cr(Mo) phases exist with irregular forms. In some eutectic cells there is primary NiAl phase, which indicates that the addition Dy and B may cause some influence on the eutectic point of the present alloy. In the primary NiAl phase and coarse NiAl dendrites, a lot of Cr particles have precipitated; while in the coarse Cr(Mo) phase in the intercellular region, many small NiAl particles precipitate as well.

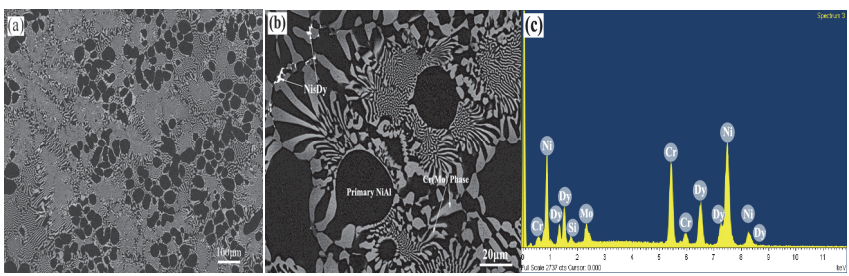


Fig. 1. SEM back-scattered electron images of NiAl-Cr(Mo)-Dy-B conventionally-cast alloy, (a) low magnification, (b) high magnification and (c) EDS of Dy richen phase.

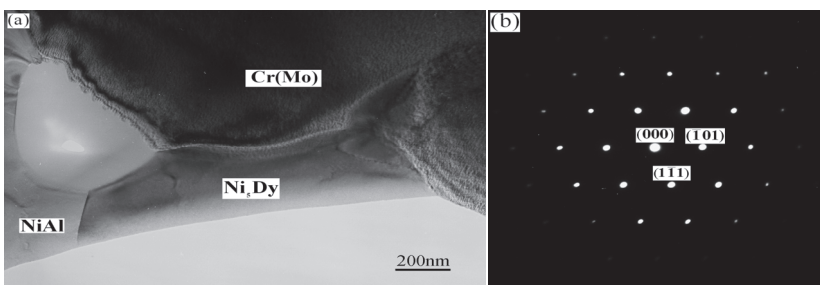


Fig. 2. TEM micrograph of (a) Dy richen phase and (b) its SADP along [121] zone axis.

In order to identify the white phase, the transmission electron microscopy (TEM) has been employed. Figure 2 shows the bright-field TEM image and

selected area diffraction pattern (SADP) along [121] zone axis of Dy rich phase. From the result, the observed white phase can be determined as Ni_5Dy, which has a hexagonal crystal structure with a=0.4856 nm, c=0.3969 nm and the space group of P6 /mmm.

The SEM images of the alloy prepared by injection casting are shown in Fig. 3. It exhibits a fine microstructure with an average eutectic cell size of about 60μm, which is less than half of the size of the conventionally cast alloy, and much more homogeneous distribution of the Ni_5Dy phase. Moreover the intercellular zone becomes narrower and Cr precipitates are seldom observed in primary NiAl phase. The previous study [9] reveals that the rapid solidification could extend the solid solution capability of the matrix, which is true for this case. The detection on composition of the different zone (Table 1) shows that the Cr content of primary NiAl phase in injection-cast alloy gets greatly increase. Further observation discovers that there are some stick like phases with stacking fault inside, distributing along the boundaries of NiAl and Cr(Mo) phases, the phase marked by a, as shown in Fig. 3(c). The selected area diffraction pattern confirms the stick like phase to be Cr_7Ni_3, which has a tetragonal crystal structure with a=0.871 nm and space group of P42/mnm. Along the Cr_7Ni_3 phases the particles of Ni_5Dy, which is marked by b, have precipitated.

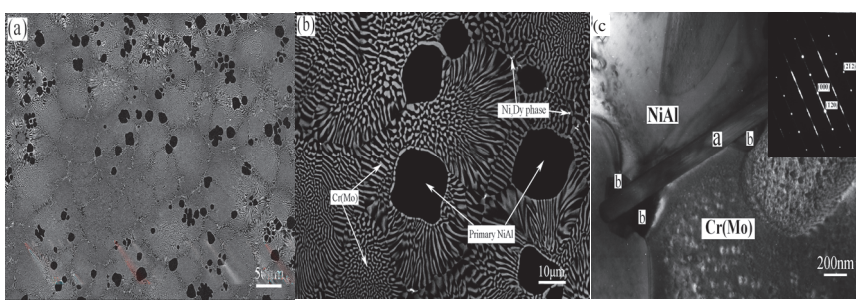


Fig. 3. SEM back-scattered electron images of NiAl-Cr(Mo)-Dy-B injection-cast alloy (a) low magnification and and (b) high magnification; (c) TEM micrograph Cr_7Ni_3 phase (Inset picture showing its selected area diffraction pattern).

Table 1. Compositions of the constituent phases in the NiAl-Cr(Mo)-Dy-B alloys.

Processing	Phase	Ni (at%)	Al (at%)	Cr (at%)	Mo (at%)
As-cast	Primary NiAl	46.7	50.6	2.7	—
	Cr(Mo)	4.18	7.82	78	10
Injectinon-cast	Primary NiAl	46.47	44.43	9.10	—
	Cr(Mo)	16.69	15.92	62.60	4.79

The compressive mechanical properties of conventionally cast and injection-cast alloy at room temperature are shown in Table 2. Compared with conventionally cast alloy, the room temperature compressive strain and yield strength of injection-cast alloy are improved significantly to be 18% and 1362 MPa, respectively, which have increased by 39.8% and 50% over the conventionally cast alloy. Such an improvement should be attributed to the microstructure optimization by the injecting casting. Based on the researches [7, 11], the compressive properties of eutectic alloy are related with its eutectic structure. The finer eutectic lamella, the higher strength the alloy can obtain. Moreover, the fine eutectic cell also could contribute to the compressive strength and ductility. The injection casting refines the eutectic lamella and eutectic cell. In addition, the Dy element in the injection-cast alloy also becomes more homogeneously, which could increase the cohesion of grain boundary.

Table 2. Results of compressive tests at room temperature under the strain rate of 10^{-3} s^{-1}.

Alloy	Yield strength (MPa)	Compressive strength (MPa)	Compressive strain (%)
Conventionally-cast alloy	987	1935	11
Injection-cast alloy	1362	2274	18

4. Summary

With addition of trace Dy element, the Ni_5Dy phases with hexagonal crystal structure have been formed along the NiAl/Cr(Mo) phases boundaries and mainly distributed in the intercellular regions. The alloy prepared by injection casting exhibits refined microstructural characteristic, i.e. refined eutectic cell size, intercellular region and Ni_5Dy phases. In addition, the high cooling rate extends the solute content in the alloy. Compared with the conventionally cast NiAl-Cr(Mo)-Dy-B alloy, the room temperature compressive strain and yield strength of the injection-cast alloy improve significantly, which can be attributed to the microstructure optimization.

Acknowledgement

The authors are grateful to the Shenzhen International Cooperative Research Project (GJHZ20140419114548516); the Strategic New Industry Development Special Foundation of Shenzhen (JCYJ20130402172114948 and JCYJ20140419164725011); the Shenzhen Technology Development Project (CXZZ20140419114548507).

References

1. R. Darolia, NiAl alloys for high-temperature structural applications, *JOM* 43(1991) 44–49.
2. L.Y. Sheng, W. Zhang, J. T. Guo, F. Yang, Y. C. Liang, H. Q. Ye, Effect of Au addition on the microstructure and mechanical properties of NiAl intermetallic compound, *Intermetallics* 18(2010)740–744.
3. L. Y. Sheng, F. Yang, J. T. Guo, T. F. Xi, H. Q. Ye, Investigation on NiAl-TiC-Al_2O_3 composite prepared by self propagation high temperature synthesis with hot extrusion, *Compos. B-Eng.* 45(2013)785–791.
4. L. Y. Sheng, F. Yang, T. F. Xi, C. Lai, J. T. Guo, Microstructure and elevated temperature tensile behaviour of directionally solidified nickel based superalloy, *Mater. Res. Innov.* 17(2013) S101–S106.
5. L.Y. Sheng, J.T. Guo, T.F. Xi, B.C. Zhang, H.Q. Ye, ZrO_2 strengthened NiAl/Cr(Mo,Hf) composite fabricated by powder metallurgy, *Prog. Nat. Sci.-Mater. Int.* 22(2012)231–236.
6. L. Y. Sheng, F. Yang, T. F. Xi, J. T. Guo, Investigation on microstructure and wear behavior of the NiAl-TiC-Al_2O_3 composite fabricated by self-propagation high-temperature synthesis with extrusion, *J. Alloys Compd.* 554(2013)182–188.
7. L. Y. Sheng, J. T. Guo, W. L. Ren, Z. X. Zhang, Z. M. Ren, H. Q. Ye, Preliminary investigation on strong magnetic field treated NiAl-Cr(Mo)-Hf near eutectic alloy, *Intermetallics* 19(2011)143–148.
8. L. Y. Sheng, F. Yang, T. F. Xi, J. T. Guo, H. Q. Ye, Microstructure evolution and mechanical properties of Ni_3Al/Al_2O_3 composite during self-propagation high-temperature synthesis and hot extrusion, *Mater. Sci. Eng. A* 555(2012)131–138.
9. L.Y. Sheng, W. Zhang, C. Lai, J.T. Guo, T.F. Xi, H.Q. Ye, Microstructure and mechanical properties of laves phase strengthening NiAl base composite fabricated by rapid solidification, *Acta Metall. Sin.* 49(2013)1318–1324.
10. L.Y. Sheng, F. Yang, T.F. Xi, Y.F. Zheng, J.T. Guo, Improvement of compressive strength and ductility in NiAl–Cr(Nb)/Dy alloy by rapid solidification and HIP treatment, *Intermetallics* 27(2012) 14–20.

11. L.Y. Sheng, L.J. Wang, T.F. Xi, Y.F. Zheng, H.Q. Ye, Microstructure, precipitates and compressive properties of various holmium doped NiAl/Cr(Mo, Hf) eutectic alloys. *Mater. Design* 32(2011)4810–4817.

12. L.Y. Sheng, F. Yang, J.T. Guo, T.F. Xi, Anomalous yield and intermediate temperature brittleness behaviors of directionally solidified nickel-based superalloy, *Trans. Nonferrous Met. Soc. China* 24(2014)673–681.

Conductive Polypyrrole Composited PET and Cotton Fabrics with Alkali Treatment

Ying Chen[a] and Jintian Tang[b†]

[1]*Institute of Medical Physics and Engineering, Department of Engineering Physics, Tsinghua University, Beijing, 100084, China*
E-mail: [a]yingchen0526@gmail.com, [b†]tangjt@tsinghua.edu.cn

Jiatong Ju[1, 2]

[2]*College of Textile and Fashion, Qingdao University, Qingdao, 266071, China*

The paper mainly discussed the preparation of conductive polypyrrole conducting fabrics which were treated with NaOH solution and prepared by in-situ polymerization. It is the first time trying to use PPy coating fabrics for electrical stimulation therapy for diabetic foot cure. FTIR spectroscopy analysis was used to investigate the existence of polypyrrole. The influence of alkali treatment on the conductive property was analyzed. The results showed that after in-situ polymerization, the surface of cotton and PET fabrics became to be black. Alkali treatment period has significant influence on surface resistance of PPy/cotton and PPy/PET fabrics. SEM showed that cells were adhered on the PET multifilament and cells could survival well with the PET/PPy materials.

Keywords: Polypyrrole; Polyester Fabric; Alkali Minimization; Electric Conductivity; Dopant.

1 Introduction

Diabetic neuropathy and peripheral vascular disease are the main etiologic factors in foot ulceration [1]. The deterioration of the wound can be greatly slowed down by electrical stimulation as the adjuvant therapy [2]. Polypyrrole (PPy) is not only possess good biocompatibility, but also can modulate multiple cellular activities which include cell proliferation, migration, and cell differentiation [3], implying a promising application in biomedical field. Wang [4] confirmed a very thin, uniform PPy could coat on the PET microfibres and average surface electrical resistivity was measured to be 63 kΩ per square; PPy-coated PET fabrics were electrically stable enough to mediate sufficient pulsed electrical stimulation.

† Corresponding author.

In this paper, polyester (PET) and cotton fabrics were chosen to use as the substrates for PPy coating which will be used for electrical stimulation therapy. However, the in situ chemical polymerization process involved many chemical agents and processing parameters. Until now the PPy coat on the fabrics were not firmly and evenly enough [5]. Alkali decrement was used in this work to increase the coating fastness.

2 Methods and Materials

The specifications of samples were shown at Table 1. Dip cleaned PET or cotton knitted fabrics in the 200 g/L NaOH solution for several minutes at 70ºC for alkali treatments; Dip alkali treated PET or cotton fabrics in 0.1 mol/L p-toluenesulfonic acid monohydrate solution (PTSA) for 1 h at 33ºC; Dry them at 60ºC. Soak above samples in 0.3 mol/L oxidant $FeCl_3 \cdot 6H_2O$ solution for 1h at 33ºC and dry them at 60ºC. Then soak them in the 0.6 mol/L pyrrole solution for 3 h at 0ºC. When the reaction completes, clean the samples with 2% ethyl alcohol solution firstly and then clean them for several times with deionized water and dry them for 2h at 60 ºC.

Table 1. Sample specifications.

Sample	Size of yarns	Density(/5 cm)	Thickness	Mass per square meter
Cotton	18.2 tex×2	48 × 60	0.715	142.5
PET	72 dtex/36f	48×68	0.822	176.6

Infrared spectra of fabrics were recorded on a Magna-IR 560 FTIR spectrophotometer. The measurements were performed at 20ºC and a relative humidity of 65%. The electric conductivity of fabrics was tested by UT151B digital multimeter and each sample was tested for 10 times.

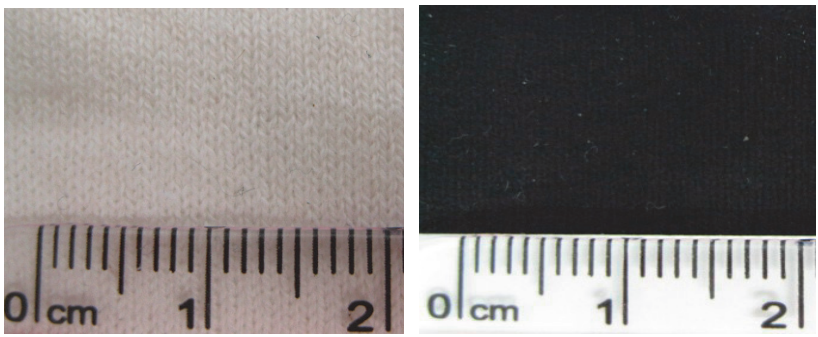
The electric currents of **e**lectric stimulus were 80 mA. The 24-well plates is used and the L929 cell density is 6×10^4/mL. There is 1.5 ml per well. 45 min electric stimulus was carried on the electric stimulus group. After the electric stimulus, change the culture solution and put the 24-well plates in the 37ºC cell incubator culturing for 24h. SEM was used to show the cell shape.

3 Results and Discussion

3.1. *The Appearance of Fabrics*

Figure 1 showed the appearance of cotton fabrics. Compared Figures 1(a) and 1(b) it can be seen that after in-situ polymerization the surface of cotton fabrics became to be black as well as the surface of PET fabrics. This is because the PPy powder is

black and it also illustrated that the PPy had been composited on the surface of fabrics.



(a) (b)

Fig. 1. The appearance of cotton fabrics: (a) cotton fabrics after cleaning; (b) conductive PPy composite cotton fabrics.

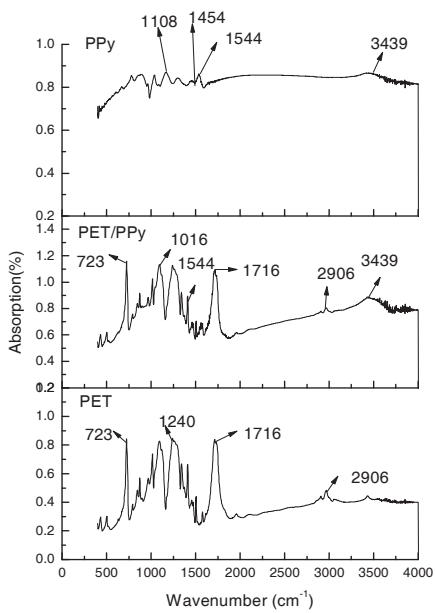
3.2. *FTIR spectra*

FTIR spectra had been used extensively to determine crystallinity and molecular orientation of various semicrystalline polymers. Figure 2(a) showed the FTIR spectra of the control PET fibers, conductive polypyrrole composite polyester fabric with alkali minimization and polypyrrole powders and in Figure 2(b) there is the same sample order for the cotton samples. Several major peaks are identified in samples which are the characteristics of PET, cotton fiber and PPy powder. In the PET FTIR spectrum, the bands at 2906 cm^{-1}, 1716 cm^{-1} , both 1240 and 1093 cm^{-1} correspond to the stretching vibration of C—H bond, C=O bond and C—O bond. The band at 1506 cm^{-1} associates with the vibration of the benzene ring, 1016 cm^{-1} associates with the in- plane banding of C—H bond in the benzene ring, and 1340 and 723 cm^{-1} associates with the surface external rocking of CH_2 bond and C—H bond in the benzene ring respectively [6]. In the cotton FTIR spectrum the wide and strong absorption peak around 3340 cm-1 corresponds to the stretching vibration of -OH bond of cellulose. 2900 cm^{-1}, 1373 cm^{-1}, 1059 cm^{-1} and 897 cm^{-1} corresponds to the stretching vibration of C—H bond, the bending vibration of -CH2 in non-crystalline region, the stretching vibration of C—O—C bond and the bending vibration of -OH bond, and the bending vibration of -CH2 band [7]. In the FTIR spectrum of PPy powder, the bands at 3439 cm^{-1} corresponds to the stretching vibration of N—H bond. The bands at 1544 and 1454 cm^{-1} correspond to the stretching vibration of 1pyrrole rings [8].

In the FTIR spectrum of the conductive polypyrrole and PET fabric, there are 3439, 1544, 1454 cm^{-1} bands associate with PPy and 2906, 1716, 1506, 1016 cm^{-1}

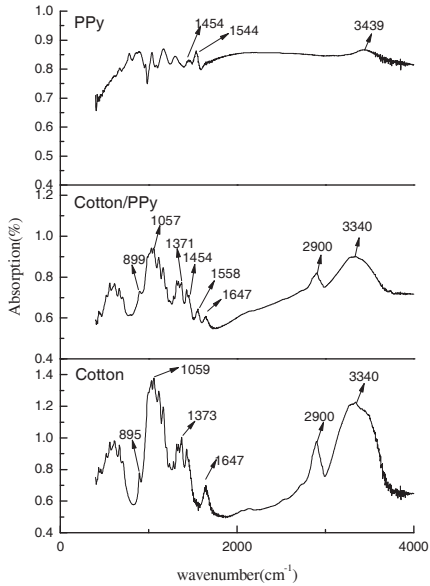
associate with PET, which illustrate that the PPy has been coated with PET fabrics. In the FTIR spectrum of the conductive polypyrrole and cotton fabric, there are 3439, 1544, 1454 cm^{-1} bands associate with PPy and 2900, 1370, 1059, 897 cm^{-1} associate with PET, which illustrate that the PPy has been coated with cotton fabrics.

Figure 3 shows the surface resistance of PPy composite polyester and cotton fabrics. With the increase of alkali treatment period, the surface resistance of PPy/PET fabrics was decreased sharply at initial and then slowly descended after 40 min. the alkali treatment could decrease the surface crystallinity and orientation of fibers; the number of polar groups on the fiber surface would be increased with the increase of hydrolysis of the ester bonds [9]. All of these changes could influence the surface properties of fibers which will be in favor of the composition of PPy. All of data were subjected to the one way ANOVA analysis. The alkali decrement time had significant influence on the surface resistance of PPy/PET fabrics. The surface resistance after 40 min, 60 min, 80 min and 100 min treatments had significant difference with that after 0 min, 20 min and 120 min treatments and it had no significant difference among 40 min, 60 min, 80 min and 100 min treatments. Considering the decease of fiber fineness and strength during alkali decrement, the time period of alkali treatment for PET fibers would be better to choose 40 min.



(a) PET fabrics

Fig. 2. FTIR curves of fabrics.



(b) Cotton fabrics

Fig. 2. (*Continued*)

However the surface resistance changes of PPy/cotton fabrics were different with that of PPy/PET fabrics. The curve was zigzag. Compared to the control sample, it was decreased except after 10 min alkali treatment. The reasons for these changes were including the surface change of fibers and the reaction of NaOH solution with the acid dopant. All of data were subjected to the ANOVA analysis. The alkali decrement time had significant influence on the surface resistance of PPy/cotton fabrics. The surface resistance after 15 min and 20 min treatments had significant difference with that after 0min, 5 min and 10 min treatments and it had no significant difference between 15 min and 20 min treatment treatments. The time period of alkali treatment for cotton fibers would be better to choose 15 min.

3.3. *Electric stimulus*

Figure 4 shows the SEM of cells after 24h cultivation. There were cells adhering on the PET multifilament, which means the PPy composited PET materials were atoxic. What's more, the cells were in the spindle - shaped state, which means the cell could survival well with the PPy composited PET materials.

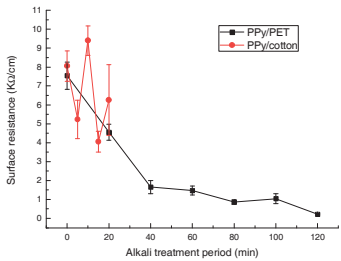


Fig. 3. The surface resistance of fabrics.

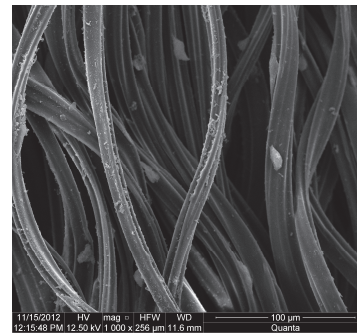


Fig. 4. SEM of cells with PPy/PET fabrics.

4 Summary

PET and cotton fabrics were chosen to use as the substrate for PPy coating which will be used for electrical stimulation therapy for diabetic foot. After in-situ polymerization, the surface of cotton and PET fabrics became to be black. The FTIR spectrum also illustrated that the PPy has been coated with cotton and PET fabrics. Alkali treatment period has significant influence on surface resistance of PPy/cotton and PPy/PET fabrics. With the increase of alkali treatment period, the surface resistance of PPy/PET fabrics was decreased sharply at initial and then slowly descended after 40 min; but for PPy/cotton fabrics the change was zigzag. SEM showed that cells were adhered on the PET multifilament and cells could survival well with the PET/PPy materials.

Acknowledgment

This project was sponsored by China Postdoctoral Science Fund (Project serial number: 2013M530637).

References

1 G. Borkow, J. Gabbay, R. C. Zatcoff, Could chronic wounds not heal due to too low local copper levels? *Med. Hypotheses*, 70(2008), 610-613.

2 F. G. Mehmandoust, G. Torkaman, M. Firoozabadi, G. Talebi, Anodal and cathodal pulsed electrical stimulation on skin wound healing in guinea pigs. *J. Rehabil. Res. Dev*. 44(2007), 611-618.

3 M. Gizdavic-Nikolaidis, J. Travas-Sejdic, G. A. Bowmaker, R. P. Cooney, C. Thompson, P. A. Kilmartin, The antioxidant activity of conducting polymers in biomedical applications. *Curr. Appl. Phys*. 4(2004), 347-350.

4 Y. Wang, M. Rouabhia, Z. Zhang, PPy-coated PET fabrics and electric pulse-stimulated fibroblasts. *J. Mater. Chem.* B. (2013), 3789-3796.

5 R. Beltran, Effect of synthesis parameters on the electrical conductivity of polypyrrole - coated poly (ethylene terephthalate) fabrics. *Polym. Int*. 52(2003), 1021-1026.

6 Y. Chen, X. Ding, Y. Li, Comparison of biostability between poly (trimethylene terephthalate) filaments and PET for vascular prostheses when exposed to hydrolytic and enzymatic degradation. *Fiber. Polym*. 13(2012), 169-176.

7 D. Tessier, L. H. Dao, Z. Zhang, M. W. King, R. Guidoin, Polymerization and surface analysis of electrically-conductive polypyrrole on surface-activated polyester fabrics for biomedical applications. *J. Biomat. Sci-polym. E*. 11(2000), 87-99.

8 U. S. Ramelow, J. H. Ma, R. Darbeau, Electrical conductivities of polypyrrole reacted with dopant solutions. *Mater. Res. Innov*. 5(2001), 40-49.

9 Z. Qin, Y. Chen, P. Zhang, Structure and Properties of Cu(II) Complex Bamboo Pulp Fabrics. *J. Appl. Polym. Sci*. 117(2010), 1843-1850.

Characterization of Structural Homogeneity of Type IV Silica Glass

Yuancheng Sun[a†], Chuandong Rao, Xuefu Song[b],
Xiurong Du, Xiaoqiang Zhang, Hui Wang

China Building Materials Academy, Beijing, China
E-mail: [a†]sunyuancheng@cbmamail.com.cn, [b]songxuefu@cbmamail.com.cn

Structural homogeneity of type IV silica glass is an important parameter and decides its usability. To characterize this parameter easily and quickly is very important. This paper discussed ways to characterize structural homogeneity of type IV silica glass. Current optical homogeneity test by interferometer, fictive temperature and stress birefringence test were compared at first. Then a new optical homogeneity test based on birefringence and image processing was present and can characterize structural homogeneity of type IV silica glass effectively and easily with low costs.

Keywords: Structure; Type IV Silica Glass, Test.

1. Introduction

Type IV silica glass[1] is synthesized by plasma chemical vapor deposition (PCVD)[2] method with silicon tetrachloride as the raw material. It is the purest silica glass and contains only about 0.4ppm OH and less than 1ppm metal impurities. Type IV silica glass has unique physical and chemical properties because of its unbroken Si-O network and has been used in inertial navigation and optical area.

Structural homogeneity of type IV silica glass is an important parameter and decides its usability. The fluctuation of Si-O bond angle and length in macroscopic dimension may cause structural inhomogeneity, although it has extremely low impurities and elements inhomogeneity is negligible. In order to improve the manufacturing level and testing efficiency, it is important to characterize structural homogeneity of type IV silica glass conveniently. This paper will analyze different methods to structural homogeneity of type IV silica glass and present a new quick method for practical use.

2. Experiment

Two kinds of type IV silica glass samples produced by horizontal and vertical process separately were prepared[3]. Sample A was produced by horizontal process

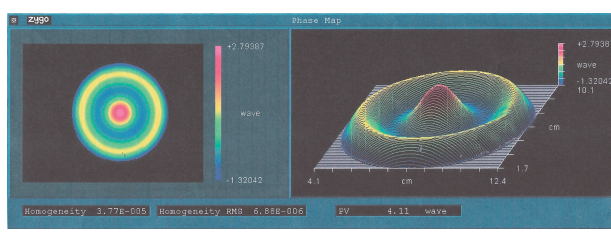
† Corresponding author.

with diameter of 100mm and thickness of 65mm. Sample B was produced by vertical process with diameter of 140mm and thickness of 19mm. Both samples were fine annealed to remove thermal stress, and then polished to get bright surfaces, whose flatness was less than λ/2. ZYGO GPI-XP laser interferometer was used to measure optical homogeneity. PE1600 FTIR spectrometer was used to measure infrared reflective spectrometer. Stress meter was used to measure structural stress and polariscope was used to get stress interference figure.

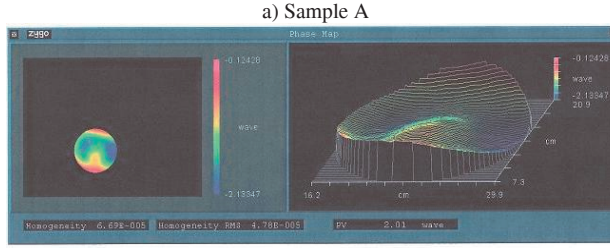
3. Results and Discussion

3.1. *Optical homogeneity*

Any fluctuation of silica structure will result in refractive index difference, so the structural homogeneity can be tested by optical method. Optical homogeneity is the parameter to characterize non-uniformity of refractive index in optical materials. Usually the value of optical homogeneity is the difference of maximum and minimum refractive index in the same sample. There are several ways to measure optical homogeneity such as collimator method, star testing method, knife-edge shadow method and interference method[4, 5]. The former three methods are qualitative test, while the interference method can give exact value of optical homogeneity. Fig. 1 shows the results of optical homogeneity tested by laser interferometer. The optical homogeneity of sample A and B are 3.77×10^{-5} and 6.69×10^{-5} separately.



a) Sample A



b) Sample B

Fig. 1. Optical homogeneity.

According to the results, the value of optical homogeneity accurately characterized the structural homogeneity of type IV silica glass. What's more, refractive index distribution of the whole surface can be seen clearly through phase map, and thus the fluctuation of silica structure is shown intuitively.

The advantage of this method is clear. Firstly, it tells accurate value to describe structural homogeneity. Secondly, it can give intuitive map of structure. Thirdly, deeper analysis such as root mean square of refractive factor can be conducted with computer. This method also has disadvantages. First of all, the requirement of sample is rigor. Surfaces must be polished precisely and have excellent surface shape, and two-sided surfaces should have required angle. So the test cycle is very long. More over, interference method needs expensive interferometer and complex operation, which are unsuitable for daily use.

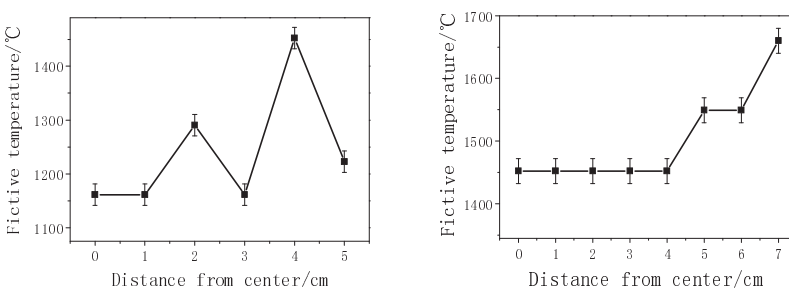
3.2. *Fictive temperature*

Tool[6] proposed fictive temperature to characterize structure of glass in 1946. If a glass has the same structure as another glass, which is in equilibrium and has the temperature of T_f, then T_f is the fictive temperature of the former glass. Agrarwal[7] used infrared reflectance spectroscopy to calculate fictive temperature of silica glass. The equation is as follows,

$$V = 1114.51 + (11603.51/T_f) \quad (1)$$

where, V is the position of stretch vibration of Si-O-Si bond near 1122cm^{-1}, and T_f is the fictive temperature of the sample.

To test fictive temperature, five points on surface of each sample were chosen and took infrared reflectance spectroscopy test. And fictive temperature was calculated use Eq. 1. The results are shown in Fig. 2. According to Fig. 2, the change of fictive temperature from center to edge of the samples represents the change of structure, which matches the results of optical homogeneity test.



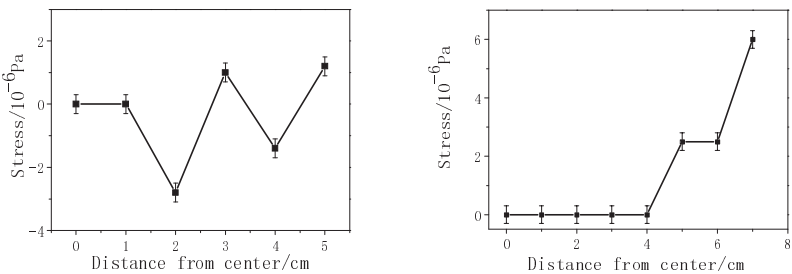
a) Sample A b) Sample B

Fig. 2. Fictive temperature.

The method of optical homogeneity test is easier than optical homogeneity method. But it should test one point each time, and it's impossible to characterize structure of the whole sample.

3.3. *Stress birefringence*

If stress exists, glass will be anisotropic like crystals, and birefringence will appear when ordinary light shines in it. After type IV silica glass is fine annealed, thermal stress disappears and only structural stress left. Then the structural homogeneity can be characterized by stress birefringence test. Fig. 3 shows the values of stress test by the stress meter. The negative value represents compressive stress and positive value represents tensile stress. According to stress birefringence test result, compressive and tensile stress alternately appears from center to edge of sample A, while sample B has tensile stress on the edge. As a result, the structure fluctuation can be characterized by stress birefringence test and agree well with optical homogeneity and fictive temperature test.



a) Sample A b) Sample B

Fig. 3. Stress.

In comparison, stress birefringence test requires lower polishing quality, so the test can be done easily and quickly. What's more, it can distinguish compressive and tensile stress. Especially for type IV silica glass, structural stress determines the structural homogeneity. But stress birefringence test still has disadvantages. It relies on human eye to get stress value and have big error. And it can only get one value each time.

3.4. *New optical homogeneity test*

To take the advantages of stress birefringence test and optical homogeneity test. This paper presents a new optical homogeneity test based on image processing. The mechanism of this test is based on that the structural fluctuation of type IV

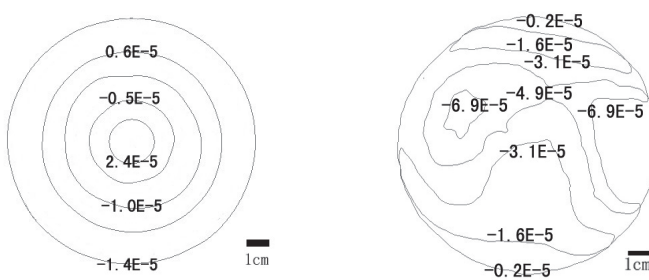
silica glass is caused by structural stress. The structural stress causes refractive factor difference at different polarizing direction and then causes optical path difference. The relation between refractive factor difference and optical path difference is as follows:

$$\Delta n_i = n_e - n_o = d\delta \tag{2}$$

where Δn_i is refractive factor difference at one stress point, n_e is refractive factor caused by stress, n_o is ordinary refractive factor, δ is optical path difference at the stress point and d is thickness.

Each optical path difference value corresponds to one interference colour under polariscope. Table of relationship between optical path difference and interference colour can be obtained use standard sample. Birefringence interference picture of the whole sample is captured by CCD camera. After that, the colour of every point can be converted to optical path difference by looking up the table with computer. And Δn_i of the whole sample can be computed use Eq. 2. The difference of maximum and minimum value of Δn_i equals optical homogeneity of the sample.

Fig. 4 shows contour maps of Δn_i tested by the new method, and optical homogeneity of sample A and B are 3.8×10^{-5} and 6.7×10^{-5} separately, which agrees with optical homogeneity test in figure 1. In addition, 3D map and statistical analysis of Δn_i can be conducted by computer.



a) Sample A b) Sample B

Fig. 4. Contour maps of Δn_i.

The advantage of this method is that it can get fairly accurate value quickly. What's more, it has lower requirements on samples and even unpolished samples can be tested.

4. Summary

Four methods to characterizing structural homogeneity of type IV silica glass were taken. Optical homogeneity test by laser interferometer gave accurate value and can take deeper analysis. But it has too much requirements on samples and should have valuable equipment. Fictive temperature and stress birefringence test are easier but can only test limited points of the sample. A new optical homogeneity test presented by this paper took the advantages of stress birefringence test and optical homogeneity test. Characterization of structural homogeneity of type IV silica glass can be done effectively and easily with low costs.

Acknowledgment

The authors would like to express their gratitude to the National Key Technology Research and Development Program of the Ministry of Science and Technology of China (2013BAE03B01), and International Science & Technology Cooperation Program of China (2012DFA51310), for their financial contribution to this study.

References

1. R. Brockner, Properties and structure of vitreous silica. *J. Non-cryst. Solids*. 5 (1970) 123-175.
2. X.Song, Y. Sun, H. Zhong, H. Wang, Z. Gu, Synthesis of silica glass by plasma chemical vapor deposition method. *J. Chin. Ceram. Soc*. 36 (2008) 531-534.
3. M. Sui, Y. Sun, X.Song, H. Wang, Study of structural homogeneity of CVD synthetic silica glass. *J. Wuhan Univ. Technol*. (2010) 106-110.
4. P. Hartmann, R. Mackh, H. Kohlmann, Advances in homogeneity measurement of optical glasses at the Schott 20 inch Fizeau interferometer. *S.P.I.E*. 2775(1996) 108-114.
5. J. Schwider, R. Burow, K.E. Elssner, R. Spolaczyk, J. Grzanna, Homogeneity testing by phase sampling interferometry. *Appl. Opt*. 24 (1985) 3059-3061.
6. A.Q. Tool, Relation Between Inelastic Deformability and Thermal Expansion of Glass in Its Anneal Range. *J. Am. Ceram. Soc*. 29 (1946) 240-253.
7. Agarwal, K.M. Davis, M. Tomozawa, A simple IR spectroscopic method for determining fictive temperature of silica glasses. *J. Non-cryst. Solids*. 185 (1995) 191-198.

Improving Water Vapor Barrier of Green-Based Nanocellulose Film via Hydrophobic Coating

Peng Lu[a] and Huining Xiao[b]

Department of Chemical Engineering and Limerick Pulp & Paper Centre, University of New Brunswick, Fredericton, NB E3B 5A3, Canada
E-mail: [a]peng.lu@unb.ca, [b]hxiao@unb.ca

Yuanfeng Pan

Guangxi Key Lab of Petrochemical Resource Processing and Process Intensification Technology, School of Chemistry and Chemical Eng., Guangxi University, Nanning 530004 China
E-mail: panyf@gxu.edu.cn

The cellulose nanofibrils (CNF)-based film is an ideal biodegradable and green packaging material. However, it is unable to withstand the influence of water vapor. The water vapor transmission rate (WVTR) of a CNF film was as high as 5088 g/m^2·24h and 332 g/m^2·24h at 38ºC (90% RH) and 25ºC (50% RH), respectively. To reduce the WVTR, a coating agent comprised of acrylated epoxidized soybean oil (AESO) and 3-aminopropyltriethoxysilane (APTS) was applied onto the CNF film using a rod coater. The effect of the APTS content on the coating property was investigated and the WVTR was reduced by 66.3% at 38ºC (90% RH) and 58.5% at 25ºC(50% RH) when the coat weight was 1 g/m^2. Moreover, the coated CNF film was highly hydrophobic along with good transparency.

Keywords: Nanocellulose; Barrier Film; 3-Aminopropyltriethoxysilane; Hydrophobic Coating; Water Vapor Resistance.

1. Introduction

Cellulose nanofibrils (CNF) is a renewable material from nature resources. The key advantages in use of CNF in packaging fields are its super strength and good film-forming property in the form of large scale films [1], nanopaper [2] and nanocomposite [3]. However, a large amount of hydroxyl groups on the CNF surface result in the poor water vapor barrier properties of CNF films. The common approaches to improve the moisture barrier capacity of CNF films for packaging applications are to treat the surfaces of CNF substrates with petrochemical-based plastics, or expensive biopolymer (e.g. polycaprolactone, poly (lactic acid), beeswax) [4] through laminating extrusion, vacuum deposition,

and multilayer coating [5]. In consideration of the packaging waste disposal problems, it is preferred to choose a material which has a high moisture barrier capacity and a potential biodegradability. Acrylated epoxidized soybean oil (AESO) is an important derivate of soybean oil, which has acrylate functional groups to polymerize/copolymerize easily via a free-radical reaction under several initiator systems. Studies reveal that under the controlled co-polymerization with other chemical could optimize the polymer properties for a surface coating [6]. These AESO-based polymers are also expected to have a proper moisture barrier capacity due to their good film-forming and hydrophobic properties. The aim of this work was to identify the optimal reaction conditions for preparing uniform water vapor barrier coating on nanocellulose films in an attempt to lower WVTR of the film and lead to hydrophobic surface.

2. Materials and Methods

2.1. *Materials*

Cellulose Nanofibrils (CNF) was obtained as aqueous suspension of the solid content at 0.6 wt% from University of Toronto. The average width of a CNF fiber is around 20 nm and several micrometers in length. Acrylated epoxidized soybean oil (AESO), 3-aminopropyltriethoxysilane (APTS), Benzoyl peroxide (BPO) and other reagents were purchased form Sigma Aldrich (Canada) and used as the coating agent without any purification.

2.2. *Preparation of films and surface coating*

The CNF film was prepared by pouring the CNF dispersion into polystyrene petri dishes and upon drying at a temperature of 23ºC and a relative humidity (RH) of 50%. In this study, the grammage (g/m^2) of the CNF film was fixed at 10 g/m^2. The coating agent which consists of varied acrylated epoxidized soybean oil (AESO), 3-aminopropyltriethoxysilane (APTS) and initiator (BPO) was applied onto the CNF film using rod coater at a velocity of 3 m/min. Immediately after the coating procedure, the films were put into the oven (80ºC) for curing 30 minutes. The coat weight was controlled to 1 g/m^2. The conversion of AESO was determined gravimetrically.

2.3. *Characterization*

The water vapor transmission rate (WVTR) was evaluated by the modified water method according to the standard ASTM E96 (2000) and ASTM D1653-03(2003). The water contact angle (WCA) of the sample was measured

using an Optical Tensiometer. A micrometer (Model 49-70, TMI., US) was used to measure the film thickness to an accuracy of 0.001 mm. The tensile strength (N/m) of the films was measured according to TAPPI Standard T220 and the tensile index (N·m/g) was obtained by dividing the tensile strength with the film grammage. To determine the morphology of the samples, AFM measurements were performed using a Nanoscope IIIa from (Veeco Instruments Inc). The images were scanned in tapping mode in air using a silicon probe (NP-S20, Veeco Instruments) with a resonance frequency of about 273 kHz.

3. Results and Discussion

3.1. *WVTR of films*

WVTR is the standard measurement by which films are compared for their ability to resist moisture transmission at specified conditions of temperature and relative humidity. Lower WVTR values indicate better moisture barrier property. The WVTR of the CNF film was 5088 g/m^2·24h at 38ºC (90% RH) and 332±7 g/m^2·24h at 25ºC (50% RH) respectively. The contact angle of pure CNF film was just 67° because of the hydrophilic nature of CNF fibers.

It is assumed that after surface reactive coating, a barrier layer could form on top of the CNF film surface which will block the pathway of the water vapor and therefore reduce WVTR. The barrier performance of the coated CNF films was determined mainly by the quality of the coating layer. Based on a previous research [7], the coating formulation especially the APTS ratio will determine the quality of the barrier layer during the curing process.

3.2. *Effect of APTS ratio on WVTR*

APTS is a bifunctional compound that possesses both the amino end which is capable of reacting with AESO and the ethoxy silane end which can be hydrolyzed to silanols and then reacted with hydroxyl bearing surfaces. It is clearly seen from Fig.1 (a) that as the APTS content increased, the WVTR of the coated CNF film first decreased to the lowest value and then went up.

When the APTS content was rather low (10 wt% of the AESO), the reduction in the WVTR was not very obvious compared with the uncoated CNF film. This is because most of the monomers were not participating in the reaction during the curing, which could be confirmed from a low conversion the AESO to polymer and a low contact angle. It was found that the contact angles for sample Co-1 Co-3 and Co-5 were 96°, 104° and 93°, respectively. Continued increase in the APTS content led to a reduction in the WVTR value and an

increase in the film hydrophobicity (high contact angle). The best result appeared at ATPS 30 wt%. Further increase in the ATPS content will not give a remarkable reduction in the WVTR due to the formation of incompact network by the reaction between AESO and APTS. Moreover, the formed barrier layer, sample Co-3, showed a fairly good hydrophobicity, which was confirmed by its higher contact angle than the others.

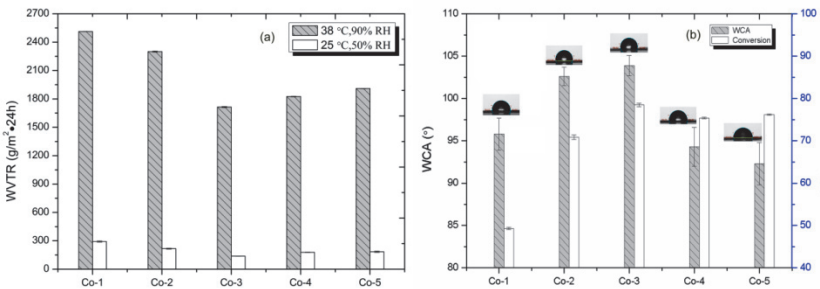


Fig.1. Effect of APTS ratio on (a) WVTR; (b) WCA and the conversion of AESO to polymer.

3.3. *AFM analysis and mechanical properties of films*

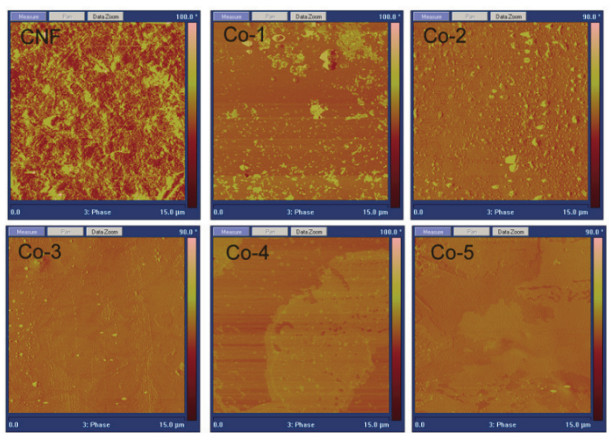


Fig. 2. The topography of the coated films with different APTS ratios.

An AFM phase image is a record of the phase lagging of the cantilever oscillation versus the phase of the driving signal. The change in the phase contrast (Fig.2) is directly corresponding to the WVTR values. As the APTS content increased (from Co-1 to Co-3), more AESO were involved in the

reaction with APTS, which finally reduced the bright domains (unreacted AESO or poly-AESO) in the matrix (cross-linked AESO-APTS) and correspondingly resulted in a decrease in WVTR. However, after APTS content was over 30 wt%, APTS patches appeared as a second phase existing amidst the continuous phase. Finally, the water vapor barrier property of the coated CNF film was flawed by those unreacted APTS patches.

3.4. *Effect of APTS ratio on CNF films qualities*

The coating layer could not only provide a good water vapor barrier property, but also make the film surface smoother. Table 1 reveals the roughness change as the APTS ratio increase. The tensile property of the coated CNF films was also higher than that of the uncoated one, which might be related to the 3-dimension network structure between the cellulose nanofibrils and AESO-based polymers. The closure of surface pores and the filling of network caused by the AESO reactive coating were also confirmed by the decrease in WVTR. On the other hand, the coated film appeared to be as transparent as the CNF films.

Table 1. Summary of CNF films qualities before coating and after coating.

Sample #	APTS [%]*	Thickness [μm]	Ra** [nm]	Tensile Index [N·m/g]	Transmittance [%]
CNF film	0	10±0.5	42.5	44.7±0.6	83.4
Co-1	10	12.1±1.1	16.8	43.1±0.4	74.7
Co-2	20	11.9±0.9	7.37	50.4±0.7	79.1
Co-3	30	12.1±0.9	38.3	56.9±0.8	81.9
Co-4	40	12.4±0.7	50.4	52.9±0.1	83
Co-5	50	12.7±0.7	24.9	45.9±0.9	86.1

* APTS[%] = APTS [g]/AESO [g]; **Ra=roughness average on a surface area of 1μm×1μm

4. Summary

A nanocellulose film with low water vapor transmission rate (WVTR) was made based on a potential biodegradable coating agent. The effect of AESO/APTS ratio on the film barrier property was revealed by AFM phase images. The coat weight at 1 g/m^2 was sufficient to reduce WVTR by 66.3% at 38ºC (90% RH) and 58.5% at 25ºC (50% RH), and improve the tensile strength of the NFC film. Moreover, the contact angle of the CNF film became higher after the AESO reactive coating, implying that the surface is more hydrophobic after the coating. The resulting film is promising as a green based packaging material.

Acknowledgments

This project was funded by NSERC Strategic Network - Innovative Green Wood Fibre Products (Canada), Chinese Scholarship Council (CSC), NSF of China (No. 21306027 & 51379077) and Guangxi NSF (No. 2013GXNSFCA019004).

References

1. Tekla Tammelin, Ulla Hippi, and Arto Salminen, Patent, *WO 2013060934* A2, (2013).
2. H. Sehaqui, A. Liu, Q. Zhou, Lars A. Berglund, Fast preparation procedure for large, flat cellulose and cellulose/inorganic nanopaper structures Biomacromolecules, 11 (2010) 2195-2198.
3. K. Larsson, Lars A. Berglund, M. Ankerfors, T. Lindström: Polylactide latex/nanofibrillated cellulose bionanocomposites of high nanofibrillated cellulose content and nanopaper network structure prepared by a papermaking route. *J Applied Polymer Science*, 125 (2012) 2460-2466.
4. W. Zhang, H. Xiao, L. Qian. Enhanced water vapour barrier and grease resistance of paper bilayer-coated with chitosan and beeswax, *Carbohydrate Polymers*, 101 (2014) 401-406.
5. Caisa Andersson. New ways to enhance the functionality of paperboard by surface treatment - a review: Packaging Technology and Science, 21 (2008) 339-373.
6. S. H. López, E. V. Santiago, Acrylated-epoxidized soybean oil-based polymers and their use in the generation of electrically conductive polymer composites. in: Soybean - Bio-Active Compounds, *INTECH open science*, 2013, pp. 231-263.
7. Peng Lu, Huining Xiao, Weiwei Zhang, Glen Gong: Reactive coating of soybean oil-based polymer on nanofibrillatd cellulose film for water vapor barrier packaging, *Carbohydrate Polymers*,111(2014), 524-529.

Synthesis, Characterization, and Catalytic Properties of MnO_x/SBA-16 for Toluene Oxidation

Yujuan Zhang, Lei Zhang, Jiguang Deng, Shaohua Xie, Huanggen Yang, Yang Jiang and Hongxing Dai†

Key Laboratory of Beijing on Regional Air Pollution Control, Beijing Key Laboratory for Green Catalysis and Separation, Key Laboratory of Advanced Functional Materials, Education Ministry of China, and Laboratory of Catalysis Chemistry and Nanoscience, Department of Chemistry and Chemical Engineering, College of Environmental and Energy Engineering, Beijing University of Technology, Beijing 100124, PR China
†E-mail: hxdai@bjut.edu.cn.

The *y*MnO_x/SBA-16 samples with high surface areas (504–835 m^2/g) were prepared using via an incipient wetness impregnation route. Compared to the bulk MnO_2 sample, the *y*MnO_x/SBA-16 samples showed better catalytic activities for the oxidation of toluene. Among all of the samples, the *y*MnO_x/SBA-16 sample with a Mn surface density of 1.21 Mn atom/nm^2 performed the best, giving a toluene consumption rate of 204.5 mL/(g_{MnO2} h) at reaction temperature = 380 ºC and space velocity = 20,000 mL/(g h). It is concluded that the high-dispersion MnO_x species, high surface area, and good low-temperature reducibility were responsible for the good catalytic performance of *y*MnO_x/SBA-16.

Keywords: Manganese Oxide; SBA-16-Supported Catalyst; Volatile Organic Compound Combustion; Toluene Combustion; High Dispersion.

1. Introduction

Bulk or supported MnO_x have wide applications in heterogeneous catalysis and electrochemistry. These materials can effectively catalyze the oxidation of CO, CH_4, and hydrocarbons, and also show activities for the decomposition of O_3, N_2O, and H_2O_2, the selective catalytic reduction of NO, and the removal of H_2S[1-8]. By comparing the catalytic activities of Pt/TiO_2 and γ-MnO_2 for the removal of volatile organic compounds (VOCs), Lahousse et al. [9] found that the latter catalyst even outperformed the former catalyst. MnO_x possesses Mn species with different oxidation states and higher oxygen storage capacity, in which the Mn^{4+}/Mn^{3+} molar ratio is dependent upon the preparation method.

It has been shown that catalytic activity of a supported catalyst is associated with the structure and dispersion of the surface metal oxide species. To some

† Corresponding author.

extent, the nature of the support exerts an important effect on the dispersion of a metal oxide. Since the discovery of the M41S molecular sieve, mesoporous materials with high surface areas, uniform pore sizes, large pore volumes, and highly ordered pore structures are promising as catalyst supports [9, 10], among which three-dimensional ordered mesoporous silica (SBA-16) shows thicker walls and better hydrothermal stability as compared to MCM-41 or MCM-48 [11]. Furthermore, SBA-16 possesses a three-dimensional and cubic mesoporous structure that is beneficial for mass transfer of reactants and products [12, 13]. Although the two-dimensional ordered mesoporous silica (SBA-15)-supported MnO_x catalysts have been reported before [14–18], rare work on the use of SBA-16 as support has been seen [19]. We here report the preparation, characterization, and catalytic performance of MnO_x/SBA-16 for the oxidation of toluene.

2. Experimental

2.1. *Catalyst preparation*

SBA-16 was synthesized using the cetyltrimethyl ammonium bromide (CTAB)-templating hydrothermal strategy. 1.21 g of F127 and 0.14 g of CTAB were dissolved in 168 mL of HCl aqueous solution (0.4 mol/L) under stirring. After complete dissolution, 4.00 g of tetraethyl orthosilicate (TEOS) was added under stirring for 5 min. The mixed solution was equally divided and placed into two Teflon-lined autoclave (100 mL) for hydrothermal treatment at 95 °C for 120 h. After being filtered, washed with deionized water, and dried at 60 °C for 12 h. The obtained solid was calcined in air at a ramp of 1 °C/min from room temperature (RT) to 550 °C and kept at this temperature for 3 h, thus obtaining white SBA-16 powders.

The yMnO$_x$/SBA-16 (y denotes the content of Mn; y = 1.5, 2.0, 2.5, 4.0, 5.5, 7.0, and 10.0 mol%) samples were prepared by the wet incipient impregnation method and subsequent thermal treatments ($Mn(NO_3)_2$ + SBA-16 → MnO_x/SBA-16). A desired amount of SBA-16 was impregnated in a given volume of $Mn(NO_3)_2$ aqueous solution (50 wt%). After being dried at 120 °C for 12 h, the solid was calcined in air from RT to to 550 °C and kept at this temperature for 5 h, thus obtaining the yMnO$_x$/SBA-16 samples. The bulk MnO_2 sample was purchased from the Beijing Chemical Reagents Company.

All of the chemicals in analytical purity were purchased from the Beijing Chemical Reagents Company and used without further purification.

2.2. *Catalyst characterization*

X-ray diffraction (XRD) patterns of the samples were recorded on a Bruker D8 Advance diffractometer with Cu Kα radiation and nickel filter (λ = 0.15406 nm). BET (Brunauer-Emmett-Teller) surface areas of the samples were determined via N_2 adsorption at −196 °C on a Micromeritics ASAP 2020 analyzer with the samples being degassed at 300 °C for 2.5 h under vacuum before measurement. Scanning electron microscopic (SEM) images of the samples were recorded on a Gemini Zeiss Supra 55 apparatus (operating at 10 kV). Transmission electron microscopic (TEM) images and selected-area electron diffraction (SAED) patterns of the samples were obtained using the JEOL-2010 equipment (operating at 200 kV). X-ray photoelectron spectroscopy (XPS, VG CLAM 4 MCD analyzer) was used to determine the Si 2p, Mn 2p, O 1s, and C 1s binding energies (BEs) of surface species using Mg Kα ($h\nu$ = 1253.6 eV) as excitation source. In order to remove the adsorbed water and carbonate species on the surface, the samples were pre-treated in O_2 (flow rate = 20 mL/min) at 450 °C for 1 h and then cooled to RT, followed by transferring the pre-treated samples into the spectrometer in a transparent Glove Bag (Instruments for Research and Industry, USA) filled with helium. The pre-treated samples were degassed in the preparation chamber (10^{-5} Torr) for 0.5 h and then introduced into the analysis chamber (3×10^{-9} Torr) for XPS spectrum recording. The C 1s signal at 284.6 eV was taken as a reference for BE calibration.

Hydrogen temperature-programmed reduction (H_2-TPR) experiments were carried out on a chemical adsorption analyzer (Autochem II 2920, Micromeritics). Before TPR measurement, ca. 0.02 g of catalyst (40–60 mesh) was loaded to a quartz fixed-bed U-shaped microreactor (i.d. = 4 mm) and pretreated in an O_2 flow of 20 mL/min at 250 °C for 1 h. After being cooled at the same atmosphere to RT, the pretreated sample was exposed to a flow (50 mL/min) of 5% H_2–95% Ar (*v*/*v*) mixture and heated from RT to 750 °C at a ramp of 10 °C/min. The alteration in H_2 concentration of the effluent was monitored online by the chemical adsorption analyzer. The reduction peak was calibrated against that of complete reduction of a known powdered CuO (Aldrich, 99.995%).

2.3. *Catalytic evaluation*

Catalytic activities of the samples for toluene oxidation (C_6H_5-CH_3 + $9O_2 \rightarrow 7CO_2 + 4H_2O$) were evaluated in a continuous flow fixed-bed quartz microreactor (i.d. = 4 mm), as illustrated in Fig. 1. To avoid the phenomenon of hot spots, 50 mg of the sample (40–60 mesh) was diluted with 0.25 g of quartz sands (40–60 mesh). Prior to the measurement, the sample was pretreated in an

O_2 flow of 20 mL/min at 250 °C for 1 h. After being cooled to a given temperature, the toluene-containing reactant gas mixture was passed through the catalyst bed. The reactant mixture was 1000 ppm toluene + O_2 + N_2 (balance), the total flow rate was 16.7 mL/min, with the toluene/O_2 molar ratio and SV being 1/200 and ca. 20,000 mL/(g h), respectively. The 1000-ppm toluene was generated by passing a N_2 flow through a pure toluene-containing bottle that was chilled in an ice–water isothermal bath. Reactants and products were analyzed online on a gas chromatograph (GC-2010, Shimadzu) equipped with a flame ionization detector (FID) and a TCD, using a stabilwax@-DA column (30 m in length) for VOC separation and a 1/8 in Carboxen 1000 column (3 m in length) for permanent gas separation. The balance of carbon throughout the investigation was estimated to be 99.5 %.

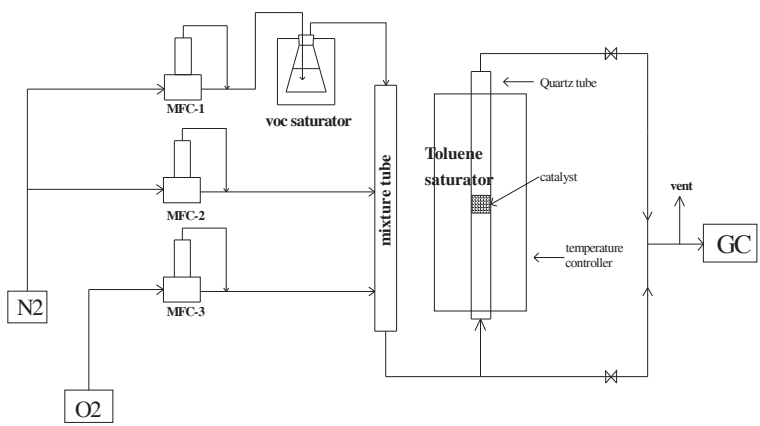


Fig. 1. Diagram of catalytic evaluation for toluene oxidation.

3. Results and Discussion

3.1. *Phase composition, pore structure, surface area, and morphology*

Fig. 2 shows the small- and wide-angle XRD patterns of the as-prepared *y*MnO_x/SBA-16 samples with different surface Mn density. There was a strong diffraction signal at $2\theta = 0.80^o$, assignable to the (110) plane of 3D cubic SiO_2 (*Im*3*m*) [20]. This result indicates that the regular mesoporous structure of SBA-16 was retained after MnO_x loading. With the rise in MnO_x loading, the intensity of the peak at $2\theta = 0.80^o$ decreased, a result due to the partial blocking of mesopores in SBA-16 [21, 22]. Although no signals due to the (200) and (211) planes were recorded, the formation of mesopores in the *y*MnO_x/SBA-16 samples could be confirmed by the typical TEM images (Fig. 3). From Fig. 2B,

one can realize that all of the samples were amorphous, and no Mn_2O_3, Mn_3O_4 or MnO_2 crystals were generated in the yMnO$_x$/SBA-16 samples with a Mn surface density of 0.18–1.91 Mn atom/nm^2. Furthermore, no MnO$_x$ crystal particles were observed on the TEM image of the yMnO$_x$/SBA-16 with a Mn surface density of 1.91 Mn atom/nm^2, and no significant diffraction rings or spots were recorded on the SAED pattern of this sample (Fig. 3). These results indicate that the MnO$_x$ species were present in an amorphous form and highly dispersed on the surface of SBA-16.

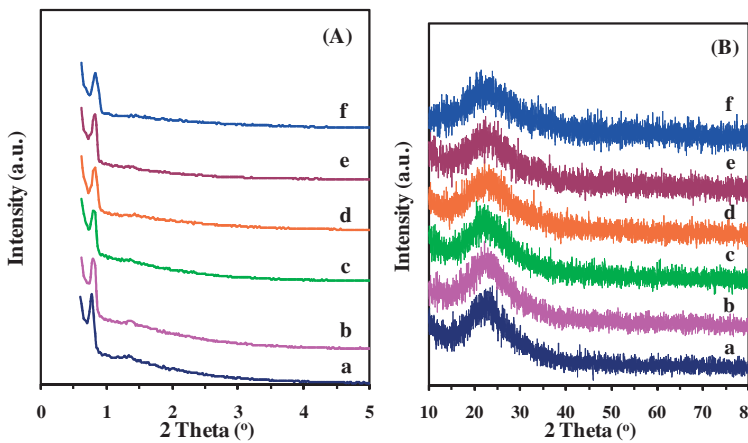


Fig. 2. (A) Small-angle and (B) wide-angle XRD patterns of yMnO$_x$/SBA-16 with the Mn surface density (Mn atom/nm^2) = 0.18 (a), 0.29 (b), 0.65 (c), 0.91 (d), 1.21 (e), and 1.91 (f).

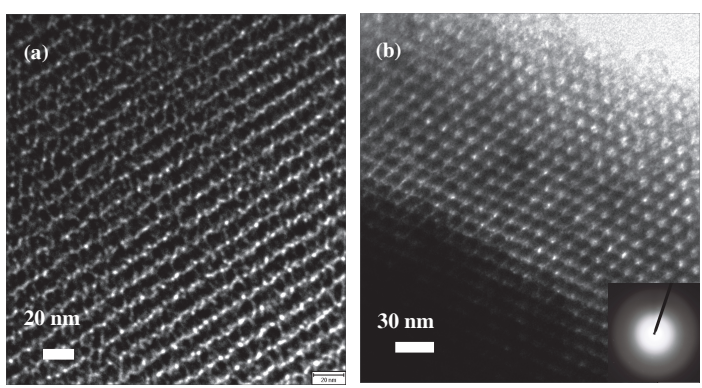


Fig. 3. TEM images of yMnO$_x$/SBA-16 with the Mn surface density (Mn atom/nm2) = 0.40 (a) and 1.91 (b).

Fig. 4. shows the N_2 adsorption-desorption isotherms and pore size distributions of the samples. It can be clearly seen that each of the samples displayed a type IV isotherm and typical a H2 histyresis loop, indicating the formation of 3D cubic mesoporous structure [13, 23]. The pore sizes of the samples were in the range of 5.6–6.0 nm (Fig. 4B). With the MnO_x loading from 1.5 to 10.0 mol%, the surface area of the sample decreased from 835 to 504 m^2/g, and the corresponding pore volume dropped from 1.22 to 0.76 cm^3/g (Table 1). But the average pore sizes of the samples increased slightly. The decreases in surface area and pore volume induced by the loading of MnO_x was due to the partial blocking of mesopores in SBA-16.

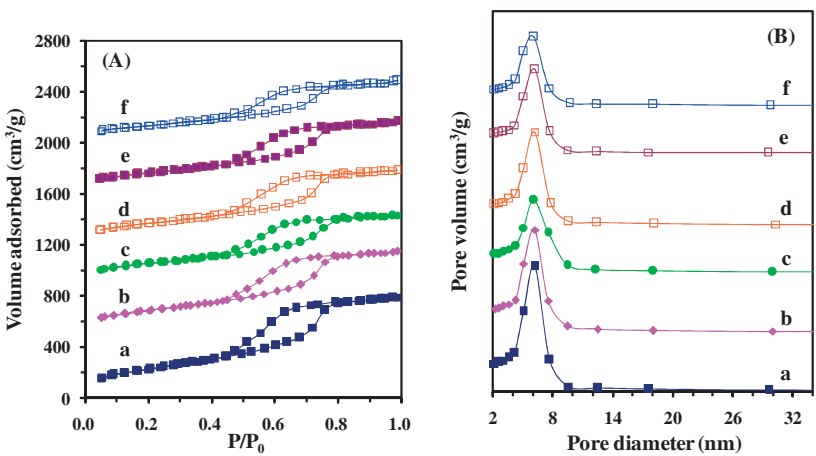


Fig. 4. (A) N_2 adsorption-desorption isotherms and (B) pore size distributions of $yMnO_x$/SBA-16 with the Mn surface density (Mn atom/nm^2) = 0.18 (a), 0.29 (b), 0.40 (c), 0.65 (d), 0.91 (e), 1.21 (f), and 1.91 (g).

3.2. *Surface element composition*

Table 2 summarizes the XPS results of the samples. The Si 2p binding energies in the yMnO$_x$/SBA-16 samples were in the range of 103.4–104.1 eV, ascribable to the surface Si^{4+} species. There was an asymmetric Mn $2p_{3/2}$ XPS signal at a binding energy of 641.8–642.5 eV, which could be decomposed into two components at binding energies of 641.6 and .2–641642.7–643.1 eV, assignable to the surface Mn^{3+} and Mn^{4+}, respectively. The O 1s binding energies (533.2–533.8 eV) of the yMnO$_x$/SBA-16 samples with the Mn surface density of 0.18–1.91 Mn atom/nm^2 were higher than that (529.8 eV) of the MnO_2 sample [17], but close to that (533.0 eV) of the SBA-16 sample [24]. Therefore, the O 1s XPS

signal was mainly from mesoporous SBA-16. Furthermore, the surface Mn/Si atomic ratios in the yMnO$_x$/SBA-16 samples were much lower than the corresponding bulk Mn/Si molar ratios. A similar result was also observed in the Mg-modified VO$_x$/SBA-15 catalysts [25].

Table 1. Physical properties of the yMnO$_x$/SBA-16 samples.

Sample	Mn surface density (Mn atom/nm^2)	BET surface area (m^2/g)	Average pore size (nm)	Pore volume (cm^3/g)
Bulk MnO_2	–	10.1	–	–
1.5MnO$_x$/SBA-16	0.18	835	5.8	1.22
2.0MnO$_x$/SBA-16	0.29	688	5.8	1.00
4.0MnO$_x$/SBA-16	0.65	602	5.8	0.88
5.5MnO$_x$/SBA-16	0.91	595	5.8	0.86
7.0MnO$_x$/SBA-16	1.21	564	5.8	0.82
10.0MnO$_x$/SBA-16	1.91	504	6.0	0.76

Table 2. XPS results of the yMnOx/SBA-16 samples.

Sample	Mn 2p$_{3/2}$ (eV)	Si 2p (eV)	O 1s (eV)	Surface Mn/Si molar ratio [a]	Bulk Mn/Si molar ratio [b]
1.5MnO$_x$/SBA-16	641.8	103.4	533.3	0.007	0.015
2.0MnO$_x$/SBA-16	641.8	104.0	533.4	0.011	0.020
4.0MnO$_x$/SBA-16	642.1	104.1	533.7	0.022	0.042
5.5MnO$_x$/SBA-16	642.1	103.7	533.2	0.030	0.058
7.0MnO$_x$/SBA-16	642.5	104.1	533.8	0.041	0.075
10.0MnO$_x$/SBA-16	642.7	104.1	533.4	0.049	0.111

[a]Estimated according to the XPS results.

[b]Calculated according to the nominal compositions.

3.3. *Reducibility*

Fig. 5A illustrates the H_2-TPR profiles of the samples. For all of the samples, there were two reduction peaks in the regions of 245–257 and 351–376 °C, assignable to the reduction of $Mn^{4+} \rightarrow Mn^{3+}$ and $Mn^{3+} \rightarrow Mn^{2+}$ [18, 26–28], respectively. With the rise in MnO$_x$ loading, the reduction peaks increased in intensity and shifted to higher temperatures, which was associated with the dispersion of the MnO$_x$ species. A quantitative analysis on the reduction peaks in the H_2-TPR profiles of the samples reveals that the H_2 consumption was in the range of 0.10–0.71 mmol/g$_{cat}$. Theoretically, the H_2 consumption of the yMnO$_x$/SBA-16 samples was 0.17–1.15 and 0.10–0.63 mmol/g$_{cat}$ if the reduction of $Mn^{4+} \rightarrow Mn^{2+}$ and $Mn^{3+} \rightarrow Mn^{2+}$ occurs, respectively. If the final reduction product were Mn_3O_4, the H_2 consumption would be 0.11–0.76 mmol/g$_{cat}$ when Mn^{4+} is reduced to Mn^{3+} and 0.07–0.21 mmol/g$_{cat}$ when Mn^{3+} is

reduced to Mn^{2+}. Apparently, the Mn in yMnO$_x$/SBA-16 was present in a mixed oxidation state (Mn^{4+} and Mn^{3+}). This deduction was in good agreement with the XPS results. The H_2-TPR profiles of supported catalysts are much more complex than those of bulk catalysts, and the nature of the support has an important influence on reducibility of the metal oxide species. For example, Trawczyński et al. [28] observed that the onset reduction temperatures of MnO$_x$ loaded on various supports were lower than those of their bulk counterparts; furthermore, the loading of MnO$_x$ on a metal oxide support could enhance the reducibility of highly dispersed active phases and the effect of the support decreased in the order of YSZ > γ-Al_2O_3 > TiO_2. Similar phenomena also took place in the yMnO$_x$/SBA-16 samples, because the active MnO$_x$ species were well dispersed on the surface of high-surface-area mesoporous SBA-16. From Fig. 5B, one can clearly see that the initial H_2 consumption rate of the sample increased with the rise in Mn surface density, and the highest value was achieved over the sample with 1.91 Mn atom/nm^2, in good consistence with their catalytic performance shown below.

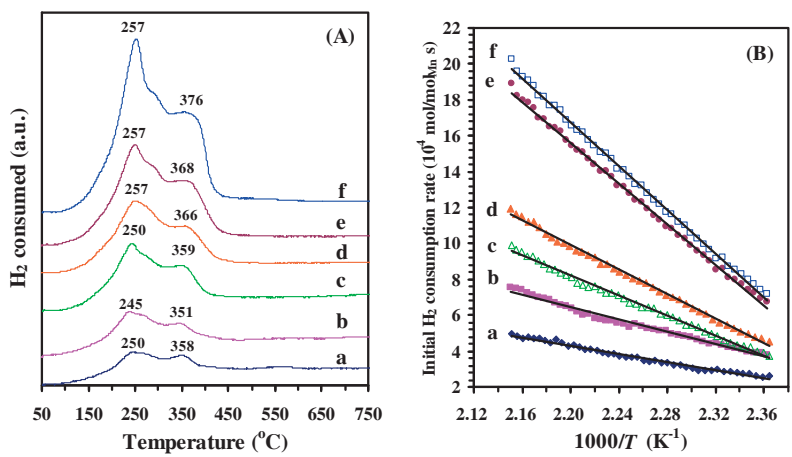


Fig. 5. (A) H_2-TPR and (B) initial H_2 consumption rate profiles of yMnO$_x$/SBA-16 with the Mn surface density (Mn atom/nm^2) = 0.18 (a), 0.29 (b), 0.40 (c), 0.65 (d), 0.91 (e), 1.21 (f), and 1.91 (g).

3.4. *Catalytic performance*

Fig. 6A shows the catalytic activities of the samples for the oxidation of toluene under the conditions of toluene concentration = 1000 ppm, toluene/O_2 molar ratio = 1/200, and SV = 20,000 mL/(g h). We use the reaction temperatures ($T_{50\%}$ and $T_{100\%}$) at toluene conversion = 50 and 100 % to evaluate the catalytic activity of the sample, respectively. It is observed from Fig. 6A that toluene

conversion increased with the rise in reaction temperature, with the highest activity ($T_{50\%}$ = 302 °C and $T_{100\%}$ =380 °C) being achieved over the yMnO$_x$/SBA-16 sample with a Mn surface density of 1.21 Mn atom/nm^2; the catalytic activity of the yMnO$_x$/SBA-16 sample with a Mn surface density of 1.91 Mn atom/nm^2 was lower than that of the yMnO$_x$/SBA-16 sample with a Mn surface density of 1.21 Mn atom/nm^2. However, the bulk MnO_2 showed a $T_{50\%}$ of 283 °C and a $T_{100\%}$ of 340 °C.

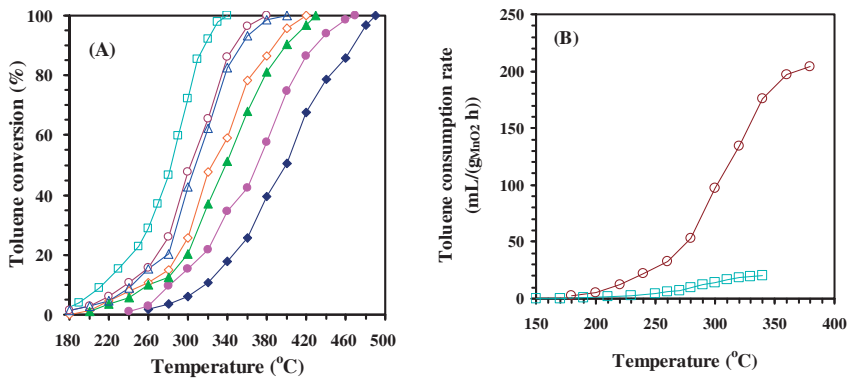


Fig. 6. Catalytic performance of (A) yMnO$_x$/SBA-16 with the Mn surface density (Mn atom/nm^2) = 0.18 (◆), 0.29 (●), 0.65 (▲), 0.91 (◇), 1.21 (○), and 1.91 (△); and (B) bulk MnO_2 (□) for toluene oxidation under the conditions of toluene concentration = 1000 ppm, toluene/O_2 = 1/200, and SV = 20,000 mL/(g h).

It is better to compare the catalytic performance of the samples by using the toluene reaction rate normalized by per gram of MnO_2. As shown in Fig. 6B, toluene reaction rate over the yMnO$_x$/SBA-16 sample with a Mn surface density of 1.21 Mn atom/nm^2 was much higher than that over the bulk MnO_2 sample. According to the H_2-TPR results, the sample with a high dispersion of MnO$_x$ was more reducible than the bulk MnO_2 sample. It is well known that the catalytic activity of a sample for the total oxidation of hydrocarbons is associated with its reducibility, and the sample with a stronger reducibility would perform better [29–31]. Therefore, the yMnO$_x$/SBA-16 sample with a Mn surface density of 1.21 Mn atom/nm^2 outperformed the bulk MnO_2 sample. Similar phenomena were also observed by other researchers [32–34]. SBA-16 possessed a 3D mesoporous structure (that facilitates the diffusion and adsorption of reactant molecules) and a high surface area (that is beneficial for the formation of highly dispersed MnO$_x$ species on its surface), thus providing a more amount of active sites as compared to the nonporous and low-surface-area bulk MnO_2 material.

Table 3. Catalytic activities at SV = 20,000 mL/(g h) and H_2 consumption estimated on the basis of the H_2-TPR profiles of the yMnO_x/SBA-16 and bulk MnO_2 catalysts.

Sample	H_2 consumption (mmol/g_{cat})	$T_{10\%}$ (°C)	$T_{50\%}$ (°C)	$T_{100\%}$ (°C)
1.5MnO_x/SBA-16	0.10	317	400	490
2.0MnO_x/SBA-16	0.14	283	372	470
4.0MnO_x/SBA-16	0.25	262	338	430
5.5MnO_x/SBA-16	0.34	256	325	420
7.0MnO_x/SBA-16	0.46	238	302	380
10.0MnO_x/SBA-16	0.71	245	308	400
Bulk MnO_2	10.9	214	283	340

To examine the catalytic stability, we carried out the 30-h on-stream toluene oxidation at 380 °C over the yMnO_x/SBA-16 sample with a Mn surface density of 1.21 Mn atom/nm^2, as shown in Fig. 7. Apparently, no significant drop in toluene conversion was observed, indicating that this sample was catalytically stable within 30 h of on-stream reaction under the adopted conditions.

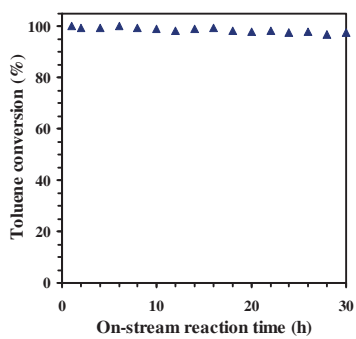


Fig. 7. Catalytic activity versus on-stream reaction time over yMnO_x/SBA-16 with a Mn surface density of 1.21 (Mn atom/nm^2) at 380 °C under the conditions of toluene concentration = 1000 ppm, toluene/O_2 = 1/200, and SV = 20,000 mL/(g h).

4. Summary

yMnO_x/SBA-16 samples with high surface areas (504–835 m^2/g) were prepared using a facile incipient wetness impregnation method. The yMnO_x/SBA-16 samples outperformed the bulk MnO_2 sample, with the yMnO_x/SBA-16 sample with a Mn surface density of 1.21 Mn atom/nm^2 showing the highest catalytic activity (toluene consumption rate = 204.5 mL/(g_{MnO2} h) at reaction temperature = 380 °C and space velocity = 20,000 mL/(g h)) in the complete oxidation of

toluene. It is concluded that the good catalytic performance of yMnO$_x$/SBA-16 was associated with their highly dispersed MnO$_x$ species, higher surface areas, and better low-temperature reducibility.

Acknowledgements

This work was supported by the NSF of China (21377008), 2013 Education and Teaching–Postgraduate Students Education–2011 Beijing Municipality Excellent Ph.D. Thesis Supervisor (20111000501), 2013 Education and Teaching–Postgraduate Students Cultivation–National Excellent Ph.D. Thesis Supervisor and Cultivation Base Construction (005000542513551), the Foundation on the Creative Research Team Construction Promotion Project of Beijing Municipal Institutions, and Scientific Research Base Construction–Science and Technology Creation Platform–National Materials Research Base Construction.

References

1. W.S. Kijlstra, D.S. Brands, E.K. Poels, A. Bliek, Mechanism of the selective catalytic reduction of NO by NH_3 over MnO$_x$/Al_2O_3, *J. Catal*. 171 (1997) 208–218.
2. S.B. Kanungo, Physicochemical properties of MnO_2 and MnO_2–CuO and their relationship with the catalytic activity for H_2O_2 decomposition and CO oxidation, *J. Catal*. 8 (1979) 419–435.
3. [A. Nishino, Household appliances using catalysis, Catal. Today 10 (1991) 107–118.
4. M.A. Baltanas, A.B. Stiles, J.R. Katzer, Development of supported manganese oxides catalysts for partial oxidation: Preparation and hydrogenation properties, *Appl. Catal*. 28 (1986) 13–33.
5. J.P. Wakker, A.W. Gerritsen, J.A. Mouljin, High temperature hydrogen sulfide and carbonyl sulfide removal with manganese oxide (MnO) and iron oxide (FeO) on gamma-alumina acceptors, *Ind. Eng. Chem. Res*. 32 (1993) 139–149.
6. G.J. Hutchings, M.S. Scurrell, J.R. Woodhouse, Direct partial oxidation of methane: Effect of the oxidant on the reaction, *Appl. Catal*. 38 (1988) 57–165.
7. I.K. Hauffe, Y. Ishikawa, Catalytic oxidation of hydrocarbons in the presence of ozone, *Chemie Ingenieur Technik* 46 (1974) 1053–1054.
8. C. Lahousse, A. Bernier, P. Grange, B. Delmon, P. Papaefthimiou, T. Ioannides, X. Verykios, Evaluation of γ-MnO_2 as a VOC removal

catalyst: Comparison with a noble metal catalyst, *J. Catal*. 178 (1998) 214–22.

9. C.T. Kresge, M.E. Leonowicz, W.J. Roth, J.C. Vartuli, J.S. Beck. Ordered mesoporous molecular sieves synthesized by a liquid-crystal template mechanism, *Nature* 359 (1992) 710–712.
10. X.Y. Hao, Y.Q. Zhang, J.W. Wang, W. Zhou, C. Zhang, S.X. Liu, A novel approach to prepare MCM-41 supported CuO catalyst with high metal loading and dispersion, *Micropor. Mesopor. Mater*. 88 (2006) 38–47.
11. D.Y. Zhao, Q.S. Huo, J.L. Feng, B.F. Chmelka, G.D. Stucky, Nonionic triblock and star diblock copolymer and oligomeric surfactant syntheses of highly ordered, hydrothermally stable, mesoporous silica structures, *J. Am. Chem. Soc*. 120 (1998) 6024–6036.
12. C.-F. Cheng, Y.-C. Lin, H.-H. Cheng, Y.-C. Chen, The effect and model of silica concentrations on physical properties and particle sizes of three-dimensional SBA-16 nanoporous materials, *Chem. Phys. Lett*. 382 (2003) 496–501.
13. T.W. Kim, R. Ryoo, M. Kruk, K.P. Gierszal, M. Jaroniec, S. Kamiya, O. Terasaki, Tailoring the pore structure of SBA-16 silica molecular sieve through the use of copolymer blends and control of synthesis temperature and time, *J. Phys. Chem*. B 108 (2004) 11480–11489.
14. G. Laugel, J. Arichi, M. Molière, A. Kiennemann, F. Garin, B. Louis, Metal oxides nanoparticles on SBA-15: Efficient catalyst for methane combustion, *Catal. Today* 138 (2008) 38–42.
15. M. Imperor-Clerc, D. Bazin, M.-D. Appay, P. Beaunier, A. Davidson, Crystallization of β-MnO_2 nanowires in the pores of SBA-15 silicas: In situ investigation using synchrotron radiation, *Chem. Mater*. 16 (2004) 1813–1821.
16. Y.-F. Han, F. X. Chen, Z.-Y. Zhong, K. Ramesh, E. Widjaja, L.W. Chen, Synthesis and characterization of Mn_3O_4 and Mn_2O_3 nanocrystals on SBA-15: Novel combustion catalysts at low reaction temperatures, *Catal. Commun*. 7 (2006) 739–744.
17. X.P. Dong, W.H. Shen, Y.F. Zhu, L.M. Xiong, J.L. Shi, Facile synthesis of manganese-loaded mesoporous silica materials by direct reaction between $KMnO_4$ and an in-situ surfactant template, *Adv. Funct. Mater*. 15 (2005) 955–960.
18. Y.-F. Han, F.X. Chen, Z.Y. Zhong, K. Ramesh, L.W. Chen, E. Widjaja, Controlled synthesis, characterization, and catalytic properties of Mn_2O_3 and Mn_3O_4 nanoparticles supported on mesoporous silica SBA-15, *J. Phys. Chem*. B 110 (2006) 24450–24456.

19. Y.J. Zhu, Y.L. Dong, L.N. Zhao, F.L. Yuan, Direct synthesis of highly ordered Fe-SBA-15 mesoporous materials under weak acidic conditions, *J. Mol. Catal*. A 315 (2010) 205–212.
20. T. Klimova, L. Lizama, J.C. Amezcua, P. Roquero, E. Terres, J. Navarrete, J. Dominguez, New NiMo catalysts supported on Al-containing SBA-16 for 4,6-DMDBT hydrodesulfurization: Effect of the alumination method, *Catal. Today* 98 (2004) 141–150.
21. C.M. Yang, H.S. Sheu, K.J. Chao, Templated synthesis and structural study of densely packed metal nanostructures in MCM-41 and MCM-48, *Adv. Funct. Mater*. 12 (2002) 143–148.
22. C.-M. Yang, P.-H. Liu, Y.-F. Ho, C.-Y. Chiu, K.-J. Chao. Highly dispersed metal nanoparticles in functionalized SBA-15, *Chem. Mater*. 15 (2003) 275–280.
23. R.M. Grudzien, B.E. Grabicka, M. Jaroniec, Effective method for removal of polymeric template from SBA-16 silica combining extraction and temperature-controlled calcinations, *J. Mater. Chem*. 16 (2006) 819–823.
24. L. Zhang, Y.H. Zhao, H.X. Dai, H. He, C.T. Au, A comparative investigation on the properties of Cr-SBA-15 and CrO_x/SBA-15, *Catal. Today* 131 (2008) 42–54.
25. W. Liu, S.Y. Lai, H.X. Dai, S.J. Wang, H.Z. Sun, C.T. Au, Oxidative dehydrogenation of *n*-butane over mesoporous VO_x/SBA-15 catalysts, *Catal. Lett*. 113 (2007) 147–154.
26. K. Ramesh, L.W. Chen, F.X. Chen, Y. Liu, Z. Wang, Y.F. Fan, Re-investigating the CO oxidation mechanism over unsupported MnO, Mn_2O_3 and MnO_2 catalysts, *Catal. Today* 131 (2008) 477–482.
27. Q.H. Tang, X.N. Huang, C.M. Wu, P.Z. Zhao, Y.T. Chen, Y.H. Yang, Structure and catalytic properties of K-doped manganese oxide supported on alumina, *J. Mol. Catal*. A 306 (2009) 48–53.
28. J. Trawczyński, B. Bielak, W. Miśta, Oxidation of ethanol over supported manganese catalysts—Effect of the carrier, *Appl. Catal*. B 55 (2005) 277–285.
29. J.J. Li, X.Y. Xu, Z.P. Hao, W. Zhao, Mesoporous silica supported cobalt oxide catalysts for catalytic removal of benzene, *J. Porous Mater*. 15 (2008) 163–169.
30. E. Finocchio, G. Busca, V. Lorenzelli, V.S. Escribano, FTIR studies on the selective oxidation and combustion of light hydrocarbons at metal oxide surfaces. Part 2. Propane and propene oxidation on Co_3O_4, *J. Chem. Soc., Faraday Trans*. 92 (1996) 1587–1593.

31. B. Solsona, T.E. Davies, T. Garcia, I. Vázquez, A. Dejoz, S.H. Taylor, Total oxidation of propane using nanocrystalline cobalt oxide and supported cobalt oxide catalysts, *Appl. Catal*. B 84 (2008) 176–184.
32. E.V. Makshina, N.S. Nesterenko, S. Siffert, E.A. Zhilinskaya, A. Aboukais, B.V. Romanovsky, Methanol oxidation on LaCo mixed oxide supported onto MCM-41 molecular sieve, *Catal. Today* 131 (2008) 427–430.
33. E. V. Makshina, S. V. Sirotin, M. W. E. van den Berg, K.V. Klementiev, V.V. Yushchenko, G.N. Mazo, Characterization and catalytic properties of nanosized cobaltate particles prepared by in situ synthesis inside mesoporous molecular sieves, *Appl. Catal*. A. 312 (2006) 59–66.
34. M. Alifanti, M. Florea, V.I. Pârvulescu, Ceria-based oxides as supports for $LaCoO_3$ perovskite: Catalysts for total oxidation of VOC, *Appl. Catal*. B. 70 (2007) 400–405.

The Preliminary Study on Polylactide/Polystyrene/Nanoclay Composites

Wenli Zhu[1, 2†]

[1]*Hubei University of Arts and Science, 296 Longzhong Road, Xiangyang, Hubei 441053, China*
[†]*E-mail: zwl829@126.com*

Xiangfang Peng[a] and Nanqiao Zhou[b]

[2]*The Key Laboratory of Polymer Processing Engineering, Ministry of Education, South China University of Technology, Guangzhou, Guangdong 510450, China*
E-mail: [a]pmxfpeng@scut.edu.cn, [b]nqzhou@scut.edu.cn

In this study, the effects of nonaclay content on compatibility of Polylactide(PLA)/ Polystyrene(PS) blends were investigated. The PLA/PS blends and their nanoclay composites were prepared through a twin-screw extruder. Thermogravimetric analysis(TGA) and differential scanning calorimetry(DSC) were performed to study the thermal properties of blends and their nanocomposites. Scanning electron microscopy (SEM) was employed to study the miscibility of PLA/PS blends on the presence of nanoclay. The research results showed that with an addition of appropriate amount of nanoclay, the compatibility of PLA/PS blends could be significantly increased.

Keywords: Polylactide; Polystyrene; Blends; Nanoclay Composites.

1. Introduction

Thanks to its biodegradability and biocompatibility, PLA has been well-known to be an eco-friendly plastic derived from a renewable plant source [1, 2]. It has attracted extensive industry interests for using in biomedical as well as commodity applications. Especially, PLA is considered to be one of the most promising substitutes for polystyrene (PS) in packaging applications, because not only its processing approaches but also its mechanical properties are comparable to PS.

Yet mass production of PLA remains challenging due to current synthesis techniques, thus results in the price of PLA is still more expensive compared to that of PS. To accelerate the replacement of PS by PLA, one of the methods is to blend it with the latter. Thus, the degrade period of blends could be dramatically

† Corresponding author.

decreased compared to that of pure PS. However, PLA is immiscible with PS and the available commercialized PS/PLA compatibilizer is too expensive to utilize in the industrial processes. Recently, it was reported that the employment of nanoclay improves the miscibility between the incompatible polymers in blends [3-5]. In addition, nanocomposites always show better mechanical properties and thermal stability as compared with unmodified polymers [6-8]. In this study, the preliminary study on PLA/PS/nanoclay composites was conducted and the effects of clay content on the blends morphology was investigated.

2. Experimental Part

2.1. *Materials*

The nanoclay used in this study was an organoclay Cloisite 20A manufactured by the Southern Clay Co. It contained the mineral (montmorillonite clay Cloisite) and 30wt% surfactant [dimethyldi-hydro di-talloammonium chloride (DMDTA)]. The PLA used in this study was 2002D (the D-lactide molar content is 4.2mol% and the molecular weight is 132,000g/mol) supplied by Naturalworks LLC. The PS used in this study was a commercialized grade PS1600 purchased from Borealis Group. The PLA and PS materials were in the form of pellets and used as received without any modification.

2.2. *Sample preparation*

After dried at 65°C in an oven for 12 hours, the PLA and PS were first dry-blended by hand and then fed into a twin-screw extruder at a weight percentage of 10:90, 30:70 and 50:50, respectively. The corresponding PLA/PS blends were extruded by a filament die and then pelletized as a pellet form, marked as P10, P30 and P50, respectively. Choosing P30 (the weight percentage of PLA:PS was 30:70) as a base material, 0.5, 1.0, 2.5 and 5.0phr organoclays were dry-blended in it and then melt-blended by the same twin-screw extruder, respectively. The produced nanocomposites pellets were marked as PN05, PN10, PN25 and PN50, respectively. For morphology analysis, a small amount of filament samples for each blend and composite was saved before pelletizing. All the blends and composites were dried properly to remove the moisture after they were collected from the pelletizer.

2.3. *Thermal analysis*

Thermogravimetric analyses (TGA) were performed on all the pure and blended materials by using a TGA Q50 (TA Instruments, New Castle, DE) with a

heating ramp of 20°C/min under the protection of nitrogen flow from room temperature to 600°C. During the heating processes, the weight percentage of indecomposable components was recorded automatically as a function of time or temperature. In addition, differential scanning calorimetry (DSC, Q2000 from TA Instruments, New Castle, DE) was used to evaluate thermal properties and crystallization kinetics. Around 15 gram materials were put into aluminum DSC pans with lids and then placed in the DSC cell. All the materials were heated with a heating rate of 10°C/min from room temperature to 200°C and kept at this condition for 10 min to erase the thermal history. They were then cooled to 40°C with a cooling rate of 10°C/min and reheated with a heating rate of 10°C/min to 200°C. All DSC runs were carried out under a nitrogen environment. During the heating and cooling processes, the heat flow of the sample was automatically recorded.

2.4. *Morphology analysis*

The entire saved filament blended and composites were dipped in liquid nitrogen and then quickly fractured in air. The exposed surfaces were sputter-coated with platinum in a mini sputter coater. Characterization for the morphology of the fracture surface was performed by utilizing a scanning electron microscope (SEM) model Hitachi 510.

3. Results and Discussion

The TGA data was plotted as temperature versus weight percentage in Fig. 1(a) for pure materials and blends and in Fig. 1(b) for 30/70 PLA/PS blends with different content nanoclays. From Fig. 1(a), it can be seen that the onset decomposition temperature of PS is dramatically higher than that of PLA. With the increase of PLA weight percentage, the onset decomposition temperature is gradually decreased. From Fig. 1(b), it can be seen that the onset decomposition temperatures of 30/70 PLA/PS blends with higher content nanoclays are slightly higher than those of blends with lower content nanoclays, indicating that the presence of clay may have influenced the blends' compatibility.

DSC reheating curves of all materials are illustrated in Fig. 2. Fig. 2(a) shows the glass transition temperature of pure PS and PLA are around 100 and 60°C, respectively. As all PLA/PS blends show two glass transition temperatures, it suggests that PLA and PS have poor compatibility. Fig. 2(b) shows the reheating curves of nanocomposites (PLA:PS=30:70). With the presence of 1phr nanoclays, a more visible endothermic peak emerged on the curve which may cause by melting the crystals produced during the heating.

When 2.5phr nanoclay was loaded in, an obvious exothermic peak in the temperature from 110 to 120°C appeared which indicates that significant cold crystallization occurred during the heating, and thus, resulted in a larger melting peak from 140 to 160°C. With further increase the loading amount of nanoclay, both the exothermic and endothermic peaks disappeared. The weakening effect of nanoclays on thermal behavior of blends indicates that the dispersion of nanoclays may play an important role on thermal properties of composites.

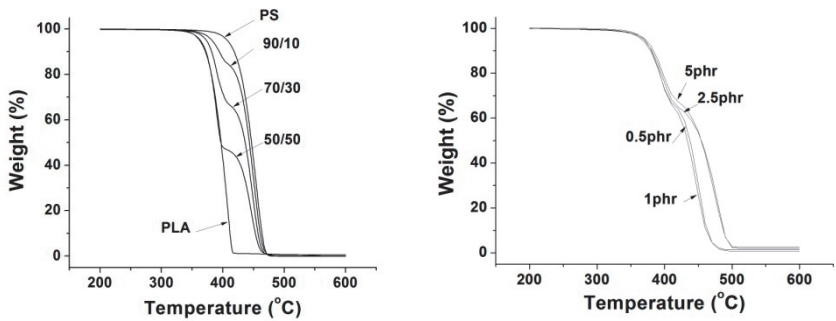


Fig. 1. TGA curves of (a) pure and blended materials, and (b) nanocomposites.

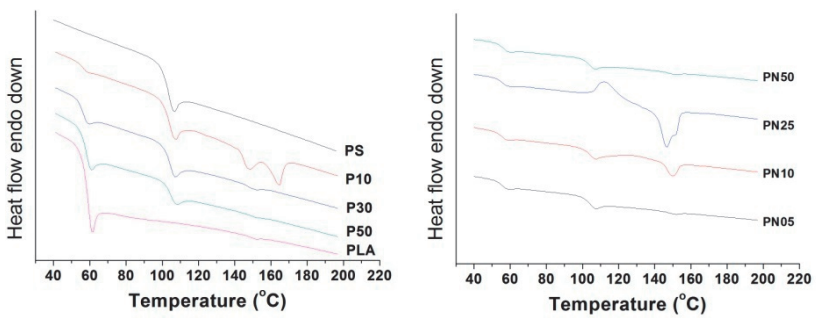


Fig. 2. DSC reheating curves of (a) pure and blended materials, and (b) nanocomposites.

PLA/PS blends morphologies are demonstrated in Fig. 3. The “white dots” present PLA domain and the “black holes” results from peeling PLA domain on the other part of the fractured sample. These photos show a typical morphology of immiscible polymer blends: PLA domains have well defined spherical shape, very broad size distribution, and also smooth fracture surface.

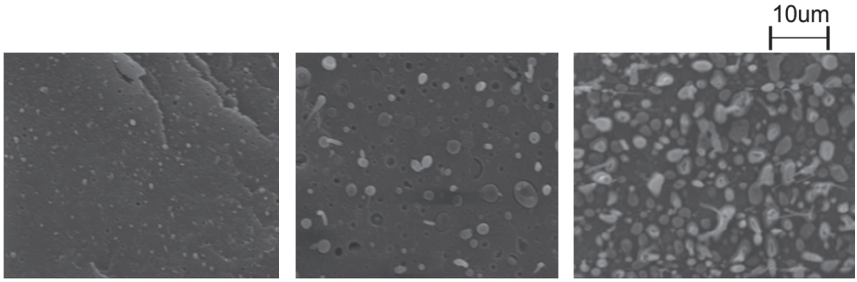


Fig. 3. SEM micrograph of PLA/PS blends.

As shown in Fig. 4, when nanoclay is introduced, the PLA domain size significantly reduces compared to the 30/70 PLA/PS blends shown in Fig. 3. When the content of nanoclay is very low, i.e. 0.5 phr, the domain size has been significantly reduced. With further increase of clay content, particularly 2.5phr, even though some small craters corresponding to PLA domains separated from PS matrix during cryofracture are seen, the interface between PLA and PS is not well defined. It is typical morphology observed for compatibilized blend systems. However, with higher content of clays, i.e. 5phr, the PLA domain size increases. This indicates that higher clay content is not desirable for compatibilizing PLA/PS blends. One of the most possible reasons is nanoclay was not well-dispersed in the blends, which resulted from the particle agglomeration due to insufficient mixing during the extrusion. This reduced the intercalation of PLA and PS chains into silicate layers, which means less wetting between two polymer phases. Further research on clay dispersion and its effects on compatibility need to be conducted to verify this hypothesis.

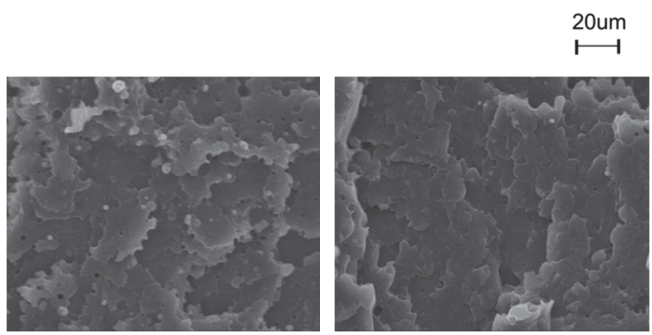
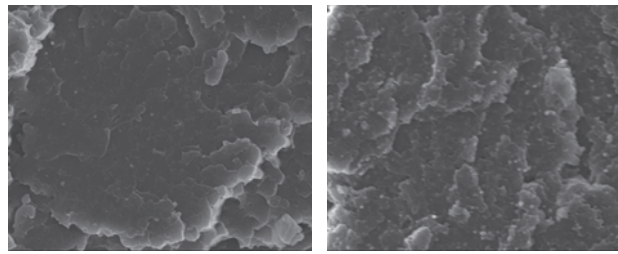


Fig. 4. SEM micrograph of PLA/PS nanocomposites.



PN25 PN50

Fig. 4. (*Continued*)

4. Summary

This work is a preliminary study on PLA/PS/nanoclay composites. The immiscible PLA and PS were melting blended through a twin-screw extruder. Organic nanoclay was employed to improve the compatability and properties of blends. TGA and DSC were performed to study the thermal properties of blends and their nanocomposites. SEM examination results showed that miscibility of PLA/PS blends could be significantly improved with loading appropriate amount of nanoclay. The future work will be the study on the effects of clay dispersion on compatibility of PLA/PS blends.

Acknowledgement

This work is supported by the Opening Project of the Key Laboratory of Polymer Processing Engineering, Ministry of Education (China), the Natural Science Foundation of Hubei Province (Grant No. 2014CFB456) and the Research and Development of Science and Technology Plan of Xiangyang City.

References

1. D. W. Hutmacher, *Biomaterials*. 21 (2000) 2529-2543.
2. K. A. Athanasiou, G. G.Niederauer, C. M. Agrawal, *Biomaterials*. 17(1996) 93-102.
3. S. M. Zhu, Y. Liu, M. Rafailovich, J. Sokolov, D. Gersappe, D. A. Winesett, H. Ade, *Abstr Pap ACS*, 218(1999)109.
4. V. Ferreiro, J. F. Douglas, E. J. Amis, A. Karim, *Macromol Symp*. 167(2001)73-88.
5. D. Voulgaris, D. Petridis, Polymer. 43(2002) 2213-2218.
6. M. Y. Gelfer, H. H. Song, L. Liu, B. S. Hsiao, B. Chu, M. Rafailovich, M. Si, V. Zaitsev, *J.of Polym.Sci.*: Part B: Polym. Phys., 41 (2003) 44-54.
7. G. Biresaw, C.J. Carriere, *Composites*: Part A. 35 (2004) 313-320.
8. K. Yang, X. Wang, and Y. Wang, *J. Ind. Eng. Chem.*, 13 (2007) 485-500.

Preparation and Catalytic Performance of Cu-supported on Manganese Oxide for Catalytic Oxidation of CO

Haixia Zhao, Lina Yan, Qing Ye†, Heng Lu, Dao Wang

Key Laboratory of Beijing on Regional Air Pollution Control, College of Environmental and Energy Engineering, Beijing University of Technology, Beijing 100124, China

†Email: yeqing@bjut.edu.cn

The manganese oxide (MnO_2) sample was synthesized by the reduction of $KMnO_4$ by $MnSO_4$. Cu doped manganese oxide materials have been synthesized by incorporation method and traditional wet-impregnation method. The structure of the catalysts was characterized by X-ray diffraction and N_2 adsorption/desorption analyses and their catalytic activities were performed by catalytic oxidation of CO. The doping Cu to manganese oxide by traditional wet-impregnation method result in a significant drop of area, due to the aggregation of copper oxides particles. Loading Cu to manganese oxide by incorporation method caused a slight change in surface area of the obtained Cu/MnO_2-Q catalysts. The catalytic activities of Cu/MnO_2 samples strongly depended upon the used methods, among which $5Cu/MnO_2$-Q catalyst, prepared by the incorporation method, was the most efficient catalyst towards the addressed reactions. The excellent performance of $5Cu/MnO_2$-Q was mainly associated with the good low-temperature reducibility, richest surface oxygen and broadly dispersed copper oxides species.

Keywords: Manganese Oxide; Copper; Carbon Monoxide; Catalytic Oxidation.

1. Introduction

Catalytic oxidation of carbon monoxide is of considerable interest due to its relevance in many industrial applications, such as gas purification in CO_2 lasers, CO sensors, air-purification devices for respiratory protection, and pollution control devices for reducing industrial and environmental emissions [1]. The catalyst employed is a key issue determining the effectiveness of catalytic oxidation technology. Manganese oxide shows good catalytic performance in a number of oxidation processes. Bulk and/or supported manganese oxides have long been used as an active catalyst for the oxidation of carbon monoxide, methane, and hydrocarbons. Since a single-component catalyst is usually hard to rival a precious metal catalyst, attempts for enhancing catalytic activity have been made by combining two or more transition-metal elements. Recently, we have prepared numerous MnO_2-supported metal catalysts and found these

materials performed well in the combustion of some typical VOCs and catalytic oxidation of CO [2]. Herein, we report the preparation, characterization, and catalytic properties of Cu/MnO_2 with various prepared methods for the catalytic oxidation of carbon monoxide.

2. Experimental

The MnO_2 catalysts were prepared via the reaction of Mn^{2+} and MnO_4^- using the HNO_3 solution as pH regulator. The above solution was refluxed and then filtered, washed, dried and calcined. The obtained samples were denoted as MnO_2. Cu/MnO_2-Q catalysts were also synthesized by refluxing mixed solution of Mn^{2+}, Cu^{2+} and MnO_4^- in the presence of concentrated HNO_3 as pH regulator. Then, this solution was filtered, washed, dried and calcined. The resulted samples were denoted as Cu/MnO_2-Q. Cu/MnO_2-H samples were using MnO_2 wet-impregnated with solution of Cu^{2+}. The samples were dried and calcined. The obtained samples were denoted as Cu/MnO_2-H. The MnO_2 catalysts are characterized by X-ray diffraction (XRD) and N_2-adsorption-desorption analytical techniques. Catalytic activities of MnO_2 catalysts for the oxidation of (1% CO + air) were evaluated. The outlet gases were analyzed on-line by GC.

3. Results and Discussion

Fig. 1 shows the XRD patterns of the MnO_2 and Cu/MnO_2 materials. As shown in Fig.1, for the support, there were significant XRD peaks recorded at 2θ = 28.7º, 37.4º, 44º, 50.0º and 62º, assigned to the (310), (211), (420), (411), and (521) planes of K_xMnO_2 with a turbostratic structure [3]. For $5Cu/MnO_2$-H samples prepared by traditional wet-impregnation method, there are weak diffraction signals due to CuO and Cu_2O phases appeared. Further increasing Cu loading to 25.0 wt% resulted in the increase in amount of the CuO or Cu_2O phases. However, for the Cu/MnO_2-Q catalysts synthesized by incorporation method, there are no significant signals assignable to CuO or Cu_2O phases. The average crystallite sizes as determined from the Scherrer equation applied to the reflection of Cu_2O (111) and CuO (111) phases for these samples are summarized in Table 1. The crystallite particle sizes of Cu_2O and CuO phases in $25Cu/MnO_2$-H were 39.00 nm and 16.5 nm, respectively.

The BET surface areas of MnO_2 and Cu/MnO_2 samples are listed in Table 1. The results are shown that the methods of preparation of Cu/MnO_2 significantly affected the properties of catalysts. It is clear that the MnO_2 support showed a high surface area of 108.7 m^2/g. Loading 5.0 wt% and 25.0 wt% Cu to MnO_2 by incorporation method caused a slight change in surface area of the obtained

Cu/MnO_2-Q catalysts. Moreover, the doping 25.0 wt% Cu to MnO_2 resulted in 25Cu/MnO_2-Q catalyst with a higher specific surface area than MnO_2. Compared with Cu/MnO_2-Q samples, the surface area of 5Cu/MnO_2-H sample decreased to 80.5 m^2/g and with a further rise in Cu loading to 25.0 wt%, the area of 25Cu/MnO_2-H catalysts was a significant drop in surface area (49.9 m^2/g), which might be due to the aggregation of copper oxides particles (Fig. 1 and Table 1). Ding et al. [4] demonstrated that the method of preparation of manganese oxides has great influence on the morphology, structural properties and catalytic activity.

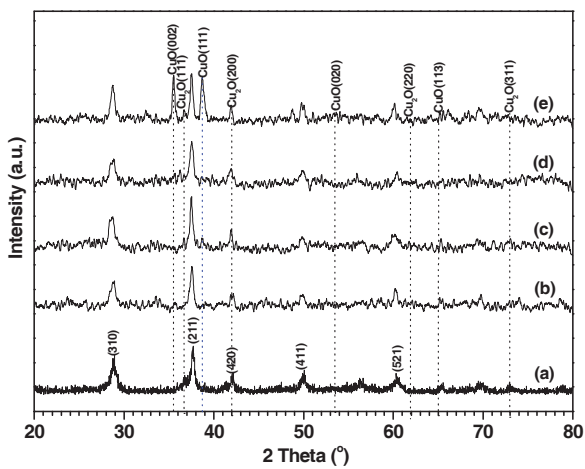


Fig. 1 XRD patterns of (a) MnO_2, (b) 5Cu/MnO_2-Q, (c) 25Cu/MnO_2-Q, (d) 5Cu/MnO_2-H, (e) 25Cu/MnO_2-H.

Ignition or light-off curves and CO conversion versus temperature are the most widespread forms of catalytic activity evaluation in catalytic oxidation studies. These curves are frequently characterised by two parameters, T_{50} and T_{100}. T_{50} refers to the temperature needed to reach 50% conversion, while T_{100} is related to the temperature required to achieve 100% conversion. The activity of the MnO_2 and Cu/MnO_2 samples in the oxidation of CO are shown in Table 1. The activities of these samples decreased in the order of 5Cu/MnO_2-Q > 25Cu/MnO_2-Q > 5Cu/MnO_2-H > 25Cu/MnO_2-H > MnO_2. Obviously, the catalytic activities of Cu/MnO_2 samples strongly depended upon the used methods, among which 5Cu/MnO_2-Q catalyst, prepared by the incorporation method, was the most efficient catalyst towards the addressed reactions. The excellent performance of 5Cu/MnO_2-Q was mainly associated with the good

low-temperature reducibility, and richest surface oxygen and broadly dispersed copper oxides species.

Table 1. BET surface areas, average crystal sizes of CuO/Cu_2O, and the temperatures (T_x) corresponding to the CO conversion over the catalysts.

Samples	Surface Area (m^2/g)	Crystall Size (nm)		Temperature of Conversion	
		CuO [a]	Cu_2O [b]	T_{50}	T_{100}
MnO_2	108.7	–	–	175	250
$5Cu/MnO_2$-Q	84.39	–	–	90	120
$25Cu/MnO_2$-Q	110.9	8	10	120	150
$5Cu/MnO_2$-H	80.45	–	–	125	160
$25Cu/MnO_2$-H	49.88	16.5	39	150	200

[a]The data were estimated sccording to the Scherrer equation using the FWHM of the (111) line for CuO.

[b]The data were estimated sccording to the Scherrer equation using the FWHM of the (111) line for Cu_2O.

4. Summary

(1) The manganese oxide (MnO_2) sample was synthesized by the reduction of $KMnO_4$ by $MnSO_4$ under acidic conditions. Cu doped MnO_2 materials have been synthesized by incorporation method and traditional wet-impregnation method.

(2) The method of preparation of Cu-doping MnO_2 has great influence on the morphology and structural properties. There are significantly CuO and Cu_2O phases over $25Cu/MnO_2$-H sample. Compared with Cu/MnO_2-H samples, with the increase of Cu loading, the surface area of Cu/MnO_2-Q sample result in a slight increase of surface area of the Cu/MnO_2-Q catalyst.

(3) The method of preparation of Cu/MnO_2 has great influence on the catalytic activity. For Cu/MnO_2-Q samples, Cu loading MnO_2 materials significantly enhance the adsorption properties of CO and lattice oxygen diffusion capacity, and improved catalysts for CO oxidation catalytic ability. The excellent performance of $5Cu/MnO_2$-Q was mainly associated with the good low-temperature reducibility, richest surface oxygen and broadly dispersed copper oxides species.

Acknowledgements

This work was supported by the National Natural Science Foundation of China (Grant Nos. 21277008 and 20777005), Beijing City Board of Education Science

and Technology Development Program (KM2013100050010) and the Project of Construction of Innovative Teams and Teacher Career Development for Universities and Colleges Under Beijing Municipality (IDHT20140504).

References

1. R. J. Farrauto, R. M. Heck, *Catal. Today* 55 (2000) 179–187.
2. Q. Ye, J. S. Zhao, F. F. Huo, J. Wang, S.Y. Cheng, T.F. Kang, H.X. Dai, *Catal. Today* 175 (2011) 603–609.
3. M. Abecassis-Wolfovich, R. Jothiramalingam, M.V. Landau, M. Herskowitz, B. Viswanathan, T.K. Varadarajan, *Appl. Catal. B: Environ*. 59 (2005) 91–98.
4. Y. Ding, X. Shen, S. Sithambaram, S. Gomez, R. Kumar, V. Crisostomo, S. Suib, M. Aindow, *Chem. Mater*. 17 (2005) 5382 –5389.

Research on Forming Process of Connecting Rod Formed by Squeeze Casting

Hong Chen[a], Shuxin Chai[b†], Tianquan Deng[c], Yuanyuan Wan[d]

Southwest Technology & Engineering Institute of China South Industries Group Corporation, Yuzhou Rd No.33, Chongqing, PR China

E-mail: [a]2897971987@qq.com, [b†]csx027@gmail.com, [c]583573494@qq.com, [d]442398348@qq.com

In this paper, we fabricate ADC12 aluminum alloy connecting rods by using squeeze casting, and compare microstructure and mechanical properties of connecting rod parts made by different processes, thereby the effect and mechanism of supercharging pressure, supercharging speed, liquid aluminum temperature to feeding capacity of pouring system is analyzed. The results indicated that, under the condition of supercharging speed 1.5-2.0m/s, supercharging pressure 90-100Mpa and liquid aluminum temperature 670-680ºC, high level quality connecting rod with dense microsturucture and high mechanical properties is achieved; proper supercharging pressure, supercharging speed and liquid aluminum temperature can improve the production quality stability.

Keywords: Squeeze Casting, Squeeze Feeding, Aluminum Alloy Connecting Rod, Engine Affect-Less.

1. Introduction

In early 1990s, squeeze casting technology was applied into aluminum alloy production by using die-casting machine in Japan, what has been developing for the manufacture of automobile, motorcycle and electric industry. A complex casting process design is necessary to reform common die-casting machine to match squeeze casting production, whose most important method is to control injection speed curve of machine, to discharge air out from mold and reduce the air volume into liquid aluminum alloy. This method has some advantages such as short production development cycle, less equipment investment etc, thus it's widely applied in the production of engine connecting rod of automobile and motorcycle.

However, it's very difficult to guarantee the quality requirement by controlling injection speed curve of die-casting machine to produce engine

† Corresponding author.

connecting rod with high strength and high reliability, shrinkage defects may occur during production process with big proportion and depth, which must be effectively found by X-ray detection, resulting in high production and quality costs, long production cycle, also damages users' interests.

In this paper, squeeze casting of aluminum alloy connecting rod is taken as the experimental object, by adjusting squeeze casting process parameters, such as supercharging pressure, supercharging speed and liquid aluminum alloy temperature etc, to research relationship between feeding channel size (feeding channel length and feeding channel diameter) and hot spot circle size, mechanical properties under condition of different temperature and alternating load fatigue test. Therefore, feeding mechanism of squeeze casting is to be investigated, to provide technical support for producing high quality and high stability aluminum alloy connecting rod.

2. Experiment

Aluminum alloy (ADC12) engine connecting rod has no bearing, whose chemical composition is shown in Table 1.

Table 1. Chemical composition of aluminum alloy ADC12. (%)

Si	Cu	Mg	Fe	Mn	Ni	Zn	Sn	Al
11.0	3.0	0.19	1.0	0.18	0.007	0.05	0.002	spare

This connecting rod requires tensile strength greater than 300MPa, elongation greater than 1% after T6 heat treatment, alternating load test of 2000 hours up. The experiment is carried out on 280 tons cold chamber die-casting machine, using mold made of H13 steel with preheating temperature 230ºC, liquid aluminum alloy 643-695ºC, supercharging speed 0.6-3.5m/s, supercharging pressure 55-178 Mpa. By adjusting the process parameters above, there three connecting rods are tested with specific experimental parameters, as shown in Table 2.

Table 2. Experimental parameters.

Process parameter	Rod No.1	Rod No.2	Rod No.3
Liquid aluminum alloy temperature (ºC)	643-650	670-680	680-695
Supercharging speed (m/s)	3-3.5	1.5-2	0.3-1
Supercharging pressure (MPa)	150-178	90-100	40-60

3. Results and Discussions

Aluminum alloy rod's structure is shown in Fig. 1. The hot spot circle's diameter is 13mm, ingates setting is allowed around rod body. The distance is 81mm from ingate to hot spot circle with draw ratio 1:1, the diameter of feeding channel from ingate to hot spot circle is 6.5mm, the ratio of feeding channel diameter to hot spot circle diameter is 0.5. The connecting rod parts in the fatigue life of sled test, as long as the connecting rod internal defects, the fatigue life of aluminum alloy connecting rod will be greatly shortened. As users continue to increase requirements to engine life, the CPK has to exceed 1.67.

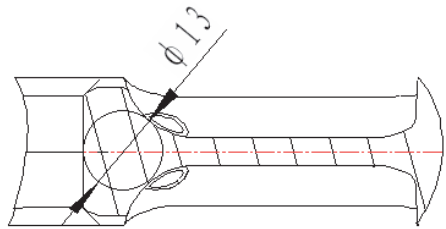


Fig. 1 Connecting rod's structure.

As shown in Fig. 2, the breakage occurs in Rod No.1 after 300 hours bench scale test; in Figure 3, cracks occur in Rod No.2 after 1256 hours bench scale test. The connecting rod fracture test were dissected, what's observed through the connecting rod low times microstructure, different specifications of shrinkage hole and shrinkage porosity defect existed inside. Because in the circulation effect of fatigue test, crack initiation source in the internal defects, leads to the connecting rod fracture prematurely (as shown in Fig. 4). A lot of experience proves, in order to make the aluminum alloy connecting rod fatigue sled test life of 2000 hours, 0.5mm shrinkage must be less than three in the range of 100mm^2 diameter, and more than 0.5mm diameter shrinkage shall not appear.



Fig. 2. The rod No.1 after 300 hours bench.



Fig. 3. The rod No.3 after 1256 hours bench.



Fig. 4. The rod No.1 after fatigue fracture.



Fig. 5. The rod No.2 after fatigue fracture.

Figure 6 show connecting rod No.3's low times microstructure cleavage fracture after fatigue sled test, it also show that the macrostructure of squeeze casting ADC12 aluminum alloy connecting rod is very tight, almost no micro defect and segregation. It explains that vast majority load was applied directly to the solid - liquid in metal solidification process, the unit load acting on the material is much bigger than which in the die casting ejection force. The load is enough to overcome deformation resistance and lead a good feeding also dense microstructure. Figure 7 and Fig. 8 show that anatomical diagrams of connecting rod in batch production using same process, which suggests its good stability.

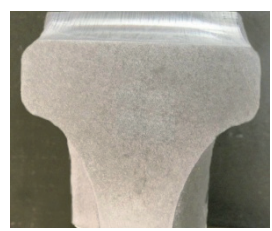


Fig. 6. Rod No.3's low times microstructure cleavage fracture after fatigue sled test.



Fig. 7. Connecting rods in batch production.



Fig. 8. Connecting rods in batch production.

The Table 2, Table 3 and Table 4 show the rules of runner system feeding size and hot spot circle diameter size, under condition that liquid temperature, supercharging speed and supercharging pressure as single argument separately.

Table 2. The relationship between supercharging pressure, ratio of feeding length to feeding channel diameter, ratio of feeding channel diameter to hot spot circle diameter.

Booster valve opening (circles)	55	70	100	140	178
Ratio of feeding length To feeding channel diameter	1.0~1.2	2.8~2.9	4.3~4.6	6.3~6.4	6.5~6.6
Ratio of feeding channel diameter to hot spot circle diameter	0.96~1	0.86~0.88	0.68~0.69	0.57~0.59	0.51~0.52

As shown in Table 2, under condition that at the same temperature of molten aluminum (690~710ºC) and at the same mold temperature (220~250ºC) with supercharging pressure increases, the ratio of feeding length to feeding channel diameter increases, accompany with the ratio of the feeding channel's diameter to hot spot circle's diameter decreases.

Table 3. The relationship between supercharging speed, ratio of feeding length to feeding channel diameter, ratio of feeding channel diameter to hot spot circle diameter.

Supercharging speed(m/s)	0.6	1.0	2.0	3.0	3.5
Ratio of feeding length To feeding channel diameter	0.8~1.1	2.8~3.1	4.4~4.5	6.3~6.4	6.5~6.6
Ratio of feeding channel diameter to hot spot circle diameter	0.95~0.97	0.82~0.84	0.65~0.68	0.57~0.61	0.50~0.53

As shown in Table 3, under condition that at the same temperature of molten aluminum (690~710ºC) and at the same mold temperature (220~250ºC) with supercharging speed increases, the ratio of feeding length to feeding channel diameter increases, accompany with the ratio of the feeding channel's diameter to hot spot circle's diameter decreases.

Table 4. The relationship between molten aluminum's temperature, ratio of feeding length to feeding channel diameter, ratio of feeding channel diameter to hot spot circle diameter.

Molten aluminum's temperature(ºC)	643	653	670	686	695
Ratio of feeding length To feeding channel diameter	0.62~0.65	0.71~0.73	0.82~0.86	0.92~0.94	0.98~1.1
Ratio of feeding channel diameter to hot spot circle diameter	5.7~6.0	5.2~5.5	4.1~4.3	3.2~3.4	2.8~3.0

As shown in Table 4, under the condition that at same supercharging pressure (150MPa), same pressurization speed (2.9m/s) and same mold temperature (220~250ºC) with the molten aluminum's temperature decreases,

the ratio of feeding length to feeding channel diameter increases, the ratio of feeding channel diameter to hot spot circle diameter decreases.

4. Results and Discussions

The biggest effect item to connecting rod quality is feeding after liquid aluminum alloy filling. During solidification, most liquid metal's volume may shrink, related to alloy composition and casting process. Insufficient feeding will lead to shrinkage defects. Therefore, thick casting head shall be set up for feeding in ordinary casting process. Nevertheless, casting head isn't needed by squeeze casting, which squeeze the liquid metal into potential shrinkage for feeding in the mechanical pressing method. Squeeze casting is completely enclosed in a squeeze casting mold, the first step of liquid metal solidification process under pressure, is crusting at the place connected cavity.[1] Then, the shell grow larger continuously into hot spot point inside. As solidification of the liquid metal is accompanied by volume shrinkage, the matching among molten metal temperature, mold temperature, boost pressure, feeding length, feeding channel's diameter and hot spot circle diameter parameters, determine feeding effect, thus affecting the parts' quality.

Under condition that certain temperature of molten aluminum and model, the pressure acting on the pressure from the beginning of the casting, at the beginning of the solidification, besides partially pressure work on crystalline part for plastic deformation by outer shell layer, most pressure still work on the liquid metal. The ratio of feeding length to feeding channel diameter increases, resulting in that during the metal solidification process, the thickness of solidified layer shell formed earlier increases, accompanied with thickness of metal liquid shell decreases constantly. The process of liquid metal solidification under pressure is a dynamic process that shell thicken and deforms, with isostatic pressing declines constantly. Assume the deformation of shell as a pipe with inner diameter r and outer diameter R, also inner surface pressure p, except the outer surface not deformed radially. According to the literature,[2] the following expression is obtained based on results related.

$$p = p_0 - \frac{\sigma_{ys}}{2\sqrt{3}}\left[\ln\frac{1}{3} + 4 - 2\sqrt{1+3\left(1-\delta'\right)^4} + \ln\frac{\sqrt{1+3\left(1-\delta'\right)^4}+1}{\sqrt{1+3\left(1-\delta'\right)^4}-1}\right]$$

In the formula(1), p means effective pressure applied to the ingot center on the solidifying liquid metal; p_0 means as a pressure acting on the ingot; δ' means the ratio of crystal layer thickness to ingot diameter, which can be also

expressed as *(R-r)/R*; σ_{ys} means yield strength of material at the deformation temperature.

As seen from Formula (1), p_0 is a constant; increases with the ratio of feeding length to feeding channel diameter, then the solidified layer thickness increases, δ' increases, so that the second item increase to a certain δ', $p = 0$ may occur. At this time, the remaining metal crystalline and solidify in the absence of pressure conditions, which is obviously disadvantageous for the internal quality of the casting. In order to compensate the pressure's declination caused by the ratio of feeding length to feeding channel diameter increase, valve shall be opened larger, that's to say there must be a higher pressing pressure. However, with pressure increases, a higher energy and higher tonnage squeeze casting equipment is needed badly. As the ratio of feeding channel to hot spot circle diameter decreases, the casting's solidification time is shortened, accompanied with δ' increases. By the same token, pressure valve shall be opened larger, which needs a higher pressure. To increase pressure works into similar effect as to increase pressure speed. With pressurization speed increases, the solidification time gets longer, which is just to make up for the pressure time delay to achieve a filling and solidification under pressure. With the extension of solidification time, the ratio of feeding length to feeding channel diameter increases, the ratio of feeding channel diameter to hot spot circle diameter decreases. The result of molten aluminum temperature increasing is similar as pressure speed increasing. However, it's not working under higher temperature. Although higher molten aluminum temperature is good for feeding hot spot, the organization may get thick and which makes parts mechanical performance worse.

5. Conclusions

In range of supercharging speed 1.5-2m/s, supercharging pressure 90-100MPa and liquid aluminum alloy 670-680ºC, with proper control of mode temperature and related auxiliary process, aluminum alloy ADC12 connecting rod, which has rarely micro defect and segregation bearing 2000 hours fatigue sled tests, is available.

Supercharging pressure and speed can significantly increase the feeding ability to complete filling and solidification under effective pressure, thereby reducing the casting shrinkage probability, increasing production quality stability. Also elevating liquid aluminum alloy temperature can achieve feeding effect, but it doesn't mean the higher the better, cause an inappropriate higher temperature may speed up microstructure bigger, to reduce the mechanical properties.

References

1. FEI Liangjun, WU Yueyi, SHEN Jianming, ZHANG Hua, A research on partial pressurization of cylinder block [J], *Special Casting & Nonferrous alloy die-casting special issue*, 2009: 197-200.
2. LUO Shoujing, CHEN Bingguang, QI Pixiang, liquid forging and squeeze casting technology, Beijing: Chemical Industry Press, 2007.
3. QI Pixiang. Squeeze Casting[M], National Defence Industry Press, 1984.
4. QI Pixiang, Squeeze casting technology facing the 21st centry[J], *Special Casting & Nonferrous Alloys*, 1998.
5. TANG Youguang, XU Zhangyi, Discussion on some technological aspects for aluminum alloy in squeeze casting[A], The 2nd International Die-Casting Conference, 2002.
6. M R GHOMASHCHI, A VIKHROV, Squeeze casting: an overview[J], *Journal of Materials Processing Techonology*, 2000, 101(3):1-9.

The Analysis of In-plane Uniaxial Anisotropy in Magnetic Thin Film Using Longitudinal MOKE and a Rotating Field (ROTMOKE)

Fang Wang[a] and Hai Wang[b†]

Department of Physics, Capital Normal University, Beijing 100048, China
E-mail: [a]1047779462@qq.com, [b†]whseal@googlemail.com

The longitudinal magneto-optical Kerr effect (MOKE) and a rotating field method (ROTMOKE) are analyzed specifically. It is found that there is a "jump" in the curve of normalized Kerr rotation angle in the case of $0.5 \leq EK/EH \leq 10$.We analyze the influence of energy competition on the "jump". In experiments, Fe films with in-plane uniaxial anisotropy induced by magnetic field are measured by ROTMOKE. Magnetic anisotropy constants $K_1=1.3\times10^3 J/m^3$ and $K_2=-0.2\times10^3 J/m^3$ are derived.

Keywords: Measurement; ROTMOKE; Fe Thin Film; Uniaxial Anisotropy; Anisotropy Constant.

1. Introduction

Magnetic anisotropy is an important feature of magnetic materials. People take various means in order to measure magnetic anisotropy constants accurately, including the ferromagnetic resonance [1, 2], the Brillouin light scattering [3] and torque magnetometry *etc*. Nevertheless surface magneto-optical Kerr effect (SMOKE) techniques have outstanding advantages such as high sensitivity, simplicity, rapid and nondestructive measurement. In addition, they can be also used to measure micro area, such as nanodot chains [4, 5] and selected regions of individual nanowire structures [6, 7]. In 1985, S.D. Bader *et al* studied magnetic properties of materials by surface magneto-optical Kerr effect [8]. Based on surface magneto-optical Kerr effect, many methods have been explored for measuring [9, 10]. R. Mattheis clearly put forward using longitudinal MOKE and a rotating field (the ROTMOKE method) to determine the anisotropy field strength in ultra-thin magnetic film in 1999 by realization of a coherent magnetization reversal (Stone-Wohlfarth-like) [11], which can obtain anisotropy constants K_1 and K_2 [12]. The ROTMOKE method can give the angular dependence of normalized saturation magnetization which is measured by longitudinal Kerr effect along the easy axis. The angle between the external

† Corresponding author.

magnetic field and easy axis is changed from 0º to 360º by rotating the field. X.L. Fan [13] *et al* showed the angular dependence of normalized saturation magnetization by rotating vibrating sample magnetometer and obtained anisotropy constants. However, as far as we know, there is no research on the influence of energy competition on "jump" of curves.

In this paper we discuss the energy competition of in-plane uniaxial anisotropy of magnetic thin film by ROTMOKE and analyze the influence of energy competition relationship on "jump" of curves of normalized Kerr rotation. We also measure Fe film with in-plane uniaxial anisotropy by ROTMOKE and obtain anisotropy constants K_1 and K_2 by fitting.

2. Sample Preparation

The samples were grown by dc magnetron sputtering (JPG600A) in 0.2Pa. The base pressure before deposition was better than 1.0×10^{-4}Pa. The power was 80 watts. The distance between the target and the substrate was set at 50mm. The polished monocrystalline silicon (110) was used as the substrate. The size was 5mm×5mm. The two bar shaped small magnet were set in silicon substrate sides. Fe films were deposited on silicon substrate under about 620Oe magnetic field. The thickness of film was measured by Alpha-Step IQ. The samples were measured by longitudinal MOKE and a rotating field (ROTMOKE) by NanoMOKE3 [14]. The spot size is 2×10^{-3} mm.

3. Theoretical Analysis

For in-plane uniaxial anisotropy of magnetic films, the total energy includes magnetic anisotropy energy E_K and the external field energy E_H in a magnetic field H. The total energy is expressed by

$$E_{total} = E_K + E_H = K_1 \sin^2\psi + K_2 \sin^4\psi - \mu_0 M_s H \cos(\alpha - \psi) \quad (1)$$

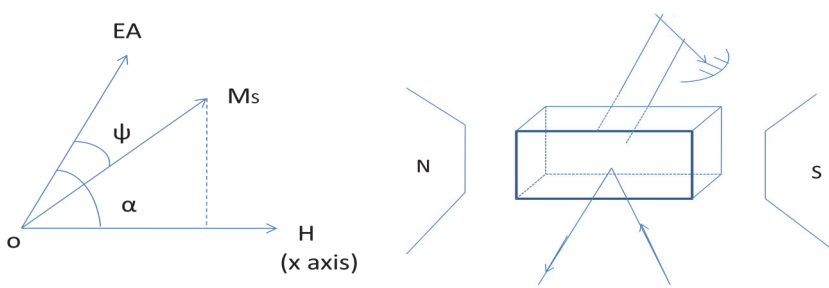


Fig. 1. (a) Magnetization vector Ms of the sample, EA and the magnetic field H are in the xy plane (b) Schematic drawing of equipment structure of NanoMOKE3.

In which, α is the angle between the magnetic field H and the easy axis. ψ is the angle between the direction of saturation magnetization and the easy axis (EA). These are shown in Fig. 1.

The direction of saturation magnetization is determined by the minimum of the total magnetic energy. That is

$$\frac{\partial E_{total}}{\partial \psi} = 0 , \quad \frac{\partial^2 E_{total}}{\partial^2 \psi} > 0 \tag{2}$$

Then,

$$K_1 \sin 2\psi + 4K_2 \sin^3 \psi \cos\psi - \mu_0 M_s H \sin(\alpha - \psi) = 0 \tag{3}$$

$$2K_1 \cos 2\psi + K_2 (3\sin^2 2\psi - 4\sin^4 \psi) + \mu_0 M_s H \cos(\alpha - \psi) > 0 \tag{4}$$

To obtain the relation between α and ψ, we require measure the Longitudinal Kerr angle under different angles α by rotating magnetic field.

$$\theta_K = \theta^{sat} \cos(\alpha - \psi) \tag{5}$$

The magnetic anisotropy constants K_1 and K_2, as well as saturation magnetization Ms can be obtained accurately by fitting the experimental θ_K/θ^{sat}–α curves with theoretical equations. Here, the magnetization M is proportional to the Kerr rotation angle θ_K [15].

The difference of energy competition relationship has an effect on magnetization behavior. Considered in the case of K_2=0, in order to better understand, the relationship of energy competition is divided into the following sections shown in Fig. 2:

In the case of $0 \leq E_K / E_H \leq 0.5$, it is shown in Fig. 2-1. When the amplitude of Ms and H is constant, the interval of Energy ratio can be converted to K_1 range interval from 0 to 1.71×10^3J/m^3. The uniaxial magnetic anisotropy energy and the Zeeman energy are competing. The former is relatively small, while the latter dominates in the region. With the angle α between the magnetic field and the EA increasing, the angle ψ between the saturation magnetization Ms and the EA is non-linearly increased. With the value of K_1 decreasing, the energy ratio of E_K to E_H decreases. When the value of K_1 is close to 0, the angle ψ varies with α linearly that the magnetic anisotropy energy is very small and the direction of Ms is close to the external field direction. When the angle α is constant, the different value of K_1 reflects different competition of the magnetic anisotropy energy E_K and the Zeeman energy E_H. The larger is the value of K_1, the smaller is the value of ψ and $\cos(\alpha-\psi)$ in the region. In Fig. 2, Ms = 1700×10^3 A/m and the external magnetic field H=20Oe are used.

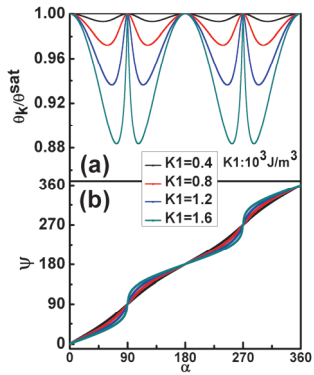


Fig. 2-1 (a) The (θ_K/θ^{sat}–α) curves (b) The equilibrium direction of magnetization ψ as a function of α in the case of 0≤EK /EH ≤0.5.

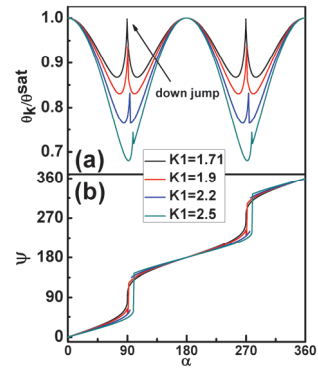


Fig. 2-2 (a) The (θ_K/θ^{sat}–α) curves (b) The equilibrium direction of magnetization ψ as a function of α in the case of 0.5≤EK /EH ≤0.78.

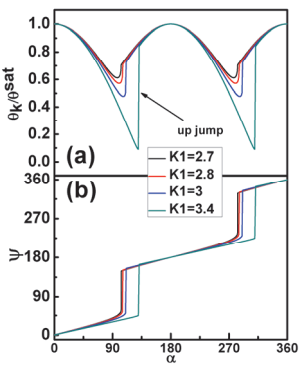


Fig. 2-3 (a) The (θ_K/θ^{sat}–α) curves (b) The equilibrium direction of magnetization ψ as a function of α in the case of 0.78≤EK /EH ≤10.

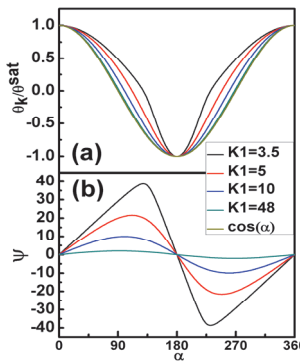


Fig. 2-4 (a) The (θ_K/θ^{sat}–α) curves (b) The equilibrium direction of magnetization ψ as a function of α in the case of EK /EH≥10.

In the case of $0.5 \le E_K/E_H \le 10$, as shown in Fig. 2-2 and 2-3, the distinguished characteristic is that the magnetic moment direction has a significant "jump" to ensure the saturation magnetization being the lowest energy state when the value of α reaches a critical value. There are two "jumps" in the θ_K/θ^{sat}–α curves. Two "down-jumps" occur in the θ_K/θ^{sat}–α curves in the case of $0.5 \le E_K/E_H \le 0.78$ (as shown in Fig. 2-2). Two "down-jumps" occur in the θ_K/θ^{sat}–α curves in the case of $0.78 \le E_K/E_H \le 10$ (as shown in Fig. 2-3). The magnetic anisotropy energy competes with the Zeeman energy. With the value of K_1 decreasing, "jump" point corresponding to the angle of the magnetic field and the EA becomes large and the magnetic anisotropy energy is reduced with respect to the Zeeman energy.

Fig. 2-4 shows the θ_K/θ^{sat}–α curves in the range of $E_K/E_H \geq 10$ corresponding to $K_1 \geq 3.41\times10^3$ J/m^3. The magnetic anisotropy energy is dominant in this region. Along with the increase of K_1, the ratio of E_K to E_H is also increased. But the angle ψ between saturation magnetization and the EA is decreased. When the value of K_1 is large enough, the direction of the magnetic moment is almost close to the easy axis. The angle ψ retains almost close to zero whatever the angle α is. At this time the angular dependence of the normalized Kerr rotation and cosine functions match well.

As the "down-jump" corresponding to the angle has an influence on accuracy of experimental data fitting and the value of K_1 and K_2, we will discuss it from the relationship of energy competition point of view.

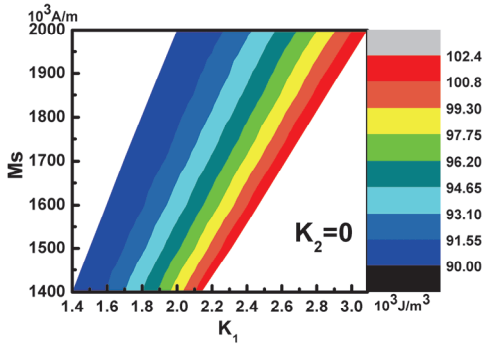


Fig. 3. Diagram with K_1-Ms. Color represents jumping point corresponding to the angle. Saturation magnetization Ms for Fe film fluctuates in the range of 20% and the field H is 20Oe.

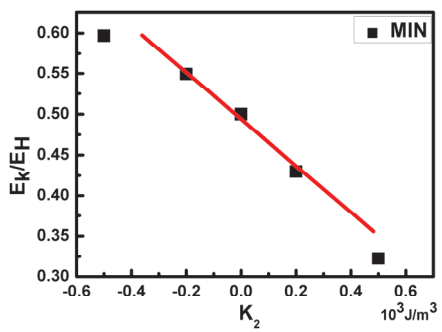


Fig. 4. E_K/E_H as a function of K_2 for jumping point corresponding to the minimum angle (black solid square). Linear fitting (Red line).

The difference of K_1 and Ms affects the interaction of magnetic anisotropy and saturation magnetization. In the case of the external magnetic field H=20Oe

and K_2=0, "down-jump" of the curves can be witnessed with the ratio of $0.5 \leq E_K/E_H \leq 0.78$. Multicolor represents jumping points corresponding to different angles which dark blue represents jumping point corresponding to the minimum angle 90° as shown in Fig. 3. The left boundary of multicolor part is the jumping point corresponding to the minimum angle meeting E_K/E_H=0.5.

Let us further consider K_2>0 and K_2<0, as K_2 influences the "down-jump" of the angular dependence of the normalized Kerr rotation. The decreasing energy ratio follows the increasing value of K_2, as is shown in Fig. 4. Although the magnetic anisotropy energy is reduced relative to the Zeeman energy, the saturation magnetization can still make a sudden deflection.

K_2 not only affects the ratio of E_K to E_H, also affects the value of K_1. In the case of fixing Ms, there is only the interaction between E_{K1} and E_{K2}. When saturation magnetization Ms is 1400×10^3 A/m, 1707×10^3 A/m or 2000×10^3A/m, jumping corresponding to the minimum angle requires to meet $\Delta K_2/\Delta K_1$=-0.5, as shown in Fig. 5. The value of K_1 is gradually decreased with the increasing value of K_2. At this time the relation of energy competition is shown in Fig. 6. With an increasing value of K_2, the energy E_{K2} accounts for the proportion to increase nonlinearly in the case of jumping corresponding to the minimum angle.

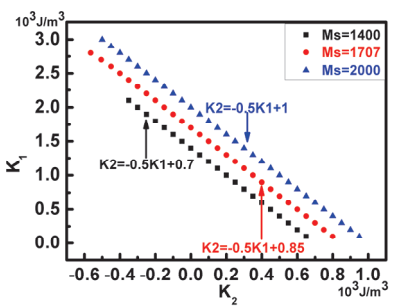


Fig. 5. K_1 as a function of K_2 at Ms=1400×10^3 A/m, 1707×10^3A/m and 2000×10^3A/m. The relation between K_1 and K_2 were obtained by linear fitting.

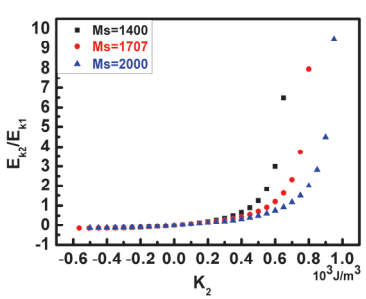


Fig.6. E_{K2}/E_{K1} as a function of K_2 at Ms=1400×10^3 A/m, 1707×10^3 A/m and 2000×10^3A/m.

4. Experiment

In-plane uniaxial anisotropy of Fe thin film is measured by ROTMOKE. The thickness of film is 100nm. We can get a series of normalized Kerr loops under different angles by applying a sufficient large rotating field. When the magnetic field is a fixed value, there are corresponding points in different normalized Kerr loops (as shown in Fig. 7-1). Different angles of α is corresponding to different points. Experimental points and fitting data are shown in Fig. 7-2. During the simulation, we use Ms =1700×10^{3}A/m for Fe film.

The fitting result shows anisotropy constants K_1=1.3×10^{3}J/m^3 and K_2=-0.2×10^{3}J/m^3 for Fe thin film with induced in-plane uniaxial anisotropy. X.L. Fan [13] *et al* studied on $Co_{92}Zr_8$ thin film with field-induced in-plane uniaxial anisotropy by rotating VSM and obtained anisotropy constants K_1=2.24×10^{3}J/m^3 and K_2=-4.7×10^{3}J/m^3. Because of the magnitude of induced magnetic field during deposition, the difference of anisotropy constants is reasonable.

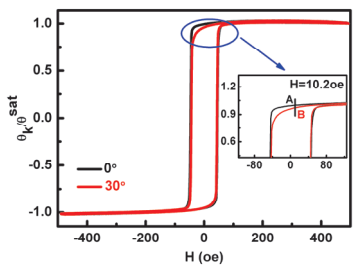


Fig. 7-1 Normalized Kerr loops of α=0°, 30°; H=10.2Oe and Kerr loops intersect at A and B.

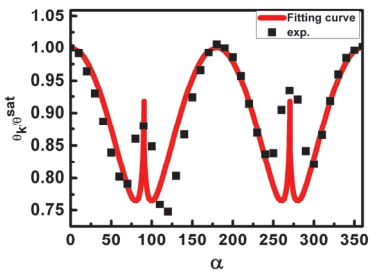


Fig. 7-2 Theoretical curve (red line) and the experimental results (black solid square) of 100nm Fe film sample at H=10.2Oe. Ms=1700×10^3 A/m.

5. Conclusions

The ROTMOKE method is a powerful tool for the measurement of magnetic anisotropy of magnetic nanomaterials. We research on the influence of energy competition relationship on the "down-jump" corresponding to angle. When "down-jump" corresponding to minimum angle occurs, the decreasing energy ratio of E_K to E_H follows the increasing value of K_2. When saturation magnetization Ms is constant, "down-jump" corresponding to the minimum angle requires to meet $\Delta K_2/\Delta K_1$=-0.5. The ratio of E_{K2} to E_{K1} increases in nonlinear way with the value of K_2 increasing. Meanwhile we measure Fe thin film by the ROTMOKE and obtain the anisotropy constants under the guidance

of theories. The research is helpful to obtain more accurate anisotropy constants for magnetic materials.

Acknowledgements

This work was finally supported by NSFC with Grant Nos. 10904097 and 11274233, and also supported by Scientific Research Base Development Program of the Beijing Municipal Commission of Education.

References

1. B. Heinrich, Z. Celinski, J.F. Cochran, A.S. Arrott, K. Myrtle, *J. Appl. Phys*. 70 (1991) 5769.
2. S.M. Rezende, J.A.S. Moura, F.M. de Aguiar, W.H. Schreiner, *Phys. Rev*. B 49 (1994) 15105.
3. B. Hillebrands, P. Baumgart, G. Gu¨ ntherodt, *Phys. Rev*. B 36 (1987) 2450.
4. Cowburn R P and Welland M E 2000 Science 2871466.
5. Cowburn R P 2002 *Phys. Rev*. B 65092409.
6. Allwood D A, Xiong G, Faulkner C C, Atkinson D and Cowburn R P 2002 Science 2962003.
7. Atkinson D, Allwood D A, Faulkner C C and Cowburn R P 2003 *Nature Materials* 285.
8. E.R. Moog, S.D. Bader, *Supperlattices Microstruct*. 1 (1985) 543.
9. S.D. Bader, E.R. Moog, P. Gru¨nberg, *J. Magn. Magn. Mater*. 53 (1986) L292.
10. W. Weber, A. Bischof, Ch. Wu¨rsch, R. Allenspach, *Phys. Rev. Lett*. 76 (1996) 1940.
11. R.P. Cowburn, A. Ercole, S.J. Gray, J.A.C. Bland, *J. Appl. Phys*. 81 (1997) 6879
12. E.C. Stone and E.P. Wohlfarth, *Phil. Trans. Roy. Soc*. A. 240, 559 (1948)
13. R. Mattheis, G. Quednaud, *J. Magn. Magn. Mater*. 205 (1999) 143
14. X.L. Fan, D.S. Xue, C.J. Jiang, Y. Gong, and J.Y. Li, *J. Appl. Phys*. 102, 123901 (2007)
15. Information from http://www.qd-china.com/products2.aspx?id=30.
16. P. Wolniansky, S. Chase, M. Ruane, and M. Mansuripur, *J. Appl. Phys*. 60, 346 (1986)

Cast Nylon/Bentonite Nanofibers Prepared for UV Resistance

Xinhua Liu[a†], Xu Yang[b] and Cuie Wang[c]

Coll. of Text. & Cloth., Anhui Polytechnic University, Wuhu 241000, China
E-mail: [a†]liuxinhua66@163.com, [b]787356809@qq.com, [c]cuiewang@126.com

Cast nylon / bentonite nanofibers were prepared by electrospinning method using formic acid and cast nylon/bentonite nanocomposite as raw materials. SEM was used to characterize the nanofibers, under the optimum reaction conditions: spinning solution concentration at 3%, voltage at 19.5kV, receiving distance at 130mm, the rate of spinning flow at 0.2ml/h, these nanofibers shows desirable dispersion and good length to diameter ratio. Furthermore, the UV resistance of the nanofibers was studied by HB902 UV resistance sunscreen testing system, the prepared composite nanofibers membrane can reach an excellent UV resistance of 280.3 UPF.

Keywords: Electrospinning; Composite Nanofibers; UV Resistance.

1. Introduction

UV could accelerate the aging of the skin and cause severe skin burns, red blisters, and even make people suffering from skin cancer. In recent years, the research on UV resistance of fabric has become a hot spot at home and abroad. R.H. Deshpande et al.[1] provided the fabric lasting UV protection by the nanometal oxide is deposited on the fabric. F.M. Meng et al.[2] obtained TiO_2 thin film containing silver by using magnetron sputtering method, and found that anti-UV properties of the film get better in a certain range. X.Y. Hu[3] gave the fabric UV resistant function by using chemical bath deposition, which enables the preparation of nano-ZnO and load of nano-ZnO on the surface of cotton fabric with one step. H. Wang et al.[4] generated CeO_2 nanoparticles on the surface of cotton fabric by a simple in situ synthesis method, which significantly promoted the cotton fabrics properties of UV resistance. D.Z. Xu[5] improved the UV resistance of the fabric by adding the modified TiO_2/ZnO composite powder in the polyester blending system.

Electrospinning is an effective method for preparing the polymer nanofibers directly and currently. Small fiber diameter, large specific surface area, which has the very high surface energy and activity, resulting in a small size effect,

† Corresponding author.

surface or interface effect, quantum size effect, etc. It has potential application value in filter, protective textiles, biological engineering and clinical medicine, etc.[6]. Our group[7] has prepared Nano TiO_2/ESBS fibe by electrostatic spinning and found the good UV resistance of nano TiO_2/ESBS fibers.

Based on the electrostatic spinning technology, cast nylon/bentonite nanofibers were prepared by using self-made nylon/bentonite nanocomposites, in this paper. We prepared cast nylon/bentonite nanofibers and studied their UV resistance that provided the scientific basis for the development of high UV resistance materials.

2. Experimental

2.1. *Materials and instruments*

Cast nylon/bentonite nanocomposite materials, manufacturing methods as shown in literature[8]. Formic acid, chemical pure, Sinopharm Chemical Reagent Co., Ltd.; Nano-TiO_2 and nano-SiO_2, chemically pure, Anhui Kena New Materials Co., Ltd. JA103 analytical balance, Shanghai Precision Instrument Co., Ltd.; KQ-400KDB high-power ultrasonic cleaning machines, Kunshan Ultrasonic Instrument Co., Ltd.; 79-1 magnetic stirrer, Jintan Jierui Er Electric Co., Ltd.; homemade electrospinning machine; Hitachi S-4800 scanning electron microscope; high power microscope (US Labomed optical microscope); DHG-9010A-type electric oven thermostat blast; HB902 UV through the tester; aluminum foil (commercially available).

2.2. *Preparation spinning solution and nanofiber membrane*

A certain quality of cast nylon/bentonite nanocomposite material which dissolved in formic acid solvent and confecting the mass fraction of 3% solution, a uniform spinning solution of nylon/bentonite was obtained by magnetically stirred until the materials completely dissolved. Then, Nylon/bentonite spinning solution were added to a certain quality of nano-TiO_2 and nano-SiO_2 to obtain nylon/bentonite/TiO_2 and nylon/bentonite/SiO_2 uniform spinning solution after ultrasonic dispersion.

The spinning solution is continuously injected into the spinneret and received on the aluminum foil. Nanofiber membrane were peeled off from the aluminum foil, then placed in dry box and set aside.

2.3. *Performance and characterization*

SEM was employed to observe the morphology of the fibers the average diameter was calculated from thirty fibers as the spinning experiment fiber

diameter with Photoshop CS6 software. Calculating the coefficient of variation as a measure of the experiment fibers spun dispersion (uniformity).

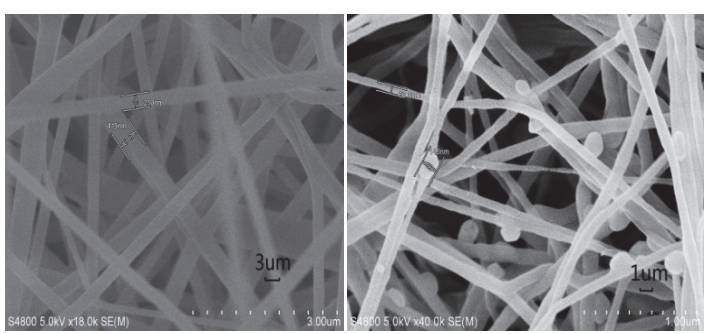
2.4. *UV resistance test*

Using GB/T 18830 standard, HB902 UV resistance sunscreen testing system is used to test UPF numerical value of UV resistance with a variety of samples.

3. Results and Discussion

3.1. *The impact of electrospinning parameters*

The impact of electrospinning voltage on fiber morphology and diameter. Nylon/bentonite uniform spinning solution was spinning in the process parameters as receiving distance at 13cm, spinning flow rate at 0.2ml/h, voltage at 14.5kV and 19.5kV, to observe the effect of voltage on the spinning system, such as the results were shown in Fig. 1, the diameter of the fibers were shown in Table 1. As we can be seen in Fig. 1, the fibers had a diameter of 321nm as voltage at 14.5kV(a); when the voltage was increased to 19.5kV(b), the fiber became thin and had a diameter of 82nm. This phenomenon occurs due to the high voltage make the electrostatic spinning solution is much greater than the surface tension, so that the jet could have a greater drawing and form smaller diameter fibers. Meanwhile, as the voltage increases, the coefficient of variation of the fiber is increased which indicate that the uniformity is deteriorated. The reason for increasing dispersion of the fibers is that jet instability was obvious as soon as the voltage was increased. Therefore, spinning voltage can be selected as 19.5kV.



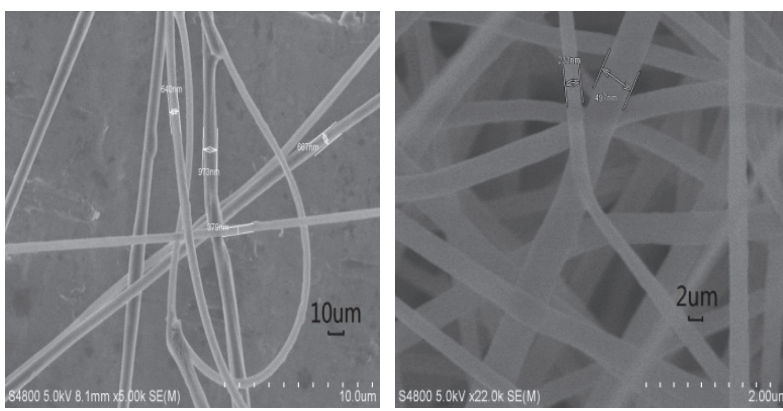
(a) (b)

Fig. 1. The SEM image of cast nylon/bentonite nanofibers at different electrospinning voltage. (a) The electrospinning voltage at 14.5kV. (b) The electrospinning voltage at 19.5kV.

Table 1. Electrospun fiber diameter at different voltage.

Voltage/(kV)	Diameter/(nm)	Variation Coefficient/(%)
14.5	321	22.30
19.5	82	24.23

The impact of electrospinning receiving distance on fiber morphology and diameter. Nylon/bentonite uniform spinning solution was spinning in the process parameters as voltage at 14.5kV, spinning flow rate at 0.2ml/h, receiving distance at 9cm and 13cm,to observe the effect of receiving distance on the spinning system, such as the results were shown in Fig. 2, the diameter of the fibers were shown in Table 2. As we can be seen in Fig. 2, the fibers had a diameter of 757nm as receiving distance at 9cm(a); When the receiving distance was increased to 13cm, the fiber became thin and had a diameter of 257nm(b). This phenomenon occurs due to the electric field in the jet can have a longer residence time in order to achieve a sufficient stretching of fibers. Meanwhile, the increasing coefficient of variation with increasing receiving distance, it indicating that the uniformity is deteriorated. The reason is that the fiber field force will be weakened by increasing receiving distance, leading to the thickness uniformity decreased of the fibers. Therefore, spinning receiving distance can be selected as 13cm.



(a) (b)

Fig. 2. The SEM image of cast nylon/bentonite nanofibers at different receiving distance. (a) The receiving distance at 9cm. (b) The receiving distance at 13cm.

Table 2. The diameter of nanofibers at different receiving distance.

Receiving Distance/(cm)	Diameter/(nm)	Variation Coefficient/(%)
9	757	22.48
13	257	25.80

3.2. *UV resistance*

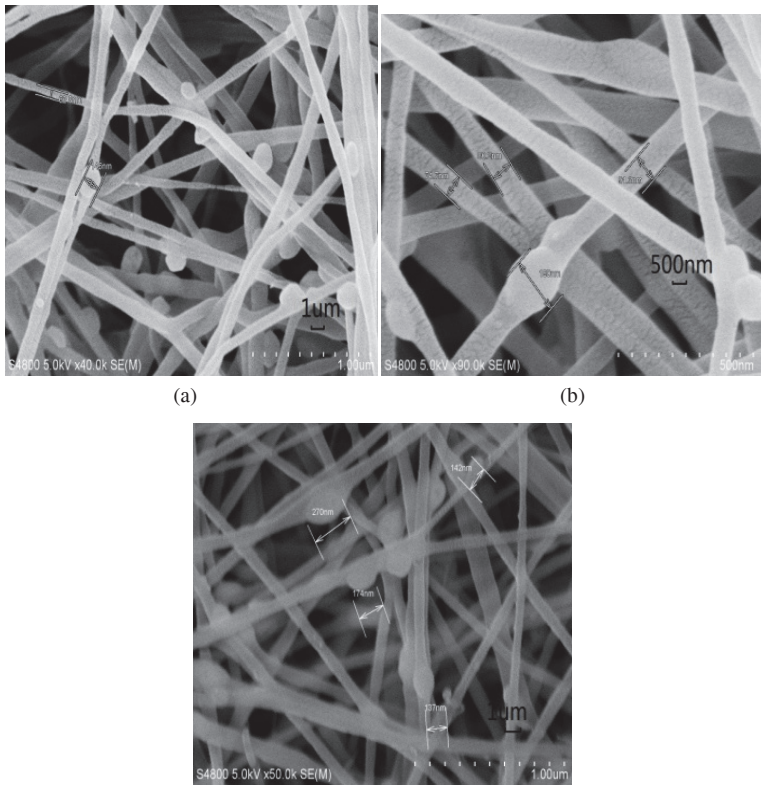
With spinning solution concentration at 3%, voltage at 19.5KV, receiving distance at 130mm, the rate of spinning flow at 0.2ml/h, cast nylon/bentonite nanofiber membrane, cast nylon/bentonite/TiO_2 nanofiber membrane and cast nylon/bentonite/SiO_2 nanofiber membrane were fabricated. The UV resistance test data obtained by UV test systems were shown in Table 3.

Table 3. The UV resistance of different nanofiber membrane.

Sample	Upf
Cast nylon/bentonite nanofiber membrane	280.3
Cast nylon/bentonite/tio_2 nanofiber membrane	40.0
Cast nylon/bentonite/sio_2 nanofiber membrane	43

As we can be seen in Table 3, the UPF of cast nylon/bentonite nanofiber membrane can reach 280.3 that shows an excellent UV resistance. According to the article of J.H. Qian[9], UV transmittance of pure polyamide film is 80% to 50%, the UV resistance of polyamide is relatively poor. Meanwhile, the UPF of nanofiber with anti-ultraviolet UV shielding agent is only about 40.

In order to analyze the differences in UV resistance, SEM image of three kind of nanofiber membrane were shown in Fig. 3. In Fig. 3(a) bentonite particles were in the uniform distribution on the surface of nylon fibers, which has small internal effects on nylon fibers. However, Fig. 3(b), (c) showed that cast nylon/bentonite/TiO_2 nanofiber membrane and cast nylon/bentonite/SiO_2 nanofiber membrane respectively. TiO_2 and SiO_2 were simply wrapped inside the fibers their UV shielding performance were greatly reduced and even disappear. UV effect is also reduced when the shape of the fiber changed after adding TiO_2, SiO_2. The different phenomenon could be understood that the layer structure of bentonite can stripe every other layers to form nanometer particles which can distribute in the fiber well. However, with the addition of TiO_2 and SiO_2, particles were gathered together because of high surface area and energy.



(a) (b)

(c)

Fig. 3. The SEM image of three kinds of nanofiber membrane. (a) Cast nylon/bentonite nanofiber membrane; (b) cast nylon/bentonite/TiO2 nanofiber membrane; (c) cast nylon/bentonite /SiO2 nanofiber membrane.

4. Summary

(1) Under the optimum reaction conditions: spinning solution concentration at 3%, voltage at 19.5kV, receiving distance at 130mm, the rate of spinning flow at 0.2ml/h, the desired nanofibers were fabricated.

(2) The bentonite particles were distributed uniformly on the surface of nylon fibers Nylon/bentonite nanofiber membrane has excellent UV resistance, the UPF value can reach 280.3.

Acknowledgements

The authors thank National Natural Science Foundation of China (Grant No. 21302001).

References

1. R.H. Deshpande, K.G. Chava and W.Q. He: Ultraviolet-blocking cotton textiles using nano-TiO2. *J. Melli and China*. 07(2014)50-52.
2. F.M. Meng, Z.Q. Sun: Enhanced photocatalytic activity of silver nanoparticles modified TiO2 thin films prepared by RF magnetron sputtering. *J. Materials Chemistry and Physics*. 118 (2009)349-353.
3. X.Y. Hu: Preparation of Superhydrophobic and UV-Blocking cotton fabrics based on nano-ZnO (MS. DongHua University, China 2013)
4. H. Wang, Y. Tao, Y.P. Xia, C. Feng, H.P. Wu and G.L. Tao: In-situ synthesis of nano-ceria on cotton fabric and its UV resistant performance. *J. Functional materials*.S3 (2010)524-526,529.
5. D.Z. Xu, Y. Luan, J. Guo and D. Li: Effects of super fine powder of TiO2/ZnO on UV-resistance and mechanics of PET fiber. J. *Journal of Dalian Polytechnic University*. 02(2009)124-127.
6. X.C. Tao, X.H. Liu, R.Y. Chen and E.Y. Chi: Preparation of nano-TiO2/ESBS composite fiber using electrostatic spinning and its ultraviolet resistants. J. *New Chemical Materials*. 40(2012)125-127.
7. Q.F. Ke, X.Y. Jin: nonwovens, second ed., Donghua University Press, Shanghai, 2010.
8. X.H. Liu: Chinese Patent 1420143. (2003).
9. J.H. Qian, Z.J. Cheng and Q.Y. Tao: Preparation and Property of Anti-ultraviolet Polyamide Chip. J. *Journal of Textile Research*. 05(2004)30-31,151.

Research on Electrical Properties of Carbon Fiber-Steel Slag Cement Based Composites

Weiguo Xing

Beijing Linkzone Technology Co. LTD,
Beijing, 100024, China
E-mail: 13910664903@139.com

Xiushu Tian, Lei Liu, Rui Shen

School of Material Science and Engineering,
Shijiazhuang Tiedao University, Hebei, 050043, China
E-mail: tianxiushu@163.com

In this paper, the effects of carbon fiber and steel slag on the electrical properties at different ages have been studied. The structures were characterized by SEM. The experimental results show that with the increasing of carbon fiber, fibers tend to lap over each other, result in the formation of the conductive channel. When the content of carbon fiber is more than 0.5%, the amount of carbon fiber is not the main factor affecting the change of resistivity, resistivity of cement mortar is obviously weakened. When the content of steel slag is low, conductive phases can not be contacted with each other, addition of steel slag and carbon fiber can not reduce the resistivity significantly. With the increasing of steel slag, the distance between conductive materials is nearer, the conductive function of carbon fiber and ferric oxide in steel slag is enhanced, the electron and the hole is conducted by means of the tunnel effect, at this time, the resistivity of cement based composites decreased rapidly, the steel slag contact with each other, forming a conductive network.

Keywords: Electrical property; Carbon fiber; Steel slag; Cement based composites.

1. Introduction

Smart concrete, is formed by adding appropriate amount of materials with special functions as carbon fibers, carbon black, steel slag or nanophase material into the concrete, which can sense its own strain and damage, is more attractive due to its strong mechanical properties and self-monitoring characteristics such as self-monitoring, self-diagnosis, self-regulation and self-healing[1-2].

Currently, researches on preparation of cement based composites by using steel slag and carbon fiber can be found at home and abroad[3-5]. Sheif Y [6] prepared a kind of conductive concrete with steel fiber and steel slag, but the stability of resistivity is relatively poor due to the corrosion of steel fiber and steel slag. Effects of steel slag on Seebeck coefficient in the heating and cooling process and resistivity of carbon fiber cement omposites were investigated by Xia qiang[7], the results showed that addition of steel slag could improve Seebeck coefficient and as steel slag increased, the Seebeck coefficient increased at first and then decreased, resistivity decreased with more steel slag and the percolation phenomenon was observed. Carbon fiber reinforced cement-based composite also is an intrinsically smart material that has many functional properties, such as high conductivity, piezoresisitivity, temperature-sensitivity and Seebeek effect [8].

However, the mechanism of steel slag and carbon fiber's role in concrete should be studied further. Therefore, carbon fiber and steel slag were used as reinforcing materials in this paper, the effects on electrical properties of cement based materials are discussed detailly.

2. Experimental Procedure

2.1. *Materials*

Steel slag, produced by Beijing Kenaikete special new material Co Ltd was used in the test. The chemical compositions of steel slag are given in Table 1.

Table1 Chemical constituent of steel slag.

Constituent	CaO	MgO	Al2O3	Fe2O3	SiO2	f-CaO	others
Content（%）	30.8	9.17	6.02	18.7	29.2	1.13	4.98

Carbon fibers of 5-10 mm in nominal length were used. Methylcellulose was used as dispersing agent.

Standard river sand was used as fine aggregates.

P•O 42.5 cement was used in the tests.

2.2. *Specimen preparation*

Cement (450g) , sand and steel slag (total amount is 1350g) , and part of the water (the water-cement ratio is 0.5) mixed 3min by cement mortar mixer, then methylcellulose-carbon fiber solution was added slowly, after adding of defoaming agent, the mortar was mixed rapidly for 3min, to ensure homodisperse cement paste can be obtained.

The electrode must be laid in the specimen and it must be protected from rusting. Therefore, the copper mesh was used as the electrode. The diameter of the holes must be greater than or equal to the maximum aggregate size of 5 mm to allow cement mortar to flow through to ensure a good bond between the electrode and the cement mortar.

Cement mortar specimens for electrical conductivity was 40×40×160 mm. After molding and curing at 20±1ºC and 95% R.H. for 1 day, the specimens were demolded and cured in natural water for 7, 14 and 28 days, three specimens of each group were tested, and finally took the average reading.

2.3. *Testing and characterization*

The flexural strength was tested by cement bending testing machine. The compressive strength was tested by NYL-60 compression-testing machine.

The four-probe method was used in this paper for measuring the conductivity of the cement mortar samples.

Calculate the conductivity as follow,

$$R = \frac{U}{I} \quad , \tag{1}$$

$$\rho = \frac{RS}{L} \quad , \tag{2}$$

Where:

ρ ... Volume resistivity [kΩ•cm],

L ... Length [cm],

S ... Area [cm2]

The microstructure of samples were determined by scanning electron microscopy (SEM: Type JSM-5610LV) with an accelerating voltage of 20kV.

3. Results and Discussion

3.1. *Effect of carbon fiber on resistivity*

Fig.1 shows the effect of carbon fiber on resistivity of 7, 14 and 28days. The resistivity of the specimens decrease with the content of carbon fiber increasing, and increase fractionally as the content is more than 0.5% (weight percent of cement).

When content of carbon fiber is less than 0.5%, carbon fiber can be dispersed uniformly in the mortar, but the quantity of overlapping fiber is less, conductive network cannot be formed. With the increasing of carbon fiber, fibers tend to lap

over each other, conductive channels are formed. When the content of carbon fiber is more than 0.5%, the amount of carbon fiber is not the main factor affecting the change of resistivity, resistivity of cement mortar is obviously weakened.

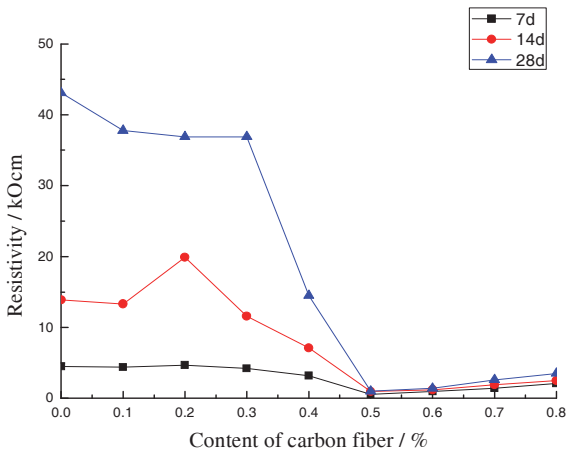


Fig.1 Effect of carbon fiber on resistivity

3.2. *Effect of steel slag on resistivity*

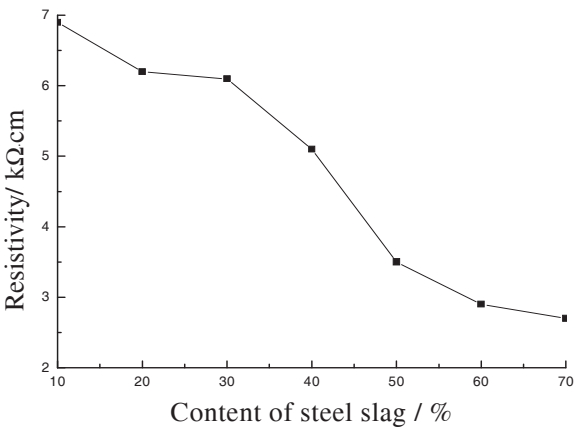


Fig.2 Effect of steel slag on resistivity

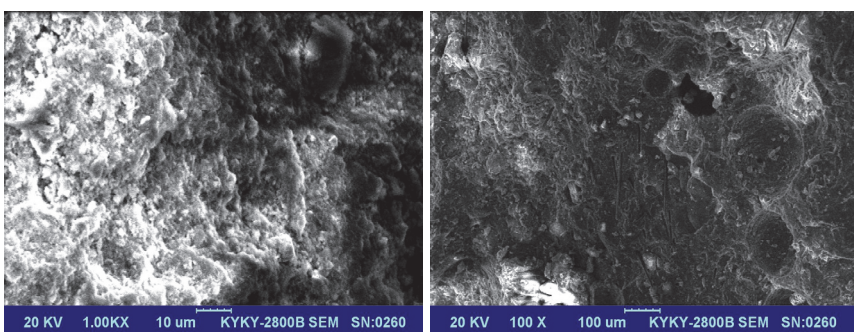
Fig.2 shows the effect of steel slag on resistivity of 28 days specimens with 0.5% carbon fiber. The resistivity of the specimens decrease with the content of steel slag increasing, and decrease slowly as the content is more than 50%. Through the experiment, it is found that steel slag-carbon fiber cement based composites has

conductivity. Cement matrix is an insulator to electricity, carbon fiber and steel slag are conductive, they superpose each other and form the conductive network, which can make the cement based material capable of conducting.

When the content of steel slag is low, conductive phases can not be contacted with each other, addition of steel slag and carbon fiber can not reduce the resistivity significantly. With the increasing of steel slag, the distance between conductive materials is nearer, the conductive function of carbon fiber and ferric oxide in steel slag is enhanced, the electron and the hole is conducted by tunnel effect, at this time, a conductive network is formed, the resistivity of cement based composites decreased rapidly. Then the steel slag continues to increase, the resistivity continues to decline, but the rate of decline is slow.

3.3. *SEM characterization*

The morphology of the hydration paste with different content of carbon fiber at 28 days are displayed in Fig.3. From Fig.3 (a), we can see that the paste has a dense structure, carbon fiber cannot overlap between each other, integrity conductive network cannot be formed, thus the conductivity is poor. From Fig.3 (b), it can be found that carbon fiber can be integrated with the cement hydration products closely, thus the electrical properties of carbon fiber-steel slag cement-based composites have been improved.



(a) SEM of paste without carbon fiber (b) SEM of paste with 0.6% carbon fiber

Fig.3 The SEM photograph of the paste with different content of carbon fiber at 28d

4. Conclusions

Steel slag-carbon fiber cement based composites have conductivity. With the increasing of carbon fiber, fibers tend to lap over each other, result in the formation of the conductive channel. When the content of carbon fiber is more than 0.5%, the amount of carbon fiber is not the main factor affecting the change of

resistivity, resistivity of cement mortar is obviously weakened. When the content of steel slag is low, conductive phases can not be contact with each other, addition of steel slag and carbon fiber can not reduce the resistivity significantly.

With the increasing of steel slag, the distance between conductive materials is nearer, the conductive function of carbon fiber and ferric oxide in steel slag is enhanced, the electron and the hole is conducted by tunnel effect, the steel slag continue to increase, the resistivity continue to decline, but the rate of decline is slow.

Acknowledgements

The writers are grateful for support provided through the youth foundation of Hebei Educational Committee (NO. Q2012023).

References

1. Han B, Yu X, Ou J. Self-Sensing Concrete in Smart Structures. Butterworth-Heinemann, 2014.
2. Chen P W, Chung D D L. Carbon fiber reinforced concrete for smart structures capable of nondestructive flaw detection. *Smart Materials and Structures*, 2(1993), 22-30.
3. Qian J, Li C, Tang Z, et al. Experimental Study on Electric Conductive Concrete Made from Steel Slag Quenching with Wind. *Journal of Building Materials*, 3(2005), 004.
4. Zuo J, Yao W, Wu K. Seebeck effect and mechanical properties of carbon nanotube-carbon fiber/cement nanocomposites*[J]. Fullerenes, Nanotubes and Carbon Nanostructures*, 2014
5. Wu J, Xu A Q. Micro-Experimentation Research on Compression Sensitivity of Carbon Fiber Concrete *[J]. Applied Mechanics and Materials*, 470 (2014), 137-140.
6. Sheif Y and Christopher Y:‘Conductive concrete overlay for bridge deck deicing’, *ACI Materials Journal*,96(1999),382-390
7. Xia Qiang and Zuo Junqing:‘Effects of Steel Slag on Temperature Sensibility of Carbon Fiber Cement Composites’, *Fly Ash Comprehensive Utilization*, 3(2014), 6-8
8. Cao H Y, Yao W, Qin J J. Seebeck effect in graphite-carbon fiber cement based composite*[J]. Advanced Materials Research*, 177(2011), 566-569.

Research on Mechanical Properties of Carbon Fiber-Steel Slag Cement Based Composites

Tian Xiushu, Meng Limin, Shen Junjun
School of Material Science and Engineering, Shijiazhuang Tiedao University, Hebei, 050043, China
E-mail: tianxiushu@163.com, 1096326983@qq.com, shenjunjun2007@126.com

In this paper, the effects of carbon fiber and steel slag on the mechanical properties at different ages have been studied. The structures were characterized by SEM. The experimental results show that the higher content of carbon fiber may enhance the strength, but dispersion of the carbon fibers in the cement matrix is difficult when the content is more than 0.6%. The strength of the specimen decrease with the content of steel slag increasing, which is due to lessen of hydration products with the decrease of cement content, when the content of steel slag is 5%~15%, the later hydration activity will be favorable to raise the 28 days strength.

Keywords: Mechanical properties; Carbon fiber; Steel slag; Cement based composites.

1. Introduction

The main by-product of the steel manufacturing process is slag. It was used in civil engineering projects tenths of years ago [1-3]. Steel slag can be used as conductive component to prepare smart cement-based materials of excellent mechanical properties. Compared to other intelligent materials (fiber grating sensor, piezoelectric materials, memory alloys), steel slag has a natural compatibility with traditional concrete materials, can be considered as an intrinsic intelligence material in concrete structure.

Currently, researches on preparation of cement based composites by using steel slag can be found at home and abroad [4~7]. Wang Fengchi [8] studied the electrical and mechanical properties of steel slag concrete with diffent ratio of slag to cement, the results show that the resistivity of the concrete is significantly reduced due to steel slag and can be further reduced through addition of fly ash. The result made by quanjuanjuan[9] shows that steel slag in the composite cement materials can actively and rapidly participate in the hydration reaction process,

hydration products generated are evenly crisscrossed together, the gel is compacted, and mechanical properties of cement stone formed is good.

However, the mechanism of steel slag's role in concrete should be studied further. The mechanical and electrical conductivity of cement based materials can be increased by adding carbon fiber [10] therefore, carbon fiber and steel slag were used as reinforcing materials in this paper, and the effects on mechanical properties of cement based materials are discussed detailly.

2. Experimental Procedure

2.1. *Materials*

Steel slag, with the grain size of less than 5mm， produced by Beijing Kenaikete special new material Co Ltd was used in the test. The chemical compositions of steel slag are given in Table 1.

Carbon fibers of 5-10 mm in nominal length were used. Methylcellulose was used as dispersing agent. The properties of carbon fiber are given in Table 2.

Standard river sand was used as fine aggregates.

P•O 42.5 cement was used in the tests. The properties of cement are given in Table 3.

Table 1 Chemical constituent of steel slag

Constituent	CaO	MgO	Al2O3	Fe2O3	SiO2	f-CaO	Others
Content（%）	30.8	9.17	6.02	18.7	29.2	1.13	4.98

Table 2 Properties of carbon fiber

Item	Tensile Strength	Content of C	Density	Resistivity
Value	3.6~3.8GPa	≥95%	1.6~1.76 g/ cm3	1.5×10 - ³Ω·cm

Table 3 Properties of cement

Item	Density	Specific Surface Area	Initial Setting Time	Final Setting Time	Cubage Stability
Value	2.90 g/ cm3	453m2/kg	2:55(h : min)	4:15(h : min)	up to standard

2.2. *Specimen preparation*

Cement (450g) , sand and steel slag (total amount is 1350g) , and part of the water (the water-cement ratio is 0.5) mixed 3min by cement mortar mixer, then methylcellulose-carbon fiber solution was added slowly, after adding of defoaming agent (0.2g), the mortar was mixed rapidly for 3 min, to ensure homodisperse cement paste can be obtained.

Cement mortar specimens was 40×40×160 mm. After molding and curing at 20±1ºC and 95% R.H. for 1 day, the specimens were demolded and cured in natural water for different ages, three specimens of each group were tested, and finally took the average reading.

2.3. *Testing and characterization*

The compressive strength was tested by NYL-60 compression-testing machine. The flexural strength was tested by cement bending testing machine.

The microstructure of samples were determined by scanning electron microscopy (SEM: Type JSM-5610LV) with an accelerating voltage of 20kV.

3. Results and Discussion

3.1. *Effect of carbon fiber on compressive strength*

Fig.1 shows the effect of carbon fiber on compressive strength of 3 and 28 days. The strength of the specimen increases with the content of carbon fiber increasing, and decrease as the content is more than 1.2% (weight percent of cement). When the content of carbon fiber is 1.2%, the 3 days cement strength increases about 40%, 28 days strength increases about 22%.

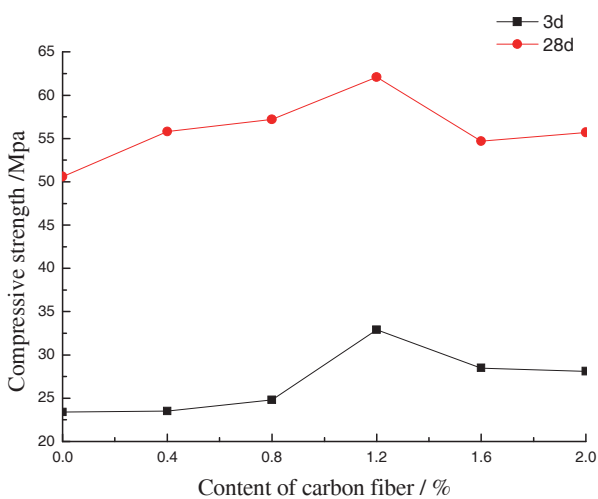


Fig.1 Effect of carbon fiber on compressive strength

It reveals that, carbon fiber makes positive contributions to the mechanical properties. When a small amount of carbon fiber is uniformly dispersed in the cement paste, the carbon fibers act as a nucleus to tightly bond with cement

hydrate and further promote cement hydration, which is favorable for the strength of cement mortar. Another reason is that the carbon fibers fill the cement pores, thus increasing the strength. But dispersion of the carbon fibers in the cement matrix is difficult when the content is more than 1.2%, thus the strength decrease.Test results also show that, the specimens without carbon fiber have fragments under stress, the specimens with carbon fiber can keep better integrity under stress.

3.2. *Effect of steel slag on compressive strength*

Fig.2 shows the effect of steel slag on compressive strength of 3 and 28 days. The strength of the specimen decrease with the content of steel slag increasing. When the content of steel slag is more than 15% (percent of aggregates), the fall tendency shows a relatively smooth change at 3 days, but sharply change at 28 days. This phnemenon is due to the lessen of hydration products with the decrease of cement content, so the hardened paste has a higher porosity, poor density and compressive strength.When the content of steel slag is 5%~15%, the later hydration activity will be favorable to raise the 28 days strength. When the content is more than 15%, steel slag cannot be well dispersed and the homogenous hydrate microstructure cannot be formed.

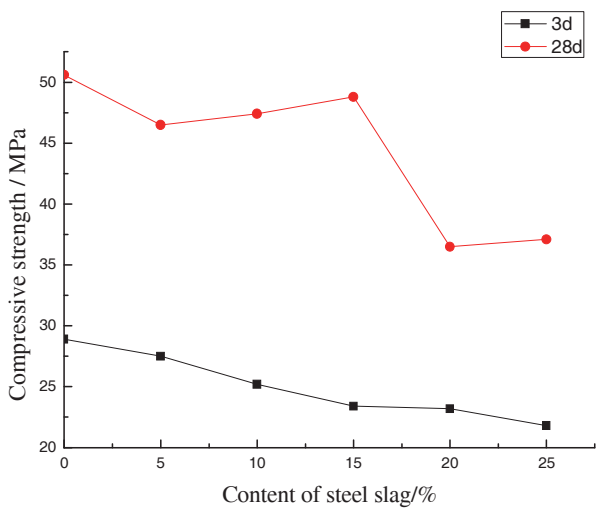


Fig.2 Effect of steel slag on compressive strength

3.3. *Effect of steel slag on flexural strength*

Fig.3 shows the effect of steel slag (with 0.5% carbon fiber) on flexural strength of 7, 14 and 28 days. When the content of steel slag is 30%, the 7d strength

increases to 4.8MPa, the 14d strength increases to 5.1MPa, the 28d strength increases to 5.3MPa.

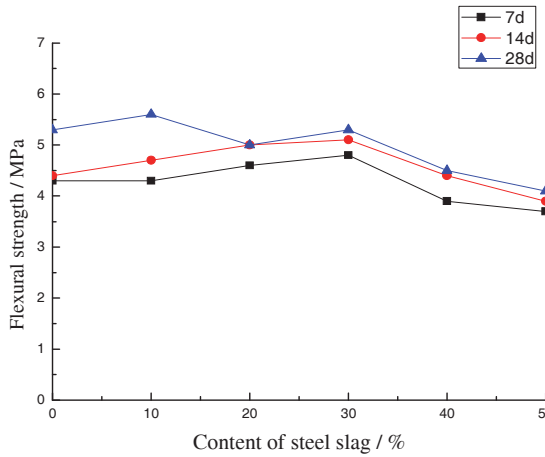
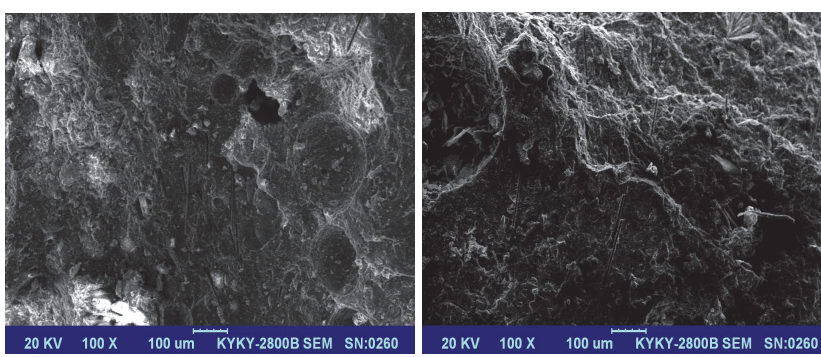


Fig.3 Effect of steel slag on flexural strength

It reveals that, when the content of steel slag is low, the network is formed by hydration products of cement and fiber, which leads to a better load-bearing capacity of composites. When subjected to flexural loading, the composites show a higher flexural strength. When the content of steel slag is high, cement paste is not sufficient to fill the voids between the steel slag, resulting in lower flexural strength.

3.4. *SEM characterization*



(a) SEM of paste with 0.6% carbon fiber (b) SEM of paste with 1.0% carbon fiber

Fig.4 The SEM photograph of the paste with different content of carbon fiber at 28d

The morphology of the hydration paste with different content of carbon fiber at 28 days are displayed in Fig.4. From Fig.4(a), we can see that the paste has a dense structure and a lower porosity when less carbon fiber dispersed uniformly. From Fig.4(b), we can see that the aggregation of carbon fiber appear in the specimen.

4. Conclusions

Carbon fiber makes positive contributions to the mechanical properties. When a small amount of carbon fiber is uniformly dispersed in the cement paste, the carbon fibers act as a nucleus to tightly bond with cement hydrate and further promote cement hydration, which is favorable for the strength of cement mortar.But dispersion of the carbon fibers in the cement matrix is difficult when the content is more than 0.6%, thus the strength decrease.

The compressive strength of cement mortar with steel slag is lower than that of plain cement mortar with the same w/c, indicating that steel slags are not valuable for reinforcing cement mortar.This phnemenon is due to the lessen of hydration products with the decrease of cement content.

When subjected to flexural loading, the composites show a higher flexural strength. But when the content of steel slag is high, cement paste is not sufficient to fill the voids between the steel slag, resulting in lower flexural strength.

Acknowledgements

The writers are grateful for support provided through the youth foundation of Hebei Educational Committee (NO. Q2012023).

References

1. Geiseler J. Slag-approved material for better future. In: Proceeding of international symposium on the utilization of metallurgical slag (ISUS 99), Beijing, China; 1999.
2. Qasrawi H, Shalabi F, Asi I. Use of low CaO unprocessed steel slag in concrete as fine aggregate[J]. *Construction and Building Materials*, 2009, 23(2): 1118-1125.
3. Manso J M, Polanco J A, Losañez M, et al. Durability of concrete made with EAF slag as aggregate[J]. *Cement and Concrete Composites*, 2006, 28(6): 528-534.
4. Tang Zuquan,Qian Jueshi,Wang Zhi, et al:‘Experimental study on electrical conduction of steel slag reinforced concrete’, *Concrete*, 6 (2006), 12-14.
5. Jia Xingwen, Qian Jueshi, Tang Zuquan, et al: ‘Research on compression sensitivity of steel slag concrete’, *Materials Review*, 22(2008), 122-124.

6. Ahmedzade, Perviz and Sengoz, Burak: 'Evaluation of steel slag coarse aggregate in hot mix asphalt concrete', *Journal of Hazardous Materials*, 165(2009), 300-305.
7. Sheif Y and Christopher Y: 'Conductive concrete overlay for bridge deck deicing', *ACI Materials Journal*, 96(1999), 382-390.
8. Wang Fengchi, Zhang Manyuan and Song Wen, et al: 'Conductive and Mechanic Properties of Steel Slag Concrete', *Journal of University of Jinan,* 4(2014), 306-310.
9. Quan juanjuan, Zhang Kaifeng, and Zhao Shiran, et al: 'Mechanism of Steel Slag in Hydration Process of Composite Binder', *Industrial Safety and Environmental Protection*, 39(2013), 41-44.
10. Sun Yafei, Huang Xin and Gao Xiang, et al: 'Optimal Dosage of Different Carbon-based Conductive Materials in Paste', *Bulletin of the Chinese Ceramic Society*, 2(2014), 261-265.

Investigation of the Structure of the Electrodeposited Alloy CoNiW by Methods HAADF STEM and AFM

Aleksey Kirillov, Evgeny Modin, Evgeny Pustovalov, Aleksandr Ferorets, Aleksandr Dubinets†, and Vladimir Plotnikov

Far Eastern Federal University, Russia
†E-mail: dubinetc.av@dvfu.ru,
E-mail: kirillov.av@dvfu.ru, modin.eb@dvfu.ru, pustovalov.ev@dvfu.ru, fedorec.an@dvfu.r, plotnikov.vs@dvfu.ru

In this paper we investigated the structure of amorphous and nanocrystalline alloys of CoNiW obtained by electrolytic deposition. Studies were performed by transmission electron microscopy in HAADF mode and atomic force microscopy. In the course of the work was to obtain new data on the structure of materials. It has been found that tungsten is more homogeneous distributed in the alloy than nickel or cobalt. This is due to higher mobility of the atoms of nickel and cobalt in the electrolyte.

Keywords: Electron microscopy, Atomic force microscopy, Amorphous alloys, Nanocrystalline alloys, Co-Ni-W, HAADF STEM.

1. Introduction

At present nanocrystalline and amorphous alloys of iron group elements and the refractory elements are advanced functional materials. Increasing interest in two-and three-component alloys with iron group metals obtained by electrochemical deposition with tungsten content. It is caused by their unique combination of tribological, electrical and electrical properties [1], which allows them to serve as an alternative to chromium coatings [2]. Also, these films with a columnar structure and a perpendicular magnetic anisotropy have a wide range of magnetic characteristics can be used for information recording devices with a high density [3]. Adding a third element to the binary alloy of tungsten in some cases it may improve the properties of the corrosive properties of such an alloy Co-Ni-W has better corrosion resistance than similar alloys electrodeposited amorphous Co-W [4]. Further, tungsten alloys may be possible alternative costly platinum and alloys containing platinum group metals [5]. Also alloys containing tungsten

obtained by electrolytic deposition may be used in the production technology of microstructures (LIGA) [6].

Method of electrolytic deposition allows to form the tungsten-containing coating on the surfaces of complex shape and significant area, and have a significant influence on the final properties of such coatings, depending on the composition of the plating tank and the deposition parameters. In [7] it is shown as the introduction of additives into the electrolyte improves the surface quality and also results in amorphization fields and increases the physical and mechanical properties of the produced coatings. Since the service properties depend on the structural features of materials, it is important to investigate the morphology and chemical composition of possible fluctuations in order to optimize the deposition parameters.

Due to the high spatial resolution the main tool for the study of surface topography on the nanometer scale is by far the atomic force microscopy (AFM). In [8-10] methods are used AFM to obtain information about the morphology of the films based on Co-W. In particular, a significant difference was shown in morphology between crystalline and amorphous films on the basis of Co-W was investigated density of nucleation of surface coatings, morphology and electrical properties of films based on Co-W, and has also been investigated relationship between impulse responses and the deposition surface morphology.

In recent years, the scan mode HAADF (high-angle annular dark field) in a scanning transmission electron microscopy (STEM) has become a popular method for the analysis of the position, the type and amount of atoms, as it provides accurate interpretable images — this is due to the fact that the intensity of the image HAADF-STEM clearly shows Z-contrast and very sensitive to the number of atoms. In published studies, showing the advantage of HAADF mode relative to the standard mode CTEM, due to the influence of the parameters of the microscope and the sample on the phase of the diffracted beams [11]. Shows the use of HAADF mode for the quantitative determination of the number of atoms and their location in the three-dimensional crystal, freeform sample without the need for calibration [12]. Also by computer simulation evaluated the accuracy of the HAADF-STEM in determining the thickness of the thin foil and the number of atoms contained in individual atomic columns [13].

2. Objects and methods

In this study we investigated the structure of the amorphous and nanocrystalline alloys of CoNiW obtained by electrodeposition from sulfuric acid solutions with the addition of sodium hypophosphite. All samples were deposited in the

conditions under which the formed amorphous alloys. System CoNiW - stationary and non-stationary mode of deposition with frequencies from 1 Hz to 10 kHz and Ni concentration from 0 to 70 at.%, acidity pH = 6.5; electrolyte temperature T = 30-40°C; cathode current density 25 mA/cm^2.

3. Discussion and conclusions

The structure of alloys of CoW-CoNiW amorphous and has defects in the form of the density fluctuations. The average size of the regions with higher density was 7 nm with a dispersion of ~ 4 nm. Analysis of the image alloys CoW-CoNiW, showed that the structure contains objects with a diameter between 5 to 100 nm.

On the HAADF-STEM image was observed structure in the form of grains with different contrast characteristic of electrolytically deposited films of this composition, Fig.1a. The film surface has a height differences, according to atomic force microscopy - more than 40 nm, Figure 1b. It was found that there inhomogeneity of chemical composition — in the dark areas of the image corresponding to thinner portions of the film, the concentration of W is observed at the 5-10% higher than the light sections. Such fluctuations in the chemical composition may be associated with features of film growth CoNiW, as for the deposition of W in the formation of such films are used modes other than the deposition Co-Ni. The structure of alloys CoNiW in the initial state is amorphous and has defects in the form of the density fluctuations. The average size of the regions with higher density was 7 nm with a dispersion of ~ 4 nm. Analysis of the image alloys CoNiW, showed that the structure contains objects with a diameter between 5 to 100 nm.

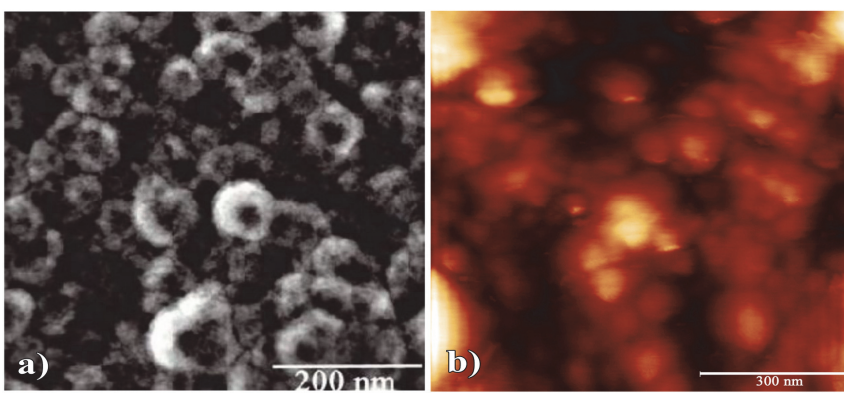


Fig. 1 Images of CoNiW film. On "a" HAADF STEM image of film. On "b" AFM image of structure CoNiW

4. Conclusions

In this paper we investigated the structure of amorphous and nanocrystalline alloys of CoNiW obtained by electrolytic deposition. Studies were performed by transmission electron microscopy in HAADF mode and atomic force microscopy. In the course of the work was to obtain new data on the structure of materials. It has been found that tungsten is more homogeneous distributed in the alloy than nickel or cobalt. This is due to higher mobility of the atoms of nickel and cobalt in the electrolyte. The thicker areas enriched nickel alloy and the finer tungsten. Thus, the structural features and the possibility obtain a surface with specified sizes of the structural elements, making these materials perspective for practical application. Also, a comparative analysis of the results obtained by scanning electron microscopy and atomic force microscopy.

References

1. Bodaghi, J. Hosseini / *Int. J. Electrochem. Sci.*, 7 (2012) 2584-2595
2. Tsynlsaru N.. Bobanova J.. Cesiulis X.Ye.H., Dikusar A., Prosycevas /., Ce/is J.-P. Surface Coatings Technology. 2009. 203(20-21), 2983-3332
3. G. Boiioni. D. Candolfo. A. Cecchetti, VM. Fedosyuk. F. Masoli. *Journal of Magnetism and Magnetic Materials.* 1993, 120, 213-216
4. Santana, R.A.C., Campos, A.R.N., Medeirosv, E.A., Oliveira, A.L.M., Silva, L.M.F., Prasad, Sh. Studies on Electrodeposition and Corrosion Behavior of a Ni–W–Co Amorphous Alloy Journal of Materials Science 42 (22) 2007: pp. 9137–9144
5. Ved, M., Sakhnenko, M., Nenastina, T., Bairachna, T., Korniy, S. Corrosion and Catalytic Properties of Galvanic Binary d6-8 Metal Alloys Physicochemical Mechanics of Materials 7 2008: pp. 346 – 353
6. Ehrfeld, W., Hessel, V., Lowe, H., Schulz, Ch., Weber, L. Materials of LIGA Technology Microsystem Technologies 5 1999: pp. 105–112.
7. Zh. I. Bobanova, V. I. Petrenko, G. F. Volodina, D. Z. Grabko, and A. I. Dikusar Properties of CoW Alloy Coatings Electrodeposited from Citrate Electrolytes Containing Surface Active Substances Surface Engineering and Applied Electrochemistry, 2011, Vol. 47, No. 6, pp. 493–503
8. Yu, Y.D., Yu, Z., Li, W., Hu, X.K., Ge, H.L., Wei, G.Y. Preparation of Co-W-P alloy films by pulse plating Surface Engineering Volume 27, Issue 9, October 2011, Pages 671-675
9. Armyanov, S., Valova, E., Franquet, A., Dille, J., Delplancke, J.-L., Hubin, A., Steenhaut, O., Kovacheva, D., Tatchev, D., Vassilev, Ts. Crystalline and

amorphous electroless Co-W-P coatings J*ournal of the Electrochemical Society* Volume 152, Issue 9, 2005, Pages C612-C619

10. Malki, M., Rozenblat-Raz, A., Duhin, A., Inberg, A., Horvitz, D., Shacham-Diamand, Y. Thin electroless Co(W,P) film growth on titanium-nitride layer modified by self-assembled monolayer Surface and Coatings Technology Volume 252, 15 August 2014, Pages 1-7
11. S.J. Pennycook, L.A. Boatner Chemically sensitive structure-imaging with a scanning transmission electron microscope Nature, 336 (1988), pp. 565–567
12. J.M. LeBeau, S.D. Findlay, L.J. Allen, S. Stemmer Standardless atom counting in scanning transmission electron microscopy Nanoletters, 10 (2010), pp. 4405–4408
13. R. Erni, H. Heinrich, G. Kostorz Quantitative characterisation of chemical inhomogeneities in Al–Ag using high-resolution Z-contrast STEM Ultramicroscopy, 94 (2003), pp. 125–133

Effect of Cooling Rate on Microstructure and Transformation Temperature of GCr15 Bearing Steel

Xiangdong Huo†, Zhenzhuo Tian

School of Material Science and Engineering, Jiangsu University, Zhenjiang 212013, China
†E-mail: hxdustb@163.com, 1040757889@qq.com

Liejun Li

School of Mechanical and Automotive Engineering, South China University of Technology, Guangzhou 510641, China
E-mail: liliejun@scut.edu.cn

Nianfu Liu

Shaoguan Iron and Steel Group Co. Ltd., Shaoguan 512123, China
E-mail: liunf2004@163.com

Gleeble-3800 thermo-simulation system was used to study the effect of cooling rate on transformation of GCr15steel. The dynamic CCT diagram was established, microstructure and hardness of experimental specimens were analyzed. As the cooling rate lower than 5ºC.s-1, the transformed microstructure is composed of pearlite colony and proeutectoid carbide precipitated on the grain boundary. The starting and finishing transformation temperature gradually decreased with the cooling rate increasing. Under higher cooling rate, partial austenite transformed to martensiteas temperature lower than 187ºC. Vickershardness increases obviously with cooling rate increasing, which can be explained by the following reasons. The diameter of pearlite colony and the pearlite lamellar spacing becomes smaller at lower cooling rate, and martensite and retained austeniteappears at higher cooling rate.

Keywords: Bearing steel; Cooling rate; Transformation; Carbide network.

1. Introduction

GCrl5 steel is a bearing steel with high carbon and highchromium. It is widely used in bearing manufacturing industry. About 80% of the bearing steel products in China are the GCrl5 steel [1-3].The cooling rate is one of important parameters during producing GCr15 bearing steel. GCrl5 is hypereutectoid steel and proeutectoid carbide precipitated firstly from austenite when it is cooled slowly

after high temperature rolling. Secondary carbide grows up along austenite grain boundary and forms network. Carbide network can cause decrease in the lifetime of bearings. In order to obtain the microstructure mainly including thin pearlite without network carbide, it is important to study the effect of cooling rate on microstructure and transformation of GCr15 bearing steel[4,5]. Unfortunately, relevant work is insufficient. In this paper, Gleeble-3800 thermo-simulation system was used to study the microstructure and transformation temperature with different cooling rate after hot compressive deformation of GCr15steel.The dynamic CCT diagram of GCr15 steel was established and continuous cooled microstructure was investigated.

2. Experimental Procedure

A commercial GCr15 high-chromium bearing steel produced by asteel company was investigated in this paper. The chemical composition of the GCr15 steel used in this study is shown in Table 1. The experiments were conducted on the Gleeble-3800 thermo-simulation system. The specimens were taken from a round bar of 50 mm in diameter and were machined to the shape and dimension as Fig. 1.

Table 1. Chemical composition of GCr15 steel investigated [wt. %].

C	Si	Mn	S	P	Cr	Ni	Cu
0.98	0.24	0.35	0.001	0.013	1.47	0.009	0.01

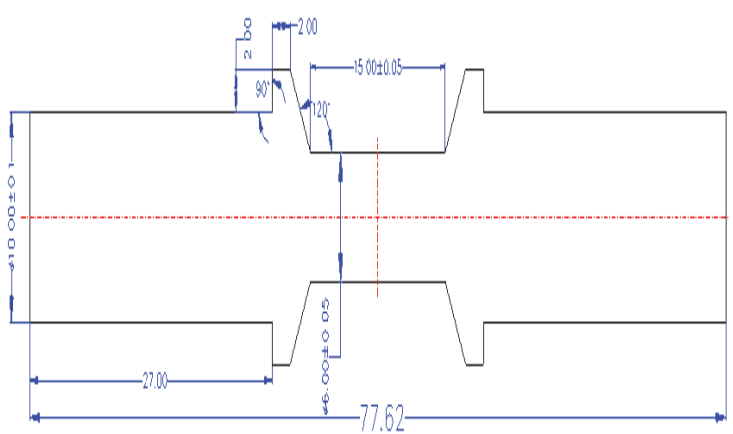


Fig. 1 The specimens for thermal simulation study.

The corresponding specimens were firstly heated to 1100ºC at the heating rate of 10ºC.s^{-1} and austenitized for 5min, subsequently were cooled to 980ºC at a rate of 10ºC.s^{-1} and deformed by approximately 40%; the stain rate is 5/s. The samples were continuously cooled to 860ºC and deformed by approximately 30% as the stain rate 8/s, then cooled to room temperature at the cooling rate of 0.5, 1, 1.5,2, 3, 5,8, 10, 15, 20ºC.s^{-1}.

The microstructure was investigated and the dynamic CCT diagram was constructed on the basis of observation by light optical microscopy and the dilatometric analysis. The specimens for metallographic examination were mechanically ground, polished and etched with a 3%Nital solution, and then observed with LEICA DM 2500M optical microscopy.

3. Results and Discussion

3.1. *Effect of cooling rate on the final microstructure*

Fig. 2 shows the microstructures of GCr15 steel formed as a result of various cooling rate. As the cooling rate changes from 0.5 to 2ºC.s-1, the transformed microstructure is composed of lamellar pearlite and white carbide distributed on the grain boundary. Proeutectoid carbide precipitated on the grain boundary forms unbroken, distinct network. The diameter of pearlite colony is large and lamellar structure of pearlite can be seen obviously.

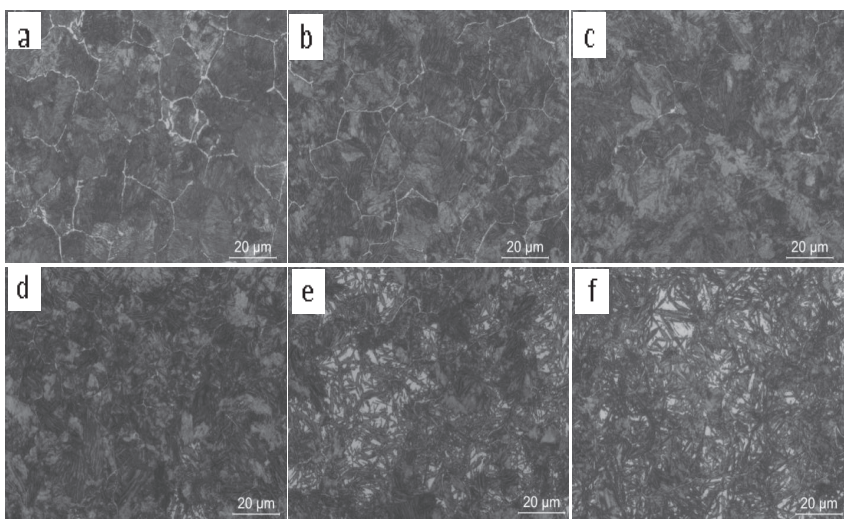


Fig. 2 The optical micrographs for GCr15 steel at different cooling rate.
(a) 0.5ºC.s^{-1}, (b) 2ºC.s^{-1}, (c) 3ºC.s^{-1}, (d) 5ºC.s^{-1}, (e) 8ºC.s^{-1}, (f) 10ºC.s^{-1}

As the cooling rate increases from 3 to 5ºC.s-1, the diameter of pearlite colony becomes smaller gradually, and the lamellar structure of pearlite can't be seen. Network carbide along grain boundary is not obvious, and rod or line proeutectoid carbide precipitated on the grain boundary.

With the cooling rate increasing, the transformation of diffusion controlling is more difficult and the transformation with shear mode is predominant. As the cooling rate increases to 8ºC.s-1, the transformed microstructure is dominated by pearlite and martensite, small amount of fine spot carbide distributes in matrix. The primary microstructure is martensite and some retained austenite as the cooling rate higher than 10ºC.s-1, and proeutectoid carbide can't be seen.

3.2. *The dynamic CCT diagram*

Fig. 3 shows dynamic CCT curves established according to transformation temperature and microstructures at different cooling rate.

As the cooling rate lower than 5ºC.s-1, the formed microstructure primary includes proeutectoid carbide and pearlite. The major transformation temperature of experimental steel ranges from 600 to 700ºC and the starting and finishing transformation temperature gradually decrease as the cooling rate increasing. As the cooling rate changes from 8 to 10ºC.s-1, the starting transformation temperature dramatically decreases and the line of finishing temperature disappears. Over-cooled austenite subsequently transforms to martensite when temperature attains to 187ºC. As cooling rate is higher than 10ºC.s-1, proeutectoid carbide and pearlite transformation are inhibited, and partial austenite transforms to martensite after the temperature lower than 187ºC. The primary microstructure is martensite and partial retained austenite.

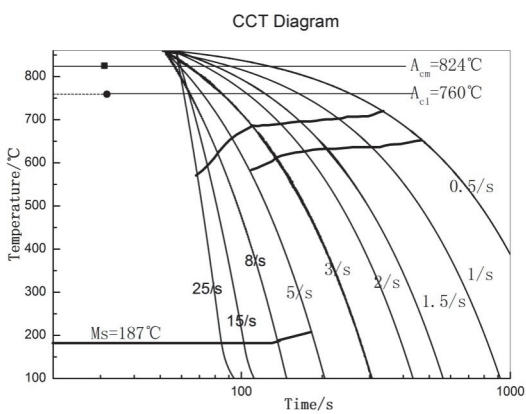


Fig. 3 The dynamic CCT diagram of GCr15 steel.

3.3. *Effect of cooling rate on hardness*

The relationship between cooling rate and hardness of experimental steel is given in Fig. 4. With the cooling rate increasing, Vickershardness of experimental steel raises obviously. The diameter of pearlite colony and the pearlite lamellar spacing becomes smaller, which is the main reason for hardness increasing as the cooling rate changes from 0.5 to 5ºC.s-1. Under the higher cooling rate, martensite and retained austenite are responsible for the high Vickers hardness.

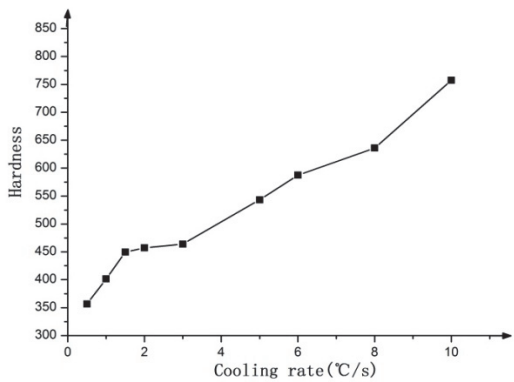


Fig. 4 Effect of cooling rate on hardness of GCr15 steel.

4. Conclusions

The microstructure and transformation temperature of GCr15steelwith different cooling rate were investigated by using Gleeble-3800 thermo-simulation system. The results can be summarized as follows.

As the cooling rate lower than 5ºC.s-1, the transformed microstructure is composed of pearlite colony and proeutectoid carbide precipitated on the grain boundary. The major transformation temperature ranges from 600 to 700ºC, the starting and finishing transformation temperature gradually decrease with the cooling rate increasing.

As the cooling rate exceed 8ºC.s-1, the finishing temperature line disappears and over-cooled austenite transforms to martensite as temperature lower than 187ºC. At higher cooling rate, the primary microstructure is martensite and partial retained austenite.

With the cooling rate increasing, Vickers hardness raises obviously. The diameter of pearlite colony and the pearlite lamellar spacing becomes smaller at

lower cooling rate, and martensite and retained austenite are responsible for hardness increasing at higher cooling rate.

References

1. Y.K. Sun and D. Wu: *J. Iron Steel Res. Int.* Vol. 16(2009), p.61
2. J.G. Zhang, D.S. Sun, H.S. Shi, et al: *Mater. Sci. Eng.* Vol. A326(2002), p.20
3. N.Q. Peng, G.B. Tang, J. Yao, et al: *J. Iron Steel Res. Int.* Vol. 20(2013), p.50
4. F. Yin, L. Hua, H.J. Mao, et al: *Materials and Design*, Vol. 43(2013), p.393.
5. C.X. Yue, L.W. Zhanga, S.L. Liao, et al: *Mater. Sci. Eng.* Vol. A499(2009), p.177

Influence of Electrical Voltage on the Wear Resistance of TA2 Alloy

Guo Xiaojuan[a], Li Muqin[b*], Wei Fanghong[c], Ma Chen[d]

College of Materials Science & Engineering,
Jiamusi University, Heilongjiang, 154007, P. R. China
*E-mail: [a]xzqgxj@163.com, [b]*jmsdxlimuqin@163.com*

The ceramic coating was in in-situ synthezed on the surface of the TA2 alloy substrate by the micro-arc oxidation technology. The silicate-aluminate solution was choosed as the electrolyte solution. The effects of in-situ micro-arc oxidation coatings thickenss on the wear resistance on TA2 alloy was investigated in details by means of pin-on-disk tester. The experimental results proved that MAO coatings were mainly consist of rutile TiO_2 phase and the thickness and content of rutile TiO_2 phase in the MAO coatings increased as the micro-arc oxidation voltage improved. The wear resistance of TA2 alloy was obviously improved when the thickness of MAO coating was closed to 10μm ~11μm.

Keywords: TA2 Alloy, MAO Coating, Wear performance.

1. Introduction

In recently, the micro-arc oxidation (MAO) has attracted more attention in virtue of its convenience and effectiveness to fabricate ceramic coatings on the surface of Ti, Al, Mg and their alloys. Micro-arc oxidation technology (MAO) was an effective method to improve the corrosion and wear resistance of the Ti, Al, Mg and their alloys. The coating properties were determinded by several factors, which included that substrate compositions, electric parameters, compositions of electrolytes solution and so on. It had been reported that ceramic coating prepared with MAO on a Ti alloy surface attaches firmly to the substrate[1-4]. The applied electric parameters had a more important influence on the properties of the resulted MAO coatings because they were related with the coating thickness, structure and surface morphologies[5, 6]. Titanium and alloys were potentially very suitable materials for load bearing implant material for the bio-medical material applications because of their high modulus of elasticity formability, good ductility and strength to weight ratio. At present, more reports about MAO technique were focused on the surface treatment of value metal Ti,

* Corresponding author.

Al, Mg and their alloys in order to improve corrosion resistance. However the applications of titanium alloys were limited due to their low hardness, high friction coefficient and relative weak wear resistance performance. So it was necessary to make effort to improve the wear resistance of titanium alloys. However, few researches could be available to concern on the effect of MAO coating thickness on the wear resistance of the bio-medical TA2 titanium. In this paper, the effect of thickness on wear resistance of the MAO coating on the surface of TA2 titanium was investigated. Meanwhile, the phase composition and the worn surface morphology of MAO coatings on TA2 alloy were analyzed.

2. Experimental Process and Characterization

The pure titanium (TA2) was utilized as substrate material, which were cut into the dimension ϕ10mm×1.5mm. Samples were ground with 800-grit SiC sandpaper and cleaned ultrasonically in acetone and de-ionized water before treatment. Electrolyte were prepared by dissolved Na_2SiO_3, KOH, Na_3PO_4 and KF solution in de-ionized water with pH value of 11-13. The concentration of the Na_2SiO_3, KOH, Na_3PO_4 and KF were 5g/L, 10g/L, 15g/L, 6g/L, respectively. The frequency and duty of the DC field were 500 Hz and 12%. The electrical voltage parameters were varied from 300V to 450 V. at the same time, the electrolyte temperature was controled in the scale of 20-40ºC. In the experimental process, the average figure of the thickness of specimens coating by 300V, 350 V, 400V, and 450V were about 6.1±0.30μm, 7.9±0.2μm, 10.4±0.3μm and 14.2±0.2μm. Each sample was oxidized for 10 min and then cleaned ultrasonically in acetone and de-ionized water before further analysis.

The phases of four specimens were evaluated by X-ray diffraction (XRD, Brooke Advance-8 style) using Cu K_α radiation, between 20° and 90° with increments of 0.02°. Microstructure of the specimens was observed using a scanning electron microscope (SEM, Hitachi JEOM, Japan). The coating thickness was measured by the TT260 digital coating thickness equipment. Balls of SAE 52 100 steel (hardness HRC 61) with a diameter of 6.0 mm was used as the counterface materials against MAO coating using the domestic SET-2M ball-on-disc tester under dry-sliding conditions. The normal load was 300g and the time was about 30min. The friction coefficient was recorded by the computer during each test. The wear tracks of the worn samples were observed and analyzed by means of a scanning electron microscopy (SEM). At least five specimens were chosen at different experimental in order to induce the experimental error.

3. Results and Discussion

The XRD patterns of the MAO coating were given in Fig.1. At the beginning of MAO surface treatment process, the rutile and anatase phases peaks formed gradually. As the electrical voltage improved, the thickness of MAO coating became large and the diffraction peak of the rutile TiO_2 strengthened gradually. This implied that the content of rutile TiO_2 was determinded by the electrical voltage during the MAO process.

Fig. 2 showed the relative curve between the friction coefficient, the thickness of MAO coating and electrical voltage. The friction coefficient of the MAO coating reduced gradually and then improved. The minimum figure was about 0.5 when electrical voltage was about 400V.When the electrical voltage was beyond 450V, the figure of friction coefficient became rebound. The MAO coating is structured with a porous loose layer in the outmost layer. With the improve of voltage, hole radial size and roughness will increase. The conclusion drawn is consistent with the result of the previous reports[5, 6]. The wear properties of MAO coating were related to the interface structure, the phase composition and coating thickness.

The wear mechanism was different under the difference of the interface bond occurred. When the electrical voltage was low, the interface force between coating and TA2 substrate was weak, so the coating was easy to pull out during the friction process. At the same time, the pull-out material became the friction media and then it accelerated friction procedure, so the friction coefficient was higher than TA2 substrate (about 6.5). When the electrical voltage was beyond 400V, the interface force between coating and TA2 substrate strengthened, so the friction coefficient was lower than the TA2 substrate.

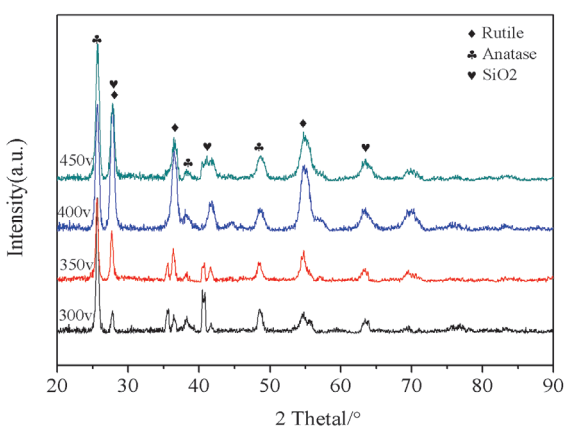


Fig. 1. XRD patterns of MAO coating with different electrical voltage.

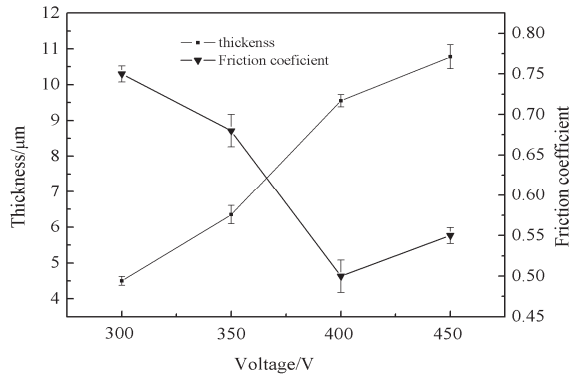


Fig. 2. Tribology test of MAO coatings and TA2 at 300Hz under 300g loading.

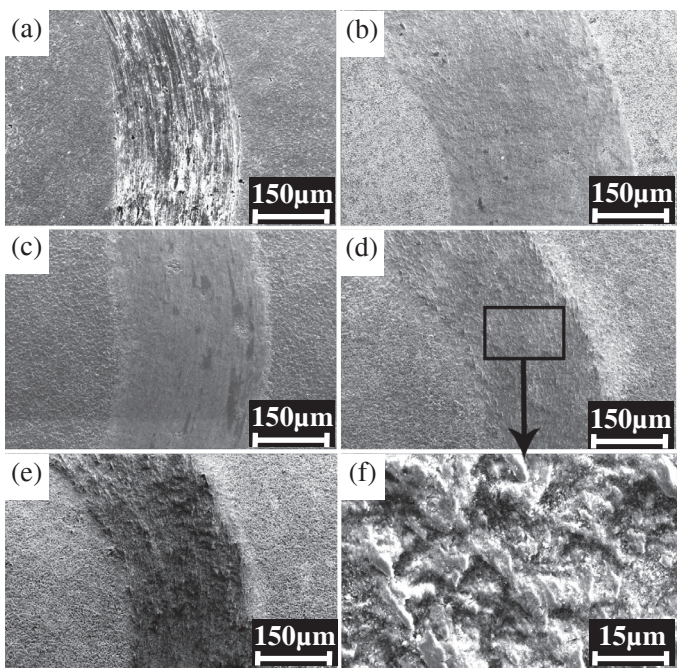


Fig. 3. SEM micrographs of worn surfaces for TA2 and MAO coating after sliding against steel ball (a) substrate (b) 300v (c) 350v (d) 400v (e) 450v.

The surface morphology of the wear tracks was listed in Fig. 3. The depth of friction ring on the TA2 substrate (Fig. 3(a)) was obviously deeper than that of MAO coating samples (Fig. 3(d)). This result was consistent with the friction coefficient of substrate and MAO coatings. The surface of TA2 substrate had

wide grooves and straight scratches while the wear tracks of MAO coatings became shallow and narrow. The adhesive and abrasive wear was the mainly mechanism during the friction process. This relative reports demonstrated that MAO process would improve the wear resistant properties. This experimental results implied that appropriate MAO treatment would improve wear performance in some degree.

4. Conclusion

(1) The MAO coating of the TA2 alloy largely was consisted of anatase and rutile phase TiO_2 and the ratio of rutile increased with its electrical voltage. At the same time, the coating thickness of the TA2 alloy increased with electrical voltage increasing.

(2) The MAO specimens showed better wear resistance than the substrate. The adhesive and abrasive wear was the mainly mechanism during the friction process after MAO specimens on the TA2 alloy.

Acknowledge

The authors were grateful for support by the graduated student innovation research projects of Jiamusi University (LZZ2014_013).The National Science Foundation of China (No.31370979, No.31370859). Heilongjiang university innovation team construction projects, biomedical materials and surface modification (2012TD010); Youth Foundation of Jiamusi University (LQ2012-41).

References

1. Y.M. Wang J.W. Gu, et al. Development and characterization of MAO bioactive ceramic coating grown on micro-patterned Ti6Al4V alloy surface [J]. *Applied Surface Science*, 2014; 299: 58–65.
2. Chail L Y, Yu X, Yang Z H, et al. Anodizing of magnesium alloy AZ31 in alkaline solutions with silicate under continuous sparking [J]. *Corrosion Science*, 2008, 50: 3274-3279.
3. Luo Z Z, Zhang Z Z, Liu W M, et al. Tribological properties of solid lubricating film/micro-arc oxidation coating on Al alloys. *Trans. Nonferrous Met. Soc. China*, 2005, 15 (6): 1231-1236.
4. Zhang Y X, Han Y, Huang P, et al. Adhesive strength and bioactivity of titania films prepared by micro-arc oxidation. *Journal of the Chinese Ceramic Society*, 2004, 32(2): 122-126.

5. WU Xiang-qing, XIE Fa-qin, et al. Effects of additives on corrosion and wear resistance of micro-arc oxidation coatings on TiAl alloy. *Transactions of Nonferrous Metals Society of China*, 2010, 20: 1032–1036.
6. Ebru Emine Demirci, Ersin Arslan, et al. Investigation of wear, corrosion and tribocorrosion properties of AZ91 Mg alloy coated by micro arc oxidation process in the different electrolyte solutions. *Thin Solid Films*. 2013; 528: 116–122.

Simultaneous Imaging Polarimeter Using an Azo-polymer Orientation Array

Peizheng Yan[a], Keyi Wang[c*], Xinyu Zhang[d] and Pengcheng Cui[e]

Department of Precision Machinery and Precision Instrumentation, University of Science and Technology of China, Hefei, 230026, China
E-mail: [a]ypz@mail.ustc.edu.cn, [c]kywang@ustc.edu.cn, [d]xinyuzh@mail.ustc.edu.cn, [e]cuei930@mail.ustc.edu.cn*

Jiangang Gao[b]

2School of Biological and Chemical Engineering, Anhui Polytechnic University, Wuhu, 241000, China
[b]gaojiangang@ahpu.edu.cn

A simultaneous imaging polarimeter based on a wave-splitting method has been proposed using an orientation array from an ordinary azo-polymer film with photo-induced optical anisotropy. The polarization states and the formation of the polarimeter have been analysed theoretically using Jones matrix calculations. The experimental results have been achieved to verify the feasibility of the proposed method, by which the azo-polymer orientation array is easy to fabricate making it convenient and low-cost. The polarimeter also demonstrates a new application of azo-polymer film.

Keywords: Anisotropic optical materials; azo-polymer film; imaging polarimeter.

1. Introduction

Azobenzene and its derivatives have attracted much attention over the past few decades due to their clean photochemical and substantial changes in material properties during light irradiation[1-5]. Fundamentally, the applications of azo-containing materials are based on the photoisomerization action of azochromophores.

In azo-polymers, there has been extensive research on the reorientation of azobenzene groups induced by linearly polarized light through photochemical trans-cis-trans isomerization. A high polarizability along the long molecular axis of the azobenzene fragments in the trans-conformation determines birefringence effects for the light outside the absorption band[1,5,6]. The large degree of optical

* Corresponding author.

anisotropy enable the creation of various types of highly efficient and functional anisotropic gratings, in which optical anisotropy is periodically modulated.

In the present paper, we focus our attention on the anisotropic gratings made of azo-polymer and its application in polarization measurement. The most general state of polarization of a light beam is conveniently described by four Stokes parameters. Imaging polarimetry has the potential to be a key sensor technology in a number of target detection applications[7]. This has typically been accomplished by manipulating a temporal sequence of images, each of which are acquired by imaging through either a rotated polarization filter or a sequence of different polarization filters. This time-sequential approach has inherent limitations when there is object motion in a scene, camera movement, or uncertainty in image registration between frames.

Another solution is to acquire the polarization data simultaneously on a single focal plane array (FPA) or multiple FPAs. Several polarimeter designs have been proposed to measure polarization simultaneously[8-10]. In this paper we describe a simultaneous imaging polarimeter using an azo-polymer orientation array.

2. Experimental Procedure

The azo-polymer (abbreviated as PCN6) used in this part of the work is a conventional side-chain liquid crystalline polymethacrylate bearing 4-(6-methacryloyloxyalkyloxy)-cyano- azobenzene groups according to the previous report [11], and the structure of PCN6 is shown in Fig. 1. The thickness of the transparent film was measured on a Shimadzu UV-2550 UV-VIS spectrophotometer to be about 2μm.

The experimental setup used to encode the birefringence in the photopolymer is shown in Fig. 2. The light of a solid-state laser (405 nm) is polarized parallel to the y-axis and azimuth of optical axis of the quarter-wave plate is $\pi/4$ with respect to the y-axis. The azo-polymer film was mounted on a precision x-y-moving stage and located in the conjugate image plane of the mask. Rotate the polarization of the laser beam to $\pi/6$, $-\pi/6$, $-\pi/3$ and $\pi/3$ sequentially by rotating the polarizer. When the azo polymer was illuminated untill it saturation, the phase retardance between its fast axis and slow axis was measured to be 110 degree for laser of 632.8nm. Before each changes of the voltage, the azo polymer was moved by T/2 along x-axis or y-axis. After four exposures, the azo-polymer was orientatied periodically to form an azo-polymer orientation array. As a result, a set of four (2×2) microretarders with the same degree of retardation, whose fast axes have four different angles, are arranged into a “unit cell”, which is repeated contiguously over the entire array shown in Fig. 3.

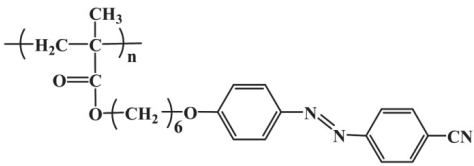


Fig. 1 Chemical structure of PCN6.

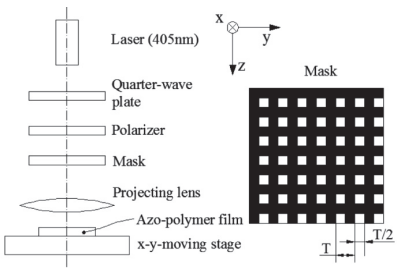


Fig. 2 Experimental setup for fabricating an azo-polymer orientation array.

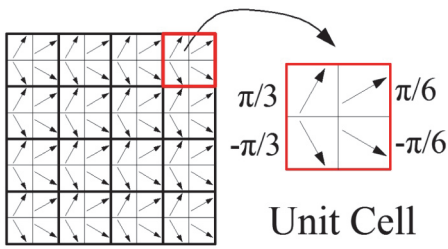


Fig. 3 Fast axes of the azo-polymer orientation array.

Using the fabricated azo-polymer orientation array, an imaging polarimeter shown in Fig. 3 is proposed and the optical axis of polarizer is parallel to the vertical direction. The azo-polymer orientation array is placed at the conjugate image plane of the CCD. Each microretarder of a uint cell is imaged to a pixel of the CCD. The unit cell can be thought of as a super-pixel. For any light illuminated onto the azo-polymer orientation array, its Stokes parameters can be calculated by the image caupured by the CCD. We have theoretically analysed this imaging polarimeter using Jones matrix calculations. An arbitrary polarization state of light with the Jones vector can be represented as :

$$E_{in} = \begin{bmatrix} E_x(t) \\ E_y(t) \end{bmatrix} = \exp(-i\omega t) \begin{bmatrix} E_x \exp(i\varphi_x) \\ E_y \exp(i\varphi_y) \end{bmatrix} = \begin{bmatrix} E_x e^{i\phi} \\ E_y \end{bmatrix}. \quad (1)$$

Let θ denotes the angle between the optical axis of azo-polymer film and the vertical direction and let δ denotes the phase retardance of the azo-polymer film. The light intensity received by CCD can be calculated using :

$$I_{out} = E_x^2 \left(\cos^2 \frac{\delta}{2} + \sin^2 \frac{\delta}{2} \cos^2 2\theta \right) + E_y^2 \sin^2 2\theta \sin^2 \frac{\delta}{2}$$
$$+2E_x E_y \sin 2\theta \sin \frac{\delta}{2} \sqrt{\sin^2 \frac{\delta}{2} \cos^2 2\theta + \cos^2 \frac{\delta}{2}} \sin \left(\arctan \left(\cos 2\theta \tan \frac{\delta}{2} \right) - \phi \right). \quad (2)$$

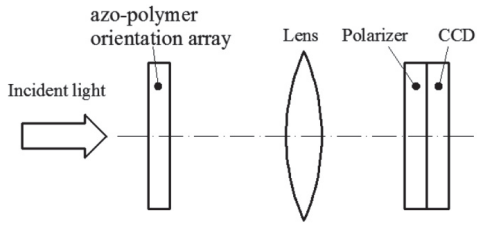


Fig. 4 Optical setup for imaging polarimeter.

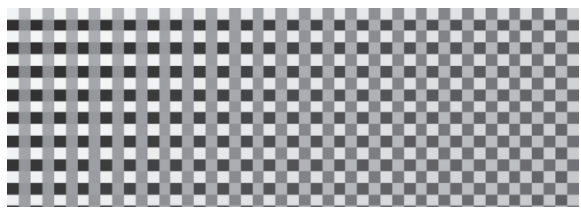


Fig. 5 Magnified area of some pixels from the CCD.

In a "unit cell" of the azo-polymer orientation array, θ is $\pi/6$, $-\pi/6$, $\pi/3$ and $-\pi/3$, respectively. The corresponding light intensity received by CCD is:

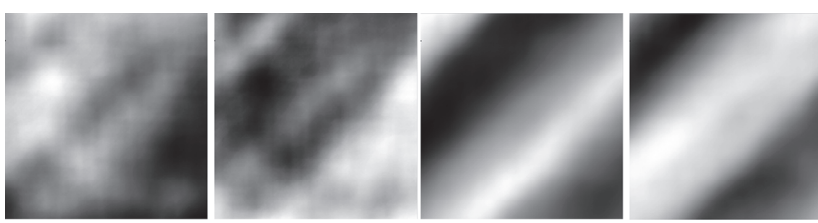
$$\begin{aligned} I_1 &= M^2 + N^2 - 2MN\sin(\phi-\alpha); I_2 = M^2 + N^2 + 2MN\sin(\phi-\alpha) \\ I_3 &= M^2 + N^2 - 2MN\sin(\phi+\alpha); I_4 = M^2 + N^2 + 2MN\sin(\phi+\alpha) \end{aligned} \quad (3)$$

where

$$M = E_x\sqrt{\cos^2\frac{\delta}{2} + \frac{1}{4}\sin^2\frac{\delta}{2}},\ N = \frac{\sqrt{3}}{2}E_y\sin\frac{\delta}{2}\ \text{ and. } \alpha = \arctan\left(\frac{1}{2}\tan\frac{\delta}{2}\right)$$

If an image is captured, we obtain ϕ:

$$\phi = \arctan\left(\frac{1}{2}\frac{I_4 - I_3 + I_2 - I_1}{I_4 - I_3 - I_2 + I_1}\tan\frac{\delta}{2}\right). \quad (4)$$



S_0 S_1 S_2 S_3

Fig. 6 Measured Stokes parameters of the incident light.

Substituting Eq. (4) into Eq. (3), E_x and E_y can also be calculated. Here, it is assumed that the amplitude and the phase of the incident light, E_x, E_y and ϕ,

have the same quantity on all four neighboring pixels. For all pixels in the image captured by the CCD, this calculation is applied. We can obtain all Stokes parameters of the light on the recording plane. Using E_x, E_y and ϕ, Stokes parameters can be calculated as:

$$S_0 = \left\langle E_x^2 + E_y^2 \right\rangle; S_1 = \left\langle E_x^2 - E_y^2 \right\rangle; S_2 = \left\langle 2E_x E_y \cos(\phi) \right\rangle; S_3 = \left\langle 2E_x E_y \sin(\phi) \right\rangle . \quad (5)$$

3. Results and Discussion

To verify the proposed polarimeter, another experiment has been made. A polarization light was made by the interference of two orthogonally polarized light beams with a wavelength of 632.8nm reflected by a flat mirror.. The angle between the two mirrors is adjusted to give several fringes of tilt and the magnified area of some pixels from the CCD array is shown in Fig. 5.

Using the theory mentioned above, four Stokes parameters of the incident light have been calculated and shown in Fig. 6. The nonuniformity of laser illuminating onto the two flat mirrors results in the nonuniform intensity of S_0 and S_1, and the corresponding results of S_2 and S_3 are two continuous fringe maps which is in accordance with the interference of two flat mirrors. The effectiveness of the proposed algorithm has been also experimentally verified.

4. Conclusions

In conclusion, a simultaneous imaging polarimeter has been presented using an azo-polymer orientation array. The polarization states and the formation of the polarimeter have also been analysed theoretically using Jones matrix calculations. Experimental verification of the proposed method has also been given, and the results support the measurement principle. This method allows the use of ordinary recording devices and material, such as CCDs and an anisotropic azo-polymer. Azo-polymer film with photo-induced optical anisotropy can be fabricated easily which reduces the cost of polarimeter and the polarimeter also demonstrates a new application of azo-polymer film.

Acknowledgement

The authors acknowledge the funding from the National Natural Science Foundation of China (NSFC) (Grant No: 51303002) and the State Key Laboratory of Modern Optical Instrumentation, Zhejiang university.

References

1. H. Ono, K. Suzuki, T. Sasaki, T. Iwato, A. Emoto, T. Shioda, N. Kawatsuki, Reconstruction of polarized optical images in two- and three-dimensional vector holograms, J. Appl. Phys. 106 (2009) 083109-1-7.
2. M. Fratz, S. Sinzinger, D. Giel, Design and fabrication of polarization-holographic elements for laser beam shaping, Appl. Optics 48 (2009) 2669-2677.
3. K.G. Yager, C.J. Barrett, Novel photo-switching using azobenzene functional materials, J. Photoch Photobio. A 182 (2006) 250-261.
4. U.A. Hrozhyk, S.V. Serak, N.V. Tabiryan, L. Hoke, D.M. Steeves, B.R. Kimball, Azobenzene liquid crystalline materials for efficient optical switching with pulsed and/or continuous wave laser beams, Opt. Express 18 (2010) 8697-8704.
5. Z.Q. Liu, N. Srisanit, X.J. Ke, P.F. Wu, S. Song, J.J. Yang, M.R. Wang, An azobenzene functionalized polymer for laser direct writing waveguide fabrication, Opt. Commun. 273 (2007) 94-98.
6. X. Pan, S. Xiao, C. Wang, P. Cai, X. Lu, Q. Lu, Photoinduced anisotropy in an azo-containing ionic liquid–crystalline polymer, Opt. Commun. 282 (2009) 763-768.
7. V. Gruev, J. Van der Spiegel, N. Engheta, Dual-tier thin film polymer polarization imaging sensor, Opt. Express 18 (2010) 19292-19303.
8. J.S. Tyo, C.F. LaCasse, B.M. Ratliff, Total elimination of sampling errors in polarization imagery obtained with integrated microgrid polarimeters, Opt. Lett. 34 (2009) 3187-3189.
9. B.M. Ratliff, J.S. Tyo, J.K. Boger, W.T. Black, D.L. Bowers, M.P. Fetrow, Dead pixel replacement in LWIR microgrid polarimeters, Opt. Express 15 (2007) 7596-7609.
10. R.C. Hardie, D.A. LeMaster, B.M. Ratliff, Super-resolution for imagery from integrated microgrid polarimeters, Opt. Express 19 (2011) 12937-12960.
11. J. Liu, K. Sun, Z.C. Li, J.G. Gao, W. Su, J. Yang, J.Y. Zhang, P. Wang, Q.J. Zhang, Banded texture of photo-aligned azobenzene-containing side-chain liquid crystalline polymers, Polymer 45 (2004) 4331-4336.

Effect of Surface Grafting on the Dielectric Properties of Barium Titanate Nanoparticles with Controllable Polymer Shielding Layers

Hailong Tang[a], Haoyu Guo[b] and Xiaobo Liu[c*]

High Temperature Resistant Polymers and Composites Key Laboratory of Sichuan Province, School of Microelectronics and Solid-State Electronics, University of Electronic Science and Technology of China, Chengdu 610054, P. R. China.

[a] E-mail: harrycoolbest@163.com, [b] E-mail: 645029719@qq.com, [c] E-mail: liuxb@uestc.edu.cn*

We developed a novel carboxyl-functionalized polyarylene ether nitrile (CPEN) as surface-grafting agent and efficiently derived a polymer shielding layer on barium titanate (BT) nanoparticle surface. The surface grafting occurs mainly via chemical bonding between the carboxyl groups in CPEN and the nanoparticle surface, as determined by FTIR and TEM, and it allows for BT nanoparticle dispersion in organic solvents, which is ideal for solution processing of polymer nanocomposites. Importantly, the degrees of surface grafting on BT nanoparticles are controllable and thus their dielectric properties are tunable.

Keywords: Barium titanate, Surface grafting, Carboxyl-functionalized polyarylene ether nitrile, Dielectric properties.

1. Introduction

Barium titanate (BT) is a typical dielectric material and is used extensively because of its high permittivity and unique ferroelectric, piezoelectric, and thermoelectric properties[1-3]. Also, BT has potential applications in electro-optical devices, because it has a high refractive index, high electro-optical coefficient, and nonlinear optical effect[4,5]. Since BT has a great many potential applications, developing techniques that manipulate its surface chemistry is essential. In general, commercial BT nanoparticles are aggregated and show poor dispersibility in most organic media. So controlled surface grafting of BT is of great interest for organic or aqueous solvent dispersion, reduced nanoparticle aggregation, and tunable electronic properties[6,7].

The most common surface-grafting agents for metal oxide surfaces are carboxylates, silanes, and phosphonates, which exhibit various bonding modes

* Corresponding author.

depending on the particle's surface characteristics[8]. However, silanes can self-condense to form ill-defined surface layers and typically are very reactive toward water. Beier and co-workers have used n-hexylphosphonic acid to give a surface coverage of 2.4 phosphonate groups/nm2 on the BT nanoparticles[9]. Carboxylates also have been used as coordinating ligands which chemisorb to the particle surface and aid in the formation of BT nanowires and nanoparticles[10,11].

In this work, we developed a novel polymeric carboxylate as surface-grafting agent and efficiently derived a polymer shielding layer on BT nanoparticle surface. The surface-grafted BT nanoparticles were characterized by Fourier transform infrared spectroscopy, transmission electron microscopy, and thermogravimetric analysis. Importantly, the thickness of polymer shielding layer on BT nanoparticle surface is controllable, and the tunable dielectric properties of surface-grafted BT nanoparticles are also investigated in detail.

2. Experimental

2.1. *Materials*

High-purity barium titanate nanoparticles was purchased in a "nanocrystal state (size distribution of 50-70 nm)" from TPL Co., USA. Phenolphthalin was prepared in our lab by reducing from phenolphthalein, according to the procedure described in literature[12].

2.2. *Synthesis of polymeric grafting agent*

The polymeric grafting agent, carboxyl-functionalized polyarylene ether nitrile (CPEN), were synthesized by the nucleophilic aromatic substitution polymerization of 2, 6-dichlorobenzonitrile (DCBN) with phenolphthalin (PPL) using anhydrous K_2CO_3 as catalyst in NMP medium, as per the procedure described in our previous literature[13]. The structure of CPEN was shown in the inset of Scheme 1. Mw=11876, Mw/Mn=1.91. Infrared absorption bands: v (cm-1) = 2231 (C≡N), 1712 (C=O), 1600, 1580 (C=C), 1500, 1460 (phenyl ring), 1243 (Ar-O), 1211, 1165, 1022 (C-O-C). 1H nuclear magnetic resonance proton (DMSO-d6): δ (ppm) = 6.71 (s, 1H, CH), 6.54-7.83 (aromatic protons), 12.98 (s, 1H, COOH).

2.3. *Surface grafting of BT nanoparticles with CPEN*

The BT nanoparticles were surface-grafted with CPEN by rotary coating technology combined with the post-treatment bonding process. In a typical

procedure, BT nanoparticles were suspended in tetrahydrofuran (THF) with the help of violent ultrasonic, and simultaneously a certain amount of CPEN was dissolved in THF with stirring. Then the CPEN solution was mixed with the nanoparticles suspension under ultrasonic treatment. Afterwards, the mixture suspension was placed in a rotary evaporator, and the surface-coated nanoparticles were obtained by rotary evaporation at 70 ºC in an ultrasonic water bath. Finally, the surface-coated nanoparticles were post-treated at 200 ºC for 4 h, and the CPEN-grafted-BT (CPEN-g-BT) nanoparticles were obtained by centrifugation and washed several times with THF, and ethanol.

2.4. *Characterization*

Fourier transform infrared (FTIR, 8000S, Shimadzu) spectra were obtained by using the KBr pellet method with 2 cm-1 resolution. Differential scanning calorimetry (DSC, model Q100, TA Instruments) was recorded at a heating rate of 10 ºC/min under flowing nitrogen. Thermogravimetric analysis (TGA, model Q50, TA Instruments) was performed at a heating rate of 20 ºC/min from room temperature to 800 ºC in air or nitrogen atmosphere. Transmission electron microscopy (TEM, G2 F20 S-TWIN, Tecnai) was performed at an operating voltage of 200 kV. Powder X-ray diffraction (XRD) was performed on a Rigaku Ultima IV diffractometer using a Cu Kα (λ = 1.54 Å) radiation source.

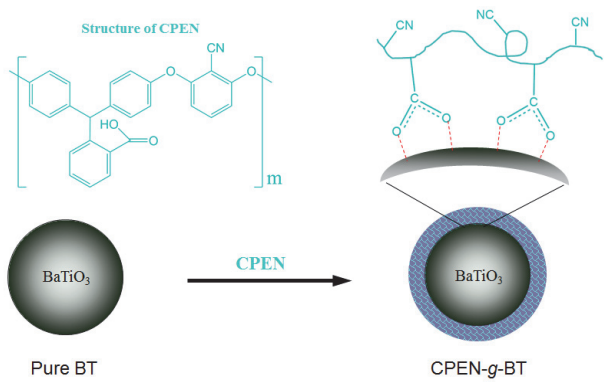
The dielectric properties (dielectric constant, dielectric loss and volume resistivity) were measured according to the ASTM D150 on a precision LCR meter (TH2819A, Tonghui). The experiments were performed at frequencies from 100 Hz to 200 kHz at 25 ºC. For sample preparation, the CPEN-g-BT compressed pellets were made by a presser with a pressure of 80 MPa using about 100 mg CPEN-g-BT crumbed powders. To fabricate the parallel plate type capacitors, colloidal silver paint was applied to both faces before annealing the pellets at 120 ºC for 1 h.

3. Results and Discussion

3.1. *Surface grafting with controllable polymer shielding layers*

As shown in Scheme 1, the BT nanoparticles were surface grafted with a polymer shielding layer through the carboxyl functional groups in CPEN, which was verified by FTIR spectroscopy. As shown in Fig. 1a, the strong absorption band at 567 cm-1 corresponds to the Ti-O vibration. The bands at 1502 and 1460 cm-1 belong to the skeleton vibration of benzene rings in CPEN, which were clearly observed in CPEN-g-BT nanoparticles. Furthermore, two characteristic bands at 1245 cm-1 and 2231 cm-1 attributed to the vibrations of aryl ether

(O-Ar-O) and nitrile groups respectively in CPEN, also clearly observed in CPEN-g-BT nanoparticles. It is worthwhile to note that the band at 1712 cm-1 belonging to free carboxyl groups in CPEN disappeared in the CPEN-g-BT nanoparticles. Moreover, there are two new bands at 1400 cm-1 and 1633 cm-1 observed in the CPEN-g-BT nanoparticles, which correspond to the symmetric and asymmetric stretching vibration of C=O, respectively. These results indicates that the BT nanoparticles were surface grafted by CPEN through the chemical bonding between the carboxyl groups and the nanoparticle surface via double coordination, as shown in Scheme 1. Moreover, powder XRD revealed that the BT nanoparticles are in the cubic perovskite phase (JCPDS no. 75-0215) and the CPEN-g-BT nanoparticles remain as phase-pure cubic BaTiO3 after surface grafting (Fig. 1b).



Scheme 1. Schematic illustration of surface grafting of BT nanoparticles with polymer shielding layer by CPEN, and the inset shows the structure of carboxyl-functionalized polyarylene ether nitrile.

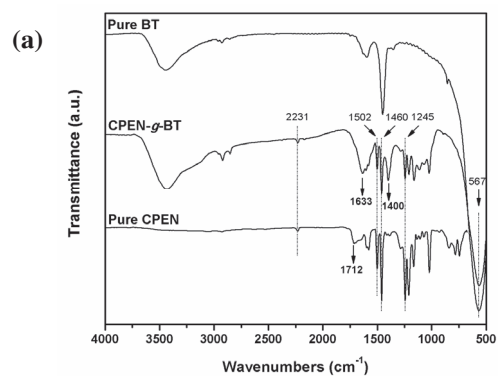


Fig. 1 (a) FTIR spectra and (b) powder XRD patterns of pure BT and CPEN-g-BT nanoparticles.

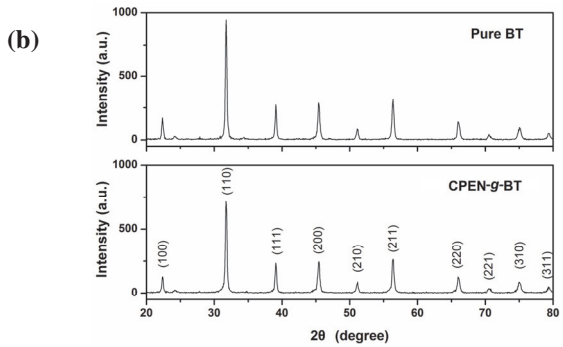


Fig. 1 (*Continued*)

The surface grafting of BT nanoparticles with polymer shielding layer was further characterized by TEM. As shown in Figs. 2a and 2b, a polymer shielding layer was clearly observed under TEM and the CPEN was uniformly covering on the surface of BT nanoparticles with a thickness of 4-7 nm. It was found that there is little weight loss of CPEN-g-BT nanoparticles in spite of repeated rinsing with THF and NMP (good solvents for CPEN). This further proves the chemical bonding between the carboxyl groups and nanoparticle surface. In addition, the dispersion of CPEN-g-BT nanoparticles in NMP can remain stable for several weeks (Fig. 2c). This indicates that the CPEN-g-BT nanoparticles become much more dispersible in organic solvents (e.g., NMP, THF, and ethanol), which is very beneficial to improve the dispersibility and compatibility of BT nanoparticles in polymer matrices.

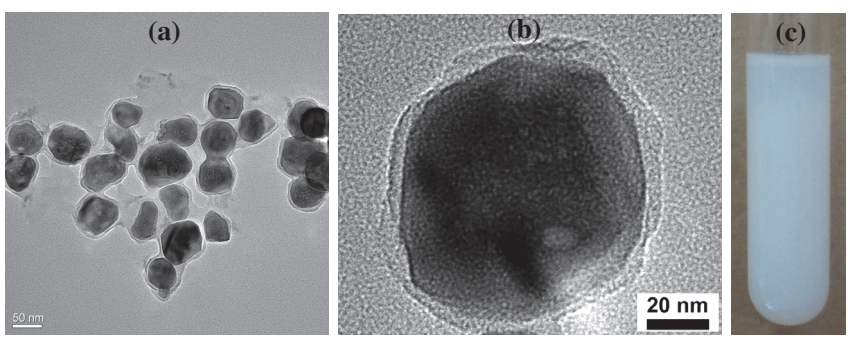


Fig. 2 TEM images of (a) CPEN-g-BT nanoparticles and (b) a single CPEN-g-BT nanoparticle; (c) dispersion of CPEN-g-BT nanoparticles in NMP after standing for five weeks.

Most important, the degrees of surface grafting of CPEN-g-BT nanoparticles, namely the thickness of CPEN polymer shielding layer, can be controllable by controlling the seeding CPEN contents. Therefore, a series of CPEN-g-BT nanoparticles with different seeding CPEN contents (Sample A: 4 wt%; Sample B: 8 wt%; Sample C: 12 wt%; Sample D: 16 wt%) was prepared and their degrees of surface grafting were determined by TGA. As shown in Fig. 3, the CPEN-g-BT nanoparticles showed a weight loss between 400 and 500 ºC under air atmosphere, which is due to the loss of surface-grafted CPEN. The weight losses of polymer shielding layer (i.e., degrees of surface grafting) of Samples A, B, C and D are 3.85%, 7.70%, 11.72%, and 15.76% respectively, which are agreement with their theoretical value (4%, 8%, 12%, and 16% respectively). Furthermore, according to the calculation from the observed ~5.5 nm thick layer on the TEM image (Fig. 2b, Sample C), the weight fraction of polymer shielding layer is about 11.5 wt%, which also match well with the TGA result. These results indicated that the thickness of the polymer shielding layer of CPEN-g-BT nanoparticles is controllable.

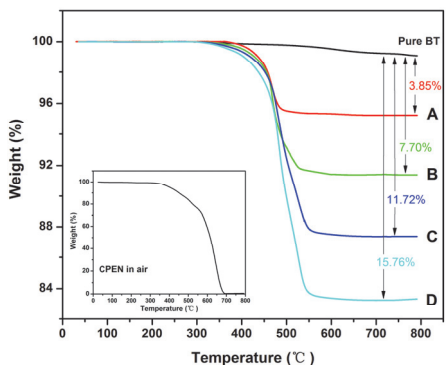


Fig. 3 TGA curves of pure BT and CPEN-g-BT nanoparticles (A: 4 wt% CPEN; B: 8 wt% CPEN; C: 12 wt% CPEN; D: 16 wt% CPEN) in air atmosphere, and the inset shows the TGA curve of pure CPEN in air.

3.2. *Dielectric properties of CPEN-g-BT nanoparticles*

The dielectric properties of the CPEN-g-BT nanoparticles were measured as a function of frequency to discern the effect of surface grafting on the nanoparticles' dielectric properties (Fig. 4). It was observed that the dielectric constant and dielectric loss of CPEN-g-BT nanoparticles have a weak frequency dependence, and gradually decrease with the increasing frequency. Furthermore, the dielectric constant obviously decreased with the increase of surface grafting degree (i.e., surface-grafted CPEN content), which is mainly due to the lower

dielectric constant of CPEN than that of BT. However, the dielectric loss have little decrease with the increase of surface grafting degree, when the surface-grafted CPEN content is over 7.7 % (i.e., Samples B, C, and D). we suspect the BT core have not been completely covered by CPEN shielding layer for Sample A, which will result in the large dielectric loss at lower frequencies due to the interfacial polarization[14]. Therefore, the CPEN-g-BT nanoparticles containing 7.7% CPEN content (i.e., Sample B) have the best dielectric properties for practical application, with relatively high dielectric constant and relatively low dielectric loss. Moreover, the volume resistivity of CPEN-g-BT nanoparticles was also measured as a function of frequency. As shown in Fig. 5, the volume resistivity of CPEN-g-BT decreases from the order of 10^9 Ω·cm to 10^5 Ω·cm with the increase of frequency from 100 Hz to 200 kHz, and slightly increases with the increase of the surface-grafting degree (i.e., surface-grafted CPEN content). In a word, the controllable surface-grafting degree of BT nanoparticles will bring their tunable dielectric properties.

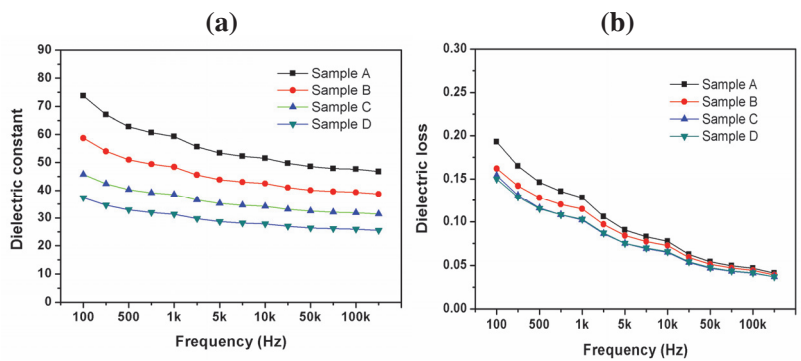


Fig. 4 (a) Dielectric constant and (b) dielectric loss of CPEN-g-BT nanoparticles as a function of frequency.

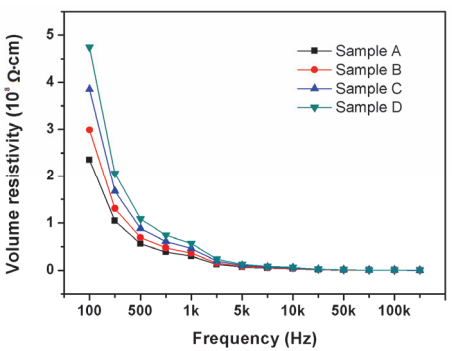


Fig. 5 Volume resistivity of CPEN-g-BT nanoparticles as a function of frequency.

4. Conclusions

In summary, carboxyl-functionalized polyarylene ether nitrile was developed as a novel polymeric surface-grafting agent to efficiently derive a polymer shielding layer on BT nanoparticles via chemical bonding between the carboxyl groups in CPEN and the nanoparticle surface. The surface-grafted BT nanoparticles can be well dispersed in organic solvents and remain stable for several weeks, which is very beneficial to improve the dispersibility and compatibility of BT nanoparticles in polymer matrices. Furthermore, their degrees of surface grafting can be controlled by controlling the seeding CPEN content, and thus surface-grafted BT nanoparticles with tunable dielectric properties can be obtained. In this view, the surface grafting of BT nanoparticles is not only a method of tailoring the surface chemistry but also tuning the dielectric properties of the material.

References

1. G. Wang, *ACS Appl. Mater. Inter.*, 2 (2010) 1290-1293.
2. Z.-M. Dang, L.-Z. Fan, Y. Shen, C.-W. Nan, Chem. Phys. Lett., 369 (2003) 95-100.
3. H.L. Tang, Z. Ma, J.C. Zhong, J. Yang, R. Zhao, X.B. Liu, *Colloid. Surface* A, 384 (2011) 311-317.
4. K.-i. Mimura, K. Hiramatsu, M. Moriya, W. Sakamoto, S. Kawado, Y. Uesu, T. Yogo, J. Nanopart. Res., 12 (2010) 1933-1943.
5. M. Zgonik, P. Bernasconi, M. Duelli, R. Schlesser, P. Günter, M. Garrett, D. Rytz, Y. Zhu, X. Wu, Phys. Rev. B, 50 (1994) 5941.
6. L.W. Chu, K.N. Prakash, M.-T. Tsai, I.-N. Lin, J. Eur. Ceram. Soc., 28 (2008) 1205-1212.
7. C. Huber, C. Elissalde, V. Hornebecq, S. Mornet, M. Treguer-Delapierre, F. Weill, M. Maglione, Ceram. Int., 30 (2004) 1241-1245.
8. M.-A. Neouze, U. Schubert, Monatshefte Chemie-Chemical Monthly, 139 (2008) 183-195.
9. C.W. Beier, M.A. Cuevas, R.L. Brutchey, Langmuir, 26 (2010) 5067-5071.
10. S. O'Brien, L. Brus, C.B. Murray, J. Am. Chem. Soc., 123 (2001) 12085-12086.
11. J.J. Urban, W.S. Yun, Q. Gu, H. Park, J. Am. Chem. Soc., 124 (2002) 1186-1187.
12. H. Tang, Z. Pu, X. Huang, J. Wei, X. Liu, Z. Lin, Polym. Chem.-UK, 5 (2014) 3673-3679.

13. H.L. Tang, J. Yang, J.C. Zhong, R. Zhao, X.B. Liu, Mater. Lett., 65 (2011) 1703-1706.
14. R.Z. Hou, P. Ferreira, P.M. Vilarinho, Chem. Mater., 21 (2009) 3536-3541.

Characterization of In situ Synthesized Nitrides Reinforced Fe Matrix Wear-resistant Coating by (Ar-N_2) TIG Arc/Cored-Wires Weld Overlaying Technology

Liu Mengru[a], Cheng Hanchi[b],

College of Materials Science and Engineering, Jiamusi University, 154007, China

E-mail: [a]liumengru1217@163.com, [b]chcjmsu@163.com

Li Lan

College of Nature Science, Jiamusi University, 154007, China

TiCN/ Fe matrix composite coatings were in-situ synthesized in the surface of Q235 steel substrate by (Ar-N_2) TIG arc/cored-wire weld overlaying process. The microstructure, microhardness and wear resistance of the weld overlay coating were investigated using SEM, XRD, Micro-hardness Tester and Pin-disc Wear Tester respectively. The results showed that when the nitrogen content in Ar-N_2 mixing arc changed between 25% to 35%, the weld overlaying coatings had a good quality without pores or cracks, but up to 40%, pores and cracks would occur in the weld overlay coating, and the TiCN particulates with size range of 1-3μm were dispersively and uniformly distributed in the Fe-matrix of the weld overlay coatings. Furthermore, the coating micro-hardness was a range of 1385HV to 1736.40HV, leading to the wear resistance significantly increasing.

Keywords: TIG/cored-wire; TiCN; In-situ synthesized; Microstructure; Wear resistance.

1. Introduction

Wear of machine components is one of the most common problems faced in industry, and the surface engineering technology by nitriding treatment is one of the important means to get the material wear-resistant[1]. In addition to the traditional nitriding, some surface engineering technology, such as laser nitriding, plasma nitriding, PVD nitriding film, PVD nitride ion implantating and thermal spraying had been researched and applied[2-6]. A few of researches demonstrated that when the strong nitride formation elements (Ti, V, Nb) were added in steels, carbonitrides would been generated, resulting in a more remarkable strengthening effect than the carbide[7].

TIG arc as a high density energy source, with the low equipment prices, fewer parameters and easy to operate, especially it could obtained a high quality weld

overlaying had been received much attention in the surface engineering[8]. A hard titanium nitride layer had been studied by melting commercial purity titanium (CP-Ti) surfaces beneath the tungsten inert gas (TIG) torch in a pure nitrogen environment[9]. Up to now, there was no report about in-situ synthesize TiCN/Fe composite coating by (Ar-N_2) TIG arc/cored-wire weld overlaying process. In this work, as the role of reactive gas, nitrogen was mixed with the argon gas to in-situ synthesize TiCN/Fe composite coating by TIG arc/cored-wire weld overlaying process, which could provides a simple and effective method to obtain a wear-resisting coating included carbonitrides, at the same time, the microstructure and properties were investigated as well.

2. Experimental Materials and Methods

2.1 Powder cored-wire material preparation

Table 1 Composition of the powders in cored-wire (wt.%).

FeTi	Mo	Cr	Ni
54.4	5.4	25.2	15

Q235 steel was used as the substrate material. The composition of the powders in cored-wire were FeTi (Ti wt.40%), Mo (wt.99.9%), Cr (wt.99%) and Ni (wt.99.9%), and the component percentage of weld overlay coating are listed in Table 1. Low carbon steel strip with 14mm×0.4mm was selected as core-wires skin, and then compressed down to a diameter of 2.8 mm by rolling.

2.2 TIG weld overlaying and coating test

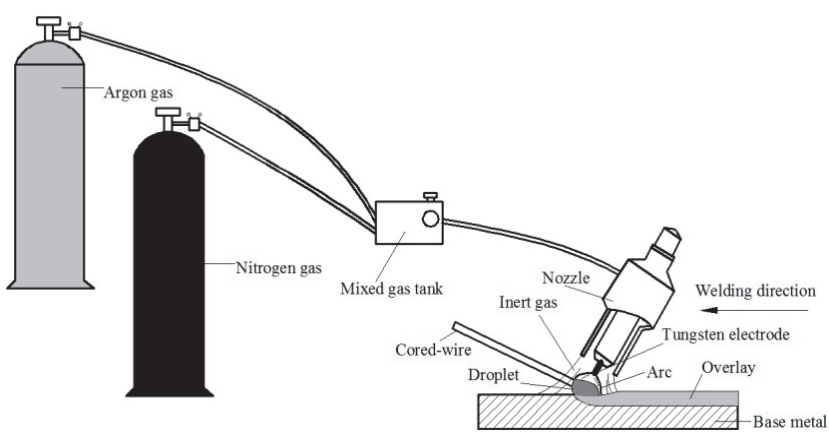


Fig.1 Schematic representation of the TIG/cored-wire weld overlaying.

Before welding the substrates were thoroughly cleaned, the coatings were carried out by Panasonic AC/DC Tungsten Inert Gas welding (TIG) machine of YC-300WP with the operating current 90 A, voltage 20–22 V, gas flow rate 10 L/min, for the amount of nitrogen gas is respectively 25%, 30%, 35% and 40%, and the other is argon gas. The welding speed is 100 mm/min. The angle of wire with welding torch and substrates was respectively 90°, 30°, the TIG welding process schematic is shown in Fig.1.

The microstructures of coatings were examined by scanning electron microscope (SEM) with FALCON60S energy dispersive spectrometer (EDS), and hard phase particles content in the weld overlaying layer was analyzed by Image analysis software. And a type of XD-2 X-ray diffraction (XRD) with Cu Kα radiation operated at 36 kV and 30 mA was used to analyze the coating phase structure. Micro-hardness along the depth of the cross-section was measured using a MHV2000 type micro Vickers. The load was 100g and loading time was 5s. An average value of hardness was taken from five different measurements. Abrasive wear experiments were done without lubrication at the room temperature and normal atmosphere conditions using a pin-disc wear tester. And the wear couple was 180 mesh of silicon carbide emery cloth, the test specimens were machined with size of 10mm×10mm×10mm. The wear conditions were a normal load of 10 N, and the time of abrasion of 2h. The quality of the samples before and after the wear test was measured using electronic scales (precision 0.0001 g).

3. Results and Discussion

3.1 Macrograph and microstructure

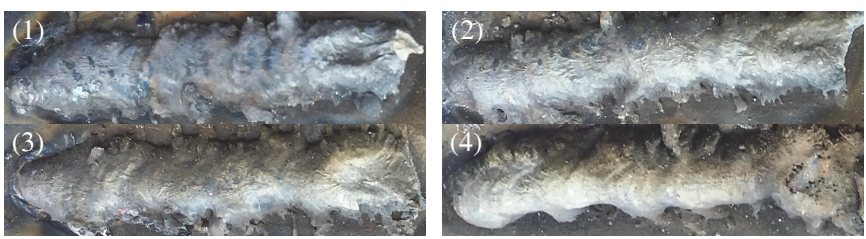


Fig.2 macrograph of the top surface of the track with different nitrogen gas content: (1) 25%; (2) 30%; (3) 35%; (4) 40%.

TiCN reinforcing Fe matrix composite coatings were in-situ synthesized in the surface of Q235 steel substrate by (Ar-N_2) TIG/cored-wire weld overlaying with nitrogen gas content changing between 25% to 40%. Fig.2 showed the surface macrograph of the weld overlay coating. It could be seen in Fig.2(4) that pores and cracks appeared when the nitrogen gas content was up to 40%, which was

possibly related to high nitrogen content and large arc heat input. Fig.3 showed the typical cross-section micrograph of weld overlay coating. It could be clearly seen that the coating has a good quality with metallurgical bonding with the substrate material and without pores or cracks, and the particles distributing uniformly.

Fig.4 showed the typical XRD spectrum of weld overlay coating, only TiCN and α-Fe (Cr, Ni) phase showed in weld overlay coating, indicating nitrogen participating synthesis reaction of TiCN in form of nitrogen ions or nitrogen atoms[10], resulting from electroionization under the TIG process, and Cr, Ni alloying elements had formed solid solution of Fe during the weld overlaying process. Fig.5 showed the scanning electron micrograph and EDS testing results of sample 2. It could be deduced that the cubic particles are TiCN with the length of 1−3 μm, and the matrix is α-Fe. The same results have also been reported by reference[11].

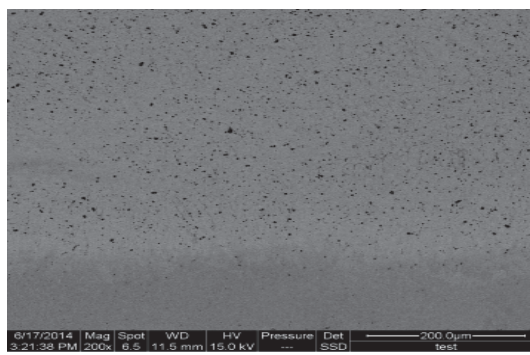


Fig.3 The typical SEM microstructure of the weld overlay coating(BSE).

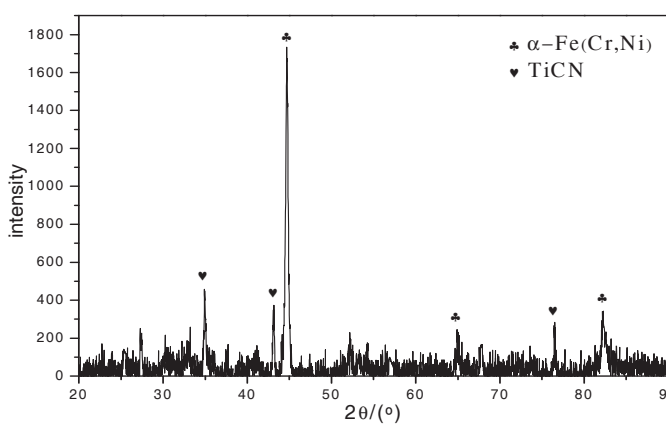


Fig.4 XRD spectrum of the weld overlay coating.

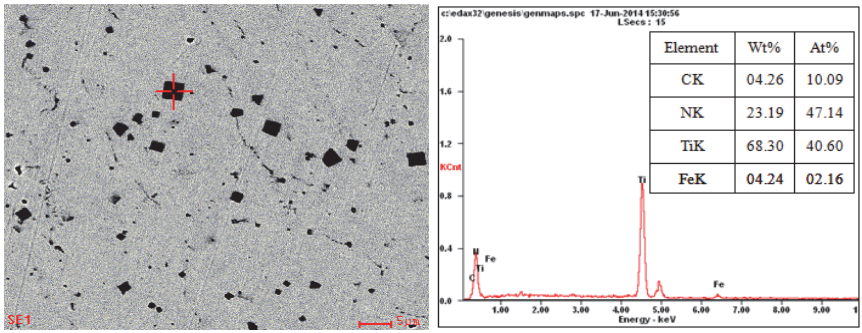


Fig.5 EDS results of the weld overlay coating.

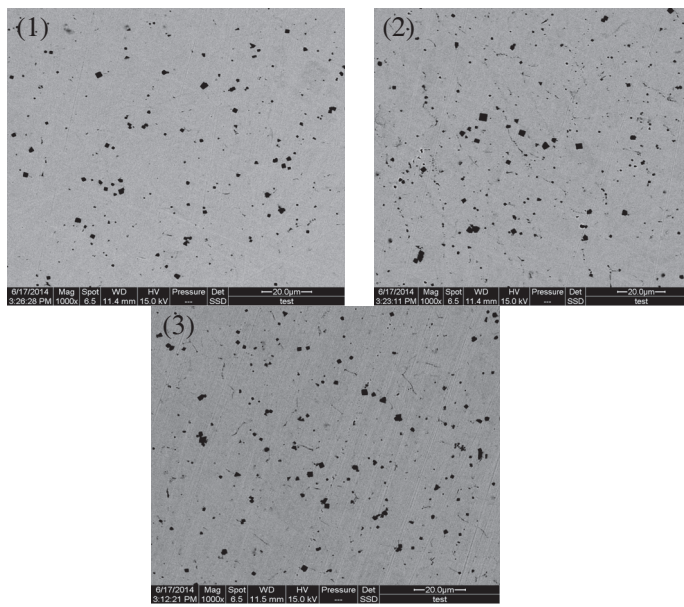


Fig.6 Typical microstructures of reinforced Fe matrix weld overlay coating (BSE) with different nitrogen gas content: (1) 25%; (2) 30%; (3) 35%.

Fig.6 showed the microstructure of the same top position of the different coating, which revealed a relatively uniform distribution of TiCN particulates in the composite coatings. It could be seen that the volume fraction of TiCN increases with the increase of nitrogen. This kind of distribution characteristics would have a good influence on the coating properties.

3.2 Hardness and wear resistance

Fig.7 showed the curves of micro-hardness profiles of weld overlay coating along the depth of cross-section. It could be seen that the micro-hardness rise gradually from exterior surface to interior, up to the culmination, then decrease mildly. Obviously, because of the coating surface directly contacting arc, the alloy elements volatilized and over burned seriously, resulting in the decrease of hard phase content. Meanwhile, the micro-hardness also increased with an increase of nitrogen gas content, attributed to the increase of hard TiCN ceramic particulates. Sample 3 had the highest hardness, which could reach1736.40HV, was 7 times higher than that of substrate. It demonstrated that the hardness development was directly related to the TiCN particulate in the weld overlay coating, which was found to decrease at deeper depths because of the lower concentration of nitrogen.

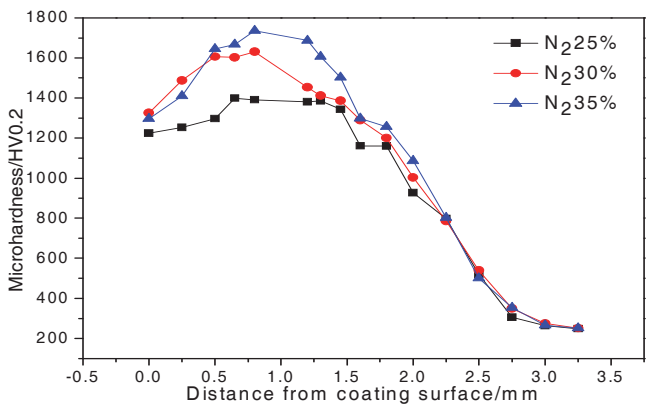


Fig.7 Microhardness curves of weld overlay coating.

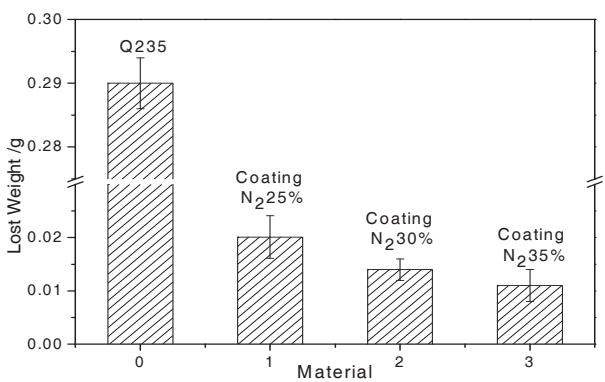


Fig.8 Wear loss of weld overlay coating and Q235 steel.

Fig.8 showed the wear loss of composite coatings and Q235 steel. It was clear that wear loss of coatings was smaller than that of Q235 steel, and the wear loss of sample 3 was the smallest, which had the same reason with micro-hardness. It could be seen that the hard phase particles in microstructure played a dominating role in the wear resistance. Hard TiCN paticulates by in-situ synthesize had strong interface with base material could successfully avoid the weld overlay coating contact with the counter surface during wear process to decrease the coatings wear loss. On the other hand, the nitrogen in the form of arc gas to join in the weld overlay coating also improved the coating matrix wear resistance, due to the nitrogen atom solid solution strengthening α-Fe matrix.

4. Conclusions

(1) TiCN/Fe matrix composite coatings were in-situ synthesized in the surface of Q235 steel substrate by (Ar-N_2) TIG/cored-wire weld overlaying with different nitrogen gas content, the coating presented a better metallurgical bond with the substrate.

(2) With the increase of nitrogen, the volume fraction of TiCN increased as well. But when the nitrogen gas content was up to 40%, pores and cracks would occur in the weld overlay coating.

(3) The weld overlaying coatings had high micro-hardness and wear resistance due to more TiCN ceramic particulates dispersively and uniformly distributed in the Fe-matrix of the weld overlay coatings.

Acknowlegement

The authors were grateful for support by the Principal Innovation and Entrepreneurship of Jiamusi university (xzyf 2013-03), and Scientific Research Fund of Heilongjiang Provincial Education Department (No.12521526).

References

1. Yutang Huang, Shangqi Zhou. The Technology and Development of Plasma Nitridin[J]. *Heat Treatment Technology and Equipment*. 2008, 29(1):48-50.
2. Dapeng Zhou, Hui Peng. Microstructure, hardness and corrosion behaviour of Ti/TiN multilayer coatings produced by plasma activated EB-PVD[J]. *Surface and Coatings Techology*. 2014, 10 (12):52-54.
3. Liu Yanzhang, Qiu Shaoyu. A Study of Effect of Nitrogen implantation on corrosion properties of Ti-Al-Zr Alloy[J].*Nuclear Physics Review*. 2006, 23(2): 202-205.

4. K.Nikolov, K.Bunk. High-efficient surface modification of thin austenitic stainless steel sheets applying short-time plasma nitriding by means of strip hollow cathode method for plasma thermochemical treatment[J]. *Vacuum*. 2014, 12: 106-113.
5. D.Höche, Jkaspar. 2-Laser nitriding and carburization of materials[J]. *Laser Surface Engineering*. 2015:33-58.
6. Chen Hailong, Yang Hui. Study on Reacting Course and Forming Mechanism of TiN Coatings Prepared by Reactive Plasma Spraying[J].*Material Heat Treatment*.2009,38(20):104-106.
7. Li Jianchang. Study on microstructure and properties of TiAl(CN)/ Fe cermet composite coating by reactive nitrogen arc cladding process[J]. *Materials science and technology*.2013, 43(3):9-12.
8. Cheng HC, Li ZX. Effects of TIG surface treating on microstructural characteristics and mechanical properties of Al_2O_3-TiB_2 coating by APS [J]. *Applied Surface Science*. 2011, 27(1):194-199.
9. S. Mridha. Titanium nitride layer formation by TIG surface melting in a reactive environment[J]. *Journal of Materials Processing Technology*. 2005, 168: 471–477.
10. Stevens S M. Forms of nitrogen in weld metal[J]. *Welding Research Council Bulletin*, 1991-1992, 369: 1-2.
11. Toit M Du, Pistorius P C. Nitrogen control during autogenous arcwelding of stainless steel[J]. *Welding Journal*, 2003, 82(8): 219-224.

Ultraviolet Light Sensing Using Gold-coated Prism Overlaid with Azo-polymer

Xinyu Zhang[a], Keyi Wang[c*] and Peizheng Yan[d]

Department of Precision Machinery and Precision Instrumentation, University of Science and Technology of China, Hefei, 230026, China
Email: [a]xinyuzh@mail.ustc.edu.cn, [c]kywang@ustc.edu.cn, [d]ypz@mail.ustc.edu.cn*

Jiajue Ma[b]

Department of Polymer Science and Engineering, University of Science and Technology of China, Hefei, Anhui 230026, China
Email: [b]jiajunma@yeah.net

A surface plasmon resonance (SPR) ultraviolet (UV) sensor based on a gold-coated prism that overlaid with azo-polymer film is constructed and tested. The change of the refractive index (RI) of the film that caused by being exposed to the UV light results in a change of the reflectivity. The rate of the reflectivity change is related to the optical power of the UV. The sensitivity, which is defined by the changing rate of reflectivity per unit UV power density, is measured to be 5.56(mv/s)/(mW/cm^2). The response time of the sensor is tested to be less than one minute.

Keywords: UV Sensing, Azo-Polymer Film, Surface Plasmon Resonance.

1. Introduction

Azobenzene is a well-known photochromic dye for its UV sensitivity. The trans-cis photoisomerization of azobenzene is reversible under cyclical irradiation of UV light and visible light, the RI of azo-polymer changes during the process of photoisomerization [1].

Side-polished fiber (SPF) has attracted a lot of interest for various reasons. For examples, the side-polished design fiber sensors have comparative higher sensitivity, it is easy to incorporate different sensing materials onto the polished area, and the advantages it inherited for being fiber-optic sensor, such as the lack of electromagnetic interference (EMI), small size, geometric versatility, and low cost [2-8]. After side-polishing, the evanescent field could leak from the fiber core,

* Corresponding author.

causing the polished area to be sensitive to the RI of the overlaid materials (e.g. azobenzene). Composed of both azobenzene and SPF, a SPF-based UV sensor is demonstrated in [9], in which an overlaid polymer containing azobenzene was used as the sensing material. Under the UV light irradiation, the RI of the dye-doped polymer within the polished area was changed and further were the fiber-optic signals. An all fiber-optic light sensor using side-polished fiber overlaid with photoresponsive liquid crystals is also introduced in [10], which has a higher sensitivity, but a much longer response time (up to 30 minutes).

SPR is another technique that is highly sensitive to the RI of the dielectric on a suitable metal surface. The attenuated total reflectance (ATR) configuration developed by Kretchmann is widely used in the designs of most SPR instruments [11]. The Kretschmann SPR configuration employs a prism with high refractive index that covered by a thin metal film, on which the sensing layer is then deposited. Changes in the reflectivity of the thin metal film are used to monitor the RI change. Compared with SPF structure, the Kretschmann SPR configuration is much easier to be fabricated.

In this paper, an UV sensor based on prism coupling SPR incorporating with an azo-polymer film is presented. The RI changes of the azo-polymer film caused by being exposed to the UV light result in changes of the reflectivity of the thin metal film in the Kretschmann SPR configuration. As the rate of the RI change of the azo-polymer is correlated to the intensity of UV light, the rate of the reflectivity change resulting from the RI change can be used to detect the intensity of the UV light. By measuring the rate of reflectivity change, an innovative method for UV sensing is developed, which has a response time less than one minute.

2. Experimental Procedure

The reflective surface of a prism is covered with a 50nm thickness gold film using Radio Frequency magnetron sputtering method, on which the above mentioned Kretschmann SPR structure is then fabricated. The refractive index of the prism is 1.83 under a wavelength of 650nm. Azobenzene-containing monomer (6CN) is synthesized using the above mentioned method [1]. Azo-polymer is dissolved in cyclopentanone, then the solution is dripped on the gold covered prism, after which the prism is placed in a constant temperature oven (set as 25 °C) for 24 hours to ensure the total volatilization of the remaining cyclopentanone. After those procedures, a Kretschmann SPR sensor overlaid with azobenzene film is obtained, as illustrated in Fig. 1, in which the theta represents the incident angle.

As shown in Fig. 2, the experiment setup is consisted of a fixed-wavelength laser diode (LD), a Glan prism, a prism and a photo detector (DET-100, Hinds Instruments). The incident light beam from the LD (with a wavelength of 650 nm)

is filtered using the Glan prism, through which only the transverse magnetic (TM) wave is kept. The LD and the Glan prism are mounted on a rotary stage, with prism fixed at the rotation center. The photo detector used to detect the reflected light beam is mounted on another rotary stage, which rotates round the same center as previous one. The UV light used for illumination is emitted by a UV LED with a fixed wavelength of 365nm.

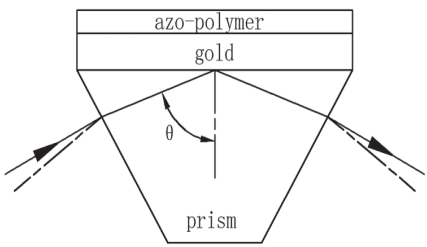


Fig. 1 Gold coated prism with azo-polymer film overlaid.

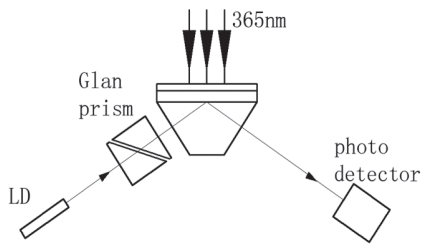


Fig. 2 Experiment setup.

3. Results and Discussion

In the first part of this experiment, the photo detector is used to measure the intensity changes of the reflected light beam versus the changes of the incident angles under two conditions: without UV irradiation and with twenty minutes of UV irradiation. Under the irradiation of 365 nm UV light, the trans-cis photoisomerization of azobenzene groups in the overlaid polymer is triggered. As a result, the refractive index of the azo-polymer declines, the reflectivity changes as well. The result is shown in Fig. 3, the optical power of UV light is 0.5mW/cm^2. As illustrated in Fig. 4, a proper incident angle (which ensures the intensity change of the reflected light is detectable for the photo detector) is chosen as 57.5º.

After fixing the incident angle at 57.5º, the intensity of reflected light is recorded while UV light (with a fixed wavelength of 365nm) is applied. The following experiments are designed to record the reflectivity changing curves under the radiation of UV light with different optical powers, the results with amplified signal from the photo detector are shown in Fig. 5. It is obvious that the changing rate of the reflectivity is correlated to the optical power of the UV light: the changing rate of reflectivity is higher with a higher optical power of UV, and vice versa. This correlation is shown in Fig. 6, the sensitivity defined by changing rate is calculated to be 5.56 (mv/s)/(mW/cm^2) within the linear variety fell in the range of 0.28 mW/cm^2 -0.55 mW/ cm^2. As the changing rate can be calculate through a few measured data, it is not necessary to take a long time to get the reflectivity stable, reflectivity data acquired within one minute is sufficient. So the response time for this UV sensor is less than one minute.

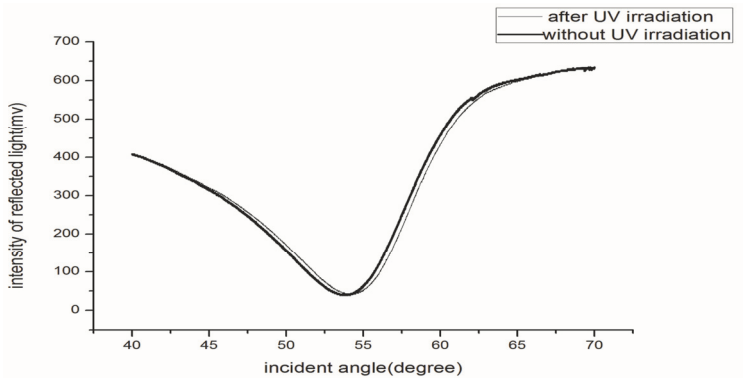


Fig. 3 Intensity of reflected light versus incident angles.

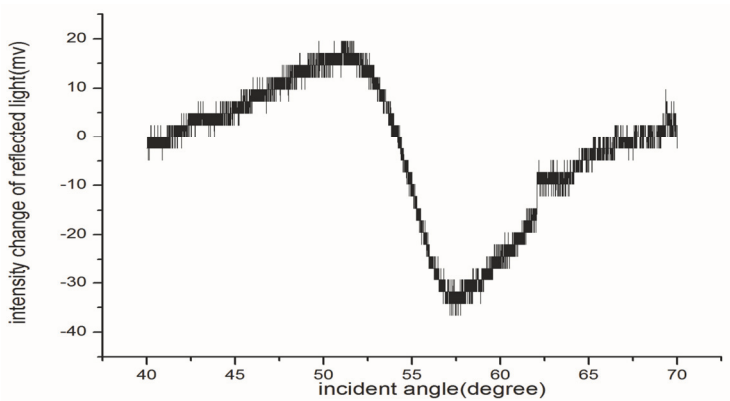


Fig. 4 Reflectivity change after UV exposure.

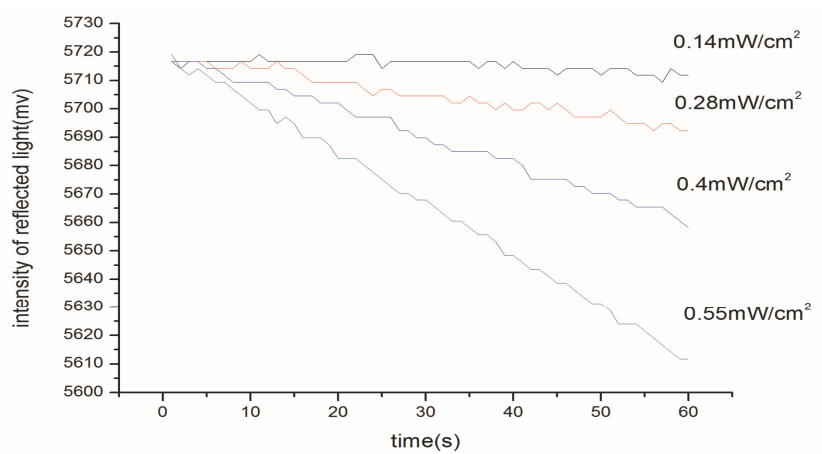


Fig. 5 Reflectivity versus time, using different optical power UV light.

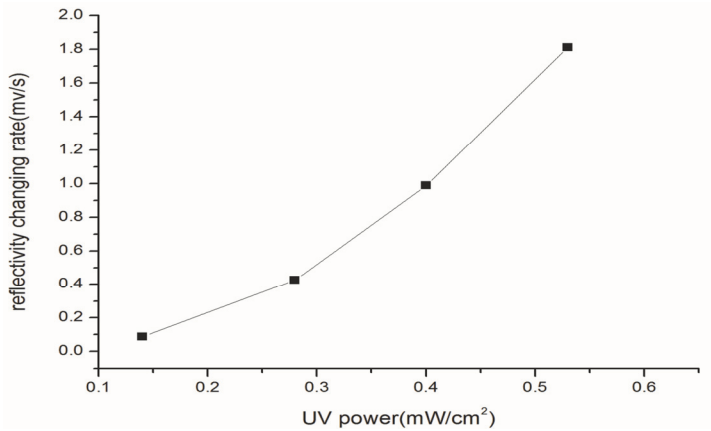


Fig. 6 Reflectivity changing rate versus UV power.

4. Conclusions

In this paper, a Kretschmann SPR UV sensor based on a gold-coated prism overlaid with Azo-polymer is built and tested. The correlation between the reflectivity changing rate and the optical power of UV light is demonstrated. The UV sensitivity is defined with the change of reflectivity changing rate caused by UV exposure. The sensitivity of the sensor is as high as 5.56(mv/s)/(mW/cm^2). The response time is less than one minute. Because the absorption and refractive index change of azo-polymer are closely related to the chemical structure of the polymer, this technique can be further used to construct UV sensors based on polymers with different chemical structures. The effect of the thickness of azo-polymer film will be analyzed in the future work as planned.

Acknowledgement

This work was supported by the National Natural Science Foundation of China (NSFC) (61275011), and State Key Laboratory of Modern Optical Instrumentation, Zhejiang University. This support is gratefully acknowledged

References

1. X.J. Tian, X.S. Cheng, W.X. Wu, Y.H. Luo, Q.J. Zhang, B. Zhu, and G. Zou, Reversible All-Optical Modulation Based onEvanescent Wave Absorption of a Single-Mode Fiber With Azo-Polymer Overlay, *IEEE Photon. Technol. Lett*. 22 (2010) 1352-1354.
2. Parriaux, S. Gidon, A.A. Kuznetsov, Distributed coupling on polished single mode optical fibers, *Appl. Opt*. 20 (1981) 2420–2423.

3. M.J.F. Digonnet, J.R. Feth, L.F. Stokes, H.J. Shaw, Measurement of the core proximity in polished fiber substrates and couplers, *Opt. Lett*. 10 (1985) 463–465.
4. S.M. Tseng, C.L. Chen, Side-polished fibers, *Appl. Opt*. 31 (1991) 3438–3446.
5. K. McCallion, W. Johnstone, G. Fawcett, Tunable in-line fiber optic bandpass filter, *Opt. Lett*. 19 (1994) 542–544.
6. N. Chen, S. Chi, S. Tseng, Wide band tunable fiber short-pass filter based on side polished fiber with dispersive polymer overlay, *Opt. Lett*. 29 (2004) 2219–2221.
7. R. Lausten, P. Rochon, M. Ivanov, P. Cheben, S. Janz, P. Desjardins, J. Ripmeester, T. Siebert, A. Stolow, Optically reconfigurable azobenzene polymer-based fiber Bragg filter, *Appl. Opt*. 44 (2005) 7039–7042.
8. K.T. Kim, S. Hwangbo, J.P. Mah, K.R. Sohn, Widely tunable filter based on coupling between a side-polished fiber and a tapered planar waveguide, *IEEE Photon. Technol. Lett*. 17 (2005) 142–144.
9. K.T. Kim, N.I. Moon, H.K. Kim, A fiber-optic UV sensor based on a side polished single mode fiber covered with azobenzene dye-doped polycarbonate, *Sens. Actuators A*. 160 (2010) 19–21.
10. Fu W, Hsiao V K S, Tang J, Wu M, Chen Z, All fiber-optic sensing of light using side-polished fiber overlaid with photoresponsive liquid crystals, *Sensors Actuators B*. 156 (2011) 423–427.
11. Kretschmann, Erwin, and Heinz Raether, Radiative decay of nonradiative surface plasmons excited by light (Surface plasma waves excitation by light and decay into photons applied to nonradiative modes), Zeitschrift fuer Naturforschung, Teil A. 23 (1968) 2135-2136.

Microstructure and Mechanical Properties of a Nickel-based Honeycomb Sandwich at High Temperature

Qiuming Zhang*
School of Chemical Engineering and Technology, Harbin Institute of Technology, Harbin, China
Email: zqmingc289@163.com

Xiaodong He, Yao Li*
Center for Composite Materials, Harbin Institute of Technology, Harbin, China
Email: hexiaodong@hit.edu.cn; liyaohit@126.com

A nickel-based superalloy honeycomb sandwich was manufactured by high-temperature brazing. The microstructure and the out-of-plate mechanical properties were determined for honeycomb sandwiches at high temperature. The maximum tensile stress was 28.5 MPa and the compressive yield strength was 29.6 MPa for the specimens at room temperature. These parameters decreased to 23 MPa and 25 MPa for specimens at 550°C, to 13.8 MPa and 19.6MPa for specimens at 850°C and to 9.3 MPa and 15.9 MPa for specimens at 900°C, respectively. With increasing temperature, the tensile elongation increased, then declined; the tensile elastic modular and the compressive modular decreased. There are intermetallic compounds and a eutectic structure in the brazing region and the critical brazing clearance is 20 μm.

Keywords: Microstructure; Mechanical Properties; Nickel-Based Honeycomb Sandwich; High Temperature.

1. Introduction

For the design and construction of lightweight transportation systems such as satellites, aircraft, high-speed trains and fast ferries, structural weight-saving is a major consideration. To meet this requirement, sandwich construction is frequently used instead of increasing the material thickness. Nickel-based superalloys have been used as materials for sandwich facings and cores that operate at higher temperature. Several core shapes and types of core material have been applied to the construction of sandwich structures. Among them, a honeycomb core consisting of very thin foil in the form of hexagonal cells perpendicular to the facings is the most popular. Superalloy honeycombs are

* Corresponding authors.

very important parts in advanced metallic thermal protection systems and their performance influences the economic efficiency and security of these systems.

Witherell [1] performed an extensive theoretical study for the structural design of an air-cushion vehicle-hull structure using aluminum honeycomb sandwich panels. Okuto et al. [2] demonstrated the validity of the so-called equivalent plate thickness method in which a honeycomb sandwich panel subjected to in-plane loads was approximately replaced by a single-skin panel with equivalent plate thickness. Elasto-plastic bending behavior of sandwich panels was studied by Kobayashi et al. [3]. Yeh and Wu [4] investigated the buckling strength characteristics of aluminum honeycomb sandwich panels in axial compression. The characteristics of the energy absorption capacity of bare honeycomb cores under lateral crushing loads was studied by Kunimoto et al. both theoretically and experimentally [5, 6]. The dynamic properties and failure behavior of composite sandwich structures were complex and test programs are destructive, time-consuming and consequently expensive for industry [7,8]. An experimental study of the impact response of metallic cellular materials was carried out by Zhao et al. [9]. Metallic sandwich panels with textile cores were subjected to combined bending and shear and then designed for minimum weight [10]. The fatigue crack growth behavior of Ni-base honeycomb panels was studied at room temperature [11]. The longitudinal shear deformation behavior and failure process of aluminum alloy honeycomb cores were investigated using single-block shear tests [12]. The bending performance of a sandwich construction with thin cellular metal cores was measured and simulated [13].

The mechanical properties for honeycomb sandwich are very important to the structure with the sandwich, especially at high temperature. To enhance the security of nickel-based honeycomb sandwich, it is thus essential to understand microstructure and mechanical properties of nickel-based superalloy honeycomb sandwich at high temperature.

For this reason, a honeycomb sandwich was fabricated from a nickel-based superalloy by high-temperature brazing and its microstructure and mechanical properties were investigated at room temperature, 550°C, 850°C and 900°C, respectively.

2. Materials and Experimental Study

A nickel-based superalloy was used for the honeycomb core and for the two face sheets comprising the sandwich sample. The cell shape of the honeycomb core was a regular hexagon, with each side 4 mm in length. The honeycomb cores were prepared by a sheet crimping process, as shown in Fig. 1. The stacked sheets were bonded by laser welding and the cores were cut and adhesively

bonded to the face sheets to create sandwich panel by high-temperature brazing. The wall thickness of the core and face sheet was 0.09 mm and 0.225 mm, respectively; Brazing was conducted with BNi-2 at 1050°C and the braze was applied uniformly over the sheets. Capillary action drew the braze into the joints, resulting in an excellent bond. During the joining process, low pressure of approximately 20 kPa was applied to thesample to ensure close contact between the face sheet and the honeycomb core. The composition of the superalloy and the brazing alloy was shown in Table 1. After brazing, the honeycomb sandwich was sectioned, polished for metallurgical examination under an optical microscope using standard procedure.

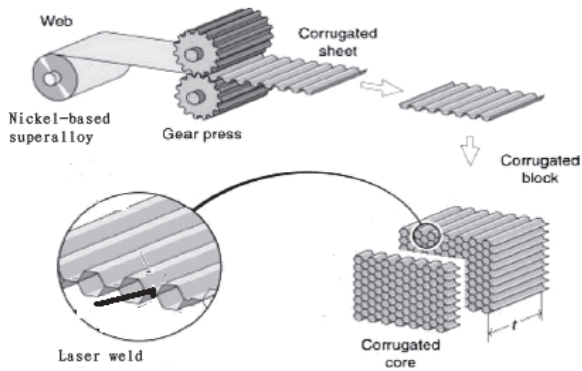


Fig. 1. The fabrication of the honeycomb core.

Table 1. Chemical composition of the superalloy and BNi-2.

Materials	Chemical Composition (%)									
	Ni	Cr	Al	Fe	Mn	Si	Zr	C	B	Y
Superalloy	75	16	4.5	3	0.5	0.2	0.1	0.05	0.01	0.01
BNi-2	82.4	7.0	---	3.0	---	4.5	---	<0.1	3.1	---

Three specimens were used in every test. The breadth and thickness of specimens for the tensile and compressive test is 30 mm and its height is 4.5 mm. The cross-head speed for the tensile and compressive test is 1mm/min. Compressive and tensile tests were carried out on a universal material testing machine (Instron 5569) at room temperature and on Instron 5510 at high temperature and atmospheric pressure.

3. Result and Discussion

A section and cross-section of the nickel-based honeycomb sandwich are shown in Figs. 2 and 3. The face sheet of the honeycomb sandwich is marked I, the

core is marked II and the brazing region is marked III. The region approaching the matrix is a solid solution and there are intermetallic compounds and a eutectic structure in the middle of the brazing region. According to the metallographic results, for brazing clearance of less than 20 μm there were no intermetallic compounds or eutectic structure present in the brazing seam, confirming that the critical brazing clearance was 20 μm. XRD pattern for the brazing region is shown in Fig. 4, indicating that there are many intermetallic compounds in the brazing region, such as Ni_2Si_3 and BCr and Cr_2Ni_3, and so on.

Tensile fracture for the honeycomb sandwich at room temperature is shown in Fig. 5. The tensile fracture for specimens at 550°C, 850°C and 900°C is shown in Figs. 6, 7 and 8, respectively. In all tensile specimens, fracture occurred wholly within the honeycomb core and no interface separation was observed, indicating that the brazing process was satisfactory. The out-of-plate tensile and compressive mechanical properties of the honeycomb sandwich are shown in Fig.9 and Fig.10, respectively.

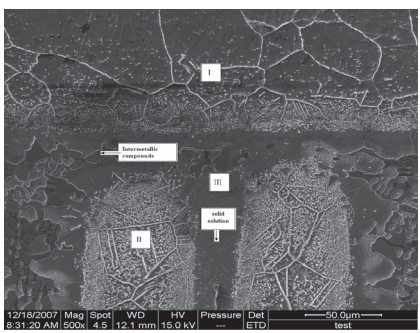


Fig. 2. Metallograph of nickel-based honeycomb in section.

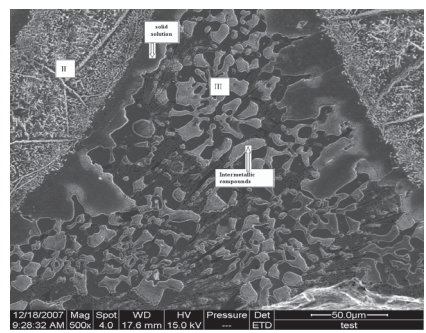


Fig. 3. Metallograph of nickel-based. honeycomb in cross-section.

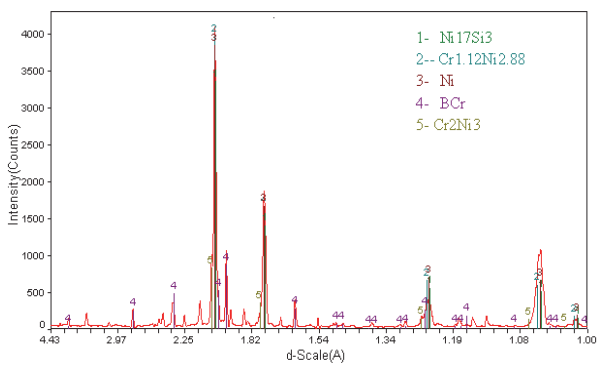


Fig. 4. XRD pattern of brazing region.

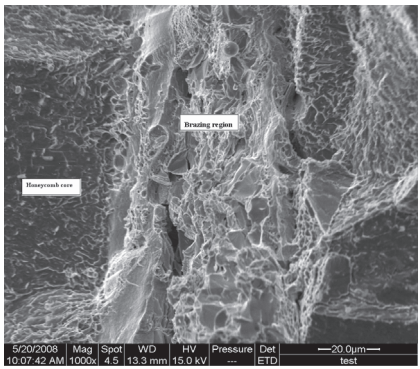


Fig. 5. The tensile fracture of specimens at room temperature.

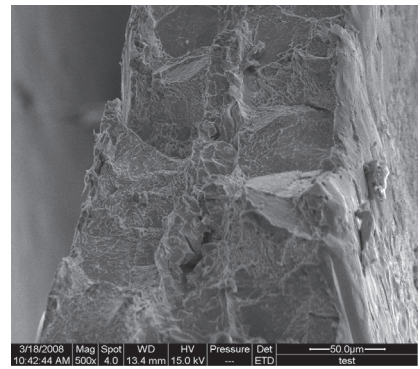


Fig. 6. The tensile fracture of specimens at 550ºC.

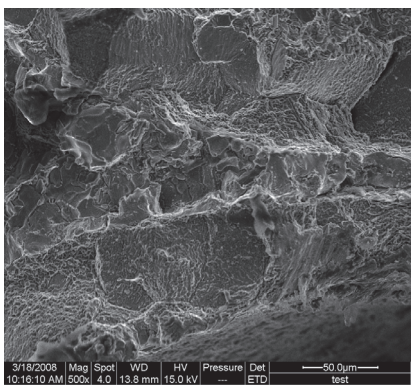


Fig. 7. The tensile fracture of specimens at 850ºC.

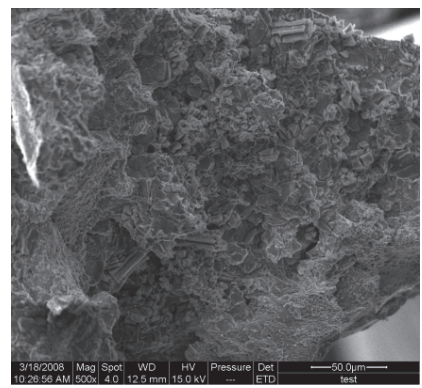


Fig. 8. The tensile fracture of specimens at 900ºC.

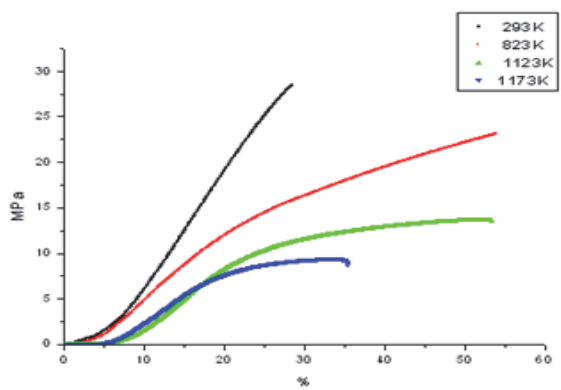


Fig. 9. The tensile stress versus strain. curves of honeycomb sandwich.

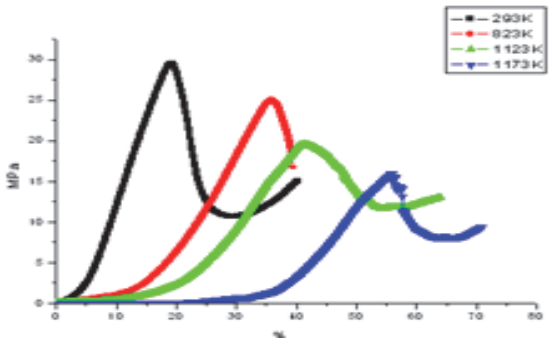


Fig. 10. The compressive stress versus strain curves of honeycomb sandwich.

There was no obvious plastic deformation in the tensile curves of the specimens at room temperature. With increasing temperature, plastic deformation in the tensile curves occurs obviously and the tensile elongation increased at first, and then declined, and the tensile elastic modular decreased gradually. This characteristic was confirmed by tensile fracture of the honeycomb sandwiches. Tensile fracture of the honeycomb core at room temperature was obviously brittle and no dimples were observed. Boundaries between the matrix and the brazing region were evident, as shown in Fig. 2 and 3. With increasing temperature, the boundary became indistinct and tensile fracture was plastic with obviously dimples.

The out-of-plate mechanical properties were given in Table 2. With increasing the temperature, the compressive elastic modular and the maximum yield strength decreased, and the tensile elastic modular and the maximum tensile strength also decreased. Compare to the maximum tensile strength, the maximum compressive yield strength was bigger at different temperature, and with increasing temperature, the difference between the maximum compressive yield strength and tensile strength increased gradually.

Table 2. The out-of-plate mechanical properties of honeycomb sandwich.

Temperature	Tensile modular (MPa)	Tensile strength (MPa)	Tensile elongation (%)	Compressive modular (MPa)	Compressive strength (MPa)
20ºC	128	28.5	29	223	29.6
550ºC	81.6	23	54	123	25
850ºC	74.9	13.8	53	110	19.6
900ºC	64.6	9.3	35	78	15.9

4. Summary

Specimens at 550°C had the following properties: tensile elastic modulus, 81.6 MPa; maximum tensile strength, 23 MPa; elongation, 54%; compressive elastic modulus, 123 MPa; and maximum yield strength, 25 MPa. Specimens at 850°C had the following properties: tensile elastic modulus, 74.9 MPa; the maximum tensile strength, 13.8MPa; elongation, 53%; compressive elastic modulus, 110 MPa; and maximum yield strength, 19.6 MPa. Specimens at 900°C had the following properties: tensile elastic modulus, 64.6 MPa; maximum tensile strength, 9.3 MPa; elongation, 35%; compressive elastic modulus, 78 MPa; and maximum yield strength, 15.9 MPa.

There are intermetallic compounds and a eutectic structure in the brazing region and the critical brazing clearance is 20 μm. No plastic deformation was observed in the tensile curve at room temperature, but obviously plastic deformation was observed in the tensile curve at high temperature, which was confirmed by the tensile fracture behavior.

References

1. Witherell PW, Air cushion vehicle structural design methods. Masters thesis, The George Washington University, December 1977.
2. Okuto K, Namba K, Mizukoshi H, Hiyama Y, The analysis and design of honeycomb welded structures. *J Light Met Welding* 29 (1991) 361–368.
3. Kobayashi H, Daimaruya M, Okuto K, Elastoplastic bending deformation of welded honeycomb sandwich panel. *J Jpn Soc Mech Eng* 60 (1994) 1011–1016.
4. Yeh WN, Wu Y, Enhancement of buckling characteristics for sandwich structure with fiber reinforced composite skins and core made of aluminum honeycomb and polyurethane foam, *J Theor Appl Fract Mech* 15 (1991) 63–74.
5. Kunimoto T, Yamada H, Study on the buffer characteristics of the honeycomb sandwich construction under dynamic loading. J Light Met 37 (1987) 327–331.
6. Kunimoto T, Mori N, Study on the buffer characteristics of the corrugated-core used for the 5051 aluminum alloy sandwich construction under dynamic loading, J Light Met 39 (1989) 687–692.
7. Wada A, Kawasaki T, Minoda Y, Kataoka A, Tashiro S. Fukuda H, A method to measure shearing modulus of the foamed core for sandwich plates. *J Compos Struct* 60 (2003) 385–390.

8. Lopatnikov SL, Gama BA, Haque MJ, Krauthauser C, Gillespie JW, Guden M, Hall IW, Dynamics of metal foam deformation during Taylor cylinder–Hopkinson bar impact experiment. *J Compos Struct* 61 (2003) 61–71.
9. Zhao H, Elnasri I, Abdennadher S, An experimental study on the behaviour under impact loading of metallic cellular materials. *Int J Mech Sci* 47 (2005) 757–774.
10. Zok FW, Rathbun HJ, Wei Z, Evans AG, Design of metallic textile core sandwich panels. *Int J Solids Struct* 40 (2003) 5707–5722.
11. Liu L, Holmes JW, Experimental investigation of fatigue crack growth in thin-foil Ni-based sandwich structures. *Int J Fatigue* 29 (2007) 1452–1464.
12. Pan SD, Wu LZ, Sun YG, Zhou ZG, Qu JL, Longitudinal shear strength and failure process of honeycomb cores. *J Compos Struct* 72 (2006) 42–46.
13. Bart-Smith H, Hutchinson JW, Evans AG, Measurement and analysis of the structural performance of cellular metal sandwich construction. *Int J Mech Sci* 43 (2001) 1945–1963.

Microstructure and Mechanical Properties of Spot Welding Joint of Dissimilar High Strength Steel

Wang Yuan[a], Qin Xinxin[b], Jiang Wenxiang[c],
Li Mengyuan[d] and Ren Jiangwei[e*]

Shanghai University of Engineering Science,
Shanghai, China
E-mail: [a]1450852770@qq.com, [b]2318821800@qq.com, [c]925198901@qq.com,
[d]394882962@qq.com, [e]jwren@163.com*

A three-layer structure consists of ultra-high strength hot stamped steel B1500HS and cold rolled high strength steel B250P1 is spot welded. Microstructure, microhardness and mechanical properties of spot welding joint are studied to find out the fracture procedure of the joint. The results show that a single nugget forms and the size of the nugget is about 6mm in diameter. Columnar grains consist of lath martensite and the microhardness is 520HV in nugget. There is softening zone in the heat affected zone of ultra-high strength steel. The crack initiates on the top of interface between different layers and propagates along the softening zone. The crack ends at the surface of ultra-high strength steel side eventually.

Keywords: Ultra-high Strength Steel; High Strength Steel; Spot Welding; Microstructure; Mechanical Properties.

1. Introduction

Lightweight automobile is one of the focuses in automobile industry in recent years. Lighting weight can reduce fuel consumption and exhaust pollution[1]. Experiments show that if 10% of automobile weight reduced, fuel efficiency can be increased by 6%–8%. Vehicle curb weight is reduced by 100 kg, fuel consumption in one hundred kilometers can be reduced 0.3–0.6 liters[2]. So, lightweight car has become a trend in the world. Meanwhile, the safety need from passengers is booming. To balance the two contradictory sides, ultra-high strength steel is widely used in automobile industry[3].

However, ultra-high strength steel, especially hot stamped steel, has specific characters in physical and chemical properties[4]. These characters of hot stamped steel lead to some complicated welding problems when it is resistance spot welded which is the most important welding technology in automobile industry.

* Corresponding author.

For example, greater electrode pressure is requested and shrink defects form easily. Moreover, the wear of electrode is intensified, which leads to the instable welding quality[5-7]. In this paper, three-layer structure consists of ultra-high strength hot stamped steel and cold rolled high strength steel is resistance spot welded. The microstructure, microhardness and mechanical properties of spot welding joint are studied to find out the fracture procedure of the joint.

2. Experimental

Ultra-high strength hot stamped steel B1500HS and cold rolled high strength steel B250P1 were used as raw materials. The chemical composition and mechanical properties of two raw materials were shown in Table1-2.

A three-layer structure consists of B1500HS and B250P1 steels was resistance spot welded. The set of three-layer structure was shown in Fig. 1. The ultra-high strength steels B1500HS which have the thickness of 1.2mm and 1.6mm were set as the top and bottom layer in the structure. The high strength steel B250P1 with the thickness of 1.0mm was set as interlayer. Single welding point was conducted at the center of overlapping area. The resistance spot welding was conducted on the ZDB-180-001-0002 energy storage spot welding machine. The welding cycles consisted of pre-heat cycle and two-pulse welding cycles. The welding parameters were shown in Table 3.

Table 1 Chemical composition of B1500HS and B250P1 (wt.%).

Materia	C	Si	Mn	Cr	Mo	B	P	S	Ait	Ti
B1500H	0.23	0.25	1.35	0.19	0.04	0.0032	-	-	-	-
B250P	≤0.008	-	≤1.20	-	-	≤0.020	≤0.12	≤0.025	≥0.015	≤0.20

Table 2 Mechanical properties of B1500HS and B250P1.

Materials	Yield Strength /MPa	Tensile Strength /MPa	Elongation /%
B1500HS (after quenching)	1500	≥1400	≥13
B250P1	250-360	≥440	≥32

Table 3 Resistance spot welding parameters.

Welding pressure	Pre-load time	Pre-heat current	Pre-heat time	Cooling time	Welding current	Welding time
3.5kN	40ms	5kA	60ms	20ms	7.1kA	300ms

After spot welding, the joint was cut along the axis of nugget on electric discharge machine. The microstructure of joint was observed on VHX-600K optical microscope. The samples used for observation were prepared according to standard procedure and etched in alcoholic solution with 4vol.% nitric acid.

Mechanical properties of spot welding joint were tested under the condition of shear according to ISO standards BS EN ISO 14272-2001. The mechanical properties testing were performed on AG-25TA universal testing machine at a constant speed 2mm/min under ambient temperature.

The microhardness of spot welding joint was measured on HX-1000 type microhardness tester with 200g load and 15s lasting time. The typical microhardness of the different zones in the joint was the average of five measurement points in each zone.

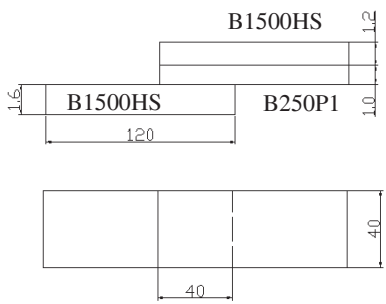


Fig. 1 Three-layer structure for spot welding (in mm).

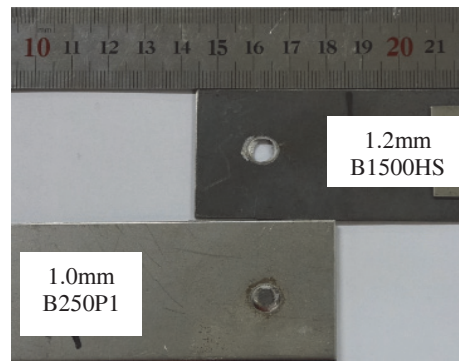


Fig. 2 Typical fracture location of spot welding joint in shear test.

3. Results and Discussion

The shear testing shows that the average shear force is 19.5kN and the standard deviation is 2.2kN. Moreover, all the seven tested joints fracture at the edge of indentation on the side of B1500HS with the thickness of 1.2mm.The typical fracture location in macro level is shown in Fig. 2.

To clarify the fracture procedure in shear test, the microstructure of spot welding joint is observed. The macrostructure of joint is shown in Fig. 3. It can be seen that a single nugget about 6mm in diameter forms because of the resistance heat in the spot welding and no shrinkage defects are found. In addition, heat affected zones in three layers are observed. The typical microstructure of joint in different zones are shown in Fig. 4.

It can be seen from Fig. 4 that the nugget has obvious character of columnar crystals. The columnar crystals consist of lath martensite. The temperature gradient existed in the sample contributes to the formation of columnar crystals. Interfaces of layers have maximum temperature and the temperature at the top and bottom surfaces is minimum because of the cooling of electrode. Moreover, the rapid cooling provided by electrode contributes to the formation of lath martensite.

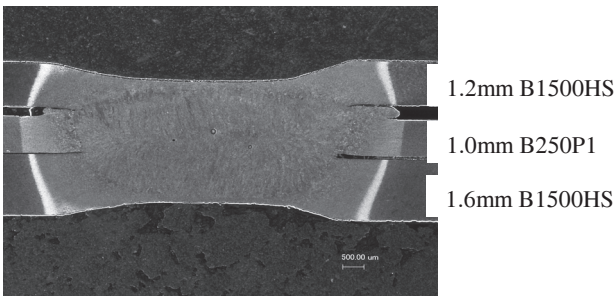
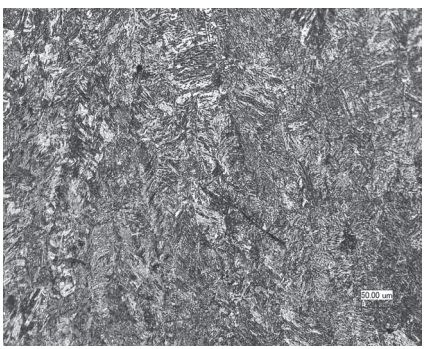
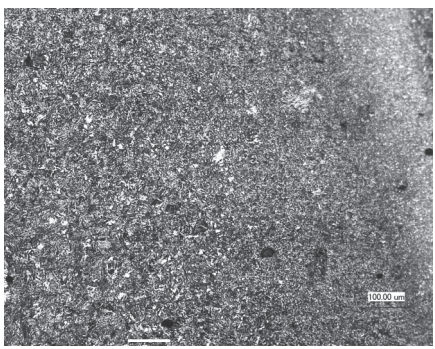


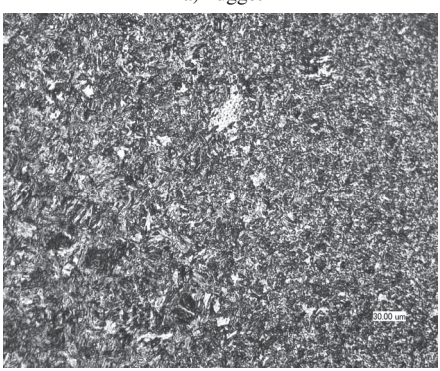
Fig. 3 Macrostructure of spot welding joint.



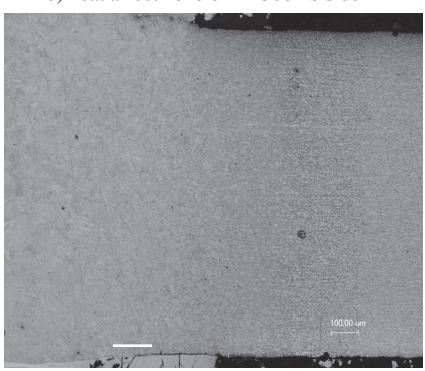
a) nugget



b) heat affect zone on B1500HS side



c) heat affect zone on B1500HS side



d) heat affect zone on B250P1 side

Fig. 4 Typical microstructure in different zones of spot welding joint.

The heat affected zone on B1500HS side can be divided into two parts. Lath martensite is observed in the part near nugget. The size of lath martensite becomes finer with the distance from nugget increases. Ferrite and bainite are observed in the part near base material. Finer martensite is found in the heat affected zone on B250P1 side. Beside, the size of martensite becomes coarser in the zone near nugget and finer in the zone near base materials.

The microhardness of the microstructure in different zones shows distinct diversity. The microhardness in nugget is about 520HV, which is higher than that of base materials B1500HS (about 495HV). The higher hardness in nugget is attributed to the martensite. The microhardness in the heat affected zone near base materials on B1500HS side decreases sharply to about 330HV, which can be attributed to the formation of ferrite and bainite. The microhardness in heat affected zone and base materials of B250P1 is about 300HV and 150-200HV respectively.

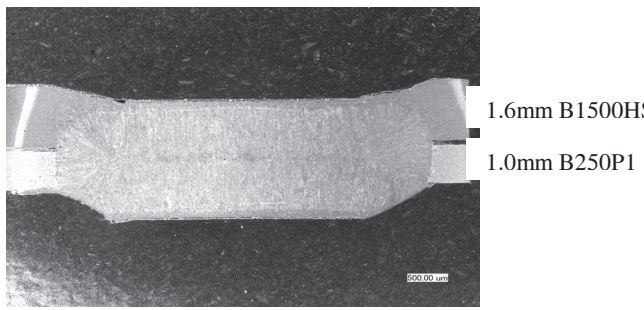


Fig. 5 Typical cross section of spot welding joint after fracture.

The typical cross section of spot welding joint after fracture is shown in Fig. 5. According to Fig. 5, the fracture procedure can be deduced based on the results on microstructure, microhardness and mechanical properties. Stress concentrates on the tip of interfaces of layers where the fracture occurs firstly during shear test. Because of the distinct softening in the heat affected zone on B1500HS side, the crack propagates along the softened zone and ends at the surface of B1500HS. However, why the crack initiates at the interface between 1.2mm B1500HS and 1.0mm B250P1 and ends at the surface of 1.2mm B1500HS? It can be explained by the relatively harder constrain provided by thicker B1500HS layer. Moreover, crack is difficult to propagate in thicker B1500HS because of the longer path. The fracture procedure results in the fracture location in macro level.

4. Conclusion

Based on the study on the microstructure, microhardness and mechanical properties of spot welding joint of ultra-high strength steel B1500HS with high strength steel B250P1, conclusion below are drawn.

(1) A single nugget forms in the resistance spot welding. The size of nugget is about 6mm in diameter

(2) Columnar grains in nugget consist of lath martensite which has the microhardness of 520HV. Softening zone exists in the heat affected zone of

B1500HS near base materials. The softening can be attributed to the formation of ferrite and bainite which has microhardness about 330HV.

(3) The crack in shear test initiates at the interface between 1.2mm B1500HS and 1.0mm B250P1. Then crack propagates along the softening zone and ends at the surface of 1.2mm B1500HS.

Acknowlegement

Thanks for the support of Shanghai University of Engineering Science under contact No.cx1405007, No.cs1405009 and No.nhky-2014-14.

References

1. T. Senuma. Physical metallurgy of iron and modern high strength steel sheets. *ISIJ International*, 41 (2001) 520-532.
2. X.Y. Zhang. Improvement of resistance spot weldability for dual-phase (DP600) steels using servo gun. *Journal of materials processing technology*, 209 (2009) 2671-2675.
3. S.P. Tewari. Resistance spot weldability of low carbon and HSLA steels. *Internation Journal of science and technology*, 15 (2010) 1-11.
4. L.J. Wang, Q.W. Cai, W. Yu, H.B. Wu, A.D. Lei. Microstructure and mechanical properties of 1500MPa grade ultra-high strength low alloy steel. Acta metal. Sinica, 46 (2010) 687-694.
5. L.J. Han, Z.W. Gu, Z.L. Zhang. Microstructure and fractography of intermediate frequency spot welding of precision ultra-high strength quenching steel. *Transactions of the China welding institution*, 31 (2010) 101-104.
6. H.P. YU, W.W. Wang, X.Y. Li, Y.H. Liu. Experiments and numerical simulation on spot-welded structure of ultra-high strength steel. *Transactions of the China welding institution*, 34 (2013) 9-12.
7. S. Xu, J. Zhi, Y.Q. Sun, K.H. Hu, T. Gong. Resistance spot welding test on ultra-high strength hot stamping steel. Research on Iron & Steel, 40 (2012) 36-40.

Effect of Cold-Rolling and Annealing on Microstructure and Texture of Interstitial Free Steel

Jiahui Qu[a], Jinqu Liu[b]

School of Equipment Engineering, Shenyang Ligong University, Shenyang 110159, China
E-mail: [a]qjh915@163.com, [b]272985361@qq.com

It was investigated and discussed systematically that the texture formation mechanism of IF steel sheet hot-rolled in ferrite region and its transformation mechanism during cold-rolling and annealing by means of the microstructure observation and orientation distribution function(ODF). The results showed that the stronger α-fibrous texture and the weaker γ-fibrous texture was both attained mainly during hot-rolling in ferrite region by the action of cross-slip with a bit of recrystallized grains found; both the fibrous textures are strengthened during cold-rolling under the joint action of cross-slip, grain rotation and shear band, the reigning fault sliding and intracrystalline; the formation of recrystallization structure and texture is mainly controlled by the mechanism of strong oriented nucleation and weak selective growth during annealing.

Keywords: Hot-Rolling; Ferrite Region; IF Steel Sheet; Texture Formation Mechanism; Cold-Rolling; Annealing; Texture Transformation Mechanism.

1. Introduction

In recent years, IF steel sheet hot-rolled in ferrite region were researched widely in the world.Through reasonably choosing hot rolling parameters (rolling temperature, rolling speed, pressure ratio, finishing temperature and lubrication, etc.), < 111 > // ND orientation and texture can be obtained,which the texture intensity is twice as much as one finishing in ferrite region[1-3]. That researches from a great amount of literature showed that the cold-rolling texture and the deep drawing performance was influenced by a different cold-rolling pressure ratio and annealing temperature on IF steel sheet. For example, a big cold-rolling pressure ratio is advantageous to the formation of <111>// ND γ-fibrous texture, and a annealing temperature impact greater than a annealing time for γ-fibrous texture[2-10]. However, that the formation mechanism of the ferrite area's hot-rolling texture, as well as the transformed process and mechanism in cold-rolling or annealing was not reported.

In this paper, the formation mechanism of the ferrite area's hot-rolling fibrous texture, as well as the transformed characteristics and mechanism in cold-rolling or annealing was are discussed, based on the deep-drawing IF steel sheet.

2. Experimental materials and methods

A IF steel sheet was used to a test materials. The chemical compositions are shown in Table 1. Its hot and cold working process is: the continuous casting billet of IF steel was heated to 1050 ºC, soon afterwards hot-rolled to 5 mm thick, and the finishing temperature of 930 ºC was controlled, the coiling temperature is 735 ºC. The hot-rolling sheet was cold-rolled to 1mm thick after the pressure ratio of 80%, and it was annealed in a box-type annealing furnace between 760 ~ 780 ºC (12 ºC/min, Heat preservation 4hour, cooling in the furnace).

Table 1 Compositions of IF steel sheet. (mass fraction, %).

C	Si	Mn	S	P	Nb	Al	Ti	N	Fe
0.004	0.016	0.13	0.006	0.006	0.005	0.034	0.060	0.002	Bal.

A large plate of hot-rolling, cold-rolling and annealing was intercepted respectively to 20 mm x 20 mm sample marked with rolling direction, then observing the microstructure and measuring the texture.

The microstructure was observed by means of optical microscope. The texture was determined by Philip company's X 'Pert PRD texture measurement instrument with Co ($K\alpha$) target. In order to eliminate the influence of stress, the specimens were washed with hydrofluoric acid after polished. The tube voltage was 35KV and the tube current was 40mA. The Schulz reflection method was used to measure three incomplete pole figures of {110}, {200} and {211} with 0°~70° of α, 0°~360° of β and $\Delta\alpha=\Delta\beta=5°$ of step. Texture analysis software of LaboTex3.0 was used to calculate orientation distribution function (ODF). The orientation densities f(g) was analyzed by selection of ODF sections with constant φ of 45°.

3. Experimental results

Fig. 1 showed the microstructure under different technological system. In Fig. 1(a), it could be seen that Area can be seen that the microstructure of hot-rolled IF steel is given priority to with fibrous tissue in ferrite region, and containing a small amount of recrystallized grains. In Fig. 1(b), it could be seen that the microstructure is a typical fiber banding structure after IF steel

cold-rolled, and that grain size obviously was refined than one of hot-rolling. In Fig. 1(c), it could be seen that the pie-grains emerge from annealing, and that the grain size trend towards the axle.

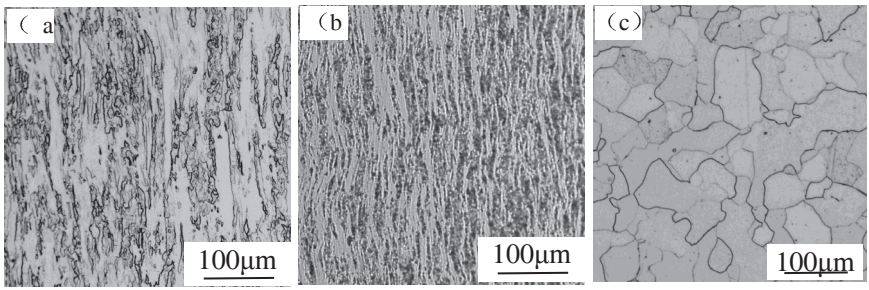


Fig. 1 Metallographic structure of IF steel sheet under different processing conditions: (a) hot-rolling in ferrite region, (b) cold-rolling, (c) annealling.

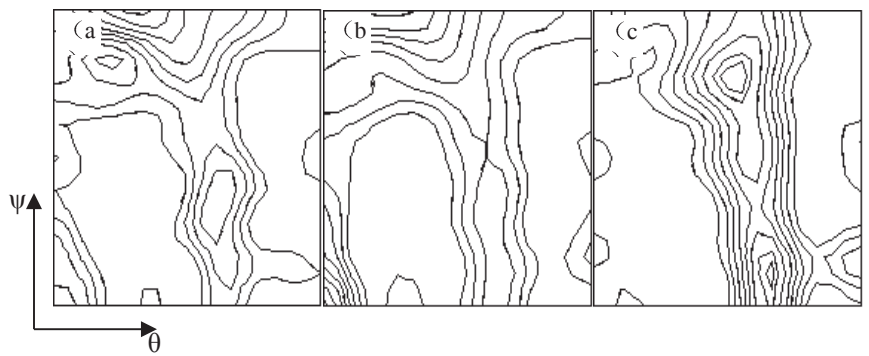


Fig. 2 ODF sectional views(φ=45°)of IF steel sheet under different processing conditions: (a) hot-rolling in ferrite region, (b) cold-rolling, (c) annealling.

Fig. 2 showed the texture test results under different process conditions of IF steel, and that the orientation density is graded 8 magnitudes in the figure. As shown in Fig. 2(a), that theα-fibrous texture {112} < 110 > corresponds to the euler angles (90 °, 40 °, 45 °) are relatively strong in ferrite region of hot-rolled IF steel, and that the texture {001} < 110 > corresponds to the euler angles (90 °, 0 °, 45 °) is very weak. At the same time, some texture were emerged for the grain orientation to deviate from rolling direction, such as the texture {114} < 131 > of the euler Angle (72 °, 18 °, 45 °). As shown in Fig. 2 (b), in cold-rolled IF steel, the α-fibrous texture are mainly the {001} < 110 > of (90 °, 0 °, 45 °) and {112} < 110 > of (40 °, 90 °, 45 °), and the are mainly the {111} < 110 > of (0 °, 55 °, 45 °) and {111} < 112 > of (55 °, 30 °, 45 °). By orientation density, it was showed that the texture {001} < 110 > of cold-rolled state was stronger than

one of hot-rolled state, and in ferrite region of hot-rolled IF steel, the texture {111} < 110 > is stronger, the texture {111} < 112 > is weaker. As shown in Fig. 2(c), after annealing, the α-fibrous texture {001} < 110 > of (90 °, 0 °, 45 °) and {112} < 110 > of (40 °, 90 °, 45 °) was obviously weakened, and the γ-fibrous texture {111} < 011 > of (0 °, 55 °, 45 °) and {111} < 211 > of (30 °, 55 °, 45 °) was clearly strengthened. Then the γ-fibrous texture was dominant after annealing.

4. Analysis and discussion

The finishing temperature in ferrite region is under $\gamma \rightarrow \alpha$ transformation temperature for hot-rolling other than the austenite[1], and namely before rolling it has been completed the $\gamma \rightarrow \alpha$ phase transition[3]. Because for the ferrite to have a body centered cubic structure and a high-level stacking fault energy, therefore, α- grain will continue to deformation and produce to dynamic restitutio in the subsequent further rolling. Under a certain condition of deformation, the ferrite generates easily dynamic recrystallization and cross-slip, so the different α-fibrous texture and γ-fibrous texture type appeared in ferrite region of hot-rolled IF steel.

Hot-rolling texture can pass on to cold-rolling texture, so this development to promote the {111} component of cold-rolling texture is very important. In the process of the cold deformation, the preferred orientation was formatted in IF steel specimen due to grain rotation, and the shear belt appears in grain due to the slip. It was confirmed by transmission electron microscopy (TEM) that the shear belt don't appear in the grain orientation of α-fibrous texture and appears only in the grain orientation of γ-fibrous texture[11]. The shear belt in crystalline helps to slip surface rotating and crystal nucleus increasing in γ-fibrous texture, so the textures between {112} < 110 > and {111} < 110 > were strengthened.

The annealing process is a very important stage to form recrystallization texture after the deformation. The energy storage is a driving force of the recrystallization on the cold rolling deformation, the formation and growth of the recrystallization crystal nucleus is a process of competition, so the final recrystallization texture are determined by the largest and fastest crystal nucleus. {111} < 112 > components have the stronger trend of development than {111} < 110 > components at the initial stage of a recrystallization and prior nucleation, so the {111} < 112 > has preference of nucleation in the grain boundary or near grain boundary. With the annealing, the γ-fibrous grain was gradually growth due to acquiring other orientation grain, thus the dominant texture having a γ-fibrous structure was formed after the recrystallization.

5. Conclusion

When the IF steel was hot-rolled in ferrite region, the fibrous deformation microstructure, the strongerα-fibrous texture and the weaker γ-fibrous texture was attained mainly under the action of cross-slip mechanism. The microstructure contains a small amount of recrystallization grain due to the presence of partial restitution and partial recrystallization, and a significant $\{110\} < 100 >$ Gauss texture and a less obvious $\{113\} < 332 >$ orientation type was appeared.

When the hot-rolling IF steel was cold-rolled, under the joint action of cross-slip, grain rotation and shear band, the reigning fault sliding and intracrystalline, the typical fibrous microstructure formed, and then betweenα-fibrous texture andγ-fibrous texture were strengthened obviously.

When the cold-rolling IF steel was annealed, the formed recrystallization microstructure and texture was controlled mainly by the stronger directional nucleation mechanism and the weaker mechanism, so the directional nucleation affected the α-fibrous texture components, and the choice growth affected the γ-fibrous texture and its adjacent components.

References

1. H Zhao, Rama S C, Barber G C, *et a1*. Experimental study of deep drawability of hot rolled IF steel[J]. *Journal of Materials Processing Technology*, 2002, 128(1/2/3): 73-79.
2. Asensio J, Romano G. Martinez V J, *et a1*. Ferritie steels optimization of hot-rolled textures through cold rolling and annealing[J]. *Materials Characterization*, 200l, 47(2): 119-127.
3. Barrett C J, Wilshire B. The production of ferrite hot rolled interstitial-free steel on a modern hot strip mill[J]. *Journal of Materials Processing Technology*, 2002, 122(1): 56-62.
4. Li B L, Godfrey A, Meng Q C, *et a1*. Microstructural evolution of IF-steel during cold rolling[J]. *Acta Materialia*, 2004, 52(4): 1069-1081.
5. Liu Y Z. SunJ H, Zhotl L Y, *et a1*. Experiment investigation of deep-drawing sheet texture evolution[J]. *Journal of Materials Processing Technology*, 2003, 140(1/2/3): 509-513.
6. Bate P S, Quinta J. Texture development in the cold rolling of IF steel[J]. *Matedals Science and Engineering A*, 2004, 380(1/2): 365-377.
7. Choi S H, Cho J H. Primary recrystallization modeling for interstitial free steels[J]. *Materials Science and Engineering A*, 2005, 405(1/2): 86-101.

8. Nave M D, Barnett M R. Texture change near grain boundaries and triple points in cold-rolled interstitial-free steel[J]. *Materials Science and Engineering A*, 2004, 386(1/2): 244-253.
9. Humane M M, Minj R K, Peshwe D R, *et a1*. Texture and formability of one-step and two-step and cold-rolled and annealed interstitial free high-strength steel sheets [J]. *Metallurgical and Materials Transactions*, 2001, A42(6): 1692-1708.
10. Pampa Ghosh, Chiradeep Ghosh, Ray R K. Thermodynamics of precipitation and textural development in batch-annealed interstitial-free high-strength steels[J]. *Acta. Materialia*, 2010, 58(11): 3842-3850.
11. Shen Kai, Duggan B J. Formation of shear band in cold rolled body-centered cubic metal[J]. *Journal of Nanjing University of Aeronautics &Aatronautics*, 2005, 37(5): 571-575.

Crystallization Behavior of Biodegradable Poly (3-hydrobutyrate-co-3-hydroxyvalerate)/Hyperbranched Poly (Ester Amide) Blends

Weilong Zheng[a], Long Chen[b*] and Zongyi Qin[c]

State Key Laboratory for Modification of Chemical Fibers and Polymer Materials, College of Materials Science and Engineering, Donghua University, Shanghai, 201620, China

E-mail: [a] flyboy123@outlook.com, [b] happyjack@dhu.edu.cn, [c] phqin@dhu.edu.cn

To enhance the toughness of poly (3-hydrobutyrate-co-3-hydroxyvalerate) (PHBV), biodegradable hyperbranched poly (ester amide) (HBPs) is blended with it by spin casting that is expected to inhibit the crystalline ability of PHBV. The differential scanning calorimetry (DSC) results show that the addition of HBPs increase the cold crystallization temperature from 45 to 56°C and decrease the melting temperature from 173.96 to 170°C. Which the enthalpy decrease indicate a lower crystallization with the addition of HBPs, to inhibit the crystalline ability of PHBV. Furthermore, the process of crystallization of the blends can be visually observed by polarized optical microscopy (POM). With the addition of HBPs, the number of PHBV spherulites decrease, its size is increased and the concentric annulus extinction is disappeared.

Keywords: Poly (3-hydroxybutyrate-co-3-hydrovalerate), Hyperchanced poly (ester amide), Crystallization behavior.

1. Introduction

With the growing environmental awareness, biodegradable polymer materials have attracted great interests such as poly (3-hydrobutyrate-co-3-hydroxyvalerate). It has many excellent features, which are biodegradability, biocompatibility, piezoelectric, optical activity, etc[1~2]. These properties make it attractive and have broad application prospects, especially in biomedical fields. However, the application of PHBV is hindered by some imperfections such as slow crystallization rate, the development of interlamellar secondary crystallization on storage, high crystallinity, and other issues[3].

Hyperbranched polymers have great potential for wide applications in materials, due to low viscosity, high functionality, good solubility characteristics

* Corresponding author.

and no chain entanglement. Especially, hyperbranched polymers can provide many terminal reactive chemical groups such as hydroxyl and carboxyl groups. They usually are used as surface modifiers and additives to improve its properties[4~7].

The present study will present the crystallization behavior of PHBV, and PHBV/HBPs blends using POM and DSC. An analysis of the crystallization ability, making use of mathematical statistics method by POM, is conducted. It will also present an analysis of the crystallization properties, making use of DSC.

2. Experimental

2.1. *Materials*

PHBV (Mn=2.67x10^5, Mw/Mn=2.30) with 1.05 mol% (3-HV) content was supplied by PHB Industrial, Tianan, China and dried in oven for 24 h at 80°C. Hybranched poly (ester amide) (HBPs), with the trade name Hybrane® PS2550, was supplied by Polymer Factory Sweden AB. Its molecular weight is 2500g/mol (Mw). The chloroform was obtained from Sinopharm Chemical Reagent Co. Ltd China.

2.2. *Preparation*

PHBV/HBPs composite was dissolved in chloroform in 5wt% (w/w). The solution heated at 56°C under vigorous stirring for 4h. Then it was stirred at room temperature for 12h. Films were prepared by spin casting and dried under room temperature for 3 days to remove residual solvent.

2.3. *Characterization*

2.3.1. *Differential scanning calorimetry*

Before testing, Samples were sealed in aluminum crucibles and put on the hot stage of 200°C for 5 min, due to without previous thermal history, and immediately put it into liquid nitrogen to ensure that the samples were amorphous. Then thermal transitions of the composites were examined by DSC (Q20, USA) under N_2 flow (40 ml/min). Samples were heated from -10°C to 200°C at a heating rate of 10°C/min.

2.3.2. *Polarized optical microscopy*

Crystallization process of PHBV/HBPs composites was studied by Olympus BX51 POM equipped with a Linkam hot stage. PHBV/HBPs films were heated

up to 200°C at 20°C/min between clean glass slides and then equilibrated at this temperature for 3 min. PHBV nucleation and spherulites growth at 70°C was examined by the POM at a rate of 100°C/min and recorded by an attached digital camera every 5s up to 30 min of PHBV crystallization.

3. Results and Discussion

3.1. *Crystallinity and Melting Behavior*

The crystallinity of the polymers has an important influence on the mechanical properties of materials. The melting curves of PHBV and PHBV/HBPs composites and the thermal parameters are shown in Fig. 1 and Table 1, respectively. The crystallinity of the blends can be calculated by the following equation (1): [8]

$$X_c = \frac{\Delta H_m}{(1-\varphi_{HBPs})\times\Delta H_f} \times 100\% \quad (1)$$

where Xc is the degree of crystallinity of PHBV and its composites. φ_{HBPs} is the weight fraction of HBPs in the blend. ΔH_m is the measured melting enthalpies and ΔH_f is the enthalpies of 100% crystalline PHBV, which is chosen as 146.6 J·g^{-1} for PHB.

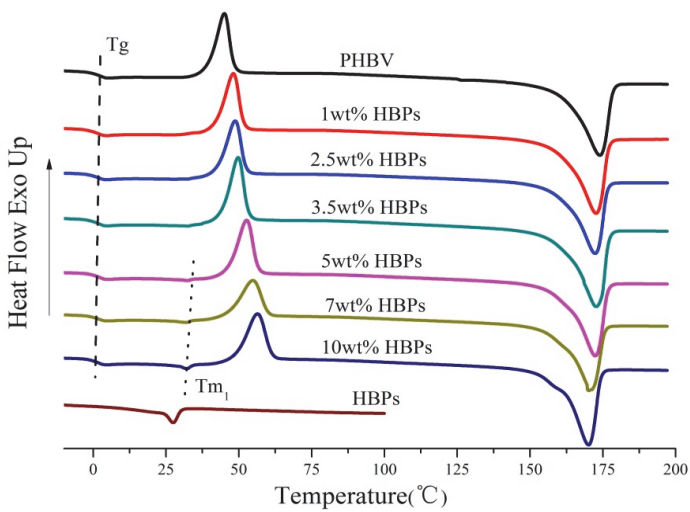


Fig. 1 DSC thermograms of neat PHBV and PHBV/HBPs composites.

As can be seen in Fig. 1 and Table 1 show that, compared with neat PHBV, the glass transition temperature (Tg) of blends didn't changed too much. The

reason was that maybe due to lower content of HBPs. But with adding the HBPs, the melting temperature (Tm_2) decreased from 173.96°C to 170.05°C. When the HBPs content more than 3.5% in the blends, it appeared a low melting temperature in low temperature region. This may be due to the agglomeration of HBPs in the blend, and meanwhile incompatible between them. The cold crystallization temperatures (Tc) of the composites increased from 45.01 to 56.32°C and the peak width became broader, which indicated that HBPs created steric-hindrance effect to hamper the crystallization of PHBV. It was consistent with the result of POM testing.

Table 1. Thermal Parameters of PHBV/HBPs Blends with Various HBPs Contents.

HBPs ratio (%)	Tg(°C)	Tm_1(°C)	Tc(°C)	Tm_2(°C)	ΔH_c(J/g)	ΔHm^a(J/g)	Xc^b(%)
0	2.96	-	45.01	173.96	42.16	106.70	72.78
1	1.95	-	48.08	172.67	39.22	94.91	65.39
2.5	1.89	-	48.70	172.36	38.77	84.51	59.12
3.5	2.03	-	49.73	172.71	38.03	82.23	58.12
5	2.46	32.56	52.65	172.40	35.98	79.48	57.07
7	2.18	32.08	54.73	170.17	33.57	76.13	55.84
10	1.60	32.36	56.32	170.05	35.73	72.65	57.34

[a] Data corrected for the percentage of PHBV in the blend.

[b] ΔH_f for 100% crystalline PHB equals 146.6J/g [8].

3.2. *Size and Morphology of Spherulite*

The process of crystallization of the blends is directly investigated by POM. PHBV spherulites with characteristic banding and Maltes cross could be clearly seen under POM (Fig. 2). Without HBPs, the number of PHBV spherulites was large and their size was relatively small. Meanwhile the concentric annulus extinction of PHBV was the rule (Fig. 2A). With the addition of HBPs, the number of PHBV spherulites decreased, their size was increased and the concentric annulus extinction was disappeared (see Fig. 2B~G).

Otherwise, through mathematical statistical method, the date gained by the POM of nucleation density as a function of the HBPs content in blends at 70°C were summarized in Fig. 3 which showed the nucleation density of the PHBV/HBPs composites as a function of the isothermal holding time. It was seen in Fig. 3 that the nucleation density of blends increased as isothermal time extended by exponential growth. Through the study of the nonlinear fitting of experimental data, with the content of HBPs increased, the nucleation density of blends decreased (Fig. 3A~B). To study the first order derivative, it could get the nucleation rate of blends (Fig. 3C~D). We could see that the nucleation rate of

blends decreased slightly with the content of HBPs increasing. Results of the POM suggested that HBPs restrained the crystallization of PHBV, likely because HBPs increased the energy barrier to form PHBV nuclei. This was in agreement with crystallization temperature (Tc in Fig. 1), which progressively increased with the addition of HBPs.

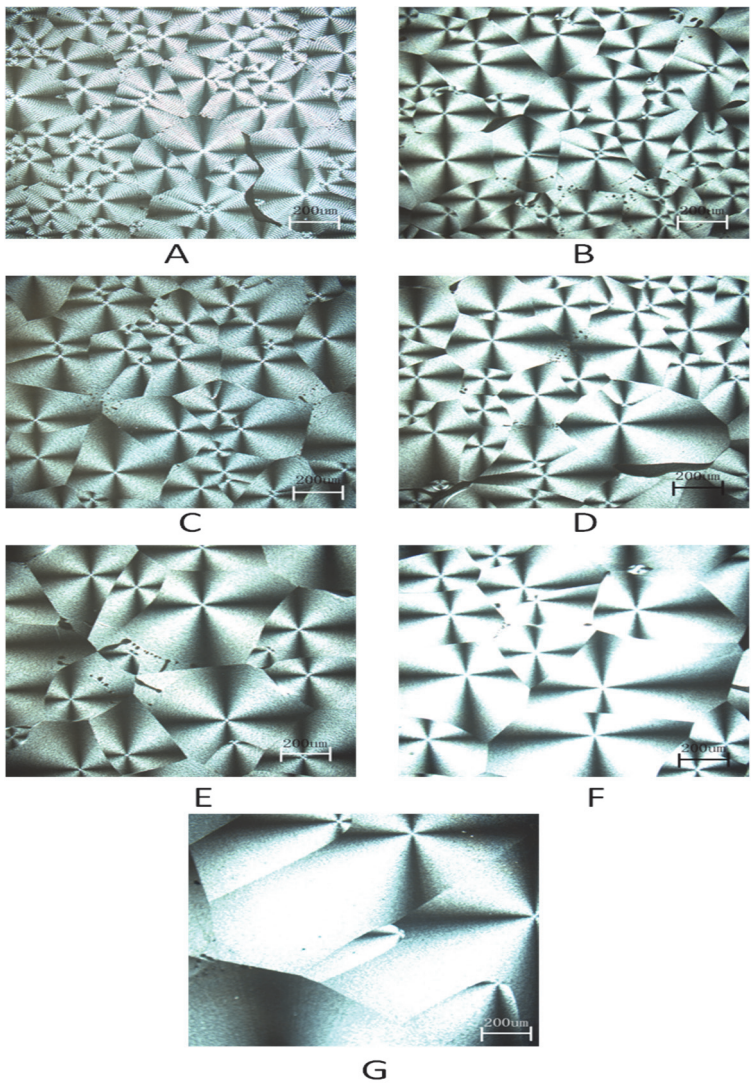


Fig. 2 Polarized optical micrographs of pure PHBV (A) with the blends (B ~ G). Isothermal crystallization at 70°C and crystallitation time: crystallization end.

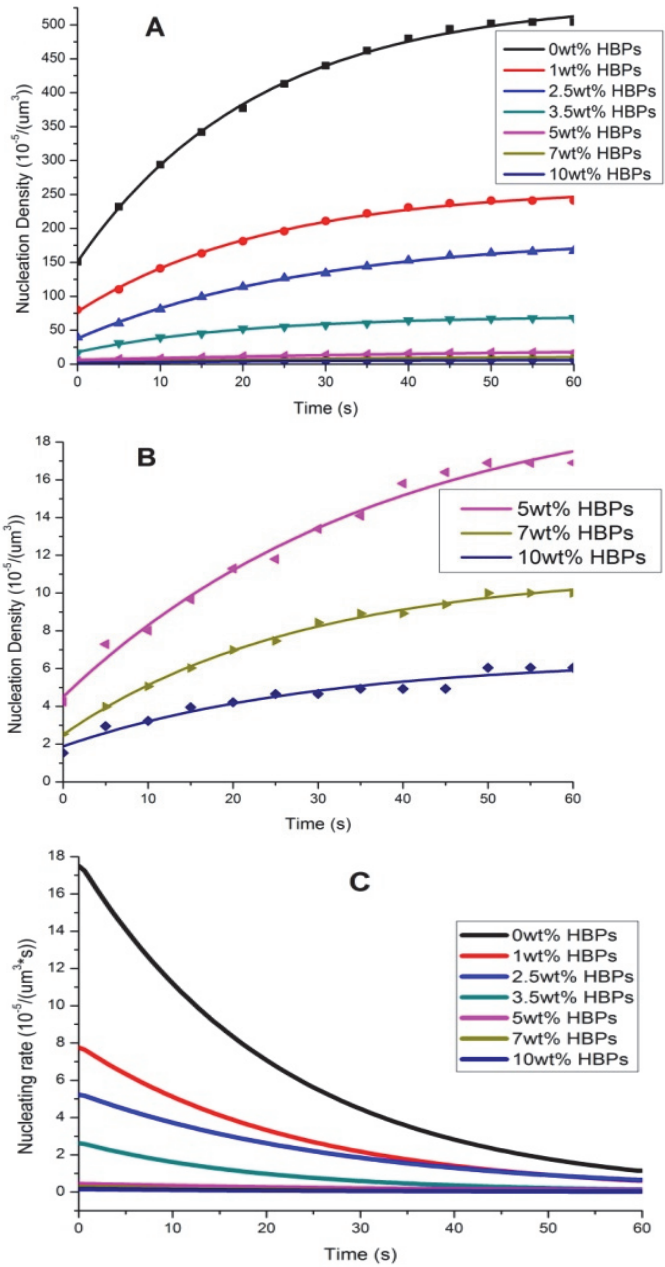


Fig. 3 Experimental and fitted curves of the Nucleation density (A, B) and the nucleation rate (C, D) of blends with different content of HBPs, solid points (experimental data) and solid lines (fitted curves).

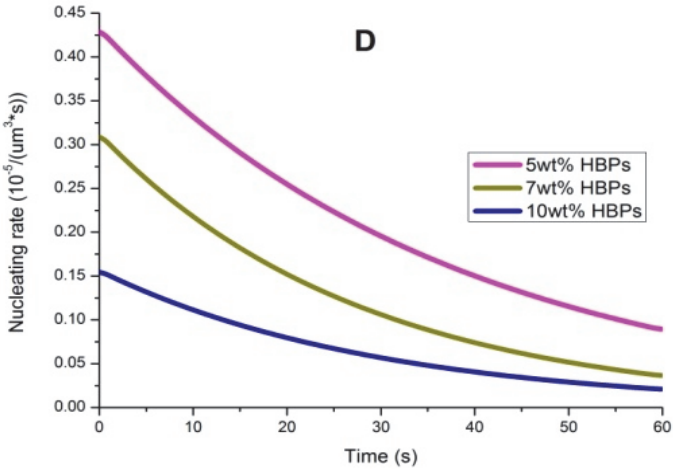


Fig. 3 (*Continued*)

4. Conclusions

The aim of this study was to analysis the crystallization behavior of PHBV/HBPs blends with the different content of hyperbranched poly(ester amide) by spin casting. The effect of hyperbranched poly(ester amide) as a nucleation inhibitor aid on PHBV was visible from DSC and POM. It showed that adding HBPs resulted in a reduction of the crystallinity of blends, comparing with pure PHBV. PHBV spherulites with characteristic banding and Maltes cross could be clearly seen by POM. With the addition of HBPs, the number of PHBV spherulites and the nucleation rate decreased more than half, their size was increased and the concentric annulus extinction was disappeared.

Acknowledgments

The authors thank the Fundamental Research Funds for the Central Universities (2232013A3-02) for financial support.

Reference

1. Doi, Y., Kanesawa, Y., Kunioka, M.; Saito, T., Biodegradation of microbial copolyesters: poly(3-hydroxybutyrate-co-3-hydroxyvalerate) and poly(3-hydroxybutyrate-co-4-hydroxy-butyrate) [J]. *Macromolecules*, 23 (1990) 26-31.
2. Choi, G. G.; Kim, H. W.; Kim, Y. B.; Rhee, Y. H., Biocompatibility of poly(3-hydroxy-butyrate-co-3-hydroxyvalerate) copolyesters produced by

Alcaligenes sp MT-16. *Biotechnology and Bioprocess Engineering* [J], 10 (2005) 540-545.

3. Bhardwaj, R., et al., Renewable Resource-Based Green Composites from Recycled Cellulose Fiber and Poly (3-hydroxybutyrate-co-3-hydroxyvalerate) Bioplastic. *Biomacromolecules* [J], 7(2006) 2044-2051.
4. Fei, Bin, Cheng Chen, et al., Modified poly (3-hydroxybutyrate-co-3-hydroxyvalerate) using hydrogen bonding monomers. *Polymer* [J], 45(2004) 6275-6284
5. Hong, Y., Cooper-White, J. J., Mackay, M. E. et al., A novel processing aid for polymer extrusion: Rheology and processing of polyethylene and hyperbranched polymer blends. Journal of Rheology[J], 43(1991) 781-793.
6. Hong, Y., et al., Film blowing of linear low-density polyethylene blended with a novel hyperbranched polymer processing aid. *Polymer* [J], 41(2000) 7705 - 7713.
7. Ying Lin, et al., Hydrogen-Bonded Blend of Polylactide with Biodegradable Hyperbranched Poly(ester amide). Macromolecules[J], 40(2007) 6257-6267
8. Shan, G., et al., Multiple melting behaviour of annealed crystalline polymers. *Polymer Testing* [J], 29(2010) 273-280.

Hydrothermal Conversion of Glucose to Lactic acid with $Al(OH)_3$

Zhengshuai Zhang[a], Guodong Yao[b] and Fangming Jin[c †]

School of Environmental Science and Engineering, Shanghai Jiao Tong University, 800 Dongchuan Road, Shanghai 200240, China

E-mail: [a]hanser108@hotmail.com, [b]ygd_sparkling@126.com, [c †]fmjin@sjtu.edu.cn

This paper investigated the hydrothermal conversion of glucose to lactic acid using $Al(OH)_3$ to exploit mild base catalysts. Results showed that the highest lactic acid yield of 17% was obtained from glucose with $Al(OH)_3$ with 35% water filling at 300 ºC for 60 s. Thus, this study may provide a promising method for lactic acid synthesis and biomass utilization under hydrothermal conditions with aluminium hydroxide.

Keywords: Biomass Utilization; Lactic Acid; Aluminium Hydroxide; Hydrothermal Conditions.

1. Introduction

In recent decades the depletion of fossil fuel reserves and global warming caused by anthropogenic CO_2 emission have urged human beings to search for renewable chemicals and energy sources.[1-2] Biomass as the most abundant green renewable source of fixed carbon has been considered as a primary candidate for the future because of its availability and its potential to produce high value products.[3-5] High-temperature water (HTW) is receiving increasing attention as a consequence of its unique inherent properties, such as a high ion product (Kw), a low viscosity, a low dielectric constant and weak hydrogen bonds, and it thus appeared to be favourable for promoting reactions even without catalysts. In this regard, hydrothermal conversion is thought to be an environmentally friendly and highly effective method for converting biomass into useful value-added chemicals[6-8].

Lactic acid has been identified as an important platform chemical and widely applied in the food, pharmaceutical, and chemical industries. Its market demand grows rapidly, particularly in consequence of its application in the synthesis of biodegradable lactic acid polymers with limited environmental impact and other commodity chemicals, including ethyl lactate (a green organic solvent) or

† Corresponding author.

1,2-propanediol. Recently, several researches[9,10] have demonstrated that biomass can be converted into lactic acid through hydrothermal reactions and alkali plays a vitally important role in the hydrothermal conversion of carbohydrate biomass to lactic acid. However, strong alkali catalysts such as NaOH[9], KOH, $Ba(OH)_2$[10], suffer from a serious disadvantage of corrosion to the reactors under hydrothermal conditions, which leads to big limitations in the application of hydrothermal process to industrial scale-up and commercialization. To advance in the commercial development of hydrothermal process it is crucial to select a mild alkali catalyst which causes less reactor corrosion and achieves good catalytic activity in the meantime.

The purpose of the present research, therefore, was to find out an appropriate catalyst along with less reactor corrosion and decent catalytic activity for the reduction of biomass to lactic acid under hydrothermal conditions. $Al(OH)_3$ (amphoteric hydroxide) for reduction of biomass into lactic acid formation is investigated in this study. The optimum reaction conditions for lactic acid production were investigated.

2. Experimental Section

2.1. *Experimental Materials*

Glucose (≥ 99.9%, Sinopharm Chemical Reagent Co., Ltd) was used as reagent and lactic acid (1.0 N) was purchased from Alfa Aesar for the qualitative analysis of the products in the liquid samples. As preliminary tests, addtives including $NaHCO_3$ (≥ 99.5%), $Al(OH)_3$(≥ 97.0%), NaOH (≥ 96.0%) were purchased from Sinopharm Chemical Reagent Co., Ltd. Deionized water was used throughout the study.

2.2. *Experimental Procedure*

Experiments were conducted using a series of batch SUS 316 tubing reactors [9.525 mm (3/8in.) outer diameter, 1 mm wall thickness, and 120 mm length] with end fittings, providing an inner volume of 5.7 mL. The schematic drawing can be found elsewhere.[11,12] The experimental procedure was conducted as follows. The desired amounts of glucose, $Al(OH)_3$, and deionized water were added to the reactor chamber. The reactor was then sealed and put into a salt bath that had been preheated to the desired temperature. In the salt bath, the reactor was vibrated and agitated during the reaction. After the preset reaction time, the reactor was removed from the salt bath and then placed into a cold water bath to quench the reaction. Afte rcooling to room temperature, the reaction liquid

sample was collected and filtered through a 0.22 μm syringe for analysis. The water filling was defined as the ratio of the volume of the water put into the reactor to the inner volume of the reactor. The reaction conditions were changed in a great range, to test the effect of different conditions for lactic acid production.

2.3. *Product Analysis*

Liquid samples were filtered and then analyzed by high performance liquid chromatography (HPLC), total organiccarbon (TOC), and gas chromatography/ mass spectroscopy (GC/MS). HPLC analysis was performed on KC-811 columns (SHODEX) with an Agilent Technologies 1200 system, which was equipped with a tunable ultraviolet/visible (UV/vis) absorbance detector adjusted to 210 nm and a differential refractometer detector. The system used a 2 mmol/L $HClO_4$ solution as the mobile phase at a flow rate of 1.0 mL/min. TOC was analyzed using a Shimadzu TOC 5000A. The Agilent 7890 GC/MS system, which was equipped with a 5985C inert mass selective detector (MSD) and a triple-axis detector, was used to investigate other possible chemicals in liquid samples.

3. Results and Discussion

Initially, the catalytic effect of $Al(OH)_3$ for the conversion of glucose (selected as the test material for biomass) into lactic acid at 300 °C for 60 s with 35% water filling in different catalyst concentration was investigated. The lactic acid yield was defined as the percentage of lactic acid to initial glucose on a carbon basis. As shown in Fig. 1, the presence of alkalicatalyst proved to increase the yield of lactic acid effectively.

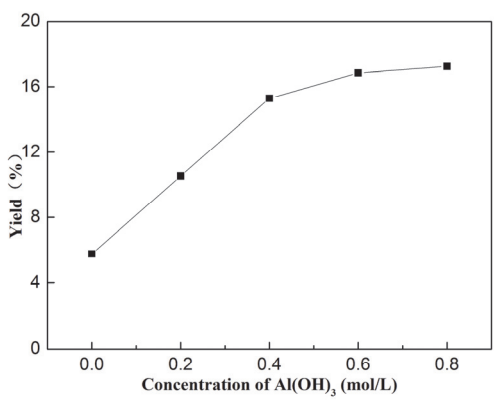
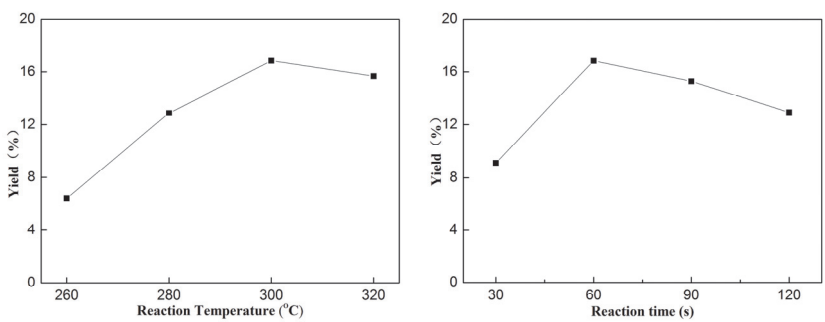


Fig. 1 Effect of $Al(OH)_3$ amount on yield of lactic acid (other conditions: 0.1mol/L glucose, reaction temperature 300 °C, reaction time 60 s, water filling 35%).

Generally speaking, the lactic acid yield increased with the initial catalyst concentration and the highest lactic acid yield of 17% was acquired when 0.8 mol/L $Al(OH)_3$ was added. For a lower yield of lactic acid with $Al(OH)_3$, a possible explanation may be it was just a low amount of $Al(OH)_3$. Thus, a further experiment with more $Al(OH)_3$ addition ranging from 1 mol/L to 2 mol/L was conducted. The highest yield remained 17%. Therefore, the lactic acid yield reached the peak at the catalyst concentration of 0.8 mol/L and no increase was observed even though more catalyst was added.

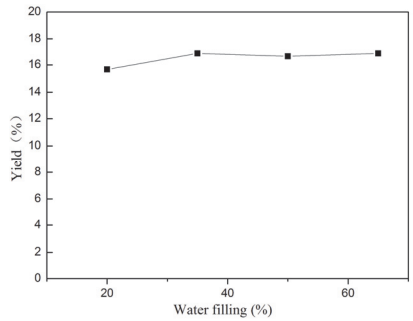
Effects of reaction conditionson the yield of lactic acid were studied to determine the optimum conditions. As illustrated in Fig. 2(a), a series of experiments were conducted at temperatures ranging from 260 to 320 °C with the addition of 0.8 mol/L $Al(OH)_3$ and a fixed reaction time of 60 s. The lactic acid yield increased remarkably with an increase in temperature and reached a maximum at 300 °C. The results showed that temperature had an obviously positive effect on the yield of lactic acid, which is possibly due to the significant change in water properties such as ion product at this temperature range in addition to theincrease in reaction rate caused by the increase in temperatures. The observed decrease in the lactic acid yield at temperatures greater than 300 °C may be attributed to the decomposition of lactic acid at higher temperatures.

The effect of reaction time on the yield of lactic acid was examined by changing the reaction time from 30 s to 120 s at 300 °C . As shown in Fig. 2(b), the reaction time also had a significant effecton the yield of lactic acid. The yield increased drastically with increasing reaction time for the first 60s, the maximum



(a) (b)

Fig. 2 Effect of process variables on yield of lactic acid: (a) reaction temperature, other conditions: 0.1mol/L glucose, 0.8mol/L $Al(OH)_3$, reaction time 60 s, water filling 35%; (b) reaction time, other conditions: 0.1mol/L glucose, 0.8mol/L $Al(OH)_3$, reaction temperature 300 °C, water filling 35%; (c) water filling, other conditions: 0.1mol/L glucose, 0.8mol/L $Al(OH)_3$, reaction temperature 300 °C, reaction time 60 s.



(c)

Fig. 2 (*Continued*)

yield was obtained at 60 s, with a value of 17%. However, the yield of lactic acid decreased as the time was further increased. The highest yield of lactic acid at 60 s is likely because lactic acid formation was faster than lactic acid decomposition during the first 60 s and after 60 s, decomposition of lactic acid may have occurred at a higher rate.

As shown in Fig. 2(c), the yield of lactic acid increased slighted when the water filling increased from 20% to 35%. The increase in water filling would lead to an increase in the reaction pressure, and thus lead to a promotion of the generation of lactic acid. However, further increase in water filling would lead to the excessive reaction pressure. Besides, excessive water filling rate of the reactor may lower the contacting possibility of reaction molecules. Therefore, no more increase in the yield of lactic acid was observed with the superfluous increase in water filling.

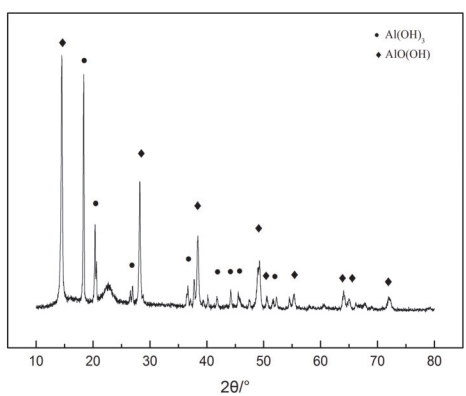


Fig. 3 XRD patterns of solid samples after reaction (Reaction condition: 0.1mol/L glucose, 0.8mol/L $Al(OH)_3$, reaction temperature 300 °C, reaction time 60 s, water filling 35%).

Additionally, recycle experiments were performed to investigate the effect of the stability and reusability of the catalyst. XRD patterns (Fig. 4) showed that part of $Al(OH)_3$ turned into AlO(OH) after four recycles under hydrothermal conditions. The lactic yield almost remained the same as 17% after four recycles. Therefore, the slight change had little effect on the loss of catalyst activity.

4. Conclusion

In summary, we developed a highly efficient conversion for the synthesis of lactic acid from biomass-derived glucosewith a mild base catalyst of $Al(OH)_3$in high temperature water. The maximum yield of 17% lactic acid was achieved in the presence of 0.8 mol/L Al(OH)3 with 35% water filling at 300 ºC for 60 s. This study provided a significant process for the conversion of biomass-derived glucose to lactic acid with little corrosion and high yield.

Acknowledgements

The authors thank the financial support of the National Natural Science Foundation of China (No. 21277091), the State Key Program of National Natural Science Foundation of China (No. 21436007), Key Basic Research Projects of Science and Technology Commission of Shanghai (No. 14JC1403100) and China Postdoctoral Science Foundation (No. 2013 M541520).

References

1. Cox, P. M.; Betts, R. A.; Jones, C. D.; Spall, S. A.; Totterdell, I. J. Acceleration of global warming due to carbon-cycle feedbacks in a coupled climate model Nature 2000, 408 (6809) 184–187.
2. Meng, M.; Niu, D. Modeling CO2 emissions from fossil fuel combustion using the logistic equation Energy 2011, 36 (5) 3355– 3359.
3. Huber GW, Iborra S, Corma A. Synthesis of transportation fuels from biomass: Chemistry, catalysts, and engineering. *Chem Rev* 106(9):4044–4098. (2006)
4. Jin FM, Enomoto H. Rapid and highly selective conversion of biomass into value-added productsin hydrothermal conditions: chemistry of acid/base-catalysed and oxidation reactions. *Energy Environ Sci* 4(2):382–397. (2011)
5. Yan X, Jin F, Tohji K, Kishita A, Enomoto H. Hydrothermal conversion of carbohydrate biomass to lactic acid. *AIChE J* 56(10):2727–2733. (2010)
6. Akiya N, Savage PE. Roles of water for chemical reactions in High-Temperature Water. *Chem Rev* 102(8):2725–2750. (2002)

7. Kruse A, Dinjus E. Hot compressed water as reaction medium and reactant—Properties and synthesis reactions. *J Supercrit Fluids* 39(3):362–380. (2007)
8. Kruse A, Dinjus E. Hot compressed water as reaction medium and reactant—2 degradation reactions. J Supercrit Fluids 41(3):361–379. (2007)
9. Yan XY, Jin FM, Tohji K, Moriya T, Enomoto H. Production of lactic acid from glucose by alkaline hydrothermal reaction. *J Mate Sci* 42(24):9995–9999. (2007)
10. Davide Esposito, Markus Antonietti. Chemical Conversion of Sugars to Lactic Acid by Alkaline Hydrothermal Processes. Chem Sus Chem, 6: 989–992. (2013)
11. Jin, F. M.; Zhou, Z. Y.; Moriya, T.; Kishida, H.; Higashijima, H.; Enomoto, H. Controlling hydrothermal reaction pathways to improve acetic acid production from carbohydrate biomass. *Environ. Sci. Technol.* 2005, 39 (6) 1893–1902.
12. Jin, F. M.; Kishita, A.; Moriya, T.; Enomoto, H. Kinetics of oxidation of food wastes with H_2O_2 in supercritical water. *J Supercrit. Fluids* 2001, 19 (3) 251–262.

Amphiphilic Conetworks Based on End-Group Cross-Linking of Polydimethylsiloxane Pentablock Copolymer and Polymethylhydrosiloxane

Ming Qiu[a] and Chunju He[b†]

State Key Laboratory for Modification of Chemical Fibers and Polymer Materials, College of Materials Science and Engineering, Donghua University, 2999 North Renmin Road, Songjiang District, Shanghai, 201620, P. R. China
E-mail: [a]qiushine890@163.com, [b†]chunjuhe@dhu.edu.cn

A series of amphiphilic conetworks (APCNs) were synthesized through cross-linking of well-defined amphiphilic pentablock copolymers via atom transfer radical polymerization (ATRP). A new ditelechelic polydimethylsiloxane macroinitiat was synthesized to initiate the polymerization of hydroxyethyl methylacrylate. The resulting triblock copolymers show well-defined molecular weight with narrow polydisperisty, which are used as macroinitiator to incorporate allyl methacrylate to get the pentablock copolymers with allyl pendant groups. Then pentablock copolymers are fully cross-linked with polyhydrosiloxanes through hydrosilylation. The so-prepared APCNs exhibit a good swelling capacity in water.

Keywords: Polydimethylsiloxane; Amphiphilic Conetwork; Atom Transfer Radical Polymerization.

1. Introduction

Amphiphilic conetworks (APCNs) as the rapidly emerging novel maetrials have three-dimensional structure covalently bonded together with the hydrophilic and hydrophobic polymer segments [1]. APCNs have many unique properties, such as swelling dependence on solvent, microphase separation structure and biocompatibility, which make them promising for applications in a wide variety of areas [2].

Most APCNs reported are synthesized by uncontrollable free radical polymerization [3], which inevitably leads to bad conformation regularity, structure defect or even loss of performance. To minimize the defects, more recently APCNs have been prepared by cross-linking polymer chains of well-defined length using controlled methods, such as quasiliving carbocationic polymerization (QLCCP), group transfer polymerization (GTP), reversible addition fragmentation chain transfer (RAFT) polymerization and atom transfer

† Corresponding author.

polymerization (ATRP) [4-6]. Among these methods, ATRP has shown outstanding capability to prepare hrdrogels and APCNs with well-defined molecular structure and good mechanical properties and the use of macroinitiator has received much attention because it simplifies the synthesis step and has a high tolerance for functional groups and impurities [7]. In this study, polydimethylsiloxane di-2-bromoisobutyrate (Br-PDMS-Br) initiate the ATRP of HEMA, and the resulting well-defined PHEMA-b-PDMS-b-PHEMA triblock copolymers is used as the macroinitiator for the ATRP of allyl methacrylate due to the preservation of active alkyl halide chain end. The introduction of PAMA units in the resulting the pentablock copolymers guarantees the full cross-linking of the resulting APCN since the allyl pendant groups act as crosslinking sites with polymethylhydrosiloxane.

2. Experimental

2.1. *Materials*

Hydroxyethyl methylacrylate (HEMA) and allyl methacrylate (AMA) were purchased from Energy Chemical Co. and purified by passing through a babic silica column to remove the inhibitor. Hydroxypropyl polydimethylsiloxane (PDMS, M_n=4000 g/mol, PDI=1.41), polymethylhydrosiloxane (PMHS, M_n=6000 g/mol, PDI=1.40) and Karstedt's catalyst (3% Pt(0) in xylene) were purchased from Gelest and were used as received.

2.2. *Synthesis of PHEMA-b-PDMS-b-PHEMA Triblock Copolymers*

The triblock copolymer was synthesized by ATRP. Br-PDMS-Br macroinitiator (1.00 g, 0.25 mmol), bpy (0.078 g, 0.5 mmol) and CuCl (0.025 g, 0.25 mmol) were added to a Schlenk flask (50 mL) equipped with a magnetic stirring bar and degassed three times. HEMA (6.55 g, 50 mmol) and a solvent mixture of MEK/1-propanol (10 mL, 7/3 v/v) were then injected into the reaction flask. The flask was placed in a thermostated bath at 60 °C for 24 h. The mixture was then diluted in MEK/1-propanol and passed through a basic alumina column to remove the copper residue. The solvents were removed in vacuo, and the polymer was then precipitated in cold hexane (100ml). The crude product was redissolved in MEK/1-propanol and precipitated in cold hexane twice, prior to being dried for 24 h in a vacuum oven. Yield: 72%.

2.3. *Synthesis of PDMS-Based Pentablock Copolymers*

The pentablock copolymers was synthesized using a molar feed ratio [AMA (0.8 g)]:[CuBr]:[PMDETA] of 50:1:1 in 8 mL isopropanol at 60 ºC involved of 2 g

triblock polymers for different time. The operations were used the same procedures as described above.

2.4. *Synthesis of Amphiphilic Conetworks*

The pentablock copolymer (1.68 g, 0,05 mmol), PMHS (0.6 g, 0.1 mmol) and Karstedt's catalyst (50 uL) was dissolved in a mixture of toluene/DMF (10 mL, 4/6 v/v) and the mixture was stirred at room temperature for 12 h. Then the homogeneous solution was poured into a Teflon mold (3×3cm) and placed in an oven at 60 ºC for 24 h. After crosslinking, the formed film was extracted by water and hexane, and dried in vacuo at room temperature.

2.5. *Characterization*

The chemical structures of triblock and pentablock copolymers were characterized by FT-IR and gel permeation chromatography (GPC). FT-IR spectra were recorded on Nicolet Instrument Nicolet 8700 spectrometer. Number-average molecular weights (*M*n) were measured by a BI-MwA Gel Permeation Chromatography (Waters, Milford, MA), equipped with a light scattering instrument (Brookhaven, Holtsville, NY), using THF as the eluent at a flow rate of 0.8 mL/min with a polystyrene standard as the reference. GPC analysis was performed after the triblock copolymers were modified with chlorotrimethylsilane through the HEMA hydroxyl moiety according to a literature because of the lack of a common solvent in which both PDMS and PHEMA are soluble.

2.6. *Measurement of the Swelling Ratio*

Swelling experiments were carried out at room temperature by immersing a pre-weighed sample in an excess of distilled water and hexane, respectively.The extent of swelling was determined by periodically taking the samples from the solvent, removing the solvent adsorbed to the surfaces by blotting with tissue paper, and weighing equilibrium swelling ratio (S_w) was recorded when the weight of the swollen samples remained unchanged. The swelling ratio was calculated as following equation:

$$S_w = \frac{m_t - m_0}{m_0} \times 100\% \quad (1)$$

where m_t is the mass of the swollen samples and m_0 is the mass of the dry sample.

3. Results and Discussion

3.1. *Polymer Synthesis*

Well-defined PHEMA-b-PDMS-b-PHEMA triblock copolymers and PAMA-b-PHEMA-b-PDMS-b- PHEMA-b-PAMA pentablock copolymers are summarized in Table 1. The pentablock copolymers were synthesized by ATRP used triblock copolymers as the macroinitiators. The number of AMA repeat units in the pentablock copolymers were controlled by varying the reaction time, i.e. 16, 34 and 52, respectively. The PDI of the pentablock copolymers remain almost the same as the triblock copolymers, indicating the polymerization is controllable. The compositions of the copolymers were first determined by FT-IR. Fig. 1 shows the FT-IR spectra of $PAMA_8$-b-$PHEMA_{63}$-b-$PDMS_{54}$-b- $PHEMA_{63}$-b-$PAMA_8$. The characteristic band of the AMA component at about 1640 cm^{-1} is observed in the FT-IR spectra.

Table 1. Characterization of the PHEMA-b-PDMS-b-PHEMA triblock copolymers and PAMA-b-PHEMA-b-PDMS-b-PHEMA-b-PAMA pentablock copolymers synthesized by ATRP.

polymer structure[a,]	reaction Time (h)	$M_{n,cal}$[b] (kDa)	$M_{n,NMR}$[c] (kDa)	$M_{n,GPC}$[d] (kDa)	PDI
H_{63}-b-D_{54}-b-H_{63}	24	22.3	20.4	30.8	1.24
A_8-b-H_{63}-b-D_{54}-b-H_{63}-b-A_8	6	25.1	22.4	33.6	1.26
A_{17}-b-H_{63}-b-D_{54}-b-H_{63}-b-A_{17}	12	27.1	24.7	35.8	1.25
A_{26}-b-H_{63}-b-D_{54}-b-H_{63}-b-A_{26}	18	28.9	27.0	37.9	1.33

[a]H, HEMA; D, PDMS; A, AMA. The subscript means the number of the unit, calculated from the NMR.

[b]Calculated from ^{1}H NMR based on PDMS unit (6H at 0.09 ppm) , HEMA unit (2H at 4.13 ppm), AMA unit (2H at 4.46 ppm).

[c]Determined by GPC measurement using polystyrene standards.

[d]Theoretical M_n= [monomer]/[initiator] × (monomer conversion) × (monomer molecular weight) + (initiator molecular weight).

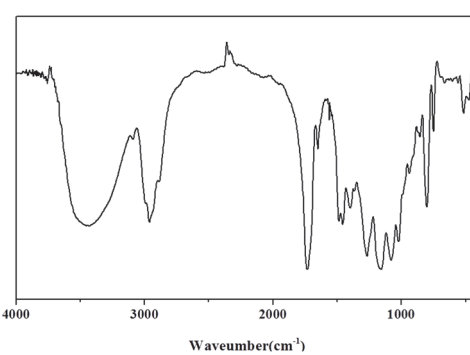


Fig. 1 The FT-IR spectra of $PAMA_8$-b-$PHEMA_{63}$-b-$PDMS_{54}$-b-$PHEMA_{63}$-b-$PAMA_8$.

3.2. *Characterization of the APCNS*

3.2.1. Sol Fraction of the Conetworks

Table 2 shows the compositions of APCNs and the sol fraction extracted from each conetwork. The sol fraction was calculated as the ratio of the mass of the extractable mixture divided by the mass of virgin conetwork. In all cases the sol fraction was relatively low, with the lowest value being as low as 5.2% and the highest 10.5%, indicating essentially complete crosslinking and control over the conetwork structure.

Table 2 Fabrication composition of conetworks and corresponding sol fraction percentage.

sample	block used (g)	PMHS crosslinker (g)	total HEMA (w %)	sol fraction (w/w %)
APCN-1	1.67	0.60	58.7	10.5
APCN-2	1.77	0.60	55.9	8.9
APCN-3	1.90	0.60	53.7	5.2

3.2.2. Characterization of the Degree of Swelling of the APCNs

One of the most attractive characteristics of APCN is its property in different solvents due to the existence of both HO and HI phases in conetworks. As shown in Fig. 2, the S_w of the conetworks in water increases with increasing PHEMA units because of the hydrophilicity of the PHEMA unit. Meanwhile, the S_w is also influenced by the cross-linking density.

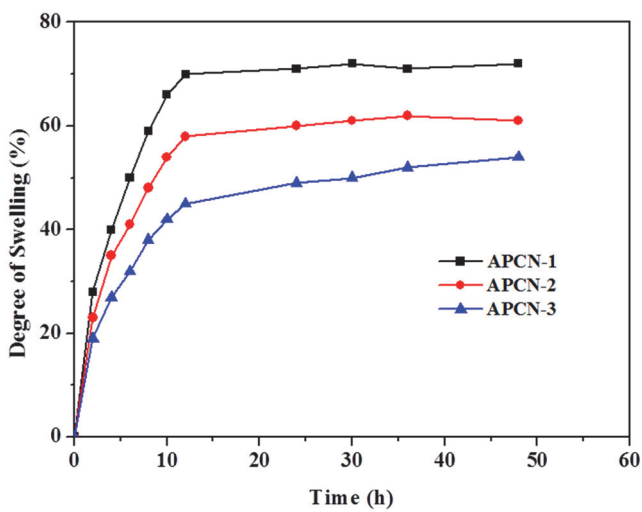


Fig. 2 Degrees of swelling of APCNs.

4. Conclusions

Conclusively, we have described the synthesis of PHEMA-involved amphiphilic conetworks through cross-linking of amphiphilic pentablock copolymers via ATRP with well-defined molecular weight and narrow polydispersity. The APCNs exhibit unique swelling behavior, which can be regulated via precise control of molecular structure.

References

1. G. Erdodi and J. P. Kennedy, Amphiphilic conetworks: definition, synthesis, applications, *Prog. Polym. Sci.* 31(2006) 1-18.
2. Y. P. Wang and J. M. DeSimone, Amphiphilic co-networks with moisture-induced surface segregation for high-erformance nonfouling coatings, *Langmuir* 27(2011) 10365-10369.
3. G. Kali, S. Vavra, K. Laszlo and B. Iván, Thermally responsive amphiphilic conetworks and gels based on poly(N-isopropylacrylamide) and polyisobutylene, *Macromolecules* 46(2013) 5337-5344.
4. A. I. Triftaridou and C. S. Paktrickios, Three different types of quasi-model networks: synthesis by group transfer polymerization and characterization, *Polym. Bull.* 58(2007) 185-190.
5. W. J. Zhao and Y. L. Yang, Amphiphilic polymer conetworks prepared by controlled radical polymerization using a nitroxide cross-linker, *J. Polym. Sci., Part A: Polym. Chem.* 48(2010) 4141-4149.
6. T. K. Georgiou, C. S. Patrickios, P. W. Groh and B. Iván, Amphiphilic model conetworks of polyisobutylene methacrylate and 2-(dimethylamino) ethyl methacrylate prepared by the combination of quasiliving carbocationic and group transfer polymerizations, *Macromolecules* 40(2007) 2335-2343.
7. K. Matyjaszewski and J. H. Xia, Atom transfer radical polymerization, *Chem. Rev.* 101(2001) 2921-2990.

The Effects of Surface Preparation on Growth of CuO Nanowires During Thermal Oxidation

C.H. Xu [a*], Y.L. Liu [c], Y. Li [d] and J.Z. Wang [d]
School of Materials Science & Engineering,Henan University of Science & Technology,
P. O. Box 53, 263 Kaiyuan Avenue,
Luoyang, P. R. China
E-mail: [a] mmcjxu@haust.edu.cn, [c] purelandliu@126.com,*
[d] wl1357102@163.com

X.L. Li[b]
Technology & Economy of Xuchang School,
Changge, Henan, P. R. China
[b] lixiangli87@126.com

In order to find the effect of surface preparation to CuO nanowire production, 4 groups of copper specimens, including non-cleaned, washed by deionized water only, washed in ethanol + 1.0 M HCl solution + deionized water, and ground on 1000# silicon carbide papers + rinsed in deionized water, were oxidized in flowing wet-oxygen at 650ºC for 3 hours. Morphologies on the surfaces of oxidized specimens were then characterized with a scanning electron microscope. Surface preparation of copper can affect the formation of CuO nanowires during thermal oxidation, significantly. The nanowires formed on non-cleaned specimens are low dense. Nanowires formed on specimens washed by deionized water only are similar to those on non-cleaned specimens. Nanowires formed on the specimens washed by ethanol + HCl solution + deionized water have medium density. Nanowires on the specimens ground by silicon carbide papers show the highest density.

Keywords: CuO nanowire, thermal oxidation, surface preparation.

1. Introduction

Cupric oxide has been extensively studied due to its interesting properties[1]. CuO is a p-type semiconductor with a narrow band gap (1.2 eV). Monoclinic CuO solid belongs to Mott insulator, whose electronic structures can't be simply described by conventional band theory[2]. Resent studies indicate that CuO can exist in three

* Corresponding author.

different magnetic phases at the different temperatures: a 3D collinear antiferromagnet, an intermediate noncollinear incommensurate magnetic phases and a 1D quantum antiferromagnetic phase[3].

One dimensional structure, such as nanorod, nanowire and nanotube, has become important building blocks for nano-devices and integrated nanosystems [4]. CuO nanowires have been research to use as a gas sensors [5], a heterogeneous catalyst to convert hydrocarbons completely into carbon dioxide and water [6], a barrier in ZnO dye-sensitized solar cells [7] and p-type field effect transistors [8]. The formation of CuO nanowires through the method of thermal oxidation has been reported recently. CuO nanowires could be formed on Cu foil or film by thermal oxidation in air [9], in N_2/O_2 [10,11]. Environmental factors, such as oxygen pressure, humidity and gas flow rate around specimens to affect formation of CuO nanowires have been reported in our previous reports [12,13]. The effect of surface preparation to CuO nanowire production during thermal oxidation is studied in this paper.

2. Experimental Procedures

Specimens were prepared with commercial Cu foil (purity: 99.9% Cu) with the thickness of 0.1 mm. The Cu foil was cut to pieces with size about 10×5 mm^2. In order to find the effect of surface preparation to CuO nanowire production, specimens were divided to 4 groups. The first group of specimens was not cleaned. The second group of specimens was washed by deionized water only. The third group of specimens was washed in ethanol, then washed in an aqueous solution of 1.0 M HCl for 1 min, rinsed in deionized water. The forth group of specimens was ground on 1000# grit silicon carbide papers, then rinsed in deionized water. All washed specimens are dried by dry nitrogen gas. After that, the specimens on an alumna crucible were oxidized in a tube furnace through flowing wet-oxygen [12] at a pressure of 1 atm. at 650℃ for 3 hours with inlet gas-flow rate range of 0.15 l/min. Wet gas used in the experiment was produced by passing the dry gas through water. Morphologies on the surfaces of oxidized specimens were then characterized with a scanning electron microscope (STEREOSCAN 440).

3. Results and Discussions

The phase of oxide nanowires formed by thermal oxidation of Cu foils is single crystalline monoclinic CuO, which has been reported in detail in our previous report, based on XRD and TEM experiments and thermodynamic analysis [12,13]. Fig. 1 shows the morphologies of oxide nanowires formed on the surfaces of 4 groups of specimens. Figs. 1 (a) and (b) are the morphology on the first group of

specimens (non-cleaned) at low and high magnifications, respectively. The sizes of nanowires are quite different: the diameters are from 0.05~0.5μm, lengths are from 1~10μm and the density is low. The morphologies of nanowires formed on the second group of specimens (washed by deionized water only) are similar to those on the first group of specimens, as shown in Figs. (c) and (d) at low and high magnifications. Figs. 1 (e) and (f) are the morphologies of the third of oxidized specimens (washed by ethanol, HCl solution and deionized water in sequence) at low and high magnifications. The sizes of nanowires are uniform: the range of diameters is from 0.3~0.5μm, lengths are from 3~20μm and the density is medium. Figs. 1 (g) and (h) are the morphologies of the third of oxidized specimens (ground by silicon carbide papers and washed by deionized water). The sizes of nanowires are uniform: the range of diameters is from 0.3~0.4μm, lengths are from 10~30μm and the density is high. Parameters of the nanowires formed in this experiment are listed in Table 1 in detail.

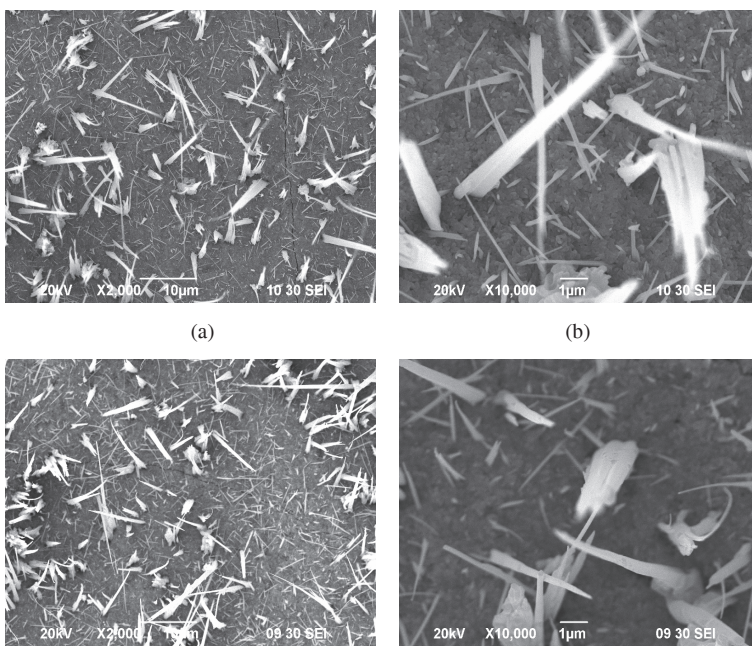
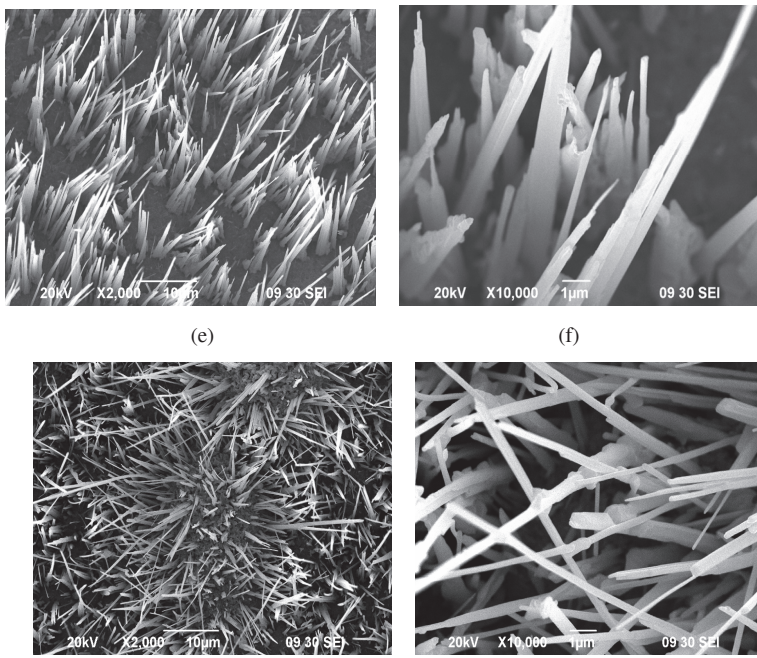


Fig. 1 The nanowire morphologies formed on Cu foil surfaces prepared by (a) and (b) non-cleaning, (c) and (d) washing in deionized water only, (e) and (f) washing in ethanol + 1.0 M HCl solution + deionized water, (g) and (h) grinding on 1000# silicon carbide papers + rinsed in deionized water.



(e) (f)

(g) (h)

Fig. 1 (*Continued*)

Table 1. Parameters of the nanowires formed in this experiment.

Specimens	Length (μm)	Diameter (μm)	Density
Group 1	0.5 - 13.6	0.05 - 0.42	low
Group 2	1.5 - 16.5	0.05 - 0.58	low
Group 3	3.4 - 23.6	0.16 - 0.89	medium
Group 4	1.84 - 30.3	0.11 - 0.63	high

It is considered that there are both thin copper oxide layer formed and organic contamination thin layer on copper surface when copper is put in air at room temperature. From the experiment results, the least dense nanowires can be found on the non-cleaned copper foil surface, suggesting that copper oxide layer and organic contamination layer on cupper surface can resist the formation of CuO nanowires during thermal oxidation process. In addition, the morphology of nanowires grown on the specimens washed by water only is similar to that on the non-cleaned specimens, suggesting that copper oxide and organic contamination layer can not be removed by water. Foil cleaned by ethanol and HCl produces medium dense nanowires, due to that ethanol can remove organic contamination

and that HCl can remove oxide on the specimen surface. Ground specimens produce the longest and most dense nanowire, due to grinding process can remove both oxide and contamination on the specimen surface.

The mechanism for whisker growth during thermal oxidation is attributed to screw dislocations emerging on the surface of a crystal [14]. The growth of nanowires may be attributed to certain defects that are active. Defects, such as dislocations may exist on the Cu foil surface, due to cool draw during foil fabrication by manufacturer. However, copper oxide layer and organic layer formed during room temperature can cover the defects to resist the formation of CuO nanowires during thermal oxidation at high temperature. When specimens were washed in ethanol and HCl, copper oxide layer and organic contamination layer can be removed, resulting in more positions for the growth of nanowires. The specimens ground on silicon carbide papers result in the appearance of more defects on the specimen surfaces, which benefit the formation of nanowires during thermal oxidation.

4. Conclusions

Surface preparation of copper can affect the formation of CuO nanowires during thermal oxidation, significantly. The density of CuO nanowires formed on non-cleaned specimens are low. Nanowires on specimens washed by deionized water only are similar to those on non-cleaned specimens. Nanowire density of specimens washed by ethanol, HCl solution and deionized water are medium. Nanowires on the specimens ground by silicon carbide papers have the highest density.

References

1. E. Rakhshani, 1986, Preparation, characteristics and photovoltaic properties of cuprous oxide—a review, *Solid State Electro*n, 29 7-17.
2. M.R. Norman and A. Freeman, 1986, *Model Supercell Local Density Calculations of the 3d Excitation Spectra in NiO*, J. Phys. Rev. B, 33 8896-8898.
3. Y.P. Sukhorukov, N.N. Loshkareva, S.N. Tugushev, 1998, *Great magnetic linear dichroism in HgCr2Se4 and construction of an IR modulator based on it* (great MLD in HgCr2Se4) J. Magn. Magn. Mater. 159 342-344.
4. X. F. Duan, Y. Huang, R. Agarwal, and C. M. Lieber, 2003, ingle-nanowire electrically driven lasers, *Nature*, 421 241-245.

5. Y. S. Kim, I. S. Hwang, S. J. Kim, C. Y. Lee, J. H. Lee, 2008, CuO nanowire gas sensors for air quality control in automotive cabin, *Sensors and Actuators B*, 135 298–303.
6. J. B. Reitz, and E. I. Solomon, 1998, Propylene Oxidation on Copper Oxide Surfaces: Electronic and Geometric Contributions to Reactivity and Selectivity, J. Am. Chem. *Soc*. 120 11467.
7. P. Raksa, S. Nilphai, A. Gardchareon, S. Choopun， 2009, Copper oxide thin film and nanowire as a barrier in ZnO dye-sensitized solar cells, *Thin Solid Films*, 517 4741–4744.
8. L. Liao, Z. Zhang, B. Yan, Z. Zheng, Q. L. Bao, T. Wu, C. M. Li, Z. X. Shen, J. X. Zhang, H. Gong, J. C. Li and T. Yu, 2009, Multifunctional CuO nanowire devices: p-type field effect transistors and CO gas sensors, *Nanotechnology*, 20 085203.
9. X. Jiang, T. Herricks, and Y. Xia, 2002, CuO nanowires can be synthesized by heating copper substrates in air, *Nano Letters* 2 1333.
10. K. Zhang, C. Rossi, C. Tenailleau, 2007, Synthesis of large-area and aligned copper oxide nanowires from copper thin film on silicon substrate P. Alphonse and J. Yves C. Ching, *Nanotechnology*, 18 275607.
11. K. Zhang, C. Rossi, C. Tenailleau, and V. Conedera, 2009, CuO nanowires grown from Cu film heated under a N2/O2 flow J. Nanosci. *Nanotechnol.*, 9 1418-1422.
12. C. H. Xu, C. H. Woo and S. Q. Shi, 2004, *The effects of oxidative environments on the synthesis of CuO nanowires on Cu substrates*, *Superlattices Microst*., 36 31-38.
13. C.H. Xu, C.H. Woo, S.Q. Shi, 2004, *Formation of CuO nanowires on Cu foil*, Chem. Phys. *Lett.*, 399 62-66.
14. P. Kofstad, 1988, High Temperature Corrosion, *Elsevier Applied Science*, London and New York.

Preparation of Uniform PMMA-SiO_2 Particles with High Content of SiO_2 via in situ Suspension Polymerization

Tao Chen[a], Yixia Wang[b], Yonghan Zhang[c], Chunjie Yan[d*]

Faculty of Material and Chemistry, China University of Geosciences, Wuhan 430074, China

E-mail: [a] taochen518@163.com, [b] Yixiawang1989@126.com, [c] yhan23@163.com, [d] chjyan2005@126.com*

Uniform poly (methyl methacrylate) (PMMA)/SiO2 particles were successfully prepared via in situ suspension polymerization. The nanosilica was modified by KH570 to make sure it's hydrophobic and better for doped into PMMA. Scanning electron microscopy (SEM) indicated that PMMA/SiO2 composite particles had good sphericity and nanosilica were evenly dispersed in microspheres and formed lots of macro porous.

Keywords: Composite microspheres, PMMA, Nanosilica, Mm-size.d

1. Introduction

Nowadays, research to investigate organic and inorganic composite particles is of great interest. Among the organic substances, poly(methyl methacrylate) (PMMA) plays an important role in the family of polyacrylic and methacrylic esters because of its satisfied properties such as exceptional optical clarity, good weather ability, high strength, excellent dimensional stability, reduced gas permeability, improved physical performance and increased heat resistance. Among the inorganic substances, nanosilica (SiO_2) is one of the most representative materials because of its great potential application in different fields including paints, catalysis, drug delivery systems, composite materials and so on[1-2].

Different synthetic procedures for preparation of PMMA/SiO_2 composites have been described in literatures: emulsion polymerization[3], sol-gel polymerization[4], static polymerization[5], suspension polymerization[6], etc. But, only a few publications about the PMMA/SiO_2 particles with Mm sized have been synthetized so far.

* Corresponding author.

In this paper, we aimed at producing Mm sized PMMA/SiO_2 particles with high content of SiO_2 via In Situ Suspension Polymerization. The formation mechanisms of composite particles were proposed and the composites exhibit a greater compressive strength and thermal stability than pure PMMA.

2. Experimental details

2.1. *Materials*

Methyl methacrylate，(MMA, 99wt. %, Sinopharm Chemical Reagent Co., Ltd, China) was purified by treating with 5% aqueous NaOH to remove the inhibitor; Nanosilica was made in Shanghai Baisen Yanling Nanotechnology Co., Ltd. Divinylbenzene (DVB, Tianjin Fuchen Chemical Regents Factory, China) and benzoyl peroxide (BPO, Tianjin Damao Chemical Regents Factory, China) were used as cross-linking agent and initiating agent, respectively. Silane coupling agent KH570 was obtained from Wuhan Geao Chemical Technology Co., Ltd (China). All other materials are analytical grade.

2.2. *Modification method of nanosilica*

A certain amount of KH570 silane coupling agent was dissolved in absolute methanol and then SiO_2 nanoparticles was added to form a suspension. The mixture was stirred at 65ºC for 24h. Then centrifuged and washed with absolute methanol. After being dried at 70ºC for 24h, KH570 modification SiO_2 nanoparticles were obtained.

2.3. *Synthesis of PMMA/SiO2 composite particles via situ suspension polymerization*

A typical preparation procedure of PMMA/SiO_2 composite particles was detailed as follows: 1.6 g NaOH and 4.0 g $MgCl2{\cdot}6H_2O$ were replaced into 120 ml deionized water at 60ºC with a vigorous stirring. Then, 0.3 g BPO and 3.0 g DVB were dissolved in 20.0 g MMA, to which modified nanosilica was added. Then the mixture was poured into the flask, heated to 80ºC and kept for 6h. Finally, the expected composite particles were obtained.

2.4. *Characterizations*

The FTIR spectrum of particles was obtained by means of a Nicolet Avatar 360 FTIR spectrometer. Three-phase contact angle, θ of the nanosilica was measured by the Contact Angle Meter. The surface morphology and microstructure of these particles were performed with field emission scanning electron microscope (FE-SEM, Hitachi SU8010).

3. Results and discussion

3.1. *Surface modification of nanosilica*

The FTIR spectra of nanosilica and modified nanosilica were shown in Fig.1. For modified nanosilica, besides the characteristic absorption peaks of Si-O at about 470cm-1, 800cm-1, 1100cm-1 and -OH at about 3430cm-1, there were absorption peaks at about 1260cm-1 and 2960cm-1, which were the characteristic peak of the C-O bond in O-C=O, and the C-H bond in -CH_2, verifying that the nanosilica were successfully modified by KH570.

Because of the abundant hydroxyl on surface, the nanosilica were hydrophilic and the three-phase contact angle was about 23.53° (Fig.2a). When nanosilica were modified by KH570, the three-phase contact angle was increased to about 118.55° (Fig.2b), meaning that the nanosilica were translated into hydrophobic.

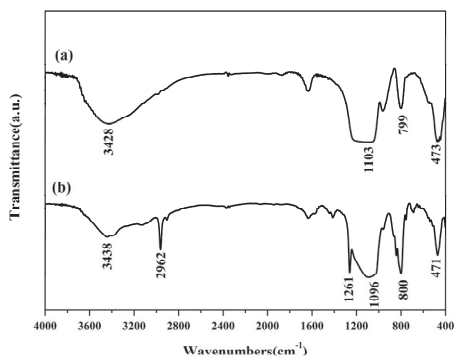


Fig.1. FTIR of nanosilica (a) and modified nanosilica (b).

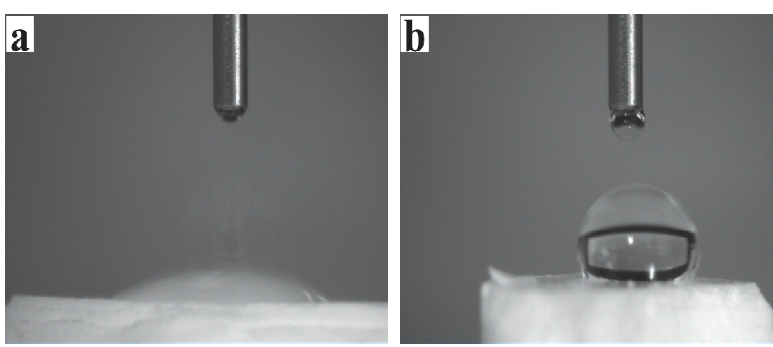


Fig.2. The three-phase contact angle determination photograph of nanosilica before (a) and after (b) modification.

3.2. *FTIR spectra analysis*

The IR analysis of pure PMMA (a), PMMA/20% SiO_2 particles (b), PMMA/40% SiO_2 articles(c) were presented in Fig.4. The characteristic adsorption peaks of pure PMMA (Fig.3a) at about 1730cm-1,1440cm-1, and 1150cm-1 were attributed to the stretching vibrations of C=O, bending vibrations of C-H in-plane, stretching vibrations of C-O, respectively. Compared with pure PMMA, PMMA/SiO_2 particles (Fig.3b) not only had characteristic absorption peaks of pure PMMA, but also had adsorption peak of SiO_2 and silane coupling agent KH570 at about 800cm-1 and 2960cm-1 respectively; Seen from (Fig.3c), with the content of nanosilica added, the typical adsorption peak intensity of modified nanosilica obviously increased, which demonstrated that PMMA particles blended with modified nanosilica.

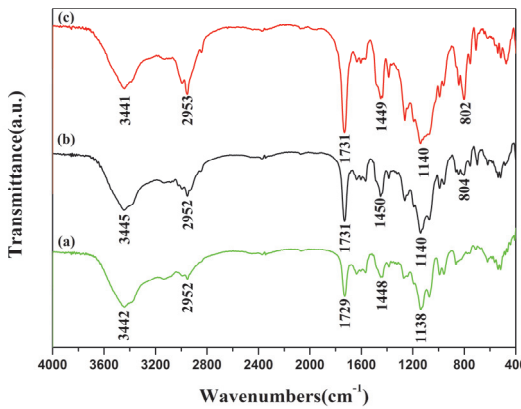


Fig.3. FTIR spectrum of: (a) pure PMMA; (b) PMMA/20% SiO_2 particles; (c) PMMA/40% SiO_2 particles.

3.3. *Morphology and properties of PMMA/SiO_2 composite particles*

The FE-SEM images of pure PMMA and PMMA/40 wt% SiO_2 composite particles were shown in Fig.4a and 4b respectively. The composite spherical particles presented 0.6-0.9 mm size and rough surface than pure PMMA due to the addition of nanosilica. It could be seen from the profile of pure PMMA (Fig.4c) and PMMA/SiO_2 composite particles (Fig.4d) that the internal structure of pure PMMA was compact, while macro porous and SiO_2 particles were observed inside the composite particles with the high content of nanosilica. That's may be explained by the adsorption air on the surface of nanosilica.

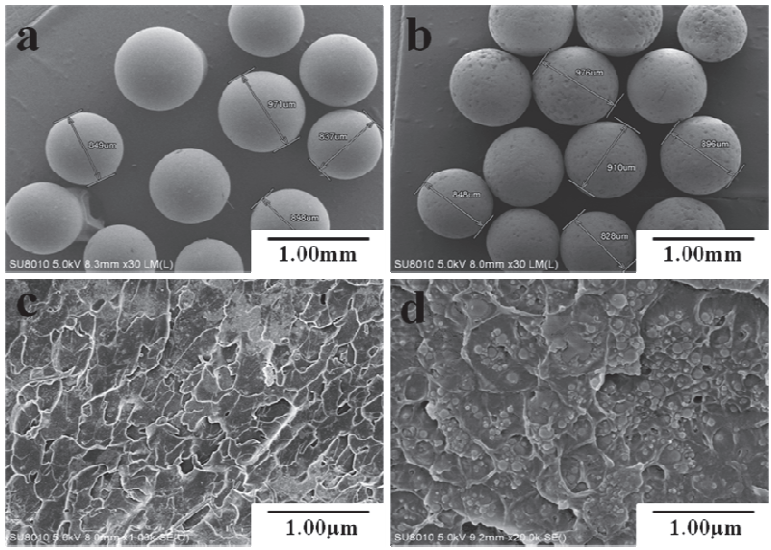


Fig.4. SEM images of composite particles prepared via situ suspension polymerization: (a) pure PMMA particles; (b) PMMA/SiO2 composite particles.

4. Conclusions

Millimeter-sized PMMA/SiO_2 composite particles were successfully prepared via situ suspension polymerization. The results suggested that these composite particles had uniform 0.6-0.9 mm size and high sphericity. The content of added midified nanosilica could higher to 40wt% and some macro porous formed inside the particles. That's may be explained by the adsorption air on the surface of nanosilica.

Acknowledgments

This work was supported by Project of China Geological Survey (12120113087100) and Public Service Project of the Chinese Ministry of Land and Resources (201311024).

References

1. T. Lin, Y. Zheng. *Synthesis and characterisation of polymethylmethacrylate/ nanosilica and nanosilica/polymethylmethacrylate core-shell structure composite microspheres. Micro. Nano. Lett. 5* (2013) 217-220.

2. J.M Zhang, J.G Gao, X.G Sun, Z Peng, J.Z Diao. *Preparation and characterization of TiO2/poly (St-co-MAA) core/shell composite particles*. *Iran. Polym.* J. 16 (2007) 39-46.
3. F.A Zhang, D.K Lee, J.P Thomas. *PMMA-mesocellular foam silica nanocomposites prepared through batch emulsion polymerization and compression molding*. *Polymer.* 50 (2009) 4768-4774.
4. M.D Morales-Acosta, C.G Alvarado-Beltran, M.A Quevedo-Lopez, B.E Gnade, A Mendoza- Galvan, R Ramirez-Bon. *Adjustable structural, optical and dielectric characteristics in sol-gel PMMA-SiO_2 hybrid films*. *J. Non-Cryst. Solids*. 362 (2013) 124-135.
5. K Shintaro, S Asumi, K Masashi. *Sparsely-distributed silica/PMMA composite particles prepared by static polymerization in aqueous silica dispersion*. *J. Colloid. Interf. Sci.* 352 (2010) 348-353.
6. Zhu A, Shi Z, Cai A, Zhao F, Liao T. *Synthesis of core-shell PMMA-SiO_2 nanoparticles with suspension-dispersion-polymerization in an aqueous system and its effect on mechanical properties of PVC composites*. *Polym. T.* 27 (2008) 540-547.

Preparation, Characterization and Photocatalytic Activity of TiO_2/Fe Composite Coatings

Liang Hao†

College of Mechanical Engineering, Tianjin University of Science & Technology, No. 1038, Dagu Nanlu, Hexi District, Tianjin 300222, China
†E-mail: haoliang@tust.edu.cn

Yun Lu[a], Sujun Guan[b]

Graduate School & Faculty of Engineering, Chiba University, No. 1-33, Yayoi-cho, Inage-ku, Chiba-shi 263-8522, Japan
E-mail: [a]luyun@faculty.chiba-u.jp, [b]guansujun1222@gmail.com

TiO_2/Fe composite coatings were prepared on Al_2O_3 balls by mechanical coating technique. SEM results showed that the composite coatings had a composite microstructure of discrete islands of TiO_2 deposited on Fe coatings. The loading amounts of TiO_2 in the composite coatings were increased by introducing Al_2O_3 impact balls. The degradation rate of methylene blue (MB) under UV irradiation was used to evaluate the photocatalytic activity of the composite coatings. Compared with TiO_2/Ti and TiO_2/Cu composite coatings made by this method, TiO_2/Fe composite coatings showed higher photocatalytic activity.

Keywords: TiO_2; Composite Coatings; Mechanical Coating; Photocatalytic Activity.

1. Introduction

Titanium dioxide (TiO_2) has been widely investigated for its potential applications from electric devices and sensors to photocatalysts. One focus of the active research in the field is the potential use as photocatalyst in decomposition of organic/inorganic pollutants, air and water purification, antibiosis, hydrogen preparation, and solar cell, among others. Many methods including physical vapor deposition (PVD), chemical vapor deposition (CVD), hydrothermal method, sol-gel method and thermal oxidation have been utilized to prepare TiO_2 nanomaterials[1].

Ball milling, frequently used in mechanical alloying, has been found its new application, such as mechanical coating. In our early work, TiO_2/Ti composite coatings[2] with high photocatalytic activity have been successfully developed by

† Corresponding author.

mechanical coating technique. Mechanical coating technique is a novel method to fabricate TiO_2/metal composite coatings. One drawback of TiO_2 as a photocatalyst is the decrease of photocatalytic activity due to the recombination of holes in the valence band and electrons in the conduction band. The recombination of electron-hole pairs can be prevented by doping with foreign metals with high electron work functions. Metals including Pt[3], Ag[4], Au[5] and Cu[6] also have been attempted.

The aim of this paper is to develop new TiO_2/Fe composite coatings with relatively high photocatalytic activity by MCT. The preparation, characterization and photocatalytic activity of the composite coatings will be discussed.

2. Experimental

Firstly, Fe coatings were developed. We used Fe powder and Al_2O_3 balls as a coating material and the substrate. The relevant parameters for development of TiO_2/Fe composite coatings are listed in Table 1 of reference[7]. A bowl made of Al_2O_3 with 250 ml in volume was used as the container of ball milling and the source materials were put into the bowl. Then the mechanical coating was performed. The sampling time was set at 4~58 hour from the start of the milling process. The ball milling was carried out by a planetary ball mill (Pulverisette 6, Fritsch, Germany). The revolution speed of the disk was set at 300 rpm (revolutions per minute). Secondly, TiO_2/Fe composite coatings were made. We applied 15.0 gAl_2O_3 balls coated with continuous Fe coatings and 13.0 g TiO_2 nanopowder (ST-01, Ishihara Sangyo, Japan) as the substrate and coating material respectively. The mechanical coating was performed by the same planetary ball mill at 400 rpm for 1, 3, 6 and 10 hour. To increase the loading amounts of TiO_2 in the composite coatings, 20 Al_2O_3 impact balls (diameter: 10 mm) were introduced into the bowl to increase the impact force of the grinding media in the contrast tests.

The loading amounts of TiO_2in the composite coatings were monitored through weighing of the samples, and the results can be accurate to 10^{-4} g. XRD, SEM and photocatalytic activity evaluation of the coatings were carried out as the description of reference [7].

3. Results and Discussion

The characterization of the continuous Fe coatings has been published in our early work[7]. Thus, it will not be involved here. The XRD patterns of the Al_2O_3 balls coated with TiO_2/Fe composite coatings after the ball milling are shown in Fig. 1. For the both cases with and without Al_2O_3 impact balls, the diffraction peaks of α-Al_2O_3, α-Fe and anatase TiO_2 were detected. It suggests TiO_2 powder

has adhered to Fe coatings. The diffraction peaks of anatase TiO_2 were rather weak which means the loading amounts of TiO_2 were slight. The diffraction peak of its (101) plane was detected near 25.3° (2θ). For the latter case, the diffraction peak of anatase TiO_2 near 25.3° was higher. It indicates that the loading amounts of TiO_2 in the case were greater than that without Al_2O_3 impact balls.

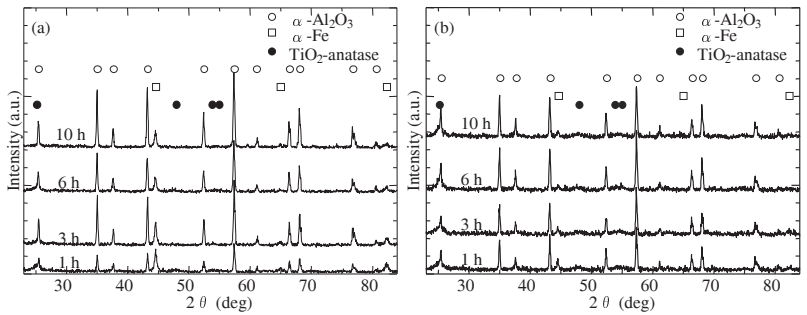


Fig. 1. XRD patterns of the Al_2O_3 balls coated with TiO_2/Fe composite coatings after the ball milling at 400 rpm: (a) and (b) without and with Al_2O_3 impact balls individually.

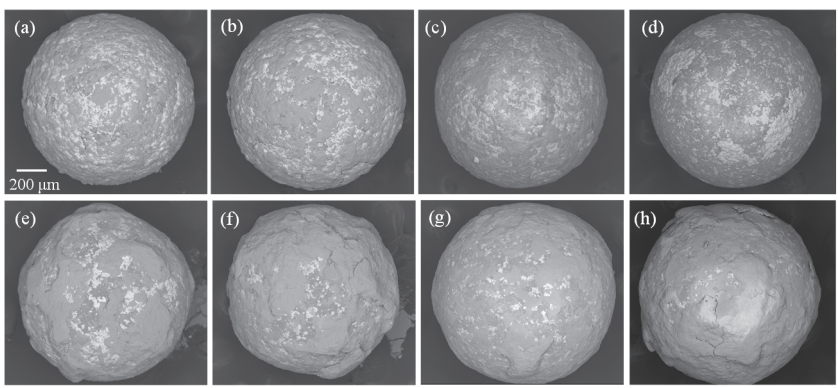


Fig. 2. Surface SEM images of the Al_2O_3 balls coated with TiO_2/Fe composite coatings after the ball milling at 400 rpm: (a) - (d) without Al_2O_3 impact balls, milling time was 1, 3, 6 and 10 h; (e) - (h) with Al_2O_3 impact balls, milling time was 1, 3, 6 and 10 h.

Fig. 2 shows the surface SEM images of Al_2O_3 balls coated with TiO_2/Fe coatings after the ball milling at 400 rpm with and without Al_2O_3 impact balls. The regions of gray and white of the balls are TiO_2 and Fe respectively, whereas the dark areas correspond to the surfaces of Al_2O_3 balls. For the both cases, TiO_2 powder particles coated Fe coatings discontinuously and formed discrete islands of TiO_2. Besides, it can be observed that the loading amounts of TiO_2 that

adhered to Fe coatings seemed to reach maximum when milling time was 3 h in the case without Al_2O_3 impact balls (Fig. 2(b)). When milling time came to 10 h, most parts of Fe and TiO_2coatings peeled off (Fig. 2(d)). However, the loading amounts of TiO_2 increased with increase of milling time to 10 h in the case with Al_2O_3 impact balls (Fig. 2(e) - (h)). It can be confirmed that the loading amounts of TiO_2 in the latter case should be more than that in the former case.

The loading amounts of TiO_2 in the composite coatings were monitored with the results shown in Fig. 3. In the case without Al_2O_3 impact balls, the loading amounts of TiO_2 increased with milling time increased to 3 h after which the loading amounts decreased. However, in the case with Al_2O_3 impact balls, it increased with the increase of milling time till reached a peak at 10 h. The introduction of Al_2O_3 impact balls did increase the loading amounts of TiO_2.

The degradation rate constants k is illustrated in Fig. 4. For the TiO_2/Fe composite coatings developed in the mechanical coating without Al_2O_3 impact balls, the degradation rate constants k reached maximum when 3 h of milling time. However, the degradation rate constants k increased with the increase of milling time to 10 h and at that time obtained a maximum value for the composite coatings made in the case with Al_2O_3 impact balls. The composite coatings made in the mechanical coating with Al_2O_3 impact balls for 10 h showed the greatest photocatalytic activity in all the samples.

Fig. 5 shows the degradation rate constants k of TiO_2/metal composite coatings developed by the same method and the TiO_2 coatings[8] as the standard of Photocatalysis Industry Association of Japan. It can be noted that the TiO_2/metal composite coatings show much higher photocatalytic activity than the TiO_2 coatings as the standard of Photocatalysis Industry Association of Japan. Compared with TiO_2/Ti and TiO_2/Cu composite coatings made by the same method before, TiO_2/Fe composite coatings show the greatest photocatalytic activity.

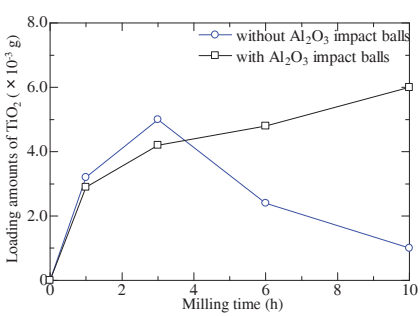


Fig. 3. Loading amounts of TiO_2 on 50 Al_2O_3 balls as a function of milling time for coating TiO_2.

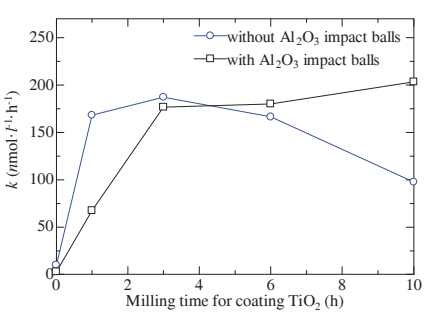


Fig. 4. Degradation rate constants k as a function of milling time for coating TiO_2.

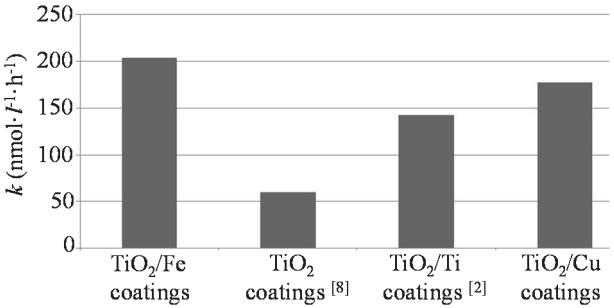


Fig. 5 Photocatalytic activity comparison of TiO_2/metal coatings and TiO_2 coatings.

It can be found from Fig. 3 and Fig. 4 that the degradation rate constants k showed the same evolution patterns as the loading amounts of TiO_2, and there is a direct proportion between them. Therefore, it can be confirmed that the photocatalytic activity of TiO_2/Fe composite coatings is directly proportional to the loading amounts of TiO_2 in the composite coatings. That is because the more the loading amounts of TiO_2, the greater the surface area of TiO_2 became. Therefore, the degradation of MB occurred on the surface of TiO_2 became quicker, which improvedits photocatalytic activity.

For the TiO_2/Ti composite coatings were prepared by mechanical coating and oxidation treatment[2], although the loading amounts of TiO_2 in the composite coatings were more than that in TiO_2/Fe composite coatings in the present work, TiO_2/Ti composite coatings showed lower photocatalytic activity than TiO_2/Fe composite coatings (Fig. 5). It may be related to the crystal type of TiO_2. The crystal types of TiO_2 in TiO_2/Ti and TiO_2/Fe composite coatings were confirmed to be rutile and anatase respectively. Rutile TiO_2 is usually considered to be less active in the degradation of some organics than anatase TiO_2[9]. Although the crystal type of TiO_2 in TiO_2/Fe and TiO_2/Cu composite coatings was anatase, TiO_2/Fe composite coatings showed higher photocatalytic activity than TiO_2/Cu composite coatings. It may relate to the effect of metal coatings.

4. Conclusions

Novel TiO_2/Fe composite coatings on Al_2O_3 balls were developed by mechanical coating. The composite coatings had a composite microstructure of discrete islands of TiO_2 and Fe coatings. Introducing Al_2O_3 impact balls into mechanical coating increased the loading amounts of TiO_2in the composite coatings. The photocatalytic activity of TiO_2/Fe composite coatings in the degradation of MB was enhanced compared with TiO_2/Ti and TiO_2/Cu composite coatings

developed by the same method. It is believed that greater loading amounts of TiO_2 and the crystal type of anatase were benefit to the enhancement of the photocatalytic activity.

Acknowledgments

This work was financially supported by the National Natural Science Foundation of China (Nos. 51404170) and the Scientific Research Foundation of Tianjin University of Science & Technology (Nos. 0001001).

References

1. X.B. Chen, Samuel S. Mao, Synthesis of titanium dioxide (TiO_2) nanomaterials, *J. Nanosci. Nanotechnol*. 6 (2006) 906-925.
2. H. Yoshida, Y. Lu, H. Nakayama, M. Hirohashi, Fabrication of TiO_2 film by mechanical coating technique and its photocatalytic activity, *J. Alloys Compd*. 475 (2009) 383-386.
3. K. Sayama, R. Abe, H. Arakawa, H. Sugihara, Decomposition of water into H_2 and O_2 by a two-step photoexcitation reaction over a Pt-TiO_2 photocatalyst in $NaNO_2$ and Na_2CO_3 aqueous solution, Catal. Commun. 7 (2006) 96-99.
4. X.W. Zhang, M.H. Zhou, L.C. Lei, Preparation of an Ag-TiO_2 photocatalyst coatedon activated carbon by MOCVD, *Mater. Chem. Phys.* 91 (2005) 73-79.
5. I.M. Arabatzis, T. Stergiopoulos, D. Andreeva, S. Kitova, S.G. Neophytides, P. Falaras, Characterization and photocatalytic activity of Au/TiO_2 thin films for azo-dye degradation, *J. Catal.* 220 (2013) 127-135.
6. S.P. Xu, J.W. Ng, X.W. Zhang, H.W. Bai, D.D. Sun, Fabrication and comparison of highly efficient Cu incorporated TiO_2 photocatalyst for hydrogen generation from water, *Int. J. Hydrog. Energy* 35 (2010) 5254-5261.
7. L. Hao, Y. Lu, H. Asanuma, J. Guo, The influence of the processing parameters on the formation of iron thin films on alumina balls by mechanical coating technique, *J. Mater. Process. Technol.* 212 (2012) 1169-1176.
8. H. Yoshida, Fabrication and performance improvement of TiO_2-metal composite photocatalysts, PhD thesis, Chiba University, Japan, 2010.
9. K. Tanak, Mario F.V. Capule, T. Hisanaga, Effect of crystallinity of TiO_2 on its photocatalytic action, *Chem. Phys. Lett.* 187 (1991) 73-76.

The Growth Control of $Zn_{1-x}Mg_xO$ Films and Photo-Electrical Property Research

Xiaoheng Wang†, Xiang Zhou and Guang Zhang
Beijing Institute of Environment Features, Beijing, China, 100854
†*E-mail: 181244898@qq.com*

Here we propose ultrasonic spray pyrolysis (USP) method to produce $Zn_xMg_{1-x}O$ films. In this work, we have grown two sets of films differ by HAc amount and Mg content in the precursor solution. By slightly increasing HAc amount it succeed in making the film thicker in the order of 10^2 nm, replacing prolonged deposition time. The energy gap of $Zn_{1-x}Mg_xO$ linearly grows from 3.13eV (x=0) to 3.35eV as Mg content increases, fitting the equation of Eg = 3.13+0.78x (eV). The blue shift of PL peaks from 380nm (x=0.0) to 364nm (x=0.28) confirms effective Mg doping. Further the un-doped ZnO film exhibit a bright band edge photoluminescence at 380nm with FWHM of 16nm without defect luminescence.

Keywords: Ultrasonic Spray Pyrolysis; $Zn_xMg_{1-x}O$ Films; Thickness of the Film; Energy gap; Photoluminescence.

1. Introduction

ZnO is a direct band-gap II–VI semiconductor material having an energy gap of 3.36 eV at room temperature with high exciton binding energy (~60 meV). Its promising properties have drawn strong commercial desire to design and fabricate efficient and lasting blue light emitting diodes (LED), short-wavelength laser diodes and photoelectric detector. Of these devices dramatically breakthroughs are continuously brought up. Energy engineering effectively regulate the energy band of ZnO while maintain the hexagonal wurtzite structure. By ternary alloying, such as introducing Mg dopant realize ZnO energy gap adjustable at the range of 3.3eV-4.0eV using MBE or PLD method [1-3]. $Zn_{1-x}Mg_xO$ is also applied as barrier layers for multiple layers such as ZnO/$Zn_{1-x}Mg_xO$ homostructure, superlattice, and multi-quantum well [4-8]. By choosing appropriate barrier height and well layer thickness, PL could be tuned in the energy range of 3.3–3.6 eV, bright PL of free excitons could be observed even at room temperature [7]. Low threshold of the stimulated emission has been also been investigated [8]. However, these structures are mainly produced by large equipments such as MBE, PLD, and their high price stops mass production.

USP method advantaging at especially low-cost, easy to control and time saving has been successfully utilized to deposit $Zn_{1-x}Mg_xO$ thin films[9], p-type ZnO films [10,11], p-n homojunctions[12,13]. However, $Zn_{1-x}Mg_xO$ as the key material of multiple layers, there is a lack of thorough research on the film thickness or surface smoothness. Here we innovate a new method by slightly adjusting HAc amount it realize the film thickness variation in the order of 10^2 nm, effectively replacing prolonged deposition time. Film surface smoothness can be achieved by make equilibrium between heat temperature and carrier gas flow rate. By introducing Mg dopant, the energy gap broadens 0.22eV fitting the linearly equation: Eg = 3.13+0.78x (eV). The linearly blue shift of PL peaks from 380 nm to 364 nm confirms Mg doping. Moreover the un-doped ZnO has a bright band edge luminescence at 380nm without defect luminescence.

2. Experiment Details

To grow $Zn_{1-x}Mg_xO$ thin films, $Zn(CH_3COO)_2$, $Mg(CH_3COO)_2$ are chosen as Zn and Mg sources, certain amount of HAc is added to control the reaction rate. The concentrations of $Zn(CH_3COO)_2$ are 0.5mol/L, 0.45 mol/L, 0.4 mol/L, 0.35 mol/L, 0.3 mol/L, 0.25 mol/L, while Mg concentrations are adjust to 0 mol/L, 0.05 mol/L, 0.1 mol/L, 0.15 mol/L, 0.2 mol/L, 0.25 mol/L respectively. The aerosol of precursor solution is generated using a commercial ultrasonic nebulizer, and transported by high purity N_2 as carrier gas at 4L/min onto the surface of glass substrate which is preheated to 300ºC, deposit for 30 min. This is the best equilibrium condition for the film deposition.

The Mg content in the films is determined by inductively coupled plasma (ICP) optical emission spectroscopy. The crystal structures of the $Zn_{1-x}Mg_xO$ films are examined by X-ray diffraction (XRD) using a D/MAX-2500 V diffraction with Cu Kα radiation. Optical transmission spectra from 330nm to 2600nm are measured at room temperature using U-4100 Spectrophotometer. Photoluminescence (PL) measurement is performed using semiconductor laser at an excitation wavelength of 266nm at room temperature.

3. Results and Discussion

Mg content in the films is examined by inductively coupled plasma (ICP) optical emission spectroscopy by dissolving the films in HNO_3 solution. Fig 1 shows the Mg content in the films as a function of that in the precursor solution. Mg content in the films increases along with that in the solution increase by the factor of about 0.5.

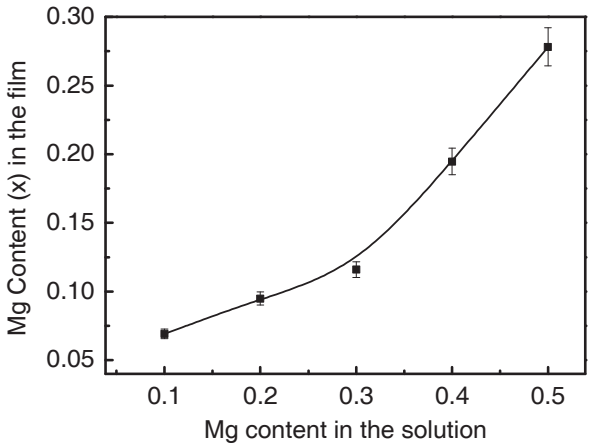


Fig 1 Mg content in the film as a function of Mg content in the precursor solution

Fig 2 shows the XRD spectra of the $Zn_{1-x}Mg_xO$ films. There are three peaks 31.74º, 34.42º, 36.20º corresponding to the (100) (002) (101) peaks of hexagonal ZnO peaks respectively without any MgO phase. The position of main peak moves towards higher diffraction degree as Mg content increased. The intensity of (100) peak is gradually reduced while the (002) and (101) peak intensity is increased relatively. The maximum Mg content (x=0.28) is significantly larger than the thermodynamic solubility limit (x=0.04)[14]. Of the $Zn_{0.88}Mg_{0.12}O$ film, the intensity of (002) peak is especially higher than the other two, with a FWHM of 0.34º. Similar $Zn_{1-x}Mg_xO$ structures are also obtained with USP method[9].

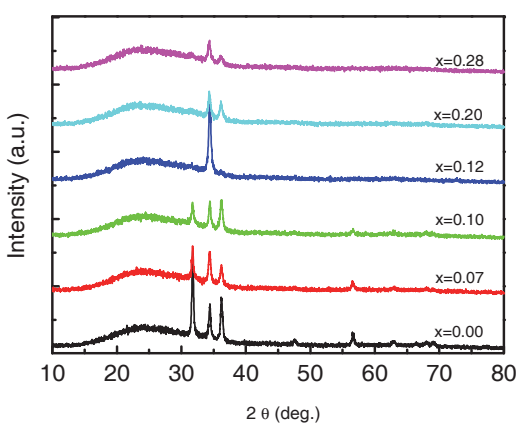


Fig 2 The X-Ray diffraction spectra of the $Zn_{1-x}Mg_xO$ films

We use the optical transmission spectra of $Zn_{1-x}Mg_xO$ film to calculating the film thickness [15,16]. There is a fringe pattern of the transmittance data in the highly transparent spectral region due to the reflection interference. The thickness of the films is given by:

$$n= [(N+N^2+s^2)^{1/2}]^{1/2}. \quad (1)$$

$$N= 2s\frac{T_M-T_m}{T_M T_m}+\frac{s^2+1}{2}. \quad (2)$$

$$d =\frac{\lambda_1\lambda_2}{2(n_2\lambda_1-n_1\lambda_2)} \quad (3)$$

where T_M, T_m are transmission data; n_1,n_2 are the refractive indexes at adjacent wave crests; s=1.52, is refractive index of glass substrate.

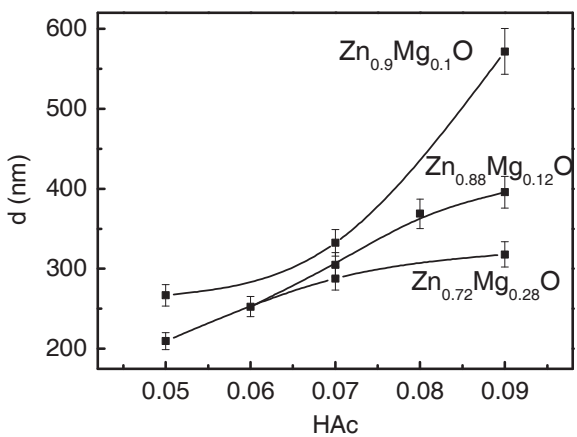


Fig 3 The film thicknesses of $Zn_{1-x}Mg_xO$ films as a function of HAc amount

Fig 3 shows the film thicknesses as a function of HAc amount. The amount of HAc varied from 0.05 to 0.09 while maintain the same Mg content. The films are thickened in the order of 10^2 nm as HAc amount slightly increases. That could be explained as follow:

The reaction for ZnO film deposition is give by:

$$Zn(CH_3COO)_2+ H_2O \overset{\Delta}{\leftrightarrow} ZnO+2\ CH3COOH$$

Since it is a reversible reaction, HAc has an influence on the reaction rate. By comparing the thicknesses of different HAc amount, we found that when the substrate is preheated to 300ºC if the amount of HAc is too less(<0.05), the film would not form for the reason that ZnO particles crystallize too rapidly thus be

taken away by the carrier gas, at the meanwhile a lot of white powder is observed at the inner-wall of the chamber; or too much HAc (>0.1) would lead to low optical transmission for the film is too thick, ZnO particles stalled at the substrate crystallize too slowly. As a result, the films grow thicker as HAc amount increases. We innovate a new way by slightly adjusting HAc amount to control the reaction rate in film deposition process replacing prolonged deposition time, succeed in making film thickness grows in 10^2 order.

The absoption edge for $Zn_xMg_{1-x}O$ is given by:

$$\alpha h\gamma = C(h\gamma - Eg)^{1/2}, \tag{4}$$

where hγ is the photon energy; α is the absorption coefficient, defined as α=1/d*ln(1/T).

Fig 4 is a conversion from T vs. λ to $(\alpha h\gamma)^{1/2}$ vs. hγ.According to Tauc method, Eg is obtained by extrapolating the linear part of the absorption edge [17,18]. As Mg content grows, the absorption edges continuously blue shift. The inset shows the energy band as a function of Mg content. Eg growsfrom 3.13eV (x=0) to 3.35eV (x=0.28) as Mg content increases, fitting the linear relationship Eg=3.13+0.78x (eV). The energy gap broadens 0.22 eV while maintain the hexagonal structure.

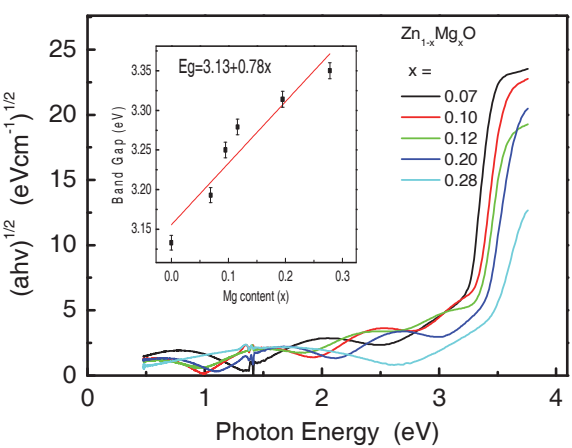


Fig 4 $(\alpha h\gamma)^{1/2}$vs. hγ plot based on the transmission spectra

Fig 5 shows the photoluminescence (PL) of $Zn_xMg_{1-x}O$ at an excitation light of 266nm at room temperature. There is a sharp and strong band edge luminescence of the un-doped ZnO at 380 nm with FWHM of 16nm without defects luminescence compared with other methods such as ALD[19]. The little

peak at 760nm is the second order diffraction. As Mg content increases, the PL peaks blue shift linearly from 380 nm to 364 nm; the intensities of the luminescence drop especially quickly (x>0.1). This blue shift to higher energy side is agreed with the broaden of energy gap causing by Mg doping.

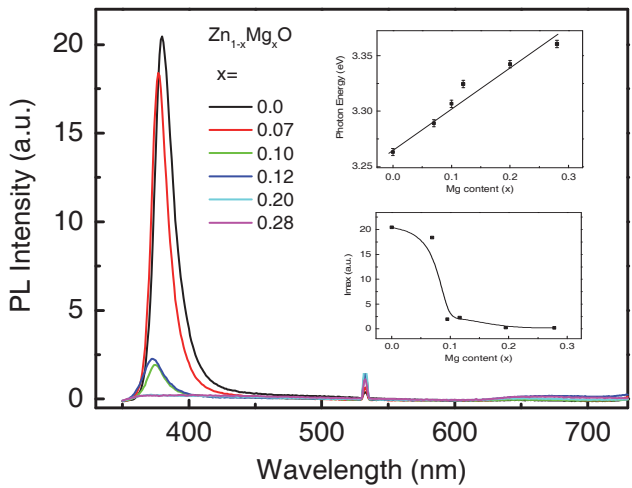


Fig 5 PL of $Zn_xMg_{1-x}O$ at an excitation light of 266nm at room temperature

4. Summary

$Zn_xMg_{1-x}O$ films have been prepared by the well-established USP method. The surface smoothness is achieved by making a balance between heat and gas flow: the substrate is preheated to 300ºC, with carrier gas at 4L/min. The film thickness is successfully managed by adjusting the amount of HAc. Slightly more HAc would stimulate a thickness growth in 10^2 nm order. Energy gap linearly grows from 3.13eV (x=0) to 3.35eV (x=0.28) as Mg content increases, fitting the relationship of Eg=3.13+0.78 x (eV). The PL peaks coordinately blue shift linearly from 380 nm to 364 nm and the intensities of the luminescence drop especially quickly (x>0.1). Strong luminescence at 380 nm of the un-doped ZnO is observed without defects luminescence.

References

1. A. Ohtomo, M. Kawasaki, T. Koida, K. Masubuchi, H. Koinuma, Y. Sakurai, Y. Yoshida, T. Yasuda, and Y. Segawa, *Appl. Phys. Lett.* 72, 2466 (1998).

2. M. Takagi, H .Tanaka, Sz. Fujita, Sg. Fujita. Jpn. *J. Appl. Phys*, Part 242, L401 (2003).
3. H. Tanaka, S. Fujita, and S. Fujita, *Appl. Phys. Lett.* 86, 192911 (2005).
4. Y.M. Lu, C.X. Wu, Z.P. Wei, Z.Z. Zhang, D.X. Zhao, J.Y. Zhang, Y.C. Liu, D.Z. Shen, X.W. Fan. *Journal of Crystal Growth* 278 (2005) 299–304.
5. Soumya Krishnamoorthy, Agis A. Iliadis, Aravind Inumpudi, Supab Choopun, Ratnakar D. Vispute, Tirumalai Venkatesan. *Solid-State Electronics* 46 1633–1637 (2002).
6. A. Ohtomo, M. Kawasaki, I. Ohkubo, H. Koinuma, T. Yasuda, and Y. Segawa, *Appl. Phys. Lett.* 75, 980 (1999).
7. T. Makino, C. H. Chia, N. T. Tuan, H. D. Sun, Y. Segawa, M. Kawasaki, A. Ohtomo, K. Tamura, and H. Koinuma, *Appl. Phys. Lett.*77, 975 (2000).
8. A. Ohtomo, K. Tamura, M. Kawasaki, T. Makino, Y. Segawa, Z. K. Tang, G. Wong, Y. Matsumoto, and H. Koinuma, *Appl. Phys. Lett.* 77, 2204 (2000).
9. Xia Zhang, Xiao Min Li *, Tong Lai Chen, Ji Ming Bian, Can Yun Zhang *Thin Solid Films* 492 (2005) 248–252.
10. J. M. Bian, X. M. Li, X. D. Gao, W. D. Yu, and L. D. Chen *Appl. Phys. Lett.* 84(4), 541 (2004).
11. X. Zhang, X. M. Li, T. L. Chen, C. Y. Zhang, and W. D. Yu *Appl. Phys. Lett.* 87, 092101 (2005).
12. J. M. Bian, X. M. Li, C. Y. Zhang, L. D. Chen, and Q. Yao *Appl. Phys. Lett.* 84(19), 3783 (2004).
13. G. T. Du, W. F. Liu, J. M. Bian, L. Z. Hu, H. W. Liang, X. S. Wang, and A. M. Liu *Appl. Phys. Lett.* 89, 052113 (2006).
14. J.F. Sarver, Fred L. Katnack, and F.A. Hummel, *J. Electrochem. Soc.*106, 960 (1959).
15. M. Mulato, I. Chambouleyron, E. G. Birgin, and J. M. Martínez *Appl. Phys. Lett.* 77, 2133 (2000).
16. R. Swanepoel *J. Phys. E: Sci. Instrum.* Vol. 16, 1983.
17. R. A. Smith, *Wave Mechanics of Crystalline Solids* (Chapman and Hall, 2nd Ed, 1969).
18. J.I. Pankove and P. Aigrain, *Phys. Rev*. 126, 956 (1962).
19. M. Godlewski, E. Guziewicz, G. Łuka, T. Krajewski, M. Łukasiewicz, Ł. Wachnicki, A. Wachnicka, K. Kopalko, A. Saremc, B. Dalati *Thin Solid Films* 518(4), 1145–1148 (2009).

Effects of Li Content on Microstructure and Corrosion Morphology of Mg-Li-Al-Ca Alloy in NaCl Solution

Yu Haixia†

Jilin Vocational College of Industry and Technology,
Jilin 132013, China
†E-mail: yhx153@126.com

The morphology of corroded surface was observed by scanning electron microscopy (SEM), and the XRD was used to analyze the composition of corrosion products. The results showed that there are a lot of bubbles and corrosion pits during corrosion process, and corrosion phenomena were observed on the pure magnesium matrix and $MgLi_2Al$ phase. XRD results showed corrosion layer consists of $Mg(OH)_2$.

Keywords: Mg-Li-Al-Ca alloy, microstructure, corrosion morphology.

1. Introduction

With the developing of urgent needs for lightweight materials and components in modern industrial field, Mg-Li alloys have been displayed the first legs in many fields, such as auto industry, medical device industry and IT industry [1,2]. But at the same time, Mg-Li alloys also own some shortcomings, such as lower strength, bad thermal stability, lower corrosion resistance [3,4]. These weaknesses severely limited the application of Mg-Li alloys. This research focus on corrosion behavior and mechanism and how to improve the corrosion resistance of Mg-Li alloys which had been a hot spots in the worldwide. The theory value and realistic directive significance of this research is very important.

2. Materials and Test Method

Table 1. Chemical composition of Mg-Li-Al-Ca cast alloy (wt %)

Alloys	Chemical Composition (wt %)			
	Li	Al	Mg	Ca
N1	7.693	3.357	81.00	0.9431
N2	8.810	2.802	81.31	0.8846
N3	10.910	3.213	78.03	0.8229
N4	11.520	3.083	70.65	0.7749

Test materials were melted with pure magnesium and pure lithium and Mg-50Ca intermediate alloy in ZG-0.01 vacuum resistance furnace, and protected by argon. Chemical composition was test by inductively coupled plasma spectroscopy instrument (ICP). The result was listed in Table 1.

3. Experimental Results and Discussion

3.1. *Effects of Li content on microstructure of as-cast*

Optical microstructure and XRD patterns of as-cast Mg-Li-Al-Ca alloys with different Li content were differently listed Fig.1 and Fig.2. α-Mg phases of close-packed hexagonal structure of Mg-Li-Al-Ca alloys varied less and less in Fig.1 and Fig.2. And β-Li of body centered cubic lattice varied more and more. According to Mg-Li binary alloy phase diagram, α-Mg phases were disappear when Li content was more than 10. 5%. Single β-Li phase can be mostly observed. The result was same with N_3.

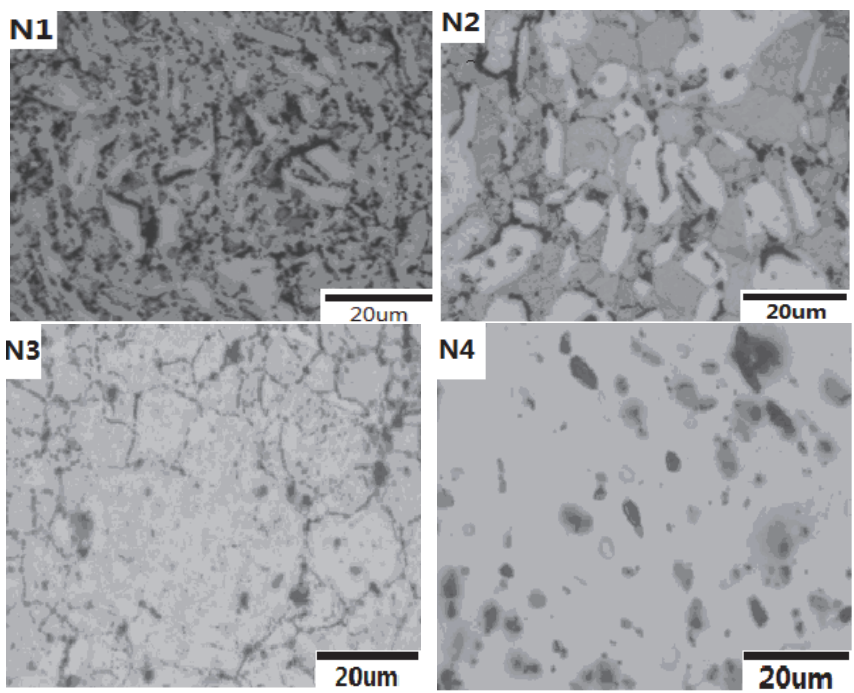


Fig.1 Optical microstructure of as-cast Mg-Li-Al-Ca alloys with different Li content

According to XRD results of Mg-Li-Al-Ca alloys' microstructure, there were a little $MgLi_2Al$ phase and Al_2Ca phase. $MgLi_2Al$ phase varied more and

more with the increase of Li content. Al and Ca were easy to segregate at crystal boundary on the base of Fig.1 and Fig.2.

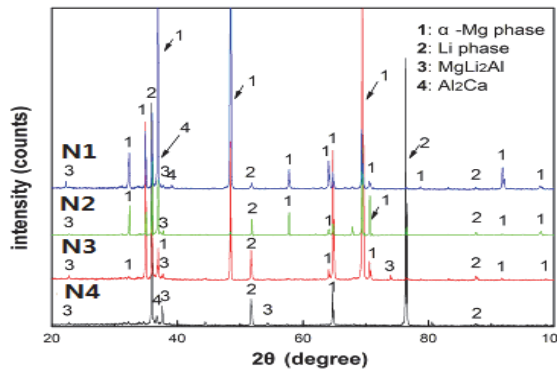


Fig.2 XRD patterns of as-cast Mg-Li-Al-Ca alloys with different Li content

3.2. *Effects of Li content on microstructure and morphology after corrosion*

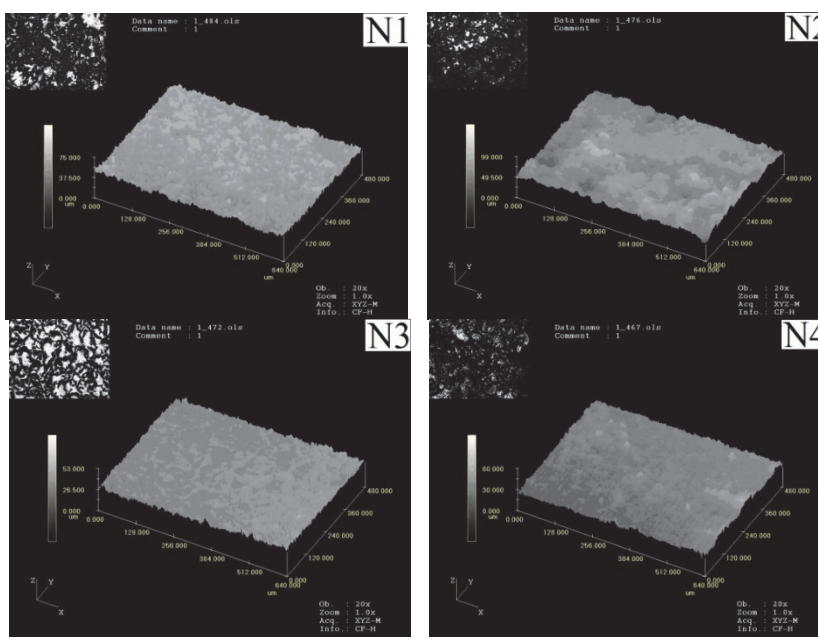


Fig.3 SEM and surface images of Mg-Li-Al-Ca alloy with different Li content upon exposure in 3.5% NaCl solution

Test patterns of as-cast Mg-Li-Al-Ca alloys with different Li content were placed into 3.5% NaCl solution. Some gas bubbles can be immediately observed at pattern surface. After a while, the surfaces of the patterns are pitted with gas bubbles, and lose metal luster. Corrosion of metals can be observed at pattern surface after some times. Corrosion time varied longer and longer with the increase of Li content, and varied from 15min of 7.63% Li content to 62min of 11.52% Li content. During corrosion test, the corrosion products began to fall, and is black.

Corrosion morphology changes of as-cast Mg-Li-Al-Ca alloys with different Li content were recorded for 4 hours in 3.5% NaCl solution. Those results are founded that, with the increase of Li content, the surface corrosion degree is weakened from N1 to N4. SEM and surface images of Mg-Li-Al-Ca alloy with different Li content upon exposure in 3.5% NaCl solution are listed in Fig.3. On the base of Fig.3, it can be observed that the corrosion phenomenon of N_1 and N_2 alloy focused on α-Mg phase, there are some corrosion holes at pattern surfaces, that accords with the characteristics of pitting. But N_3 and N_4 alloy corrosion phenomenon occurred at the whole surface of the pattern. These phenomena accord with uniform corrosion.

It is recorded in Fig.4 that XRD patterns of Mg-Li-Al-Ca alloy with different Li contents upon exposure in 3.5% NaCl solution for 48h. According to Fig.4, N1 and N2 alloys corrosion products are α-Mg and $Mg(OH)_2$ and β-Li, and N_3 alloy corrosion products are $Mg(OH)_2$and β-Li, N4 alloy corrosion products are $Mg(OH)_2$、β-Li and $Al(OH)_3$. This shows that the corrosion phenomenon occurred in the pure magnesium matrix and $MgLi_2Al$ phase. The corrosion of Li is not found in the test. This result is consistent with many scholars' [5,6].

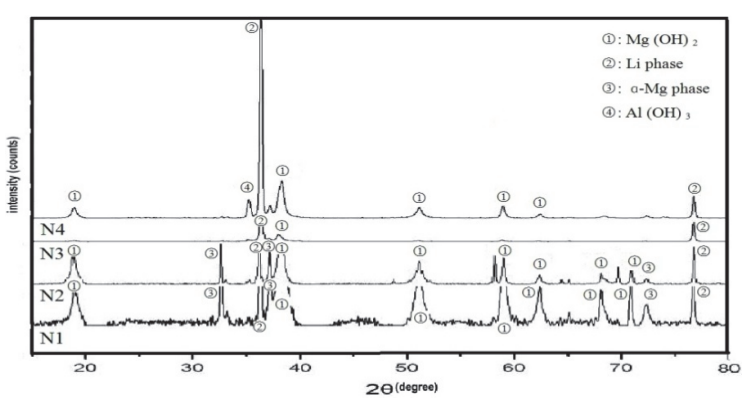


Fig.4 XRD patterns of Mg-Li-Al-Ca alloy with different Li contents upon exposure in 3.5% NaCl solution for 48h

4. Conclusions

The α-Mg phase gradually decreased with the increase of Li content in microstructure of Mg-Li-Al-Ca alloys, and β-Li phase gradually increased. And the corrosion process varied from pitting to uniform corrosion.

Acknowledgments

The authors would like to thank Prof. Zhan-yi Cao for reviewing the manuscript.

References

1. Yao Lei, Hao Hai, Gu Song-Wei, et al, Effects of electromagnetic stirring on microstructure and mechanical properties of super light Mg-Li-Al-Zn alloy, *Transactions of nonferrous metals society of China*. 20(2010) 388-392.
2. Ma Chunjiang, Zhang Di, Qin Jining, et al, Aging behavior of Mg-Li-Al alloy, *Transactions of nonferrous metals society of China*. 9 (1999) 772-777.
3. Yu Haixia, Yang Yunlong, Cheng Liren, et al, Effects of Li content on microstructure and mechanical properties of Mg-Li-Al-Ce-Ca alloy, *Hot working technology*. 42 (2013) 109-111.
4. YANG Guang-yu, HAO Qi-tang, JIE Wan-qi, Study Status of Mg-Li System Alloys, *Foundry technology*. 25 (2004) 19-21.
5. MA Yi-bin, LI Ning, LI De-yu, et al, Corrosion Behavior of Mg-14-1Al-0.1Ce Alloy in NaX (X=F, Cl, Br and I) Solutions, *Corrosion science and protection technology*. 23 (2011) 467-470.
6. Rong-Chang Zeng, Lu Sun, Yu-Feng Zheng, et al, Corrosion and characterisation of dual phase Mg-Li-Ca alloy in Hank's solution: The influence of microstructural features, *Corrosion Science*. 79 (2014) 69-82.

Effect of Low Content SiO_2 on the Crystallization Behaviour and Dynamic Mechanical Properties of Polyurethane/SiO_2 Composites

Yuhua Yi†

School of Mechanical and Automotive Engineering, South China University of Technology,Guangzhou, 510640, China
GuangZhou SCUT Bestry Technology Co.Ltd, Guangzhou,510640, China
†E-mail: mmyhyi@scut.edu.cn

A series of polyurethane/SiO_2 composites with SiO_2 content no more than 1 wt % were prepared via in situ polymerization through a prepolymer process. Morphology of the nanocomposites were characterised by SEM. The effect of SiO_2 on crystallinity and dynamic mechanical properties of polyurethane/SiO_2 composites was investigated. It was found that SiO_2 dispersed in polyurethane matrix uniformly. With the addition of SiO_2, the crystallization degree of the polyurethane decreased, the tanδ peak which associated with the glass transition temperature (Tg) of the polyurethane soft segment shifted obviously to the lower temperature. The optimum SiO_2 content was 0.5wt %. At this content, the decline of the crystallization degree was 9%, the shift of the tanδ peak was 8ºC.

Keywords: Polyurethane, SiO_2, Morphology, DMA

1. Introduction

Polyurethanes are organic polymers that contain the urethane group in the structure [1]. The urethane linkage is the fundamental group in polyurethane chemistry which formed by the reaction between the hydroxyl groups of the polyol and the NCO groups of the diisocyanate [2].

SiO_2 is a synthetic, amorphous material that has spherical particles, which form chain-like, branched aggregates. The SiO_2 is nano size and containing hydroxyl functional groups on the particle surface. Due to the hydroxyl groups at the surface, silica can be grafted to the polyurethane chain by chemical reaction with NCO gruops. As a result, the thermal, rheological, mechanical, and adhesion properties of polyurethane can be improved [3-5]. The SiO_2 content in previous studies normally between 1~10 wt %. The effect of SiO_2 on the dynamic mechanical properties which is very important for products used under

dynamic condition usually to be negative. Polyurethane composites with low SiO_2 content have been rarely studied.

In this work, MDI based polyurethane/SiO_2 nanocomposites with SiO_2 content no more than 1 wt % were prepared via in situ polymerization process, The structure and properties of the composite were investigated in terms of morphology, crystallinity and dynamic mechanical properties.

2. Experimental Procedure

2.1. *Materials*

Polyethyleneglycol adipate (PEA) with relatively molecular weight of 1,000, carbodiimide modified MDI (C-MDI), hydroquinone dihydroxyethylether (HQEE)

2.2. *Pretreatment of SiO_2*

SiO_2 used in this work is HB615. First put HB615 into the muffle furnace at 250ºC for 2 hours. Then mix the HB615 with PEA by the high-speed shear disperser about 15~20min with the rotational speed of 4000~4500rpm. The content of HB615 is 0.5 wt % and 1 wt % respectively.

3. Preparation of Polyurethane/SiO_2 Nanocomposite

In this study, the polyurethane/SiO_2 nanocomposite elastomer was prepared via in situ polymerization and prepolymer process. First, polyethyleneglycol adipate premixed with HB615 was input into a reacting chamber, heated to 120 to 130ºC and stirred in a vacuum of –0.095 to –0.098 Mpa for 2 to 2.5 hours to dehydrate. Then, polyethyleneglycol adipate was cooled to 60ºC, mixed well with stoichiometric amount of carbodiimide modified MDI, the molar ratio of NCO/OH was 2:1, stirred and heated to 80 ±2ºC for 2 hours to obtain the polyurethane pre-polymer.

The prepolymers were then mixed with hydroquinone dihydroxyethylether (HQEE) at 95% theory based on measured NCO content of these prepolymers. These mixtures were casted onto a teflonated mould preheated at 100ºC and maintained at this temperature for 15 hours to produce test specimens.

4. Characterization

The morphology was characterised by SEM (FEI Nova Nano SEM430). The crystallization behaviour was determined by a WAXD instrument (Rigaku D/max-2500), using Cu-Ka radiation of a wavelength of λ=0.154 nm. Dynamic

mechanical properties were determined with a DMA242 dynamic mechanical analyzer made by Germany NETZSCH company and according to standard method (GB 9870-88). The size of specimens was 10×10×2 mm, the temperature heating rate was 5ºC/min and the frequency was 10 Hz.

5. Results and Discussion

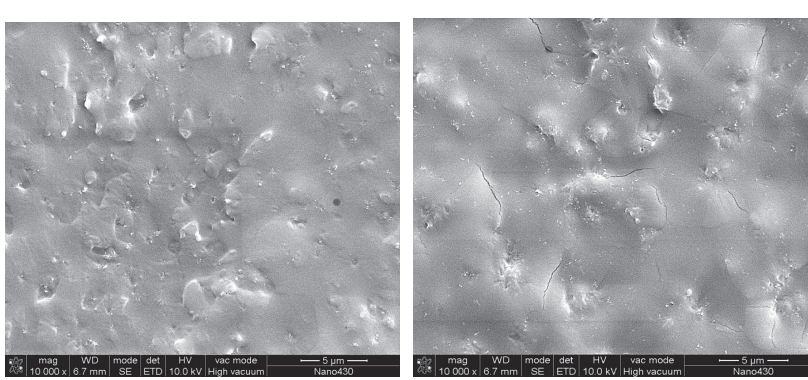
5.1. *Morphology of polyurethane/SiO_2 nanocomposites*

Table 1 shows the different formulations of polyurethane/SiO_2 composite samples.

Table 1. Different formulas formulations of polyurethane/ SiO_2 composite samples

Sample	PU01	PU02	PU03
SiO_2 [wt%]	0	0.5	1

SEM images of cryogenically fractured surface of polyurethane/SiO_2 composite elastomer with varying SiO_2 content were shown in Figure 1. It was found that SiO_2 dispersed uniformly in polyurethane matrix and there was no obvious aggregation. The boundary of polyurethane/SiO_2 was diffused, indicating of the formation of the strong interfacial bonding between the two phases. In this work, polyurethane/SiO_2 composite elastomer were prepared via in situ polymerization process, which was benefit for dispersion of nanofillers in polyurethane matrix. The interfacial bonding of the two phases can thus be improved. Furthermore, the hydroxyl groups of SiO_2 could react with NCO group, which improved the dispersible uniformity of SiO_2 in the polyurethane matrix greatly.



0.5wt% SiO_2 1wt% SiO_2

Figure 1. SEM micrographs of the polyurethane/ SiO_2 nanocomposites

5.2. *The crystallization behavior of polyurethane/SiO_2 nanocomposites*

The crystallinity of polyurethane/SiO_2 nanocomposites was investigated by a Philips Xray diffractometer and show in Figure 2.

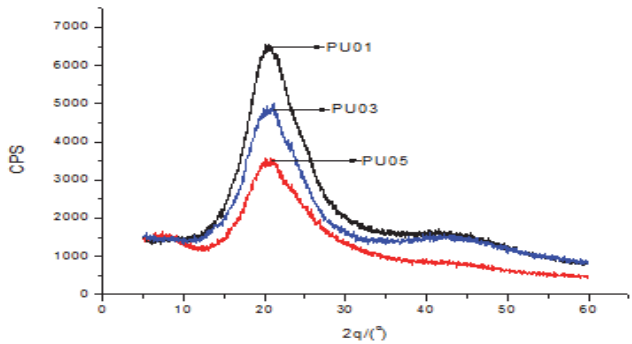


Figure 2. WAXD of the polyurethane/ SiO_2 nanocomposites

WAXD shows significant change with various content of SiO_2 (Figure 2), there is a clear effect of the nano SiO_2 on the crystalline component. A crystalline peak at 20.4 was found for all samples. As to the pure polyurethane elastomer system (PU01), this peak at 20.4 is clear and sharp. By addition with nanosilica, this feature progressively weakens and broadens.

In this work, the polyurethane/SiO_2 nanocomposites was prepared via in situ polymerization, the chemical reaction between silica and polyurethane is benefit to form high interaction between silica and polyurethane hard segment. The interaction at the hard segment–silica interface can change the molecular mobility. Which make the movement of the polyurethane chain more difficultly, takes place that reduces crystalline domains in the polyurethane matrix. The crystallization degree calculated by JADE5.0 method for neat polyurethane (PU01) is 35.7%, with the addition of 0.5 wt % nanosilica (PU02), the crystallization degree decreased to 32.5%. When the SiO2 content increased to 1wt% (PU03), the crystallization degree decreased greatly, only 28.7%, an approximately 20% decline in the crystallization degree is observed with 1 wt % silica content.

5.3. *Dynamic mechanical properties of polyurethane/SiO_2 nanocomposites*

Dynamical mechanical analysis provides information on the glass transition and damping properties of a polymer. The dynamical mechanical properties of polyurethane/SiO_2 composite elastomer with varying SiO_2 content were shown in Figure 3.

Figure 3 shows that all the samples exhibited only one tanδ peak, the tanδ peak is associated with the glass transition temperature (Tg) of the polyurethane soft segment. The peaks changed with the addition of SiO_2, and the content of SiO_2 had little influence because the content of SiO_2 is low in this research. It is clear that the tanδ values of the polyurethane/SiO_2 nanocomposites are lower than that of the neat polyurethane. Tg for the neat PU (PU01) is 26.2ºC, whereas the same for the nanocomposite having 0.5wt% addition of nanosilica (PU02) is 18ºC, which for 1wt% (PU03) is 17ºC. An approximately 9ºC shift is observed with 1wt% silica content. This is mainly attributed to the good interaction between the polyurethane hard segment and the silica particles. As a result of which the nanometer-sized particles can restrict the segmental motion near the

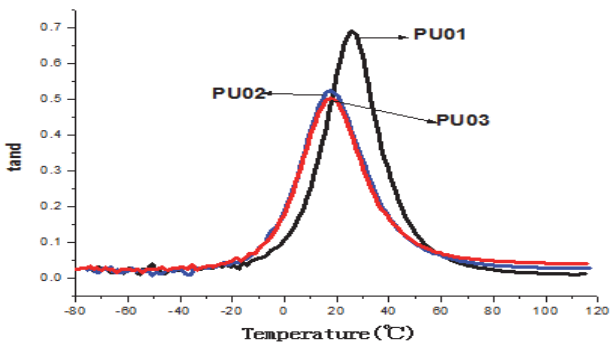


Figure 3. Tan delta curves of the polyurethane/SiO_2 nanocomposites

organic inorganic interface. As a result, the crystallization degree of the polyurethane hard segment declined, which make the motion of the soft segments more easily. This is in agreement with the WAXD results in the earlier paragraph. Maji et al.[6] reported the same trend for the polyurethane nanocomposites with nanoclay loading.

6. Conclusions

MDI based polyurethane/SiO_2 nanocomposites with SiO_2 content no more than 1 wt % were prepared via in situ polymerization process. Morphology of the nanocomposites were characteried by SEM, it was found that SiO_2 dispersed in polyurethane matrix uniformly. The effect of SiO_2 on crystallinity and dynamic mechanical properties of polyurethane/SiO_2 composites was investigated by WAXD and DMA. With the addition of SiO_2, the crystallization degree of the polyurethane decreased, the tanδ peak which associated with the glass transition temperature (Tg) of the polyurethane soft segment shifted obviously to the lower temperature. The optimum SiO_2 content was 0.5wt%. At this content, the

decline of the crystallization degree was 9%, the shift of the tanδ peak was 8ºC. The experimental result is valuable for the polyurethane products used under dynamic conditions such as tires, rollers and SPS composite structure.

Acknowledgements

The authors thank to GuangZhou SCUT Bestry Technology Co.Ltd for the unselfish assistance. This research is supported by the National Science Foundation (Project No. 51278201)

References

1. I.R. Clemitson. *Castable pPolyurethane Elastomers*. 2008, New York.
2. Cristina. Prisacariu. Polyurethane Eastomers from Morphology to Mechanical Aspects'. 2011, New York.
3. Jingjing Ding, Lin Ye. Structure and Property of Polyurethane/SiO2 Composite Elastomer Prepared via in Situ Polymerization. *J. Appl. Polym. Sci.*, 2013(127): 2732–2738
4. Sanja Lučić Blagojevic, Zrinka Buhin, Ružica Lukic Kovačić. Influence of Nanosilica on the Morphology, Thermal and Mechanical Properties of Polyurethane Elastomer', *J. Appl. Polym. Sci.*, 2012(125): 181–190.
5. Sanja Lučić Blagojević, Zrinka Buhin, Ivona Igrec. Influence of Silica Nanofiller on the Isothermal Crystallization and Melting of Polyurethane Elastomer', *J. Appl. Polym. Sci.*, 2013(129): 1466–1475.
6. Pradip K. Maji, Prasanta K. Guchhait, and Anil K. Bhowmick. Effect of Nanoclays on Physico-Mechanical Properties and Adhesion of Polyester-Based Polyurethane Nanocomposites: Structure-Property Correlations', *J. Mater. Sci.*, 2009(44): 5861–5871.

Spectral Extinction Coefficient Test of the Photoelectric Jamming Aerosol

T. Zhang†, X.D. Dai, L. Chen, C.S. Chen, H.F. Liu, M.Y. Dai, L.N. Ren
State Key Laboratory of NBC Protection for Civilian, Beijing 102205, China
†*E-mail: tong_zhang@126.com*

The attenuation performance and extinction coefficient of a photoelectric jamming aerosol were studied in narrow spectral bands by using IR radiometers and smoke box test system. The experimental results showed that the infrared transmittance and extinction coefficients of the photoelectric jamming aerosol can be successfully tested at each spectral band in this method, much more accurate than those tested by traditional thermal imagers in wide wavelength range. The measured extinction coefficients of the photoelectric jamming aerosol were very consistent in three experiments of different concentrations, indicating that the method has higher accuracy and repeatability.

Keywords: spectral extinction coefficient; photoelectric jamming material; aerosol; smoke.

1. Introduction

In the atmosphere, micro and nano articles can easily form aerosols, of which the absorption and scattering effects will result in certain attenuation to the light in infrared spectral bands [1]. Some of such functional materials with higher concentrations will form effective shield and jamming effect against the detection and guidance from the air and the space. [2-4]

In the performance evaluation of photoelectric jamming aerosol, the extinction coefficient is very important for evaluating the jamming and attenuation effect. However, limited to the laboratory equipment and test conditions, the extinction coefficient in current research can only be obtained by calculating the average value over a wide spectral band without effective methods to obtain the extinction coefficients in narrow spectral bands, which cannot meet the requirement of the fight against high-resolution spectroscopy detection.

In this paper, the infrared jamming performance of a new type of photoelectric jamming aerosol was measured with spectral range of 8~12um and spectral resolution accuracy of 0.06um by using a high-resolution infrared

spectrum radiometer [5]. Based on this, the spectral extinction coefficients test methods were established and the extinction coefficients of the infrared jamming aerosols was finally obtained.

2. Experimental Procedure

2.1. *Experimental Instrument*

SR-5000N IR radiometer (Israel CI Company) was selected in the test of blackbody radiation intensity. Specifically, InSb and MCT detectors were used in spectrum measurement mode, and narrow field of view of 2-7mRad was selected with a spectral range of 1.4-13um, spectral resolution of 0.8% wavelength and chopper frequency of 1800Hz.

SR 200 (Israel CI) was applied as the standard blackbody to be calibrated and tested, whose diameter was 22.2mm, emission rate was 0.99 and temperature readout resolution was 0.1ºC.

2.2. *Test Method*

A new type of nano-shell material was selected as the photoelectric jamming aerosol, and its performance was tested in a smoke box test system. The test steps are as follows:

(1) Set up the blackbody at a designated position and set the temperature at 400ºC. Set up and commission SR-5000N IR radiometer, data acquisition and processing system before completing their focusing, calibration and zeroing;

(2) Weigh a certain quality of sample, and fill it into the cyclone dispersion device and tighten it;

(3) Turn on the IR radiometer and test blank for more than 5s;

(4) Spray the sample rapidly, and turn on the stirring fan for 10s to make the smoke dispersed equably in the smoke box and then record the data;

(5) Open the air sampling pump at 25s after smoke spraying, collect aerosol articles for 30s, and calculate the mass concentration based on the membrane mass obtained before and after the smoke spraying.

2.3. *Calculation*

The spectral extinction coefficient indicates the smokescreen shielding area per unit mass, and characterizes the attenuation ability of smoke aerosol against electromagnetic radiation. Higher value means better attenuation performance. According to Lambert-Beer's law,

$$\tau = \exp(-\alpha C_m L) \quad (1)$$

where, τ is the transmittance, Cm is aerosol mass concentration; L is the optical path. Formula (1) represents that the transmittance is determined by the extinction coefficient α with the certain aerosol concentration and smoke thickness.

3. Results and Discussion

3.1. *The Test Mass Concentration*

Three test experiments named T1, T2 and T3 were conducted. In each test the photoelectric jamming aerosol was selected with the same material of novel semiconductor particles with the same material parameters, except that the mass concentration was respectively 0.13, 0.53 and 0.8g/m^{-3}.

3.2. *The Infrared Transmittance Calculation*

The spectral radiation intensity of standard blackbody was measured with SR5000N IR radiometer. In three tests experiments T1, T2 and T3, different concentrations of aerosol produced different attenuation effects to the spectral radiation at different wavelengths. With these values the transmittance of the aerosols at different spectral wavelength were calculated, and the results are shown in Fig.1, Fig.2 and Fig.3.

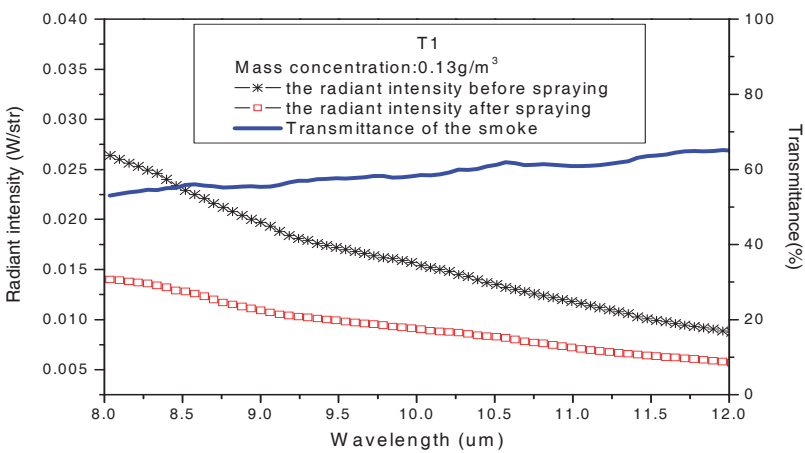


Fig.1 The blackbody radiation intensity and transmittance changes curves (0.13g/m3 in T1 experiment).

As shown in Fig.1, when the aerosol was not sprayed, the radiation intensity of standard blackbody was about 0.01~0.027 W/str, indicating that the radiation intensity of blackbody was stronger in short wave bands. However, after the smoke was sprayed for 25s, the radiation intensity of blackbody at each wave band reduced to 0.006 W/str to 0.014 W/str due to the jamming effects of smoke, indicating that the aerosol material plays an important role in attenuating the spectral radiance at any band of 8~12μm. And from the transmittance curve, it was found that with the increase of the wavelength, the transmittance also increased, indicating that the smoke aerosol has stronger attenuation performance at short wavelength than that at long wavelength. To explain this, the size of the smoke aerosol with the diameter of 1~2μm should be considered, which is easier for jamming the short wavelength. Furthermore, the shortwave infrared has stronger electron energy, which was more easily absorbed by the smoke articles, to bring lower transmittance at the shorter wavelength.

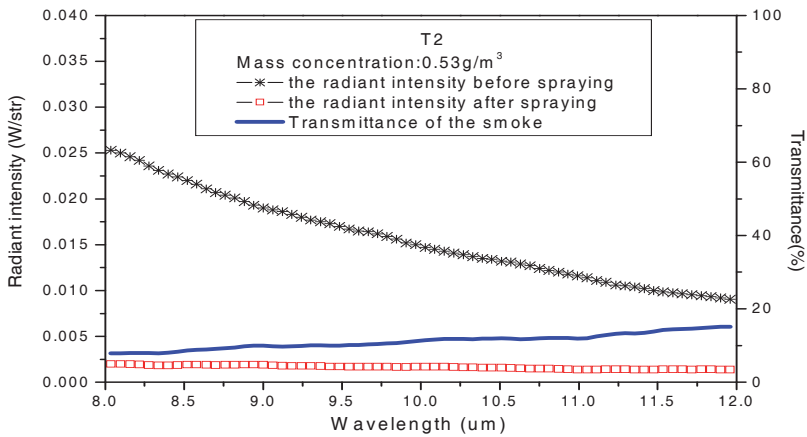


Fig.2 The blackbody radiation intensity and transmittance changes curves (0.53g/m3 in T2 experiment).

Fig.2 shows the blackbody radiation intensities and transmittance changes curves with mass concentration of 0.53g/m3 in T2 experiment. It can be found that the blackbody radiation intensity before spraying is substantially the same as that in Fig.3, but the values reduces significantly after the smoke aerosol was sprayed with the data range is less than 0.0025W/str. This is due to the concentration of smoke was increased to 0.53g/m3 after spraying in T3 experiment, producing more absorption and scattering to each spectral radiance. The calculated smokescreen transmittance was significantly reduced to less than 20%, but still showed a gradual increasing trend, verifying the above analysis of the jamming mechanism of the smoke material.

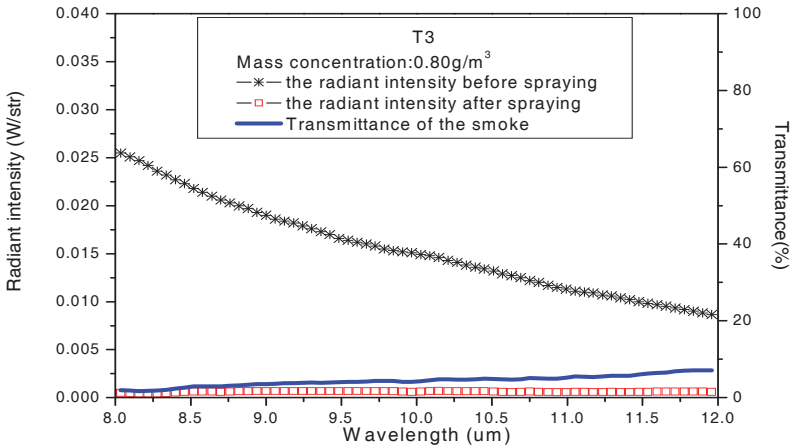


Fig.3 The blackbody radiation intensity and transmittance changes curves (0.80g/m3 in T3 experiment).

As shown in Fig.3, the radiation intensity of blackbody before spraying remained consistent with the previous two experiments, but was significantly reduced after spraying and further approaching 0, showing that when the smoke concentration is increased to 0.80g/m3, the jamming and shielding effect of the smoke aerosol were further enhanced. It can be seen from the transmittance curve that the IR transmittance of each band were lower than 7% after the spraying and even lower than 2% at 8μm, indicating that the smoke material a high efficient infrared jamming material that can form significant shadowing effects on 8~12μm spectral radiance.

3.3. *Mass Extinction Coefficient Calculation*

According to equation (1), the mass extinction coefficient curve can be obtained with the data measured in the T1, T2 and T3 experiments, as shown in Fig.4.

As can be seen from Fig.4, the spectral extinction coefficient calculated is higher with the range of 1.1~1.6m2/g, further indicating that the material owes high infrared jamming performance. The three curves are basically the same values and trends, and can be considered that the extinction coefficient at each wavelength is a constant, illustrating the data measured by the test method in this paper have high accuracy and consistency, and also verifying the spectral transmittance of the smoke is only related to the light distance and mass concentration in Lambert-Beer's law. It also can be found that with the increase of the wavelength, the extinction coefficient was reduced from 1.6m2/g at 8μm

to 1.1m2/g at 12μm, showing the value of the extinction coefficient is different at various wavelengths and exhibit different infrared jamming and shielding effect.

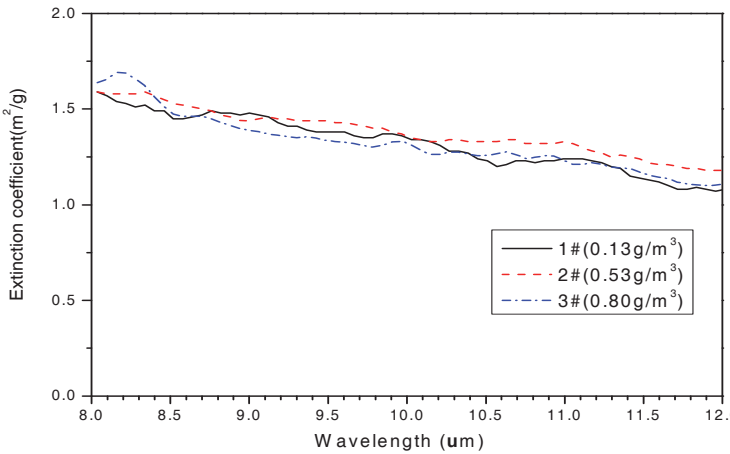


Fig.4 Mass extinction coefficient of the samples.

4. Conclusions

By using smoke box test system and SR5000N IR radiometer, the spectral transmittance and spectral extinction coefficient of photoelectric jamming aerosol were studied in three different mass concentration conditions. The results showed that with the increase of mass concentration, the infrared transmittance was significantly reduced, and even to less than 7% when the mass concentration reaches 0.8g/m3, indicating that such aerosol is a high efficient infrared jamming material. Besides, the extinction coefficients calculated in three experiments are basically the same, proving that this test method can be taken to test and calculate extinction coefficients accurately at each narrow band, which are very useful for designing new types of infrared jamming materials.

Acknowledgments

Project supported by the National Natural Science Foundation of China (Grant No. 51103176, 41205097).

References

1. A.A. Rafati, A.R.A. Borugeni, M. Najafi, et al, Ultrasonic/surfactant assisted of CdS nano hollow sphere synthesis and characterization, *Materials Characterization*, 2011, 62, 94-98.
2. H.X. Wang, D.Z. Liu, Z.B. Song, Infrared images shielded characteristics of carbon nano-materials, *Chinese Journal of Energetics Materials*, 2008, 16, 588-591.
3. J.J. Qiu, J.T. Mei, Interference of the smoke screen confronting infrared guided weapons, *Infrared and Laser Engineering*, 2006, 35, 212-215.
4. X.Y. Wang, G.P. Pan, Y.L. He, Infrared extinction characteristic of nanometer aluminas, *Chinese Journal of Energetic Materials*, 2005, 13, 312-315.
5. P. Liang, T.L. Hu, Property of optical structure of portable IR spectroradiometer, *Journal of Applied Optics*, 1999, 20, 22-25.

Research on Tensile Properties for Low-Alloy Steel after Fire Damage

Chen Wang[a1], Jin Chen[b], Yinpei Wang[c]

Key Lab of Safety Science of Pressurized System, Ministry of Education, School of Mechanical Engineering, East China University of Science and Technology, Shanghai, 200237, China

E-mail: [a]cwang@ecust.edu.cn; [b]chenjin@ecust.edu.cn; [c]ypwang@ecust.edu.cn*

In chemical processing plants and petroleum refineries, the pressure vessels and pipelines suffered often from fire accidents and thus resulted in the metal materials were in overheating state. Elevated temperature could cause the changes in metallographic structure and have unfavorable effects on material mechanical properties. In order to understand better the influence laws of overheating on metallographic structures and material mechanical properties, the methods of theoretical analysis and experimental research were used and the effects of thermal exposure temperature, duration time and cooling rate on microstructure and mechanical properties of low-alloy steel 12MnNiVR, were studied systematically. In the paper, mechanical testing are carried out to understand changes in the mechanical properties that would be observed in the metal exposed to elevated temperatures during a fire accident. The study can provide basis data for the material properties database of metal material suffered from fire accident, and afford technical supports in the key technologies on fire damage FFS (Fitness-For-Service) integrity assessment.

Keywords: 12MnNiVR; Material Degradation; Low-Alloy Steel; Fire Damage.

1. Introduction

12MnNiVR is the low-alloy steel with high strength for large oil storage tanks. Based on C-Si-Mn alloying series and supplemented by Mo,V,B,Ni,Ti and other micro-alloying elements, steel 12MnNiVR can obtain high tensile strength above 610MPa by reasonable heat treatment with quenching and tempering. Alloying elements can be dissolved fully in austenite with elevated temperature and precipitated as carbides and nitrides particles during cooling and thus can improve the strength and other mechanical properties of steel 12MnNiVR [1-2]. Studies have

[1] Corresponding author.

shown that the steel possesses excellent comprehensive performance, such as high strength, high toughness and good weldability under high heat input, and also can withstand the large external energy input during welding [3-5,17].

In chemical processing plants and petroleum refineries, the oil storage tanks suffered often from the fire accidents [6] and thus resulted in the metal materials were in overheating state. Elevated temperature could cause the changes in metallographic structure and have unfavorable effects on material mechanical properties (such as decreasing strength and toughness) and thus the tanks could not continue to be in service properly. In order to correctly assess whether the crude oil storage tank works safely after the fire damage, and to understand better the influence laws of overheating on metallographic structures and material mechanical properties, it is necessary to research on the material degradation associated with fire accident environment.

Referencing to the research results existed and relevant standards [6-8] and using a combination method of theoretical analysis and experimental testing, the material deteriorating of steel 12MnNiVR with elevated temperature were researched in the paper. The thermal simulation experiments were made with different heat treatment methods, and the effects of thermal exposure temperature (700ºC, 830ºC, 950ºC, 1000º,1100ºC), duration time (2h, 4h, 8h, 12h) and cooling rate (air-cooled and water-cooled) on mechanical properties of low-alloy steel 12MnNiVR, were studied systematically. Mechanical tests (hardness tests) are carried out to understand the changes in mechanical properties that would be observed in the metal exposed to elevated temperatures during a fire accident. The studies can provide basis data for the material properties database of metal material suffered from fire accident and afford technical supports in the key technologies on fire damage FFS integrity assessment.

2. Chemical composition, original microstructure and mechanical properties

The chemical composition analysis of sample taken from steel plates in supplier states were made, and the results are shown in the Table 1.

The metallurgical structure of steel plates in supplier states is composed of tempered sorbite, a small amount of ferrite, tiny carbides and nitrides, as shown in Fig. 1. The actual austenite grain size tests were carried out by oxidation method [12], and the actual austenite grain appearance is shown in Fig. 2. Using the comparative method [12], the average actual austenite grain-size number of original state was evaluated for 8.5.

Table 1. Chemical composition of the tested steel (mass%).

Element	C	Si	Mn	P	S	Cu	Ni	Cr	Mo	V
Content	0.092	0.180	1.500	0.009	0.001	0.025	0.210	0.029	0.100	0.042
GB19189-2011[11]	≤0.15	0.15~0.40	1.20~1.60	≤0.020	≤0.010	≤0.25	0.15~0.40	≤0.30	≤0.30	0.02~0.06

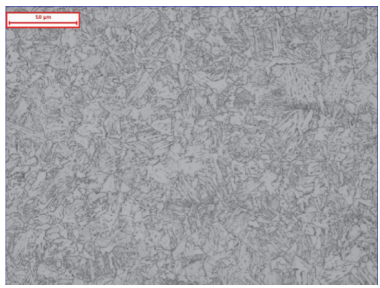


Fig. 1 Original metallurgical structure.



Fig.2. Original austenite grain appearance.

The mechanical properties tests [13-15] were carried out for steel plate 12MnNiVR in supplier states (thickness 21mm), and some of experiment data are shown in Table 2. The vickers hardness values are 208HV10, 210HV10, and 204HV10 respectively, and the average vickers hardness is 207HV10.

Table 2. Experiment data of steel 12MnNiVR in original state.

Sampling Direction	Tensile Test at Room Temperature			Impact Test	
	Proof Strength R_{eL}/MPa	Tensile Strength R_m/MPa	Elongation A/%	Temperature (ºC)	CVN Absorbed Energy KV_2/J
Lateral	546,545,543 (545)	631,630,630 (630)	24,26,25 (25)	20	> 300, > 300, > 300
				-20	> 300,263,256
Longiintudal	535,536,544 (538)	621,622,629 (624)	26,26,25.5 (26)	20	> 300, > 300, > 300
				-20	> 300, > 300, > 300
GB19189-2011	≥490	610~730	≥17	-20	≥80

3. Effects of thermal exposure temperature, duration time and cooling rate on mechanical properties

The thermal simulation experiments were carried out in accordance with the test plan. Followed corresponding standards, the mechanical property tests of samples with different heat treatment were made, and the test data are shown in Fig. 3-Fig. 4. When the temperature is heated to 700ºC, which the temperature is below the critical phase transition temperature AC1 [16], there is no phase transition occurring in the whole process of thermal simulation, so the cooling rate has no

effects on mechanical properties and microstructures of steel. With the extension of heat preservation time, the cementite gathered grows up and coarsen gradually (as shown in Fig. 5), and thus have adverse effects on mechanical properties of materials. At the same time, due to high temperature tempering decreases dislocation density in ferrite matrix, therefore the strength is weakened and lower than the original ones, but with a little change, thus shows good tempering stability.

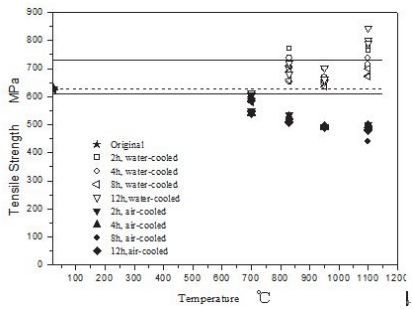


Fig. 3 Tensile strength test data duration.

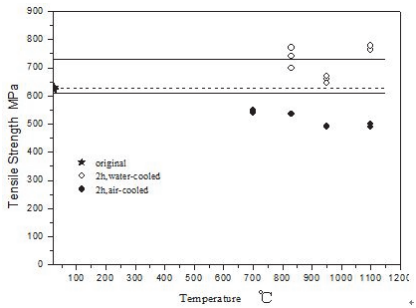


Fig. 4 Part tensile strength test data (2h).

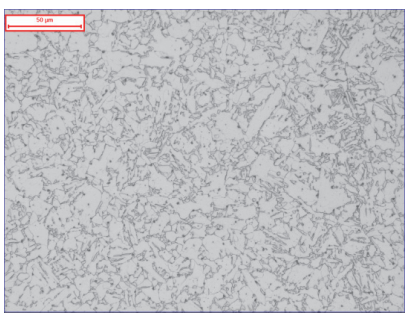


Fig. 5 Microstructure with 12hours 700ºC, air-cooled.

When the heating temperature exceed the phase change temperature A_{C1}, the austenite transforms to martensite and bainite in the process of water cooling, so the strength of the sample are higher than those of original state, and the opposite trend can occur when the ferrite phase is emerged during air cooling. Due to the second phase of granular dispersed particles, which is formed by micro-alloying elements V,Cr,Mo,Ti, etc, can effectively prevent the grain and microstructure growth and coarsening, therefore, the influences of heat preservation time on mechanical properties of steel are small. With the increasing of thermal simulation temperature, the strength of sample decrease under the condition of air cooled, and increase with the increasing of martensite and bainite under the condition of water

cooled, but when the temperature exceeds 950ºC, the strength decrease slightly as the microstructures of sample grow up. In the individual sample, due to lack of martensitea and bainite in the microstructure, the strength decrease after cooling.

4. Conclusion

Based on the analysis of test data, when the thermal exposure temperature is below the critical phase transition temperature AC1, the cooling rate has no effects on mechanical properties and microstructures of steel. When the thermal exposure temperature is higher than the critical phase transition temperature AC1, and under the different cooling rate, there is a big difference in mechanical properties due to the difference of microstructure. When the air cooling is adopted, the mechanical properties of sample are lower than that of the original state, and when the water cooling is adopted, the strength of sample is greater than that of original state.

Acknowledgement

This work was sponsored by the important project of 12th National Science and Technology Support Plan Program (2012BAK03B02).

References

1. Zhang Xiaohu, Li Xiaoyan. Exploitation and Application of High Input Energy Welding Steel Plate for Oil Storage. *Pressure Vessel Technology*, 2003, 20(1): 16-19 (In Chinese).
2. Zhao Yanling. Effect of Micro-alloying Elements on the Properties of Quenched and Tempered Low Alloy High Strength Steel. *Wide and Heavy Plate*, 2004, 10(5): 14-19.
3. Wang Hui, Zheng Yunlong, Pu Huaquan, et al. Research on Welding Crack Test of 12MnNiVR Steel. *Pressure Vessel Technology*, 2003, 20(7): 19-23.
4. Yan Han, Zhao Wengui, Hua Yanping et.al., Weldability of 610MPa Grade High Strength Plate Steel 12MnNiVR for Oil Storage Tanks. J*ournal of Iron and Steel research*. 2011, 18 (S1-2): 769-772.
5. Zhang Xiaohu, Gu Xianshan. Brief Introduction of GB 150.2-2011 Pressure vessels-Part 2: *Materials. Pressure Vessel Technology*, 2012, 29(4): 42-52.
6. Xuedong Chen, Zhibin Ai, Zhichao Fan et.al. Integrity Assessment of Pressure Vessels and Pipelines under Fire Accident Environment. *Proceeding of the ASME 2012 Pressure Vessels & Piping Conference*. 2012.
7. Tsutomu Kikuchi et al., Fitness-For-Service Assessment for Fire Damage in Pressure Equipemnt. ICPVT-13.
8. API 579-1/ASME FFS-1. Fitness-For-Service. *API/ASME*, 2010.

9. GB/T20123. Steel and iron-Determination of total carbon and sulfur content Infrared absorption method after combustion in an induction furnace (routine method), 2006 (National Standard, In Chinese).
10. GB/T4336. Standard test method for spark discharge atomic emission spectrometric analysis of carbon and low-Alloy steel (routine method), 2002 (National Standard, In Chinese).
11. GB19189. Quenched and tempered high strength steel plates for pressure vessels, 2011 (National Standard, In Chinese).
12. GB/T6394. Metal-methods for estimating the average grain size, 2002 (National Standard, In Chinese).
13. GB/T4340.1. Metallic Materials-vickers hardness test, Part 1: test method, 2009 (National Standard, In Chinese).
14. GB/T228.1. Metallic materials-Tensile testing, Part 1: Method of test at room temperature, 2010 (National Standard, In Chinese).
15. GB/T229. Metallic meterials-Charpy pendulum impact test method, 2007 (National Standard, In Chinese).
16. Zhang Zhimin, Cai Qingwu, Yu Wei. Continuous cooling transformation behavior and transformation kinetics of 12MnNiVR steel. *Transactions of Materials and Heat Treatment*, 2013, 34(4): 143-147.
17. Yiang Yunqing, LiuJiwen, Zhang Yongwei, et al. Heat Treatment Properties of Steel 12MnNiVR and Its Toughness in Welding Corse Region. *Pressure Vessel Technology*, 2013, 30(9): 11-19 (In Chinese).

Preparation of Nanoporous Nickel Phosphates with Surfactants and Application in Intumescent Flame Retardant Polypropylene Composites

Shibin Nie[a†], Xiang Dong[b], De-yi Wang[d*], Chao Peng[e]

Key Laboratory of Coal Mine Safty and Efficient Exploitation of Minstry of Education, School of Energy Resources and Safety, Anhui University of Science and Technology, Huainan, Anhui 232001, China

E-mail: [a†]nsb@mail.ustc.edu.cn; [b]654091832@qq.com; [d]23941517@qq.com; [e]541182587@qq.com

Lei Liu[c]

School of Mechanics, Southeast University, Nanjing 210096, China

E-mail: [c]liulei@seu.edu.cn

Nanoporous nickel phosphates with Surfactants OA-12, CAB-35 and OP-10 have been synthesized. The structure and morphology of nanoporous nickel phosphates were investigated. Then the synthesized nanoporous nickel phosphates were applied in intumescent flame retardant polypropylene (PP) composites. The flame retardant properties of PP composites were investigated by LOI test. The structure of nanoporous nickel phosphates does not greatly influenced with the addition of OA-12, CAB-35 and OP-10, but the morphology of nanoporous nickel phosphates shows some changes. The result of LOI test show that nanoporous nickel phosphates with CAB-35 can improve the intumescent flame retardant PP composites better.

Keywords: Nanoporous Nickel Phosphates; Intumescent Flame-retardant; Polypropylene.

1. Introduction

Nanoporous nickel phosphates with high thermal stability has structure like zeolites [1] and has excellent prospects of applications in many areas, such as ion exchange, hydrogen deposit [2], as well as catalytic properties [3]. In our previous work, one kind of nanoporous nickel phosphates-VSB-1 had demonstrated that had an excellent synergistic effect with traditional intumsecent flame retardant based on ammonium polyphosphate (APP) and pentaerythritol PER [4]. However, intumsecent flame retardants based on APP and PER have some shortcoming, such as low water resistance.

† Corresponding author.

CFA and silica-gel microencapsulated APP (Si-MCAPP) microencapsulated by SiO_2 gel has been used to form novel intumescent flame retardant system (IFRs), and the research demonstrates the IFRs have excellent water resistance [5]. However, the flame retardant efficiency of IFRs still needs to be further improved.

So in this work, nanoporous nickel phosphates with surfactants OA-12 (N, N-dimethyldodecylamine-N-oxide sol.), CAB-35 (cocoamidopropyl betaine) and OP-10 (alkylphenol ethoxylates) were synthesized. The structure and morphology of nanoporous nickel phosphates were investigated. Then the synthesized nanoporous nickel phosphates were applied in intumescent flame retardant polypropylene (PP) composites.

2. Experiments

2.1. *Materials*

PP (homopolymer, melt-flow rate=2.5g/10min) was supplied as pellets by Yangzi Petrochemical Co. (China). CFA and Si-MCAPP were synthesized in our lab [6, 7]. Nickel nitrate hexahydrate ($Ni(NO_3)_2 \cdot 6H_2O$, 98.5%) was bought from Sinopharm Chemical Reagent Co. Ltd. Phosphoric acid (H_3PO_4, 8%), NH_4F (96%) and ammonia were bought from Wuxi Zhanwang Chemical Reagent Co., Ltd. OA-12, CAB-35 and OP-10 were provide by Kehongda Co. Ltd.

2.2. *The synthesis of nanoporous nickel phosphates*

Surfactant (OA-12, CAB-35 or OP-10) was dissolved with deionized water, and $Ni(NO_3)_2 \cdot 6H_2O$, H_3PO_4 and NH_4F were added to the above solution. Then ammonia was dropped to adjust the pH to 2.5. Making the molar ratios of the mixture to be $1.0H_3PO_4$:1.0 $Ni(NO_3)_2$: $1.0NH_4F$: 0.1Surfactant:$40H_2O$. The mixture was sealed in Teflon-lined stainless steel autoclaves at 180ºC for 4 days. The solid was obtained after washing with plenteous deionized water and dried at 80ºC for 12h. The samples were named NiP-1 (with OA-12), NiP-2 (with CAB-35), and NiP-3 (with OP-10).

2.3. *The preparation of samples*

PP, Si-MCAPP, CFA and nanoporous nickel phosphates were dried in vacuum oven at 80ºC before use. Then PP, Si-MCAPP, CFA and nanoporous nickel phosphates were melt-mixed in a twin-roller mill (XSS-300, China) for 10 min at 175ºC. The samples are listed in Table 1.

Table 1. Formulations of the flame retardant PP composites (IFR: Si-MCAPP /CFA=3/1, by weight).

Samples	Compositions
PP1	PP+IFR(30.0%)
PP2	PP+IFR(29.0%)+ NiP-1(1.0%)
PP3	PP+ IFR(29.0%)+ NiP-2(1.0%)
PP4	PP+ IFR(29.0%)+ NiP-3(1.0%)

2.4. *Characterization*

LOI was measured according to ASTM D2863, and the apparatus used was an HC-2 oxygen index meter (Jiangning Analysis Instrument Company, China). The specimens dimensions used for test were 100×6.5×3 mm^3.

The scanning electronmicroscopy (SEM) image of the residue after the LOI test was taken using a KYKY-2800B scanning electron microscope produced by Zhongke Keyi Company. The char was adhibitted on the copperplate, and then coated with gold/palladium alloy ready for imaging.

3. Results and discussion

3.1. *Characterization of the NiP*

Fig.1 shows the XRD patterns of nanoporous nickel phosphates The XRD patterns show the nanoporous nickel phosphates have good crystallinity, and diffraction peak at a small angle in 2θ means the framework structure inner may be more open. The position of diffraction peaks appearing in Fig. 1 is just like the report in the literature [8], demonstrating the synthesis of nanoporous nickel phosphates has the same structure as VSB-1. It can be observed from Fig. 1, the structure of nanoporous nickel phosphates does not greatly influenced with the addition of OA-12, CAB-35 and OP-10.

The SEM photographes of nanoporous nickel phosphates are shown in Fig. 2. The morphology of nanoporous nickel phosphates is influenced by surfactants. The morphology of NiP-1, NiP-2 and NiP-3 shows some differences. NiP-2 has a large mushroom shape formed by gathering a lot of sharp needle-shaped particles. NiP-1 also has a mushroom shape, but the shape is different from that of NiP-2. It is just like part of NiP-2. NiP-3 has kinds of morphologies, such as needle-shape, part of mushroom shape and mushroom shape.

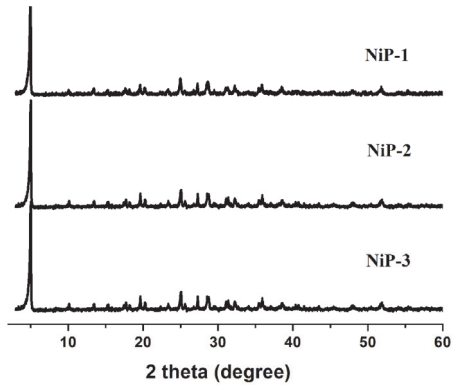


Fig. 1 XRD patterns of nanoporous nickel phosphates.

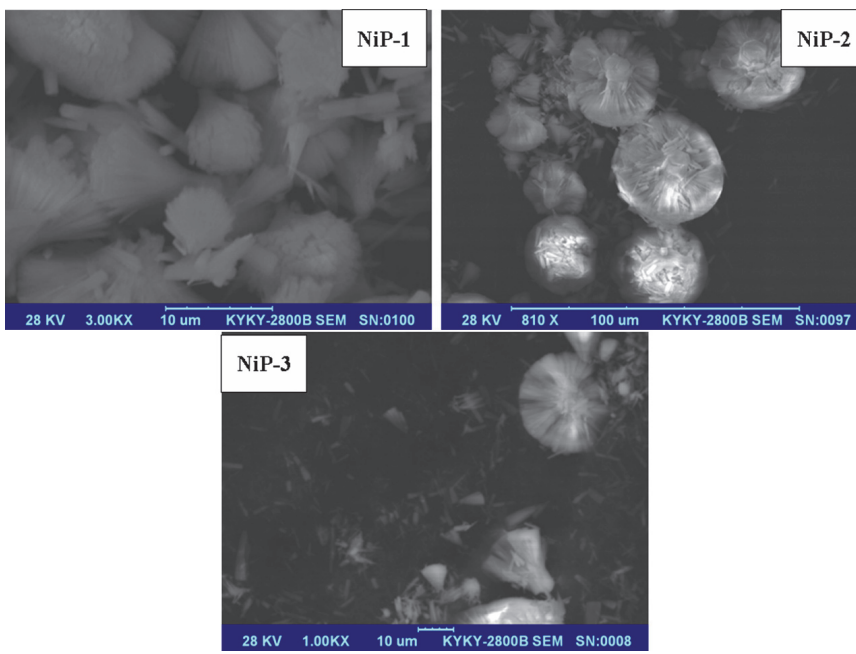


Fig. 2 The SEM photographes of nanoporous nickel phosphates.

3.2. *LOI analysis*

The LOI results of flame retardant PP composites are shown in Fig. 3. PP is a kind of combustible polymer matrix, and the LOI value is about 17.5%. With addition of 30% IFRs, the LOI value of PP1 without nanoporous nickel phosphates is

40.0%. Keeping the total amount of additives as 30wt% unchanging, with the addition of 1 wt% nanoporous nickel phosphates, the LOI value of PP2, PP3 and PP4 is 41.3%, 42.6% and 41.5% respectively. The LOI value of flame retardant PP composite increases meaning the improvement of flame retardant PP composites. It can be observed from the above results that NiP-2 shows the better synergistic effect with novel intumescent flame retardants.

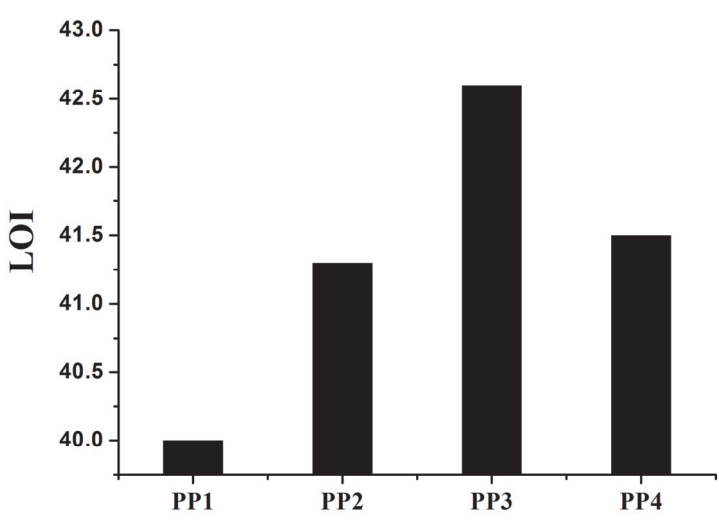


Fig. 3 The LOI results of flame retardant PP composites.

4. Conclusions

Nanoporous nickel phosphates with Surfactants OA-12, CAB-35 and OP-10 have been synthesized. Then the synthesized nanoporous nickel phosphates were applied in intumescent flame retardant PP composites. The structure of nanoporous nickel phosphates does not greatly influenced with the addition of OA-12, CAB-35 and OP-10, but the morphology of nanoporous nickel phosphates shows some changes. The result of LOI test show that with the addition of nanoporous nickel phosphates, the flame retardant property of PP composite increases. NiP-2 shows the better synergistic effect with novel intumescent flame retardants.

Acknowledgements

The work was financially supported by National Natural Science Foundation of China (No.51303004, U1332134), the Specialized Research Fund for the

Doctoral Program of Higher Education of China (No.20133415120001) and the revitalization plan in Anhui.

References

1. N. Guillou, Q. Gao, M. Nogues, R. E. Morris, M. Hervieu, G. Férey, Zeolitic and magnetic properties of a 24-membered ring porous nickel(ll) phosphate, VSB-1. *C. R. Acad. Sci.* Paris 2, (1999) 387–392.
2. P.M. Forster, J. Eckert, J.S. Chang, E.S. Park, G. Férey, A.K. Cheetham, Hydrogen Adsorption in Nanoporous Nickel(II) Phosphates, *J. Am. Chem. Soc.* 125 (2003) 1309–1312.
3. X.L. Wang, Q.M. Gao, Preparation and photocatalytic activity of titanium oxide anchored on the channel surface of nanoporous material VSB-1, *Materials Letters*, 59 (2005) 446–449.
4. S.B. Nie, Y. Hu, L. Song, S.Q. He, D.D. Yang, Study on a novel and efficient flame retardant synergist-nanoporous nickel phosphates VSB-1 with intumescent flame retardants in polypropylene, *Polym. Adv. Technol.* 19 (2008) 489–495.
5. S.B. Nie, P. Chao, S.J. Yuan, M.X. Zhang, Thermal and Flame Retardant Properties of Novel Intumescent Flame Retardant Polypropylene Composites, *J Therm Anal Calorim.* 113 (2013) 865–71.
6. P. Bai, B. Li, S.L. Gao, M. Lin, M. Wang, Investigation on flame retardancy and antidripping of new intumescent flame retardant polypropylene film, *Polymers & Polymer Composites,* 18 (2010) 469–476.
7. J.X. Ni, L.J. Chen, K.M. Zhao, Y. Hu, L. Song, Preparation of gel-silica/ ammonium polyphosphate core-shell flame retardant and properties of polyurethane blends, *Polym. Adv. Technol.* 22 (2011) 1284–1231.
8. X.L. Wang, Q.M. Gao, C.D. Wu, J. Hu, M.L. Ruan, Preparation, channel surface hydroxyl characterization and photoluminescence properties of nanoporous nickel phosphate VSB-1, *Micro. Meso. Mater* 85 (2005) 355–364.

Precipitate Analysis of Nanoparticle-Reinforced Tin Bronze Using Atom Probe Tomography

Kai-Xuan Chen[a], Ya-Wei Niu[b], Ding Ding[d] and Zi-Dong Wang[e*]

School of Materials Science and Engineering, University of Science and Technology Beijing, Beijing 100083, People's Republic of China

E-mail: [a]974235951@qq.com

[b]niuyawei0322@hotmail.com

[d]109428436@qq.com

[e]wangzd@mater.ustb.edu.cn*

Xiao-Hua Chen[c]

State Key Laboratory for Advanced Metals and Materials, University of Science and Technology Beijing, Beijing 100083, People's Republic of China

E-mail: [c]2837783219@qq.com

In this paper, APT (atom probe tomography) plays a key role in researching the nanoparticles in new ZCuSn10Zn2FeCo alloy. In the alloy, Fe and Co are used to strengthen ZCuSn10Zn2 alloy by improving convective condition during solidification to obtain in-situ iron-rich nanoparticles embedded inside the micrometer-sized grains. The TEM and HRTEM results show that the mosaic structure of a large number of in-situ generated iron nanoparticles embedded in the copper matrix grain and the coherent interface between the nanoparticle and copper matrix. The composition, size, shape and distribution of iron nanoparticles were analyzed by APT which reveals the iron-rich phase precipitation mechanism and identify the two types of iron nanoparticles reinforcement mechanism: The iron nanoparticles hinder the Sn segregation leading the disappearance of continuous hard brittle δ phase and promote grain refinement through heterogeneous nucleation effect. The character of other elements in the alloy was also analyzed by APT technology.

Keywords: Tin Bronze Alloy; Three-dimensional Atom Probe; Nanoparticles.

1. Introduction

Tin bronze alloy with excellent process ability and good corrosion resistant performance is widely used to make wear-resisting components, corrosion resistant components, electrical devices and other components, such as ship pump body, contact wire used in high-speed train and conductive switch, etc [1].

* Corresponding author.

Nowadays, the development of modern technology not only depends on the performance of metal materials, but also need to develop higher performance and more comprehensive metal materials [2]. For the higher performance of Tin bronze alloy, new in-situ iron nanoparticle reinforced Cu–3Sn–8Zn–6Pb alloy has been fabricated by centrifugal casting in a vacuum chamber with a medium frequency electrical furnace, and a uniform distribution of nanoparticles have been observed in the such alloy which exhibits an excellent comprehensive mechanical properties [3]. These particles appeared to be iron-rich phase, with a cubic lattice and a parameter of 2-20 nm, and they were generated by the in situ method during solidification [3]. It was reported [3] that the formation of these very fine particles led to an increase in strength of 420 MPa and no decrease in plasticity of 25.4%. However, the detailed analysis of these particles has not been performed to date due to their nanoscale size. Fortunately, Atom-probe tomography (APT) could provide unparalleled insights into the three-dimensional nanoscale structure which has not only revealed phenomena that could only be hypothesized, such as clustering phenomena, grain boundary segregation, nanostructural evolution, and the chemistry of buried interfaces, but has also allowed the observations of atoms and defects in 3D with accuracy never achieved heretofore [4]. In this work, in-situ iron-rich nanoparticle strengthened ZCuSn10Zn2 alloy was manufactured using centrifugal casting method. APT will be used to carry out a detailed investigation of precipitates formed in cast Tin bronze alloy containing additions Fe and Co.

2. Experiments Procedure

The investigated Tin bronze alloys, containing Cu-10Sn-2Zn wt.% and Cu-10Sn-2Zn-1.5Fe-0.5Co wt.%, were fabricated by centrifugal casting in a vacuum chamber (ultimate vacuum level 6.0×10^{-2} Pa) with a medium frequency electrical furnace. The microstructure was characterised by Optical Microscope and TEM. The atomic level of particle characterisation was performed at the University of Shanghai using a local electrode atom probe (LEAP 4000XHR). APT was carried out using a pulse repetition rate of 200 kHz and a 20% pulse fraction on the sample with temperature of 50 K. The extent of solute-enriched regions (radius of gyration) and the local solute concentrations in these regions were estimated using the maximum separation envelope method with a grid spacing of 0.1 nm. A maximum separation distance between the atoms of interest of d_{max} = 0.6 nm and the smallest atom number of clusters of N_{min}=10 was used.

3. Results and Discussion

3.1. *Microstructure of the as-cast samples*

The OM photos of the cast CuSn10Zn2 alloys without iron and with 1.5% Fe are shown in Fig. 1(a) and (b), respectively. In the white region of Fig. 1(a), the typical dendritic casting structure with various orders of the developed dendrite arms is shown. The microstructure of cast CuSn10Zn2Fe1.5Co in Fig. 1(b) is mainly with equiaxed crystallites with the average grain diameter from 40 to 100 μm. Besides, there is a decrease of δ phase (tin-rich phase) of CuSn10Zn2 with iron compared to that of virgin CuSn10Zn2 alloy. Fig. 2(a) shows the well-dispersed particles with very small size of 2-20 nm distribute in copper matrix. HRTEM micrograph of a nanoparticle is been shown in Fig. 2(b), in which the iron nanoparticle has a coherent or semi-coherent relationship with copper matrix.

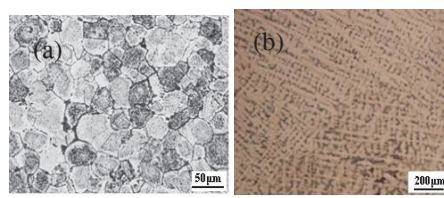


Fig. 1. OM micrographs of the copper alloys: (a) ZCuSn10Zn2 and (b) ZCuSn10Zn2Fe1.5Co.

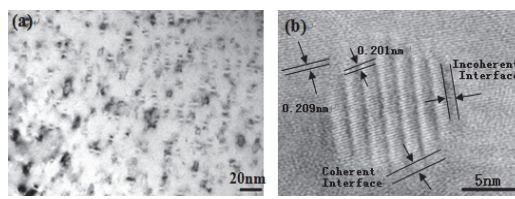


Fig. 2. HRTEM micrographs of iron nanoparticles

3.2. *APT analysis of the as-cast samples*

Two sets of simples sectioned from the different part of cast CuSn10Zn2Fe1.5Co were analyzed by atom probe tomography. Fig. 3 shows APT characterisation of particles in two sets of simples, the APT study revealed the formation of nanoscale particles containing Fe, Co atoms (Fig. 3). Based on the maximum separation method, ~10 particles were investigated (Fig. 3(b) and (c)). The precipitates showed an almost rounded or planar shape and a crystallographic arrangement of atoms (Fig. 3(d)). Fe-Co particles with different size distribute homogeneously, the equivalent radius Rp [6] of these Fe-Co particles in the form of spherical shape was calculated and is about 0.21~0.66 nm.

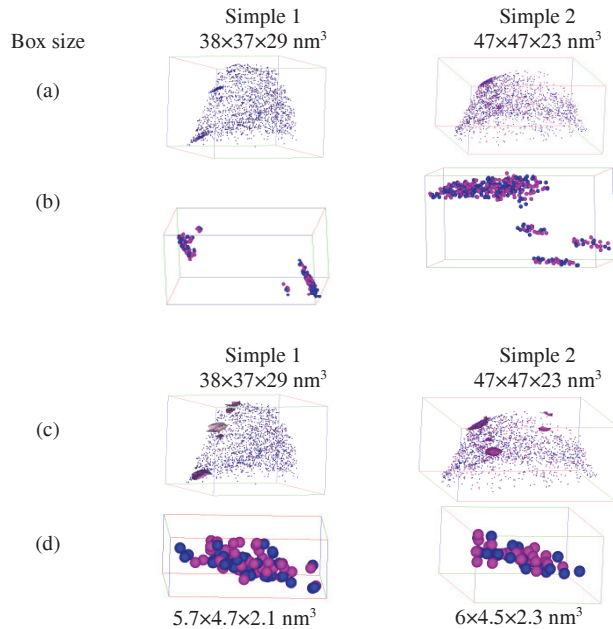


Fig. 3. APT characterisation of particles: (a) Fe, Co atom map; (b) Fe, Co particles; (c) corresponding 2 at.% Fe-Co iso-concentration surface; (d) selected atom map of Fe-Co particle. The matrix atoms for (b)–(d) were suppressed with the maximum separation method with d_{max}= 0.6 nm. The total number of atoms analysed in (a) is 1007992.(Fe; Co)

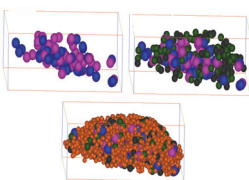


Fig. 4. A 3D atom map reconstruction of a volume containing a single.3.582-nm-diameter Fe-Co.particle.using.2.at.%.Fe alloy isoconcentration surface as the precipitate/matrix interface. (Cu; Fe; Co; Sn; Zn)

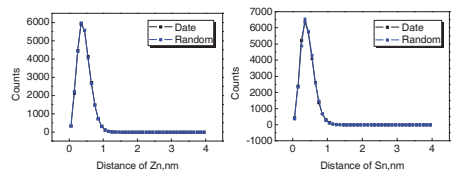


Fig. 5. Solute NND analysis of Zn,Sn in ZCuSn10Zn2Fe1.5Co.

A 3D atom map reconstruction of a Fe-Co particle (selected from Fig. 3(b)) adding Cu, Sn, Zn atoms is been displayed in Fig. 4. The particle exhibits a core-shell distribution in which Fe, Co atoms arrange alternately forming the core, copper atoms wrap in the Fe-Co core periphery, which visually illustrates iron particles serve as nucleation centers of the copper matrix, and a small

amount of Zn, Sn atoms segregated at copper/Fe-Co core interface which necessarily affect lattice misfit between iron nanoparticle and copper matrix [7].

The Guinier radius [6,8], which represents the actual size of particles, was calculated using data for radius of gyration obtained by the maximum separation envelop method [6]. The average Guinier radius of particles (contain Cu, Sn, Zn, Fe, Co atoms) was 1.34 ± 0.97 nm, some of which was not detected using TEM. The compositional analysis of all particles revealed that the average composition of these particles was 31.03±7.52 at.% Fe, 41.07±7.1 at.% Cu and 23.99±6.91 at.% Co with a trace of Zn, Sn. It's known that Fe, Co have a similar melting point (Fe 1534ºC, Co 1495ºC) much higher than copper (1083ºC), in other words, they almost have a same higher solidification point resulting the prior in-situ precipitation in copper liquid at the same time [9]. Additionally, FCe and Co are with belong iron group metals with ferromagnetism, so the magnetic coupling effect between teeny magnetic Fe clusters and Co clusters may promote the combination of them resulting the phenomenon above [10].

Solute NND analysis [11] of Zn, Sn in ZCuSn10Zn2Fe1.5Co alloy are been displayed in Fig. 5 which showed that experimental atom distance curve of Sn, Zn was almost consistent with atomic distance curve at random distribution state, so there was no obvious segregation or aggregation of Sn, Zn in ZCuSn10Zn2Fe1.5Co alloy. Fig. 4 shows a tin segregation at the iron nanoparticles, in other words, iron nanoparticles have a role in hindering tin segregation.

According to the melting point and the atomic radius of each element [9,12] combining with the above analysis, the formation process of nanoparticles could be speculated as following: Firstly, Fe, Co atoms with high melting point dissolved out from high temperature copper liquid and these Fe, Co atoms or small particles combined to form nanocluster cores; Liquid Cu, Zn, Sn atoms met with Fe-Co clusters and migrated into vacancies of the clusters during their migration process, while it was hard for them to squeeze into atomic interstice of Fe, Co clusters because of their biggish atomic radius; Then Cu atoms contacted directly with Fe-Co clusters dissolved out with the temperature decrease, stacking in the periphery of Fe-Co nanocluster cores or staying in the Fe-Co vacancies; Liquid Zn, Sn atoms in Fe-Co clusters vacancies were still been trapped by solid Fe, Co, Cu atoms until the room temperature and eventually became part of the nanoparticles.

3.3. *Effect of iron nanoparticles on the grain refinement*

In the metal casting industry, it is common practice to introduce nucleating agents to a liquid metal, referred to as inoculation, for the formation of fine,

uniform and equiaxed non-dendritic grains [13]. There are many dispersed spherical nanoparticles and a relatively small number of micron particles as shown in Figs. 1(a), 2, 3. Furthermore, these iron particles precipitate before the copper precipitation. Similar as the grain refined effect from spherical Zr particles on magnesium matrix [13-15], Cu and Fe, Co have the same type of crystal structure and almost identical lattice constants at high temperature(T≥916ºC) [12], and iron nanoparticles in Fig. 2(b) has a better coherent relationship with copper matrix. Because of the very similar crystallographic characteristics, it is reasonable to assume that iron particle could be the potent heterogeneous nucleation substrate for copper [13]. As shown in Fig. 1, the grains of ZCuSn10Zn2Fe1.5Co are almost equiaxed crystallites with smaller size compared to the thick dendrites of original ZCuSn10Zn2, we believe that these iron nanoparticles play a significant role in the grain refinement by acting as nucleating centers during the solidification of the copper matrix.

3.4. *Effect of iron nanoparticles on the tin segregation*

Compared with the original ZCuSn10Zn2 alloy, the bright white δ phase of new ZCuSn10Zn2Fe1.5Co alloy is decrease. Sn in ZCuSn10Zn2Fe1.5Co alloy distributes fairly uniform from the NND analysis (Fig. 5). According to the above analysis, we assume that the prior precipitating of a large number of iron nanoparticles in metallic melt is the main reason of δ phase reduction. In the solidification process of ZCuSn10Zn2Fe1.5Co alloy, nanoparticles consisted of Fe and Co would precipitate in priority. Soon afterwards, because of the coherent structure and similar crystallographic characteristics between the nanoparticles and the copper matrix, it is reasonable to assume that nearly complete wetting occurs on all crystalline faces of the iron substrate exposed to molten Cu [13]. According to the solute redistribution theory and solute trapping models [12,16], solid/liquid (S/L) interface advances into liquid with the velocity of $V_{S\text{-}L}$ as the copper grain growth, at the same moment, low-melting-point Zn, Sn atoms continuously move away from S/L interface and diffuse into liquid phase, doing random Brownian motion. With the presence of large number of iron nanoparticles in the S/L interface forefront, most of the Sn atoms would meet with these uniform distributed nanoparticles with large specific surface area, some of Sn atoms attach into vacant site on the surface of the nanoparticles and are swallowed by the further growing of the particles, which is coincided with the tin segregation at the iron nanoparticles shown in Fig. 4; the other part of Sn atoms would be bounced back by the nanoparticles and have no forward

diffusion. Eventually, all nanoparticles and most of Sn atoms would be engulfed by solid phase and there will be an obvious reduction of tin segregation. Without these iron nanoparticles, however, Sn atoms would move away from the solid phase and diffuse forward to the grain boundary without obstacle, forming larger scale tin-rich δ phase at grain boundary.

4. Conclusion

The characterisation of iron nanoparticles in Tin bronze were analyzed detailedly by APT, which reveals these iron nanoparticles uniformly dispersed in copper matrix have a positive effect on the copper grain refinement and hard brittle tin-rich δ phase reduction.

Acknowledgments

This work was supported by the Specialized Research Fund for the Doctoral Program of Higher Education of China (No. 20100006110026). The authors thank Doctor Li for the APT examination at the University of Shanghai and for helpful discussions.

References

1. Sadykov F A, Barykin N P, Aslanyan I R, Wear of copper and its alloys with submicrocrystalline structure, *Wear*, 225-229(Part1) (1999) 649-655.
2. Lu K, The future of metals, *Science*, 328 (2010) 319-320.
3. Zidong Wang, Xuewen Wang, Qiangsong Wang, I Shih and J J Xu, Fabrication of a nanocomposite from in situ iron nanoparticle reinforced copper alloy, *Nanotechnology*, 20 (2009) 1-6.
4. Emmanuelle A. Marquis, Michael K. Miller, Didier Blavette, Simon P. Ringer, Chantal K. Sudbrack, and George D.W. Smith, Structural Materials: Understanding Atomic-Scale Microstructures, *MRS BULLETIN,* 34 (2009) 725-730.
5. Jang Sik Park, Cheol Woo Park, Keun June Lee, Implication of peritectic composition in historical high-tin bronze metallurgy, *Materials characterization*, 60 (2009) 1268-1275.
6. M.K. Miller, Atom Probe Tomography, Kluwer, Academic/Plenum Press, New York, 2000.
7. H.-T. Li, Y. Wang, Z. Fan, Mechanisms of enhanced heterogeneous nucleation during solidification in binary Al-Mg alloys, *Acta Materialia*, 60 (2012) 1528-1537.

8. I.B. Timokhina, P.D. Hodgson, S.P. Ringer, R.K. Zheng and E.V. Perelom, Precipitate characterisation of an advanced high-strength low-alloy (HSLA) steel using atom probe tomography, *Scripta Materialia*, 56 (2007) 601-604.
9. Guo Qingwei, Phase diagram manual of binary metal system, first ed., *Chemical industry press*, Beijing, 2009.
10. Zou Chang-Wu, Yao Ya-Dong, Meng Xiao-peng, Gong Yi-Chao, The synthesis of carbon encapsulated cobalt iron nanoparticles and an examination of their magnetic properties, Jo*urnal of Sichuan University* (Natural Science Edition), 50 (2013) 1075-1078.
11. Zheng Z Q, Liu W Q, Liao Z Q, Ringer S P, Sha G, Solute clustering and solute nanostructures in an Al–3.5Cu–0.4Mg–0.2Ge alloy, *Acta Mater*., 61 (2013) 3724-3734.
12. Geng-xiang Hu, Xun Cai, Yong-hua Rong, Fundamentals of materials science, third ed., *Shanghai Jiao Tong University Press*, Shanghai, 2010.
13. Ma Qian, Heterogeneous nucleation on potent spherical substrates during solidification, *Acta Materialia*, 55 (2007) 943-953.
14. Qian M, StJohn DH, Frost MT, Characteristic zirconium-rich coring structures in Mg–Zr alloys, *Scripta Mater*, 46 (2002) 649-654.
15. Qian M, StJohn DH, Frost MT, Heterogeneous nuclei size in magnesium–zirconium alloys, *Scripta Mater*, 50 (2004) 1115-1119.
16. M. J. Aziz, Model for solute redistribution during rapid solidification', *J. Appl. Phys*, 53 (1982) 1158-1168.

The Complex Band Structure of $Hg_{1-x}Cd_xTe$ Material

Xuebo Wang, and Tongsheng Xia*

School of Electronic Information Engineering, BeiHang University, Beijing 100191, China

*E-mail: wxb2013@buaa.edu.cn; *xiatongsheng@buaa.edu.cn*

The CdTe/HgTe quantum well structure has attracted a rapid growing interests due to its unique edge states and transport property. In this work, we calculated the complex band structure of $Hg_{1-x}Cd_xTe$ alloy bulk materials using six band k·p model in an envelope function approach. The complex bands of $Hg_{0.88}Cd_{0.12}Te$ (x=0.12) and CdTe(x=1) near the center of the Brillouin zone in the [001] direction are shown. The imaginary curves connect real parts of the complex bands across the band gaps. Our results will be helpful for designing CdTe/HgTe quantum well structures with better performance later.

Keywords: K. P model; Complex Band Structure; $Hg_{1-x}Cd_xTe$

1. Introduction

To understand the electronic and transport properties of surface and interface states, the imaginary electronic band structure of the constituent materials will be as important as the real part of the band structure [1], especially when it needs to take the tunneling into consideration. As discussed before, the Bloch functions with complex wave vector $\vec{k}$ can provide an effective way to deal with open quantum systems, such as, in our earlier work, we showed that due to the effect of tunneling through the complex band structure, the Id-Vg curves of CNTFETs drop to the minimum but then increase again [2]. Calculating the material complex band structure can be taken as the first step to further consider the quantum transport behavior in constituent materials.

Recently, topological insulator (TI) has attracted enormous attention in condensed matter physics. It has great potential application in semiconductor spintronics due to its peculiar gapless Dirac fermion states on the surface [3, 4, 5]. The topological insulator was first demonstrated by a two-dimensional $CdTe/Hg_{1-x}Cd_xTe/CdTe$ quantum well (QW) structure. The most intriguing thing of the $CdTe/Hg_{1-x}Cd_xTe/CdTe$ QWs is it exhibits quantum phase transition. It has shown that when the quantum well length exceeds a critical value, it becomes a topological insulator, and it exhibits the quantum spin Hall effect

(QSHE)[4]. Phase change is a very interesting thing and may be very useful. It has also found that the phase change can be made by other ways, such as, by coupling the Poisson's equation with Schrödinger's equation, Li and Chang have shown that the external applied electric field can cause a quantum phase transition for the CdTe/$Hg_{1-x}Cd_xTe$/CdTeQWs[6].This is important, and we think it will be even more interesting to calculate the quantum transport behavior in this kind of quantum well structure. Before that, however, we will use this paper to show our results on the complex band structure calculations on the materials of CdTe and $Hg_{1-x}Cd_xTe$, which we think are the first important step to further think about the quantum transport behaviors in structure and devices made with these materials. The complex band structure based on the multiband K·P model is calculated in section II, and results and conclusions are made in section III.

2. Multiband K·P Model

We use the six band k·p model for the band structure calculation. It is based on an envelope function approach introduced by Burt [7]. The strong coupling between the lowest conduction band and the highest valence band is included in the framework of the k·p theory. The corresponding effective Hamiltonian in *k*-space we used can be found in Li *et al*'s work [8].

The band structure parameters for HgTe and CdTe at 0K used in our calculation are list in Table I. The Kane parameters of $Hg_{1-x}Cd_xTe$ are assumed to be x-independent. The band gap (Eg) of $Hg_{1-x}Cd_xTe$ as a function of temperature T and stoichiometry x [9] is given by:

$$\begin{aligned} E_g(x,T) &= -303(1-x)+1606x-132x(1-x) \\ &+[4.95(1-x)+3.25x-3.93x(1-x)] \\ &\times 10^{-1}T^2/[11(1-x)+78.7x+T]. \end{aligned} \tag{1}$$

T=0K and x=0.12 or x=1 are chosen for the calculations. The wave function Ψ has the usual six-band basis set.

$$\varphi_1 = \left|\frac{1}{2},\frac{1}{2}\right\rangle = |S\uparrow\rangle, \qquad \varphi_2 = \left|\frac{1}{2},-\frac{1}{2}\right\rangle = |S\downarrow\rangle,$$

$$\varphi_3 = \left|\frac{3}{2},\frac{3}{2}\right\rangle = \frac{1}{\sqrt{2}}|(X+iY)\uparrow\rangle, \qquad \varphi_4 = \left|\frac{3}{2},\frac{1}{2}\right\rangle = \frac{i}{\sqrt{6}}|(X+iY)\downarrow -2Z\uparrow\rangle,$$

$$\varphi_5 = \left|\frac{3}{2},-\frac{1}{2}\right\rangle = \frac{1}{\sqrt{6}}|(X-iY)\uparrow +2Z\downarrow\rangle, \quad \varphi_6 = \left|\frac{3}{2},-\frac{3}{2}\right\rangle = \frac{i}{\sqrt{2}}|(X-iY)\downarrow\rangle.$$

If taken Z axis as the transport direction, the Hamiltonian can be quantized, extend $H\Psi = E\Psi$ matrix to six, coupled, one-dimensional Schrödinger equations. And the Schrödinger's equation can be discretized as:

$$[\mathrm{T}^{\dagger}][\Psi(n-1)]+([\mathrm{D}]-\mathrm{EI})[\Psi(n)]+[\mathrm{T}][\Psi(n+1)]=0. \tag{2}$$

where

$$T=\begin{bmatrix}
-\frac{\hbar^2}{2m_0}\frac{(2F+1)}{\Delta^2} & 0 & 0 & -i\sqrt{\frac{2}{3}}P\frac{1}{2\Delta} & 0 & 0 \\
0 & -\frac{\hbar^2}{2m_0}\frac{(2F+1)}{\Delta^2} & 0 & 0 & \sqrt{\frac{2}{3}}P\frac{1}{2\Delta} & 0 \\
0 & 0 & \frac{\hbar^2}{2m_0}(\gamma_1-2\gamma_2)\frac{1}{\Delta^2} & \frac{\hbar^2}{2m_0}\sqrt{3}k_-\gamma_3\frac{1}{\Delta} & 0 & 0 \\
-i\sqrt{\frac{2}{3}}P\frac{1}{2\Delta} & 0 & -\frac{\hbar^2}{2m_0}\sqrt{3}k_+\gamma_3\frac{1}{\Delta} & \frac{\hbar^2}{2m_0}(\gamma_1+2\gamma_2)\frac{1}{\Delta^2} & 0 & 0 \\
0 & -\sqrt{\frac{2}{3}}P\frac{1}{2\Delta} & 0 & 0 & \frac{\hbar^2}{2m_0}(\gamma_1+2\gamma_2)\frac{1}{\Delta^2} & -\frac{\hbar^2}{2m_0}\sqrt{3}k_-\gamma_3\frac{1}{\Delta} \\
0 & 0 & 0 & 0 & \frac{\hbar^2}{2m_0}\sqrt{3}k_+\gamma_3\frac{1}{\Delta} & \frac{\hbar^2}{2m_0}(\gamma_1-2\gamma_2)\frac{1}{\Delta^2}
\end{bmatrix}$$

$$D=\begin{bmatrix}
A+\frac{\hbar^2}{2m_0}(2F+1)\frac{2}{\Delta^2} & 0 & i\frac{1}{\sqrt{2}}Pk_+ & 0 & i\frac{1}{\sqrt{6}}Pk_- & 0 \\
0 & A+\frac{\hbar^2}{2m_0}(2F+1)\frac{2}{\Delta^2} & 0 & -\frac{1}{\sqrt{6}}Pk_+ & 0 & -\frac{1}{\sqrt{2}}Pk_- \\
-i\frac{1}{\sqrt{2}}k_-P & 0 & B+\frac{\hbar^2}{2m_0}(\gamma_1-2\gamma_2)\frac{-2}{\Delta^2} & 0 & \frac{\hbar^2}{2m_0}(\sqrt{3}\mu k_+^2-\sqrt{3}\gamma k_-^2) & 0 \\
0 & -\frac{1}{\sqrt{6}}k_-P & 0 & C+\frac{\hbar^2}{2m_0}(\gamma_1+2\gamma_2)\frac{-2}{\Delta^2} & 0 & \frac{\hbar^2}{2m_0}(\sqrt{3}\mu k_+^2-\sqrt{3}\gamma k_-^2) \\
-i\frac{1}{\sqrt{6}}k_+P & 0 & \frac{\hbar^2}{2m_0}(\sqrt{3}\mu k_-^2-\sqrt{3}\gamma k_+^2) & 0 & C+\frac{\hbar^2}{2m_0}(\gamma_1+2\gamma_2)\frac{-2}{\Delta^2} & 0 \\
0 & -\frac{1}{\sqrt{2}}k_+P & 0 & \frac{\hbar^2}{2m_0}(\sqrt{3}\mu k_-^2-\sqrt{3}\gamma k_+^2) & 0 & B+\frac{\hbar^2}{2m_0}(\gamma_1-2\gamma_2)\frac{-2}{\Delta^2}
\end{bmatrix}$$

$A=E_c(z)+\dfrac{\hbar^2}{2m_0}(2F+1)k_{||}^2$, $B=E_v(z)-\dfrac{\hbar^2}{2m_0}(\gamma_1+\gamma_2)k_{||}^2$, and $C=E_v(z)-\dfrac{\hbar^2}{2m_0}(\gamma_1-\gamma_2)k_{||}^2$. $\Psi(n)$ is the wave function at n^{th} grid point in 1D grid along z direction. The relation between two wave functions at grid points separated by Δ can be written as $[\Psi(\mathrm{n}+1)]=e^{ik_z\Delta}[\Psi(\mathrm{n})]$. (Eq.2) can also be rewritten as:

$$\left(\frac{[\mathrm{T}^{\dagger}]}{\lambda}+([\mathrm{D}]-\mathrm{EI})+\lambda[\mathrm{T}]\right)[\Psi(n)]=0. \tag{3}$$

here λ denotes $e^{ik_z\Delta}$. (Eq.3) is a polynomial eigenvalue problem for a given value of E, which can then be represented as a generalized eigenvalue problem as:

$$\begin{bmatrix} [D]-E & [T^{\dagger}] \\ I & 0 \end{bmatrix} \begin{pmatrix} \Psi(n) \\ \Psi(n-1) \end{pmatrix} = \lambda \begin{bmatrix} -[T] & 0 \\ 0 & I \end{bmatrix} \begin{pmatrix} \Psi(n+1) \\ \Psi(n) \end{pmatrix}. \quad (4)$$

Out of the twelve solutions obtained, only six are physical. These physical solutions appear as negations of each other. The non-physical solutions can be discarded by inspection.

Table I. Six-band K·P parameters for $Hg_{1-x}Cd_xTe$ (Ref.10) and CdTe (Ref.8) at 0K.

Material	E_g	F	$E_p = 2m_0P^2/\hbar^2$	γ_1	γ_2	γ_3	E_v	κ
$Hg_{1-x}Cd_xTe$	-	-0.8	19 [eV]	3.3	0.1	0.9	0	-0.4
CdTe	1.606[eV]	-0.09	8 [eV]	1.47	-0.28	0.03	-0.57	-1.31

3. Results and Conclusion

Figure 1 shows the complex band structure obtained from equation (Eq.4) by this six band K·P model. In the plot, we simply show the results with $k_{//}=(0,0)$. The complex band structure of $Hg_{0.88}Cd_{0.12}Te$ is shown in Figure 1(a), while the complex band structure of CdTe is shown in Figure 1(b). The imaginary part of the complex band structure is shown in the left part of the figure, while the real part is shown in the right part of the figure. CdTe has a large direct band gap, and the band gap of $Hg_{0.88}Cd_{0.12}Te$ is negative. For $Hg_{0.88}Cd_{0.12}Te$, the energy of the conduction-band edge is -87.86 meV and the valence-band edge is 0 eV. The loop (*abc*) on the left and the line (*rst*) on the right are the imaginary part of the band gap states for the subbands of $Hg_{0.88}Cd_{0.12}Te$ and CdTe, respectively. As expected, the imaginary dispersion curves connect bands across the band gaps.

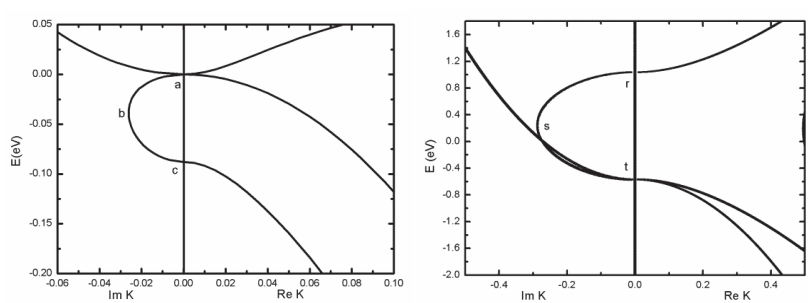


Figure 1: Complex band structure of $Hg_{0.88}Cd_{0.12}Te$ (a) and CdTe (b) in the [001] direction for complex wave vector with $k_{//}=(0,0)$.

In summary, we show the complex band structure of $Hg_{1-x}Cd_xTe$ materials. A detailed description has been presented within a six-band k·p model in the

envelope function approach. This will be useful for our later quantum transport calculation on the CdTe/HgTe QWs.

Acknowledgements

This work is support in part by Beijing natural science foundation (4122045).

References

1. Y. C. Chang andJ. N. Schulman: 'Complex band structures of crystalline solids, An eigenvalue method', *Phys.* Rev. B, 1982, 25, 3975-3986.
2. T. S. Xia, L. F. Register and S. K. Banerjee: 'Calculations and applications of the complex band structure for carbon nanotube field-effect transistors', *Phys*. Rev. B, 2004, 70, 045322.
3. C. L. Kane and E. J. Mele: 'Quantum Spin Hall Effect in Graphene', *PRL*, 2005, 95, 226801.
4. B. A. Bernevig, T. L. Hughes and S. C. Zhang: 'Quantum spin Hall effect and topological phase transition in HgTe quantum wells', *Science*, 2006, 314, 1757-1761.
5. L. Fu, C. L. Kane, and E. J. Mele: 'Topological Insulators in Three Dimensions', *PRL*, 2007, 98, 106803.
6. J. Li and K. Chang: 'Electric field driven quantum phase transition between band insulator and topological insulator', *Appl. Phys. Lett*., 2009, 95, 222110.
7. M.G. Burt: 'Fundamentals of envelope function theory for electronic states and photonic modes in nanostructures', *J. Phys.: Condens. Matter,* 1999, 11, 53-83.
8. E. G. Novik, A. Pfeuffer-Jeschke and T. Jungwirth, et al: 'Band structure of semimagnetic $Hg_{1-y}Mn_yTe$ quantum wells', *Phys.* Rev. B, 2005, 72, 035321.
9. C. R. Becker, V. Latussek, A. Pfeuffer-Jeschke, G. Landwehr, and L. W. Molenkamp: 'Band structure and its temperature dependence for type-III $HgTe/Hg_{1-x}Cd_xTe$ superlattices and their semimetal constituent', *Phys.* Rev. B, 2000, 62, 10353-10363.
10. *II-VI and I-VII Compounds, Semimagnetic Compounds*, Landolt-Börnstein, Group III, edited by U. Rössler (Springer, Berlin, 1999), Vol. 41B.

Mechanical and Structural Evolution of SiC/Zr-Si-C Coated C/SiC Composites under Thermal Shock Tests

Xiang Yang[a*], Cao Feng[b]

Science and Technology on Advanced Ceramic Fibers and Composites Laboratory, National University of Defense Technology, Changsha 410073, Hunan, P. R. China

[a] E-mail: shmily_0427@163.com, [b] E-mail: fcao@china.com*

SiC/Zr-Si-C coatings were fabricated on the surface of C/SiC composites by molten salt method and CVD method, and then mechanical and structural evolution of SiC/Zr-Si-C coated C/SiC Composites under thermal shock tests were studied. The results showed the degradation of the flexural strength properties and no mass variation. The composition of SiC/Zr-Si-C coatings was characterized by SEM and XPS. The results showed that the main constitute of the coatings was not changed after thermal shock tests. The structural of coating was changed owe to the tensile stress. Due to the debonding of the coating-matrix interfaces, the flexural strength decreased after thermal shock tests.

Keywords: C/SiC composites; Coating; Molten Salt; CVD; Thermal shock.

1. Introduction

Owe to their low density, excellent corrosion resistance, high strength and good fracture toughness, carbon fiber reinforced silicon carbide (C/SiC) composites were considered candidate materials for high temperature structural components [1-3]. However, at higher temperatures (>1200ºC), the oxidation of the fiber, interphase and matrix cooperatively influence the oxidation behavior of C/SiC composites [4,5]. Consequently, C/SiC composites need anti-oxidation protection when used to high temperature environment.

In early paper [6], we reported a new multilayer coating, which was dense SiC layers alternated with porous Zr-Si-C layers. The dense SiC layers were prepared by chemical vapor deposition (CVD) and the porous Zr-Si-C layers were made by molten salt reaction. The Zr-Si-C layers in the new multilayer coating were porous, which were obviously different from the traditional dense and crack-free coatings.

* Corresponding author.

And the study showed that the linear and mass ablation rates were much lower than those of uncoated composites [6].

However, the anti-oxidation performance of coating was commonly tested at an invariable temperature [4-8]. While, most space vehicles worked at low-earth orbit environment, where the pressure reached 10-7 Pa, the temperature cycles between -160ºC and 200ºC, and so on [9]. However, the mechanical and structural evolution of SiC/Zr-Si-C coated C/SiC composites under space environments were still unknown.

In this paper, the thermal shock induced deformation and damage of SiC/Zr-Si-C coated C/SiC composites was studied, and the effect on their flexural property and microstructures was discussed. Up to now, no bulletin about the effect of thermal shock on flexural property and microstructures of C/SiC composites was reported.

2. Experimental Procedures

2.1. *Preparation of C/SiC Composites*

Polycarbosilane (PCS) (molecular weight: 1742, soften point: 175ºC) was synthesized in National University of Defense Technology. Xylene was used as the solvent for PCS. C/SiC composites denoted as raw samples were prepared using 9~12 cycles of infiltration of PCS-Xylene solution (mass ratio 1:1), and then pyrolysed at 1200ºC under N2 (purity: 99.99%) atmosphere [3].

The samples were cut from C/SiC composites (density: 2.01 g/cm^3, open porosity: 11.4%).

2.2. *Preparation of SiC/Zr-Si-C Coating*

SiC/Zr-Si-C coating was used by molten salt and CVD method. As for Zr-Si-C coating process, a mixture of equimolar KCl-NaCl, sponge Zr and 20wt.% K_2ZrF_6 was put in the alumina crucible and heated to 1100ºC under an Ar atmosphere. The samples were immersed in the bath of molten salt for 3h [6]. As for the CVD SiC process, Methyltrichlorosilane (MTS, CH_3SiCl_3) was carried by H_2, and the molar ratio of H_2: MTS was 10; Ar was used as the dilute gas to slow down the chemical reaction rate during the deposition. The parameters were: deposition temperature 1100ºC; deposition time 5h; deposition pressure 3 kPa [4].

2.3. *Procedures for Thermal Shock Tests and Characterization*

Thermal shock tests were used to simulate the space environment. Alternating hot and cold range from -100ºC to 100ºC, high and low end of the holding time was

10min, temperature change rate was 50ºC/min, thermal shock times was 200 times.

The samples were weighed by an electronic balance (sensitivity: ±0.001g). The flexural strength of C/SiC composites were evaluated by three-point bending tests. The microstructures and fracture surfaces of the specimens were examined on scanning electron microscopy (SEM, S4800). The elements of samples after tests were identified by XPS (K-Alpha 1063, 12,000 V, 72 W, 0.5 eV, and 10-9 mBar).

3. Results and Discussion

3.1. *Composition and Microstructure of SiC/Zr-Si-C Coatings*

Fig. 1 shows the microstructure images of SiC/Zr-Si-C Coatings. Zr-Si-C coating shows a porous structure (Fig. 1(a)), and no visible cracks exist in the surface of the coatings (Fig. 1(b)).

The coatings are about 100 μm thick, which show a sandwich-like structure, dense CVD SiC coating alternates with Zr-Si-C coating. The type of coating is SiC/Zr-Si-C/SiC.

Obvious interface is found in Fig. 1(c), which exists between the SiC bonding coating and the SiC substrate, between SiC coating and Zr-Si-C coating. The average diameter of SiC coating is 40μm and the average diameter of Zr-Si-C coating is only 16μm.

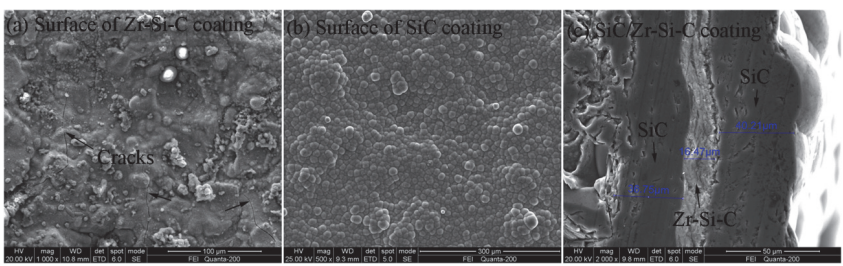


Fig. 1 SEM of SiC/Zr-Si-C coatings.

The Zr-Si-C coating and SiC coating are confirmed by EDS (Fig. 2 and Fig. 3). EDS (Fig. 2) results show that there are C, Zr and Si, which can be confirmed that Zr-Si-C coating have been formed by molten salt method.

This method involves the following steps: (1) the dissolution of Zr in molten salt; (2) the diffusion of Zr atoms toward to the surface of SiC; (3) the formation of Zr-Si-C coating by the reaction between Zr and SiC.

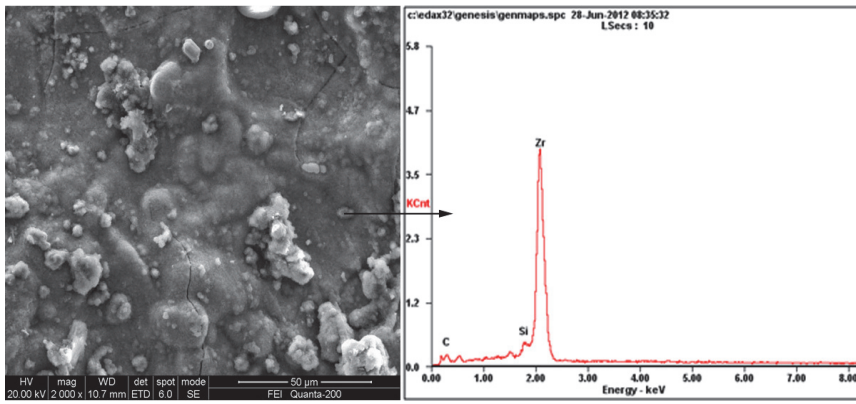


Fig. 2 EDS of Zr-Si-C coating.

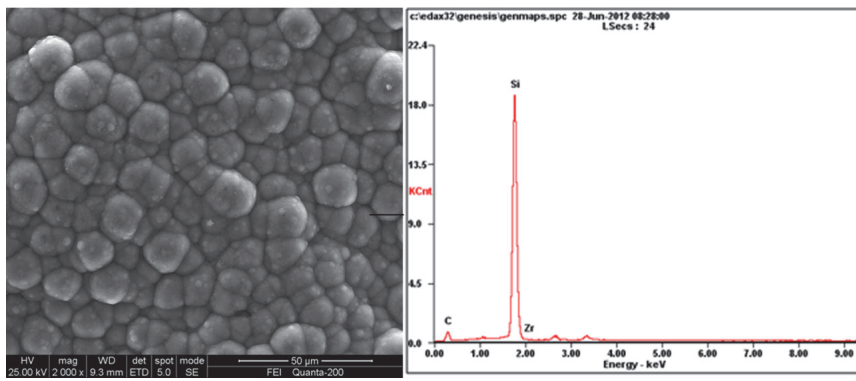


Fig. 3 EDS of SiC coating.

EDS (Fig. 3) results show that there are C and Si, which indicated that the coating is SiC.

Therefore, the results show that the SiC/Zr-Si-C coatings can be fabricated by CVD method and molten salt method.

3.2. *Residual Flexural Strength and Mass Variation*

Table 1 shows the mass variation of the materials before and after tests. The results of the mass variation show that no oxidation reaction occurs in the tests.

The flexural strength property after the thermal shock tests is determined by measuring the residual flexural strength. Fig. 4 shows the load-displacement curves of coated samples thermally shocked for 200 cycles. After tests, the samples show typical ductile fracture behaviors.

The flexural strength of coated C/SiC composites is 650.1MPa before the tests; while the strength decreases to 495.4MPa after tests, and then the flexural strength retention is 76.2%. There is obvious effect of thermal shock on flexural strength of coated C/SiC samples.

While compared to uncoated C/SiC composites, there is no significant effect. The flexural strength of uncoated C/SiC composites was 533.1MPa [4], the strength of the coated samples is 495.4MPa after thermal shock tests, which still show higher strength even after thermal shock tests.

Table 1. The mass variation of the material after thermal shock.

Samples	Before Tests(g)	After Tests(g)	Mass Retention Rate (%)
SiC/Zr-Si-C coated C/SiC composites	3.365	3.364	100.0
	3.377	3.375	99.9
	3.384	3.383	100.0
	3.375	3.373	99.9
	3.376	3.375	100.0
	Average		100.0

The results show that SiC/Zr-Si-C coatings can improve the mechanical properties of C/SiC composites.

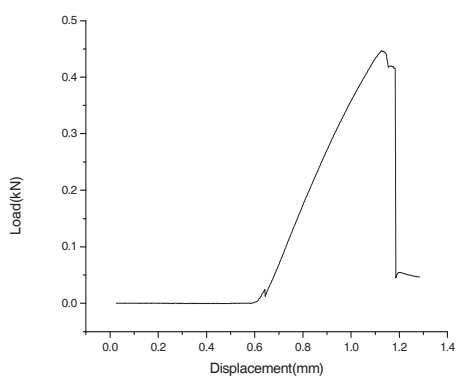


Fig. 4 Load–displacement curves of coated C/SiC composites after thermal shock tests.

The fracture surface of samples before and after tests is showed in Fig. 5. The pull-out of carbon fibers from SiC matrix can be obviously found, which is accordant with its fracture characteristic. Meantime, the pull-out mechanism is not changed.

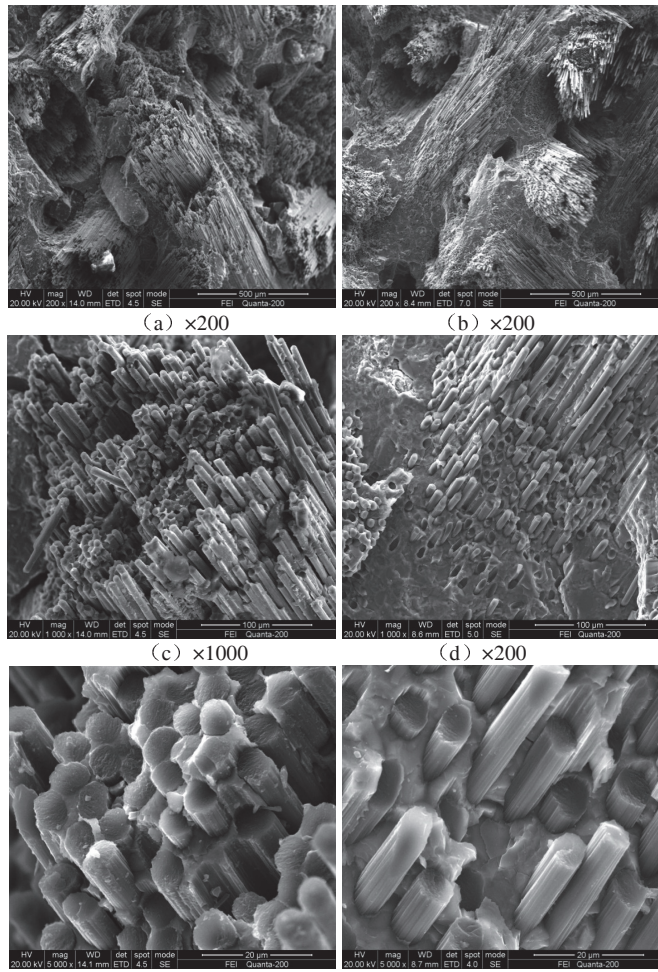


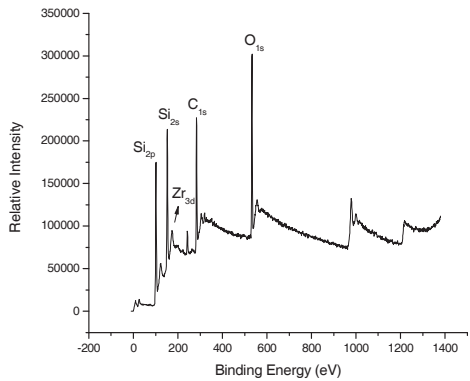
Fig. 5 SEM of coated C/SiC composites before and after thermal shock tests (a), (c) and (e) Before thermal shock tests (b), (d) and (f) After thermal shock tests.

As stated above, after the tests, coated C/SiC samples show the degradation of the flexural strength properties and no mass variation.

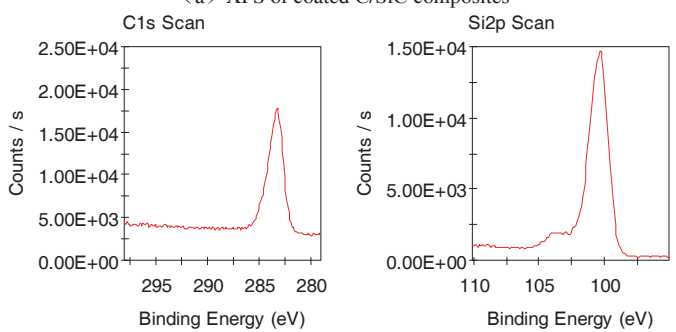
3.3. *Evolution of Coating Characteristics of Coated C/SiC Composites After Tests*

The XPS is also be used to testify the element of coating after tests, which reveals the composition of the most external surface of the products. Fig. 6 is the XPS

patterns of the coating after tests. Data from the XPS survey of the composites indicate that the major peaks in the spectra were due to the C1s (~284eV and 283.2eV), O1s (~532eV), Zr3d (186.2eV and 182.8eV) as well as Si2p (~100.4eV) photoelectrons. The results show that the ZrC and Zr2Si are observed in the coating.



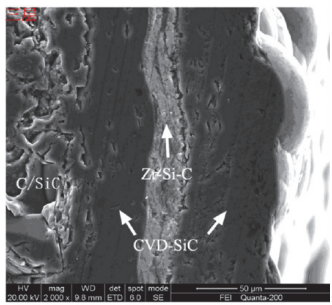
（a）XPS of coated C/SiC composites



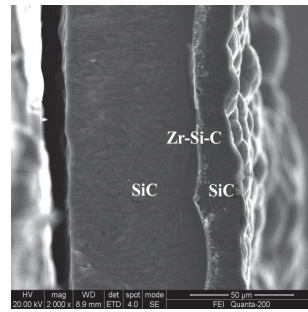
（b）C phase　　（c）Si phase

Fig. 6 XPS of coated C/SiC composites after thermal shock tests.

Fig. 7 shows SEM of the coated samples before and after the thermal shock tests between -100ºC and 100ºC for 200 times. The thickness of Zr-Si-C is attenuation (From 10μm to 1μm), and the interfacial bonding between SiC coating and Zr-Si-C coating is changed, which caused the degradation of mechanical properties.



(a) Before thermal shock tests



(b) After thermal shock tests

Fig. 7 SEM micrographs of coated C/SiC composites.

The degradation of mechanical properties was closely related to the evolution of the damage in the coating[10-12].

It was clear that the density of C/SiC composites increased with different coatings[4]. At the same time, the flexural strength of C/SiC composites greatly increased with the coatings, because porosity between the fibers and matrix was filled [4].

The coating of the composites is changed due to the tensile stress after thermal shock tests. During the thermal shock tests, the repeated tensile stresses in the interfaces of coating/matrix can weaken the interface bonding, which lead to delamination and debonding of coating/matrix interface.

The results show that the damage of SiC/Zr-Si-C coating can reduce the mechanical property of coated C/SiC composites under thermal shock environment.

C/SiC composites, as the aero-engines and space shuttles materials, suffer the worse working conditions, such as ultra-high temperature, high pressure and high speed. It is necessary to research and develop the high-temperature, long-life and highly reliable anti-oxidation coatings to satisfy the use requirements.

Therefore, it is necessary to develop anti-oxidation coatings with higher stability and melting temperature, multilayer coatings seem to be a promising strategy for the protection C/SiC composites in the space environment. And the thermal expansion coefficients of the materials should be took into account.

4. Conclusions

SiC/Zr-Si-C coated C/SiC composites under thermal shock were studied, and the flexural property and microstructures were discussed. The following conclusions had been reached:

(1) SiC/Zr-Si-C coated C/SiC samples showed the degradation of the flexural strength properties and no mass variation.

(2) The main constitute of the coating was not changed after thermal shock tests. While the structural of coating was changed owe to the tensile stress. The flexural property of C/SiC composites was reduced by the damage of SiC/Zr-Si-C coating under thermal shock tests.

(3) It is necessary to develop anti-oxidation coatings with higher stability and melting temperature, for C/SiC composites using in the space environment.

Acknowledgements

The authors are grateful to National Natural Science Foundation of China (51402357) for financial support. The authors are also grateful to Aid Program for Innovative Group of National University of Defense Technology and Aid Program for Science and Technology Innovative Research Team in Higher Educational Institutions of Hunan Province.

References

1. G.D. Li, C.R. Zhang, H.F. Hu, *Preparation and mechanical properties of C/SiC nuts and bolts*, *Materials Science and Engineering*: A. 547 (2012) 1-5.
2. G.D. Li, Y.D. Zhang, C.R. Zhang, *Design*, *preparation and properties of online-joints of C/SiC-C/SiC with pins*, Composites Part B: Engineering. 48 (2013) 134-139.
3. K. Jian, Z.H. Chen, Q.S. Ma, *Effects of polycarbosilane infiltration processes on the microstructures and mechanical properties of 3D-Cf/SiC composites*. Ceramics International. 33 (2007) 905-909.
4. X. Yang, L. Wei, W. Song, Z.H. Chen, *Oxidation behavior of oxidation protective coatings for PIP–C/SiC composites at 1500ºC*. Ceramics International 38 (2012) 9-13.
5. Q. M. Liu, L.T. Zhang, J. Liu, *The Oxidation Behavior of SiC–ZrC–SiC Coated C/SiC Minicomposites at Ultra high Temperatures*. J. Am. Ceram. Soc. 93 (2010) 3990-3992.
6. X. Yang, W. Li., S. Wang, Z. H. Chen, Y. Z. Zhang, *Ablation Behavior and Mechanism of SiC/Zr-Si-C Multilayer Coating for PIP-C/SiC Composites Under Oxyacetylene Torch Flame,* Composites: Part B. 2013 doi:. http://dx.doi.org/10.1016/j.compositesb 2013.10.033
7. Y. Blum and J. Marschall, Low Temperature, *Low Pressure Fabrication of Ultra High Temperature Ceramics (UHTCs)*, AFRL-ML-WP-TR-2006-4200 (2006) 1-116.

8. X. Yang, H.F. Hu, Y.D. Zhang, *Thermal Shock Properties of 3D-C/SiC Composites Prepared via Polymer Infiltration Pyrolysis,* Ceramics International. 40 (2014) 9087–9094.
9. B. F. Zhang, S. Wang, W. Li, *Mechanical behavior of C/SiC composites under simulated space environments, Materials Science and Engineering A.* 534 (2012) 408-412.
10. C.Y. Zhang, X.W. Wang, B. Wang, *Thermal Shock Properties of a 2D-C/SiC Composite Prepared by Chemical Vapor Infiltration,* Journal of Materials Engineering and Performance. 22 (2013) 1680-1687.
11. H. Wang and R.N. Singh, *Thermal Shock Behavior of Two Dimensional Woven Fiber-Reinforced Ceramic Composites*, J. Am.Ceram. Soc. 79 (1996) 1783-1792.
12. Y. Kagawa, N. Kurosawa, T. Kishi, *Thermal Shock Resistance of SiC Fiber-Reinforced Borosilicate Glass and Lithium Aluminosilicate Matrix Composites,*J. Mater. Sci. 28 (1993) 735-741.

The Crystal Structure of the $PrAl_8Cu_3Ni$ Quaternary Compound

Bing He[a], Changsheng Qin[b], Degui Li[c], Lei Hu[d], Ming Qin[e*]

Department of Physics and Communication Engineering,
Baise University, Baise, Guangxi 533000, PR China
E-mail: [a]bsxyhb@21cn.com; [b]87629749@qq.com; [c]lidegui354@163.com;
*[d]894879712@qq.com; [*e]qm6327@sohu.com*

A new quaternary compound $PrAl_8Cu_3Ni$ was synthesized and studied by means of X-ray powder diffraction technique using Reitveld methods. The quaternary compound $PrAl_8Cu_3Ni$ crystallizes in the tetragonal structure, space group *I4/mmm*. with the $Mn_{12}Th$ structure type and lattice parameters a=8.79261(3)Å, c=5.16605(2)Å, V = 399.387Å^3, z=2 and ρ_x=5.042 g/cm^3.

Keywords: Crystal structure; X-ray diffraction; Reitveld methods.

1. Introduction

The tetragonal $ThMn_{12}$-Type RT_4Al_8 (R=rare earth metal, T=transition metal) compounds received serious attention in recent years due to these compounds display a wide variety of magnetic properties depending on the kinds of R and T elements [1]. Among them $CeCu_4Al_8$ has been reported [2] to exhibit such heavy fermion like behavior that the specific heat divided by temperature C/T attains a large T→0 value of 0.3J/K^{2}mol with abroad maximum of 0.95J/K^{2}mol at T_{max}= 1.1K without showing magnetic ordering down to 30 mK,and the characteristic temperature (T_k) was estimated to be about 6K from the low-temperature broad maximum of the electrical resistivity [3]. Mössbauer spectroscopy, magnetization and AC-susceptibility measurements performed on $DyFe_xAl_{12-x}$($4 \leq x \leq 4.7$) polycrystalline samples ($ThMn_{12}$-type structure), revealed a complex magnetic behaviour dependent on applied field, temperature and composition [4]. To the best of our knowledge, quaternary intermetallic compound $PrAl_8Cu_3Ni$ have not been reported in literature. This work reports on the crystal structure of $PrAl_8Cu_3Ni$.

* Corresponding author.

2. Experimental Details

Sample with $PrAl_8Cu_3Ni$ nominal compositions was synthesized by arc melting the stoichiometric amount of the elements (with purity of at least 99.9%) on a water-cooled copper crucible under a pure argon atmosphere. To ensure homogeneity the sample was turned upside down and melted three times. The weight loss during melting was less than 1%. Following the melting, the ingot was wrapped in a tantalum foil, sealed under vacuum in a silica tube and annealed at 1073 K for 4 weeks., then cooled down at a rate of 10 K/h to room temperature. Sample composition of $PrAl_8Cu_3Ni$ was examined by means of scanning electron microscope (SEM) and energy dispersive X-ray spectroscopy (EDS). The sample composition (7.6 at. % Pr, 61.2 at.% Al, 23.2 at.% Cu and 8.0 at.% Ni), analyzed by SEM-EDS with ZAF matrix correction method, was very close to the nominal composition of the $PrAl_8Cu_3Ni$ compound (7.69 at. %Pr, 61.54 at.% Al, 23.06 at.% Cu and 7.69 at.% Ni). High-quality powder X-ray diffraction patterns of the sample were collected at room temperature using a Rigaku Smart Lab 2006 powder diffractometer equipped with a Cu Kα radiation and a graphite monochromator. The scan range was from 10.00º to 110.00º (2θ) with a step size of 0.02º and a count time of 4 s per step.

3. Results and Discussion

The powder X-ray diffraction pattern of $PrAl_8Cu_3Ni$ was successfully indexed using the Jade 5.0 [5] program in a tetragonal unit cell with the lattice parameters a=8.79261(3)Å, c=5.16605(2)Å. Reflection conditions (hkl: h + k + l = 2n; hk0: h + k = 2n; 0kl: k + l = 2n; hhl: l = 2n; 00l: l = 2n; h00: h = 2n) pointed to 5 space groups I4/mmm (no. 139), I422 (no. 97), I-4m2 (no. 119), I-42m (no. 121), and I4mm (no. 107). By comparing crystallographic characteristics of the $PrAl_8Cu_3Ni$ compound with those presented in the structure type database it was found that $PrAl_8Cu_3Ni$ and $CeCu_4Al_8$ [2] have the same structure type (space group I4/mmm, ThMn12-type structure). Structure refinements of $PrAl_8Cu_3Ni$ was then performed using the DBWS9807 program [6]. Several compound modes for Cu and Ni at 8f, 8i and 8j sites were tested. When the 8(f) site occupied by 75% Cu and 25% Ni, the 8(i) and 8(j) positions occupied by Al atoms and the 2(a) positions occupied by Pr atom, the goodness-of-fit parameters of these refinements led to the best values: Rp=4.95%, Rwp=6.64%, RB=7.35%, RF=6.35%. Early research on the structure determinations of RT_4Al_8 [7, 8] shows that the T atoms in RT_4Al_8, occupy the 8(f) position, the aluminum atoms being restricted to the 8(i) and 8(j) positions. Similar results were obtained also from X-ray single-crystal data on $CaMn_4Al_8$ [9]. Obviously, the results of structure determinations for $PrAl_8Cu_3Ni$ are in good

agreement with that obtained from the structure investigation of RT4Al8. Refined parameters of $PrAl_8Cu_3Ni$ are summarized in Table 1. The observed, calculated, and residuals X-ray powder diffraction patterns of PrAl8Cu3Ni are shown in Fig. 1 A set of interatomic distances in $PrAl_8Cu_3Ni$ is given in Table 2. The xz-plane projection of the $PrAl_8Cu_3Ni$ structure is shown in Fig. 2.

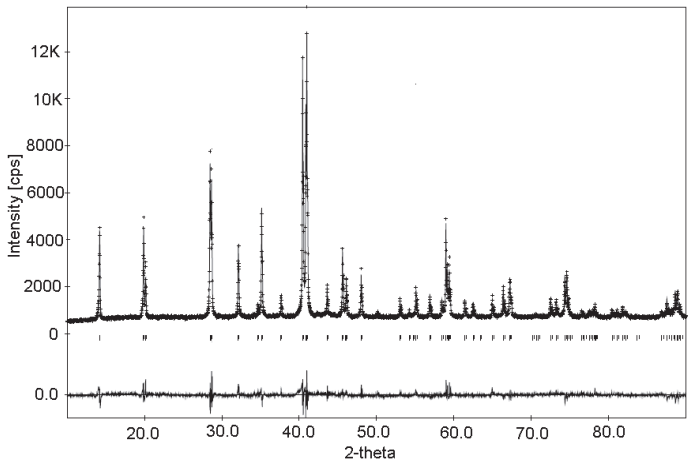


Fig. 1 Observed, calculated and residuals X-ray powder diffraction patterns of $PrAl_8Cu_3Ni$.

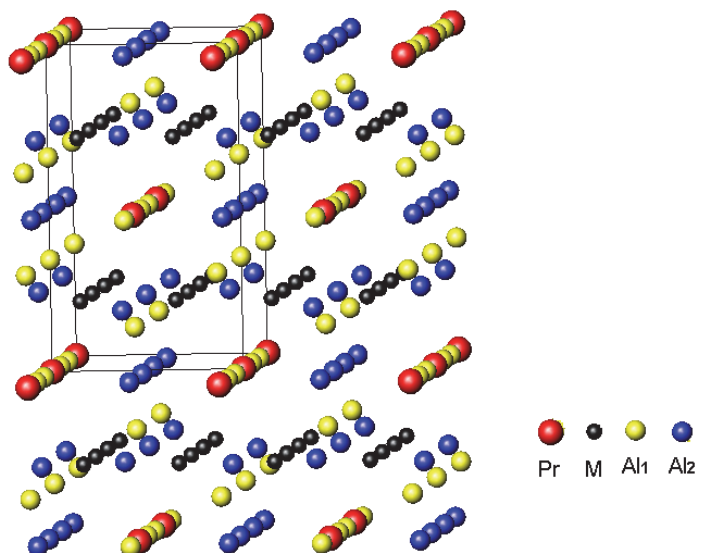


Fig. 2 Projection of the $PrAl_8Cu_3Ni$ structure on the xz-plane (M=75%Cu+25%Ni).

Table 1. Refined atomic parameters for $PrAl_8Cu_3Ni$, Space group: *I4/mmm*, a=8.79261(3)Å, c=5.16605(2)Å, Rp=4.95%, Rwp=6.64%, R_B=7.35%, R_F=6.35%.

Atom	position	X	Y	Z	Occ.	B[Å^2]
Pr	2a	0	0	0	1	0.19（6）
Cu	8f	0.25	0.25	0.25	0.75	0.38（7）
Ni	8f	0.25	0.25	0.25	0.25	0.38（7）
Al	8i	0.3431(5)	0	0	1	0.88（9）
Al	8j	0.2682(4)	0.5	0	1	0.37（8）

Table 2. Selected interatomic distances (Å) for PrAl8Cu3Ni.

Atom-atom		Distance[Å]	Multiplicity	Atom-atom		Distance[Å]	Multiplicity
	- Pr	3.017(2)	×1		- Pr	3.290(3)	×2
	- M	2.678(5)	×4		- Al_2	2.882(2)	×2
Al_1	- Al_1	2.759(1)	×3	Al_2	- Al_1	2.762(3)	×2
	- Al_2	2.762(3)	×2		- Al_1	2.732(2)	×2
	- Al_2	2.732(2)	×2		- M	2.555(4)	×4
	- Al_1	2.678(5)	×4		- Al_1	3.017(2)	×4
M	- Al_2	2.555(4)	×4	Pr	- Al_2	3.290(3)	×8
	- Pr	3.366(6)	×2				
	- M	2.583(2)	×2				

Acknowledgments

This work was supported by the Scientific Foundation of Guangxi High Education (No. 2013ZD070).

References

1. I. Felner, I. Nowik, J. *Phys. Chem. Solid*, 40 (1979) 1035.
2. U. Rauchschwalbe, U. Gottwich, U. Ahlheim, H. M. Mayer, F. Steglich, J. *Less-Common Met*., 111 (1985) 265.
3. H. Ido,T. Nishioka, Kontani, *Journal of Magnetism and Magnetic Materials*, 177-181 (1998) 385-386.
4. S. Se′ rio, L.C.J. Pereira , M. Godinho, J.C. Waerenborgh, *Intermetallics 16* (2008) 1219–1226.
5. Jade5, XRD Pattern Processing, *Materials Data, Inc*., 1999.
6. R.A. Young, A.C. Larson, C.O. Paive-santos, User's Guide to Program DBWS9807 for Rietveld Analysis of X-ray and Newtron Powder Diffraction Patterns with a PC and Various Other Computers, School of Physics, *Georgia Institute of Technology*, Atlanta, GA, 2000.
7. K. H. J. Buschow, J. H. N. van Vucht and W. W. van den Hoogenhof, J. *Less-Common Met.*, 50 (1976) 148.
8. O. S. Zarechnyuk and P. I. Kripyakevich, Sov. P*hyx-Crystallogr*., 7 (1963) 436.
9. E. Chech, G. Cordier and H. Schafer, J. *Less-Common Met.*, 90 (1983) 109.

Simulation of Melt Flow and Interface Shape of 450 mm Czochralski Grown Silicon Single Crystal

X. Y. Zhang[a], X. J. Guan[*b], J. Wang[c]

School of Materials Science and Engineering, Shandong University, Jinan 250061, China

*E-mail: [a]zhangxiangyu0012@163.com; [*b]xjguan@sdu.edu.cn; [c]vwang@126.com*

Z. B. Pan

Institute of Crystal Materials Shandong University, Jinan 250100, China

Q. K. Zeng

School of Aeronautics, Shandong Jiaotong University, Jinan 250357, China.

The utilization of numerical simulation to investigate 450 mm Czochralski grown silicon single crystals has gained significant interests due to the fact that the growth process of 450 mm Czochralski grown silicon single crystals is much more complicated: the melt flow is strong and complex, and its technical parameters fluctuation range is small. A group of 2D axisymmetric simulations were carried out to study the effects of crystal/crucible rotation on the melt flow pattern and interface shape. The results show that the interface maximum deflection for 450 mm Si growth is much more sensitive than smaller ingot growth. The natural convection dominates the flow pattern in the simulations of small crucible rotation rate. An optimum condition with the lowest deflection for 40" hot zone can be achieved by proper combination of crystal rotation and crucible one.

Key words: Numerical Simulation; 450 mm; Crystal Rotation; Crucible Rotation; Vortex; Interface Deflection.

1. Introduction

In recent years, semiconductor industry has rapidly developed, the feature size of integrated circuit is advancing to 10 nm or even smaller, leading to a larger silicon wafer size. In 2008, Intel Corp, Samsung Electronics, and TSMC had entered into an agreement to start a pilot line in 2012[1], but due to the limitation of technology and research funds, this ambitious target has been postponed.

* Corresponding author.

Compared with experiments, numerical simulation has its unique advantages of low cost, short test period and high repeatability to be extremely useful and really a key to the R&D of 450 mm silicon ingot.

The 450 mm silicon crystal is estimated to be about 200 cm long and 800 kg heavy[2]. Large amount of molten silicon in the crucible could bring about strong convection and complex flow to enhance the scale and intensity of vortex. Furthermore, big diameter silicon crystal shows a obvious increase of temperature gradient, which would result in bigger interface deflection and thermal stress. Zheng Lu, StevenKimbel et al[3] successfully grown a 450 mm silicon single crystal and discussed the change law of hot zone along with increasing crystal diameter. E Kamiyama, J Vanhellemont et al[4] indicated the small size and low density of the formed voids when pulling crystals close to the Voronkov criterion conditions were a challenge for wafer surface inspection tools and discussed possible solutions. Liu，Kakimoto et al[5] performed 2D model of small ingot to investigate the change law of interface shape under different crystal and crucible rotation. Omidreza Asadi Noghabi, Mohammed M'Hamdi et al.[6] employed a 2D model of 6" ingot and investigated the impacts of crystal and crucible rotations on melt flow and interface deflection. In this paper, we carried out a 2D model for 450 mm silicon growth, and observed the change law of melt flow and interface shape under different combinations of crystal/crucible rotations to demonstrate the optimal combination.

2. Model description

A 2D axisymmetric model, adopting a quasi-steady approximation, was constructed by a commercial software CGSim. The predictions simulated by the software, such as the growth rate, flow pattern and power consumption of silicon crystal growth, have been confirmed by actual experiments[7-9]. Fig. 1 shows the main structure of the furnace. Relevant heat transfer phenomena including conduction, convection and radiation as well as crystallization and associated latent heat release are considered. A one equation turbulence model based on RANS approaches is employed for the melt flow. The exterior temperature is set to 300 K and shielding gas Ar is blown at a constant rate. The energy balance[7] at the melt/crystal interface is given by

$$k_{crys}\frac{\partial T}{\partial n}\Big|_{crys} - k_{melt}\frac{\partial T}{\partial n}\Big|_{melt} = \rho_{crys} L_H V_n \qquad (1)$$

where T is the temperature; $\boldsymbol{n}$ is the normal vector at the crystallization front; L_H is the silicon latent heat and V_n is the local crystallization rate normal to the melt/crystal interface; k_{crys} and k_{melt} is the crystal conductivity and melt one, respectively.

Simulations have been performed at middle stage of crystal growth at the height of 500 mm. Table 1 gives the process parameters used in the simulation for growth control. All the process parameters are kept constant in the simulations, except for crystal rotation and crucible one.

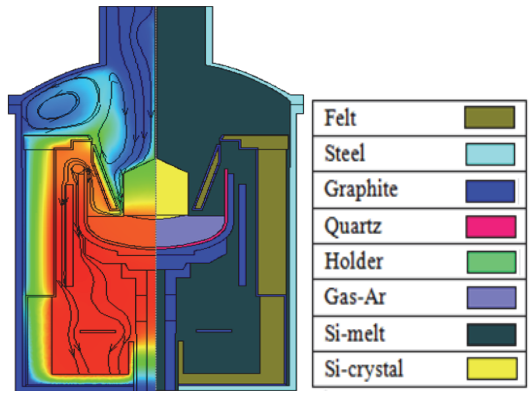


Fig. 1 Furnace geometry (crystal height = 500 mm), predicted thermal field and streamlines in the argon gas.

Table 1. Operational parameters used in simulation.

Parameter (unit)	Value
Crucible diameter (in.)	40
Crystal hight (mm)	1000
Pulling rate (mm/min)	0.3
Silicon charge (kg)	400
Crystal rotation (rpm)	1-20
Crucible counter rotation (rpm)	1-5
Average heat power (kW)	120
Atmosphere pressure (Pa)	1000

3. Results and discussion

3.1. *Impacts of rotation rates on convection*

Along with crystal rotation increasing, fast-flowing zone moves toward to the deep of the melt, the maximum flow rate reaches 0.02-0.03 m/s. Three dominating vortexes are observed, when crystal rotation rate varies from 1 rpm to 10 rpm and crucible rotation rate varies from 2 rpm to 5 rpm, as shown in Fig. 2. Vortex 1: natural convection and forced convection (crucible rotation), Vortex 2: natural convection, gas shear stress and Marangoni effect (thermocapillary force). Vortex 3 : natural convection, gas shear stress, forced convection driven by crystal rotation and crucible one.

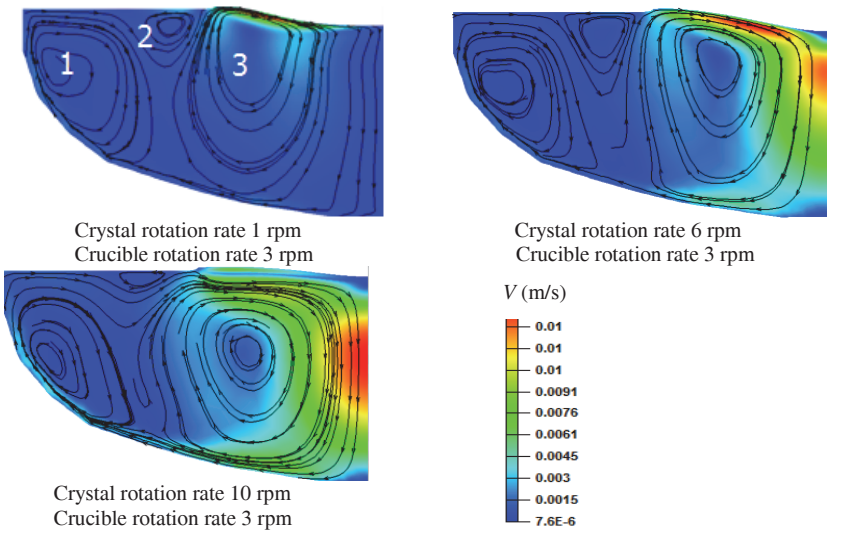
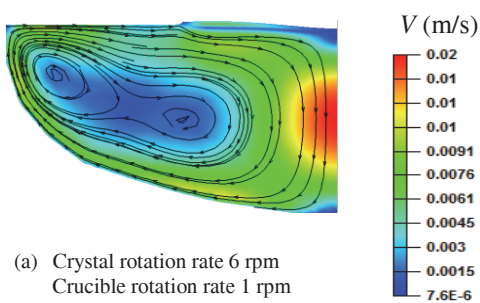


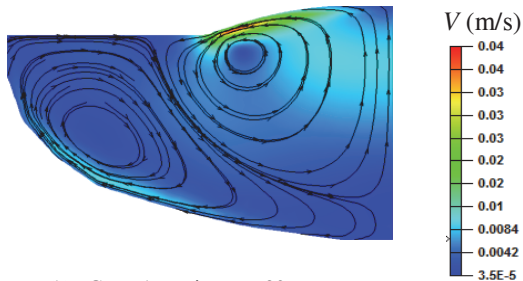
Fig. 2 Melt flow pattern at 500 mm crystal height for crucible rotation rate is kept 3 rpm.

When crucible rotation rate is set to 1rpm, the simulated results show that the vortexes have different characters, as shown in Fig. 3(a). Vortex 1 and vortex 3 gradually roll into one clockwise vortex with increasing crystal rotation to 15 rpm，while vortex 2 is not observed. We can see from Fig. 3(b) that with continually rising crystal rotation, a new anticlockwise vortex caused by forced convection of crystal rotation appears in the vicinity of interface, and its size and intensity increase synchronously. The increasement of crystal rotation does not result in any obvious change in the number and distribution of vortex, except for weakening vortex 2, when crucible rotation is higher than 2 rpm.



(a) Crystal rotation rate 6 rpm
Crucible rotation rate 1 rpm

Fig. 3 Melt flow pattern at 500 mm crystal height.



(b) Crystal rotation rate 20 rpm
Crucible rotation rate 1 rpm

Fig. 3 (*Continued*)

When the crystal rotation keeps in constant and the crucible rotation varies from 2 rpm to 5 rpm, three typical vortexes are all clearly observed. The intensity of forced convection increases with higher crucible rotation rate, and both the size and intensity of vortex 2 is enhanced, meanwhile, vortex 1,and vortex 3 show signs of compression.

3.2. *Impacts of rotation rates on crystal/melt interface deflection*

The curved interface is considered to be a locus of stress concentration, which significantly affects the quality of silicon single crystal. Compared to small diameter silicon single crystal growth, a much lager maximum deflection is observed in 450 mm. It is of great interest to investigate the feature of 450 mm silicon growth interface change under different crystal/crucible combinations.

Large thermal field and complex convection determine small range of process parameter variation. To investigate the effects of crystal rotation and crucible one on interface deflection, several groups at low crystal/crucible rotation rate were adopted in the simulations. Crystal rotation rate was varied from 1 rpm to 20 rpm, and crucible rotation rate was varied from 1 rpm to 5 rpm.

The simulated interface shape for different crucible rate (crystal rotation rate was kept content for 10 rpm) is plotted in Fig. 4. It is seen that the central zone of interface generally moves down along with increasing crucible rotation rate, making ingot grow deeper into the melt. Fig. 5 shows the change law of interface shape at different crystal rotation rate (crucible rotation rate was kept content for 3rpm). The interface change from concave to convex with increasing the crystal rotation rate. The same change rule is also observed in the experiments of smaller diameter silicon growth [10], but the interface deflection of 450 mm silicon single crystal growth is much more sensitive to crucible/crystal rotation changes.

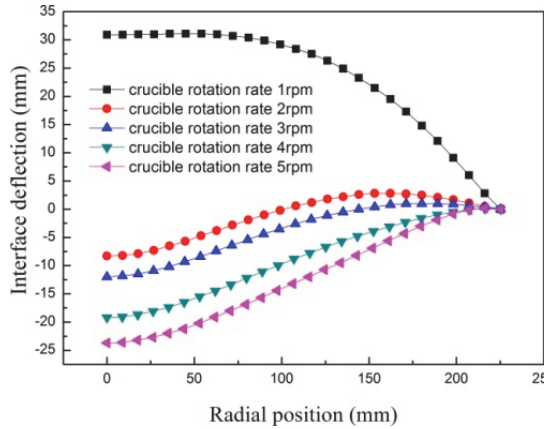


Fig. 4 Interface shape (crystal rotation rate =10rpm).

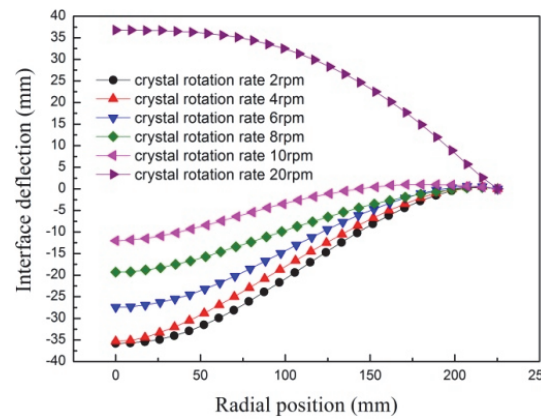


Fig. 5 Interface shape (crucible rotation rate =3rpm).

This phenomenon is caused by the forced convection which the crucible (crystal) rotation brings about, so that convective type start to change from natural convection to forced convection with crucible (crystal) rotation increasing. Concave interface shape enables a bigger pulling speed to raise silicon single crystal production.

In order to minimize the deflection in the process of crystal growth, Fig. 6, in which the negative value means concave interface shape and the positive value stands for convex interface, illustrates the combined influence of crucible/crystal rotation on interface deflection. It is of great interest that the deflection is smaller at stronger crucible rotation, but a too high crucible rotation rate is unacceptable considered the stability of mechanical system. The

coordinate of interface's central point generally reaches the lowest position when crystal rotation rate is between 3-5 rpm. For the present crystallization position, the minimum interface deflection for a 500 mm high crystal occurs at the crystal rotation rates between 3 and 5 rpm and the crucible rotation rate of approximately 5 rpm.

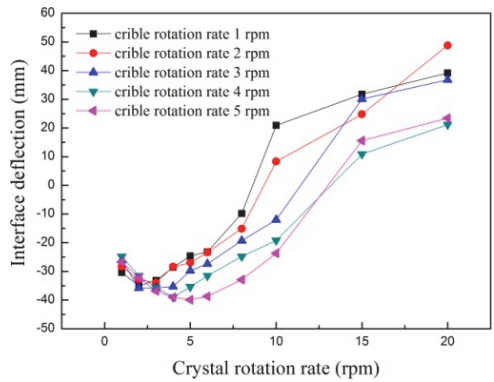


Fig. 6 Maximum interface deflection for 500 mm height crystal.

4. Conclusions

Crystal and crucible rotations have significant impacts on thermal field, silicon melt flow pattern and interface shape in 450 mm CZ Si growth. Compared with the previous studies[6-9], the interface maximum deflection is much more sensitive than that of smaller ingot growth process, which determines the narrower range of process parameters variation for 450 mm silicon growth. The natural convection dominates the flow patterns at small crucible rotation rate. An optimum condition with the lowest deflection can be achieved by proper combination of crystal rotation and crucible one, that is, that the smaller crucible rotation rate and crystal rotation rate between 3-5 rpm is the optimum combination for 40" hot zone. Although 2D analysis does not fully describe the complex 3D interactions in the hot zone of the 450 mm Czochralski silicon growth, the present work founds a good basis for subsequent in-depth analysis and experiments.

References

1. X. Dai and Q. Chang: 'Growth of 450mm CZ Si single crystal of IC grade', *J. Mater. China*, 2010, 29, 10, 21-24.

2. M. Watanabe and S. Kramer: ‘450 mm silicon: An opportunity and wafer scaling’, *J. Int. Electrochem. Soc.*, 2006, 15, 4, 28-32.
3. Z. Lu and S. Kimbel: ‘Growth of 450mm diameter semiconductor grade silicon crystals’, *J. Cryst. Growth*, 2011, 318, 1, 193-195.
4. E. Kamiyama, J. Vanhellemont, and K. Sueoka: ‘Thermal stress induced void formation during 450 mm defect free silicon crystal growth and implications for wafer inspection’, *Appl. Phys. Lett.*, 2013, 102, 8, 082108.
5. L. Liu and K. Kakimoto: ‘Effects of crystal rotation rate on the melt–crystal interface of a CZ-Si crystal growth in a transverse magnetic field’, *J. Cryst. Growth*, 2008, 310, 2, 306-312.
6. O. Asadi Noghabi, M. M'Hamdi, and M. Jomâa: ‘Effect of crystal and crucible rotations on the interface shape of Czochralski grown silicon single crystals’, *J. Cryst. Growth*, 2011, 318, 1, 173-177.
7. O. A. Noghabi, M. Jomâa, and M. M'hamdi: ‘Analysis of W-shape melt/crystal interface formation in Czochralski silicon crystal growth’, *J. Cryst. Growth*, 2013, 362: 77-82.
8. W. T. Chung, Y. H. Wu, and Y. C. Chen: ‘Investigation of the 22 inch hot zone simulation and experiment of the CZ silicon crystal growth process’, *37th IEEE Photovoltaic Specialists Conf. on ‘latest technology in the field of Photovoltaics’*, Washington, USA, Jun 2011, paper: 2142.
9. D. P. Lukanin, V. V. Kalaev, and Y. N. Makarov: ‘Advances in the simulation of heat transfer and prediction of the melt-crystal interface shape in silicon CZ growth’, *J. Cryst. Growth*, 2004, 266, 1, 20-27.
10. R. Teng, X. Dai, and Q. Xiao: ‘Numerical Simulation of Melt/Crystal Interface and Melt Flow during Large Diameter Single Silicon Crystal Growth’, *J. Synth. Cryst.*, 2013, 4, 015.

Thermal Structural Analysis of Surface of Pulling-Straightening Roller Based on ANSYS

Wang Li-Yan[a], Yu Bai-Shui[b], Chen Hua[d*]

School of Material Science and Engineering,
Changchun University of Technology,
Changchun 130012, JiLin, China
*E-mail: [a]10521773@qq.com; [b]1527607498@qq.com; [*d]chenhua@mail.ccut.edu.cn*

Liu Li-Ping[c]

Changchun Vocational Institute of Technology,
Changchun 130033, JiLin, China
E-mail: [c]63824397@qq.com

Using the heat analysis function of ANSYS software, the temperature field simulation analysis was carried out for 0Cr13Ni4MoN welding on surface of 42CrMo pulling-straightening roller. The influence of 200ºC and 400ºC preheating on temperature field distribution were studied. Experiments showed that "Birth and Death loading method" heat source model can realistically simulate the process of surfacing layer growth for pulling-straightening roller. Preheating way can increase the overall temperature of welding roller and reduce the temperature range, as well as temperature distribution of welding sample tended to be uniform. Based on simulation calculation, a dynamic simulation method which is a feasible two-dimensional (2D) welding temperature field was established. And application of the finite element analysis technology in the field of welding analysis was promoted.

Keywords: Pulling-straightening Roller; Surfacing; Birth and Death Element; Finite Element Analysis.

1. Introduction

Since working conditions of continuous casting pulling-straightening roller is complicated，it bear mechanical loads, thermal loads and friction loads when working. At blooming stage, surface of hot roller directly contact with 900~1200ºC steel, and then rapidly is cooled by water. The pulling-straightening roller continuously experience alternating effect of heating and cooling, therefore, the main damage form of hot roller is thermal fatigue damage which occur peeling and cracking. Meanwhile, roller scrapped because of excessive wear and it's also one of its major causes of failure. The local damage of roller

* Corresponding author.

will cause serious loss. Surface welding method can not only restore size of roller, and also obtain specific performance alloy layer which include wear resistance, heat resistance, corrosion resistance, etc.

In the literature, many reports are available that focus on the roll overlaying welding simulation technology. Tang professor calculated the quasi-steady temperature field for thin sheet by finite element method, but he did not consider nonlinear of thermal physical properties and surface heat loss of material [2]. Chen Chu et al studied two-dimensional nonlinear steady-state and transient temperature field by finite element analysis [3].

J. B. Leblon investigated the theory and numerical simulation way of plastic behavior of phase transformation, and developed SYSWELD software. According to research, J. B. Leblon studied coupling effects between temperature, transformation and thermal stress by using SYSWELD software [5]. Based on the finite element method, Yukio Ueda first put forward a thermal elastic plastic analysis theory which considered the material mechanical properties relating to the strength, so that made the analysis of complex dynamic stress and strain welding process possible [6].

2. The simulation analysis of temperature field

2.1. *Preprocessor of numerical simulation*

Before the simulation analysis of the temperature field for pulling-straightening roller welding process was built by software ANSYS13.0, following hypothesis was done:

- A sample did not contain impurities and defects, there was no internal larger cracks, and was isotropic.
- The simulation analysis did not consider arc radiation and the effect of metal filling, flowing and cladding on weldment.
- A sample was thick, and the crack appeared on surface in general, so it was treated as a simulation of two-dimensional plane.

Established model was shown in Fig. 1.

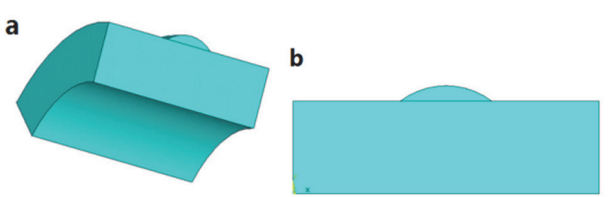


Fig. 1 Finite element model (a) Solid model; (b) Two-dimensional model.

2.2. *Element type analysis*

Choice of element type was one of the most important aspects during simulating surfacing process of pulling-straightening roller. After the establishment of the preprocessor physical model, element type was selected. ANSYS13.0 offers nearly 200 kinds of element types; usually the choice of element type depends on the geometry and freedom. In surfacing analysis, the following factors should be considered:

- The element must be two-dimensional unit;
- The element could do thermal analysis;
- The element met need of temperature analysis;
- The element also should be able to do transient nonlinear analysis

According to these requirements, this paper chose the four nodes number 13 2D coupling element Vector Quad 13 (Fig. 2).

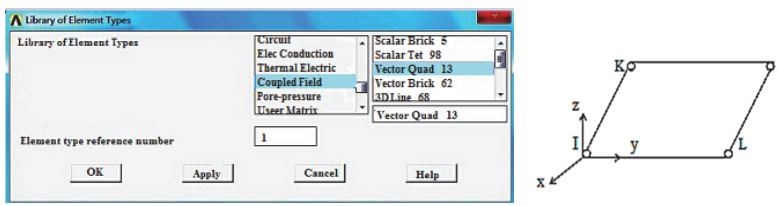


Fig. 2 Coupling field analysis element.

Table 1. Vector Quad 13 element properties.

The Quantity of Node	4
Element function	coupling field, including temperature, displacement, magnetic, electric; iterative calculations; calculation of the “birth and death”
Species can be applied load	temperature, heat rate, heat flux, pressure, convection
Physical properties	density, thermal conductivity, modulus of elasticity, linear expansion coefficient, specific heat, Poisson's ratio
DOF	displacement, temperature

2.3. *The surfacing materials properties of the pulling- straightening roller*

Test base metal was 42CrMo pulling-straightening roller; welding material was 1Cr13Ni4MoN. Due to large temperature changes during welding process, it’s necessary to consider physical properties with varying temperature. In addition, because convergence calculation for a nonlinear is difficult, the parameters of high-temperature were dealt with. Fig. 3 were material properties which obtained by ANSYS13.0 software.

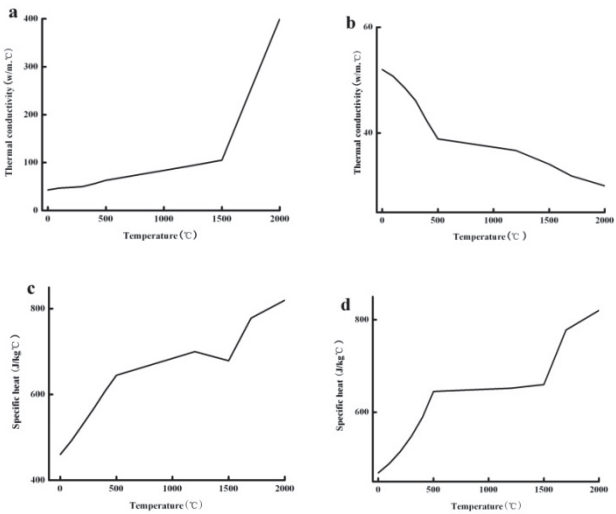


Fig. 3 The material physical properties curves of high-temperature which obtained by the interpolation and extrapolation method. (a) 0Cr13Ni4MoN thermal conductivity, (b) 42CrMo thermal conductivity, (c) 0Cr13Ni4MoN specific heat capacity, (d) 42CrMo specific heat capacity.

2.4. *Meshing*

After element type and material properties were defined, the continuum model was meshed. There were two kind of meshing ways to software ANSYS13.0. One way was mapping method, another way was freedom method. If the geometric model was regular, the first method should be used. If the shape of the geometric model was more complex, you could use the second method.

Simulation results depended on the total number and size of the grid. Because of uneven welding temperature field, solder layer, heat-affected zone and the contact surface should select compact grid. Temperature of model rim was relatively small, therefore, it could adopt sparse element grid accuracy of the result was ensured under control, and long time computing could not lead to crash. Finite element model grid was shown in Fig. 2-4.

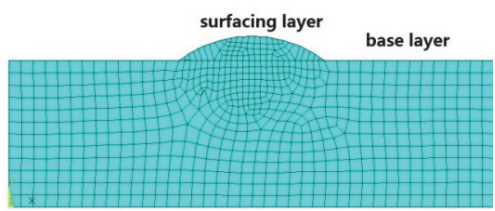


Fig. 4 Finite element mesh generated.

Using list functionality of ANSYS13.0 software the statistical results were: finite element mesh generated 645 units and 781 nodes; the mesh size was 1mm × 1mm in the center of the welding layer.

2.5. *Selection of heat source*

Gaussian heat source model and "birth and death" loading method were chosen. Boundary condition was the temperature of surrounding medium, and in this paper the temperature chose 20ºC. During welding, the surface temperature of the roller increased gradually, however the air which contact with the roller was still room temperature, so the heat power of roller surface will spontaneously released into the air through heat convection. There were two manners in heat exchange of the weldment including convection and radiation. Experiments show that the welding heat radiation loss was more than convection. Generally radiation and convection heat transfer was calculated in different ways. In order to facilitate the calculation, the overall heat transfer coefficient should be considered. Thus, the heat loss due to heat the boundary can be expressed as:

$$q_s = \beta(T - T_a) \tag{1}$$

where; β — surface heat transfer coefficient, the unit is *W/cm·ºC*; T — surface temperature for the weld part;

T_a — ambient temperature, the unit is *W/cm·ºC*;

β_C — convection heat transfer coefficient; $\beta = \beta_C + \beta_E$

β_E — radiation heat transfer coefficient. From heat transfer theory, we know that

radiation heat flux density is:

$q_r = \varepsilon\sigma[(T+273)^4 - (T_a+273)^4]$

Therefore

$$\beta_E = \varepsilon\sigma\left[(T+273)^2 + (T_a+273)^2\right]\left[(T+273)+(T_a+273)\right] \tag{2}$$

where, ε — the emissivity of the object surface; σ — Stefan-Boltzann constant, is approximately 5.67. $w/cm^2 \cdot k^4$

As the convective heat transfer coefficient is dependent on temperature. In the calculation, surface heat transfer coefficient with changing temperature must be given.

2.6. *Analysis of simulation results with preheating conditions*

Fig. 5 and Fig. 6 showed the temperature field distribution at different times during heating process under preheating 200ºC and 400ºC, respectively. In the figure the area enclosed by the same color was isothermal region, the

temperature values of various colors were listed at the legend bottom. Findings from analysis of simulation results are as follows:

- In the initial welding stage, the solder is gradually accumulated to the surface of roller, and its temperature change dramatically. And the temperature of contact surface and the bonding surface rise very quickly, but the temperature of the bonding surface is significantly higher than the contact surface temperature.
- With welding process, a certain thickness of the cladding layer is formed, and heat-affected area gradually is expanded, local high temperature zone expand to the surrounding environment. With increasing of welding time, the liquid nugget expanded rapidly along the axis and radial direction.
- In the later stage of welding, as time goes on, the welding heat-affected areas are gradually weakened.

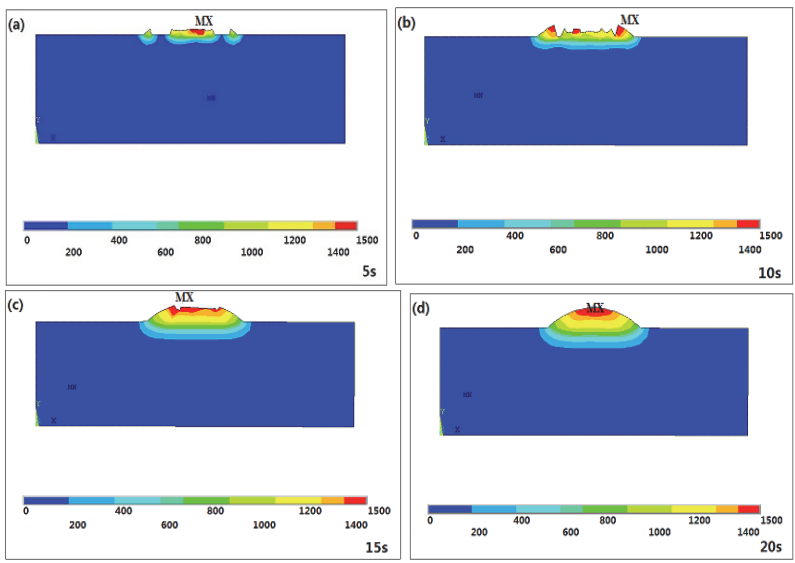


Fig. 5 The temperature distribution under preheating 200ºC
a) 5s; b) 10s; c) 15s; d) 20s.

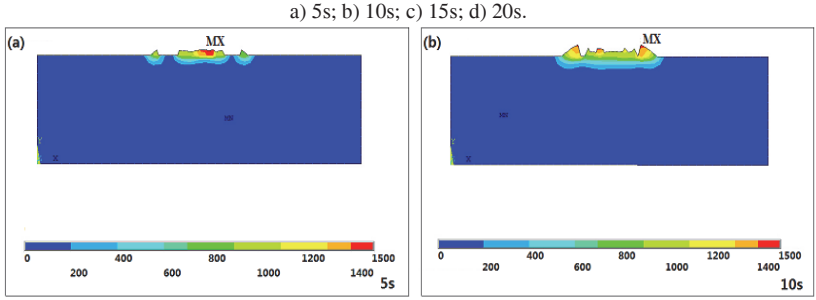


Fig. 6 The temperature distribution under preheating 400ºC
a) 5s; b) 10s; c) 15s; d) 20s.

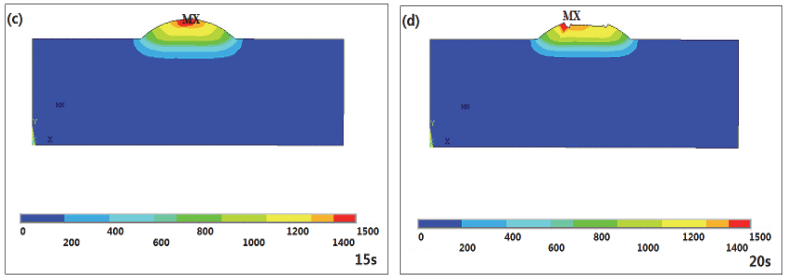


Fig. 6 (*Continued*)

3. Conclusion

- "Birth and Death loading method" heat source model can realistically simulate the process of surfacing layer growth for pulling-straightening roller.
- Preheating way can increase the overall temperature of welding roller and reduces the temperature range, as well as temperature distribution of welding sample tend to be uniform.
- Compared with un-preheating, the laws of residual stress distribution is basically same under preheating condition. And the maximum residual stress occurs near the heat affected area.

Acknowledgements

This work was financially supported by the natural science foundation of Jilin Province (No 201115143).

References

1. Guo Zheng hong. Progress in the Pearlitic Transformation Mechanism in Steels [J]. *Transactions of Materials and Heat Treatment*, 2003(3): 1-2
2. Q X Yang, M Yao, Park Joongkeun. Numerical simulation on residual stress distribution of hard-face-welded steel specimens with martensite transformation [J]. 2004: 1-2
3. D Rosenthal, H Schmenber. Thermal Study of Arc Welding [J]. 1938(04):1-3
4. Z Paley. Computation of Temperature in Actual Weld Designs [J]. 1975(03): 1-3
5. U shio, M Proc. Metallo-thermo-mechanics application to phase transformation incorporated processes [J]. 1996: 1-6
6. B K Jones, A F Emery, S I Marburger. An analytical and experimental study of the effects of welding parameters on fusion welds [J]. 1993(02): 1-3

7. Lin Yong-cheng, Chen Ming-song, Zhong Jue. Investigation on metadynamic recrystallizaton behavior of 42CrMo steel [J]. *Transactions of Materials and Heat Treatment*, 2009(4):2-6
8. Zhang Wei-ping, Liu Shuo, Ma Yu-tao. Strengthening Mechanism of Particle Reinforced Metal Matrix Composite Coating by Laser Cladding [J]. *Transactions of Materials and Heat Treatment,* 2005(02):2-6
9. B N Napuohob.Novel Technique for measuring the residual stress and the strain-optic coefficient profile of an optical fiber [J]. 1979(11):2-6
10. P Petrov. Numerical modeling of temperature distributions electron beam welding [J]. 1992(12):3-6

Evaluation Method on Anti-Icing Effects of Hydrophobic Coating

Chunhua Xiao*

State Key Laboratory of Aerodynamics,
Chinese Aerodynamics Research and Development Center,
Mianyang, 621000, China
*E-mail: *dragoner76@163.com*

Anti-icing effects of different nano coatings on a rectangle test model have been investigated experimentally in an icing wind tunnel under different icing weather conditions. The shape of ice accretion on the test model are measured and compared respectively. A quantitative method of evaluating anti-icing effect is established on the basis of nine geometric characteristic parameters of ice profile. The nondimensional deviation of the nine parameters are calculated and analyzed on the coated model and the clean model respectively. The results demonstrate that the anti-icing nano coatings can effectively reduce the icing velocity and intensity, but not eliminating the icing phenomena completely. The silicone rubber coating has a little anti-icing capability, while better performance can be achieved once different proportion of nano molecules is added in, which is a valuable way of fabricating anti-icing coatings. The best coating tested in this study for anti-icing is the silicone rubber coating added in 10% cetane and 10% octadecane. The conjugation of cetane and octadecane in the silicone rubber makes this coating better ice-repellent capacity. But the dimethyl silicones added in the coating decrease or delay the releasing of the nanoparticles and hence make the anti-icing capacity unstable.

Keywords: Nano Coating; Hydrophobic Coating; Anti-Icing; Evaluation Method.

1. Introduction

Ice accretion on the surfaces of aircraft components will significantly reduce the aerodynamic performance [1]. Hydrophobic anti-icing coating is one of the most studied methods in the last decade. It can reduce the icing phenomenon by changing the physical and chemical characteristic of a solid surface and thus reducing the adhesion of the water. David et al. [2] investigated experimentally the anti-icing performance of low adhesion coating under the conditions of static and droplet impingement icing. Jennifer et al. [3] developed a novel coating that could reduce the freezing point of the water by releasing the tripropene ethylene glycol

and propanetriol from the surface. The performance of anti-icing is highly dependent on the releasing velocity. Cao, et al. [4] validated the anti-icing performance of the polymer with nanoparticles in both laboratory conditions and natural environments respectively. Their study showed that the anti-icing performance relied not only on the hydrophobic property but also on the size of nanoparticles. Rachid et al. [5] studied experimentally the hydrophobic coating on the wind turbine blade under the cold weather. The test results showed that the coating with good hydrophobic performance could reduce the shear strength between the ice and the blade surface. Varanasi et al. [6] studied the frost formation and ice adhesion on superhydrophobic surfaces. The result showed that these coatings could effectively restrain rime and decrease the adhesion. These works promoted the development of anti-icing coating fabrication and its anti-icing mechanism. We will investigate the anti-icing effect of nano coating and set up a quantitative evaluation method on anti-icing effect coupled the ice profile geometric characteristics.

2. Experimental facility

2.1. *Wind tunnel*

The tests are taken in the 0.3m×0.2m icing wind tunnel which is a closed-loop circuit wind tunnel with the maximum wind speed of 60m/s. The tunnel is located at China Aerodynamics Research and Development Center. The icing wind tunnel has a length of 8m and a width of 3.2m. An evaporator is fabricated between the third corner and the fourth corner, and a spray system is equipped in the settling chamber. The refrigerated temperature in the test section can be adjusted to -20ºC.

2.2. *Test model*

The test model is a rectangular pane with the size of 200mm(height)× 60mm(width)×20mm(thickness) which is made of aluminum alloy material. The pane model is installed vertically between the ceiling and the floor in the test section.

2.3. *Measurement instruments*

The shape of the ice on the model is measured by a heated knife blade, a scaled chipboard, a vernier caliper and a pencil through cutting the ice shape on the test model. The icing process is recorded by a 5,184×3,456 high resolution digital camera.

3. Test methods and conditions

3.1. Test method

The flowfield of the icing wind tunnel is first calibrated to obtain the airflow speed and the cooling system is set up to assure the ambient temperature. The spray system is adjusted to assure the icing cloud parameters such as Mean Volumetric Diameter and Liquid Water Content of droplet by changing the water and air pressure. The icing process is recorded by the camera under required airflow and icing cloud parameters. The profile of ice on the central cross-section of the model is traced by the ice profile tracing equipment. The ice is cut by the heated knife and measured by the scaled chipboard inserted into the melted gap. The ice profile is described by the pencil and digitized by a professional sofware before stored in a computer.

3.2. Test condition

The tests are carried out at the two wind speed of 20m/s and 30m/s for each coating respectively. The ambient temperature is settled to be around -10ºC, the uncertainty is about ±1ºC. The mean volumetric diameter of droplet is 40μm and the density of the liquid water is 0.7g/m3. The nano coating provided by China National Center for Nanoscience and Technology is made of silicone rubber polymer composite added in different nanoparticles. Four prescriptions are used to validate the anti-icing effect of the coatings: No.1 coating is pure silicone rubber; No.2 coating is silicone rubber added in 20% cetane; No.3 coating is silicone rubber added in 10% cetane and 10% octadecane; No.4 coating is silicone rubber added in 10% cetane and 10% octadecane and 10% dimethyl silicone.

4. Evaluation method of anti-icing effect

The ice profile of the cross section on the test model is obtained by ice profile tracing equipment. Fig. 1 presents the ice profile geometric characteristic parameters of an ice accretion. There are nine parameters defined as ① the ice thickness on stagnation point, ② the maximum ice thickness, ③ the maximum ice width, ④ the impingement range on upper edge, ⑤ the impingement range on lower edge, ⑥ the upper ice horn length, ⑦ the lower ice horn length, ⑧ the upper ice horn angle and ⑨ the lower ice horn angle.

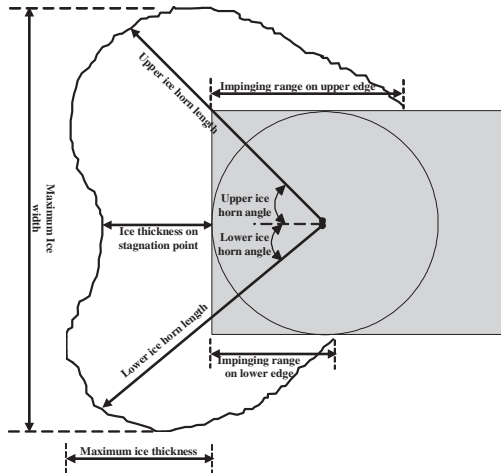


Fig. 1 Geometric characteristics of an ice accretion

The quantitative evaluation method on the anti-icing effect is set up by the nondimensional deviation of the ice shape geometric characteristic. The deviation of each parameter is computed and non-dimensionalized by the following formula.

$$\Delta X_i = \left| \frac{X_{iC} - X_{iN}}{X_{iN}} \right| \times 100\% \tag{1}$$

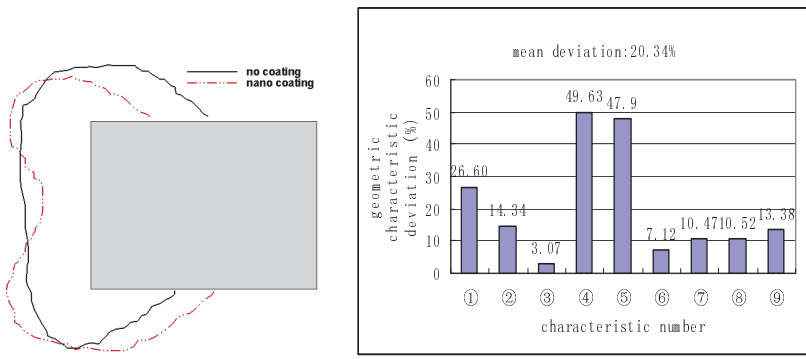
where XiC and XiN represent the characteristic parameters on the test model with and without nano coating respectively.

5. Test results and discussions

The ice profiles and the geometric characteristic deviation on all the coatings are obtained at two wind speeds of (U=)20m/s and 30m/s respectively. For No.1, No.2 and No.4 coating, at U=20m/s, the difference of the ice profile between the clean model and the coated model is very small. However, at U=30m/s, the size of the ice accretion and the mean deviations become larger. It indicates that the anti-icing performance is not unstable at two wind speeds.

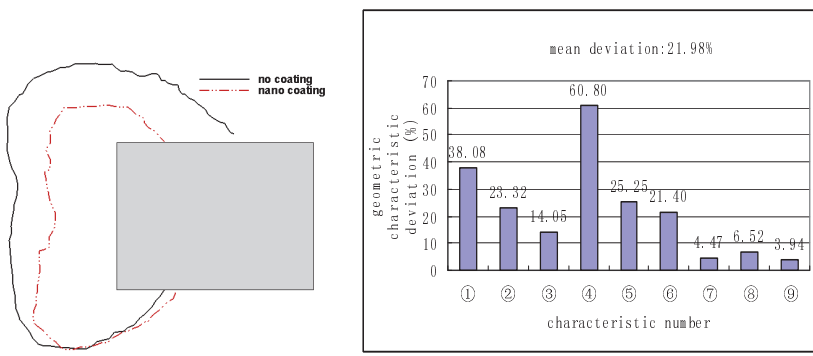
In order to improve the anti-icing performance, we added in 10% cetane and 10% octadecane to the silicone rubber coating. It can be seen from Fig. 2(a) that the ice shape difference between the clean model and the coated model is not small, and the mean deviation of 20.34% shown in Fig. 2(b) indicates better anti-icing effect with respect to the definition of the anti-icing performance introduced. With increasing of the wind speed to 30m/s, both the ice accretion and the shape difference between the clean model and the coated model increase, as shown in

Fig. 3. Mean deviation of 21.98% also indicates good performance on anti-icing effect. It can be seen that the mean deviation with this nano-coating is further increased by 2.5% and 0.5% at (U=) 20m/s and 30m/s respectively when compared to the silicone rubber+20% cetane.



(a) Ice profiles (b) Ice profiles geometric characteristic deviation

Fig. 2 Ice profiles and its geometric characteristic deviation on silicone rubber coating added in 10% cetane and 10% octadecane(U=20m/s)

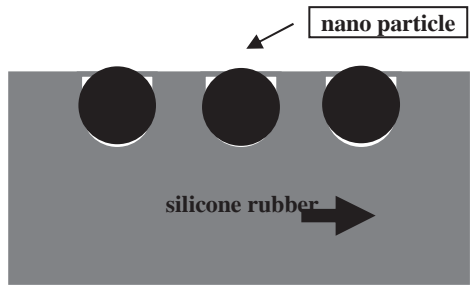


(a) Ice profiles (b) Ice profiles geometric characteristic deviation

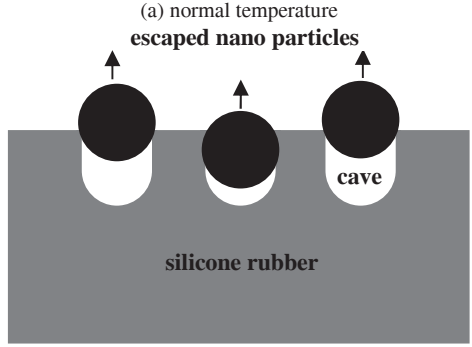
Fig. 3 Ice profiles and its geometric characteristic deviation on silicone rubber coating added in 10% cetane and 10% octadecane(U=30m/s)

Fig. 4 presents the anti-icing mechanism of the new coating with nanoparticles. The black circles represent the nanoparticles, and the gray substrate is the silicone rubber coating. During the preparation of the material, large amounts of nanoparticles are added to the silicone rubber, thus forming many caves in the coating under normal temperature, as shown in Fig. 4(a). When the ambient temperature drops below the frozen point, some nanoparticles added in the coating will be gradually released to the coating surface, and form a kind of

micro-nano-structure on the surface of the coating, as shown in Fig. 4(b). The micro-nano-structure has the effectiveness of water-repellent and anti-icing, thus preventing or significantly reducing icing on the surface. The anti-icing performance is highly dependent on the number and uniformity of escaped nanoparticles.



(a) normal temperature



(b) temperature below 0ºC

Fig. 4 Schematic of anti-icing principle of silicone rubber coating added in nanoparticles

6. Summary

(1) The quantitative evaluation method can provide useful guidance as to the experimentally observed behavior of the anti-icing effect with nano coatings based on the nondimensional deviation of ice shape geometric characteristic.

(2) Both silicone rubber coating and silicone rubber coating added in different nano molecules have some certain anti-icing effect. The better performance with the latter is due to the micro-nano-structure formed by the nanoparticles which prevents icing on the solid surface.

(3) Anti-icing effect can be achieved by improving the surface hydrophobic performance of composite polymer material. However, water phobic is not equal to ice phobic. Once ice accretion appears on the surface of coating, the surface hydrophobic characteristics will be changed. Therefore, the nano coating can only decrease or delay the icing speed on the surface.

Acknowledgement

This work is supported by China National Science Funding (Project No: 61179075).

References

1. Kind RJ, Potapczuk MG, Feo A, Golia C and Shah AD. Experimental and computational simulation of in-flight icing phenomena, *Progress in Aerospace Sciences*, 1998, 34:275-345.
2. David N.Anderson, Allen D.Reich. Tests of the Performance of Coating for Low Ice Adhesion, AIAA-97-0303, 1997.
3. Jennifer Ayres, W. H. Simendinger, C. M. Balik. Characterization of titanium alkoxide sol–gel systems designed for anti-icing coatings: II. Mass loss kinetics. *Journal Coat Technology Research*, 2007, 4 (4): 473–481.
4. Liangliang Cao, Andrew K. Jones, Vinod K. Sikka, Jianzhong Wu, Di Gao. Anti-Icing Superhydrophobic Coatings. *Langmuir Letter*, 2009, 25(21), 12444–12448.
5. Rachid Karmouch, Simon Coudé, Gilles Abel, et al. Icephobic PTFE coatings for Wind Turbines operating in cold climate conditions. *IEEE Electrical Power & Energy Conference*，2009.
6. Varanasi K K, Deng T, Smith J D, et al. Frost Formation and Ice Adhesion on Superhydrophobic Surfaces, *Applied Physic Letters*, 2010, 97(23).

Characterization and Property of Mg-Doped Cu_2SnSe_3 Bulks with the Mg Substitution at the Sn Site

Dong-Hau Kuo*, Walelign Wubet

Department of Materials Science and Engineering, National Taiwan University of Science and Technology, Taipei 10607, Taiwan

** E-mail: dhkuo@mail.ntust.edu.tw*

$Cu_2(Sn_{1-x}Mg_x)Se_3$ (Mg-*x*-CTSe) bulks at x = 0, 0.05, 0.1, 0.15, and 0.2 were prepared at 550 °C for 2 h. Defect chemistry was studied by measuring structural and electrical properties of Mg-doped Cu_2SnSe_3 as a function of the dopant concentration. Mg-*x*-CTSe pellets were *p*-type at x = 0, 0.05, and 0.1 and *n*-type at x = 0.15 and 0.2. The low hole concentration of 3.18×10^{17} cm^{-3}, high mobility of 387 cm^2 V^{-1} s^{-1}, and low conduction of 20 S cm^{-1} were obtained for $Cu_2(Sn_{1-x}Mg_x)Se_3$ bulks at x= 0.1 (5% Mg), as compared to 1.06×10^{18} cm^{-3}, 209 cm^2 V^{-1} s^{-1}, and 36 S cm^{-1} for undoped one. The explanation based upon the Mg-to-Sn antisite defect for the changes in electrical properties was declared.

Keywords: Cu_2SnSe_3; Reactive Sintering; Microstructure; Electrical Property; Extrinsic Defect.

1. Introduction

The CdTe and $CuIn_{1-x}Ga_xSe_ySe_{2-y}$ (CIGS) absorber systems have been developed for thin-film PV devices, but may be limited in the long term by the scarcity of Te, Ga, and In [1]. Ternary semiconductors of the family I_2–IV–VI_3 (I = Cu, Ag; IV = Ge, Sn; VI = S, Se, Te) have found applications in the fields of photovoltaics, Li-ion batteries, thermoelectrics, and in acousto-optic devices [2].

Cu_2SnSe_3 (CTSe) in particular is a *p*-type semiconductor and has a band gap ranging from 0.8 to 1.7 eV, a high optical absorption coefficient (10^4–10^5 cm^{-1}), and relatively high hole mobility [3]. There are different reports on the electrical properties of CTSe. Kuo *et al.* found the values of 8.33 S cm^{-1}, 1.8×10^{19} cm^{-3}, and 2.9 $cm^2V^{-1}s^{-1}$, for the electrical conductivity (σ), hole concentration (n_p), and hole mobility (n_p), respectively [4]. Kim *et al.* found the values of 10^{17}-10^{21} cm^{-3} and 6.3-14 cm^2V^{-1} s^{-1} for n_p and μ, respectively [5]. Babu *et al.* prepared CTSe films and their films were found to be *p*-type with n_p of 1.85×10^{20} cm^{-3} and μ of 1.79 cm^2 V^{-1} s^{-1} [6]. G. Marcano and C. Rincón found n_p of 8×10^{19} cm^{-3} [7].

Various methods were reported for the preparation of undoped CTSe in the forms of thin film as well as powder. CTSe thin films were deposited by

using different techniques such as DC magnetron sputtering from the targets composed of Cu_2Se and $SnSe_2$ [4] and high purity elemental targets [8] and co-evaporation from pure elements [5,6]. CTSe powders were prepared by using the vertical Bridgman–Stockbarger technique at high temperature [7,9] and colloidal synthesis [2,3]. However, to the best of our knowledge there are no reports on doped CTSe.

To enhance sintering at lower temperature, sintering aids need to be added to assist the densification by liquid-phase reactive sintering. In this study, we report results on polycrystalline $Cu_2(Sn_{1-x}Mg_x)Se_3$ (x = 0–0.2) bulks, which show enhanced electrical properties due to the Mg doping. In the present paper, we also present results of the structural and compositional characteristics of Mg-CTSe.

2. Experimental Section

Magnesium-doped CTSe materials with the formula of $Cu_2(Sn_{1-x}Mg_x)Se_3$ were prepared in the form of bulk pellets with x values of 0, 0.05, 0.1, 0.15, and 0.2 *via* a two-step liquid-phase reactive sintering at 550ºC for 2 h with a holding at 300ºC for 1 h. These constituent powders were separately milled by a planetary ball-milling machine for 6 h to achieve very fine powders and then were mixed by a conventional ball milling machine for 12 h. The selenides weighing were based on the actual formula of $Cu_2[(Sn_{0.95-x}Mg_x)Sb_{0.05}](Se_{2.875}S_{0.075}Te_{0.05})$ with x at 0, 0.05, 0.1, 0.15, and 0.2 after considering the compositions of sintering aids. The specimens were symbolized in terms of Mg-x-CTSe.

The composition and growth morphology of Mg-x-CTSe pellets were characterized by scanning electron microscopy (SEM; JEOL JSM-6390LV) equipped with an energy dispersive spectroscope (EDS). Crystal structure was analyzed by X-ray diffractometry (XRD; Bruker D2). A Hall effect measurement system (ECOPIA HMS 2000) was used to measure the conductivity, mobility, and carrier concentration.

3. Results and Discussion

Fig. 1 shows a series of XRD patterns related to Mg-x-CTSe pellets after sintering at 550ºC for 2 h. The XRD result was used to identify the formation of a solid solution. The major XRD diffraction peaks appeared at 2θ of 27.2°, 45.1°, 53.4°, 65.5°, and 72.3°, which could be attributed to the (111), (220), (311), (400), and (331) planes, respectively, of CTSe and consistent with the data file of PDF #65-4145.

The concentrations of Cu, Mg, Sn, Sb, and total anions (Se, S and Te) for Mg-x-CTSe pellets were shown in Fig. 2. The constituent elements with the

relative errors at about 5% was recorded by averaging the areal regions covering more than 8 grains in order to achieve much factual data. The [Mg]/([Cu]+[Mg]+[Sn]+[Sb]) ratios were 0, 0.012, 0.014, 0.035, and 0.042 and the [Sn]/([Cu]+[Mg]+[Sn]+[Sb]) ratios were 0.30, 0.29, 0.28, 0.27, and 0.24 for Mg-*x*-CTSe at 0, 0.05, 0.1, 0.15, and 0.2, respectively. The amounts of other constituent elements of the pellets such as Cu and Sb and the total amount of anions (S, Te, and Se) were almost constant. The Mg-*x*-CTSe materials sintered at such a low temperature remained favored and had the composition close to our design formulation.

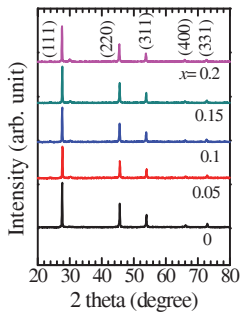


Fig. 1 XRD patterns of Mg-*x*-CTSe (*x* = 0–0.2) pellets.

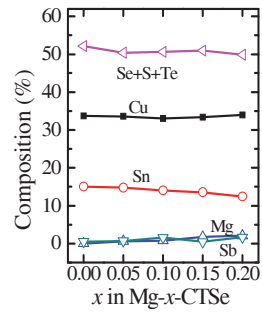


Fig. 2 EDS composition analyses of Mg-*x*-CTSe.

Fig. 3 displays SEM surface images of Mg-*x*-CTSe pellets with *x* values of (a) 0, (b) 0.05, (c) 0.1, (d) 0.15, and (e) 0.2. There was a change in the grain size as the *x* value increased. The grain sizes were 2.1±0.5, 2.3±0.4, 2.8±0.5, and 3.0±0.6 μm at $x = 0$, 0.05, 0.1, and 0.15 respectively. Mg-0-CTSe had the microstructure with compact and large grains. The grain size, grain boundary, and densification were improved for Mg-*x*-CTSe at $x = 0.05$. The pellets at $x = 0.1$ and $x = 0.15$ (Fig. 3(c) and (d)) also exhibited good grain growth with smooth surfaces. A slightly porous pellet with loose grains was observed for Mg-0.2-CTSe, as shown in Fig. 3(e). All the pellets had smooth surfaces with clearly defined grain boundaries and they were dense enough to be used for electrical property measurements. The precipitation of second phases of MgSe and SnSe might occur for Mg-*x*-CTSe at $x \geq 0.1$.

Fig. 4 shows the conductivity, mobility, and carrier concentration (n_p and n_e) for Mg-doped CTSe pellets at different doping concentrations. Electrical properties were measured using the van der Pauw method [10]. The Mg-*x*-CTSe pellets at $x = 0$, 0.05, and 0.1 exhibited *p*-type conductivity whereas CTSe pellets at $x = 0.15$ and $x = 0.2$ showed the *n*-type conductivity, which indicated that the Mg dopant acted as a donor to transform the *p*-type to the *n*-type. The

Mg-*x*-CTSe has a $p \rightarrow n$ transition after adding 7.5% Mg ($x = 0.15$), this is due to the formation of Mg_{Cu}^{+} donor defect at $x = 0.15$ and 0.2 in addition to the Mg_{Sn}^{2-} defect when the Mg content increased. However, there is a question for small Sn^{4+} ion to enter to the quite bigger Cu^{1+} site. The Sn_{Cu} defect has not been observed in $A_2^{I}B^{II}B^{IV}C_4^{VI}$ and $A^{I}B^{III}C_2^{VI}$. For the net hole concentration, the n_p values were 1.1×10^{18}, 5.1×10^{17}, and 3.2×10^{17} cm^{-3} for Mg-*x*-CTSe at $x = 0$, 0.05, and 0.1. The n_e values were 1.1×10^{18} and 3.2×10^{18} cm^{-3} for Mg-*x*-CTSe at $x = 0.15$ and 0.2. There was a continuous decrease in n_p when the x value of Mg-*x*-CTSe increased from 0 to 0.1. With increasing the Mg dopant concentration, n_e became dominant over n_p to show the net *n*-type behavior. For the Mg content at $x \geq 0.15$, the net n_e value remained relatively unchanged. The $p \leftrightarrow n$ transition leads to a minimum in carrier concentration. The electrical mobility is an important electrical property to evaluate a semiconductor used for the solar cell devices. Electrical mobility (μ) of Mg-*x*-CTSe pellets were 348, 386, 207, and 215 $cm^2\ V^{-1}\ s^{-1}$ at the $x = 0.05$, 0.1, 0.15, and 0.2, respectively, as comparing with 209 $cm^2\ V^{-1}\ s^{-1}$ for Mg-free CTSe. The Mg doping in CTSe enhanced electrical mobility and led to a high mobility of 386 $cm^2\ V^{-1}\ s^{-1}$ for Mg-0.1-CZTSe. The data indicates that the 5% Mg ($x = 0.1$) dopant is a special donor to lower n_p and enhance mobility. The slight decrease of mobility at the higher Mg content can be caused by the increase in the concentration of scattering centers from the Mg dopant and the occurrence of possible precipitates of MgSe and SnSe. The high mobility in Mg-0.1-CTSe can be attributed to the low atomic scattering factor of Mg. Electrical conductivity (σ) of Mg-*x*-CTSe pellets were 36, 29, 20, and 38 S cm^{-1} at $x = 0.05$, 0.1, 0.15, and 0.2, respectively, comparing with 67 $S \cdot cm^{-1}$ for the undoped one. The lowest conductivity at $x = 0.1$ is mainly contributed from its lowest carrier concentration. The carrier concentration, mobility, and electrical conductivity therefore depend on the variations of the tin and magnesium contents in Mg-*x*-CTSe.

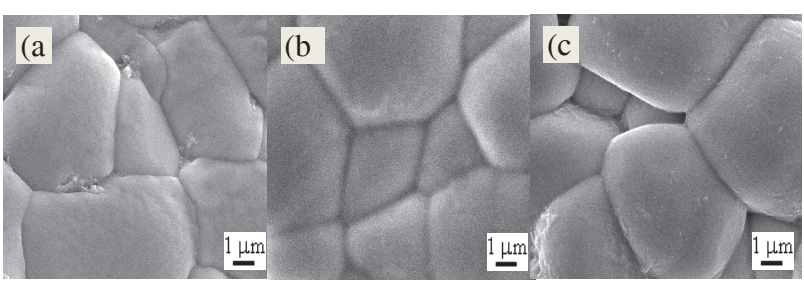


Fig. 3 SEM surface images of Mg-*x*-CTSe pellets at (a) $x = 0$, (b) $x = 0.05$, (c) $x = 0.1$, (d) $x = 0.15$, and (e) $x = 0.2$ after sintering at 550ºC for 2 h

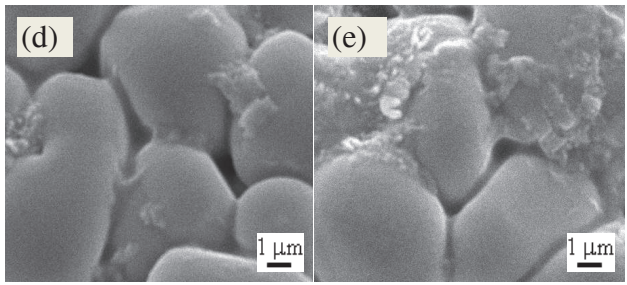


Fig. 3 (*Continued*)

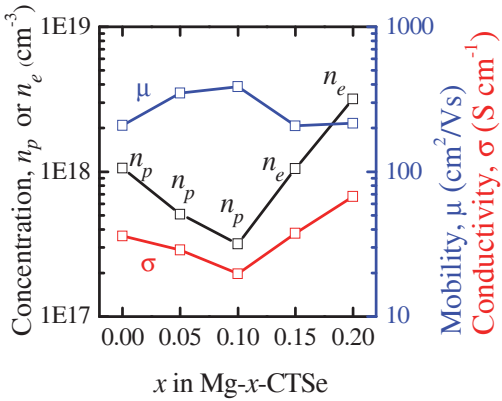


Fig. 4 Electrical properties of Mg-*x*-CTSe (x = 0.0–0.2) pellets after Hall effect measurements

4. Summary

$Cu_2(Sn_{1-x}Mg_x)Se_3$ bulks (x = 0–0.2) were fabricated by a liquid-phase reactive sintering at 550ºC for 2 h. Mg-*x*-CTSe pellets at x = 0, 0.05, and 0.1 exhibited *p*-type conductivity and they were *n*-type at x = 0.15 and 0.2. Our study showed that Mg-*x*-CTSe bulk at x = 0.1 had the lowest carrier concentration of 3.2×10^{17} cm^{-3}, the highest mobility of 386 cm^2 V^{-1} s^{-1}, and the lowest electrical conductivity of 20 S cm^{-1}. The minimal hole concentration at x = 0.1 was attributed to the formation of the Mg_{Cu}^{+} donor defect, which was supported by the data of electrical property and the XRD peak shift. Finally, our material-selection study can provide a quick approach, not the time-consuming thin-film technique, to evaluate the absorbers for a thin-film solar cell device.

Acknowledgments

This work was supported by Ministry of Science and Technology of the Republic of China under grant numbers 102-2221-E-011-019-MY2 and103-ET-E-011-008-ET.

References

1. J.T.R. Dufton, A. Walsh, P.M. Panchmatia, L.M. Peter, D. Colombara, M.S. Islam, *Phys. Chem. Chem. Phys*. 14 (2012) 7229–7233.
2. M. Ibáñez, D. Cadavid, U. Anselmi-Tamburini, R. Zamani, S. Gorsse, W. Li, A.M. López, J.R. Morante, J. Arbioldg, A. Cabot, J. Mater. *Chem. A 1* (2013) 1421–1426.
3. J. Wang, A. Singh, P. Liu, S. Singh, C. Coughlan, Y. Guo, K. M Ryan, J. *Am. Chem. Soc.* 135 (2013) 7835–7838.
4. D.H. Kuo, W.D. Haung, Y.S. Huang, J.D. Wu, Y.J. Lin, *Thin Solid Films 518* (2010) 7218–7221.
5. K.M. Kim, H. Tampo, H. Shibata, S. Niki, T*hin Solid Films 536* (2013) 111–114.
6. G.S. Babu, Y.B.K. Kumar, Y.B.K. Reddy, V.S. Raja, Mater. *Chem. Phys.* 96 (2006) 442–446.
7. G. Marcano, C. Rincón, L. M. de Chalbaud, D. B. Bracho, G. S. Peŕez, *J. Appl. Phys.,* 90 (2001) 1847–1853.
8. R.A. Wibowo, S. Moeckel, H. Yoo, A. Hoelzing, R. Hock, P.J. Wellmann, *J. Alloy. Compd*. 588 (2014) 254–258.
9. G.E. Delgadoa, A.J. Mora, G. Marcanob, C. Rincón, *Mater. Res. Bull. 38* (2003) 1949–1955.
10. L.J. Van der Pauw, Philips Res. Rep.13 (1958) 1–9.

A Facile Synthesis of Mesoporous Silica Nanoparticle and its Morphology Manipulation by Varying pH Value

Zhifeng Yi[a†], Chunfang Feng[b], and Lingxue Kong[c†]

Institute for Frontier Materials, Deakin University, Geelong Campus at Waurn Ponds, Geelong, VIC 3216, Australia

E-mail: [a†]yzhi@deakin.edu.au, [b]chunfang@deakin.edu.au, [c†]lingxue.kong@deakin.edu.au

David Cahill[‡]

Centre for Chemistry and Biotechnology, School of Life and Environmental Sciences, Deakin University, Geelong Campus at Waurn Ponds, Geelong, VIC 3216, Australia

[‡]E-mail: david.cahill@deakin.edu.au,

Mesoporous silica nanoparticles (MSNs) with particle size of 20 nm have been synthesised through the template directed method at low temperature. The pH value of the reaction solution was found to have a great impact on the morphology of the final products. The morphology of resultant MSNs were investigated through transmission electron microscope. The mesoporous structure was examined by Brunauer-Emmett-Teller and Barrett–Joyner–Halenda methods. The results suggested that the high pH value had a great effect on the morphology of the final MSNs. Higher pH value intensified the interaction between particles. The pH value less than 10 is good for the formation of nanoparticles, while at pH 12, a silica framework with heterogeneous mesopore structure can be obtained.

Keywords: Mesoporous Silica Nanoparticles; Surfactant Template; pH Effects; Agrochemical Delivery System.

1. Introduction

Silica based nanomaterials have attracted the researchers' attention in recent decades due to the high surface area, quantum dot effects, controllable structure, and low toxicity [1]. Mesoporous silica nanoparticles (MSNs) with the pore diameter between 2 and 50 nm, as the most important candidature in this field, have tuneable porous and particulate structure and compelling applications in terms of biosensing, treatment of waste water and controlled drug delivery systems [2]. The MSNs with particle size less than 50 nm possess the excellent permeability. However, the synthesis of MSNs with the particle size less than

50 nm, especially as small as 20 nm, is still very challenging. It is because the porous structure at such a tiny particle size tends to collapse [3] and the interaction between particles will intensify the aggregation. Chiang et al. [4] have prepared MSNs with the particle size of 16.9 nm, but the surface area and pore size of these nanoparticles cannot be characterized, which means the unattended porous structure. A recently study from Ma and Wiesner [5] described the synthesis of MSNs with the particle size less than 10 nm. The size of the smallest MSNs they fabricated is around 6.6 nm. Only half or one pore were formed in one particle because of the sub-10 nm particle size, which impairs the ability of MSNs to be the carriers of agrochemicals. Therefore, the most challenging issue to prepare MSNs with 20 nm particle size is the maintenance of mesoporous structure.

The size of the resulted MSNs is associated to several factors such as the pH value, ionic strength, and temperature. Herein, CTAB was chosen as the surfactant template to form mesopores, and phosphate buffer solution and ammonia solution were used to as catalyst to accelerate the reaction of the silica source. We synthesized MSNs with 20 nm particle size and undamaged mesoporous structure in a facile and simple way. Also, the effects of pH value on the particle morphology were investigated. The relationship between experimental conditions and the final morphology of MSNs was also discussed based on the existing theory about the growth of MSNs.

2. Materials and Methodology

2.1. *Materials*

Cyltrimethylammonium bromide (CTAB, ≥99%) and tetraethyl orthosilicate (TEOS, 98%) were purchased from Sigma-Aldrich. Sodium hydroxide (NaOH), potassium dihydrogen phosphate (KH_2PO_4), ethanol and hydrochloric acid are the AR grade. All the chemicals are used without further purification.

2.2. *Synthesis of MSNs under Different pH Value*

The synthesis process of MSNs was based on the previous studies with modification [6]. We increased the concentration of CTAB, which provides more spots for silica nucleation, in turn leading to the formation of small particles. The effects of pH value on the morphology of MSNs was also investigated. Specifically, the phosphate buffer solution was obtained from mixing 1.74 g NaOH and 10.2 g KH_2PO_4 in 1.5 L Milli-Q water (final pH value is 7.2). The pH of the previously obtained phosphate buffer solution was adjusted by adding 2 M of NaOH aqueous solution to 9, 10 and 12. Then, 2.96 g of CTAB was dissolved in

100 mL of this buffer solution. The mixture was heated to 80 °C for 30 min to stabilize CTAB micelles. Then CTAB solution was cooled to 30 °C. TEOS (1.86 mL) was added into CTAB solution dropwise. The reaction was maintained at 30 °C for 4 h. The as-made MSNs were collected by the centrifugation and washed with ethanol for several times to remove the unreacted TEOS and free CTAB. The experimental parameters are listed in Table 1. To remove the CTAB templates inside MSNs, the as-made MSNs were redispersed into a mixture of 100 mL of absolute ethanol and 1 mL of hydrochloric acid. The mixture was stirred at 60 °C overnight. The final MSN powders without CTAB templates were centrifuged and washed with ethanol and dried under vacuum.

Table 1 Experimental parameters of MSN synthesis

Samples	pH	Temperature (°C)	CTAB (mM)	TEOS (mM)	Reaction time (h)
MSN-PH7	7.2	30	80	80	4
MSN-PH9	9	30	80	80	4
MSN-PH10	10	30	80	80	4
MSN-PH12	12	30	80	80	4

3. Results and Discussion

The morphology of the MSNs synthesized with different pH can be seen from Figure 1. At pH 7.2, spherical nanoparticles with the particle size of around 20 nm can be seen (Figure 1 A). At pH of 9 and 10, the branched morphology started to form and the nanoparticles were bonded chemically, which deteriorated their dispersity (Figure 1 B and C). Mesopores (white dots) can also be seen under TEM. An interesting finding is that the continuous increase of the pH to 12 led to a collapse of the particulate shape and the super-branched silica framework was detected (Figure 1 D). The mesoporous structure of all the samples can also be seen from the TEM images (white dots). These results suggested that the higher pH intensify the interaction between particles and form branched silica framework because the high pH increased the ionic strength of the reaction solution, which in turn screened the charges on the surface of adjacent particles, leading to the aggregation. The SAXS patterns of all the MSN samples (inset in Figure 1) were obtained at Australian Synchrotron possess uniform scattering, which suggested the isotropic mesoporous structure without any orientation.

The adsorption properties of these MSNs were investigated through nitrogen sorption isotherms. All isotherms exhibit typical type IV adsorption curve (Figure 2 A) according to IUPAC classification. The hysteresis loops at the relative pressure higher than 0.8 indicate the inter-connected porous structure [7]. For the MSNs synthesized at pH 7.2, 9 and 10, the main pore size distribution is at around 2-3 nm, while the MSNs synthesized at pH 12 possess a textural porous structure

that is indicated by the pore size at around 30 nm (Figure 2 B). The high pH dose not only affect the particle and pore formation, but also leads to the interaction between particles to form heterogeneous mesopore structure.

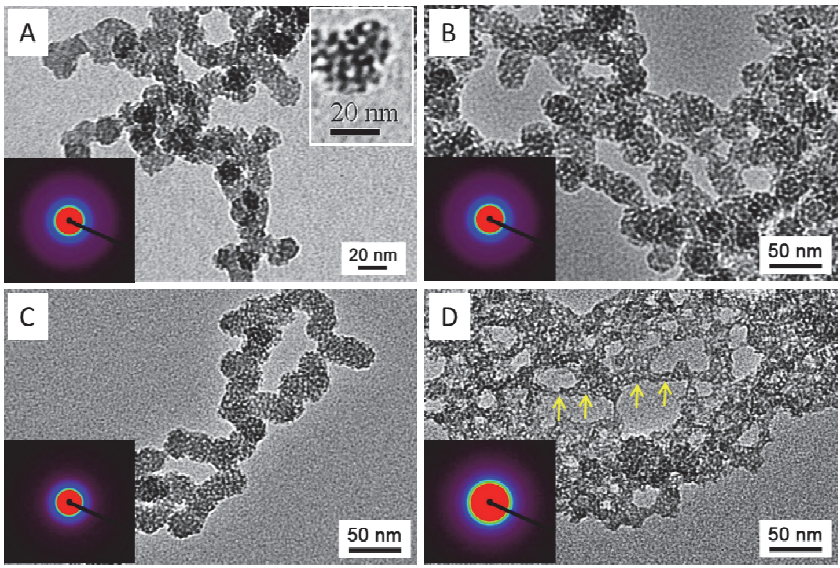


Figure 1 TEM images of MSNs synthesized in the phosphate buffer solution under different pH value. The inset figure at the top right in A is HRTEM image to show mesoporous structure. The inset figures at bottom left are the scattering patterns for the corresponding MSNs at SAXS with a synchrotron source. The yellow arrows in D indicate the super-branched mesoporous silica networks.

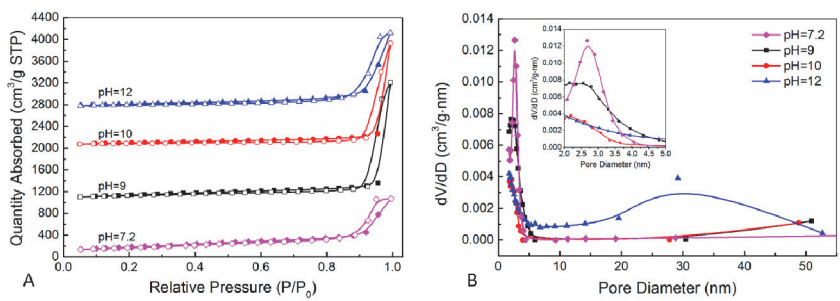


Figure 2 Nitrogen isotherms of MSNs synthesized at different pH (A) and the corresponding pore size distribution (B).

The surface area and pore volume is calculated from the nitrogen sorption isotherms (Figure 3). The surface area of MSNs decreases with the increase of pH value because inter-particle connections decrease the surface of each particle. The

pore volume of these MSNs is nearly the same at pH 7.2, 9 and 10, but it increases to about 1.29 cm^3/g when the pH reaches 12, due to the presence of the large pores formed by the silica framework.

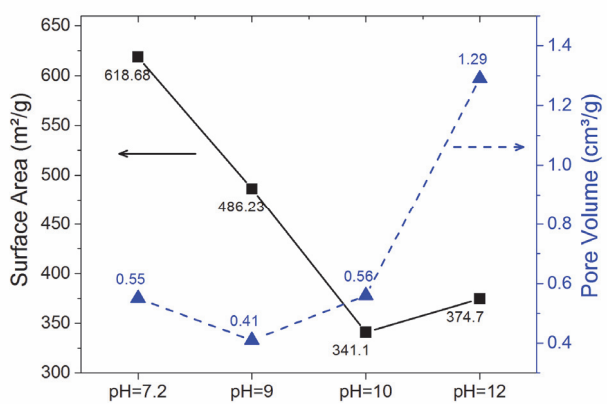


Figure 3 BET surface area and pore volume of MSNs synthesized at different pH value.

4. Conclusion

A facile and simple method to synthesize MSNs with small particle size and tunable mesopore structure has been proposed in the study. The particle size of MSNs was decreased because of the increased amount of CTAB micelles as the silica nucleation spots. By varying the pH value, the interaction between particles is intensified, and a heterogeneous mesopore structure can be obtained at pH 12, which can potentially offer heterogeneous catalyst ability for the further work.

Acknowledgements

We acknowledge the Institute for Frontier Materials, Deakin University for providing scholarships. The authors thank Rosey Van Driel (Institute for Frontier Materials, Deakin University) for helping with the characterization on TEM. We also acknowledge the beamtime provided by Australian Synchrotron under the grant M6410 in August 2013.

References

1. T. Barik, B. Sahu, V. Swain, Nanosilica—from medicine to pest control, Parasitology Research 103 (2008) 253-258.
2. L.D. Bonifacio, B.V. Lotsch, G.A. Ozin, *Periodic Mesoporous Materials*: Holes Filled with Opportunities, in: L.A. David, D.S. Gregory, P.W. Gary

(Eds.), Comprehensive Nanoscience and Technology, Academic Press, Amsterdam, 2011, pp. 69-125.
3. H. Jervis, S.G. Kazarian, K.L.A. Chan, D. Bruce, N. King, Water vapour-induced mesoporous structure collapse observed by VGI and FT-IR spectroscopy, *Vibrational Spectroscopy* 35 (2004) 225-231.
4. Y.-D. Chiang, H.-Y. Lian, S.-Y. Leo, S.-G. Wang, Y. Yamauchi, K.C.W. Wu, Controlling Particle Size and Structural Properties of Mesoporous Silica Nanoparticles Using the Taguchi Method, *The Journal of Physical Chemistry* C 115 (2011) 13158-13165.
5. K. Ma, H. Sai, U. Wiesner, Ultrasmall Sub-10 nm Near-Infrared Fluorescent Mesoporous Silica Nanoparticles, *Journal of the American Chemical Society* 134 (2012) 13180-13183.
6. Q. He, X. Cui, F. Cui, L. Guo, J. Shi, Size-controlled synthesis of monodispersed mesoporous silica nano-spheres under a neutral condition, *Microporous and Mesoporous Materials* 117 (2009) 609-616.
7. J. Hu, F. Gao, Y. Shang, C. Peng, H. Liu, Y. Hu, One-step synthesis of micro/mesoporous material templated by CTAB and imidazole ionic liquid in aqueous solution, *Microporous and Mesoporous Materials* 142 (2011) 268-275.

Investigation on Microstructure and Properties of X90 High-Strength Pipeline Steel Welded Joints

Z. Y. Bi[1, 2]

[1]*National Engineering Technology Research Center for Petroleum and Natural Gas Tubular Goods, Baoji 721008, Shaanxi, China*
[2]*Steel Pipe Research Institute of Baoji Petroleum Steel Pipe Co., Ltd., Baoji 721008, Shaanxi China*
Tel: (0917)3398455, E-mail: bsgbzy@cnpc.com.cn

The low temperature toughness and micro structure feature of base metal, weld seam and HAZ (heat affected zone) of X90 high-strength pipeline steel spiral welded pipe produced by industrial experiment were investigated. The results indicate that low temperature impact toughness of base metal is best, HAZ better weld seam poor at same temperature. The microstructure of near fracture zones of base metal was composed of fine acicular ferrite (FAF), quasi-polygonal ferrite (QPF), lath bainite (LB) and a small fine granular M-A (martenite / austenite) structure. The microstructure of near fracture zones of weld seam was composed of AF, and the form of M-A constituents shows diversity, cusp-clear and the size increased. The microstructure of near fracture zones of coarse-grain HAZ was composed of granular bainite (GB), and the square, wedged and bar M-A constituents distributed on the inside-grain and grain boundary, the size of M-A structure larger than that of base metal. The poor impact toughness of weld seam and HAZ specimen results from large size and cusp type M-A structure, while the existences of inclusion in weld seam make impact toughness worse.

Keywords: X90 Pipeline Steel; Impact Toughness; Welded Joints; Acicular Ferrite.

1. Introduction

Along with the growing demand for energy, the pipelines of oil and gas will inevitably forward high strength, high toughness, large wall thickness, large diameter and large throughput. Currently, the X90 of a new generation of high-strength pipeline steel is research and development in domestic. The series of research have started about X90 pipeline steel, mainly focused on the basic research of raw materials [1,2], and the system study on microstructure and properties of welded joints are not reported. Taking X90 SAWH base metal, weld seam and HAZ as the research object, through the system contrast study to explore the pipe characteristics in base metal, and the weld and HAZ and impact fracture toughness variation rule, providing the theoretical reference to X90 pipeline steel development engineering application.

2. Experimental

The X90 SAWH of with Ø1219 mm (pipe diameter) ×16.3 mm (wall thickness) for this experiment, and its chemical composition is for the mass fraction (%): 0.05C, 0.26Si, 1.93Mn, 0.22Ni, 0.34Cr, 0.23Cu, 0.34Mo, 0.018P, 0.001S, 0.12 (Nb+V+Ti). Adoption the high-strength and high-toughness of special welding wire and fluorine alkaline welding flux which were developed by Steel Pipe Research Institute of Baoji itself for X90 pipeline steel welding in this experiment. The chemical compositions of special welding wire for the mass fraction (%): 0.049C, 0.45Si, 1.84Mn, 2.2 (Ni+Cr+Mo), 0.018P, 0.009S, 0.06 (Nb+V+Ti+B). The welding flux brand BG - SJ101H2. Impact test according to *Metallic Materials-Charpy Pendulum Impact Test Method* (GB / T229-2007), using 10 mm × 10 mm × 55 mm Charpy V notch impact specimens, the test is carried out on NAI500F Charpy impact test machine. Using LeicaMEF-4M optical microscope and Hitachi S4300 cold field emission scanning electron microscope to observe fracture profile at first, then using EDAX Genesis6.0 type spectrometer (EDS) for incusion EDS analysisthe profile near the fracture and microstructure of M-A component is observed by JEM-200CX transmission electron microscope (TEM).

3. Results and discussion

3.1 Charpy impact experimental analysis

Table 1 shows the Charpy impact energy values in base metal, weld and HAZ. The impact energy in base metal and HAZ is relatively concentrated and dispersion is very small, which means toughness is stable, while impact energy in weld is scattered, which means poor stability in toughness. It follows that the toughness in base metal is the best, HAZ comes second, and weld is the worst.

Table 1 Data of impact experiments of base metal, weld seam and HAZ of X90 pipeline steel

Sampling Location	Test Temperature(ºC)	Impact Absorbing Energy(J)					
Base metal	-10	325	333	331	306	286	303
Weld seam	-10	181	192	131	77	182	176
Heat-affected-zone	-10	287	280	263	270	267	269

3.2 Features of fracture surface

Figure 1 shows the macro photos of impact specimen at fracture surface from base metal, weld and HAZ. Observed the figure we can find that the impact fracture surface of base metal and HAZ are similar, the characteristics of shear

lip area and fiber area is obviously and the area occupation is as high as 90%, both sides of the fracture surface area are raised and the middle region is sunken, serious deformation; while the fracture of weld impact specimen is relatively flat, deformation less, the proportion of radiation area is significantly increased, therefore, the toughness of weld is worse than that of base metal and HAZ.

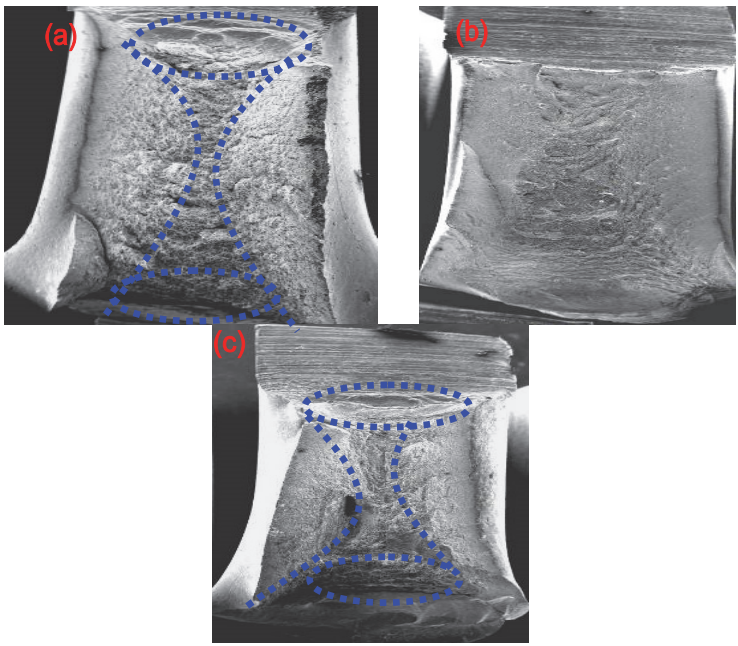


Fig. 1 Impact fracture surface of base metal (a), weld seam (b) and HAZ (c) samples

3.3 Fracture morphology and microstructure of base metal and HAZ in near fracture zone

The fracture morphology of base metal is given in Fig. 2a. It can be found that the characteristics of fracture surface is axised dimple, the large and deep dimples show a mosaic distribution. They are connected by fine and densely dimple surface. The microstructure characteristics of the near fracture zone of base metal are shown in Fig. 2b and 2c. It can be seen from the figures that the microstructure is fine acicular ferrite (FAF) + quasi polygonal ferrite (QPF) + lath bainite (LB) + a small amount of M-A structure. The group M-A structure is granular, flaky distributed in austenite grain, grain boundary and within lath boundary, and its size is small. Acicular ferrite microstructure has a high ability to prevent cracking, its composition is mainly composed of finer ferrite lath with

a wedge shaped M-A structure, with fine sub unit and high density of dislocations, and the effective grain size is smaller than other organizations [3]. The acicular ferrite which are intersecting and engagement with each other and their distribution state can effectively extend the crack propagation path, increase the crack extension resistance, can effectively improve the toughness of materials [4,5]. This is also one of the main reasons that the low temperature impact toughness of base metal is better than that of weld and HAZ.

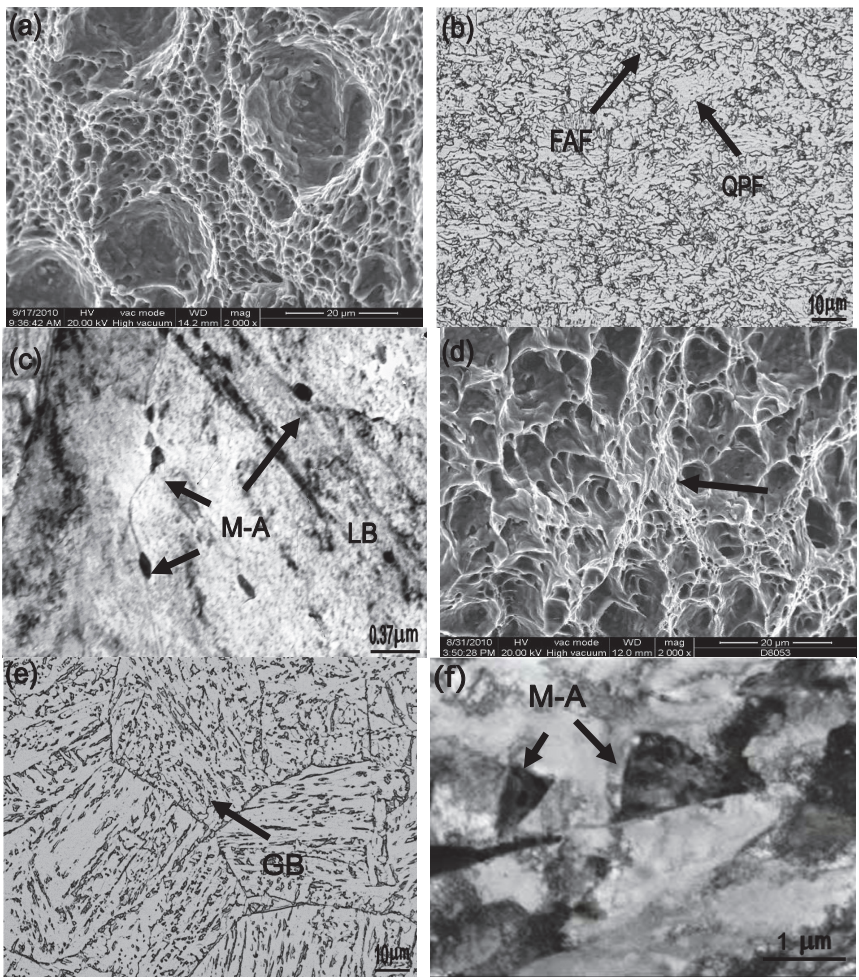


Fig. 2 Fracture morphology (a), OM (b) and TEM (c) micrographs in the near fracture zone impact sample of base metal and fracture morphology (d), OM (e) and TEM (f) micrographs in the near fracture zone impact sample of coarse-grain HAZ

Figure 2d shows the fracture morphology of impact specimen in the HAZ. In the figure, the feature of fracture surface in HAZ is ductile microvoid, which is parabolic and combined with tearing ridges, these tearing ridges becoming together and bigger, and there is no tiny dimples on them. It is with obvious difference when compared with feature of fracture surface in base metal.

The coarse grains locate zone where are closest to the fusion zone. Their peak welding temperature is higher (>1150ºC), this cause the grain size is much bigger than original base metal grains. Studies have reported that the weakest area of weld mechanical properties located in the weld coarse grain area and the critical area [6, 7]. From Fig. 2e and 2f the microstructure of HAZ is granular bainite (GB). In the figure, the original austenite grain boundary can be clearly observed, in the intracrystalline and grain boundary, M-A structure distribute in square, wedge and strip. As shown in figure in the arrow, compared with the base metal, HAZ grain size is bulky, M-A structure with a long and thin strip distribution in the grain boundaries and inside the grains, the size become bigger significantly, and with a certain direction. Large size cusp corner type M-A structure is easy to cause dislocation pileup and produce micro-stress field which provides conditions for micro-crack intiation [8]. This has certain damage on the material toughness.

3.4 Fracture morphology and microstructure of weld specimen in near fracture zone

Figure 3a shows the fracture morphology of weld impact specimens. As can be seen from the figure, the surface of weld specimens is characterized by intensive small dimple and the dimple is parabolic, there are torn edges as shown by the arrows connected between dimple and dimple. We can find granular inclusions at the bottom of the larger dimple. Chemical composition of the weld is significantly different from the HAZ and the base metal because it's deposited metal. We design the welding wire by using multiple alloying + micro-alloying method and adding lanthanon and micro-alloying elements Nb, V, Ti , B etc to make the chemical composition of the weld deposited metal is similar with the base metal and ensure enough weld toughness[3]. Fine Nb, V, Ti of C, N compounds formed during the welding will effectively pinning the austenite grain boundaries and prevent austenite grain coarsening. There will be a large number of precipitations in the subsequent continuous cooling process, the pinning dislocation play precipitation strengthening role. Mo alloyed has become a mature pipeline alloy design. Studies have shown that Mo can reduce the phase transition temperature of supercooled austenite, inhibit the formation

of polygonal ferrite and promote acicular ferrite transformation. Further, Mo can increase the solubility of C, N and Nb compound in austenite, reduce the precipitation temperature of Nb carbides and Nb nitrides, and improve precipitation strengthening effect of Nb carbides and Nb nitrides.

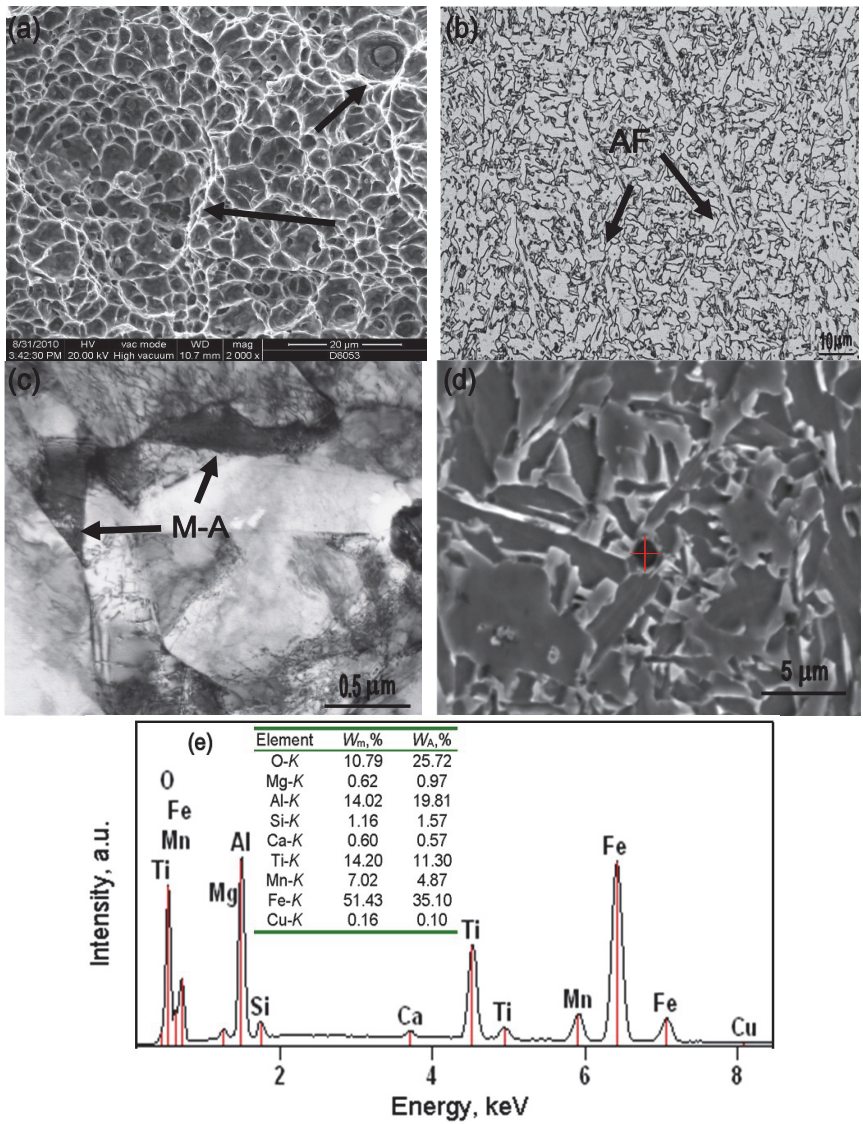


Fig. 3 Fracture morphology (a), OM (b), TEM (c) micrographs and the EDS results of inclusions in Fig. 3(d), 3(e) in the near fracture zone impact sample of weld seam

Multi-alloying and micro-alloying design of welding wire ensures weld metal can form a certain amount of inclusions as acicular ferrite nucleation centers. Figure 3d shows that the size of spherical inclusion is about 1.5μm, there is acicular ferrite radial grows around the inclusions. Figure 3e is EDS analysis of the weld inclusions. It shows that the composition of the weld inclusions is mostly oxide, including Al_2O_3, MgO, Ti_2O_3, MnO, SiO_2, etc by EDS analysis. There are in-depth study and detailed discussion by the author in the literature [3] Chapter 3. Inclusions are the most advantageous position for microporous to form and grow up together, under the effect of stress, it can easily cause local stress concentration to produce microscopic stress field, so the opportunity to form micro-cracks in the material significantly increased to do harm to the toughness of the material. Inclusions can easily speed up the connection and development of micro-cracks, forming the main crack, subsequently leading to fracture [8].

Figure 3b and 3c show the microstructure morphology for impact specimen near the fracture area in weld zone. The figure shows that microstructure in weld zone is mainly composed of densely acicular ferrite and M-A structure. Inclusions not only act as the nucleus promoting ferrite formation, but also create conditions for the formation and growth of microporous, which simultaneously enhances toughness and increases the damage to toughness at the same time. In conclusion, when designing composition of welding wire, it's important to determine appropriate alloying elements not only to realize the appropriate inclusions in weld zone, but also to guarantee good toughness in weld zone.

4. Conclusions

(1) For X90 high strength pipeline steel, the fracture morphology of base metal appear in large and deep dimple distribution characteristics. The fracture morphology of weld seam present a parabola type close-set tiny dimple and tearing ridge connected and larger granular inclusions dimples at the bottom. The HAZ fracture surface features to assemble and tear of the overgrowth of connected edges of parabolic toughening distribution. The impact toughness of base metal is stable and the best, the HAZ is better, the weld seam is poor.

(2) The raw material specimens near the fracture zone microstructure is fine acicular ferrite + Lath bainite + a small amount of M-A structure, M-A structure is in the granular and flaky, tiny dimension. The specimen of weld near the fracture zone is acicular ferrite, M-A component with diversity shapes, distribution in close-set and disorder, and its size is larger than that of base

metal. The microstructure of near fracture zones of coarse-grain HAZ was composed of granular bainite (GB), M-A component diversity in shapes, distributed inside-grain and grain boundary with some direction, the size of M-A conponent larger than that of base metal. The poor impact toughness of weld seam and HAZ specimen results from large size and cusp type M-A structure.

(3) The existance of inclusions in the weld provides conditions for acicular ferrite element shape, but to the impact toughness with great damage.

Acknowledgments

This work was supported by the National Science & Technology Pillar Program (No. 2011BAE35B01) Fund.

References

1. Y. F. Li, Q. Q. Wang, Q. G. Wang, X. B. L, R & D of X90 SAWH Pipes, *Steel Pipe*. 40 (2011)25-28.
2. Z. F. Gao, W. Huang, Study on Microstructure and Mechanical Property in Hot Affected Zone (HAZ) of Welded Joint of High Strength Pipeline Steel Produced in Russia, *Welded Pipe and Tube.* 35(2012)67-72.
3. Z. Y. Bi, *Welding Technology for Line Pipe*, first ed., Beijing Petroleum Industry Press, 2013.
4. D. V. Edmonds, R. C. Cochrane, Structure-property relationships in bainite steels, *Metall Mater Trans A*, 21(1990)1527-1540.
5. W. Deng, X. H. Gao, X. M.Qin, D. W. Zhao, L. X. Du, *et al*. Impact fracture behavior of X80 Pipeline steel, *Acta Metall Sin*, 46(2010)533-540.
6. Z. Y. Bi, X. T. Jing, X. L. Xu and S. L. Jin, Microtructure and Performance on Weld of Reheated X80 Steel, *Journal of Iron and Steel Research*, 5(2010)27-31.
7. Y. Q. Chen, Z. Y. Du, L. H. Xu, Microstructure and mechanical properties of heat affected zone for X80 pipeline steel, *Transactions of the China Welding Institution*, 5 (2010)101-105.
8. Z. Y. Bi, J. Yang, J. Niu, J. X. Zhang, Fracture toughness of welded joints of X100 high-strength pipeline stee, *Acta Metall Sin,* 5(2013)576-582.

Parameter Optimization Research of Oil Spill Tracking Buoy

Rui Yang† Qun Gu
No.8, Xitucheng Road, Haidian District,
Beijing, China Waterborne Transportation Institute
E-mail: †yangr@wti.ac.cn, 68861452@qq.com

Based on the study of technical characters and research situation of oil spill tracking buoy, the technique parameters of tracking buoy has been optimized by a hydrodynamic method through hybrid adaptive ant system algorithm. To achieve an all-weather whole procedure monitoring propose for oil spill by using of satellite positioning communication mode, provides an effective technical method for the rapid response of oil spill emergency.

Keywords: Tracking Buoy; Parameter Optimization; Oil Spill; Adaptive; Ant System Algorithm.

1. Introduction

China's crude oil imports reached 285 million tons in 2013, which rose 6.8% from a year earlier. Crude oil import dependence may top 60 percent, meaning that the risk of the oil spill accidents is obvious. The oil spill accidents have significant impact on marine environment, property and people health, and will cause serious pollution damage to the marine ecological environment and fishery resources.

The oil tracking buoy[1] is a kind of water surface drifting buoy. It utilizes satellite positioning communication techniques and can effectively track the oil under different sea states. The tracking buoy provides an effective technical measure for the oil spill events. It can track the oil spill drift location fast and accurately, which enable us to take measures earlier to reduce accident damage and warn the sensitive areas, reducing or avoiding pollution. Through the buoy, the contingency cleaning plans can be launched immediately and the effective commands can be made, effectively stopping the spread the spill oil. At the same time, the oil track buoy can also improve the cleaning efficiency, reducing the pollution and the cleaning cost.

Ant System algorithm[2], declared by Dr. M. Dorigo from Italy, is a new simulate evolution algorithm to resolve complex optimization, and he was

enlightened from biology evolution. This algorithm simulates the action of finding food of real ant system in nature. It using man-made ant with memories, finds the shortest path from ant hole to food source through the information communion and cooperation of each ant. Today, man-made ant system algorithm has been applied to a series of optimizing combination problems such as discrete traveling salesman problem[3], quadratic assignment problem[4] and network routing, and shows advantage of ant system algorithm partly. Meanwhile, it also shows a low convergent speed and lack of pheromone in the beginning at the same time.

2. Ant System Algorithm

The research on finding food of ants by biologists indicated that the reason why ant system can find the shortest path from hole to food source without any notice. When single ant searches the food, it will release a special secretion which we called pheromone. The probability of after ants choosing this path is in direct ratio to the thickness of pheromone. With the accumulation and volatilization of pheromone, the ant systems find the shortest path finally.

2.1. *Artificial Ant System Algorithm*

The phenomenon above produces the man-made ant system algorithm. Defines the probability of k^{th} ant as:

$$p_{ij}^{(k)} \leftarrow \frac{\left(\tau_{ij}^{(k)}(t)\right)^{\alpha}\left(\eta_{ij}^{(k)}(t)\right)^{\beta}}{\sum_{r}\left(\tau_{ir}^{(k)}(t)\right)^{\alpha}\left(\eta_{ir}^{(k)}(t)\right)^{\beta}} \quad r \in allk \tag{1}$$

In the Eq. (1), $allk$ is the set of the selected path of kth ant from i to j; $\tau_{ij}^{(k)}$ is the thickness of pheromone of this ant from i to j; $\eta_{ij}^{(k)}$ is the weigh of the ant from i to j; $i, j \in \Omega$.

So, there are some advantages of ant system algorithm on the problem optimization. Firstly, ant system algorithm holds a selection system. The more pheromone thickness, the more selection probability, and it is a regenerative feedback. Secondly, it holds an intact pheromone thickness refreshing system. The pheromone thickness on path will increase with the increasing of the times of ants passing, and will decrease with time coming by, which reduces the probability that a longer path is selected.

2.2. *Hybrid Adaptive Ant System Algorithm*

Hybrid Adaptive Ant System Algorithm is based the origin man-made ant system algorithm. Importing a weight multiplier of normal distributing ξ_{ij} :

$$\xi_{ij} \leftarrow \frac{\sum_{k}^{m} \Delta\tau_j}{\sum_{1}^{m} \Delta\tau_i} \tag{2}$$

Then import the weight multiplier into selection probability equation. Now selection probability of the k[th] ant from i to j below:

$$p_{ij}^{(k)} \leftarrow \frac{\xi_{ij}\left(\tau_{ij}^{(k)}(t)\right)^{\alpha}\left(\eta_{ij}^{(k)}(t)\right)^{\beta}}{\sum_{r}\xi_{ij}\left(\tau_{ir}^{(k)}(t)\right)^{\alpha}\left(\eta_{ir}^{(k)}(t)\right)^{\beta}} \qquad r \in allk \tag{3}$$

From Eq.(3), after the multiplication of weight multiplier by pheromone and weigh, the effect of selection probability for k[th] ant by pheromone τ_{ij} ,and weigh η_{ij} ant increase with ξ_{ij} , which increase the selection process.

2.3. *Functions Global Optimum Value Problem*

The Hybrid Adaptive Ant System Algorithm this paper purposed can apply to multi-extremum continuous functions and nonlinear continuous function. Let weigh is $\eta_{ij} \leftarrow Z_i - Z_j$, Z_i is the value of object function when searching function in position i.

The process of applying it to multi-extremum continuous functions and nonlinear continuous function is as follows. First, diffuse the ant number to the answer's definition area equably, and get the best value of object function. Then, choose ant base on the selection probability with local searching to get better answer. Finally, update the pheromone thickness and selection probability dynamic in normal school, then make ant system find the best answer through repetition and iterative continuously.

Test function is $z = 0.5 - \frac{\sin\sqrt{x^2+y^2} - 0.5}{[1+0.001(x^2+y^2)]^2}$ x, y∈ (-10 10) (4)

The plots of the functions are showed in Fig. 1. From Table 1, the function have infinite general max values Vmax=1.9360, spreading at a circle with center is origin and radius is 4.6850.

Table 1 is the result of simulation.

Table 1 Result of simulation in function by Hybrid AS

subject	*parameter*
Average Times	1.6
Cycle Time (S)	0.578
Expectation	1.9360
Square Error	0
Ratio of Maximal Value	100%

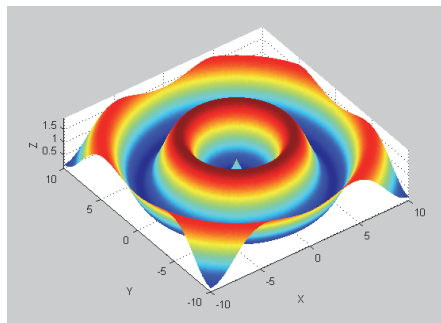


Fig. 1 The plots of test functions

3. Oil Spill Tracking Buoy

3.1. *Buoy Structure Study*

Maritime Tracking and positioning buoy must have the similar drift characteristics of the spilled oil it tracks with simple structure, light weight, good drift property as far as possible. According to the specific characteristics of buoy, the design of overall parameters of buoy such as: water area, frontal area, the water height, mass balance should be optimized and modified basing on the hydrodynamic performance of the drift buoy. The overall 3D effect design of tracking positioning buoy is shown in Fig. 2.

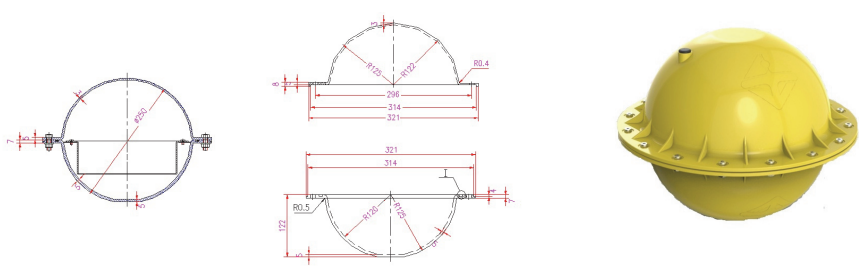


Fig. 2. 3D effect design of tracking positioning buoy

Based on its hydrodynamic utilized satellite positioning communication technique, the oil tracking buoy has a good tracking ability in different regions, under different sea states and for different oil film.

3.2. *Hydrodynamic Performance of Buoy*

The tracking motion of a buoy in the sea water will be affect by wind and water below the surface of water[5]. If the buoy could follow the spilled oil film perfectly, then the buoy velocity is equal to the velocity of oil film. The sea water force on the buoy could be expressed as:

$$F_{water} = \frac{1}{2}\rho_{water}\left(V_o - V_{water}\right)^2 A_1 C_{Dc} \tag{5}$$

A_1 : water area, C_{Dc} : sea water resistance coefficient of buoy.

With the equivalent wind velocity of V_{10} and current velocity:

$$F_{water} = \frac{1}{2}\rho_{water}\left[(\zeta - \alpha)V_{10}\right]^2 A_1 C_{Dc} \tag{6}$$

ζ : wind coefficient with an area of 1.6%-3.5%,mainly depending on the depth of oil film.

The direction of resistance applied on the buoy by different sea water is opposite with the relative velocity of buoy and seawater. From the wind force on buoy point of view, take the uniform motion of buoy into consideration, the wind force and water resistance should be equal:

$$\rho_{water}\left[(\zeta - \alpha)V_{10}\right]^2 A_1 C_{Dc} = \rho_{air}\left[(1-\zeta)V_{10}\left(\frac{8h}{150}\right)^{1/7}\right]^2 A_2 C_{Da} \tag{7}$$

For $\alpha < \zeta < 1$, then:

$$\frac{\zeta - \alpha}{1-\zeta} = \left(\frac{\rho_{air} A_2 C_{Da}}{\rho_{water} A_1 C_{Dc}}\right)^{1/2}\left(\frac{8h}{150}\right)^{1/7} \tag{8}$$

It could be found that the tracking characters (wind coefficient) of buoy are mainly decided by its design parameters (the height of buoy above water, the shape of buoy above and below water etc.).The required high tracking accuracy could be optimized by the geometric parameters of buoy and sea state parameters in the design process.

4. Parameter Optimization Research

Based on the hydrodynamic study of buoy, the micro sea oil spill positioning and tracking buoy has been developed and practiced in an oil spill emergency test, which achieved good experimental results and practical experience.

The steps of buoyparameter optimization using ant system algorithm is: first, generate M dot random, then put M ants on hydrodynamic performance functions; secondly, each ant choose next dot base on probability, which depends on thicker pheromone thickness; then, when all of ants complete a searching, update the pheromone thickness. Each ant releases pheromone inverse ratio to length of the path. Finally, each ant begins a new searching until the stop condition satisfied.

The result of oil spill tracking buoy based on hybrid adaptive ant system algorithm are showed in Table. 2.

Table. 2. Parameter optimization result of spherical buoy in diameter 250mm

Weight /kg	*A2/mm2*	*A1/mm2*	*A2/A1*	*h/mm*	*CDC/CDa*	*k*	ζ
8	3980	45083	0.0882	34	0.0117	0.000450002	0.0164
7	10183	38880	0.2619	65.3	0.2587	0.004000775	0.0199
6	15574	33489	0.4650	88.7	0.4778	0.007569109	0.0234
5	20605	28458	0.7240	109.3	0.7394	0.012104676	0.0278
4	25519	23544	1.0838	129	1.0485	0.018058705	0.0335
3	30605	18458	1.6580	149.5	1.6017	0.028193913	0.0430

5. Conclusion

The ocean environment is very complicated. The environment and climate are different at different area in different season under different weather conditions. The differences of environment and climate have influences on the drift of spill oil. The oil tracking buoy is a fast effective approach for the oil spill events, which is also stable, reliable and inexpensive. The oil spill track buoy utilizes satellite positioning communication techniques, which makes it have good tracking ability under different sea states.

Reference

1. Test Report with oil spill tracking buoy in East China Sea, China Waterborne Transportation Institute, 2014.1
2. Dorigo M, Maniezzo V, Colorni A. Ant system: optimization by a colony of cooperating agent *[J]. IEEE Trans on Systems, Man , and Cybernetics*, 1996, 26 (1): 29-41

3. Dorigo, M., & Gambardella, L. M. A cooperative learning approach to the traveling salesman problem *[J]. IEEEE Trans on Evolutionary Computation*, 1997, 1(1):53–66.
4. V. Maniezzo and A. Colorni, "The Ant System Applied to the Quadratic Assignment Problem," *IEEE Transactions on Knowledge and Data Engineering*, vol.11, pp.769-778, 1999.
5. Wang Tianlin, Liu Yindong, Improving effectiveness of oil-spill tracking buoys, *Journal of Harbin Engineering University*, 2009 (9) :986-990

Mechanism of Pump Efficiency Promotion by Multi Traveling Valve Device

Xiaolong Li[a*], Xiaoqiang Liu, Liping Zhou, Huaru Xu
China University of Petroleum (East China), School of Petroleum Engineering, ShanDong QingDao 266580, P.R.China ;
Email: [a]lixiaolong199041@foxmail.com,

Wen Xiao[b]
Research Institute of Oil Production Technology, Shengli Oil Field Branch, SINOPEC Group, ShanDong DongYing 257000, P.R.China
Email: [b]xiaow0811@hotmail.com

Leakage of pump, low efficiency of rod pump system are serious problems in the procedure of oilfield development at present. Multi traveling valve is a new kind of low-cost and convenient method which is escalated from conventional rod pump. It is effective in the aspect of stroke loss reducing, leakage mitigating, pump efficiency improving, segmentation-lifting and so on. Through theoretical analysis, formula derivation and practical applications, draw the conclusion: the ranges of installations number is 4-6, maximum of efficiency promotion is about 11%.

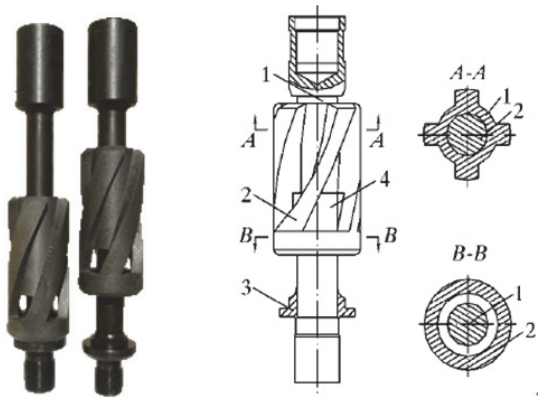
Keywords: Multi Traveling Valve; Leakage; Pump Efficiency; Segmentation-Lifting.

1. Introduction

Conventional rod pump system consist of 4 parts: rod, piston, traveling valve and standingvalve[1].Wellbore fluid will all load on traveling valve when sucker upstroke. Therefore traveling valve load large and attrition easily. And then abrasion of traveling valve causes leakage, low pump efficiency and other serious problems especially in deep well or heavy loads well[2]. Large stroke, low times of strokes and pump inspection are common methods to solve these problems in oil field[3,4].

Multi traveling valve is a new kind of low-cost and convenient method which is escalated from conventional rod pump. Multi traveling valve device installed on rod equips the centralizer and changeover function due to its structural characteristics. Multi traveling valve devicehas been put into use[5].

* Corresponding author.



1- Cartridge; 2- Traveling valve; 3- Valve seat; 4- Trepanning

Fig.1 Multi traveling valve device

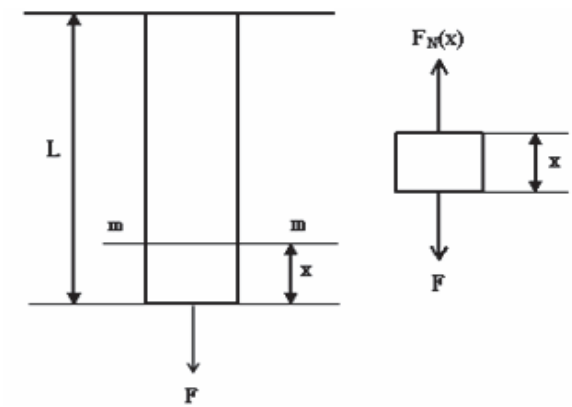


Fig.2 Force model of sucker rod

2. Mechanism of Multi Traveling Valve Device

As seen in Fig.1, Multi traveling valve device consists of cartridge, traveling valve and valve seat. It is connected with the rod up and down. Traveling valve is coated in the middle of cartridge and vertically movable. There are trepanning for fluid flowing on the traveling valve. Valve seat and cartridge are integrative in the device. The traveling valve assemblage consists of traveling valve and valve seat.

When unloading in downstroke, traveling valve goes upward by friction and pressure underlying. Then traveling valve assemblage open up and fluid flows from the trepanning. When loading in upstroke traveling valve goes downward by friction and liquid head upside until it is packed with valve seat. Then

traveling valve assemblage block up and fluid column goes upward with upstroke.

Joint multi traveling valve device and rod is equal to disperse the liquid head on sucker to the devices. Reduce the loss of plunger stroke and improve pump efficiency[6].

Dead load of rod can't be omitted. Axial force is not a constant on different cross-section. Firstly compute the elastic elongation of infinitesimal which length is *dx*, and then compute the elastic elongation of whole rod by integrating.

Compute the axial force on cross-section m-m. Assumptions are upstroke, constant diameter, inertial load omitted. According to force balance rule:

$$F_{\mathrm{x}} = A\gamma x + \rho g S L \tag{1}$$

A stands for dimensions of rod cross-section, m^2; γ stands for specific weight, $\gamma = \rho_{\mathrm{rod}} g$, N/m^3; ρ stands for density of wellbore liquids, kg/m^3; S stands for cross-section of well bore liquids, m^2; L stands for length of whole rod, m.

Application of Hooke's law:

$$\Delta(x) = \frac{F_{\mathrm{x}}}{EA} dx \tag{2}$$

E stands for elastic modulus of rod, N/m^2.

Assume that liquid in wellbore is monophasic fluid, omit leakage. Compute the elongation of rod which length is L:

$$\Delta L = \int_1 \frac{F_x(\mathrm{x})}{EA} dx = \frac{1}{2}\frac{\gamma}{E} L^2 + \frac{\rho g S}{EA} L^2 = (C_1 + C_2)\ L^2 \tag{3}$$

C_1, C_2 are abbreviation of elastic elongation modulus.

The elastic elongation can't be eliminated. But the elastic elongation caused by load of liquid head can be reduced according to formula 3. Reduce the elastic elongation by decrease the load of liquid head and then improve the pump efficiency[7].

The elastic elongation caused by load of liquid head is:

$$\Delta L_\gamma = \frac{F_\gamma}{EA} L = \frac{\rho \mathrm{g} L S}{EA} L = \frac{\rho \mathrm{g} S}{EA} L^2 \tag{4}$$

F_γ is the force caused by load of liquid head, N.

From wellhead to the bottom, every elastic elongation caused by load of liquid head between two devices is:

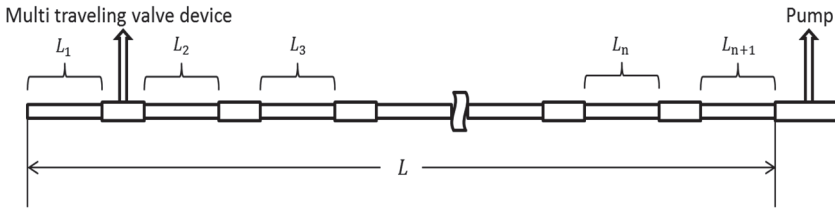


Fig.3 Schematic diagram of devices installation

$$\Delta L_{n+1} = \frac{\rho g S(L - L_1 - L_2 - \cdots - L_n)}{EA} L_{n+1} \tag{5}$$

Omit the dead load of devices because their quality are small compared to the whole rod. Then the whole elastic elongation caused by load of liquid head is:

$$\Delta L_z = \Delta L_1 + \Delta L_2 + \Delta L_3 + \cdots + \Delta L_{n+1} = \frac{\rho g S}{EA}(L^2 - \sum_{\substack{i=1, j>i \\ j \le n+1}}^{n} L_i L_j) \tag{6}$$

The difference between before and after installation of devices is:

$$\eta = 1 - \frac{\Delta L_z}{\Delta L_y} = \frac{\sum_{\substack{i=1, j>i \\ j \le n+1}}^{n} L_i L_j}{L^2} = \frac{M}{L^2} \tag{7}$$

Reducing the elastic elongation is equivalent to enlarge the effective stroke, scilicet larger the value η. And then improve the pump efficiency. Value η is equal to efficiency values.

The number of devices (n) correspond different extrmum M. Assume M_1 stands for extremum of one device, M_2 sands for extremum of two devices, so:

From formula 7 $\eta = 1 - \frac{\Delta L_z}{\Delta L_y} = \frac{\sum_{\substack{i=1, j>i \\ j \le n+1}}^{n} L_i L_j}{L^2} = \frac{M}{L^2}$, then:

$$M_{n\max} = \frac{M_{n+1}^2}{(n+1)^2} L^2 = \frac{1}{2} g \frac{1}{1 + \frac{1}{n}} L^2$$

Thus

$$M_{\max} = \lim_{n\to+\infty} \frac{M_{n+1}^2}{(n+1)^2} L^2 = \lim_{n\to+\infty} \frac{1}{2} g \frac{1}{1+\frac{1}{n}} L^2 = 0.5L^2, \quad \eta_{\max} = \frac{M_{\max}}{L^2} = 50\%$$

Consider the ratio between load of liquid head and whole load (consist of dead load and liquid load),

$$K = 1 - \frac{1}{1+\frac{\rho g S}{EA} \Big/ \frac{\gamma}{2E}} = 1 - \frac{1}{1+2\rho g S/\gamma A} \approx 0.228 .$$

Then

$$\eta'_{\max} = K\eta_{\max} \approx 11.4\%$$

As seen from Fig.4, the preferred number of devices is 4-9. The devices significantly improve the efficiency when the number is 4-9 and theoretically the maximum of improved efficiency is 11.4%.

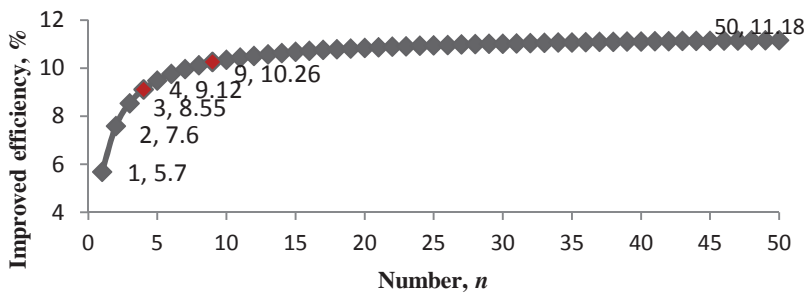


Fig.4 Relation between number of devices and efficiency

3. Conclusion

(1) Multi traveling valve device is effective in the aspect of stroke loss reducing, leakage mitigating, pump efficiency improving, segmentation-lifting, sucker lifetime extension and so on.

(2) The devices significantly improve the efficiency when the number is 4-9 and theoretically the maximum of improved efficiency is 11.4%.

(3) The optimization of installation is even placed.

References

1. Sofiane Benhaddad, Glen Lee, Role of microstructure in sucker rod string failures in oil well production [J]. *Practical Failure Analysis*, 2001, Vol.1 (2)
2. Zhang AD, Li P, Xiao YJ, et al. Forces exerted on eccentrically worn pumping rod and reasons [J]. *Petroleum Drilling Techniques*, 2004, 32(6): 38-40.
3. Chen Yong Ming. Discusson improving the efficiency of the system by pumping process [J]. *China Petroleum Machinery*, 2009, 37(10): 90-91.
4. Pan JL, Jin GJ, Jing WS. Analysis and economic evaluation of sucker rod stress [J]. *Oil-Gas Field Surface Engineering*, 2006, 25(11): 12-14.
5. Zhu MH, Gong XF, Lu GH, et al. Centralizer of Sucker rod [J]. *China Petroleum Machinery*, 2004, 32(10): 62-63.
6. Sun WJ, Ma LZ, Tang HB. Analysis on common subsurface failure of sucker rod pumping installation [J]. *Oil Field Equipment*, 2002, 31(4): 59-61.
7. Qu ZQ, Li XL, Cheng YH, et al. Mechanism and application of rod system efficiency promotion by Stimulative nipple [J]. *Fault-Block Oil & Gas Field*, 2014, 21(1): 133-136.

Characteristics and Advances of Graphene

Li Liu†

School of industrial manufacturing,
Chengdu University, Chengdu
†E-mail: 843814006@qq.com

Chang Chun Zhou

National Engineering Research Center for Biomaterials,
Sichuan University, Chengdu
E-mail: 20296317@qq.com

Graphene as a new carbon material allotropism body has many unique properties. The material structure of graphene is a two-dimensional crystal structure with carbon atom superposition in monolayer mode. This special structures exhibit many unique physical and chemical properties, etc. This paper introduced the special physical and chemical properties of graphene, and reviewed the research progress and applications of graphene in the high-tech fields.

Keywords: Graphene; Characteristic; Structure; Research progress.

1. Introduction

The new material is the new industry development foundation of 12th five-year plan of seven big strategic. The quality of carbon materials is light and exist in many forms with large reserves in the nature, such as fullerenes[1,2], carbon nanotubes (CNT)[3,4], etc. Have always been the goals of science and technology research and development. In recent decades, CNT has long been regarded as one of the most likely to be used for nano electronics materials. CNT, however, because the separation is very difficult to get uniform CNT material structure and performance, It becomes the biggest bottleneck of the CNT.

In October 2004, British scientists first reported a new carbon material-graphene[5] (graphene) in the journal Science. Graphene's special structure form makes it the world's most hard qualities, but also has a strong toughness, conductivity and thermal conductivity. Graphene is a two-dimensional single

atomic layer structure that makes up of sp2 hybridization carbon atoms that are connected in a six-party lattice honeycomb shown in Figure 1[6].

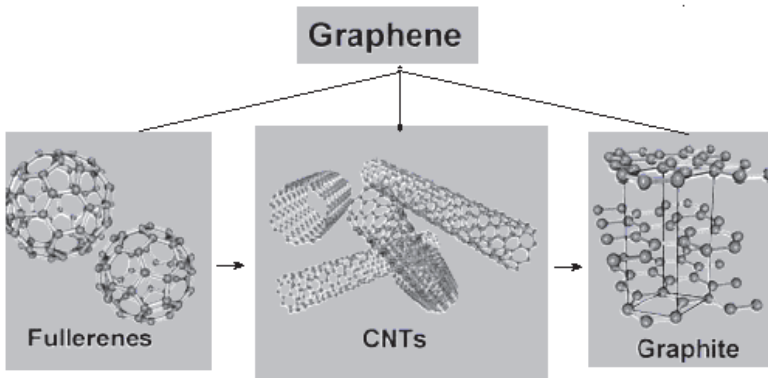


Figure 1. Graphene and other carbon

2. Characteristics of Graphene

2.1. *Chemical Properties*

Graphene's structure is similar to graphite，its surface can absorb and strip can be all kinds of atoms and molecules. From the surface chemical point of view, graphene is similar to the properties of graphite, can use graphite to estimate the properties of graphene. But due to lack of applicable to traditional chemical methods of samples, so the characterization of graphene chemistry is still fraught with difficulties.

2.2. *Electrical Conductivity*

Strictly two-dimensional material can't exist independently, this is because the 2D structure is the thermodynamic instability of material structure [7]. Graphene is found for the first time in human history the most close to the two-dimensional material in a strict sense; it has many unique electrical properties. The resistivity of grapheme is about 10^{-6} Ω. cm, with half integer quantum hall effect, will never disappear conductivity; Its more than 15000 cm2 / V • s electron mobility, but silicon electron mobility of 1400 cm2 / V s, therefore is widely applied in communication technology[8]. Graphene present relatively some opacity, light transmittance as high as 98%, it absorbs about 2.3% of visible light, is expected to be used in the field of modern electronic technology applications.

Another feature of graphene is the carry electronic rate is high, its carry electronic speed reached 1/300 of the speed of light, far more than the electronic speed in general conductor, this makes material has efficient conduction efficiency. Electrons in graphene (load sub-electric charge carrier), its nature is similar to relativity nature of neutrinos.

2.3. *Mechanical Properties*

Graphene's intensity is the highest substance known to mankind, it is hard than diamonds and more than the best steel in the world high strength on 100 times. The physicist of Columbia University test on graphene showed that added 55 Newton's pressure to make 1 microns long graphene fracture.

2.4. *Memory Effect*

Determination of the thermal ionization mass spectrometry, the memory effect is mainly adsorbed by the sample surface and the graphene deposition caused by two factors. Performance of a memory effect measurement results of Sample affected isotype measured over the remaining sample in the ion source, the current measured after the sample isotopic abundance greater the difference, to bring the greater memory effect. When contact with the inner surface of the steam and some strong activity ion source compound adsorbed, the number of materials and finish in addition to the amount of adsorption on the nature of the compound, and with the inner surface on the ion source.

2.5. *Micro-Graphene and Graphene Sheet*

Graphene made of the carbon atoms in single flake structure, is only a carbon atom thickness of 2D materials; And graphene micro film is refers to the carbon layer more than 10 layer, thickness within 5-100 nanometer thin deposit of graphene layer. Micro-graphene and graphene sheet are two kinds of different material, icro-graphene has a distinct competitive advantage.

3. Application of Graphene

In the past, the main research field of graphene has been focused on the fundamental physics and electronics[9]. Due to the excellent electrical properties, graphene has a broad applications in the next generation of nanoscale electronic devices, high-speed transistors, solar cells, display technology, flexible touch screen, and other fields.

4. Summary

Since the discovery of graphene in 2004, Graphene found that since 2004, in order to be able to apply the nature of the graphene is excellent in reality, people by constantly changing the methods of preparation of graphene in the preparation of large area high quality graphene. Due to domestic institutions mainly engaged in research on graphene for some of the major scientific research institutions and graphite products production enterprises, only a small amount of production of graphene samples, and no large-scale production capacity, also does not have the formation of the downstream application and demand, so the graphene scale requires at least eight to 10 years to realize industrialization. All kinds of manufacturing methods of graphene also need to solve problems, and various improvement techniques also in development, industrialization is most likely to use of graphene downstream industry is composite material field and display technology.

Graphene fast growth to science from a newborn star, graphene is special characteristics of discovered and developed gradually, but in the research and application of graphene still exists a lot of challenges, there exist many problems, needs to be further in-depth study, the organic chemist, materials chemists and engineers is to work together.

References

1. Thrower P A. Novel carbon materials — what if Carbon, 1999.37: 1677~1678.
2. Kroto H W, Heath J R, O'Brien S C, et al. C60: Buckminsterfullerence. *Nature*, 1985. 318: 162~163.
3. Iijima S. Helical microtubules of graphic carbon. Nature, 1991. 354: 56~58.
4. Iijima S, Ichihashi T. Single-shell carbon nanotubes of 1-nm diameter. *Nature*, 363: 603~605.
5. Novoselov K S, Geim A K, Morozov S V, Jiang D, Zhang Y, Dubonos S V, Grigorieva I V, Firsov A A. Electric field effect in atomically thin carbon films. *Science*, 2004. 306: 666~669.
6. Seyller Th, Bostwick A, Emtsev A K, et al. Epitaxial graphene: a new material. *Phys. Stat. Sol.* (b), 2008. 245:1436~1446.
7. Born M, Huang K. *Dynamical Theory of Crystal Lattices*, Oxford University Press, Oxford, UK 1998.
8. Liao Qing, Investigations on the growth of graphene and related structures, [D], Zhejiang University, 2011.
9. http://www.icgoo.net.

Radiation in a Thermal Analysis of a Power Box

Bo Chen†

The Key Laboratory of Microwave Remote Sensing, Chinese Academy of Sciences, Beijing 100190, China
†E-mail: chenbo@mirslab.cn, cbo_111@163.com

Ning Li

National Space Science Center, Chinese Academy of Sciences, Beijing 100190, China
E-mail: lining@mirslab.cn

It is discussed whether outside radiation of the surface of a satellite borne power box which will be located inside the satellite could be dis-considered while analyzing temperature of the box. Results show that when the outside radiation of the box is computed the maximum temperature is 67.6ºC, and when the outside radiation of the box is not considered the maximum temperature is 67.7ºC. The maximum difference of key components is much less than 1ºC. After the finite element computed, the scope of outside temperature of box was gotten, then the resistance of conduction of the whole box and the resistance of outside radiation of the box are calculated referring with equations. The radiation resistance is 0.86ºC / W and the conduction resistance is only 0.02ºC / W, show that the heat will transfer mainly through conduction. Radiation could be ignored when doing thermal analysis of this kind of satellite borne boxes. It could save some computing time when do such analysis.

Keywords: CAE; Thermal Modeling; Radiation.

1. Introduction

In this paper the problem is discussed whether outside radiation could be ignored while analyzing temperature of a satellite borne power box.

2. Methods and Processes

2.1. *The Main Structure*

Material is aluminum and main structure is a box, 226mm×185mm×167mm. Total power consumption is 42 W, including two main thermal consumption PCBs (shown in Fig. 1 and Fig. 2), and some modules on PCBs (shown in Table. 1).

2.2. *Expressions*

The thermal contact resistance R_c could be computed referring with Eq. 1 shown below:

$$R_c = \frac{1}{hA_c} \tag{1}$$

where h is thermal contact conductance coefficient, A_c is the contact area.

The radiation resistance could be computed approximately referring with Eq. 2 shown below:

$$R_r = \frac{T_i - T_x}{A_i \varepsilon_i \sigma (T_i^4 - T_x^4)} \tag{2}$$

where A_i is the radiation area, ε_i is the infrared emissivity, σ is the Stefan-Boltzmann constant, T_i is the surface temperature, and the T_x is the environment temperature, which is valued 45ºC when analyzing the high temperature work case.

2.3. *Processes*

Firstly, build a finite element model in computer. Secondly, compute the temperature results of the structure, including one considering outside radiation and the other dis-considering outside radiation. Finally, the resistance of conduction and the resistance of radiation of the box are also calculated by equations (referring with Eq. 1 and Eq.2).

Only the conduction and radiation would been computed because of the vacuum environment for this satellite equippments.

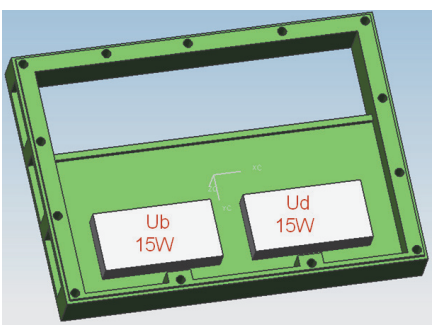


Fig. 1 PCB one (30W)

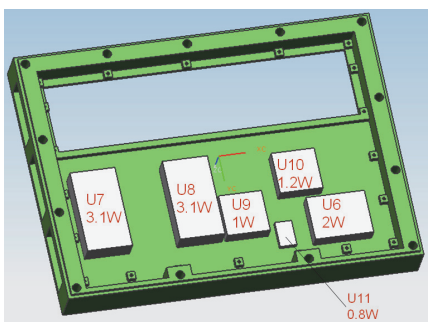


Fig. 2 PCB two (12W)

Table 1. Information of modules

No.	Q [W]	Dimention [mm×mm×mm]	R_{jc} [ºC/W]	$T_{j-permitted}$ [ºC]
Ub	15	76×38×13	0.38	85
Ud	15	76×38×13	0.38	85
U7	3.1	54×29×13	1.15	85
U8	3.1	54×29×13	1.15	85
U9	1	27×27×9	3.7	85
U10	1.2	27×27×9	3.7	80
U6	2	37×29×9	2	80
U11	0.8	17×11×3	6.2	80

where Q is heat power consumption; R_{jc} is thermal resistance junction to case; and $T_{j\text{-permitted}}$ is derated maximum junction temperature.

3. Results and Discussion

3.1. *Results of Analysis*

The temperatures are from 45ºC to 67.6ºC when considering radiation and 45ºC to 67.7ºC when dis-considering radiation (shown in Fig. 3 to Fig. 6).

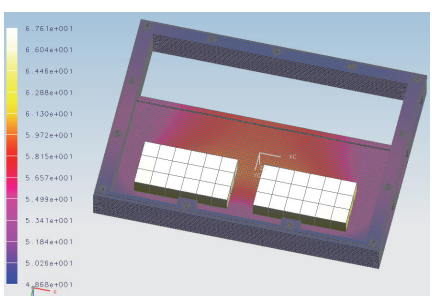


Fig. 3 PCB one (radiation)

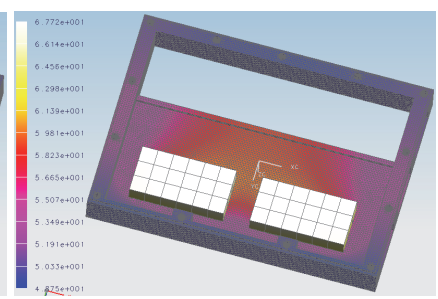


Fig. 4 PCB one (dis-radiation)

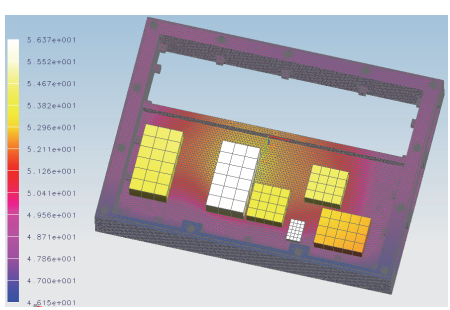


Fig. 5 PCB two (radiation)

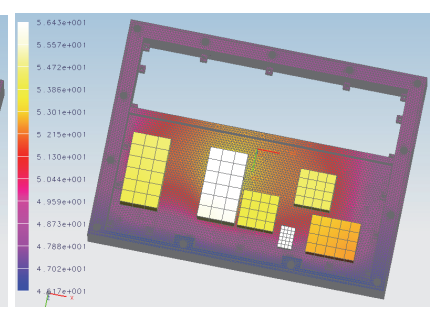


Fig. 6 PCB two (dis-radiation)

Table 2. Differences between radiation and dis-radiation

No.	$T_{c-radiation}$ [ºC]	$T_{c-dis-radiation}$ [ºC]	$T_{c-dis-radiation}$ - $T_{c-radiation}$ [ºC]
Ub	67.6	67.7	0.1
Ud	67.6	67.7	0.1
U7	54.4	54.6	0.2
U8	56.2	56.3	0.1
U9	53.9	54.0	0.1
U10	54.3	54.4	0.1
U6	52.9	53.0	0.1
U11	56.4	56.4	0

3.2. *Discussion*

The case temperature of the key components is shown in Table 2. The maximum difference is only 0.2ºC which is much less than 1ºC. After the finite element compute, the surface temperature of the box was gotten, which is no more than 47.0ºC. Then the resistances of conduction and radiation are computed referring with Eq.1 and Eq.2. The radiation resistance is 0.86ºC / W and the conduction resistance is only 0.02ºC / W, showing that the heat will transfer mainly through conduction. The results show that the outside radiation could be ignored when doing the thermal analysis of this kind of satellite borne boxes heat of which transfer mainly through conduction.

4. Conclusions

(1) The problem whether outside radiation could be ignored while analyzing temperature of a satellite borne power box is discussed. (2) A finite element model was built and the results show that the maximum temperature is 67.6ºC when the outside radiation of the box is computed, and the maximum temperature is 67.7ºC when the outside radiation of the box is not considered. The maximum difference is much less than 1ºC. (3) The conduction resistance of the whole box is only 0.02ºC / W which is much less than the outside radiation resistance of the box which is 0.86ºC / W, which show that the heat transfer mainly through conduction. (4) Outside radiation could be ignored when doing the thermal analysis of this kind of satellite borne boxes heat of which transfer mainly through conduction. It could save some computing time when do such analysis.

Acknowledgements

This paper is supported by Youth Innovation Promotion Association, Chinese Academy of Sciences and the Knowledge Innovation Program of the Chinese Academy of Sciences.

References

1. Z.Q. Hou and J.G. Hu, Spacecraft Thermal Control Technology: *Theories and Applications* , Chinese Science Technology Publishers, China 2007 (Chinese)
2. J. Meseguer, I. Perez-grande and A. Sanz-Andres, *Spacecraft Thermal Control*, Woodhead Publishing Limited, UK 2012

Design of the Charger with MPPT Function for Photovoltaic Power Generation

Zhang Bo†

Department of Electronic, Suzhou Vocational University, Suzhou Jiangsu, China
†E-mail: zhangbo1221@126.com,

Wang Yi-wang

Jiangsu Photovoltaic Power Generation Engineering Technology Research and Development Centers, Suzhou Jiangsu, China
E-mail: 99806239@qq.com,

Zhang Shuai

Suzhou Hosola New Energy Co., Ltd. , Suzhou Jiangsu, China
E-mail: 76163186@qq.com

In the photovoltaic power generation, in order to solve the time mismatch of power supply and demand, the energy storage method is adopted. The maximum power point tracking (MPPT) method is used for realizing the low-cost system. Therefore, the charger with the function of MPPT is developed. Compared with other works, the Boost circuit and the open-circuit voltage method are used to realize MPPT. Meanwhile, the battery is charged using three-stage method. The MSP430G2553 is used as the core of the controlling. The experiments indicate that the charging power of this charger, under the same condition, is increased by about 11% compared with that without MPPT function. Meanwhile, the increase of its cost is very low.

Keywords: Solar Charger; MPPT; Boost Circuit; Open-circuit Voltage Method.

1. Introduction

With the gradual lack of the global energy source and the more severe situation of the environment contamination, the solar energy, which is clean and regenerate, has been received more and more attentions[1]. The technology of the photovoltaic power generation is the significant way of the application of the solar energy and becomes the focus of recent researches. The power of PV system is influenced greatly by the weather conditions, such as the light intensity. This frequently leads to the lack of the power generation in the high demand of the electricity and the surplus of the power generation in the low demand[2]. To solve this problem, the energy storage is introduced. Meanwhile,

the cost of solar cells is very high in PV system. To low the cost, the maximum power point tracking (MPPT) method should be used. Therefore, the charger with the function of MPPT, which is used in the photovoltaic power generation, is developed in this paper.

2. The Method of MPPT and the Solution of the Control

Photovoltaic cells are not constant-voltage sources, and also not constant-current source. There is only one maximum power point in its output power under a certain light intensity and temperature . The cost of solar cells is high. Therefore, to achieve the same aim, the number of solar cells adopted should be as small as possible. That demands that the solar cells are operated on the maximum power point under various light intensity and temperature, i.e.. So a certain control method and the corresponding circuit should be used to realize the MPPT of the photovoltaic cells.

According to the principles of circuits, when the impedance of the load matches to the internal impedance of the photovoltaic cells, the load obtains the maximum power. The method to realize MPPT is to insert DC/DC converter into the photovoltaic cells and the actual load. The DC converter and the actual load are as the load of solar cells. The corresponding control method is applied to modulate the duty cycle of the DC/DC converter and match the total impedance of the load to the impedance of the solar cell at that moment[3]. Due to the fairly small power consumption of DC/DC converter, the maximum power is obtained in the actual loads.

The ordinary control methods are the constant voltage method, the open-circuit voltage method, the disturbance observation method, the conductance enhancement method, the fuzzy control method, the practical measurement method, and so on[4]. According to the characteristics of the solar cell, when the temperature changes little and the output power of solar cells reaches the maximum, the operating voltage, which is marked as U_m, is almost the same under various light intensities. Therefore, the output voltage of the solar cell can be set as U_m by controlling the DC/DC converter, as makes the solar cell operate under the maximum power. However, the effects of the temperature are not considered, so it brings the large errors. The improvement is the open-circuit voltage method. With the analysis of the characteristics of the photovoltaic cell, with whatever light intensity and temperature, the operating voltage of the solar cell is 0.76 times of its open-circuit voltage (error ±2%) when the output power of the solar cell is maximum. The light intensity and the temperature can be considered as a constant during a small period. So, the measurement of the open-circuit voltage need only at every interval. And then

control the operating voltage of the solar cell at 0.76 times of its open-circuit voltage by DC/DC converter. The open-circuit method considers the effect of the temperature, superior to the constant voltage method theoretically[5,6]. Other controlling methods are either too immature, or the demand of the measurement precision is too high[7]. So the open-circuit method is adopted in this solution.

3. The Choice of the Main Circuit of the DC/DC Converter

There are many topologies in DC/DC converters. Non-isolated inputs and outputs, such as Buck, Boost, Buck-Boost, Cuk, etc. Input and output isolation, such as single-ended flyback, single-ended forward, push-pull, half-bridge and full-bridge, etc[8]. Boost circuit has the following advantages. (1) The input current is continuous. If the inductance is large enough, the fluctuation of the current of the DC input source can be small. This is very helpful in realizing the MPPT of solar cells[9]. (2) The power switch is directly grounded and convenient for driving. Moreover, since the structure of the Boost circuit itself is simple, Boost circuits are applied in many occasions to realize MPPT.

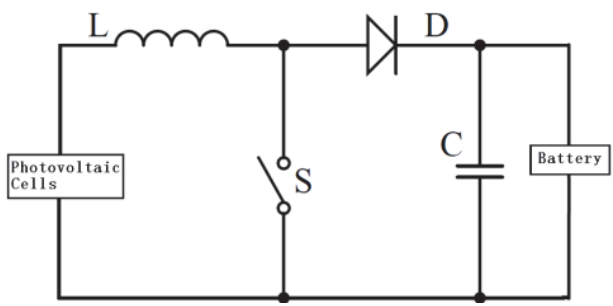


Fig. 1 The diagram of Boost circuit to realize MPPT

Eq. 1 is the input and output relationship of the Boost circuit.The voltage of battery, such as the output voltage $U_{o,}$ can be considered as a constant in a Small interval. The MPPT is realized by

$$U_o = U_i / (1-D) . \tag{1}$$

modulating the duty cycle to vary the input voltage U_i of the Boost circuit, i.e. the output voltage of the solar cells.

4. The Integral Design of the System

The system structure is shown in Fig. 2. The main circuit consists of the photovoltaic array, the Boost circuit and the battery. The control circuit consists

of the microprocessor, the sampling circuit, the driving circuit, and so on. There is also the protecting circuit. Since the main circuit is the boosting circuit, the voltage of the selected maximum power point of the photovoltaic array is absolutely not higher than the voltage of the battery.

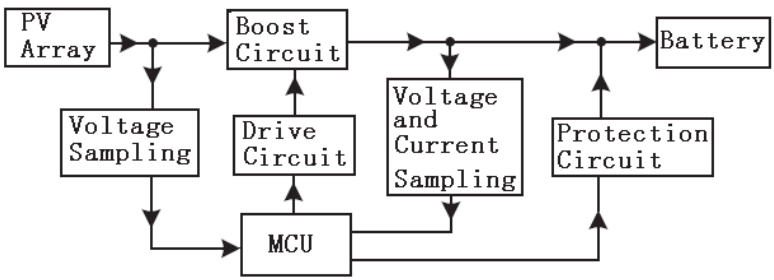


Fig. 2 The diagram of the integral structure of the system

There are three sections in the sampling circuit, sampling the output voltage of the photovoltaic array, the output voltage of the Boost circuit (i.e. the charging voltage of the battery) and the output current of the Boost circuit (i.e. the charging current of the battery). Sampling the photovoltaic array is mainly for realizing MPPT. Sampling the output of the Boost circuit is mainly for prolonging the use of the battery by selecting the proper charging method. The forms of the circuit these three designed sections adopt are the same, including proportional integral circuit (mainly proportional circuit) composed of the operational amplifier. The current sampling is to sample the voltage of the resistor, which is a milliohm level resistor cascaded in the circuit. The outputs of the sampling circuit are all sent to microchips.

The microprocessor adopts the MSP430G2553 mixed-signal processor. The lifetime of the battery is short in the PV system[10]. The proper method of the charging ought to be used to prolong its lifetime. Here,three-stage method is adopted. MPPT control stage (large current stage), high constant voltage stage, and low constant stage (trickle charging).When the battery voltage is not high, the MPPT control is adoptted, a large current charging, so that the maximum efficiency of solar cells. When large current charging, when the battery voltage rises to a certain value, turn to the high voltage charging stage. This stage use control Boost circuit output voltage instead of MPPT, using a relatively high voltage charging.When the high voltage charging, when the charge current is less than a certain value,turn to low voltage charging. The only difference between this phase and the previous phase is that the charging voltage is relatively low, trickle charge. MPPT stage is usually the longest time, the battery

get most power in this stage. And if the charging current is too large in MPPT control stage, the high constant voltage charging is used to limit the charging current.

After the system is powered on, the microprocessor blocks the PWM signal and control the battery open. So, the battery is not charged. At this time, the voltage of the battery is examined to determine the charging stage. Meanwhile, the open-circuit voltage of the photovoltaic cell is examined[11]. The controlling of the MPPT adopts the open-circuit method as mentioned above. The microprocessor blocks the PWM signal and control the battery open once a time at every interval, such as half an hour, during the large current charging. In this way, the voltage of the open circuit due to the light intensity and the temperature is examined.When charging is abnormal or the battery is overcharging, or When the need to measure the open circuit voltage of the battery,the protection circuit make the battery open.

5. Result and Discussion

In our experiment, the programable DC source CHROMA 62150H-600S is adopted to simulate the solar cell, open-circuit voltage of the solar cell is equal to 12.8V, the short-circuit current is 1.689A, the maximum power point voltage is 10.1V. The I-V curve and the P-V curve at a moment in the maximum power point tracking process are shown in Fig. 3, Solar cell output voltage and current, respectively11.44V, 1.096A.The I-V curve and the P-V curve in the stable state in the maximum power point tracking process are shown in Fig. 4, Solar cell output voltage and current, respectively 10.11V, 1.479A. The experiment indicates that the charging power of this charger, under the same condition, is increased by about 11% compared with that without MPPT function.

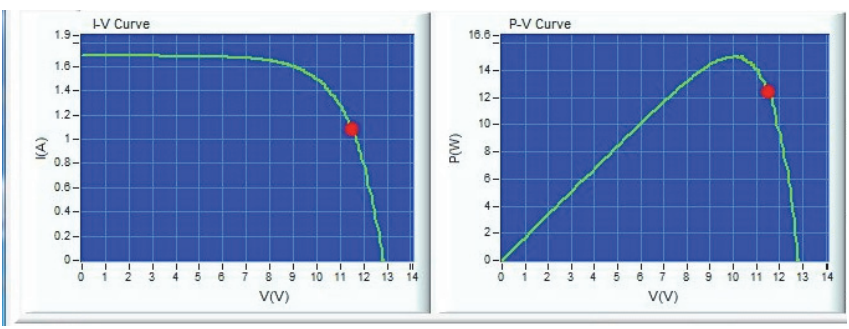


Fig. 3 The I-V curve and the P-V curve at a moment in the maximum power point tracking process

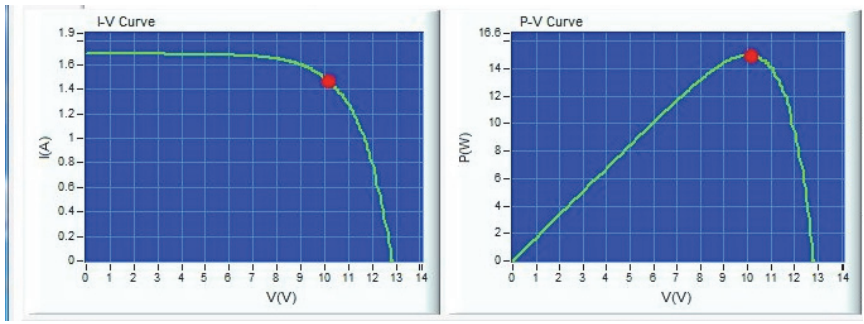


Fig. 4 The I-V curve and the P-V curve in the stable state in the maximum power point tracking process

This design realizes the MPPT of the photovoltaic cell and the intelligent charging control of the battery at the same time,with a very little increase of the cost.Its performance is stable, and with the high ratio of performance to value. So the charger is very competitive in PV systems.

References

1. Xiang yang-gong, Design optimization of a large scale rooftop photovoltaic system, *Solar Energy*, Vol.78, pp.362-374,2005.
2. M E Glavin, W G Hurley, Ultra capacitor Battery Hybrid for Solar Energy Storage[C], *Universities Power Engineering Conference*, pp.791-794, 2007
3. Zhang bo, Wang Yi-wang, Li Xiang. Research and design of small wind/PV hybrid independt generating system, *Modern Electric Power*, Vol.30, pp.29-32,2013
4. Rong Yajun, Chen Le, Cui Mingyong, etc., A battery charging control strategy based On maximum power tracking, *Power System Technology*, Vol.38, pp.347-351,2014.
5. Cheng Qi-ming, Cheng Yin-man, Wang Ming-mei, etc., Survey on MPPT methods of photovoltaic cells, *Journal of Shanghai University of Electric Power*, Vol.25, pp.346-352,2009.
6. Zheng Shi-cheng, Liu Wei. Research and implementation of photovoltaic charging system with maximum power point tracking[c], *The 3rd IEEE Conference of Industrial Electronics and Applications, Singapore,* pp.619-624, 2008
7. Liu Xue-jun. An Improved Perturbation and Observation Maximum Power Point Tracking Algorithm for PV Panels[D]. Concordia University,2004

8. Liu S L, J, Chen Y B. An improved boost DC-DC converter based on intrinsic safety and its design[C]. *Proceedings of the IEEE Region 10 conference, Hongkong, China*, pp.99-103, 2012.
9. Zhao hong, Pan Junming, Photovotiac maximum power point tracking system using boost converter, *Power Electronics*, Vol.38, pp.55-57,2004.
10. Huang Yinghua,Wang Liangyu, Han Fei, The study of battery charging control in photovoltaic power penetration systems, *Journal of North China Institute of Science And Technology*, Vol.10, pp.67-71,2013.
11. Lu Lin, Shu Guo-hua, Zhang Shi-wen, Research on Max Power Point Tracking for Solar-Electric Charging System based On Micro-Controller, *Power Electronics*, Vol.41, pp.96-98,2007.

Review and Prospects: Application and Research of Heat Pumps in China

Yuanyuan Sun[a], Ronghua Wu[b], Chunjin Sun
College of Mechanical and Electrical Engineering, Qingdao University, Qingdao, China
E-mail: [a]251941811@qq.com, [b]wuronghua18@126.com

Heat pump systems offer economical and environmental way to utilize green energy. But many problems still exist in the development of heat pumps of our country. Summarized the status of different kinds of heat pumps at home and abroad; put forward new classification method of heat pump system and analyzed the merits and demerits of different kinds of heat pumps; pointed out the key problems of the current heat pump system such as low operating efficiency, poor operation management and so on; from the aspects of energy saving, and rational planning and peak shaving, presented the future developments of heat pump system, and put forward the views of the influence on system operational efficiency by transportation energy consumption.

Keywords: Heat Pump; Application of Heat Pumps; Transportation Energy Consumption; System Operational Efficiency.

1. Introduction

Heat pump system offers high efficiency and environmental protection way to take advantage of energy through the consumption of a small part of driving energy (electricity) for heat transfer from low grade energy to the middle grade energy. However, there are still many drawbacks in the development progress of China's heat pump system, and the most striking point is the lack of systematic study of heat pumps.

To solve the problems of the irrational design and operation of heat pump systems and the inefficient operation of the whole system, summarized development status of advanced technology of heat pumps at home and abroad, and raised a new method to refine the classification of the heat pump. Based on the different types of heat pump system, we pointed out the main ideas for further development of the system.

Nowadays, the application of heat pump system is becoming a new trend in the field of energy utilization in China. Because of its energy saving and environmental protection, the government gradually start to attach importance to

the development and application of heat pump. And heat pump system is planned to be included in the city central heating system. Consequently, the heat pump will have a broader prospect for development in China.

2. Basic Principle

Heat pump is an energy utilization device that consumes a small part of high grade energy to transfer energy from low grade energy to the middle grade energy that is consuming a small part of driving energy to supply user heat from driving energy and low grade energy.

Based on the second law of thermodynamics[1], while energy transfer direction and the temperature gradient are in the same direction, certain power is needed to be input. Currently, the efficiency of heat pump systems in engineering applications (usually a vapor compression heat pump system) is high, and the COP is generally more than 4, compared with the coal-fired, oil-fired boiler, the heat pump can save about 40% of primary energy, carbon dioxide emissions can be reduced by 68%, sulfur dioxide emissions can be reduced by 93%, and nitrogen dioxide emissions can be reduced by 73%[2].

3. Classification and Characteristic

According to the working principle of heat pump, heat pump systems can be divided into vapor compression heat pump, absorption heat pump, steam jet pump, and other heat pumps etc.

3.1. *Vapor Compression Heat Pump*

Vapor compression heat pump is formed by a closed loop consists of a compressor, condenser, evaporator, throttle expansion components and other parts, in which fills the cycle refrigerant (such as R22 or R134a), and the compressor work to promote the refrigerant in the circulation flow. Vapor compression heat pump system using electric energy as the driving energy, the system efficiency is very high (COP≥ 4).Vapor compression heat pump has been widely used in cooling and heating field in China instead of boiler and water chilling unit.

3.2. *Absorption Heat Pump*

The absorption heat pump is divided into two categories: the first kind absorption heat pump, using steam, fuel, waste hot water or steam as the driving source. Second class absorption heat pump uses a lot of intermediate temperature waste heat and low temperature heat.

According to estimates, heat supplied by absorption heat pump is equal to the absorption heat from low temperature waste heat and compensation heat of the driven heat that is to say supplied heat was always greater than the consumption of high grade heat (COP＞1).

3.3. *Steam Jet Heat Pump*

Steam jet heat pump, which is composed of nozzle, a receiving chamber, mixing chamber, a diffusion chamber and other components, is a kind of thermal equipment [3] with the advantages of simple structure, small volume, no moving parts, energy saving and environmental protection, and running stable; the main disadvantage is its low thermal coefficient.

3.4. *Other Heat Pumps*

Chemical heat pump is a new type of heat pump[4], refers to the heat pump using chemical phenomena, such as chemical reaction, absorption, adsorption, concentration and other chemical phenomena. The basic principle of thermoelectric heat pump is the Peltier effect[5], thermal power unit is the basic unit of work by the thermoelectric effect.

4. Current Research and Application

The most widely used system is the vapor compression heat pump system, as a result of more available heat source, the development direction of vapor compression heat pump system is also diversified.

4.1. *Ground Source Heat Pump*

Buried pipe of ground source heat pump system, we usually refer to simply as the ground source heat pump (GSHP). Embedded the plastic pipe in the underground vertically or horizontally, tube in which refrigerant, and make it become the heat exchanger[6] of circulating working medium and soil. It was the realization of consuming the storage of summer in winter or consuming the storage of winner in summer, so it seems that the soil is more like an energy storage device[7.8]. The heat pump can absorb heat from the soil surface, and the continuous heat absorbing soil rate is generally at about 25W/m^2[9].

To improve the engineering application value of ground source heat pump system requires us to start from reduce initial investment, make fully combination with building foundation [10], take local natural climatic conditions for foundation design, and maximize the use of resources and capital. Through the heat pump

coupled with solar, air source or other species, forms a set of comprehensive utilization and delivery device of low grade energy. The problems of GSHP are unstable operation and low running efficient.

4.2. *Surface Water Heat Pump*

The energy source of surface water heat pump system is the surface water from pond, lake, and river[11]. Distribution of river, lakes and other surface water relating to the geographical factors, surface water heat pump system is often affected by these limitations. Compared with the air, specific heat capacity of water is higher to several orders of magnitude. Compared to the groundwater, water quality is difficult to guarantee, which requires water treatment device, such as filtration device or intermediate anti blocking, heat exchanger etc. Design method for the improvement and optimization of system transmission pipeline, development of low temperature difference, big flow, small flow high efficiency heat exchange equipment, will become the key breakthrough of the future development of surface water source heat pump system.

4.3. *Sewage Source Heat Pump*

Sewage source heat pump is to utilize the heat directly from the city sewage for civilian heating, which is an important part of comprehensive utilization of sewage.

There are two key problems in utilization of sewage source heat pump:

1) *Blocking and pollution.* Sewage is two-phase fluid, carrying dirt of both large scale and small scale[12], which is easy to trap the heat exchanger, and pollute the pipe wall.

2) *Flow and heat transfer problems.* The sewage is a kind solid multi-component fluid flow, and compared with clean water, it is difficult to make sure the sewage heat transfer and flow characteristics accurately.

To achieve safe and reliable application of sewage source, these breakthroughs must to be done[13.14]:

1) *Develop the new design idea of city sewage heat pump system.* Improve existing technology and insufficient to ensure that the operation of heat pump system is more safe and reliable.

2) *Deep study on characteristics of flow and heat transfer characteristics of sewage.* To understand the characteristics of sewage through the experimental method, is the basis to know scientific theory of sewage comprehensive development of the necessary.

3) *Structure design of sewage heat exchanger.* Sewage heat exchanger as the most efficient and safest means to utilize sewage waste heat, is already embodied the development potential and economic benefits of its own. Through the optimization of heat exchanger entrance shape, passage shape, pipe material, size parameters, so that the heat exchanger has better ability to prevent blocking, dirt and corrosion, and also has better heat transfer characteristics.

4.4. *Sea Water Source Heat Pump*

With the help of heat pumps, sea water source heat pump take heat from sea for heating and cooling. According to estimates, as the cooling water temperature is a reduction of 1ºC, the refrigeration coefficient can be increased by about 2%~3%[15].

Energy-saving and environmental protection, stable running are the outstanding characteristics of the seawater source heat pump. At present, the sea water source heat pump is also facing the problem of "THREE—ANTI". Because of the high natural level of seawater, it will seriously affect the thermal performance of heat transfer equipment. The heat transfer process is different from that of water[16], with the characters of small temperature difference and large flow. The complex flow and heat transfer characteristics is becoming another important key problem hindering the development of seawater source heat pump.

4.5. *Composite Heat Pump*

In practical applications, a single heat source heat pump system exists problems in their own, such as air source heat pump outdoor heat exchanger in winter frost and defrost, sewage source heat pump "Three Prevention" and so on, which restricts its further development and engineering application. At present, the compound source heat pump technology has become one of the development trends of the HVAC industry research[17-19].

But because of the more complex system[20.21], higher operation control requirements, and higher initial investment and long payback period, advances in the application of this technology have been very slow. In addition to a more in-depth and widely study based on a technical point of view, and optimization of system component matching, relevant supporting incentives formulated by our government are still needed, so as to promote research and application progress of the energy saving and environmental protection technology.

5. Prospects

The overall development trend of heat pump technology is more efficient, more energy-saving, more environmental protection, and the overall trend of heat pump system is a systematic, holistic, diversification.

Suitable construction. The so-called suitable, is to act according to circumstances, which requires that the selection and design of heat pump system should be suitable to the environment and climate of the local topography of the heating project. In the early planning of the project, a comprehensive investigation of the implementation of the project is needed to be executed, focusing on the two aspects of location selection and source selection to make a preliminary positioning of the planning and construction of the project.

System energy conservation, improve the overall efficiency of energy utilization. The main energy consumption equipment in heat pump system are the units and pumps (including circulating pumps, water intake pumps and so on), whose energy consumption accounted for 98% of total energy system. The efficiency of heat pump (COP) has reached a very high level at the average of 4.5~5.0. In the design process, they did not pay attention to energy consumption blindly, leading to selected pump energy consumption more than the suitable pump, which makes the system COP large amplitude attenuation. According to the research and application examples of heat pump systems, it is not energy-saving, until the transportation energy consumption is less than 25% of the total energy consumption.

Therefore, pay attention to matching of water pump and units, design the energy-saving system based on the COP, so as to maximize the efficient use of heat pump system.

Rational planning and operation regulation. System planning work should be done mainly at the initial stage of the construction. In the construction of the project, it is common that the total amounted is less than the design heating load requirements. And the best solution is operation regulation, for there is an obvious difference between actual operation process condition and the theoretical design conditions. Reasonable matching of macro planning heat amount and total heating load, to the auxiliary heat source, adaptive peak, so as to realize the comprehensive use of energy, and can realize the maximum amplitude use of low temperature heat source, improving energy efficiency at the greatest degree, and the promotion of the energy-saving effects of the system.

Heat pump units classified design. Heat pumps circulating on the market today are mostly based on the groundwater condition, and the groundwater due to its limitations has been replaced by other new heat source. Now sewage, surface

water, and sea water has become the mainstream of the low temperature heat source. On the basis of the characteristics of the different heat sources, make classification of heat pump units in details, and promote the industrialization of heat pump units suitable to different sources.

6. Conclusions

Heat pump unit is a new mode of energy utilization, whose energy efficiency has reached a consensus in the field of industry, but there are still some problems at the present stage of the development of the heat pump system.

However, the development potential has not been fully excavated in heat pump, and the heat pump system has a very broad space for development as well. Based on the overall study of heat pump system, from several aspects of location, selection of heat source, energy saving system and operation management, make a constructive direction for the future development of heat pump system. Puts forward the innovation idea of the influence system energy consumption on the system operational efficiency, and points out the stage limitations of the design and production. Raises the conception of detailed classification, and heat pump units should be adapted with the heat source.

Acknowledgments

This work was financially supported by the Twelfth Five Year National Science and Technology Support Program (sq2011sf14b00503).

References

1. Yao Yang, Ma Zuiliang. *HVAC* 2002(03).
2. Qin Wang, Wei He, Yuqian Liu, Guofeng Liang, Jiarong Li, Xiaohong Han, Guangming Chen.. *Renewable and Sustainable Energy Reviews* 16 (2012) 6522–6538.
3. Abdulateef JM, Sopian K, Alghoul MA, Sulaiman MY. *Renew Sust Energy Rev* 2009;13(6–7):1338–49.
4. C.W. Chan, J. Ling-Chin, A.P. Roskilly. *Applied Thermal Engineering* 50 (2013) 1257-1273.
5. Dongliang Zhao, Gang Tan. *Applied Thermal Engineering*, 66, Issues 1–2, May 2014, 15-24.
6. M.R. Errera, S. Lorente, A. Bejan. *International Journal of Heat and Mass Transfer* 75 (2014) 327–336.
7. Ioan Sarbu, Calin Sebarchievici. *Energy and Buildings* 70 (2014) 441–454.
8. Yang W, Zhou J, Xu W, Zhang G. *Energy Policy* 2010;38(1):323–32.

9. Xu Bangyu, Lu Yajun, Ma Zuiliang. *Heat Pump* [M]. Beijing: Chinese Building Industry Press 1988.
10. Jiang Yi. *HVAC* 2005(05).
11. Sun Dexing, Wu Ronghua, Zhang Chenghu, Liu Zhibin. *China survey and design*, 2006, 21(5):30–32.
12. Lei Tian, Xiao Dong Chen, Qian Peng Yang, Jin Chun Chen, Qiong Li, Lin Shi. *Chemical Engineering Journal*, Volume 188, 15 April 2012, Pages 47-56.
13. Wu Ronghua, Sun Dexing, Zhang Chenghu, Ma Guangxing. *Journal of Harbin institute technology* 2006(08).
14. Zhibin Liu, Liangdong Ma, Jili Zhang. *Applied Thermal Engineering*, Volume 62, Issue 2, 25 January 2014, Pages 747-757.
15. Young-Jin Baik, Minsung Kim, Ki-Chang Chang, Young-Soo Lee, Ho-Sang Ra. *Renewable Energy* 65 (2014) 236-244.
16. Xuejing Zheng, Shijun You, Jian Yang, Gaofeng Chen. E*nergy and Buildings*, Volume 68, Part A, January 2014, Pages 147-155.
17. Qiang Si, Masaya Okumiya, Xiaosong Zhang. *Energy and Buildings* 70 (2014) 237–245.
18. Daniel Carbonell, Michel Y. Haller, Daniel Philippen and Elimar Frank. *SHC 2013, International Conference on Solar Heating and Cooling for Buildings and Industry*. September 23-25, 2013, Freiburg, Germany. Energy Procedia 48 (2014) 524 – 534.
19. Qu Yunxia, Fang Zhaohong. *Renewable energy* 2003(01).
20. Li H, Yang H. *Appl Energy* 2010; 87(9):2818–25.
21. Yang L, Zhang X.S. *Patent application* CN201010277418.9; 2010.

Ab Initio Molecular Dynamics Simulation on Carbothermal Reduction Mechanism of Fluorapatite in Vacuum

Xiaohui Zhu[a], Qian Bai, Bi Jing, Qiuxia Li[b*]

College of Chemistry and Chemical Engineering, Yunnan Normal University, Kunming 650092, China
E-mail: [a]jingibbso@yeah.net; [b]qiuxiali03@163.com

Yucheng Liu

Bio-Chemistry Department, Wenshan University, Wenshan 663000, China

This report aims to analyze carbothermal reduction mechanism of fluorapatite under high temperature and vacuum process by using ab initio molecular dynamics simulation. The rerults of PDOS calculations in the vicinity of the Fermi level show that the Ca atom and P atom , C atom does not form a covalent bond and there is no intermediate like Ca_3P_2 and CaC_2 in dynamic simulation results; Speculates that carbothermal reduction mechanism of fluorapatite with ab initio molecular dynamics simulation.The reaction process is $PO_4^{3-} \rightarrow PO_3^{2-} \rightarrow PO_2^{-} \rightarrow PO \rightarrow P$ after C reacted with phosphate. Meanwhile, C combines with O^{2-} generating CO, Ca^{2+} combines with O and F generating CaO and CaF_2 separately.

Keywords: Ab Initio Molecular Dynamics; Fluorapatite; Carbothermal Reduction; Deoxidization Mechanism; Phosphorus.

1. Introduction

In the study of preparing phosphorus by carbothermal reduction mechanism of fluorapatite, according to the experimental studies, Jinrong Zhang, etc, proposed two kinds of carbothermal reduction mechanisms of fluorapatite [1]. The first one is carbon reacts with fluorapatite directly generating P_2, CaO, CO and CaF_2, another one is to generate intermediate Ca_3P_2 and CaC_2 firstly, Ca_3P_2 and CaC_2 then continue to react with fluorapatite generating P_2. Xiaojun Bao's studies suggest that carbothermal reduction mechanism of fluorapatite is that the thermal decomposition of $Ca_5(PO_4)_3F$ generate P_2O_5, CaO and CaF_2, afterward,

* Corresponding author.

P_2O_5 reacts with C generating P_2 [2]. Yucheng Liu, etc. studies have a completely different opinion, they think $Ca_5(PO_4)_3F$ reacts with C firstly generating P_2, CO, CaO and CaF_2, the CaO combines with SiO_2 generating $CaSiO_3$ [3].

In recent years, with the rapid growth of computer operation speed, as well as the relevant theories and numerical algorithms developing in leaps and bounds, some theoretical calculations like quantum chemistry, molecular dynamics, and ab initio molecular dynamics have become conventional computing research tools in the study of reaction kinetics and materials science. The content of the studies involve electronic structure, reaction kinetics and other aspects, for instance, according to the experimental studies, E.Scheepers, etc. used computational fluid dynamics to carry on the preliminary calculation towards the thermodynamic properties of phosphate rock and dynamics [4, 5]. In addition, Donald Mkhontohas researched the structure and adsorption properties of fluorapatite. In the study of reaction kinetics, due to the difficulties of high temperature experiments as well as the complexity of heterogeneous reaction, computer simulation calculation is becoming an important method in the process of studying reaction kinetics [6]. In 1985, R.Car and M.Parriinello [7] combined molecular dynamics method with density functional theory, which made ab initio molecular dynamics become a reality. A lot of literatures and experimental data show that: his calculation results and the experimental data of this method can be a very good match, but also overcome many defects of the Monte Carlo method and the classical molecular dynamics [8, 9]. Ab initio molecular dynamics has been widely used in all kinds of solid and liquid. The author used both quantum chemical calculation and ab initio molecular dynamics firstly to study carbothermal reduction mechanism of fluorapatite under high temperature and vacuum.

2. Calculation Method

Using Material Studio software Package CASTEP (Cambridge Serial Total Energy Package) module, applying density functional theory (DFT) the generalized gradient approximation (GGA),calculating with the NPT ensemble [10], temperature of 1723 K and 1223 K, the pressure of 50 Pa, the optimum condition based on thermodynamics calculation, thermodynamics calculation will be published elsewhere, ime of 0.5ps ~1ps, time step is 1fs, steps number is 1000, using Andersen pressure control method [11, 12] and temperature controlling method for the Nose [13]. The structure of $Ca_5(PO_4)_3F$ and C interactions in different situations is conducted by ab initio molecular dynamics simulations, calculated with the density of states (DOS), partial density of states (PDOS).

3. Results and Discussion

State density analysis can obtain the electronic structure distribution in the material properties, electronic reactivity is strongest near the Fermi level, herefore, we can know the reactivity of the atom through the analysis of electronic density of states near Fermi level.

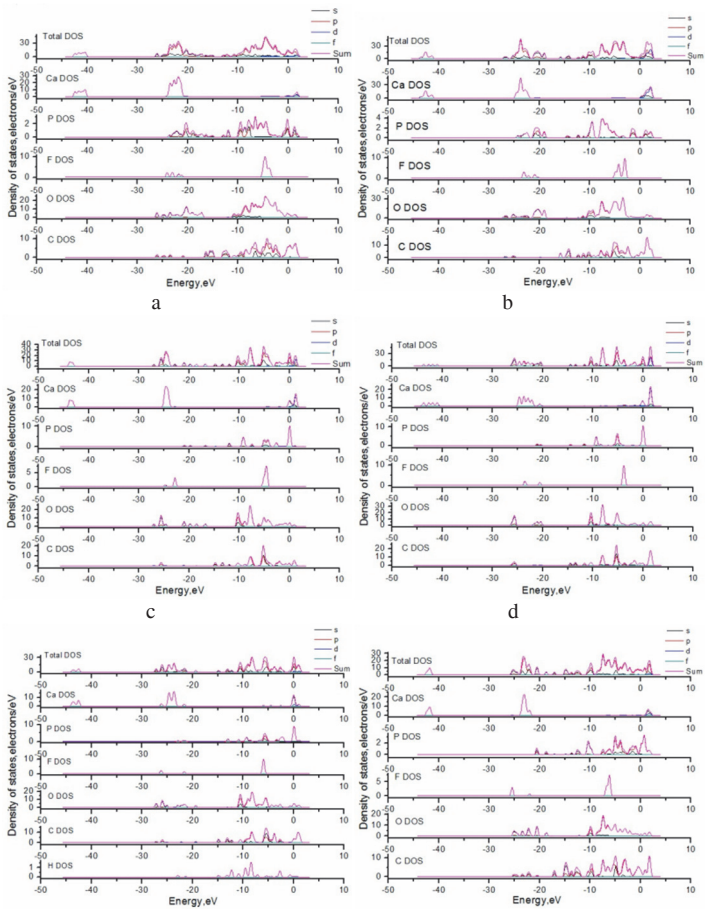


Fig.1 PDOS of carbothermal reduction of fluoraptite with different molar ratio of $Ca_5(PO_4)_3F$ and C, and different condition

(a:X=1:5 at 1723 K, 50 pa ; b:X=1:7.5 at 1223K, 50Pa; c:X=1:12 at 1723K, 50Pa; d:X=1:12 at 1223K, 50Pa;e:X=1:12 at 1223K, 50Pa; f:X=1:16 at 1723K, 50Pa)

The dynamics simulation results of carbothermal reduction (the molar ratio of $Ca_5(PO_4)_3F$ and C is 1:5 at 1723 K, 50 pa) show that after a period of reaction

under 1723k, C atoms combined with oxygen atoms quickly, while P-O bond length in which a group of bond length becomes shorter, forming P-O molecule, the rest of the P-O bond become longer, C-O bond length become shorter, indicating that C atoms and oxygen atoms on the phosphate radical form CO. Density of states in Fig. 1a shows that near the Fermi level below, P atoms appear wide phenomenon distinctly; the Fermi level bonding and anti-bonding part of C atoms are contributed by 2s orbitals. State density of O atoms broaden, and two groups of state density close to each other, which explains that C and O atoms form a stable covalent bond, and P-O bond is weakened with the increase of C atoms.

The dynamics simulation results of carbothermal reduction (the molar ratio of $Ca_5(PO_4)_3F$ and C is 1:7.5 at 1223K, 50Pa) show that after a period of reaction under 1723 K, C atoms combine with O atoms quickly, P-O bond length becomes longer while C-O bond length becomes shorter, which implies that C atoms react with oxygen atoms on the phosphate radical generating CO. From the density of states in Fig.1b, we can know that near the Fermi level and above, all atoms above broaden in different degrees, therefore, P-O bond is weakened while C-O bond form a covalent bond. From contrast state density in Fig.1a, at low temperatures, near the Fermi level, broadening degrees of state density increase with temperature rise, the weakened level of P-O bonds also will increase.

The dynamics simulation results of carbothermal reduction (the molar ratio of $Ca_5(PO_4)_3F$ and C is 1:12 at 1723K, 50Pa) show that there exist ions and products like F^-, Ca^{2+}, P and $CO_{(g)}$ at the reaction temperature 1723K; atoms combine with O atoms quickly, P-O bond length become longer while C-O bond length become shorter. Besides, from the density of states in Fig.1c, we can know that under the Fermi level, state density of O and C atoms broaden forming a stable C-O bond, which shows that C atoms and O atoms are in the form of covalent bond. In other words, O atoms in phosphate combine with C atoms forming $CO_{(g)}$. P atoms broaden distinctly, indicating that P-O bond formed by the combination of P atoms and O atoms is unstable. Above Fermi level, Ca atoms and P atoms appear negative shift phenomenon distinctly, P atoms negative shifting, below the Fermi level, however, O atoms broaden, indicating that P-O bond is weakened while C-O bond strengthen under the reaction of C atoms.

The dynamics simulation results of carbothermal reduction (the molar ratio of $Ca_5(PO_4)_3F$ and C is 1:12 at 1223K, 50Pa) show that after the temperature dropped to 1223K, bond length do not change a lot, there is no any new substance formed. From the density of states in Fig. 1d, the appearing of mixed

state near Fermi level means that there exists hybridization phenomenon between orbitals, namely the bonding effect of different states, in other words, negative shift can be found above Fermi level, wherears broadening phenomenon appears under Fermi level. P-O bond is weakened while C and O atoms broaden, implying that C-O bond formed a stable covalent bond.

The dynamics simulation results of carbothermal reduction (the molar ratio of $Ca_5(PO_4)_3F$, C and H is 1:12:5 at1723K, 50Pa) show that after a period of reaction under 1723 k, bond length do not change a lot. From the density of states in Fig. 1e, the top of valence band, O atoms broaden. Meanwhile, the broadening phenomenon of C atoms above Fermi Level appears distinctly, therefore, the weakened extent of P-O bond enhance compared with the situation of without H atoms, C-O bonding is very obvious.

The dynamics simulation results of carbothermal reduction (the molar ratio of $Ca_5(PO_4)_3F$ and C is 1:16 at 1723K, 50Pa) show that after a period of reaction under 1723K, C atoms combine with O atoms quickly, a group of P-O bond length become shorter which form PO molecules, the rest are longer. Thus, C atoms react with O atoms in phosphate forming CO. In addition, from density of states in Fig. 1f, below Fermi Level, P atoms appears broadening phenomenon distinctly. Because of each state density of fluorapatite atoms above the Fermi level appearing a negative shifting and broadening phenomenon below the Fermi level and the wide phenomenon, C and O atoms are in the form of covalent bond. In other words, O atoms combine with C atoms, forming $CO_{(g)}$, P-O bond is unstable and the extent of weakening is deeper.

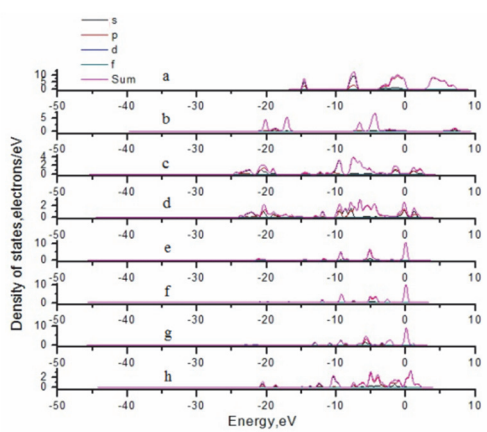


Fig.2 PDOS of P atoms at 1723K, 50Pa
(a:P; b:$Ca_5(PO_4)_3F$; c:$Ca_5(PO_4)_3F$:C=1:7.5,1223K;d:$Ca_5(PO_4)_3F$:C=1:7.5,1723K;
e:$Ca_5(PO_4)_3F$:C=1:12,1223K; f:$Ca_5(PO_4)_3F$:C=1:12,1723K;
g:$Ca_5(PO_4)_3F$:C:H=1:12:5,1723K; h:$Ca_5(PO_4)_3F$:C=1:16,1723K)

Fig. 2 is the PDOS of P atoms at 1723K, 50Pa. a is the PDOS figure of P atoms, the valance band in -8~-6eV is contributed by P atoms 3s orbitals, near Fermi level, P atoms are mainly contributed by 3p orbitals, the width of state density is bigger, P atoms are in an unstable state; b is the PDOS figure of P atoms in $Ca_5(PO_4)_3F$, comparing with a, it's obvious that the P atoms in b negative shift below Fermi Level with energy reducing. Therefore, the P atoms in b are in a stable state. The P states of P atoms in c, d, h, l constitute a strong correlation function at the Fermi leve. From figure c, d, h, the density states of P atoms broaden where the electron in Valence band can occur transitions; The P atoms in figure e, f, g do not form intermediate level in Fermi Level, which implies that the electron will not occur transitions, at the same time, the width of P atoms density states decreases and the P-O bond is weakened mostly, which is the optimum reaction. Either carbon too much or too little has an effect on carbothermal reduction of fluoraptite. Carbothermal reduction with $Ca_5(PO_4)_3F$ and C molar ratio is 1:16 at 1723K, the effect of reduction reaction will reach the best.

4. Conclusion and Prospect

(1) We conducted a preliminary study of carbothermal reduction mechanism of fluorapatite by using ab initio molecular dynamics simulation, the results indicate that: there is an obvious interaction between $Ca_5(PO_4)_3F$ and C at 1723K, which implies that $Ca_5(PO_4)_3F$ did not have interaction with the product CO; The results of PDOS show that Ca atoms did not form cavalent bond with P atoms and C atoms, therefore, there was no intermediates like Ca_3P_2 and CaC.

(2) From the results of dynamics simulation we can know that: during the process of $Ca_5(PO_4)_3F$ carbonthermal reduction, the O atoms in $Ca_5(PO_4)_3F$ were reduced by C atoms one by one; From calculating results of ab initio molecular dynamics, we can speculate carbothermal reduction mechanism of fluorapatite. First of all, C atoms react with $Ca_5(PO_4)_3F$, removing the O atoms in phosphoric acid root continuously, $PO^4 \rightarrow PO^3 \rightarrow PO^2 \rightarrow PO \rightarrow P$, afterward, C combines with O^{2-} forming CO, meanwhile, combines with O^{2-} and F^- generating CaO and CaF_2 respectively.

(3) This work outlines an preliminary exploration concerning preparing phosphorus by the carbothermal mechanism of fluorapatite in vacuum. Next, we will deeply research following topics of: controlling PO reduction to generate P_2; analyzing how P gather to generate P_2, P_3 and P_4; and

simulating the process of various components of ore influencing the fluorapatite carbothermal reduction.

Acknowledgements

This work financially supported by the Applied Basic Research Project of Yunnan Province, China (2011FZ080).

References

1. Zhang Jinrong. Research on phosphate rock reduction mechanism[J]. *Chinese Journal of Applied Chemistry*, 1986, 3 (3): 86. (In Chinese)
2. Bao XiaoJun, Yuan Xiaochun, Wang Shumin. Research on molten state reduction kinetics of phosphate rock and the reaction mechanism [J]. *Journal of the Chemical Fertilizer Industry*, 1987, (6): 2-5. (In Chinese)
3. Liu Yucheng, Li Qiuxia, Liu Yongcheng. Fluorapatite carbon-thermal reduction mechanism in vacuum[J]. *Chinese Journal of Vacuum Science and Technology*, 2012, 49 (3): 84-87. (In Chinese)
4. E. Scheepers, A. T. Adema, Y. Yang, et al. The development of a CFD model of a submerged arc furnace for phosphorus production[J]. *Minerals Engineering*, 2006, (19): 1115-1125.
5. E. Scheepers, Y. Yang, M.A. Reuter, et al. A dynamic-CFD hybrid model of a submerged arc furnace for phosphorus production[J]. *Minerals Engineering*, 2006, (19): 309–317.
6. Donald Mkhonto, Phuti E. Ngoepe, Timothy G. Cooper, et al. A computer modelling study of the interaction of organic adsorbates with fluorapatite surfaces[J]. *Phys Chem Minerals*, 2006, 33: 314-331.
7. Zou Weidong. Theoretical basis of ab initio dolecular dynamics[J]. *Journal of Xianning Teachers College*, 2001, 21 (6): 13 to 18. (In Chinese)
8. Hammond B L, Lester W A Jr, Reynolds P J. Monte carlo method in ab initio quantum chemistry[J]. *Singapore: World Scientific Publishing Co*, 1994: 1-15.
9. Fan Kangqi, Jia Jianyuan. Main technology of classical molecular dynamics simulation[J]. *Journal of Device and Technology*, 2005, (3): 133-138. (In Chinese)
10. H. C. Andersen. Molecular dynamics at constant pressure and/ or temperature[J]. *J Chem Phys*, 1980, (72): 2384-2393.
11. V. Anisimov,J. Zaanen, O. K. Andersen. Band theory and mott insulators: hubbard U instead of stoner[J]. *Phys Rev B*, 1991, (44): 943.

12. J. P. Perdew, K. Burke, M. Emzerhof. Generalized gradient approximation made simple[J]. *Phys Rev Lett*, 1996, (77): 3865-3868.
13. S. Nosé. A molecular dynamics method for simulations in the canonical ensemble[J]. *Mol Phys*, 1984, (52): 255-268.

Methods of Estimating VaR Based on Gray Peaks over Threshold Model

Ruiqing Wand[a†] and Ziqian Xiao[b]

Department of Software Engineering, Hainan College of Software Technology, Qionghai, China

E-mail: [a†]ayrqing@163.com, [b]xiaoziqian1234@163.com

A two-stage model of estimating VaR based on grey system and extreme value theory is proposed. Firstly, in order to capture the dependencies, seasonalities and volatility-clustering, an GM(1,2) model is used to filter price series. In this way, an approximately independently and identically distributed residual series with better statistical properties is acquired. Then peaks over threshold is adopted to explicitly model the tails of the residuals of GM(1,2) model, and accurate estimates of value-at-risk can be produced. The empirical analysis shows that the proposed model can be rapidly reflect the most recent and relevant changes of prices and produce accurate forecasts of value-at-risk at all confidence levels, and the computational cost is far less than the existing two-stage value-at-risk estimating models, further improving the ability of risk management for electricity market participants.

Keywords: Value-At-Risk; Grey System Theory; Extreme Value Theory; GM(1;2); Peaks Over Thresholds.

1. Introduction

Value-at-risk (VaR) is a risk management tool to quantify the level of risk exposure in advance. Extreme value theory (EVT) provides a theoretical foundation to study the asymptotical distribution of extreme value for order statistics. EVT allows extrapolation beyond the sample and can accurately describe the behavior of the tails of the real data. Rozario R. [1] estimated the VaR of electricity market using a EVT technique known as peaks over thresholds (POT), showing that the estimated results perform well for moderate to very high confidence levels (95-90%), but struggle at higher levels (>99%) owing to the extreme clustering and other dependence evident in the data. Bystrom Hans N.E. [2] extended the classic unconditional EVT approach by first filtering the data via GARCH specification to capture some of the dependencies in electricity return series, and thereafter applying ordinary EVT techniques. In this way the independently and identically distributed (IID) assumption behind the EVT-based tail-quantile estimator is less likely to be violated, and the better tail

estimates in-sample and better predictions of future extreme price changes can be acquired. To describe the leverage effects of volatility of electric power price, an EGARCH specification [3] is used to filter the return series to obtain nearly IID residuals, showing that EGARCH-EVT model can rapidly reflect the most recent and relevant changes of electricity prices and produce accurate forecasts of VaR in the more volatile markets. Up to now electric power energy cannot be stored economically and electricity price exhibits considerably richer structure than load curve. To obtain an approximately IID residual series with better statistical properties, an ARMAX-GARCH model with Gram-Charlier series expansion of normal density function and skewed student-t distribution over the error items is used to pre-filter the raw data to capture the dependences of electricity price series, further improving the effectiveness of the VaR estimates via POT model [4, 5]. But the high non-linearity for the GARCH models leads to very large computational costs and hinders the wide application in practice.

In this paper a gray system and extreme value theory based two-stage model (GM(1,2)-POT-VaR) for estimating VaR is proposed. In stage one, considering that the properties of incomplete and uncertain information for the spot prices are in line with the characteristics of grey variables and the spot prices strongly depend on the system loads, a gray GM(1,2) model is used to pre-filter the electricity price series. In stage two, an EVT based POT model is employed to explicitly deal with the right tail of the residuals of the GM(1,2), and accurate estimates of VaR in electricity market can be produced. The empirical analysis indicates that the GM(1,2)-POT-VaR model can rapidly reflect the most recent and relevant changes of electricity prices and can produce accurate forecasts of VaR at all significance levels. Moreover, the computational costs is far less than the proposed models in [4, 5], further improving the risk management ability of electricity market participants. These results suggest that the proposed approach is robust and therefore useful.

2. GM(1,2) Model

The grey model is a modeling method based on the concept of grey generating function and differential fitting. Let the series of electricity prices and load be $X_1^{(0)} = \{x_1^{(k)}(1)\}$ and $X_2^{(0)} = \{x_2^{(k)}(1)\}$ respectively, then the dynamic process of $x_1^{(1)}(k)$ can be described by the GM(1,2) model [6]:

$$x_1^{(0)}(k) + az_1^{(1)}(k) = bx_2^{(1)}(k), \tag{1}$$

where $$X_2^{(1)} = \{x_2^{(1)}(k) \mid x_2^{(1)}(k) = \sum_{j=1}^{k} x_2^{(1)}(j)\}$$

$z_1^{(1)}(k) = \lambda x_1^{(1)}(k) + (1-\lambda)x_1^{(1)}(k-1)$ $(0 \le \lambda \le 1)$ is the background value, a and b are the model parameters to be estimated,. Let $\hat{a} = [a,b]^T$, then the estimated values by least squares method is $\hat{a} = (B^T B)^{-1} B^T Y_N$, in which,

$$Y_N = [x_1^{(0)}(2), x_1^{(0)}(3), \cdots, x_1^{(0)}(n)]^T,$$

$$B = \begin{bmatrix} -\lambda x_1^{(1)}(2) - (1-\lambda)x_1^{(1)}(1) & x_2^{(1)}(2) \\ \vdots & \vdots \\ -\lambda x_1^{(1)}(n) - (1-\lambda)x_1^{(1)}(n-1) & x_2^{(1)}(n) \end{bmatrix}.$$

After calibrated $\hat{a}$, the solution to Eq. 1 with initial condition $x_1^{(1)}(1) = x_1^{(0)}(1)$ is

$$\hat{x}_1^{(0)}(k+1) = \hat{x}_1^{(1)}(k+1) - \hat{x}_1^{(1)}(k). \tag{2}$$

3. POT Model

There exists strong temporal dependence in the electricity price series due to the specific features of electric power. It violates the underlying assumption that the data series to which EVT is applied should be a sequence of IID random variables. In this paper, a two-stage approach, provided by McNeil and Frey [7], is used to this problem. Firstly, the heteroscedasticities, skewnesses, lepkurtosises and seasonalities of electricity price series are filtered by the GM(1,2) model to obtain a nearly IID normalized residual series. In stage two, the EVT framework is applied to the standardized residuals to better capture the heavy-tails and improve the accuracy of VaR estimation.

POT is to model the excess distribution for the IID sample data that exceed a high threshold. Given the distribution function $F_z(z)$ of a random variable Z, the distribution function of values of z above a certain threshold u, $F_u(y)$, is called the conditional excess distribution function and is defined as

$$\begin{aligned} F_u(y) &= \text{Prob}(Z-u \le y \mid Z > u) = \frac{F_z(u+y) - F_z(u)}{1 - F_z(u)} \\ &= \frac{F_z(z) - F_z(u)}{1 - F_z(u)}, \forall 0 \le y \le z_F - u, \end{aligned} \tag{3}$$

where Z is a random variable, u is a given threshold, $y = z\text{-}u$ are the excesses and $z_F \le \infty$ is the right endpoint of $F_z(z)$.

The theorem of Balkema-De Haan-Pickands states that for large u the conditional excess distribution function $F_u(y)$ is well approximated by the

generalized Pareto distribution (GPD). If T is the total number of observations and T_u the number of observations above the threshold u, the value of $F_z(u)$ can be well approximated by the estimate $(T\text{-}T_u)/T$ for sufficiently high u. Replacing $F_u(y)$ by the GPD and $F_z(u)$ by $(T\text{-}T_u)/T$, we obtain the estimate of $F_z(z)$ from Eq.3

$$F_z(z) = 1 - \frac{T_u}{T}\left(1 + \frac{\xi}{\sigma}(z-u)\right)^{-1/\xi} \qquad \forall z > u. \tag{4}$$

Having determined a threshold, the estimates of ξ and σ of the GPD can be obtained by applying maximum likelihood estimation for the excesses of a threshold u. Replacing the values of parameters by their estimates and inverting Eq. 4 for a given probability c, the estimates of the c-th tail quantile for the sample distribution can be gotten,

$$F_z^{-1}(c) = u + \frac{\sigma}{\xi}\left(\left(Tc/T_u\right)^{-\xi} - 1\right), \tag{5}$$

which is valid for positive excesses, that is $z > u$.

4. GM(1,2)-POT-VaR Estimating Model

For a given time horizon t, suppose that the system demand for electricity is Q_t, the retail price to ultimate customers is P_0, the spot price is $p_t=\mathrm{E}(p_t|I_{t\text{-}1})+\varepsilon_t$, where $\mathrm{E}(\cdot)$ is the conditional expectation operator, $I_{t\text{-}1}$ the information set available at time t-1 and ε_t the random shock. The trading losses of an electric utility over the target horizon t is $\Delta P_t = Q_t\left(\mathrm{E}(p_t \mid \mathrm{I}_{t-1}) + \varepsilon_t - P_0\right)$. As P_0 is a regulated price and Q_t can be accurately forecasted, Q_t and P_0 can be regarded as constant. Let $f_\varepsilon(\varepsilon_t \mid I_{t\text{-}1})$ denote the conditional probability density function of ε_t conditional on $I_{t\text{-}1}$. The VaR of an electric utility in the specified period t with the pre-assigned probability level c, denoted by $VaR_{c,t}$, is

$$1 - c = \mathrm{Prob}(\Delta P_t \geq VaR_{c,t}) = \int_{\frac{VaR_{c,t} - Q_t(\mathrm{E}(p_t|\mathrm{I}_{t-1}) - P_0)}{Q_t}}^{\infty} f_\varepsilon(x \mid \mathrm{I}_{t-1})dx. \tag{6}$$

Now inverting Eq. 6 for the given probability c, we obtain

$$VaR_{c,t} = Q_t\left(\mathrm{E}(p_t \mid \mathrm{I}_{t-1}) - P_0 + F_\varepsilon^{-1}(c \mid \mathrm{I}_{t-1})\right), \tag{7}$$

where $F_\varepsilon(\cdot)$ is the conditional cumulative distribution function of ε_t, F_ε^{-1} is the quantile function defined as the inverse of the distribution function F_ε.

The expected values of the electricity spot price $E(p_t|I_{t-1})$ and the c-quantile $F_{\varepsilon}^{-1}(c \mid I_{t-1})$ of the residual series ε_t can be estimated by Eq. 2 and 5. Then we can calculate the VaR of an electric utility in the specified period t by Eq. 7.

5. Empirical Results

In this paper, a total of 1197 observations of average daily electricity spot prices and loads in PJM markets are employed to validate the performance of the VaR calculating model. The sample period begins on 1st June 2007 and ends on 9th September 2010. Table 1 lists the Ljung–Box Q statistics for the residuals of GM(1,2) model, showing that the Ljung–Box Q statistics for the residual are far less than the daily average electricity spot price series.

Table 1. Ljung-Box test for residuals of GM(1,2) model.

Statistics	Electricity prices ($/MWh)	Residuals ($/MWh)
Ljung-Box Q(6)	3868.28(0)	28.87(0.00007)
Ljung-Box Q(24)	11348.94(0)	51.21(0.001)
Ljung-Box Q2(6)	3117.13(0)	1.37(0.96756)
Ljung-Box Q2(24)	7892.50(0)	3.62(0.99999)

From a closer inspection of the sample mean excess function for the residuals of the grey GM(1,2) model, we fix the threshold u to 3.837. The estimates of the shape and scale parameters, ξ and σ, can be determined by fitting the GPD to the residuals via maximum likelihood estimator. Inserting the estimates of ξ and σ into Eq. 5, the tail quantiles of the residual series at a given confidence level c can be calculated. The Kupiec's test results for actual and forecasted losses are shown in Table 2. Summarizing the results for the Kupiec's tests, the VaR predictions are insignificantly different from the proposed downfall probability, but the GM(1,2)-POT-VaR model is easier to deal with and possesses the advantages of less computational costs.

Table 2. Backtests of estimated VaRs.

Confidence level	Statistics	ARMAX-GARCHSK	ARMAX-GARCH-st	GM(1,2)-POT-VaR
95%	Expected	60	60	60
	Real	59	60	59
	LR	0.013	0.000	0.013
97.5%	Expected	30	30	30
	Real	28	30	28
	LR	0.130	0.000	0.130
99%	Expected	12	12	12
	Real	13	13	12
	LR	0.087	0.087	0.000

6. Discussion and Conclusion

The distinctive characteristics of electric energy make electricity price present highly volatility, thus volatility of price risk management in electricity market is more important than in financial markets. A gray system and extreme value theory based two-stage model for estimating VaR is proposed. In stage one, a gray GM(1,2) model is used to pre-filter the electricity price series. In stage two, an EVT based model is employed to explicitly deal with the right tail of the residuals of the GM(1,2). The empirical analysis indicates that the GM(1,2)-POT-VaR model can rapidly reflect the most recent and relevant changes of electricity prices and can produce accurate forecasts of VaR at all significance levels. Moreover, the computational costs is far less than the proposed models in [4, 5], further improving the risk management ability of electricity market participants.

Acknowledgements

This work is supported by the natural science foundation of Hainan Province, China (611126).

References

1. R.D. Rozario, Estimating value at risk for the electricity market using a technique from extreme value theory on http://www.sal.tkk.fi/publications/pdf-files/eleh07.pdf.
2. H.N.E Bystrom, Extreme value theory and extremely large electricity price changes. I. *Rev. Econ. & Fin.*, 14 (2005) 41-55.
3. K.F. Chan, P. Gray, Using extreme value theory to measure value-at-risk for daily electricity spot prices, I. *J. Forecasting*, 22(2006) 283-300.
4. R.Q. Wang, X. Wang, Y.Z. Li, Risk measure of electricity market based on ARMAX-GARCH model with skewed-t distribution and extreme value theory, *Syst. Protect. & Contr.*, 41(2013) 1335-1440.
5. R.Q. Wang, F.X. Wang, M.C. Xu, ARMAX-GARCHSK-EVT Model Based Risk Measure of Electricity Market, *Proc. of 32nd Ch. Contr. Conf.*, Xi'an, China, July 26-28, 2013: 8284-8288.
6. S.F. Liu, N.M. Xie, *Grey system theory and its application*, first ed., Science Press, Beijing, 2008.
7. A.J. McNeil, R. Frey, Estimation of tail-related risk measures for heteroscedastic financial time series: an extreme value approach, *J. Empirical Fin.*, 7(2000) 271-300.

Effect of Nozzle on Performance of Swirl-Cooled Combustor

Kai Li†, Yi-hua Xu
Aircraft Engineering College, Nanchang Hangkong University, Jiangxi Nanchang 330063, China
†E-mail: 1020385704@qq.com

Zhuo-xiong Zeng
College of Power and Mechanic Engineering, Shanghai University of Electric Power, Shanghai, 200090, China

In order to study the influence of nozzle size on performance of swirl-cooled combustor chamber, Reynolds stress model (RSM) is used to carry out simulations of swirl-cooled combustor chamber with different stretching lengths and diameters of nozzle. The results showed that: nozzle extended into the combustion chamber could increase the combustion efficiency and improve the cooling effect for the wall. Reducing the diameter of nozzle can improve the combustion efficiency. When nozzle diameter is between 44% and 62% of the combustion chamber diameter is beneficial to get better cooling effect of the wall. Nozzle diameters larger than 80% of combustion chamber diameter may damage the cooling effect for the wall. Tangential velocity in the annular space has a greater effect on the cooling effect of the wall, and the tangential velocity in core of inner swirl is an important factor to affect the combustion efficiency.

Keywords: Swirl-Cooled; Size of Nozzle; Cooling Effect of Wall; Combustion Efficiency; Vortex Velocity.

1. Introduction

Vortex-cooled technology is a relatively new combustor cooling method. It could keep combustion within the vortex core by the inner and outer vortex, the outer vortex prevented high temperature gas from contacting with the wall surface to achieve the objective of cooling the wall. Meanwhile, the engine applied vortex-cooled technology had characteristics of low cost, good maintenance and long performance life [1-3].

In recent years, the vortex-cooled technology applied to combustor has been intensively investigated. LI Jia-wen et al. [4, 5] completed the 20s ignition experiments, results show that vortex-cooled thrust chamber worked steadily,

oxygen formed effective cold vortex, the temperature of outer wall of the cylindrical segment temperature rose 5K; studies also showed that among the three analyzed injection plates, the maximum efficiency of combustor is 97.6% when the injector distribution diameter is the largest. Anderson et al. [6] utilized tracer particles to make cold flow experiments on thrust chamber and obtained vortex structure. LI Gong-nan et al. [7] carried out a three-dimensional simulation study of vortex-cooled thrust chamber, verified the existence of bidirectional vortex structure.

Currently, vortex-cooled technology is mainly used for rocket engine thrust chamber. Its rear often used Laval nozzle, and in order to prevent the directly effluence of tangential inlet oxidant. Therefore, it needs to design appropriate convergent nozzle segment [8]. Further, since the particular organization of air in vortex-cooled combustor, resulting in its shortcoming: poor mixing of the fuel. So its combustion efficiency can be further improved. Thus, this paper presented swirl-cooled combustor through studies of cyclone separator and vortex-cooled thrust chamber. That is applied the exhaust pipe of cyclone to the vortex-cooled thrust chamber, instead of the original Laval nozzle. And it uses a new fuel injection method, in order to improve combustion efficiency. After that, the vortex-cooled technology can be applied to aero-engine and more combustion devices.

In this paper, simulations about stretching length and diameter of the nozzle were carried out to explore the influence of nozzle size on performance of swirl-cooled combustor. The results could provide technical support for the practical application and design of swirl-cooled combustor.

2. Model Description and Calculation Methods

The structure of swirl-cooled combustor is shown in Fig. 1. Taking the round face's center of the combustor head as coordinate origin, the combustor model was established along the Z-axis positive direction. Two tangential air intake manifolds were built at the bottom of the combustor barrel, fuel is injected into the annular hole from the head, the center hole is for air jet. The specific size of combustor parameters are as follows: the combustor barrel is 45mm diameter, 164mm height; the tangential air intake manifold is 12.5mm length, 8mm width; the nozzle is 50mm height; circular hole is 32mm outside diameter, 30mm inside diameter; central air jet hole is 2mm diameter. The values of stretching lengths(S) and nozzle diameters(D_1) are shown in Table 1 and 2.

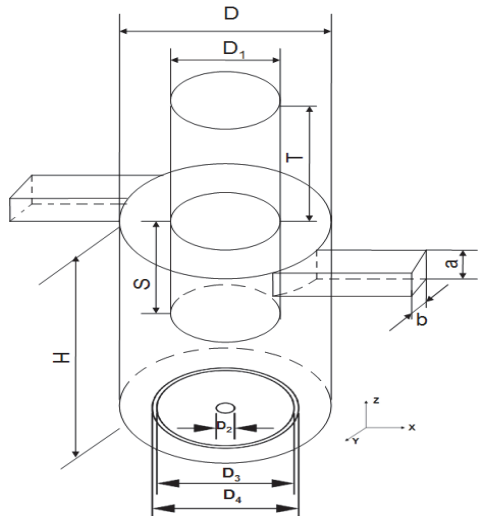


Fig. 1. Structure of swirl-cooled combustor.

Table 1. Values of stretching lengths.

D_1/mm	S/mm	S/H
24	0	0%
24	5	3%
24	10	6%
24	15	9%
24	20	12%
24	25	15%
24	30	18%
24	35	21%
24	40	24%

Table 2. Values of nozzle diameters.

S/mm	D_1/mm	D_1/D
30	16	36%
30	20	44%
30	24	53%
30	28	62%
30	32	71%
30	36	80%
30	40	89%

3. Computation Model and Boundary Conditions

In order to effectively simulate flow field which exists swirl, flow separation and recirculation zone, high-precision turbulence model should be used. Due to isotropic characteristics, the most widely used K-ε model has large deficiencies in solving flow problems with high speed gradients and strong swirl. Reynolds stress model (RSM) is suitable for solving anisotropic, flow lines bend, strain rate mutation and swirl flow, a lot of researches also showed that RSM can accurately describe the behavior of swirling fluid flow [9]. Therefore, the numerical simulation of swirl-cooled combustor should utilize Reynolds stress model (RSM).Combustion model chose finite chemical reaction rate model,

turbulence-chemical interaction chose eddy-dissipation model. Near the wall used standard wall function method, diffusion terms used second-order central difference scheme, convection terms used QUICK format, speed-pressure coupling method used SIMPLEC, combustor wall used adiabatic wall, the velocity take no-slip condition. All entrances used velocity inlet. Air inlet velocity is 19m/s; central air jet velocity is 80m/s, the equivalent ratio of the total combustor is 0.67. Nozzle outlet used pressure outlet boundary condition, the outlet pressure was set to atmospheric pressure. The inlet temperature of air and methane are 300K.

4. Results and Discussion

4.1. Numerical verification

The above method was utilized to carry out simulations of the vortex cold-wall combustor in literature [10]. In Fig. 2, the temperature of the A point near the wall is 385.6K. It is close to the temperature of 373K measured by literature [10]. The total temperature obtained through numerical simulation is 3096.3K. It is close to the theoretical total temperature of 3179.98 K calculated by thermal calculation software CEA. The results show that the simulation method chosen by this paper is credible.

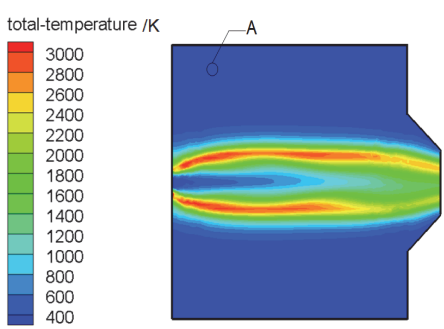


Fig. 2. Temperature distribution of vortex cold-wall combustion chamber.

4.2. Influence of nozzle stretching length

The key to realize the swirl-cooled effect is forming inner and outer swirl structure in swirl-cooled combustor. In order to investigate the inner and outer swirl structure and the internal flow characteristics, envelope surface of zero axial velocity, distribution of streamlines, axial velocity distribution in the radial direction and tangential velocity distribution in the radial direction are introduced.

To make the graphics clearly, only partially representative conditions are selected to analyze.

Fig. 3 shows the axial velocity of the dark areas is greater than zero; light area represents the axial velocity is less than zero, and its interface is the envelope surface of zero axial velocity, that is, the dividing line between the inner and outer swirler. According to the axial velocity distribution in the radial direction (Fig. 5), the zero points could be used to calculate the width of inner swirl. Due to the width of inner swirl in the combustor is substantially same (Fig. 4), so the width of the inner swirler(r) on section Z/H=50% is used to characterize the width of the combustor. Z represents the length direction of the combustor. Fig. 6 shows the ratio of the width of the inner swirl and combustor radius (R). With the increase of nozzle stretching length, the ratio of the width of the inner swirl and combustor radius increases. The growth rate is rapid at the beginning, up to a certain value the growth rate slows down. The wall extending into the combustor blocks the spread of the inlet air to the center.That makes the inlet air flow downward close to the wall, and reduces the thickness of the outer swirl.

For convenience, the the radial velocity distribution on section Z/H=25% are selected to analyze. In Fig. 7, tangential velocity rises rapidly from the wall to interior, then the change of tangential velocity enters relatively stable stage. Finally, it declines rapidly.Tangential velocity in the core area of inner swirl is proportional to the distance from the combustor center. It is called forced vortex. Tangential velocity in outer swirl is inversely proportional to the distance from the combustor center. It is called free vortex.This is basically the same with the conclusions of inner and outer swirl can be simplified as outer free vortex and inner forced vortex in literature. The tangential velocity in intermediate region is



Fig. 3. Envelope surface of zero axial velocity.

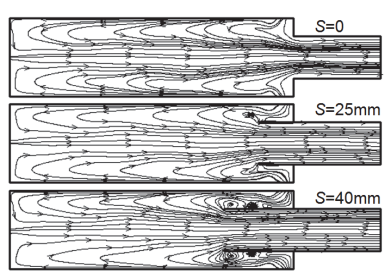


Fig. 4. Distribution of streamlines with different stretching lengths.

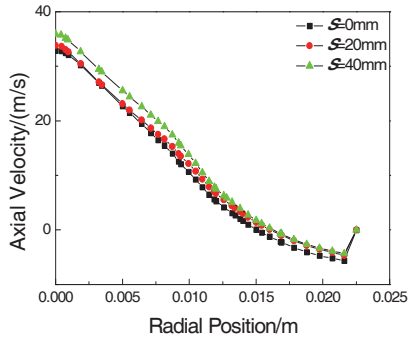


Fig. 5. Axial velocity distribution with different stretching lengths.

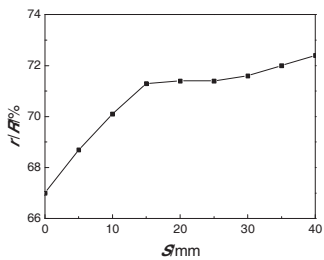


Fig. 6. Ratio of half-width of inner swirl and radius with different stretching lengths.

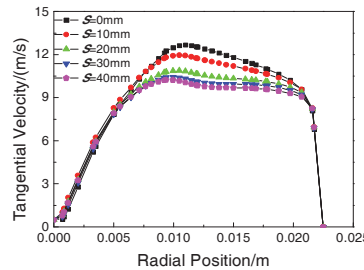


Fig. 7. Tangential velocity distribution at section local of Z/H=25% with different stretching lengths.

relatively stable. It is the transition region of inner and outer swirl. It is called annular space of the double swirl.According to Fig. 7, with the increase of nozzle stretching length, tangential velocity in annular space increase; The trends of tangential velocity in the core area of inner swirl and the outer swirl are basically same.

Total pressure loss is one of the performance parameters of the combustor.In order to study the total pressure loss of swirl-cooled combustor, total pressure loss coefficient is introduced.The formula can be expressed as:

$$\delta=\frac{P_1^*-P_2^*}{P_1^*} \tag{1}$$

p_1^* is the combustor inlet total pressure, p_2^* is the combustor outlet total pressure.

Fig. 9 shows that, with the increase of nozzle stretching length, total pressure loss coefficient increases gradually.The increase of nozzle stretching length limits the discharge capacity of the combustor, and results in recycle stream (Fig. 4). Recycle stream will bring more energy loss, then it makes total pressure losse

increase. However, this effect is slight, the total pressure loss coefficient is maintained at between 0.55% to 0.6%. This shows that the simple structure of swirl-cooled combustor has low resistance characteristic.

Combustion efficiency is also one of the combustor performance parameters. As shown in Fig. 9, the combustion efficiency presents an upward trend with the increase of nozzle stretching length, and the combustion efficiency increases significantly when nozzl begins to extend into the combustor. When the stretching length increase to a certain value, the growth rate begins to slowdown. At this time, the combustion efficiency will remain at 96.5%. The reasons are that, the increase of stretching length makes the volume of combustor reduce, and it limits the discharge capacity of the combustor, so that the combustion chamber pressure increases.The increase of pressure can increase turbulence speed, and reduce laminar flame propagation speed. The comprehensive effects improve the turbulent flame propagation speed. Thereby, burning rate is increased, and combustion performance is improved. So the combustion efficiency increases by increasing nozzle stretching length.

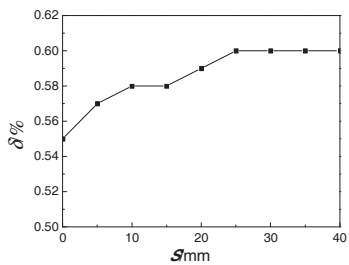


Fig. 8. Total pressure loss coefficient different stretching lengths.

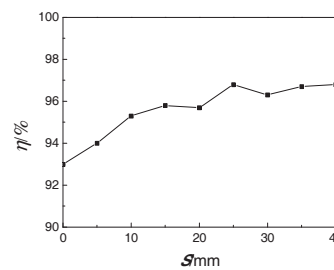


Fig. 9. Combustion efficiency with different stretching lengths.

Temperature distribution on center plane of symmetry is selected to observe the cooling effect for the wall.With the increase of stretching length, the temperature near the wall is gradually decreased, as shown in Fig. 10-11. The temperature in the core area of inner swirl is basically same. It only has a slight increase with the increase of stretching length.In the annular space,the temperature vary greatly. With the increase of stretching length, the temperature drop rapidly. Known from the above analysis, the tangential velocity in annular space decreases with the increase of stretching length. And tangential velocity is an important factor of fuel blend [7], larger tangential velocity is conducive to burning vigorously in annular space (Fig. 6). These high-temperature product will soon transfer heat to the outer swirl, which is close to the annular space. It leads to rapid temperature rise and the damage of the cold wall effect.In Fig. 10, when S=0mm and S=5mm,

the temperature near the wall on section Z/H=25% exceeds the maximum operating temperature of the conventional flame tube material, which is required to below 1200K . So increasing nozzle stretching length could improve the cooling effect for the wall.

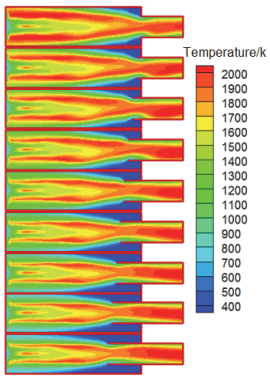


Fig. 10. Temperature distribution of the whole combustor with different stretching lengths.

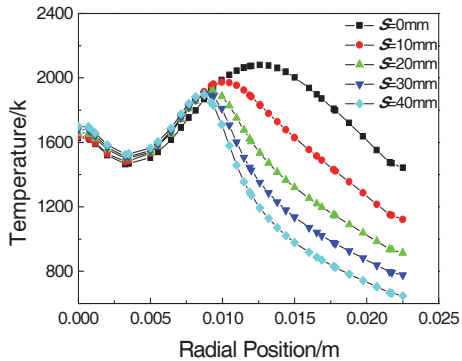


Fig. 11. Temperature distribution at section of Z/H=25% with different stretching lengths.

4.3. Influence of nozzle diameter

According to Fig. 12, with the increase of nozzle diameter the tangential velocity in the core area of inner swirl decreases. But when the nozzle diameter is 40mm, the tangential velocity has a slight increase.In the annular space, the trend of tangential velocity is irregular. The vortex velocity in outer swirl remains the same.

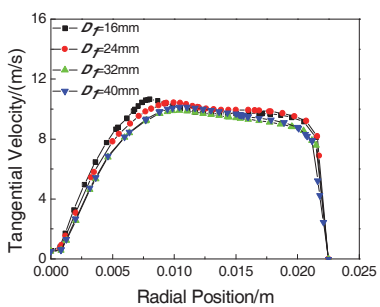


Fig. 12. Tangential velocity distribution at section of Z/H=25% with different diameters.

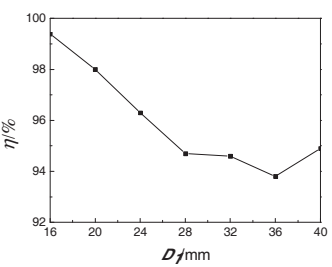


Fig. 13. Combustion efficiency with different diameters.

In Fig. 13, combustion efficiency decreases with the increase of nozzle diameter. Finally, it has a slight rise.Under the condition of the nozzle diameter is

16mm, the maximum combustion efficiency reaches 99.4%. While increasing nozzle diameter, the minimum combustion efficiency is only 93.8%. The reasons are as follows: Reducing the nozzle diameter will decrease the discharge capacity of the combustor. It plays a role in improving combustor pressure and improving combustion performance. So the combustion efficiency is improved. On the other hand, most fuel are concentrated in the central area under this fuel injection method. The greater tangential velocity is beneficial for the mixing of the fuel, which can help the combustion efficiency improve. So the tangential vortex in the core area of inner swirl plays a decisive role on the combustion efficiency. Known from the above analysis, the trend of combustion efficiency corresponds to the trend of tangential velocity in the core area of inner swirl. This indicates that tangential velocity in the core area of inner swirl has a greater effect on combustion efficiency.

According to Fig. 14, it is not a linear relationship between the temperature near the wall and nozzle diameter. The best swirl-cooled effect occurres in the conditions of moderate nozzle diameter. Too small and too large nozzle diameter will cause poor swirl-cooled effects, or even destroy the cooling effect for the wall. The effects of nozzle diameter on the cooling effect for the wall is the combined effect of multiple factors. On the one hand, the tangential velocity in annular space plays a role in swirl-cooled effect. But it does not exhibit regularity at different nozzle diameters. On the other hand, the tangential velocity in the core area of inner swirl affects the fule mixing and the fuel concentration distribution in the annular space. Thereby, it can affect the combustion in annular space. Furthermore, the variation of combustor pressure can change combustion speed and combustion performance. Thus it can affect the cooling effect for the wall.

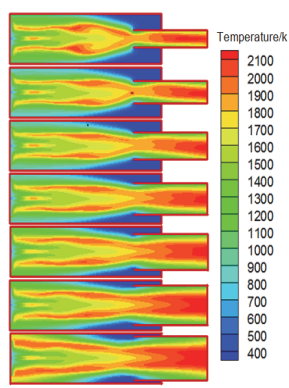


Fig. 14. Temperature distribution with different diameters.

5. Conclusions

(1) Under the condition of D_1/D=53%, the minimum combustion efficiency is 93%(S=0). Increasing the nozzle stretching length can improve the combustion efficiency and swirl-cooled effect , the maximum combustion efficiency is 96.8%. (2) Under the condition of S/H=15%, reducing the nozzle diameter will help improve combustion efficiency. When D_1/D=36%, the maximum combustion efficiency is 99.4%. (3) When D_1/D is between 44% and 62%, the swirl-cooled effect is optimal. When D_1/D>80%, it may destroy the swirl-cooled effect. (4) Tangential velocity in annular space plays a role in swirl-cooled effect, and tangential velocity in the core area of inner swirl the most important factor of combustion efficiency.

References

1. Chiavertini M J, Malecki M J, Sauer J A, et al. Vortex Combustion Chamber Development for Future Liquid Rocket Engine Applications[R]. AIAA 2002-4149.
2. Munson S M, Saucer J A, Rocholl J D, et al. Development of a Law-Cost Vortex-Cooled Thrust Chamber Using Hybrid Fabrication Techniques[R]. AIAA 2005-4131.
3. Dechuan Sun, Shang Liu. Experimental Research on Bidirectional Vortices in Cold Wall Rocket Thruster[J]. *Aerospace Science and Technology*, 2012, 18(1): 56-62.
4. Li J W, Tang F, Yu N J. Experiment study on vortex-cooled thrust chamber[J]. *Journal of Propulsion Technology*, 2012, 33(6): 956-960.
5. Li J W, Wang H Y, Ye H Y, et al. Combustion efficiency analysis on vortex-cooled thrust chamber[J]. *Journal of Propulsion Technology*, 2013, 34(11):1507-1512.
6. Anderson M, Rom C, Bonazza R, et al. Vortex Chamber Flow Field Characterization Using Laser Diagnostics[C]. Las Vegas: *52nd JANNAF propulsion meeting*, 2004.
7. Li G N, Yu N J, Lu Q. Simulation study of flow characteristics and performance of vortex cooling thrust chamber[J], *Journal of Aerospace Power*, 2014, 29(2): 420-426.
8. BAI R B. Numerical simulation of the ignition process in a GOX/CH4 vortex cold-wall thruster[D]. Shanxi: Northwestern Polytechnical University, 2011.
9. SUN D C, BAI R B, LIU S. Numerical simulation of vortex cold-wall rocket combustor[J]. *Journal of Projectiles, Rockets, Missiles and Guidance*, 2011, 31(2): 111-113, 116.
10. Yang J W. Vortex cold-wall rocket engine experimental study[D]. Xi'an: Northwestern Polytechnical University, 2010.

Experimental Study on the Pyrolysis Characteristics of Demineralized Phragmites

Jinming Shi, Min Lin, Yunsheng Xie, Xiping Xi, Heli Wang, Yuanyuan Gong
Institute of Energy, Jiangxi Academy of Science, Jiangxi Nanchang 330096 PRC
NO. 7777, Changdong Road, Nanchang City, Jiangxi Province, China
†E-mail:shijinming0012@163.com

Based on washing and pickling, the Phragmites samples were prepared, and these characteristics of pyrolysis reaction were researched in thermogravimetric analyzer. The influence of reaction factors, such as the metal salt components, metal salt elution rate, biomass samples pore size distribution, heating rate, on the pyrolysis characteristics was investigated. Results showed that, the demineralized methods had significant effects on minerals and the pore structure. The pickling efficiency was 99.8%. Original positions of minerals formed new holes after elution, thus leading to the adsorption quantity of elution sample greater than raw sample. With the demineralizing degree increasing, the mesopore proportion decreased gradually. Improving the heating rate was helpful for pyrolyzing of Phragmites raw samples and elution samples.

Keywords: phragmites; pyrolysis; pickling; washing; mineral.

1. Introduction

Because of the huge population, environment friendly, renewable, biomass has been paid more attention. Using biomass in an effective way is a challenge for the energy industry. Biomass energy conversion technologies especially pyrolysis and gasification have been substantially studied to promote renewable energy utilization and solving partially the environmental issues.

Poyang Lake is the largest freshwater lake in China, aquatic plants resources rich. With popularizing and applying phytoremediation technology, the biomasses resources quantities are increased. But the large number of biomasses can't be used reasonably. The biomasses are usually used by incinerating in the fall and the winter, causing environmental pollution and a lot of resources waste. Therefore, utilizing the aquatic plant resources of Poyang Lake reasonably is beneficial to adjust the energy structure of Jiangxi province, but also enrich the biomass pyrolysis gasification database.

Phragmiteses were picked from southern rocky mountain wetland in Poyang Lake, and the wetland has a large number of deposits substances, such as N, P, alkali metals, heavy metals, leading to the initial substances content in Phragmites more than terrestrial plants, and these elements rich rally had certain influence on the pyrolysis characteristics. Therefore, it is significant to study the characteristics of Phragmites pyrolysis.

Recently, the study was paid more attention to the agriculture and forestry waste pyrolysis and gasification [1-5], but few to aquatic plants pyrolysis and gasification [6,7]. Zhao Hui et al. [7] found that compared with corn straw, sawdust and other typical terrestrial biomasses, enteromorpha had the lowest thermal stability, and the catalytic effect of Al_2O_3 to enteromorpha was better than that to corn straw. Wang Xianhua [8] found that mineral matters have great influences on biomass pyrolysis. Amounts of alkali metals, such as K, Ca and Mg, resulted in biomass pyrolysis reaction activation energy and reaction activation temperature dropping. Pickling and washing to remove minerals made the pore structure increasing, which easy to release the volatile matters, and resulted in the maximum pyrolysis rate increasing significantly [8]. Yang Haiping et al. [9] had used the main organic components (hemicellulose, cellulose and lignin) in biomass as model biomass samples to research the catalytic mechanism of alkali salts addition on biomass pyrolysis, and the results showed that K_2CO_3 had obvious role in promoting hemicellulose and cellulose pyrolysis. T. d. Hengel et al. [10] used the pickling method to remove the minerals in coal, and ammonium acetate was used to replace AAEMs (alkali and alkaline-earth metals) in lignite, to research the mineral catalytic properties of lignite.

The recent studies were focused on terrestrial biomasses, but rare to aquatic plants. Based on the previous researches and the current situation, this paper studied Phragmites pyrolysis process using thermogravimetric analyzer. Through washing and pickling, pore structure analysis, the influences of minerals on the pyrolysis characteristics are analyzed.

2. Experiment and Instrument

2.1. *Sample preparation*

2.1.1. *Raw sample preparation*

Phragmites in Poyang Lake was chosen as the research object. In order to demonstrate conveniently, Phragmites samples were marked as P. After grinding and sieving, Phragmites samples particle size was controlled in 180 ~ 200 μm. These samples were dried at constant temperature 333K for air dry basis.

2.1.2. *Sample demineralization*

Demineralization by Washing*:* A slurry of 40g raw Phragmites sample and 500ml of distilled water was stirred for 2h at 333K and then filtered. After filtering, the demineralization sample was washed with 2000ml of hot distilled water.

Demineralization by Pickling*:* A slurry of 40g raw Phragmites sample and 500ml of 6M HCl was stirred for 2h at 333K and then filtered. The biomass was subsequently mixed with 500ml of 10M HF, stirred at 333K for 6h, and then filtered. After filtering, the demineralization sample was washed with 2000ml of hot distilled water [10]. The samples were dried at 333K in oven for several hours. The proximate and ultimate analysis results are presented in Table 1.

Table 1 Proximate analysis and ultimate analysis

Sample	Proximate analysis/ %				Ultimate analysis/ %				
	Mad	Vad	Aad	Fcad	Cad	Had	Nad	Sad	O*ad
P.R	6.22	68.15	14.91	10.72	44.83	5.71	0.32	0.05	34.18
P.W	6.26	71.64	13.05	9.05	46.44	5.77	0.35	0.06	34.33
P.A	5.43	80.58	0.03	13.96	49.08	6.16	0.37	0.05	44.31

*Calculated by difference

P.R represented the raw biomass sample, P.W represented the washing sample, and P.A represented the pickling sample.

2.2. *The sample analysis*

2.2.1 *1 low-temperature ashing*

EMITECH K1050X low-temperature-ashing instrument was used to ash Phragmitess raw sample, washing sample and pickling sample respectively. Then, the ash content will be determined by XRF analysis.

2.2.2 *XRF analysis*

Low-temperature-ashing samples were analyzed with EAGLE III X-ray Fluorescence analysis, to determine the percentage of the oxide content in the ashes.

2.2.3 *BET analysis*

The samples were analyzed with the Micromeritics ASAP 2020 (Micrometer Co. in the United States), to determine the specific surface and pore size of the raw sample and bio-chars. Nitrogen (purity > 99.99%) was used for the adsorption medium in the instrument, and the relative pressure is between 0.01 ~ 0.995.

2.2.4 *Pyrolysis experiments*

Pyrolysis experiments were carried on with NETZSCH STA449F3 thermogravimetric analyzer (Germany). The reaction medium was N2, and the flow rate was 100 ml/min. Samples were added into the alumina crucible with 5±0.5 mg. In the beginning, the high purity N2 was pumped for 30 min, scavenging air in the reactor. Then, the temperature was rise programmed to 900ºC, and later, the residence time was controlled within 30 min. The heating rate was controlled 10ºC/min, 20ºC/min, 30ºC/min, respectively.

3. Results and Discussions

3.1. *The influence of elution treatment on ash*

Table 1 listed the ash content of Phragmites raw samples, washing samples, pickling samples after low temperature ashing. It could be seen from Table 2, there were different deashing effects to Phragmites in different elution processes. Washing deashing efficiency was 12.47%, and pickling deashing efficiency reached 99.8%, and the resident 0.03% minerals may be the organic salts. It found that the effect of pickling was superior to washing, and the rate of SiO2 and insoluble salt of Phragmites minerals was nearly 87.06%.

Table 2 Ash content of samples

Biomass	Ash content/ %			Efficiency/ %	
	(R)	(W)	(A)	(W)	(A)
Phragmites	14.91	13.05	0.03	12.47	99.8

3.2. *The ash composition changes*

According to the principle of low-temperature- ashing, under the effect of high frequency electric field, organic matters can be oxidized to oxide in the sample in low temperature. Thus the ash compositions were shown in the form of oxide. The results analyzed by XRF were shown in Fig. 1.

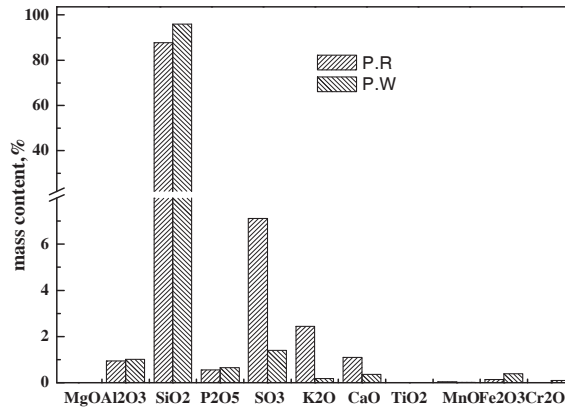


Fig. 1 The compositions content in ash of P.R and P.W (P.R represented the raw biomass sample, P.W represented the washing sample)

The compositions content in ashes of Phragmites raw sample and washing sample were shown in Fig. 1. Due to pickling deashing efficiency of 99.8% to the raw sample, it could not be shown in this Figure. It could be seen that, the main components of minerals in Phragmites was Si, and others were S, K, Ca, Al, P, Fe and Mn, and the content order was descending. But it should be pointed out, due to the other components removed, the total ash content decreased led to some compositions percentage increasing. The actual content should be calculated as follow:

$$Ar = Ad \bullet (1\text{-}x)$$

Ar was the actual ash content, and Ad was the measured ash content, and x was deashing efficiency.

Compared Phragmites raw sample with washing sample, the influence of washing on Al, Si, P, Fe and Mn was not remarkable, but obvious on S, K and Ca. It can be concluded that there are soluble salts composed of S, K, Ca in minerals.

Experimental results showed that, the alkali metals or alkaline earth metals elements and a small amount of sulfate in Phragmites could be removed after washing. Phragmites minerals may be composed of 99.8% inorganic minerals and 0.2% organic minerals.

3.3. *The influence of elution treatment on pore structures*

Figure 2 showed the Isothermal adsorption curve and Isothermal stripping curve of the Phragmitess samples. In Fig. 2, the adsorption isotherm, although a slight difference in the shape, but showed the S type, which is same as II type isotherm of gas adsorption isotherm by S. Brunauer [11]. It was suggested that Phragmites pore

system was complex and the pore size distribution was continuous and complete. The adsorption quantity of washing sample was the largest, but the raw sample minimal. This showed that there was a new pore formed in the minerals original position after washing or pickling process.

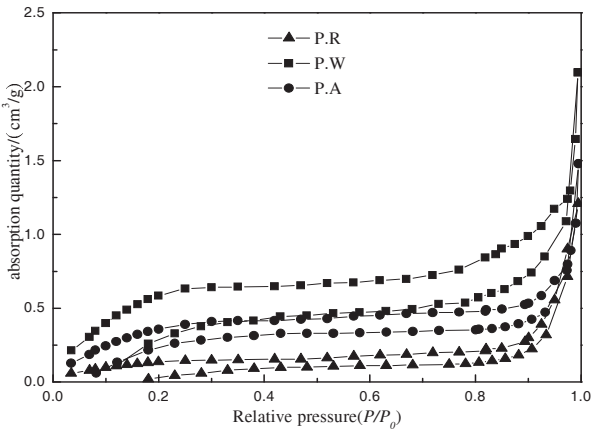


Fig. 2 Isothermal adsorption curve and Isothermal stripping curve of P.R, P.W and P.A

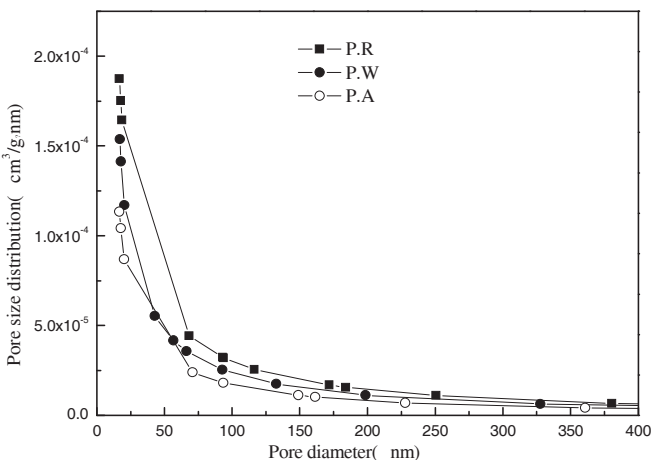


Fig. 3 Pore size distribution of P.R, P.W and P.A

Figure 3 showed the pore size distribution of Phragmites raw sample and elution samples. There was the similar pore size distribution in the Phragmites and elution samples particles, very few micropore and mainly 15 to 25 nm mesopore. With the demineralization degree increasing, the proportion of mesopore reduced gradually. Compared with Fig. 2, it could be found that a major contribution to the adsorption quantity of washing sample was the formed new mesopores in

removing minerals. But inorganic minerals almost removed completely in pickling process, the formed new pore should be greater than washing sample. It could be very unstable, or collapse occurred at the same time. Thus the adsorption quantity of the pickling sample is lower than washing sample. Through the above analysis, with the demineralization degree increasing, the number of different size pores was changed, and the quantity of large pore and mesopore was increasing relatively.

3.4. *The influence of demineralization on pyrolysis characteristics of Phragmites*

Figure 4 showed DTG curves of the Phragmites and elution samples under a heating rate. It suggested that, there were obvious weightlessness between 180 ~ 500ºC, which was the volatile matters releasing process, due to the thermal decomposition reaction of hemicellulose and cellulose. After 500ºC, for biomass carbonization stage, the DTG curve was relatively flat, which was due to the slow decomposition of residues, mainly formed coke and ash.

The raw sample had wide volatile releasing zone, but the weightlessness rate smallest. The volatile releasing zone of pickling sample was 250 ~ 400ºC, and the weightlessness rate was the largest. When the temperature above 500ºC, the thermal decomposition reaction of hemicellulose and cellulose almost ended, and lignin pyrolysis become the main reaction in pyrolysis. Because of more coke formed during the thermal decomposition of lignin, the pyrolysis weightlessness rate curve was gentle in high temperature.

The results showed that under the same heating rate, the volatile release of raw sample was ahead of elution samples, but the releasing rate was the minimum. This was mainly related to the pore structure, as shown in the Fig. 3, the 15~25 nm mesopore was the most in raw sample. Compared with the elution samples, volatile could be easy to release. And in Fig. 2, the adsorption quantity of raw sample was the minimum, which reflected the minimum pore volume, and it resulted in the minimal releasing rate of volatile.

In addition, the volatile releasing of pickling sample in pyrolysis process ended first and the second was the washing sample. At the same time, according to the integral area of weightlessness rate curve, it was found that the volatile release of each sample was not very obvious. This was to say, it had significant effect on the demineralization of Phragmites, but will not affect the total precipitation of volatile.

Compared with the DTG curves of samples under a heating rate, improving the heating rate could be helpful for pyrolysis reaction, and shorten the reaction

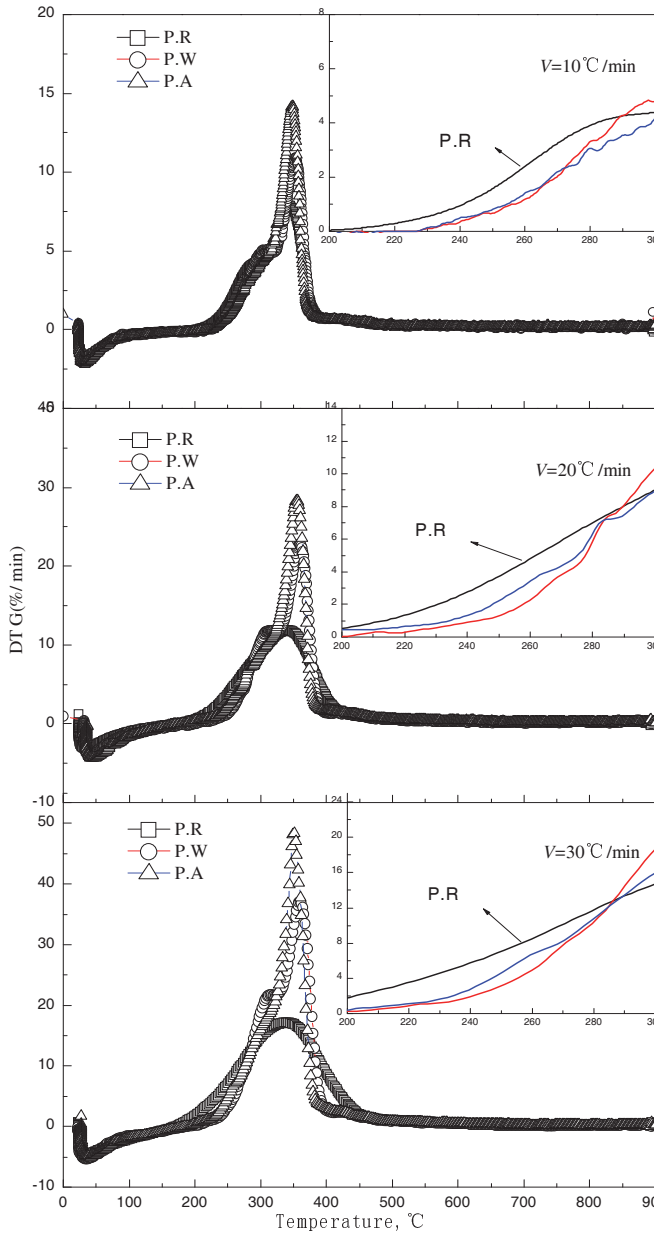


Fig. 4 Pyrolysis DTG curves of different samples at a heating rate

time to required temperature, but also may cause thermal hysteresis phenomenon, which was due to the reaction degree was low in the short reaction time, affected the pyrolysis reaction of biomass samples particles inside effectively [12].

In Fig. 4, there were common characteristics of pyrolysis reaction under different heating rate, such as the larger the heating rate was, the greater the weight loss rate was. It proved that the increase of heating rate was helpful for pyrolysis reaction [12]. For the raw sample, when the heating rate increased more than 20ºC/min, the twin peaks in DTG curves disappeared, which were the cellulose and hemicellulose pyrolysis reaction peaks. With the improvement of heating rate, pyrolysis reactions of cellulose and hemicellulose would be conducting simultaneously, thus making the twin peaks associating.

But for elution samples, when heating rate under 30ºC/min there was not similar phenomenon, twin peaks were still apparent. This was mainly caused by pore structure changed. The original structure was destroyed, and the pore volume increased, more in favor of heat and mass transfer. Therefore, volatile released more easily. In Fig. 4, it could also be proved by the weight loss rate of elution samples under the same heating rate higher than the raw sample.

4. Conclusions

The demineralizing efficiency was 12.47% by water, and the pickling demineralizing efficiency reached 99.8%. There were 0.2% organic minerals in Phragmites. The main components of minerals in Phragmites were Si, and others were S, K, Ca, Al, P, Fe and Mn. K and Ca mainly existed with the form of soluble salt.

There was a new pore formed in the minerals original position after washing or pickling process, which led to the absorption quantity of elution samples larger than the raw sample. With the demineralization degree increasing, the proportion of mesopore reduced gradually.

Weight loss rate of raw sample was the smallest and pickling sample maximum. After 500ºC, thermal decomposition reaction of lignin become the main pyrolysis reaction. The volatile release of raw sample was ahead of elution samples, but the pore volume led to the minimum releasing rate. Improving the heating rate was helpful for the biomass pyrolysis.

Acknowledgment

This project is supported by National Nature Science Foundation of China (51166004) and supported by Nature Science Foundation of Jiangxi Province of China (20133BAB21002).

References

1. Nandi S. P., Onischak M., Gasification of chars obtained from maple and jack pine woods. [A]. *Fundamentals of thermochemical biomass conversion*. [C], New York: Elsevier, 1985, 567-587.
2. Gaur S., Rao T. R., Phragmites T. B., et al. kinetics of corn cob char gasification in carbon dioxide*[J]. Fuel Science & Technology International*, 1992, 10(9): 1461-1499.
3. Huang Yanqin, Yin Xiuli, Wu Chuangzhi, et al. Effects of metal-salt catalysts on CO2 gasification reactivity of fir char. *Acta Energiae Solaris Sinica*, 2010, 31(11): 1385-1390.
4. ZhaoHui, Han Shuxin, Zhou Jingsong, Sheng Shuiping, Luo Zhongyang, Cen Kefa. Investigation of emission behavior of inorganic element during biomass entrained flow gasification*[J]. Acta Energiae Solaris Sinica*, 2011, 32(4):456-462.
5. Zhang Yanping, Jin Baosheng, Liu Renping. Factors affecting alkali release and transformation during corncob combustion. *Acta Energiae Solaris Sinica*, 2009, 30(2):261-265.
6. Shijinming, Xie Yunsheng, Ao Ziqiang. Experimental study on the Transforming Characteristics of Alkali and Alkaline Earth Metallic Species during Isothermal Pyrolysis of Typical Biomass*[J]. Chinese Society of Engineering Thermophysics*, Beijing, 2012.
7. Zhao hui, Yan Huaxiao, Liu Ming, Zhang Mengmeng, Tian Yuanyu, Qin Song. Effect of Al2O3 on pyrolysis characteristics of enteromorpha clathrata. *China Biotechnology*, 2010, 30(8):37-41.
8. WANG Xianhua, CHEN Hanping, WANG Jing, XIN Fen, YANG Haiping. Influences ofm ineralmatters on biomass pyrolysis characteristics. *Journal of Fuel Chemistry and Technology*, 2008, 36(6):679-683.
9. YANG Hai-ping, CHEN Han-ping, DU Sheng-lei, CHEN Ying-quan, WANG Xian-hua, ZHANG Shi-hong. Influence of Alkali Salts on the Pyrolysis of Biomass Three Components. *Proceedings of the CSEE*, 2009, 29(17):70-75.
10. T. D. Hengel, P. L. Walker, Jr. Catalysis of lignite char gasification by exchangeable calcium and magnesium. *Fuel*, 1984, 63(9):1214-1220.
11. Brunauer S., Deming L. S., Deming W. E., et al. On a Theory of the vander Waals Adsorption of Gases*[J]. J. Am. Chem. Soc.* 1940, 62(7): 1723-1732.
12. Wang wei, Lan Yuxin, Li Ming. Pyrolysis fo Pine Sawdust by TG-FTIR Analysis. *Journal of Agro-Environment Science*, 2008, 27(l):350-384.

Application of Array Sonic Logging in the Study of Regional Geostress in Nanpu Sag

Jiming Yao[a*], Weihua Zhang[c] and Sen Wang[d]

College of Mining Engineering, Hebei United University, Tangshan, Hebei 063009, China
[a] E-mail: jimingy@126.com,
[c] E-mail: zhangweihuanancy@126.com, [d] E-mail: wangsen@heuu.edu.cn

Xianxian Tao[b]

PetroChina Xinjiang Oil field Company, Karamay, Xinjiang 834000, China
[b] E-mail: sxyttxx@petrochina.com.cn,

In the petroleum industry, the design of drilling technology, reservoir fracturing, and development design are closely related to the present-day stress field of the oil field. The S-wave splitting phenomenon can be used to evaluate the state of the stress in rocks, including strata naturally fractured, rocks with uneven tectonic stress, and rocks with high-angle dipping. This paper used the data of the split fast and slow S-wave components extracted from array sonic logging waveforms to evaluate the anisotropic characteristics of the strata. Based on the data from array sonic logging, the direction and magnitude of the maximum horizontal stress are calculated in Nanpu sag. Our results are consistent with other methods. Therefore, our study provides reliable results that are important to be considered for future drill plans and reservoir fracturing in the study area.

Keywords: array sonic logging, anisotropic characteristics of strata, geostress, S-wave splitting.

1. Introduction

During the early time of the 1920s, one of pioneer geologists of China, Li Si-guang, firstly introduced the concept of geostress. He proposed that the stress in the lithosphere has caused the earth crust to overcome the resistance and led to constant deformation. He believed that the strain in present-day's crust, such as fold and fault, is a reflection of the past stress in the lithosphere[1]. For the

* Corresponding author.

petroleum industry, the direction and the magnitude of maximum horizontal stress are of great significance for design of drilling plan, reservoir fracturing, development design and so on[2,3]. According to incomplete statistics, there are 145 casing-damaged wells occurred in Nanpu sag (649 wells in total), making a damage rate of 22.4% for the oil and water wells in this oilfield[4]. These damaged wells have caused significant economic losses for the company and they also continue to have an influence on the daily production of this oilfield in future. With the recent development of technology in this field, we are now able to image in detail the anisotropic characteristics of the strata by analyzing results from array sonic logging. This new technique provides us an opportunity to understand the state of stress in the underground rocks[5,6]. Results from array sonic logging can be used to accurately determine the direction and magnitude of the regional principle stresses, particularly the maximum horizontal stress in wells. These results provide important data for us to understand the orientation of potential deformation in these undrilled wells[7]. This will help us to improve well optimization of structure, design and testing height of artificial fractures in formation[8,9].

2. The Principle of Geostress Estimation Using Array Sonic Logging

2.1. *Determination of Geostress Direction*

The orientation of S-wave velocity is usually anisotropic in anisotropic strata. In fractured strata, the polarized S-wave parallel to fractures travels faster than that perpendicular to fractures. This phenomenon is called S-wave splitting[10]. Beside the fractured formation, the S-wave splitting phenomenon also occurs in rocks with uneven tectonic stress and rocks with high-angle tilt. This phenomenon is the physical basis of our evaluation of horizontal geostress by array sonic logging. Essentially, the S-wave that generated by dipole source in anisotropic strata will split into two orthogonal components along X and Y axis of polarization (Fig. 1). One of the components travels fast along the strike of fractures and it is called fast-shear wave. The other one perpendicular to fractures travels slowly and it is called slow-shear wave. Occurrence of s-wave splitting in the formation rocks suggests that these rocks show anisotropy. The level of anisotropy is indicated by the degree of splitting and difference between fast-shear wave and slow-shear wave are controlled by velocity.

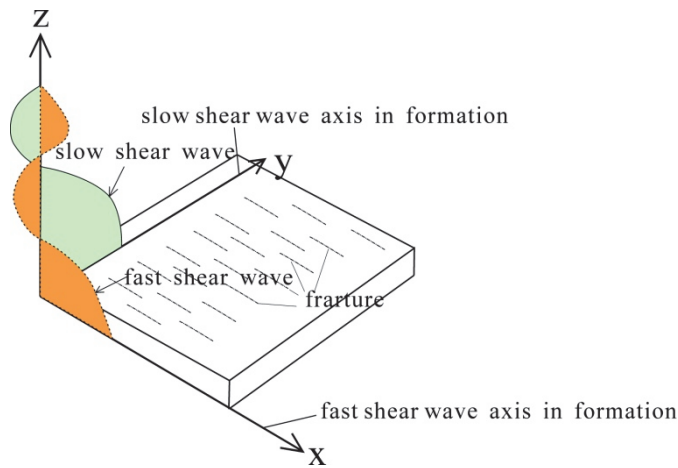


Fig. 1 The S-wave splitting in anisotropic strata

We use dipole shear sonic imager (DSI) to measure the shear moveout of any direction perpendicular to borehole axis, and to calculate the anisotropy parameters of energy, stepout and time by use of stepout-time coherence technology (STC). STC is the analysis of multi-channel signal correlation in a time domain. The fundamental principle of this analysis is that, at first, we select a reference wave train in a set of array wave train, then use time window to intercept every wave train in turn, suppose time window is recorded as τ on the position of the reference wave train, on the other wave train, moving time window as s, the length of time window as Tw, similarity degree of waveform in time window as F, thus, there is a mathematical relationship for these parameters:

$$F^2(s,\tau)=\frac{\frac{1}{N}\int_0^{T_w}\left\{\sum_{n=1}^{N} r_n\left[t+s(n-1)\Delta z+\tau\right]\right\}^2 dt}{\sum_{n=1}^{N}\int_0^{T_w}\left\{r_n\left[t+s(n-1)\Delta z+\tau\right]\right\}^2 dt} \tag{1}$$

In the equation: F is correlation coefficient, $0\leqslant F\leqslant 1$; s is time window slowness (μs/m); τ is the location of time window in the first wave train(μs); N is the number of receiving probes; Δz is spacing between probes; Tw is window length(μs); rn is discrete value of wave signal(μs); t is time(us).

If F=0, there is no correlation between the waveforms. If F=1, the waveforms are the same. In general, 0<F<1.

The anisotropy values of S-wave can be directly calculated by using the array acoustic logging data. This calculated is based on the fact that the travel direction of fast S-wave is the same as the maximum stress and the amplitude of S-wave anisotropy is proportional to the stress. Determination of the maximum horizontal stress using array acoustic logging required an assumption that S-wave anisotropy in the strata results from uneven stresses. However, this is not always this case. S-wave anisotropy can be caused by many other features in formation rocks. As compared to anisotropy from other reasons, the anisotropy that caused by uneven stresses is characterized by great change of S-wave velocity at the borehole walls and about 15% speed difference between fast and slow S-wave[11].

2.2. *Calculate the Magnitude of Geostress*

(1) Calculate the physical parameters of the rocks

$$E = \frac{\rho_b \left(3\Delta t_s^2 - 4\Delta t_p^2\right)}{\Delta t_s^2 \left(\Delta t_s^2 - \Delta t_p^2\right)} \times \eta \tag{2}$$

$$\mu = \frac{0.5\Delta t_s^2 - \Delta t_p^2}{\Delta t_s^2 - \Delta t_p^2} \tag{3}$$

In the equation: ρb is the formation bulk density; Δ ts is the shear wave offset time in formation; Δ tp is the primary wave offset time in formation.

Where: if ρb in g/cm3, Δ t in s/m and E in psi, the value of η is 1.34× 1010; if ρb in g/cm3, Δ t in s/m and E in MPa, the value of η is 9.29× 107.

(2) Calculate the magnitude of geostress

$$\sigma_v = P_o = g \times \int_0^H \rho_b(h)dh \tag{4}$$

$$\sigma_h = \frac{\mu}{1-\mu}(\sigma_v - \alpha P_p) + P_p \tag{5}$$

$$\sigma_H = \lambda \sigma_h \tag{6}$$

$$\lambda = \frac{\sigma_H}{\sigma_h} = 1 + k\left[1 - \left(\frac{D_{\min}}{D_{\max}}\right)^2\right]\frac{E}{E_{ma}} \tag{7}$$

In the equation: μ is the poisson's ratio of the formation; Pp is the pore fluid pressure in formation; α is Boit coefficient or effective stress concentration coefficient ($0 \leqslant \alpha \leqslant 1$); λ is stress non-equilibrium coefficient; k is calibration factor ($1 \leqslant k \leqslant 3$).

3. Evaluate Geostress State by S-Wave Anisotropy

The main oil-producing interval in Nanpu sag is characterized by strong anisotropism, resulting in the low production of a single well. In order to improve oil-field development efficiency, acid fracturing is an effective method to reform reservoir and an important stimulating method to improve the production of oil (gas) well. Thus, the evaluation of regional geostress would be particularly important.

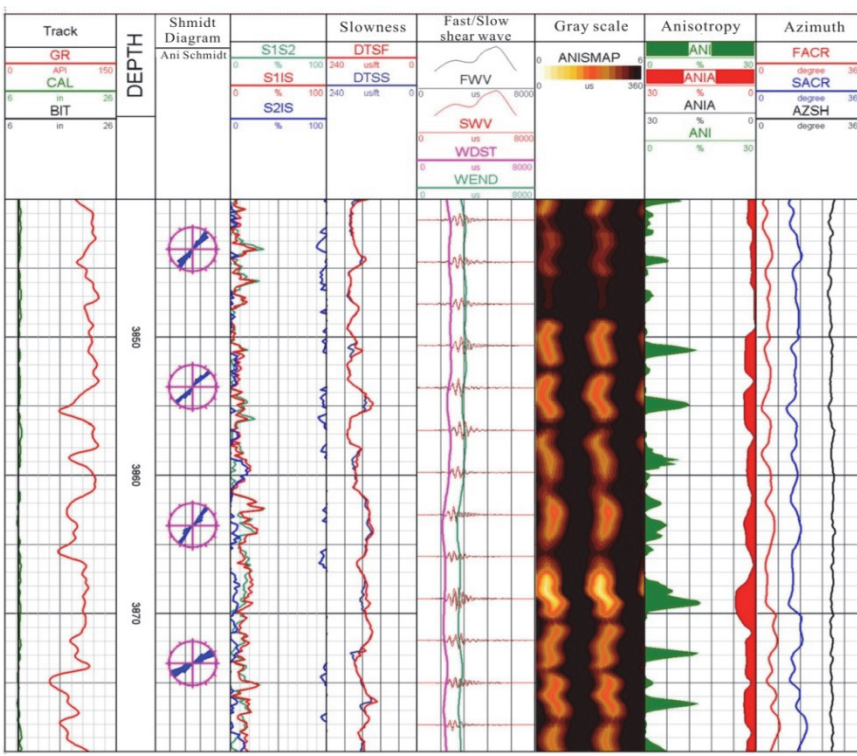


Fig. 2 The anisotropy of S-wave picked from cross-dipole acoustic logging data in well A of Nanpu sag

There are relatively abundant array acoustic logging data in Nanpu sag. These data provide an important basis for regional stress evaluation. Core data indicate poor fracture development in the studied strata of the area. Together with array acoustic logging imaging, geologists believe that the anisotropy in the studied strata is caused by uneven stress. The direction of the maximum horizontal stress in Nanpu sag is NE to NNE. This direction is generally consistent with the regional principal stress in the region. Fig. 2 shows the results of calculated maximum horizontal stress in the third section of Shahejie Formation in Nanpu sag by using the method of array acoustic logging above. These results show that the direction of the maximum horizontal stress in this well is mainly from NE 30 to NE 80, and the value of this stress range from 64.7 MPa to 78.3 MPa, with an average value of 70.4MPa. Our inferred direction of the maximum horizontal stress is nearly the same as the strike of induced joint from the analysis of the imaging logging (Fig. 3, 4). Moreover, according to the analysis of rock acoustic emission experiment, the value of the maximum horizontal stress is between 55.2 MPa to 81.4 MPa, with an mean value of 68.3MPa, which is close to our calculated value. These comparisons indicate that using array acoustic logging data to determine the maximum horizontal stress (both the direction and the magnitude) is reliable.

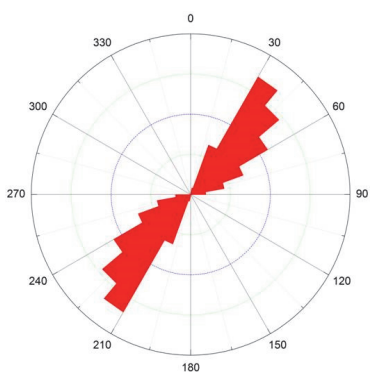


Fig. 3 The rose diagram for anisotropy evaluation in X well

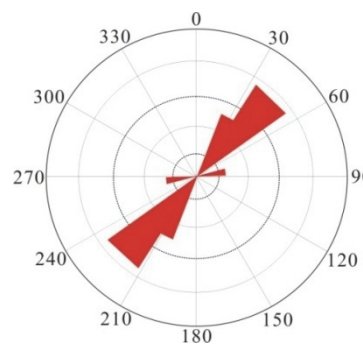


Fig. 4 The rose diagram for strike of induced joint in X imaging logging

4. Conclusion

(1) In anisotropic strata, S-wave splitting phenomenon will occur and form fast S-wave and slow S-wave. The S-wave splitting phenomenon in formation is the basis on which stratum horizontal stress is evaluated by array acoustic logging. The S-wave splitting phenomenon can happen in fissured formation, tectonic

stress unbalanced formation and high angle stratum. The premise which strata horizontal stress is evaluated by use of cross-dipole acoustic logging must be that the shear-wave anisotropy is caused by uneven stresses in formation.

(2) According to the cross-dipole acoustic logging analysis, in horizontal plane, the orientation of larger horizontal principal stress of Nanpu sag is about the NE and NNE, which has the basically same direction with regional stress. The regional maximum principal stress direction are mainly distributed in between NE 30 to NE 80 based on the array acoustic logging judgment, the value of larger horizontal principal stress is between 64.7 to 78.3 MPa, and the average is 70.4MPa. The evaluation result by use of cross-dipole acoustic logging is credible comparing to imaging logging and rock acoustic emission experiment.

References

1. Chen Qingxuan, Wang Weixiang, Sun Ye et al. Rock mechanics and tectonic stress field analysis[M]. Beijing: *Geological Publishing House* (in Chinese), 1998.
2. Zhang Jinghe, Application of geostress and fracture testing technology in petroleum exploration and development[M]. Beijing: *Petroleum Industry Press (in Chinese)*, 2001: 121-128.
3. Li Zhiming, Zhang Jinzhu. Geostress and petroleum exploration and development[M]. Beijing: *Petroleum Industry Press (in Chinese)*, 1997.
4. Yang Liangjie, Wang Ximao, Cui Zhandong, et al. Current and comprehensive regulation measures of casing damage in Jidong oilfield[J]. *Oil drilling & production technology (in Chinese)*, 2003, 25(2): 79-81.
5. Gu Jiayu, Zhang Guangya, Li Xiaodi, et al. Theory technology and petroleum exploration breakthrough—taking the Tarim basin, northwest China as an exemple[J]. *Acta Petrolei Sinica (in Chinese)*, 2002, 23(1): 6-10.
6. Zhao Jun, Qin Weiqiang, Zhang Li, et al. Anisotropy of dipole shear wave and its appl ication to ground stress evaluation[J]. *Acta Petrolei Sinica (in Chinese)*, 2005, 26(4): 54-57.
7. Shen Jianguo. Basic of applied acoustics -real axis integration and the two-dimensional spectrum technology[M]. Tianjin: *Tianjin University Press (in Chinese)*, 2004
8. Zhu Liufang, Shen Jianguo. The method processing the slowness of P- and S-wave from waveforms of array sonic logging[J]. *Well Logging Technology (in Chinese)*, 2004, 28(5): 373-377.

9. Dong Jingli. Processing of multipole array acoustic log data and its application[J]. *Well Logging Technology (in Chinese)*, 2009, 33(2): 115-119.
10. Esmersoy, C·Koster, K·Williams, et al. *Dipole shear anisotropy logging[J]*.Oilfield Review, 1990, 2(4): 9-12.
11. Wang Xiaojie, Peng Shimi,Lv Benxun, et al. Researching earth stress field using cross dipole acoustic logging technology[J]. *Journal of China University of Petroleum (in Chinese)*, 2008, 32(4): 42-48.

Monitoring for Transmission Line Galloping Based on Monocular Vision

Xie Kai*, Lv Zhong-bin, Yang Wei, Shao Ying-biao, Song Gao-li
Equipment status evaluation center, State grid hennan electric power research institute, Zhengzhou, Henan, 450052, China
Email: hetaoyuanhit@163.com

With the development of power grid construction, the frequency and intensity of transmission line galloping increased significantly, and transmission line galloping has become one of the most main factors threaten the security of power grid. Now, the monitoring technique for transmission line galloping is not mature, and has many defects and problems. A new method based on monocular vision technique is proposed in this paper. The results of on-site test have shown that the proposed method is feasible and effective.

Keywords: Transmission Line; Line Galloping; Monocular Vision.

1. Introduction

Galloping, which is low frequency and large amplitude wind-induced vibration of ice-accreted transmission lines, usually occurs in moderately strong and steady wind, and is well recognized as one of the major wind-induced vibrations to cause failure [1, 2]. It is frequently reported that the amplitude of galloping of ice accreted transmission lines could be very large, sometimes in the order of the sag of the line, offering the possibility of short circuiting among different phases. Galloping of ice-accreted transmission lines is a major concern to the power industry.

Galloping is one of the classical problems in overhead transmission lines under certain climatic conditions, and has been studied by many researchers through field observations, wind-tunnel experiments and numerical analyses. In order to develop an effective method of controlling or minimizing galloping, it is indispensable to monitor its characteristics such as galloping orbit, frequency, amplitude and mode of vibration [3]. But because of the complexity of the galloping, there are no more successful conductor galloping monitoring system which can be used to verify the mechanism and anti-galloping results [4, 5].

The traditional way of the power transmission line patrol requires the worker to detect equipments on the site regularly. That not only consumes a lot of manpower and material resources, but also can not monitoring incidents timely and brings some unnecessary delays, even will expand the fault coverage[6]. Camera technology is adopted in the monitoring of galloping in practice, by which the qualitative results of galloping on the spot can be gained. Then the judgments and measurement can be made by staffs to prevent the galloping in the light of the photograph at the scene. This technology can not gain the quantitative information of galloping, and then the accurate information is lack, which limits the technology to be spread in engineering practice. The on-line monitoring technology based on wireless network is a hot study on galloping in recent years comparatively, in which all kinds of date including pressure, vibration frequency, ambient information and others on the spot are monitored, by which the galloping can be calculated in the light of the three degrees of freedom mathematical model[7]. Because of imperfect of galloping mechanism and mathematic model as well as the affection of micro-meteorological conditions, there are some limitations in application and promotion of the technology.

In this paper, a new method based on monocular vision technology is proposed for monitoring transmission line galloping. Compared with traditional video technology, the method can get galloping characteristics such as galloping orbit, frequency, amplitude and mode of vibration.

2. Monitoring for Transmission Line Galloping Based on Monocular Vision

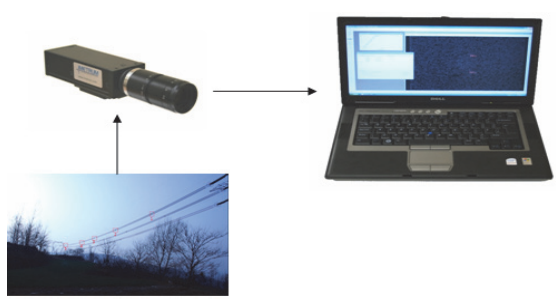


Fig. 1 The structure of whole system

The structure of monitoring system for transmission line galloping based on monocular vision is shown in Fig. 1, and the system includes one camera, the host station, which is a personal computer (PC) equipped with video analysis software. The basic working process principle using the system to monitoring is as follows: The on-site staff chooses a good viewing spot, in which the camera can take the

whole line between the two iron towers. The camera records the galloping video of the transmission. By measuring some space parameters, the background software can calculate the key characteristics of galloping.

2.1. *System calibration*

Because of the difference of the observation point and the camera angle, the corresponding relation between image size and actual size will be different. Therefore, when the observation point and the camera angle are determined, the system needs to be calibrated. According to the basic principle of the pinhole camera model, the relationship between the 2D image coordinates and the 3D world coordinates can be determined.

The vertical displacement calibration coefficient K of any point inside the space is:

$$K = \frac{b \times D}{f} \times \cos\alpha \tag{1}$$

where

K the vertical displacement calibration coefficient of any point inside the space

b the pixel size of CCD

α the elevation angle of CCD

f the focal length of CCD

D the distance of the camera to plane of measurement

$$D = d \times \cos\beta - \frac{f}{1000} \tag{2}$$

where

d the distance of the camera to measured point

β the angle between the measured point and the optical axis of camera

$$\beta = \sqrt{(x - x_0)^2 + (y - y_0)^2} \times \tan^{-1}\frac{b}{f} \tag{3}$$

where

x, y the 2D image coordinates

x_0, y_0 the principal point coordinates of the camera

Through the above three equations, the vertical displacement calibration coefficient K is

$$K = \frac{b \times \left\{ d \times \cos \sqrt{(x - x_0)^2 + (y - y_0)^2} \times \tan^{-1} \frac{b}{f} - \frac{f}{1000} \right\}}{f} \times \cos \alpha \qquad (4)$$

In this equation, only d and$\alpha$is unknown. So, the two parameters need to be measured on-site. Based on the same principal, the horizontal displacement calibration coefficient is calculated.

2.2. *Image processing*

Image processing software consists of feature selection and image matching, etc. Feature selection is to choose the characteristic area on the transmission line, and the diagram is shown in Fig. 2. Image matching is to search the same characteristic area in different frame images, and the diagram is shown in Fig. 3.

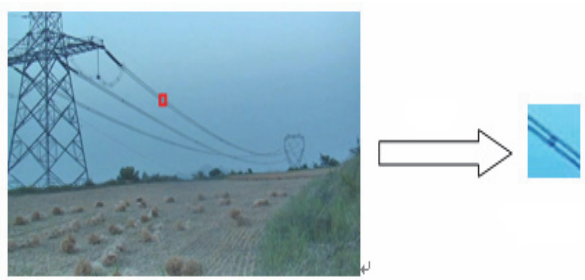


Fig. 2 The diagram of feature selection



Fig. 3 The diagram of image matching

3. On-Line Tests

In order to test the feasibility and effectiveness of the proposed system, the monitoring system for transmission line galloping based on monocular vision is firstly applied at Transmission Line Galloping Prevention Technique Laboratory, State Grid, China.

3.1 *South phase galloping between #3 tower and #4 tower, January 12, 2013*

In the video, spacer selected as feature points, and the galloping trace of the spacer is calculated through calibration and calculation. The spacer distribution diagram is shown in Fig. 4. Through curve fitting, the trace about vertical variation of every spacer can be obtained, which is shown in Fig. 5. From Fig. 5, the galloping mode can be obtained, which is two, and the galloping amplitude of spacer 2 is largest. By date analysis, the largest galloping amplitude of spacer 2 is 4.88m. The vertical variation trace of spacer 2 is shown in Fig. 6, and the galloping frequency is 0.38Hz calculated from the figure.

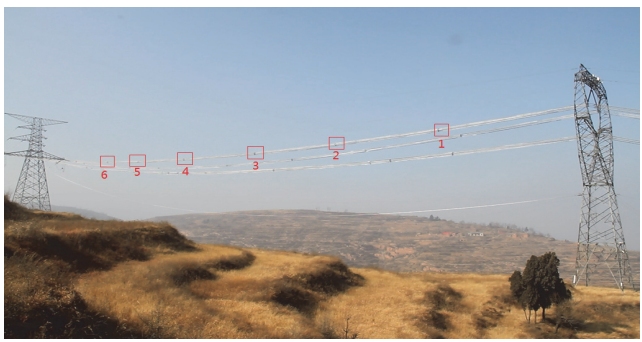


Fig. 4 The diagram of spacer distribution

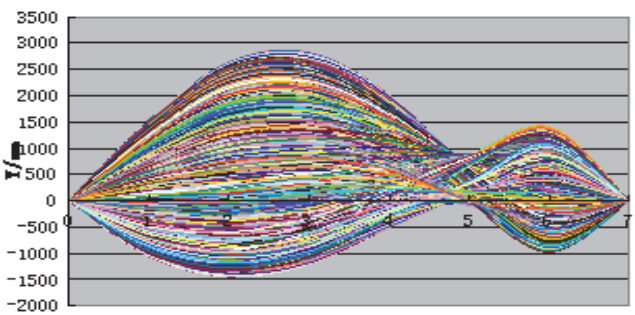


Fig. 5 Galloping trace diagram of transmission line

3.2 *South phase galloping between #2 tower and #3 tower, march 21, 2013*

In the video, spacer selected as feature points, and the galloping trace of the spacer is calculated through calibration and calculation. The spacer distribution diagram is shown in Fig. 7. Through curve fitting, the trace about vertical variation of every spacer can be obtained, which is shown in Fig. 8. From Fig. 8, the galloping mode

can be obtained, which is five, and the galloping amplitude of spacer 4 is largest. By date analysis, the largest galloping amplitude of spacer 4 is 2.82m. The vertical variation trace of spacer 5 is shown in Fig. 9, and the galloping frequency is 0.56Hz calculated from the figure.

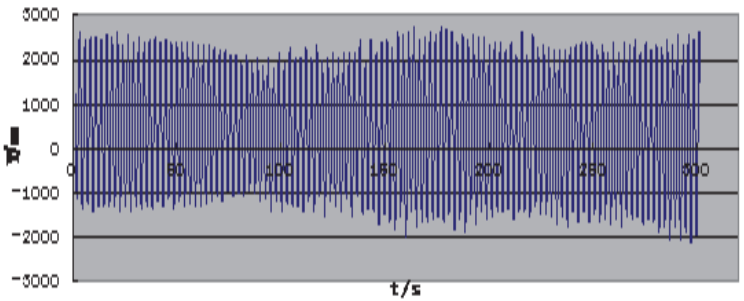


Fig. 6 The vertical variation trace of spacer 2



Fig. 7 The diagram of spacer distribution

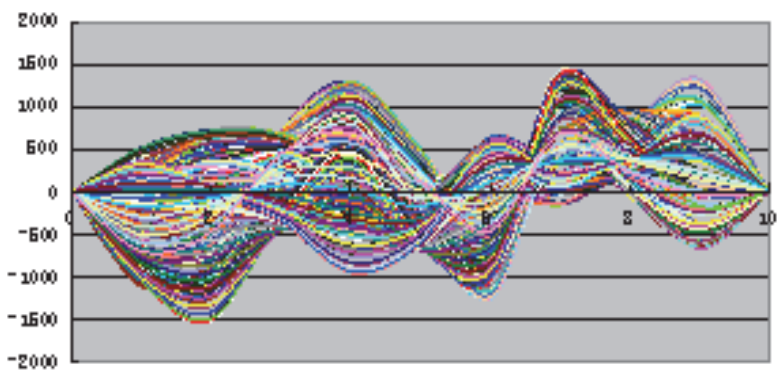


Fig. 8 Galloping trace diagram of transmission line

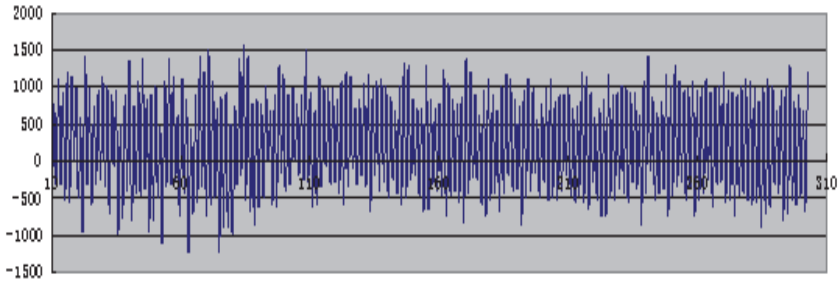


Fig. 9 The vertical variation trace of spacer 4

4. Conclusion

This paper described a new method based on monocular vision for monitoring transmission line galloping, which can execute simply. Compared with other monitoring methods, the system can get galloping characteristics such as galloping orbit, frequency, amplitude and mode of vibration. The results of on-site test have shown that the proposed system is feasible and effective.

References

1. Pasha Ma, How to tame galloping of transmission conductors, *Electric World*, 1989, 203(7), 43-6
2. Wang J, Lilien JL, Overhead electrical transmission line galloping: A full multi-span 3-DOF model, some applications and design recommendations, *IEEE Trans Power Delivery*, 1998, 13(3), 909-16
3. C.B. Gurung, H. Yamaguchi, T. Yukino, Identification of large amplitude wind-induced vibration of ice-accreted transmission lines based on field observed dada, *Engineering Structures*, 24(2002)179-188
4. Lu Mingliang, The study on monitoring technique of transmission line's galloping, *Electric power*, 1994(6), 39-43
5. Xinbo Huang, Guanbo Huang, Yun Zhang, Designation of an on-line monitoring system of transmission line's galloping, ICEMI2009, (1)655-659
6. Rawlins CB, Analysis of conductor galloping field observations-single conductors, *IEEE Trans Power Apparatus System*, 1981, 100(8), 80-9
7. Wang Feng, He Wei, Hu Zewei, Wen jun, Lin Wei, The high voltage overhead power transmission lines galloping monitoring system, *Measurement & Detecting Technics*, 2010, 32(1), 66-68

Energy Flow Modeling and Analysis of Electrical Hydraulic Power Steering System for Electric Bus

Zhulong Jiang, Guobiao Shi
Beijing Institute of Technology
E-mail: jiangzl_bit@163.com; sgb@bit.edu.cn

With the development of electronic control technology, electrical hydraulic power steering system (EHPS) on electric bus has been widely used, but there is a large energy loss in EHPS system. In order to improve energy efficiency of EHPS system, this paper established a control model of EHPS system on electric bus, analyzed the energy flow and major power loss, and proposed ways to reduce energy consumption. Finally, real vehicle tests prove the feasibility of energy-saving methods. The results for development of energy-saving EHPS system on electric bus have certain significance.

Keywords: Electric Bus; EHPS System; Energy Flow.

1. Introduction

With the application of the power steering system in car, how to improve the performance of the power steering system and reduce the power consumption has become a matter of growing concern. In recent years, thanks to the development of electronic control technology, electrical hydraulic power steering system (EHPS) on electric bus has been extensively studied [1] [2]. However, research shows that there is a large energy loss in EHPS system. The loss will not only increase heat, reduce the service life, but also increase noise and exhaust emissions [3]. Foreign scholars have carried out some useful exploration in reducing EHPS system energy consumption [4] [5], but domestic scholars focus on control theory, relatively few on reducing energy consumption [6] [7] [8] [9]. This paper established a control model of EHPS system on electric bus, analyzed the energy flow and major power loss, and proposed ways to reduce energy consumption. Finally, the real vehicle tests determine the sensitivity of the main performance parameters for EHPS system energy consumption. The conclusions provide a theoretical basis for the installation of new energy-saving EHPS system on electric bus.

2. Construction and Principle of EHPS System

The EHPS system with lower energy consumption studied in this paper is provided by an electric pump which is driven by a motor, rather than the traditional EHPS system powered by an engine. Fig. 1 shows the construction and principle of EHPS system.

This EHPS system includes mechanical part, hydraulic part and electrical part. mechanical part mainly includes recirculation ball steering gear and rod; hydraulic part mainly includes control valve, steering cylinder, pressure limiting valve, hydraulic pump, storage tank and tubing; electrical part mainly includes brushless DC motor, sensors(include vehicle speed sensor, angle sensor) and electronic control unit(ECU) [10]. The electric pump including storage tank, hydraulic pump, pressure limiting valve, brushless DC motor and ECU will make the construction more compact and portable, and the installation flexibility much greater [11].

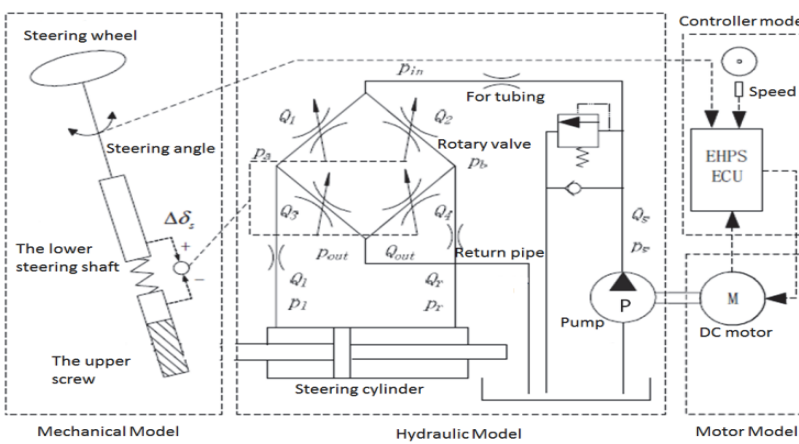


Fig. 1 Construction and principle of EHPS system

According to vehicle speed and steering wheel, ECU changes the steering pump flow by controlling the drive motor speed, achieving that low-speed, high traffic, steering lightweight; high-speed, low traffic, improving road feel and reducing energy consumption.

3. Establish EHPS System Model

The force caused by the steering wheel is equivalent to the force on the nut screw, EHPS system can be divided into four parts: mechanical steering, hydraulic system, motor and controller. Therefore, in order to facilitate research,

mechanical steering model, hydraulic system model, motor model, controller model is established.

3.1. *Mechanical steering model*

For recirculating ball steering gear, the study ignores the gaps and friction. Fig. 2 shows the movement of screw, nut and tooth fan.

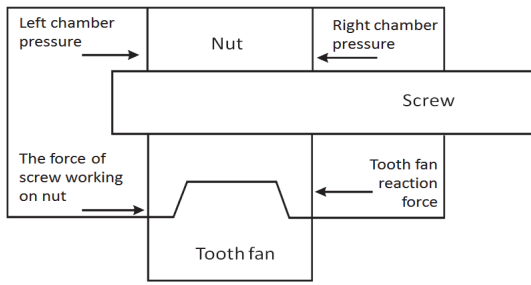


Fig. 2 The movement of screw, nut and tooth fan

According to Newton's second law, the balance equation of nut force:

$$M\ddot{x} = F_L - F_R + F_{sita} - F_{zhu} - C_r\dot{x}$$

Where M = the mass of nut and solid even parts; x = nut displacement; F_L = left chamber pressure; F_R = right chamber pressure; F_{sita} = the force on the nut screw; F_{zhu} = the force of tooth fan acting on the nut; C_r = damping piston.

The driving relationship of nut displacement and steering wheel angle:

$$x = S\theta_w / 2\pi$$

Where S = screw lead; θ_w =steering wheel angle.

Left and right cylinder chamber pressure booster formula:

$$F_L = p_L A; \quad F_R = p_R A$$

Where p_L = left chamber pressure; p_R = right chamber pressure; A = the effective area of piston.

3.2. *Hydraulic system model*

3.2.1 *Steering valve model*

Fig. 3 shows the steering valve equivalent model. In the bridge model, the steering model includes four variable orifices. Steering torque causes the

deformation of the torsion bar, the angle difference of steering valve is formed, the two valve port will open, while the other two will close. The actual steering valve includes a plurality of valve ports, each valve port comprises four parallel valve ports.

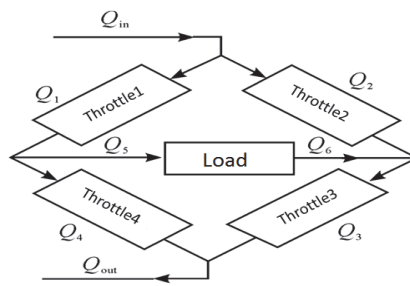


Fig. 3 Steering valve equivalent model

$$\begin{aligned} Q_{in} &= Q_1 + Q_2 \\ Q_L &= Q_1 - Q_4 \\ Q_R &= Q_2 - Q_3 \\ Q_{out} &= Q_3 + Q_4 \end{aligned} \qquad \begin{aligned} Q_1 &= C_d A_1 \sqrt{2(p_{in} - p_L)/\rho} \\ Q_2 &= C_d A_2 \sqrt{2(p_{in} - p_R)/\rho} \\ Q_3 &= C_d A_3 \sqrt{2(p_R - p_{out})/\rho} \\ Q_4 &= C_d A_4 \sqrt{2(p_L - p_{out})/\rho} \end{aligned}$$

Where Q_{in}, Q_{out} = the rotary valve oil flow; $Q_{i(1,2,3,4,)}$ = the flow through the throttle valve i; Q_L, Q_R = the flow of booster cylinder left and right chambers; $A_{i(1,2,3,4)}$ = the area of throttle valve i; C_d = flow coefficient; ρ = hydraulic oil density; p_{in}, p_{out} = the pressure of steering valve.

3.2.2 *Pump model*

Pump is a very important part of EHPS system, pump' steering speed determines the oil pressure of hydraulic inlet tubing, determines the size of the assist force.

Pump flow equation:

$$Q_P = qN - K_3 p_P$$

Where Q_P = pump oil flow; q = pump displacement; N = pump steering speed (motor steering speed); K_3 = pump drain coefficient; p_P = the output pressure of hydraulic pump.

Hydraulic pump formula:

$$p_P = 2\pi T K_4 / q$$

Where T = pump output torque (motor output torque); K_4 = pump torque coefficient.

Pump homeostasis formula:

$$Q_P - Q_{in} = \frac{V_P}{K_5} \cdot \frac{d_{p_P}}{d_t}$$

Where V_P = pump volume; K_5 = pump volume coefficient.

3.3. *Motor model*

This system uses brushless DC motor, this motor is a PMSM, which has no excitation loss, small thermal resistance, no radio interference, long life, reliable operation, easy maintenance.

$$N = \left[U_s - (R_C + R_M) I_M \right] / K_1$$

Where U_s = supply voltage; R_C = the resistance between the supply voltage and the motor; R_M = motor resistance; I_M = motor electric current; K_1 = motor speed coefficient.

$$T = K_2 I_M$$

Where K_2 = motor torque coefficient.

Increasing supply voltage is available to a larger motor torque and motor speed stability.

3.4. *Controller model*

ECU is the control core of the entire steering system, signal acquisition system provides data signals to ECU through a series of sensors, after logical analysis and calculation, ECU controls the motor speed by sending control signals to executive body through drive circuit. Actually, ECU is a discrete-time sampling control system, when the sampling period is much shorter than the time constant of the continuous part, the control system can be approximated as a continuous-time system. Control system should have strong anti-jamming capability (robustness) to adept the changeable driving environment. Control algorithm should be fast and accurate for real-time control requirement, and can effectively help to achieve the desired patterns and characteristics [12].

4. Analysis of EHPS System Energy Flow

Energy input of EHPS system is divided into electric energy input by pump and mechanical energy input by driver, the final energy output of EHPS system is represented by the output of boost power. Fig. 4 shows the energy flow of EHPS system.

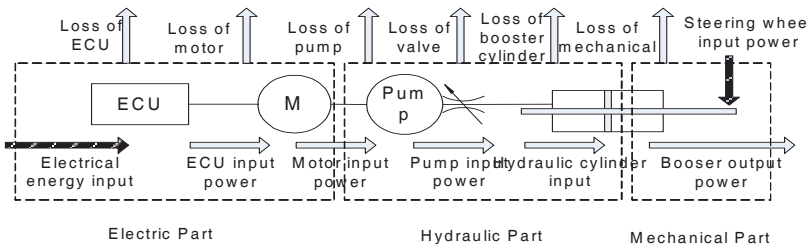


Fig. 4 EHPS system energy flow

In the non-steering condition, system does not need help, boost power output is 0, EHPS system stays in standby mode. At this time, motor speed is very low, all of the input power becomes useless power dissipating in the ECU, brushless DC motor and hydraulic system.

In the steering condition, the output boost power is from the power of hydraulic system and input torque power of driver. The power supply send the energy to motor through the ECU, output power of the motor is delivered to hydraulic system, finally, the combination of the output power of hydraulic system and the input power of driver is the output boost power of EHPS system. Fig. 4 shows that the energy consumption of EHPS system mainly includes mechanical energy consumption, transfer valve energy consumption, pump energy consumption, motor energy consumption, controller energy consumption, this paper analyzes five energy consumption above and proposes methods to reduce the energy consumption.

4.1. *Analysis of mechanical energy consumption*

Mechanical energy consumption is almost caused by the vice screw nut drive of recirculating ball steering gear, vice fan drive gear nut, vice piston drive of power cylinder and friction of tie rod ends, reducing the friction of system can be helpful for reducing the mechanical energy consumption effectively. However, smaller friction of steering system is not possible, if the friction is too small, system can not obstruct the tiny vibrations from ground to steering wheel, it will increase the burden on the driver. Therefore, the friction should be determined by the driver' s subjective judgment.

Efficiency of mechanical transmission can be used to indicate the friction energy consumption of mechanical part:

$$P_{ms} = P_a \eta_m$$

Where P_{ms} = mechanical power consumption; P_a = total power consumption of steering system.

4.2. *Analysis of hydraulic energy consumption*

The establishment of hydraulic system model based on the following assumptions: ignoring liquid compression factor and inertia; consistent characteristic of the rotary valve outlet and inlet; uniform flow distribution valve circuit; pump leakage and system pressure is proportional; the torque loss of pump and motor is considered in motor model; unified consideration of inlet and outlet oil pressure. Fig. 5 shows the hydraulic system model.

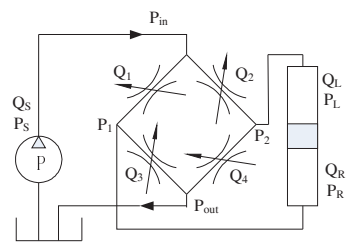


Fig. 5 hydraulic part schematic of EHPS system

4.2.1. *Analysis of valve power*

Study the rotary valve, each valve port's pressure:

$$\Delta p_i = \frac{\rho Q_i^2}{2C_d^2 A_i^2}$$

The power loss of the rotary valve:

$$P_{V-loss} = \sum_{i=1}^{4} Q_i \Delta p_i = \sum_{i=1}^{4} \frac{\rho Q_i^3}{2C_d^2 A_i^2}$$

The formula above shows that the power loss of rotary valve is mainly caused by the differential pressure of valve port, however the valve has to produce enough differential pressure to get enough pressure, increasing valve port area and reducing traffic are helpful to reducing energy consumption at the condition of enough steering assistant pressure.

4.2.2. *Analysis of pump power*

The torque of pump:

$$T = \frac{p_P q}{2\pi K_4}$$

The input power to pump:

$$P_{P-in} = T\omega_P = qNp_P / K_4$$

Where ω_P = the angular velocity of pump.

The output power of pump:

$$P_{P-out} = Q_P p_P = qNp_P - K_3 p_P^2$$

The power loss of pump:

$$P_{P-loss} = P_{P-in} - P_{P-out} = qNp_P / K_4 - qNp_P + K_3 p_P^2$$

The formula above shows that the power loss of pump is mainly caused by the pump drain, reducing the pump drain can be helpful to reduce the energy consumption of pump. Therefore, installation control valve on pump will eliminate the need for pipeline between pump and rotary valve, reduce cost and drain, decrease pipeline oil pressure. And, reducing the mechanical friction will decrease the energy consumption. So, the pump gear should be double arc sine curve tooth, in meshing process, there is no sliding and wear between tooth profile surfaces. Pump will work smoothly with no trapped fluid phenomena, low noise, long life and high efficiency.

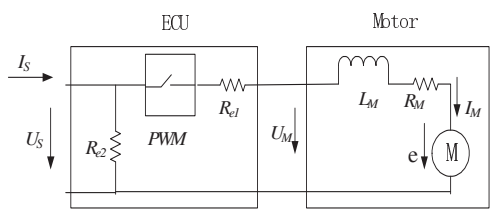


Fig. 6 electric part schematic of EHPS system

4.3. *Analysis of electrical energy consumption*

The electric part of EHPS system is mainly composed by the motor and the controller, the energy consumption is caused by the two parts. Fig. 6 shows the electric part model.

Where I_s = supply current; R_{e1} = power switch resistance; R_{e2} = equivalent total resistance; U_M = motor drop; L_M = motor armature inductance; e = motor EMF.

Input power of motor:

$$P_{M-in} = U_M I_M$$

Power loss of motor:

$$P_{ME-loss} = I_M^2 R_M$$

Friction torque power loss of motor:

$$P_{MM-loss} = B_M \omega_M^2$$

Where B_M = motor viscous friction coefficient; ω_M = motor angular velocity.

Total power loss of motor:

$$P_{M-loss} = P_{ME-loss} + P_{MM-loss} = I_M^2 R_M + B_M \omega_M^2$$

The formula above shows that the power loss of motor is related to armature current, armature voltage, motor speed and viscous friction coefficient. Changing these parameters will reduce the power loss of motor. The assistant power of steering system is determined by the current driving condition. However, torque is determined by armature current, the motor speed (pump oil) is determined by the voltage. Therefore, the supply voltage, armature current and motor drop can not be changed. Through the analysis above, the methods to decrease the power loss of motor are decreasing the armature resistance and viscous friction coefficient, choosing efficient motor.

4.4. *Analysis of controller power*

Voltage regulation of motor can change the motor speed, voltage regulation is controlled by the PWM of the ECU. PWM system is mainly composed by the power switch, the energy loss of the power switch is the main part of controller's energy loss.

Input power of the controller:

$$P_{ECU-in} = U_s I_s$$

Power loss of the power switch:

$$P_{R_{e1-loss}} = I_s^2 R_{e1}$$

Power loss of equivalent total resistance:

$$P_{R_{e2-loss}} = \frac{U_s^2}{R_{e2}}$$

Total power loss of the controller:

$$P_{ECU-loss} = P_{R_{e1-loss}} + P_{R_{e2-loss}} = I_s^2 R_{e1} + \frac{U_s^2}{R_{e2}}$$

The formula above shows that the method to reduce the energy consumption of the controller is to decrease the resistance of the power switch and increase the equivalent total resistance.

5. Conclusion

According to the energy flow, this paper established the models of mechanical steering, rotary valve, pump, motor and controller combining with the characteristic of electric bus EHPS system. The research results shows the most power loss is caused by the rotary valve, and decreasing the valve port area is quite helpful to reduce the energy consumption of the rotary valve. Meanwhile, choosing efficient motor and advanced pump, designing excellent controller has a pronounced effect on reducing the energy consumption of system. This paper provides a theoretical basis to reduce the energy consumption of electric bus EHPS system.

Acknowledgement

This work was financially supported by the National High Technology Research and Development Program of China (863 Program): Research and Development of Electric Power Steering System for Electric Vehicle (Project Number 2011AA11A244).

References

1. Guoyu DAI. "*Overall Design of KLQ6129GQEV2 Pure Electric Bus*," Bus & Coach Technology and Research, No.6, pp.21-23, 2012.
2. Benxiang XU. "*Design of NPS6100SHEV Extended Range Electric Bus*," Bus & Coach Technology and Research, No.6, pp.14-16, 24, 2011.

3. Ranyi LI, Long QUAN. "*Analyzing and comparing energy-dissipat –ing character of hydraulic power steering system*," Journal of Engineering Design, vol.9, No.3, pp.131-135, 2002.
4. Inaguma, Y., Suzuki, K., and Haga, K., "*An Energy Saving Technique in an Electro-Hydraulic Power Steering (EHPS) System*," SAE Technical Paper 960934, 1996, doi: 10. 4271/960934.
5. Bootz, A., Brander, M., Stoffel, B., "*Efficiency Analyses of hydraulic power steering system*," The Eighth Scandinavian International Conference on Fluid Power. Tampere Finland, 2003.
6. Peiji SHI, Guobiao SHI, Yi LIN, Wanzhong ZHAO. "*Modeling and Characteristics of Hydraulic Lines of EHPS*," Transaction of the Chinese Society for Agricultural Machinery, No.10, pp.174-177, 2008.
7. Feng GAO, Yahui LIU, Xuewu JI, Xiaolin GUO. "*Primary calculation of electronically controlled hydraulic power steering*," Journal of Beijing University of Aeronautics and Astronautics, No.5, pp.605-607, 2007.
8. Yong HUANG, Quanshi CHEN, Bin QIU, Fuhu CHEN. "*Control of Electro-hydraulic Power Steering System in Electric Vehicle*," Journal of Highway and Transportation Research and Development, No.10, pp.147-150, 2005.
9. Hao WANG, Runtao DING, Zhijie LI, Yan ZHOU, Yan JIAO. "*Simulation of Electro-hydraulic Power Steering System*," Journal of Tianjin University, No.5, pp.627-630, 2008.
10. Zhongming ZHU. Analysis and Controller Design of Electro-hydraulic Power Steering System[D]. Zhenjiang: Jiangsu University, 2009.
11. Yi LIN, Guobiao SHI. "*Development Status and Tendency of Electric Power Steering*," Journal of Highway and Transportation Research and Development, No.2, pp.79-82, 2001.
12. Junjun ZHANG. Design and Research of Electro-hydraulic Power Steering System[D]. Zhenjiang: Jiangsu University, 2009.

Experimental Research on Coal Water Slurries Prepared by Single and Blended Coals

Yaxuan Hu, Jianzhong Liu*, Jiaoyan Lin, Junhu Zhou, Kefa Cen

State Key Laboratory of Clean Energy Utilization, Zhejiang University, Hangzhou, Zhejiang, China
*E-mail: *jzliu@zju.edu.cn*

As coal water slurries (CWSs) are mostly prepared by blended coals in practical application, studying the preparation characteristics of blended coal water slurry (BCWS) has realistic significance. Four coals of different rank, including Wucaiwan coal (WCW), Huangling coal (HL), Guizhou coal (GZ), and Tianchi coal (TC), were chosen to prepare CWSs. Results showed that the slurryability of these four coals was significantly different. The slurry concentration was only 52.4% for WCW, while it was up to 68.2% for TC. With increasing coal rank and decreasing moisture and oxygen content, the slurry concentration increased. Four coals were blended with each other to prepare BCWSs, and the slurryability of the BCWSs was studied. Different blending pattern showed different slurryability. Blending WCW into HL decreased the slurry concentration of HL, whereas blending TC into HL increased the slurry concentration of HL. Research on the stability of CWS indicated that, the stability of CWS made of coal with lower Zeta potential was better. Coal blending also had effects on the stability of CWS, and a rational blending method can improve the stability.

Keywords: Coal Water Slurry; Coal Blending; Slurryability; Stability.

1. Introduction

Coal water slurry (CWS) is widely applied in boiler combustion as a fuel to substitute for petroleum [1]. As a kind of clean and efficient way of coal gasification, CWS gasification technology has attracted a wide attention [2]. Rheological properties are important properties of CWS and the viscosity is desired to be as low as possible [3]. Transportation by pipelines plays an important role in application of CWS, and the viscosity of CWS directly affects the resistance of the pipeline [4-6].

In the industrial application, it is desirable that the CWS has high solid concentration and low viscosity. Generally, the viscosity of CWS is expected to be 1000mPa·s [7]. CWS is a kind of complex non-Newtonian fluid [8], and its viscosity is affected by many factors. Researches show that, the viscosity of CWS depends on coal category (mainly coal rank), moisture, oxygen content,

additive, and so on. Mishra et al. [9] found that higher ash content increased the hydrophilicity of coal, and then decreased the free water of CWS. Less free water increased the viscosity of CWS. Chen Jun et al. [10] reported that with increasing pore fractal dimension, specific surface area and pore volume of the coal, the slurry viscosity increased and solid concentration of CWS decreased. In addition, the slurryability of coal got worse with increasing moisture and oxygen content and decreasing Hardgrove Grindability Index (HGI). Moreover, the coal properties including particle size, particle surface potential, fusinite content, and SiO_2 content in coal ash, also affected the viscosity of CWS [7, 11, 12]. Additives used in the preparing process of CWS also had effects on the properties of CWS [13, 14]. As a kind of solid-liquid two phase suspension, CWS belongs to unstable thermodynamic so that it leads to solid-liquid separation related to the stability, and CWS with poor stability is unable to meet the requirement of pumping and spraying in application [15].

Most of the existing researches focus on the slurry properties of CWS made of single coal, but CWS used in actual application is mostly prepared by blended coals at present. Preliminary researches indicate that blending coals is a simple and economic method to improve slurry ability of coals, especially for the coals with poor slurry ability, and thus expand coal adaptability to preparing CWS which meets requirement in industrial application [16, 17]. In this paper, four coals were chosen to blend with each other at different ratios, and the blended coals were used to prepare BCWSs. The slurryability and stability of BCWSs were studied, and at the same time, the slurrying influence factors and mechanism were analyzed.

2. Experimental

2.1. *Materials*

Four different coals, including Wucaiwan coal (WCW), Huangling coal (HL), Guizhou coal (GZ), Tianchi coal (TC), were selected to prepare CWS. These coals have different ranks. WCW is collected from open-pit mine of ZhunDong coalfield in XinJiang, and it has the lowest rank in the four coals. HL from ShanXi is bituminous coal. GZ and TC are two kinds of anthracitic coal. Table 1 shows the proximate analysis and ultimate analysis results of these coals.

The particle size of four coals was measured by Mastersizer 2000 and result was shown as Fig. 1. The volume average particle diameter of these four coal, i.e., WCW, HL, GZ and TC, was 23.844μm, 25.550μm, 30.880μm and 17.241μm respectively.

Table 1. Proximate Analysis and Ultimate Analysis of Coals

Sample	Proximate analysis [%]				Ultimate analysis [%]				
	Mad	Aad	Vad	FCad	Cad	Had	Nad	St,ad	Oad
WCW	8.35	7.70	28.59	55.36	64.01	3.34	0.50	0.23	15.87
HL	3.48	29.57	23.02	43.93	54.88	3.53	0.85	0.47	7.22
GZ	2.78	21.59	8.15	67.48	76.89	2.52	0.92	1.79	3.51
TC	1.38	28.74	9.34	60.54	70.64	3.02	1.09	0.98	4.15

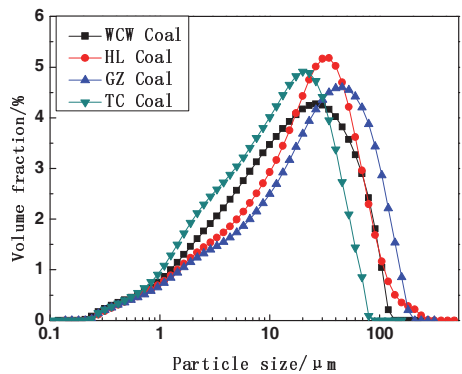


Fig. 1. Particle Size of Four Coals

2.2. *Preparation of CWS*

Copolymer of methylene naphthalene, sulfonate styrene, and sulfonate maleate (NDF) was used as the additive of CWS. Additive was added into coal powders at the weight ratio of 0.8:100 (additive: coal), and then deionized water was poured into the mixture of coal powders and additive. The coal water mixture was then stirred for 15 minutes at 800-1000r/min to form uniform suspension.

During preparing BCWS, the mass ratios of 2:8, 4:6, 5:5, 6:4, and 8:2 were selected for coal blending.

2.3. *Viscosity of CWS*

The viscosity of CWS was tested by HAAKE VT550 viscometer at (20±0.1) ºC. The shear rate of rotor rose from 0 to 100s-1 steadily while testing. When the shear rate was 100s-1, 10 values of viscosity were recorded subsequently, and the average of these 10 values was taken as the viscosity value at 100s-1 to evaluate the slurryability of the coals.

2.4. *Solid concentration of CWS*

CWS sample of (3.0±0.2) g was weighted, and then dried to constant weight at 105ºC ~ 110ºC in a dry oven. The mass ratio of dried sample to original sample was taken as the solid concentration of CWS.

2.5. *Stability of CWS*

In the paper, the stability was measured by water separation method. The CWS sample was put in a sealed container, and after two weeks, supernatant was generated on the top of CWS. The stability of the slurry samples was assessed basing on the water separation rate (WSR), which was defined as the mass ratio of the supernatant to the total water in the test slurry.

2.6. *Zeta potential*

Dilute suspension of coal powders was prepared, and after standing for some hours, the supernatant was used to determine the Zeta potential on the coal particle surfaces. The Zeta potential was measured by Powereach JS94H micro-electrophoresis meter (ZhongChen Digital Technology Equipment Corporation, ShangHai).

3. Results and Discussion

3.1. *Slurryability of single coals*

Fig. 2 shows the relationship between viscosity and solid concentration for CWS prepared by single coal. The experimental results revealed that the viscosity of CWS increased with increasing the solid concentration. This is because that increasing solid concentration resulted in the number of coal particles increasing and the water in the slurry decreasing. Water played a lubrication role to decrease the frictions between the solid particles. Decreasing water content led to slurry viscosity increasing. The solid concentration of CWS at 1000mPa·s was considered as the solid concentration, and it was calculated by linear interpolation method. The slurry concentration of these four single coals is shown in Table 2. The slurry concentration of WCW was the lowest of all, only 52.4%. The slurry concentration of TC and GZ coal was up to 68.2% and 66.5%, respectively. The results indicated that the slurryability of different coals was significantly different. The slurry concentration of low rank coal was low, and it increased as the coal rank increased.

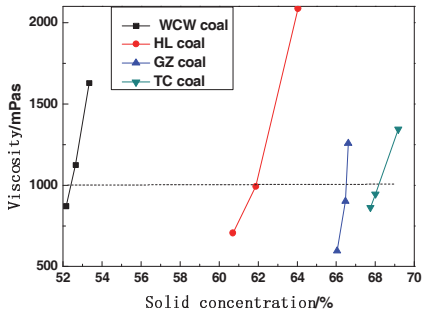


Fig. 2. Relationship Between Viscosity and Solid Concentration of CWS Prepared by Single Coal

Combining with the properties of coals, it was concluded that the slurry concentration decreased as the moisture of coals increased, which was shown as Fig. 3. The coal with higher moisture content had stronger water binding capacity. In the CWS made of this coal, more water was bound on the coal particles and thus the free water which lubricates the solid particles in the slurry decreased. Therefore, the viscosity of CWS increased and the slurry concentration decreased. Moreover, the oxygen content of coal also affected slurry concentration. The slurry concentration decreased as the oxygen content increased. Higher oxygen meant more oxygen-containing functional groups in the coal, which made the coal more hydrophilic, leading to decreasing the slurry concentration [18].

Table 2. Slurry Concentration of Coals

Coal category	WCW	HL	GZWY	TC
Slurry concentration [%]	52.4	61.9	66.5	68.2

3.2. *Slurryability of blended coals*

Fig. 4 shows the slurryability of blended coals, including blending two bituminous coals (WCW and HL), blending two anthracitic coals (GZ and TC), and blending a bituminous coal with an anthracitic coal (HL and TC). The slurry concentration is low for WCW and HL, especially only 52.4% for WCW. When these two coals was blended and prepared slurry, the slurry concentration decreased as the proportion of WCW increased. After blending with TC, the slurry concentration of HL increased, and the slurry concentration was higher when more TC was blended. Blending TC into HL increases the hydrophobicity of coal, which increases the free water of CWS, so the blended coal has higher concentration. However, the slurry concentration of the blended coal was lower than that of TC single coal. The slurry concentration was high for these two

anthracitic coals, GZ and TC. When blending these two coals at different ratios, all the slurry concentration stayed constant approximately between 68.5% and 69%, which is slightly higher than that of the two single coals. Apparently, different blending method had different effect on the slurryability of the coals.

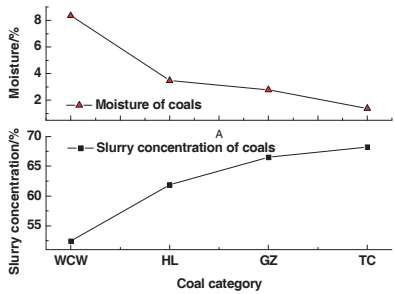


Fig. 3. Relationship Between Slurry Concentration and Moisture of Coals

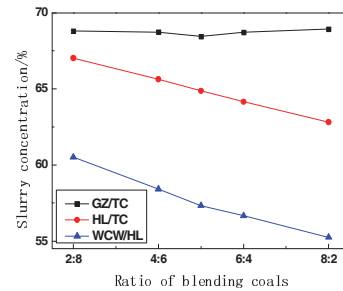


Fig. 4. The Slurry Concentration of Blended Coals

3.3. *Stability*

WSR reflected the stability of CWS, and Lower WSR implied better stability [19].

3.3.1. *Stability of CWS made of single coals*

The relationship between WSR and viscosity of CWS is shown as Fig. 5. To the same CWS, the WSR of CWS with higher viscosity was lower, which indicated that the CWS had better stability. This is because that, the solid particles in CWS constructed a kind of spatial net structure. The structure was stronger when the viscosity of CWS was higher, and the resistance which particles needed to overcome for sedimentation increased, and therefore, the stability of CWS was better. The surface of low rank coal, especially brown coal, exhibited strong hydrophilcity because of hydrophilic groups, i.e., -COOH, -OH. In the CWS, coal particles, water, and additive formed three-dimensional net structure with a certain strength by the dipole of the polar groups and the function of the hydrogen bonding, so the slurry had high viscosity and static stability [20].

At the same viscosity, the WSR of CWS made of different coals was also different. The WSR of CWS at 1000mPa·s was calculated as the fixed-viscosity WSR by using linear interpolation method, which was shown as Table 3. The WSR of WCW coal was the lowest of all, which indicated its stability was the best, and the WSR of TC coal was the highest, which indicated its stability was the worst.

3.3.2. *Stability of BCWS*

Fig. 6 shows the fixed-viscosity WSR of BCWSs. When blending two bituminous coals, WCW and HL, the WSR of the BWCS was between that of the two single coals, and the WSR of the BCWS increased as the proportion of HL increased. This indicated that increasing HL proportion decreased the stability of CWS. Blending GZ and TC presented the similar results. The WSR of CWS made of blended coal of HL and TC was higher than that of the two single coals, and with increasing TC proportion, the WSR of the BCWS increase firstly and then decreased. When the ratio of HL to TC was 4:6, the WSR was highest. This indicated that the stability of BCWS made of blended coal of HL and TC was worse than that of the two single coals and when the ratio was 4:6, the stability was the worst.

3.4. *Relationship between Zeta potential and stability*

Zeta potential was electrokinetic potential in colloidal dispersions, and it was the electric potential in the interfacial double layer at the location of the slipping plane relative to a point in the bulk fluid away from the interface.

The Zeta potential of four coals is shown in Table 3. It is found that when the coal with lower Zeta potential was prepared into CWS, the WSR was lower, and the stability was better. Lower Zeta potential meant the surface charges on the coal were more, and the repulsion between the coal particles was bigger, which made the particles harder to agglomerate and easier to disperse, therefore, the stability of CWS was better.

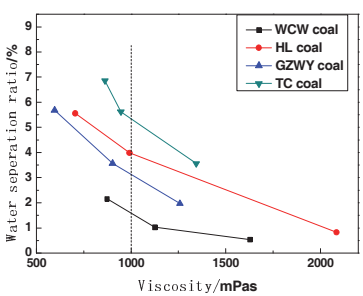


Fig. 5. Relationship Between WSR and Viscosity of CWS Prepared by Single Coals

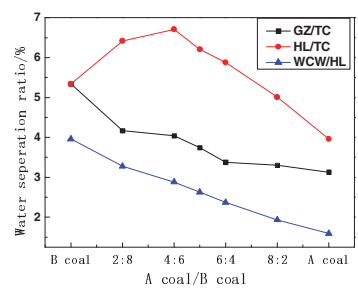


Fig. 6. Fixed-viscosity WSR of The BCWS

Table 3. Fix-viscosity of CWS and Zeta Potential of Different Coals

Coal category	WCW	HL	GZ	TC
Zeta potential [mV]	-76.61	-48.04	-50.85	-45.22
Fixed-viscosity WSR [%]	1.59	3.96	3.13	5.34

4. Conclusion

(1) Because of the effect of the coal quality, the slurryability of different coals was different. Generally, coal with low rank, high moisture and oxygen content was hard to prepare CWS, and the slurry concentration was low. Anthracitic coals were easier to prepare CWS than bituminous coals, and the slurry concentration of low rank coal, such as brown coal, was the lowest.

(2) Different blending method had different effects on the slurryability. The slurry concentration of blending coal of WCW and HL increased with increasing the proportion of HL, but it was still lower than that of HL single coal. After blending anthracitic coal, TC, into HL, the slurry concentration increased, and the slurry concentration was more when more TC was blended. When GZ and TC were blended at different ratio, all the slurry concentration of blended coal stayed constant approximately between 68.5% and 69%, which was slightly higher than that of the two single coals.

(3) The stability of CWS increased with increasing the viscosity. At the same viscosity (1000mPa·s), the stability of different CWS was different. The coal with lower Zeta potential had bigger repulsion which made the particles harder to aggregate, and thus the stability was better.

(4) Different blending method had different effects on the stability. The stability of BCWS made of blended coal of WCW and HL decreased with increasing the HL proportion. After blending HL and TC, the stability of BCWS was worse than that of the two single coals, and when the ratio was 4:6, the stability was the worst.

The effect of blending coals on the CWS preparation was complex, and it was unable to summarize simply into a pattern. However, a rational blending method can effectively improve the fixed-viscosity concentration and stability of CWS.

Acknowledgement

The authors wish to thank the National Basic Research Program of China (Grant No. 2010CB227001) for their financial support.

References

1. Cheng J., Zhou J. H., Li Y.C., et al. Effects of pore fractal structures of ultrafine coal water slurries on rheological behaviors and combustion dynamics, *Fuel*, 87 (2008): 2620-2627.

2. Zhao H., Liu H.F., Xu J.L., et al. Breakup and atomization of a round coal water slurry jet by an annular air jet, C*hemical Engineering Science*, 78 (2012): 63-74.
3. G. Atesok, F.Boylu, A.A. Sirkec, and H. Dincer. The effect of coal properties on the viscosity of coal–water slurries, *Fuel*, 81 (2002): 1855-1858.
4. Liu M., and Duan Y.F.. Resistance properties of coal–water slurry flowing through local piping fittings, *Experimental Thermal and Fluid Science*, 33 (2009): 828-837.
5. Chen L.Y., Duan Y.F., Liu M., et al. Slip flow of coal water slurries in pipelines, *Fuel*, 89 (2010): 1119-1126.
6. Chen L.Y., Duan Y.F., Zhao C.S., et al. Rheological behavior and wall slip of concentrated coal water slurry in pipe flows, C*hemical Engineering and Processing: Process Intensification,* 48 (2009): 1241-1248.
7. F. Boylu, H. Dinçer, and G. Ateşok. Effect of coal particle size distribution, volume fraction and rank on the rheology of coal–water slurries, *Fuel Process Technology*, 85 (2004): 241-250.
8. Zhao H., Liu H.F., Xu J.L., et al. Secondary breakup of coal water slurry drops, *Physics of Fluids*, 23 (2011): 113101.
9. S.K. Mishra, P.K. Senapati, and D. Panda. Rheological Behavior of Coal-Water Slurry, *Energy Sources*, 24 (2002): 159-167.
10. Cheng J., Chen X.G., Liu J.Z., et al. Impacts of pore fractal structures of pluverized coal water slurry properties, *Proceedings of the CSEE*, 28 (2008): 60-64.
11. Li Y.C., Zhou Z.Q., Cheng J., et al. Infuence of the coal's physical chemistry propertyto its slurrying quality, *Coal Conversion*, 32 (2009): 35-39.
12. Yu Chi W., Li B.Q., Li W., et al. Analysis of coal characteristics on the properties of coal water slurry preparetion with different coal ranks, *Journal of Fuel Chemistry and Technology*, 35 (2007): 146-154.
13. Ma S.D., Zhao P., Guo Y., et al. Synthesis, characterization and application of polycarboxylate additive for coal water slurry, *Fuel*, 111 (2013): 648-652.
14. D.F. Umar, H. Usui, Y. Komoda, et al. Effect of dispersing and stabilizing additives on rheological characteristics of the upgraded brown coal water mixture, *Fuel Process Technol*, 90 (2009): 611-615.
15. Li P.W., Yang D.J., Lou H.M., et al. Study on the stability of coal water slurry using dispersion-stability analyzer, *Journal of Fuel Chemistry and Technology*, 36 (2008): 524-529.

16. Li Y.C., Cheng J., Liu J., et al. Improve the coal's slurrying concentration by coal blending, *Coal Conversion*, 33 (2010): 41-44.
17. Hu Y.X., Liu J.Z., Wang R.K., et al. Effects of blending coals on the behavior of coal water slurry, *Proceedings of CSEE*, 32 (2012): 31-38.
18. Yu Y.J., Liu J.Z., Wang R.K., et al. Effect of hydrothermal dewatering on the slurryability of brown coals, *Energy Conversion and Management*, 57 (2012): 8-12.
19. Wang R.K., Liu J.Z., Gao F.Y. et al. The slurrying properties of slurry fuels made of petroleum coke and petrochemical sludge, *Fuel Process Technology*, 104 (2012): 57-66.
20. Yang B.L., Gong K.F., Zhou J.H., et al. Slurryability of lignite and petroleum coke mixture, J*ournal of Fuel Chemistry and Technology*, 36 (2008): 391-396.

Feasibility Study and Development of Eolic Energy in the Ponza

Colantoni Andrea[a*], Cossio Filippo[b],

Department of science and technology for Agriculture, Forests, Nature and Energy University of Tuscia, S. Camillo De Lellis s.n.c., Viterbo, Italy
Tel. +39 0761 357356
E-mail: [a]colantoni@unitus.it, [b]filippocossio@libero.it,*

Menghini Giuseppina[a], Suraci Vincenzo[b]

S.P.S. (Solar production systems) Italy S.r.l., S. Erasmo 12, 00186 Rome, Italy
Tel. +39 06 45439628 Fax +39 06 97270381
E-mail: [a]giusymenghini@unitus.it, [b]info@spsitaliasrl.it

The core of the present work focuses on the detailed analysis on the wind power potential of the Ponza Island. The results have been obtained thanks to the use of advanced software tools developed specifically for the purpose of wind data elaboration. The main output of this analysis is a detailed map representing the wind farm locations and an estimation of 4,5 MW of installed wind power equivalent to an annual production of 9 GWh of electric power (that is the 90% of the annual demand of the entire island). Finally the work presents an innovative way of project-financing making the whole project feasible and easy to adopt for the public administration.

Keywords: Rational Use of Energy, Renewable Energy Sources, Wind energy, Electric energy.

1. Introduction

The economic development of a territory must consider a series of national and international instruments directed to a reduction of greenhouse gases and protection of the natural resources. The most known are the protocol of Kyoto, the conventions on Biodiversity, Desertification, Agenda 21, the protocol on the species protected of the Mediterranean (SPA Protocol that is one of the instruments of the Convention of Barcelona), the Habitat Directive and the Water

* Corresponding author.

Framework Directive. All these legislative instruments, of opportunely applied, represent an incentive for a new economic development more respectful for the natural resources and able to create new markets for Italian suppliers of technology. The present document aims to introduce, as much as possible in procedural terms, the use of new and renewable energetic sources (NRES) and a rational use of energy (REU) to define the elements of an extract of the Environmental Energetic Plan of Ponza Island through the Integrated Management of the territory [5], [6], [7]. The Environmental Energetic Plans (E.E.P.), have the scope to propose to communal level, complex and structured participations, finalized in reducing the energetic consumptions of primary sources in the examined territory and to pursue the objective of reducing the emissions of greenhouse gases and improve the environmental impact. The legislative and environmental motivations that lead the EE.LL to formulate a proposal of energetic action plans oriented to improve the use of renewable energetic sources and a rational use of energy, will be inquired The scope of such surveying is to find the restrictions and the sphere of action to define a Communal EEP.

2. Eolic Energy

Italy has ratified the Kyoto protocol and in matters of reduction of greenhouse gases emissions, Eolic energy plays a fundamental role, furthermore it allows to pursue the production of electric power by renewable sources according to the National White Book. Eolic energy, as biomasses, represents actually the only source capable to supply an amount of electric power such as fossil fuels. In this way is possible to reduce emissions in atmosphere of greenhouse gases and pollution.

To the end of 2001 in Italy turned out to be installed, on firm earth, more than 1.240 aero generators, able to supply a total power estimated in 700 MW. Our country was able, in year in advance, to reach the first objective indicated in the White Book approved from the CIPE in the '98 for year 2002. Due to the installation of ulterior 270 MW of power in 2001, it was to gain a 60% increment in comparison with the previous year. In 2002 there was a further installation of 88 MW, taking the total power provided to 785 MW [1], [2], [3], [4].

3. Analysis Instruments

Different projects and investigations to establish the energetic potential of NRES and REU, to find out the best strategies for an energetic and environmental sustainable development, will be inquired. The aspects developed in this section are:

- Analysis of the legislative references: in this section will be shown the sources of information to consult and publications about legislative problematic, concerning the use of renewable sources and energetic saving. The last aim is to show how to find the normative outline for an E.E.P.C. proposal.
- Analyses of energetic problems of the territory: will be illustrated the methods of search and evaluation to write down an energetic and environmental and social outline of the territory of Ponza Island.
- Study of territory and energetic sources: evaluation of NRES and REU action plans and of the real economic/environmental saving.
- To realize an Action plan, it's foreseen the use of specific software to analyze: the potentialities of every renewable energetic sources available in the island of Ponza, the evaluation of the obtainable energetic saving and the reduction of greenhouse gases.

4. Material and Methods

The existence of a direct relationship between the wind variations and the cost production of electric power makes necessary, in order to carry out a correct technical and economic evaluation, to determine the anemology of a territory. The first step is to realize an eolic map of Ponza Island then a qualitative and quantitative wind analysis. The creation of the eolic map will be realized through the WAsP software that turns out to be the main and the most complete instrument available on the market. The same software has been used to realize the European Atlas of Wind too; the aim of the Atlas is to promote the market of electric power produced by aerogenerators and the development of new technologies. A naturalistic and historical surveying of the territory, the orography of the island and data about wind speed and direction have been used as inputs for the realization of the map.

5. Preliminary Study

Like already pointed out, the first fundamental step to determine the technical-economic feasibility of an Eolic plant is the creation of an Eolic map representing the distribution of the resource wind on territory. In order to draw it, the table (scale 1:25000) 170-III-SO of Military Geographic Institute (IGM), representative the territory of Ponza island, has been converted in raster, then in vectorial and finally georeferenced. (Figure 1). The anemometer data considerated go from 1993 to 2002, they are hourly (for every hour we have a single value) and represent the medium value of the previous ten minutes. To obtain a detailed description of the wind characteristics it is necessary to gain the following fundamental parameters: annual average speed; the annual maximum speed;

distribution of frequency of the intensity (describable with a Weibull curve) and distribution of frequency of the wind direction.

By the analysy of anemometer data we have obteined the wind rose (Figure 2) and the curve (Figure 3) representing the speed frequency (Weitbull curve).

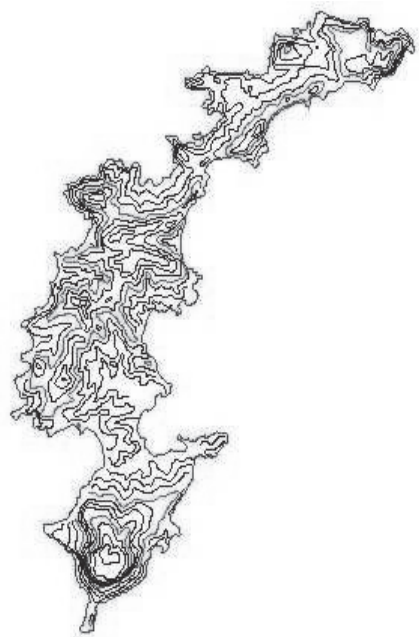


Figure 1 Map of Ponza Island

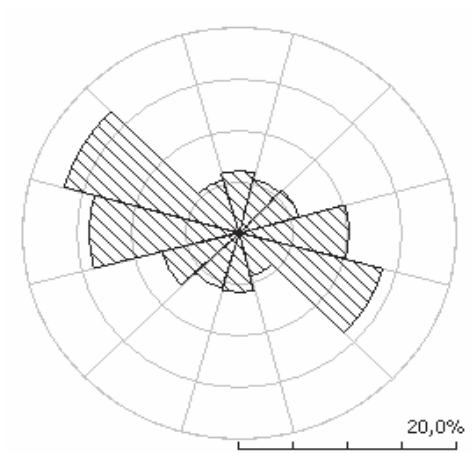


Figure 2 Wind rose

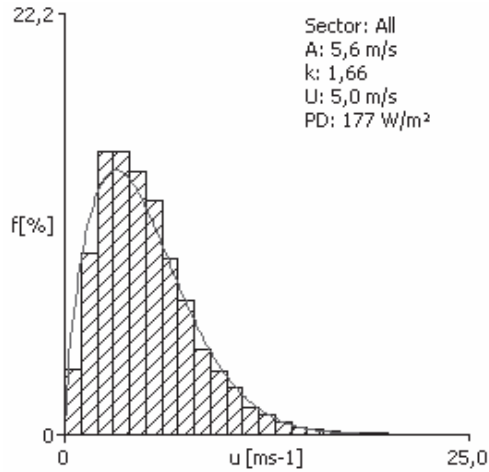


Figure 3 Weibull curve

To set up an eolic map of a territory is necessary to calculate in several points the aeolic potential highlighting the changes of speed and direction. Then we must insert the orography and realize a grid to define the above mentioned points. Once obtained the map it has been possible to estimate the following potentialities:

- a total power of 4,5 MW, composed by eighteen 250 kW aereogenerators;
- a gross annual production estimated to 9 GWh;
- an annual net production of energy equal to 7,65 GWh (15% loss).

The aerogenerators actually installed on firm earth, with a power of 1 MW each, can't be used in Ponza for these reasons:

- Transport costs (via sea and earth);
- Narrow roads with problems of stability with elevates weights;
- Considerable environmental impact due to the dimensions of the whole aerogenerators.

For these reasons the preliminary projects have been carried out with models of 250 kW aerogenerators. In this way the visual impact and the problems of transport have been reduced.

6. Definition of Action Plans and Specification of Feasible Projects

In this section will be exposed the guide lines of action plans useful to the Local Body (Town council of Ponza) for planning and scheduling all the necessary actions.

Generally an action plan needs:

- Identify feasible plans;

- Identify the existing barriers and the necessary innovations;
- Computing sectorial forms;
- Computing technologic forms.

It is opportune a planning using forms that could help to find out the kind of intervention needed. The forms must consider the following aspects:

Action objectives and the intervention proposed:

- Timing and priority of every action;
- Operators involved or to involve;
- Actions effect (energy saving, pollution reduction, new work positions);
- Costs, problems, previous experiences, results verification;

7. Action Plan for Eolic Technology

According to the preliminary study the most windy areas have been found; the aerogenerators in these areas should guarantee at least 2,000 working to produce a power of 250 kW each. The island has been divided in seven areas. In each of them it was possible to determine the number of aerogenerators to install.

The action plan has been divided in three parts:

1) "EOLO PONZA 1" project: 6250 kW aerogenerators for an amount of 1,5 MW;

2) "EOLO PONZA 2" project: 6250 kW aerogenerators for an amount of 1,5 MW;

3) "EOLO PONZA 3" project: 6250 kW aerogenerators for an amount of 1,5 MW. The projects are in succession will be described only the first because it has same technical aspects for all eolic plants.

"Eolo Ponza 1" Project

On the basis of the following factors:

- Anemologic data
- Low environmental impact
- Accessibility to the involved areas
- Sinergy with other projects

Three areas of particular interest have been found.

A 250 kW aerogenerator will be installed in each one of this locality, the existamated production of energy is around 510 MWh that are equivalent to approximately 2000 hours of work. The total energy produced annually from the three wind farm will be of approximately 3 GWh, the 30% of the island total consumptions in one year. The coverage can reach the 50% during winter months.

Subsequently a feasibility study will be carried out with the cooperation town council technicians to verify the practicability, productivity and the business plan of the project. The production of electric energy with fossil fuels implies the

emission of polluting substances and greenhouse gases. The emission level depends on combustible, combustion and fumes control. The values of the main emissions associated to the generation of electric energy are:

- CO_2 (carbon dioxide): 1,000 g/kWh
- SO_2 (sulphur dioxide): 1.4 g/kWh
- NO_2 (nitrogen oxides): 1.9 g/kWh

The most important is the carbon dioxide, the progressive increment of which could contribute to the greenhouse effect and to cause dramatic climatic changes.

The sequence of activities to develop the project are:

- Study of Feasibility;
- Definitive Plan and publication of the ban;
- Executive Planning after the assignment of the ban and relative authorizations;
- Yard opening, closing works;
- Test and inflow in energy net.

The economic prevision of the entire system, is based on the following voices of unit cost:

- Cost of a single machine (250 kW),
- Assembly;
- Transformer and Cabin Electric;
- Roads and Pits;
- Reinforced concrete;
- Electric trellis;
- Planning and survey.

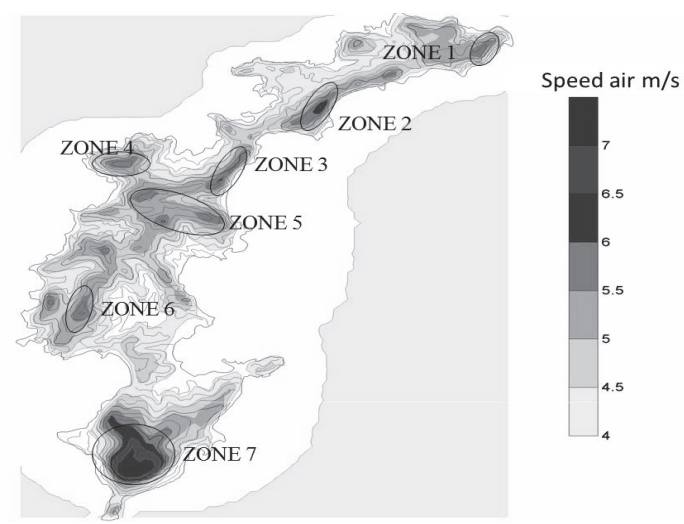


Figure 4 Intervention areas with installation of eolic plants

The total turnkey cost of the plant (7 aerogenerators (Figure 4), 250 kW each) is estimated in 1,920,000 € (320,000 € each generator) and, with 4% financial ni terests for 8 years and 2250 hours of annual operation of the system, is estimated a gross margin of 1,572,000 € after 20 years. A project financing will be launched to find private funds. The land owners will be compensated with a 30 years rent contract. The town council will be partner of the project.

8. Environmental Aspects

Negative environmental effects due to the use of wind turbines are primarily acoustic noise emission, visual impact, and electromagnetic interference influencing the reception of radar, radio and television signals. However, aero-acoustic research has provided design tools and blade configurations that make blades considerably more silent. So wind turbines can now be installed within 200 meters of houses. Because of electromagnetic interference, wind farms should not be built near airports. A primary impact of wind turbines on Ponza island is visual. This is exacerbated by the need to site wind farms in the windiest areas, which are usually exposed high areas, which themselves often have a natural beauty. Where possible wind farms on islands, indeed anywhere, should not be sited within or near nature reserves, protected areas or special areas of conservation.

During normal operation a wind turbine causes no emissions.

9. Detailed Analysis

The choice of a suitable site to install a wind turbine is conditioned by several factors in addition to a high wind resource. For example, various urbanistic, environmental and landscape constraints must be born in mind, about which people's sensitivity has increased a lot during the last years.

Power density remains quite high in every month, the highest values occur from November to April, with a peak in February, equal to 726.9 W/m^2, while the lowest values occur from May to October, with a minimum in September, equal to 365.6 W/m^2. Furthermore, the wind could allow a wind turbine to supply power almost continuously throughout the year. In fact, with a cut-in speed equal to 2.5 m/s and a cut-off speed equal to 17 m/s, the working time varies from the lowest value of 0.74 in December to the highest value of 0.84 in May and June. However, the values of the cut-in speed and cut-off speed should be chosen from the values of commercial wind turbines so as to optimize the annual energy supplied by the turbine in terms of costs. With regard to the hourly variability, Fig. 5 shows that in each month the highest values of the available wind power density are reached in

the afternoon, mostly with a peak at 15:00, while the lowest values are reached in the late evening.

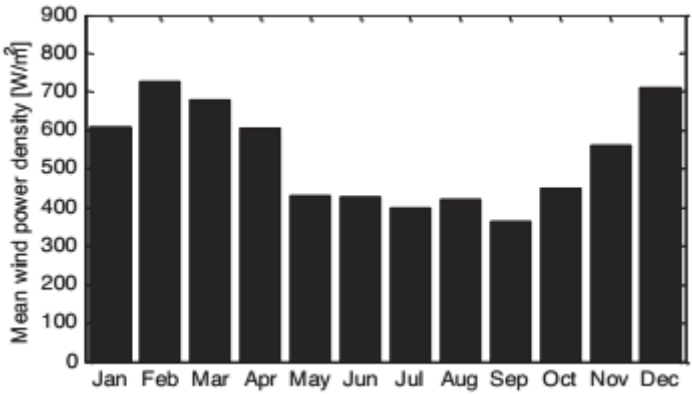


Figure 5 Available wind power density in each month at Ponza Island

10. Conclusions

Wind energy is an attractive, clean, indigenous energy source for Ponza Island that have the required wind regime. The primary regional wind systems are the NE trades that form a relatively stable wind regime.

Coastal sites on the islands tend to have strong diurnal variations in wind speed with the strongest winds occurring between 9:00 am and 4:00 p.m., whilst there is little wind during the rest of the 24 hour day.

The cost of wind turbines and ancillary equipment has fallen significantly over the past decade and this trend is continuing. The cost of electricity produced from wind energy has fallen even faster, not only because of lower wind turbine prices, but also because of higher turbine efficiency and availability, larger turbines intercepting increased wind speeds, and lower operation and maintenance costs.

The present preliminary study permitted to focalize, on demand of Ponza city council and the necessary elements to realize the energetic and environmental plan of Ponza Island. With this document the potentiality of the New and Renewable Energy Sources (NRES) and of Rational Energy Use (REU) have been analyzed.

References

1. J. Cai, R. Liu, and C. Deng, An assessment of biomass resources availability in Shanghai, *Renewable and Sustainable Energy Reviews* (2008), 12, 1997–2004.

2. Y. Yanli, Z. Peidong, Z. Wenlong, T. Yongsheng, Z. Yonghong, and W. Lisheng, Quantitative appraisal and potential analysis for primary biomass resources for energy utilization in China, *Renewable and Sustainable Energy Reviews* (2010), 14, 3050–3058.
3. N. Bilanzdija, N. Voca, T. Kricka, a. Matin, and V. Jurisic, Energy potential of fruit tree pruned biomass in Croatia, *Spanish Journal of Agricultural Research* (2012), 10, 292–298.
4. M. Petriccione, L. F. Ciarmiello, P. Boccacci, A. De Luca, and P. Piccirillo, Evaluation of 'Tonda di Giffoni' hazelnut (Corylus avellana L.) clones, *Scientia Horticulturae* (2010), 124, 53–158
5. D. Monarca, M. Cecchini, A. Colantoni. Plant for the production of chips and pellet: technical and economic aspects of a case study in the central Italy, *Computational Science and Its Applications* (2011), IV, 296–306.
6. Marucci, A., Carlini, M., Castellucci, S., Cappuccini, A. Energy efficiency of a greenhouse for the conservation of forestry biodiversity (2013), 2013 *Mathematical Problems in Engineering*.
7. Monarca, D., Cecchini, M., Colantoni, A., Marucci, A. Feasibility of the electric energy production through gasification processes of biomass: Technical and economic aspects". *Lecture Notes in Computer Science* 6785, 307–315.

Study on Piezoelectric Harvesting Mechanism of Nonlinear Cantilever Harvester

Sun Chun-hua[a*], Liu Jie[b], Wang Hong-bing[c], Shang Guang-qing[d]
Department of Mechanic and Electronic Engineering,
Suzhou Vocational University, 215104, China
E-mail: [a]sunch@jssvc.edu.cn, [b]liuj@jssvc.edu.cn,
[c] whb@jssvc.edu.cn, [d]shanggq@jssvc.edu.cn

To improve resonance band and harvested energy efficiency, an nonlinear cantilever's piezoelectric system is studied. A permanent magnet is set as a mass on the free tip of the oscillator, which suffers the nonlinear repulsive magnetic force during vibrating. The mathematic model of harvesting energy is proposed based on the lumped parameter model for this nonlinear system. The effective factors of the bistable characteristic are discussed and the stochastic resonance action is analyzed. The optimized parameters for generating bistablity are also deduced. The correction of the model is verified by experimental results. The studied result shows that affable parameters of structure and space between two magnets are chosen and the device becomes a bistable system which possesses lower natural frequency and wider frequency band. This study can be generally applied to improve the integrated voltage output.

Keywords: Nonlinear Piezoelectric Oscillator; Energy Harvest; Stochastic Resonance.

1. Introduction

Up to now, study on the technology of energy harvesting from vibration has been mostly focused on linear piezoelectric oscillator, which theory is based on linear piezoelectric equation[1-4].The relative research[5] shows that a linear oscillator possesses the following characteristics: 1) the resonance frequency is higher and wave band is narrower. 2) the maximum electrical power is generated under the resonance state. While in the non-resonance condition, the electric energy output decreases obviously. That makes application of the linear piezoelectric vibrator be badly restricted.

Nonlinear stochastic resonance piezoelectric technology is one of the frontier topics. This research shows that a nonlinear piezoelectric vibrator has bistable behavior and decreases the resonance frequency while increases waveband[6-8]. This work proposes a stochastic nonlinear oscillator and discusses its piezoelectric energy harvesting mechanism.

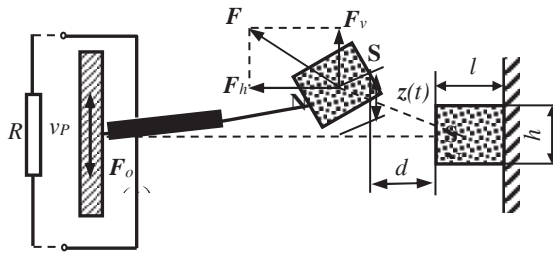


Fig.1 Nonlinear piezoelectric cantilever beam

2. Nonlinear Piezoelectric Harvesting Model

Figure 1 shows a cantilever beam, of which a permanent magnet is positioned on the free end. The other one with opposite polarity is fixed at a distance d along the beam axis.

The forces of the harvesting system are analyzed in Fig.1. The repulsive force F between the two magnets is[9]

$$F = \frac{1.5}{1+3d} \times \frac{wh}{2\mu_0}\left\{\frac{B_r}{\pi}\left(\tan^{-1}\frac{wh}{2d\sqrt{w^2+h^2+4d^2}} - \tan^{-1}\frac{wh}{2(l+d)\sqrt{w^2+h^2+4(l+d)^2}}\right)\right\}^2 \quad (1)$$

Where, l, w, h are length, width and height of the magnets. $\mu_0 = 4\pi \times 10^{-7} N/A^2$ is vacuum permeability. $B_r = 1.25T$ is property parameter of the permanent magnet.

The vertical component F_v of the repulsive force F is

$$F_v = F \times \frac{z}{\sqrt{z^2+d^2}} \quad (2)$$

F_v is a nonlinear odd function of the tip displacement z as shown in Equ.(2). According to 2nd law of Newton's motion, the motion equation of the nonlinear piezoelectric cantilever beam is constructed based on the lump parameter model as following

$$F_o(t) - \Theta v_p + F_v = M_{eq}\ddot{z}(t) + \eta_{eq}\dot{z}(t) + K_{eq}z(t) \quad (3)$$

Where $F_o(t)$ is input mechanical excitation, Θ is electromechanical coupling constant, v_P is output voltage of PZT, M_{eq} is equivalent mass of

cantilever beam, η_{eq} is equivalent damping, K_{eq} is equivalent stiffness, $z(t)$ is equivalent displacement.

Based on Kirchhoff's first law, the equivalent circuit of piezoelectric oscillator meets

$$\Theta \dot{z}(t) = C_P \dot{v}_P + v_P / R_L \tag{4}$$

Where, C_P is equivalent capacitance and R_L is an external resistor.

Equations of (1) - (4) describe commonly the harvesting mechanism of the nonlinear piezoelectric cantilever beam.

3. Influence Factors of the Bistable Characteristics

The generated potential energy of nonlinear piezoelectric cantilever beam under the comprehensive effects of weight, elastic restoring force and magnetic force can be expressed by

$$V(z) = \frac{1}{2} K_{eq} z^2 + M_{eq} g z - F \cdot (\sqrt{z^2 + d^2} - d) \tag{5}$$

Figure 2-4 show the potential energy V simulated by using MATLAB software.

From the above figures, some results can be obtained: 1) the potential V shows a symmetric double well with two stable equilibrium points at suitable parameters of $d = 4-5mm$, $l = 4-7mm$ or $h, w = 4-8mm$; 2) Effect of parameters of d, h (w), l on bistable behavior gradually decreases. Therefore, when the permanent magnet is selected, it is a effective way to change the bistable behavior by adjusting distance d between two permanent magnets.

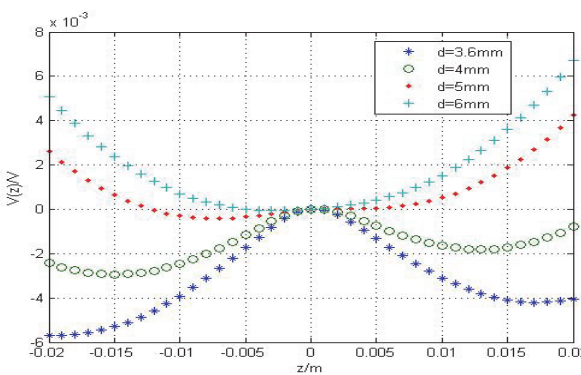


Fig.2 Effect of *d* on potential energy

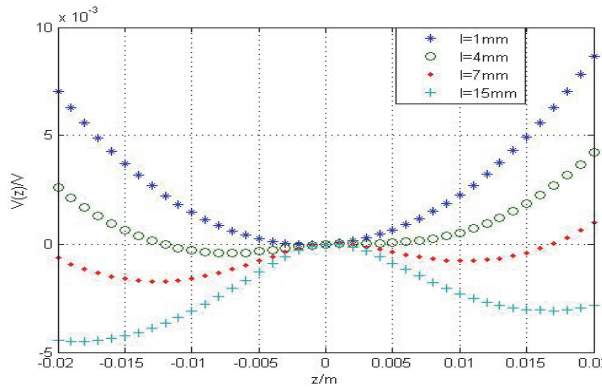


Fig.3 Effect of *l* on potential energy

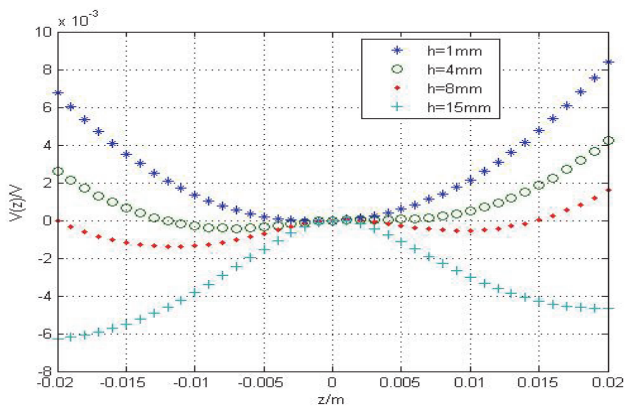


Fig.4 Effect of *h*(or *w*) on potential energy

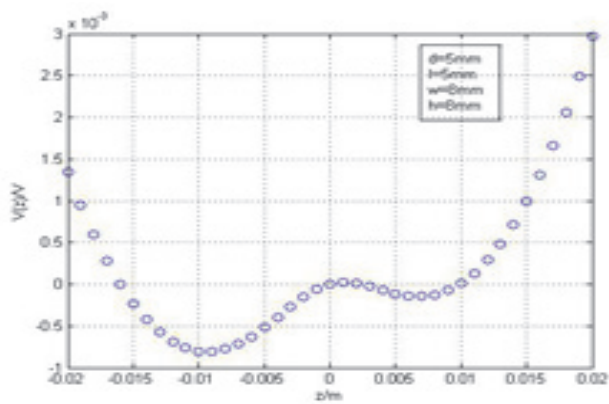


Fig.5 Bistable characteristic with optimized parameters

The optimized parameters of nonlinear piezoelectric cantilever beam are $l = 5mm$, $w = h = 8mm$ and $d = 5mm$. Figure 5 shows potential function V for the optimized parameters and implies better bistablity.

4. Analysis of Nonlinear Characteristic

The nonlinear switching mechanism is analyzed when a white noise vibration source is applied in the cantilever base. Figure 6 and Fig.7 show the output voltage v_P in the linear case and in presence of nonlinearity, corresponding respectively to exceedingly large and finite distance d.

The conclusion reduced from the two figures can be listed as following: 1) resonance phenomenon does not occur under the stochastic vibration source when the distance d=12mm is not small enough to generate magnetic force on the cantilever system. In the case, the system can be taken as a linear piezoelectric oscillator. The output voltage v_P is much less and has no regular variation, as shown in Fig.6; 2) while the output voltage v_P changes with cycle and emerges the resonance phenomenon when the distance d=5mm is changed to generate bistable behavior. The value v_P in this case is two times of the linear system. The maximum voltage is up to 15V, as shown in Fig.7.

Moreover, Fig.8 reports the responses in the frequency domain in bistable vibrations of the nonlinear cantilever beam. The nonlinear case provides a wider spectrum to produce a improved effectiveness in converting wide-spectrum vibrations.

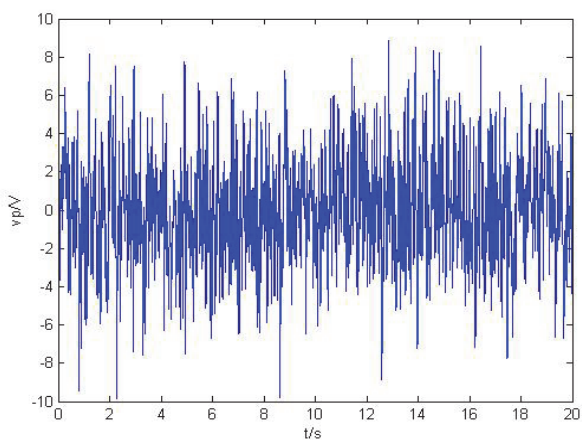


Fig.6 Output voltage v_P with non-bistablity

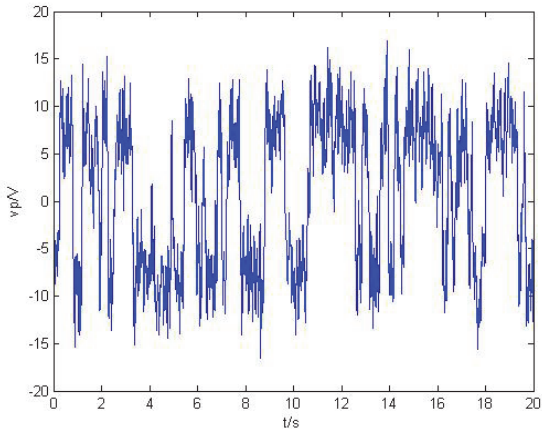


Fig.7 Output voltage v_P with bistablity

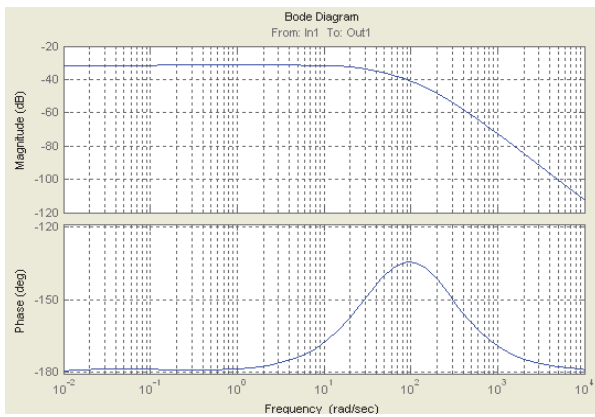


Fig.8 Amplitude-frequency characteristic with bistablity

5. Experimental Validation

To experimentally evaluate the proposed model and its characterization, a experimental setup is done, as shown in Fig.9. The piezoelectric bimorph were realized by screen printing low-curing-temperature PZT films on steel cantilevers. A permanent magnet was pasted on the cantilever free tip while an external one with opposite polarity was fixed on a stage. The oscillator was excited at the base by mechanical vibrations using a electrodynamic shaker. The distance d is set up by varying the distance between the cantilever tip and the fixed permanent magnet.

Figure 10 shows the measured open-circuit output voltage v_P of the oscillator with different values of distance d under the same stochastic vibration



Fig.9 Experimental equipment

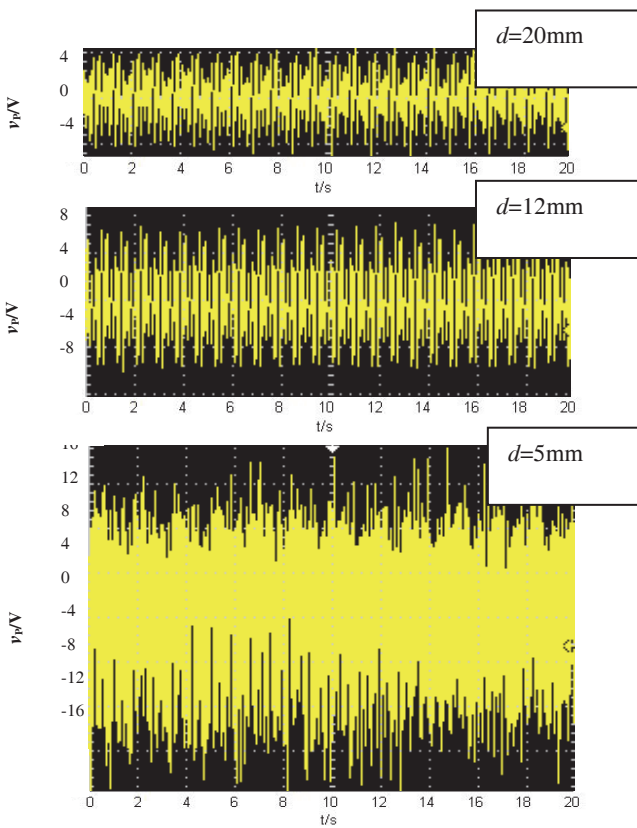


Fig.10 Output voltage v_d with different d

source. The oscillator does not be effected by the magnetic force when d =20mm. The oscillator is not be excited to generate resonant vibration, so that a smaller voltage v_P is obtained. When the distance d decreases to d =12mm, the oscillator is gradually effected by the magnetic force and the output voltage v_P increases with decreasing d. Until the distance is up to d =5mm, the stochastic resonance phoneme happens and the output voltage v_P is nearly twice of the value with non-resonance. The experimental results shown in Fig.10 are very consistent with the simulation results of Fig.6-7.

The measured natural frequency is $f_n = 28Hz$ when there is no magnetic force on the oscillator. Meanwhile, the natural frequency is $f_n = 25Hz$ and $f_n = 19Hz$ when d =12mm and d =5mm, respectively. This proves that a lower natural frequency and a wider spectrum for the bistable system in contract to the linear case can be obtained.

6. Conclusion

Linear piezoelectric cantilever beam has been widely used for energy harvesting application. To overcome its poor output power outside of the resonance frequency range, a magnet is set on the free tip as the cantilever mass. A other magnet is fixed opposite to the one to generate the repulsive magnetic force for increasing the cantilever stiffness. In this study, the enhanced output voltage and wider waveband are demonstrated with the numeric simulation and experiment results. The constructed model of nonlinear energy harvesting system is correctly verified by the experimental results. The principle of nonlinear piezoelectric energy harvesting technology may be generally applied to improve the integrated voltage output.

The further work is to array piezoelectric cantilever beams for scavenging mechanical vibration on larger range.

Acknowledgements

This research was supported by the National Natural Science Foundation of China (No.51175359). The 4th "333 Engineering" Research Funding Project of Jiangsu Province (BRA2014086).

References

1. Y.M. Liu, Active energy harvesting. University Park: the Pennsylvania State University, 2006
2. Choi W.J., Jeon Y., Jeong J. H., et al. Energy harvesting MEMS device based on thin film piezoelectric cantilevers[J]. J. *Electroceram.*, 17(2006) 543–548.

3. H.D Zhao, J.Yu, J.M. Ling. Finite element analysis o f cymbal piezoelectric transducers for harvesting energy from asphalt pavement[J]. *J of the Ceramic Society of Japan*, 118 (2010)909-915.
4. C.H.Sun, J.H. Du, H.B.Wang, et al. Properties analysis of piezoelectric energy harvesters from pavement vibration[J]. *Piezoelectrics & Acoustoptics*, 35(2013) 556-560. (in Chinese)
5. S.Roundy, On the effectiveness of vibration-based energy harvesting. *J of Intelligent Material Systems and Structures*, 16(2005)809-823.
6. C.R.McInnes, D.G.Gorman, M.P.Cartmell, Enhanced vibrational energy harvesting using nonlinear stochastic resonance. *Journal of Sound and Vibration*, 318(2008)655-662.
7. L.Gammaitoni, I. Neri, H.Vocca, Nonlinear oscillators for vibration energy harvesting. *Applied Physics Letters*, 94(2009) 164102.
8. Z.S. CHEN, Y.M. YANG, Stochastic resonance mechanism for wideband and low frequency vibration energy harvesting based on piezoelectric cantilever beams. *Acta Phys. Sin*., 60(2011), 074301.
9. Y. WANG, Calculation of Magnetic Force of Permanent Magnet Devices. *Magnetic Material & Device*, 38(2007) 49-51. (in Chinese)

Analysis on the Response Time of the Battery Energy Storage System

Song Li[1,a], Wang Zhiming[2,b] and Luo Weihua[3,c*]

[1] *The Nanjiao Street No. 81, Liaoyang City, Liaoning Province, China*
[2] *Ningbo Road 18, Heping District, Shenyang City, China*
[3] *Ningbo Road 18, Heping District, Shenyang City, China*
E-mail: [a]songli20020708@163.com, [b]wzm2@ln.sgcc.com.cn, [c]whluo2000@126.com

At home and abroad, there are few experimental on the actual storage system of the vanadium redox flow battery (VRB). In this paper, using the scientific method to test the charging response time and the discharging response time of the VRB storage system. The VRB system which was been tested is largest VRB in the world. Its capacity is 5MW/2h. The test results show that the charging response time is 2221ms, and the discharge response time is 571ms. It is an advanced the international level.

Keywords: Vanadium Redox Flow Battery (VRB).Test. The Charging Response Time. The Discharging Response Time.

1. Introduction

When the global environment concern and fossil energy shortage, wind power is facing with a great developing opportunity. It changes traditional electric power industry from growth to quality. Wind power is a random and intermittent energy sources, wind farm output prediction accuracy is not yet able to meet the purpose of engineering applications.[1] With lately progress in energy storage technology, battery energy storage systems (BESSs), which is prominent with high energy density, flexible allocation of power and capacity and quick response, have been utilized in power systems for wind dispatch ability enhancement.[2] e.g. load shifting, wind power volatility alleviation, power system stability control, etc. Combination wind farm with various ESSs has been regarded as one potential solution[3], which to mitigate such negative impacts. And the application of BESSs has become one of the most relevant research subjects.

In this paper, the application of battery for frequency regulation is studied. A control strategy is proposed for the battery energy storage system for the

* Corresponding author.

frequency control purpose. The results are obtained for different parameters based on the proposed method.[4]

The organization of this paper is as follows. In Section II, battery energy storage system is presented. The charge Response Time Test of VRB is provided in Section III. The discharge Response Time Test of VRB is provided in Section IV. Conclusion in Section V. Acknowledgment in Section VI.

2. Battery Energy Storage Technologies

A range of options for small-scale renewable energy storage are available by means of battery energy storage technologies. With high energy densities and relative ease of use, they present a viable option for small-scale renewable energy integration.[5] The characteristics of batteries that needs to be used for comparative assessment are power rating and energy storage capacity, cost, cycle lifetime, safety and licensing, size and operational and maintenance requirements.[6]

The vanadium redox flow battery (VRB) is discussed in this paper. It is a flow battery that is capable of storing energy in multi megawatt ranges and for durations of hours or days.[7] The stored energy can be returned to the grid or supplied to a load as required and directed. The present form (with sulfuric acid electrolytes) was patented by the University of New South Wales in Australia in 1986. An earlier German Patent on a titanium chloride flow battery was registered and granted in July 1954 to Dr. Walter Kangro, but most of the development of flow batteries was carried out by NASA researchers in the 1970s. Although the use of vanadium in batteries had been suggested earlier by Pissoort, by NASA researchers and by Pellegri and Spaziante in 1978, the first known successful demonstration and commercial development of the all-vanadium redox flow battery employing vanadium in a solution of sulfuric acid in each half was by Maria Skyllas-Kazacos and co-workers at the University of New South Wales in the 1980s.[8]

The VRB is capable of being charged as quickly as it was discharged and is able to respond to all forms of power quality variations and can be operated in a UPS mode as well. For loads which require reactive energy, the VRB can provide VARS on a continuous basis either when charging or discharging.

VRB's are based on the patented vanadium-based redox regenerative fuel cell that converts chemical energy into electrical energy.[9] Redox is the term used to describe electrochimical reactions in which energy is stored in two solutions with electrochemical potentials sufficiently separated from each other to provide an electromotive force to drive the oxidation-reduction reactions. In the VRB energy is stored chemically in different ionic forms of vanadium in a

dilute sulfuric acid electrolyte. This creates a current that is collected by electrodes and made available to an external circuit. The reaction is reversible allowing the battery to be charged, discharged and recharged.

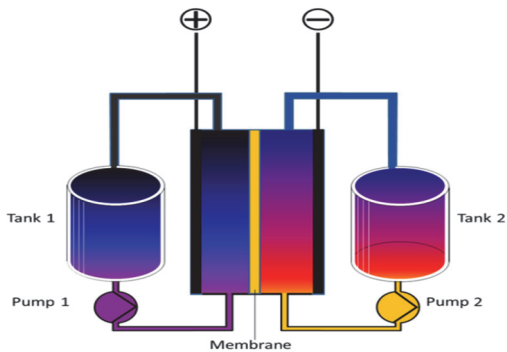


Fig. 1 The vanadium redox flow battery

In Fig. 1, the vanadium redox battery exploits the ability of vanadium to exist in solution in four different oxidation states, and uses this property to make a battery that has just one electro active element instead of two. The main advantages of the vanadium redox battery are that it can offer almost unlimited capacity simply by using larger and larger storage tanks, it can be left completely discharged for long periods with no ill effects, it can be recharged simply by replacing the electrolyte if no power source is available to charge it, and if the electrolytes are accidentally mixed the battery suffers no permanent damage.

The VRB has an availability of greater than 98%. It is designed for unattended operation with very low maintenance costs. No degradation from repeated deep charges and discharges. The system can be discharged and charged greater than 13,000 times (20% to 80% SOC) without deterioration in system efficiencies. System round-trip efficiencies between 70% - 78%.[10] The VRB-ESS has a charge/discharge window of 1:1 - allowing off-peak charging for on-peak dispatch - a fraction of the time required by other battery systems and ideal for wind generation applications. Cross mixing of electrolytes does not lead to contamination of electrolytes. Indefinite life of electrolyte (no disposal or contamination issues). Once charged, the electrolyte remains fully charged with low self-discharge.

3. The Charge Response Time Test of VRB

It is in a wind farm do the experiment in Shenyang. The capacity of the wind farm is 49.5MW, and the storage capacity of the system is 10MW.

3.1. *Test Scheme*

In this experiment, the charge response time of energy storage system can be obtained. Test point as shown in Fig. 2. The energy storage system was charging in 500kW when SOC of VRB is more than 50%. After 10 minutes, the energy storage system was charging in 4500kW.

Charging power from the 775kW jump to 5285kW storage active power curve and energy storage system instantaneous current waveform curve as shown in Fig. 3 and Fig. 4 shows, response time in storage system transient current waveform curve analysis and statistics.

3.2. *Analysis results*

Energy storage exists overshoot phenomena to a certain extent of charging system response time in the testing process, the charging power from 775kW to 6531kW in time for the super 626ms, stable to 5285kW need 2221ms, as shown in Fig. 5 and Fig. 6.

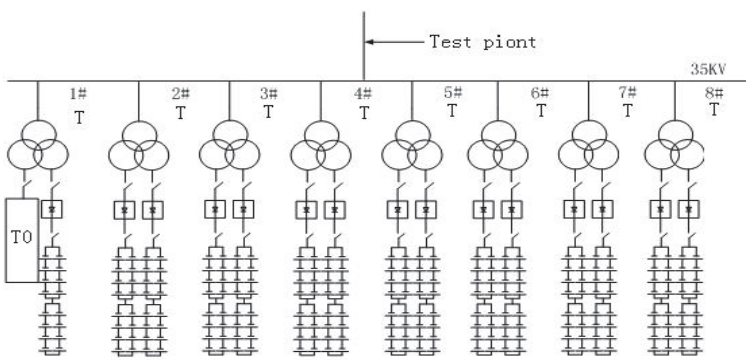


Fig. 2 The point diagram of the response time test

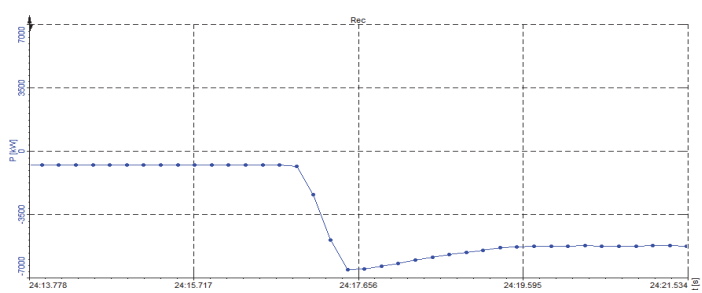


Fig. 3 The power curve of charging transition

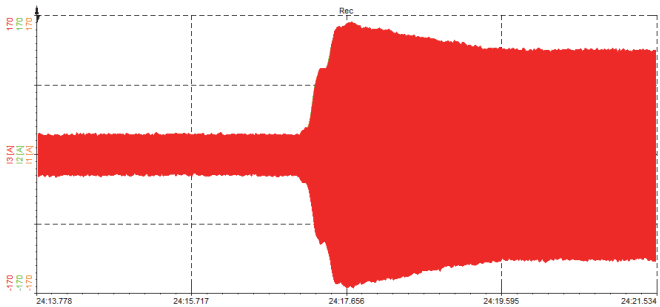


Fig. 4 The current waveform curve of charging system transition

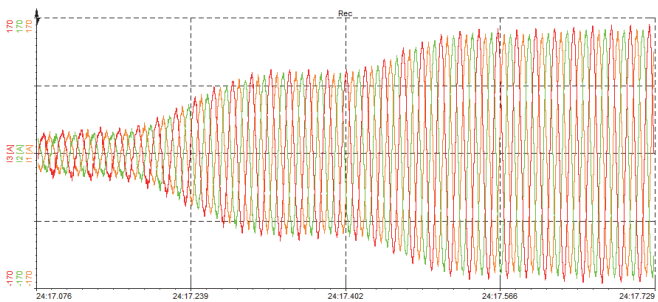


Fig. 5 The instantaneous current waveform from charging jump to.the overshoot

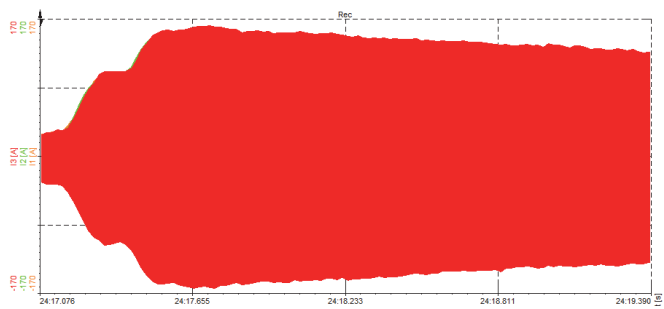


Fig. 6 The instantaneous current waveform charging jump to stability

4. The Charge Response Time Test of VRB

4.1. *Test Scheme*

In this experiment, the discharge response time of energy storage system can be obtained. Test point as shown in Fig. 2. After a full charge, the energy storage system was charging in 500kW. After 10 minutes, the energy storage system was discharging in 4500kW.

The discharge power from the 285kW jump 4373kW storage active power curve and energy storage system instantaneous current waveform curve as shown in Figure 7 and figure 8 shows, response time in storage system transient current waveform curve analysis and statistics.

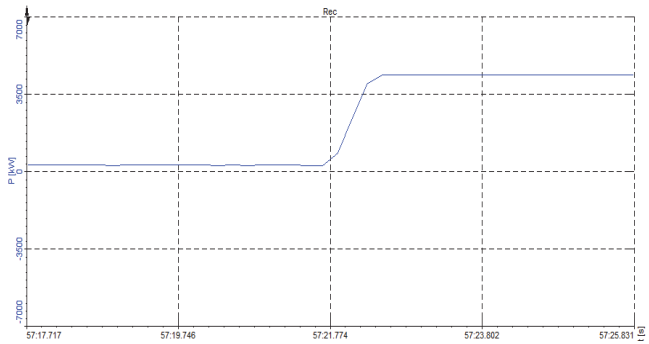


Fig. 7 The power curve of discharging transition



Fig. 8 The current waveform curve of discharging system transition

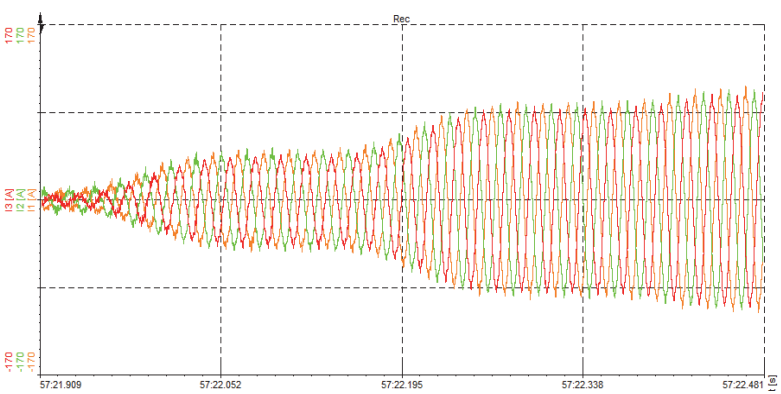


Fig. 9 The instantaneous current waveform from discharging jump to the overshoot

4.2. *Analysis results*

Energy storage system discharge response time testing process is relatively stable, the discharge power from the 285kW stable to 4373kW need 571ms, as shown in Fig. 9.

5. Conclusion

The charge storage system response time is 2221ms (to overshoot is 626ms), discharge response time is 571ms, In response to the power set state changes, the existence of overshoot phenomena to a certain extent, and the charging discharging response time was significantly longer than the other three response time.

Acknowledgment

This work was supported by China's National High Technology Research and Development Program (20l1AA05Al12). as well as science and technology projects of State Grid Corporation and Liaoning Electric Power Co., Ltd. of China.

References

1. Y. N. Chi, Y. H. Liu, W. S. Wang, etc., "Study of impact of wind power integration on power system," *Power System Technology*, vol. 31, pp. 77-81, Mar. 2007.
2. ZENG Jie, "Application of Energy Storage Technologies in Power Grids," Guangdong Electric Power, Nov. 2010, vol. 23, pp.1-5.
3. Yang, T.c. "Initial study of using rechargeable batteries in wind power generation with variable speed induction generators". *lET Renewable Power Generation*, vol. 2, no. 2, pp. 89-101. 2008.
4. E. Ela, B. Kirby, E. Lannoye, M. Milligan, D. Flynn, B. Zavadil, and M. O'Malley, "Evolution of operating reserve determination in wind power integration studies," in Proc. 2010 *lEEEPower and Energy Society General Meeting Conj*, pp. 1-8.
5. S. Teleke, M. E. Baran, S. Bhattacharya, and A. Q. Huang, "Optimal Control of Battery Energy Storage for Wind Farm Dispatching," *IEEE Trans. Energy Conversion*, vol. 25, pp. 787-794, 2010.
6. K. Yoshimoto, T. Nanahara, and G. Koshimizu, "New Control Method for Regulating State-of-Charge of a Battery in Hybrid Wind Power/Battery

Energy Storage System," in Proc. 2006 *IEEE Power Systems Conference and Exposition Conf.*, 2006, pp. 1244-1251.

7. P. J. Hall and E. J. Bain, “Energy-storage technologies and electricity generation,” *Energy Policy*, vol. 36, pp. 4352-4355, 2008.
8. H. Ibrahim, A. Ilinca, and J. Perron, “Energy storage systems-Characteristics and comparisons,” *Renewable and Sustainable Energy Reviews*, vol. 12, pp. 1221-1250, 2008.
9. J. P. Barton and D. G. Infield, "Energy storage and its use with intermittent renewable energy," in *IEEE Transactions on Energy Conversion*, vol. 19, pp. 441-448, 2004.
10. J. Baker, “New technology and possible advances in energy storage,” *Energy Policy*, vol. 36, pp. 4368-4373, 2008.

A Rapid Calculation Method of Wind Farm Collector Lines Maximum Length Applied to Planning and Design

Guodong Liao[a], Xintao Xie & Mengjiao Li

State Grid Hunan Electric Power Corporation Economic & Technical Research Institute, Changsha, Hunan, 410004 China
E-mail: [a]lgd_1981@163.com

Longyuan Li[b*], Peng Ai & Yun Lu

School of Electrical Engineering, Southwest Jiaotong University, Chengdu, Sichuan, China, 610031
E-mail: [b]lilongyuan2012@gmail.com

Grasping the maximum length of each wind farm collector lines which can be extended is of great importance to wind farm planning and design, especially for siting of booster substation and determination that whether adjacent wind farms could share one booster station to send out wind power rapidly. To overcome the deficiencies of the existing technology, this paper proposes a method for rapid calculation of maximum length of collector lines in wind farm. This method establishes relation between voltage of the tail wind generator collecting point and the maximum length of collector line based on voltage equation of π-type equivalent circuit, accurately taking the power loss of box-transformer, collector lines ground capacitance, booster transformer and transmission line into account, together with grid power system parameters, which have impacts on wind farm voltage distribution. This method makes up the defect of excessive error of usual engineering estimation method and reduces the calculation complexity of detail method greatly. Taking an actual wind farm in Hunan China as an example, the calculated results show that the proposed method has high-er precision compared with the engineering method, and it can be used for the planning and design of wind farm.

Keywords: Wind Farm Planning and Design; Voltage of the Tail Wind Generator Collecting Point; Collector Lines Maximum Length; Voltage Equation; Π-Type Equivalent Circuit.

1. Introduction

For purpose of orderly development and co-ordination sent of wind power, the planning and design of transmission is required for those geographically concentrated wind farms, which studies the mode of collecting and sending wind

* Corresponding author.

power and voltage level of transmission line [1]. For example, Hunan Energy Agency organized a study of transmission planning for wind farms in the whole Hunan province. The capacity of wind generator (WG) is small but the number of WGs in a wind farm is big, which is quite different from traditional thermal power. Powers of WGs in wind farm are strung together by collector lines to booster transformer and then would be sent out to grid. Due to the high R/X of collector line, the voltage of collecting point of WGs strung in the same collector line reduces from the tail to the head, and the longer collector line is, the higher voltage of WG collecting point in the tail is [2-4]. Thus, the distance between WG in the tail and booster transformer should be considered in transmission planning to ensure that WGs in the wind farm could operate safely and reliably. What's more, altitude of mountain wind farm is relatively high, and WGs are generally set on a ridge. If booster substation of wind farm is too close to the ridge, transmission line of wind farm could freeze easily [5-7]. If booster station is too close to the mountain foot, collector line could be too long, which makes the voltage of WG collecting point in the tail become out of limit. So it's really important for planning and design of wind farm to grasp the maximum length of collector line could be extend, especially for siting of wind farm and judging that whether adjacent wind farms could share the same booster station to send out wind power rapidly.

The maximum length that each collector line can extent in wind farm can be theoretically obtained by the follow procedure: firstly, build the power flow model with WG including collector system [8-10] and outside power grid in the flow calculation of business program like PSS/E, BPA, and so on; then repeatedly adjust the length of collector lines with the goal that the voltage of WG collecting point in the tail reach the allowable upper limit value. However, this calculation method is very complicated and the modeling is also a great amount of work. What's more, since the R/X ratio is relatively large, the flow power of large grid with wind farm including collector system will be difficult to converge. However, the study of wind farm collector system focus on optimizing its layout at present [11-16], and the calculation of the maximum length of collector lines may rely on engineering estimates. In the planning and design of wind farm, to reduce the calculation complexity, power loss of collector line ground capacitances and box-transformers are ignored, and it's assumed that the wind farm boost transformer low voltage side of the bus is infinite bus (constant voltage). Then the maximum length of collector lines which meets the voltage requirements is calculated. However, the power loss of ground capacitance has a great impact on wind farm voltage distribution and in fact the voltage of the wind farm booster transformer bus is not constant. So it has the disadvantage that the error is too large and it is particularly significant for mountain wind farms which have a large-scale use of cables.

To make up the deficiencies of the existing technology, this paper proposes a method for rapid calculation of the maximum length of wind farm collector lines. Firstly, the equivalent wind farm model used for assessment is established and the parameters configuration method is given. Then, based on π-type equivalent circuit voltage equation, the equation about the maximum length of collector lines is established, considering the maximum voltage of tail WG collecting point in collector line. In these equations, collector lines ground capacitance, box-transformer, booster transformer and transmission line are taken into account, which have impacts on wind farm voltage distribution. And the extended maximum length of wind farm collector lines is calculated by numerical method. Finally, simulations of an actual wind farm in Hunan China have been done to verify the accuracy of the proposed method in this paper.

2. Modeling of Equivalent Wind Farm

The actual wind farms have diverse structure and numerous t-connections, and the lengths between each WG of the same collector line are different. Therefore, as a relatively rough tool of assessment of wind farm collector lines maximum length, the workload of modeling the actual structure of wind farm is too heavy. Moreover, some of the wind farms are also still in the plan, yet the layout of wind farms and related data to establish the actual wind farm model is more out of the question. Thus, when calculating the wind farm collector lines maximum length, making the wind farms be equivalent to simple symmetrical series structure is feasible and necessary.

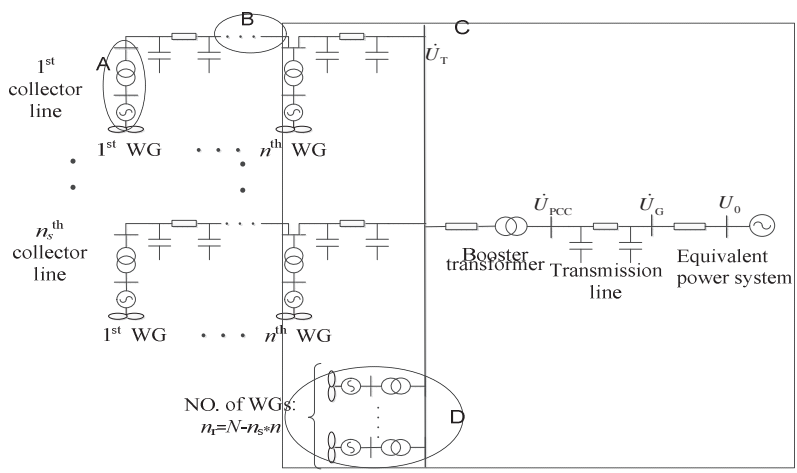


Fig. 1. Schematic of equivalent wind farm

Structure of the equivalent wind farm is shown in Fig. 1, which contains of N WGs, n_s collector lines, and each collector line contains n WGs. Wind farm is completely symmetrical structure, which means the structure and the parameters of every collector line are identical. Therefore, this situation may occur, N is not exactly divisible by n_s, that means in addition to the $n_s \cdot n$ WGs connected to the collector lines, but also the excess of $n_r = N - n_s \cdot n$ ($n_r < n_s$) WGs. Approach in this paper is attaching the WGs directly to the low voltage bus of booster transformer of the wind farm.

Lines are represented by π type circuits, and ground capacitances and reactive power losses are taken into account, which can improve accuracy. In order to avoid calculation of large power flow, external system of wind farm transmission line is represented by a simple line transmission system, which reduces complexity of the calculations greatly.

Some basic parameters of equivalent wind farm are set according to actual wind farms or typical values. Number of WGs connecting to each collector line n is rounded down by the average number of WGs connecting to each line in the wind farm to be assessed.

The number of collector lines which connect WGs and booster transformer of the equivalent wind farm n_s should not more than $\left[\frac{N}{n}\right]$, Where N is the total number of WGs in the wind farm to be assessed. The distance l_k (k=1, 2, …, n-1) between adjacent WGs connecting to the same collector line of the equivalent wind farm is the average distance between the WGs in the wind farm to be assessed. For planning wind farm, the typical values of n, n_s and l_{ave} can be set to 8 (when the rated power of WG is 2MW), the maximum value and 0.8 km.

3. Calculation Method of Wind Farm Collector Lines Maximum Length

3.1 *Calculation of Box-type Trans-former Injecting into Collector Lines Power*

The WG converge into collector lines by box-type transformer, as shown in part A in Fig. 1, shown in detail in Fig. 2, where R_t, X_t and k_t are resistance, reactance and nonstandard ratio of box-type transformer; $\dot{U}_1$ and $\dot{U}_2$ are the voltage of WG terminal (box-type transformer low-voltage-side) and box-type transformer high-voltage-side respectively; P_1 and Q_1 are output active power and reactive power of WG; P_2 and Q_2 are active power and reactive power of box-type transformer high-voltage-side injecting into collector lines.

Let $\dot{U}_1 = U_1\angle\theta$ and $\dot{U}_2 = U_2\angle 0°$, in which P_1, Q_1 and U_2 are known, U_1, θ and P_2, Q_2 are unknown, P_2 and Q_2 are to be calculated.

Both the current and voltage fall have two calculation methods, as shown in Eq. 1-2.

$$\dot{I} = (P_2 - jQ_2)/(U_2/k_t) = (P_1 - jQ_1)/U_1\angle -\theta \tag{1}$$

$$\Delta\dot{U} = \dot{U}_1 - U_2/k_t = \left[(P_2R_t + Q_2X_t) + j(P_2X_t - Q_2R_t)\right]/(U_2/k_t) \tag{2}$$

Simplify Eq. 1-2, eliminate U_1 and θ, and get Eq. 3 about P_2 and Q_2. Now the two equations are both quadratic equations, which can be solved to get P_2 and Q_2 by using the root formula.

$$\begin{cases} \left(R_t^2 + X_t^2\right)P_2^2 + \left[2(Q_1R_t - P_1X_t)X_t + R_tU_2^2/k_t^2\right]P_2 \\ + \left[(Q_1R_t - P_1X_t)^2 - P_1R_tU_2^2/k_t^2\right] = 0 \\ \left(X_t^2 + R_t^2\right)Q_2^2 + \left[2(P_1X_t - Q_1R_t)R_t + X_tU_2^2/k_t^2\right]Q_2 \\ + \left[(P_1X_t - Q_1R_t)^2 - Q_1X_tU_2^2/k_t^2\right] = 0 \end{cases} \tag{3}$$

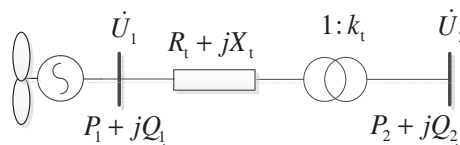


Fig. 2. Schematic of WG and box-type transformer

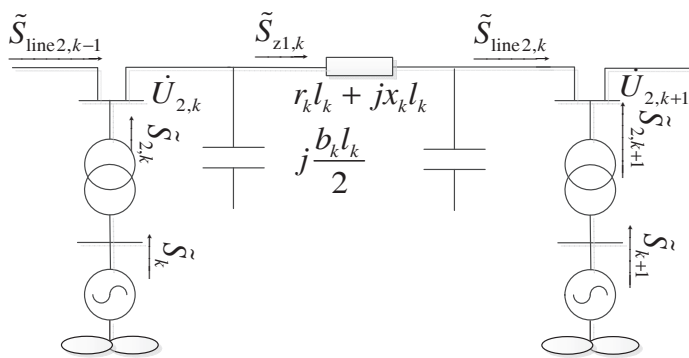


Fig. 3. Schematic of k^{th} collector line

3.2 *Flow Recursive Calculation of Series Collector Lines*

Power injects into collector lines from box-type transformer high-voltage-side. The k^{th} collector line is shown in part B in Fig. 1 and details are in Fig. 3, where r_k,

x_k and b_k are the resistance, reactance and ground susceptance of per unit length of the k^{th} collector line respectively; l_k is the length of the k^{th} collector line.

The active power $P_{z1,k}$ and reactive power $Q_{z1,k}$ at the end of k^{th} π-type equivalent collector line impedance are

$$P_{z1,k} = P_{\text{line2},k-1} + P_{2,k} \tag{4}$$

$$Q_{z1,k} = Q_{\text{line2},k-1} + Q_{2,k} + U_{2,k}^2 b_k l_k / 2 \tag{5}$$

where $P_{\text{line2},k\text{-}1}$ and $Q_{\text{line2},k\text{-}1}$ are the active and reactive power at the head of k-1^{th} collector line, when k=1, $P_{\text{line2},0}$=0, $Q_{\text{line2},0}$=0; $U_{2,k}$ is the voltage of the k^{th} box-type transformer high voltage side, when k=1, $U_{2,1}$= $U_{2,\max}$ i.e. the voltage at the end of series collector lines is the acceptable maximum; $P_{2,k}$ and $Q_{2,k}$ are the active power and reactive power of k^{th} box-type transformer high voltage side injecting into collector lines, which can be got from Eq. 3.

The voltage of the k+1^{th} box-type transformer high voltage side (i.e. the voltage at the head of k+1^{th} collector line) $U_{2,k+1}$, the active and reactive power $P_{\text{line2},k}$ $Q_{\text{line2},k}$ at the head of k^{th} collector line are

$$U_{2,k+1} = \sqrt{\left[U_{2,k} - \left(P_{z1.k} r_k l_k + Q_{z1.k} x_k l_k\right)/U_{2,k}\right]^2 + \left[\left(P_{z1.k} x_k l_k - Q_{z1.k} r_k l_k\right)/U_{2,k}\right]^2} \tag{6}$$

$$P_{\text{line2},k} = P_{z1,k} - \left(P_{z1,k}^2 + Q_{z1,k}^2\right) r_k l_k / U_{2,k}^2 \tag{7}$$

$$Q_{\text{line2},k} = Q_{z1,k} - \left(P_{z1,k}^2 + Q_{z1,k}^2\right) x_k l_k / U_{2,k}^2 + U_{2,k+1}^2 b_k l_k / 2 \tag{8}$$

Finally, the voltage $U_{2,n}$ of the n^{th} box-type transformer high voltage side, the active power $P_{\text{line2},n\text{-}1}$ and reactive power $Q_{\text{line2},n\text{-}1}$ at the head of n-1^{th} collector line.

3.3 *Establish Equation of Collector Lines Maxmium Length*

The n_s collector lines converge into the booster transformer which connect to the equivalent power system by transmission line as shown in part C in Fig. 1, shown in detail in Fig. 4, where r_n, x_n and b_n are the resistance, reactance and ground susceptance of per unit length of the n^{th} collector line respectively, which is the nearest to the booster transformer; l_n is the length of the n^{th} collector line which is the only parameter to be calculated; R_T and X_T are the resistance and reactance of the booster transformer; r_G, x_G and b_G are the resistance, reactance and ground susceptance of per unit length of the wind farm transmission line, and l_G is the

length of the wind farm transmission line; U_0 is the voltage of the equivalent source of power system; R_0 and X_0 is the equivalent resistance and reactance of power system.

$U_{2,n}$, $P_{\text{line2, }n\text{-1}}$ and $Q_{\text{line2, }n\text{-1}}$ are obtained by the calculation in 3.2. As shown in Fig. 4, the active power $P_{\text{z1},n}$ and reactive power $Q_{\text{z1},n}$ at the end of n^{th} π-type equivalent circuit impedance are

$$P_{\text{z1},n} = P_{\text{line2},n-1} + P_{2,n} \tag{9}$$

$$Q_{\text{z1},n} = Q_{\text{line2},n-1} + Q_{2,n} + U_{2,n}^2 b_n l_n / 2 \tag{10}$$

where, $P_{2,n}$ and $Q_{2,n}$ are the active power and reactive power of the n^{th} WG unit injecting into the collect line, which can be calculated by Eq. 3. The active power $P_{\text{line2},n}$, reactive power $Q_{\text{line2},n}$ at the head of n^{th} π-type equivalent line and the voltage U_{T} of booster transformer low voltage bus are respectively

$$P_{\text{line2},n} = P_{\text{z1},n} - \left(P_{\text{z1},n}^2 + Q_{\text{z1},n}^2\right) r_n l_n / U_{2,n}^2 \tag{11}$$

$$Q_{\text{line2},n} = Q_{\text{z1},n} - \left(P_{\text{z1},n}^2 + Q_{\text{z1},n}^2\right) x_n l_n / U_{2,n}^2 + U_{\text{T}}^2 b_n l_n / 2 \tag{12}$$

$$U_{\text{T}} = \sqrt{\left[U_{2,n} - \left(P_{\text{z1}.n} r_n l_n + Q_{\text{z1}.n} x_n l_n\right)/U_{2,n}\right]^2 + \left[\left(P_{\text{z1}.n} x_n l_n - Q_{\text{z1}.n} r_n l_n\right)/U_{2,n}\right]^2} \tag{13}$$

In the equivalent model, the wind farm has n_{s} series collector lines, and each line has n WGs. What's more, the rest $n_{\text{r}} = N - n_{\text{s}} \cdot n$ WGs and box-transformer directly connect to the booster transformer low voltage bus, which is shown in part D of Fig. 1. The calculation method of injecting power $P_{2,\text{rate}}$ and $Q_{2,\text{rate}}$ are basically similar to the other WGs, which can be obtained by Eq. 3. The difference is that the voltage of the box-transformer high voltage bus is its ratings. And then the active power P_{T} and reactive Q_{T} injecting into the low voltage bus of booster transformer are respectively

$$P_{\text{T}} = n_{\text{s}} P_{\text{line2},n} + \left(N - n_{\text{s}} n\right) P_{2,\text{rate}} \tag{14}$$

$$Q_{\text{T}} = n_{\text{s}} Q_{\text{line2},n} + \left(N - n_{\text{s}} n\right) Q_{2,\text{rate}} \tag{15}$$

The booster transformer, transmission line, and equivalent power system are shown in Fig. 4. The voltage, output active power and reactive power of the point of common coupling (PCC) U_{PCC}, P_{PCC} and Q_{PCC}, voltage, output active power and reactive power of power grid substation U_{G}, P_{G} and Q_{G} are respectively:

$$U_{\mathrm{PCC}} = k_{\mathrm{T}}\sqrt{\left[U_{\mathrm{T}} - \left(P_{\mathrm{T}}R_{\mathrm{T}} + Q_{\mathrm{T}}X_{\mathrm{T}}\right)/U_{\mathrm{T}}\right]^2 + \left[\left(P_{\mathrm{T}}X_{\mathrm{T}} - Q_{\mathrm{T}}R_{\mathrm{T}}\right)/U_{\mathrm{T}}\right]^2} \quad (16)$$

$$P_{\mathrm{PCC}} = P_{\mathrm{T}} - \left(P_{\mathrm{T}}^2 + Q_{\mathrm{T}}^2\right)R_{\mathrm{T}}\Big/U_{\mathrm{T}}^2 \quad (17)$$

$$Q_{\mathrm{PCC}} = Q_{\mathrm{T}} - \left(P_{\mathrm{T}}^2 + Q_{\mathrm{T}}^2\right)X_{\mathrm{T}}\Big/U_{\mathrm{T}}^2 \quad (18)$$

$$U_{\mathrm{G}} = \sqrt{\left[\frac{P_{\mathrm{PCC}}x_{\mathrm{G}}l_{\mathrm{G}} - \left(Q_{\mathrm{PCC}} + b_{\mathrm{G}}l_{\mathrm{G}}U_{\mathrm{PCC}}^2/2\right)r_{\mathrm{G}}l_{\mathrm{G}}}{U_{\mathrm{PCC}}}\right]^2 + \left[U_{\mathrm{PCC}} - \frac{P_{\mathrm{PCC}}r_{\mathrm{G}}l_{\mathrm{G}} + \left(Q_{\mathrm{PCC}} + b_{\mathrm{G}}l_{\mathrm{G}}U_{\mathrm{PCC}}^2/2\right)x_{\mathrm{G}}l_{\mathrm{G}}}{U_{\mathrm{PCC}}}\right]^2} \quad (19)$$

$$P_{\mathrm{G}} = P_{\mathrm{PCC}} - \left[P_{\mathrm{PCC}}^2 + \left(Q_{\mathrm{PCC}} + U_{\mathrm{PCC}}^2 b_{\mathrm{G}}l_{\mathrm{G}}/2\right)^2\right]r_{\mathrm{G}}l_{\mathrm{G}}\Big/U_{\mathrm{PCC}}^2 \quad (20)$$

$$Q_{\mathrm{G}} = Q_{\mathrm{PCC}} + U_{\mathrm{PCC}}^2 b_{\mathrm{G}}l_{\mathrm{G}}/2 + U_{\mathrm{G}}^2 b_{\mathrm{G}}l_{\mathrm{G}}/2 - \left[P_{\mathrm{PCC}}^2 + \left(Q_{\mathrm{PCC}} + U_{\mathrm{PCC}}^2 b_{\mathrm{G}}l_{\mathrm{G}}/2\right)^2\right]x_{\mathrm{G}}l_{\mathrm{G}}\Big/U_{\mathrm{PCC}}^2 \quad (21)$$

Finally, the higher degree equation with an unknown l_n, the length of the n^{th} collector line which is closest to booster transformer, is obtained, which is

$$f\left(l_n\right) = U_0 - \sqrt{\left[U_{\mathrm{G}} - \left(P_{\mathrm{G}}R_0 + Q_{\mathrm{G}}X_0\right)/U_{\mathrm{G}}\right]^2 + \left[\left(P_{\mathrm{G}}X_0 - Q_{\mathrm{G}}R_0\right)/U_{\mathrm{G}}\right]^2} = 0 \quad (22)$$

where, U_0 is the voltage of power system equivalent source, which is known.

3.4 *The Calculation of the Collector Lines Maxmimum Length*

Eq. 22 is a higher degree equation which has not the general solution, so it only can be solved by numerical methods. Two-point secant method is a root-finding method without derivative operations. For equation $f(x)$=0, two-point secant method use not only the previous step function values at x_{k-1}, but also the function value at x_k to construct iterated function, which can improve the convergence rate of iteration. The iterative formula of two-point secant method is

$$x_{k+1} = x_k - f\left(x_k\right)\cdot\left(x_k - x_{k-1}\right)\Big/\left[f\left(x_k\right) - f\left(x_{k-1}\right)\right] \quad (23)$$

$$tol_{k+1} = \left| x_{k+1} - x_k \right| \tag{24}$$

When satisfying the convergence conditions $tol \le \varepsilon$, the iteration ends, where ε is a small positive number.

Finally, the maximum length L of collector line, from the extremity WG of collector line to the booster transformer, is obtained

$$L = \sum_{k=1}^{n-1} l_k + l_n \tag{25}$$

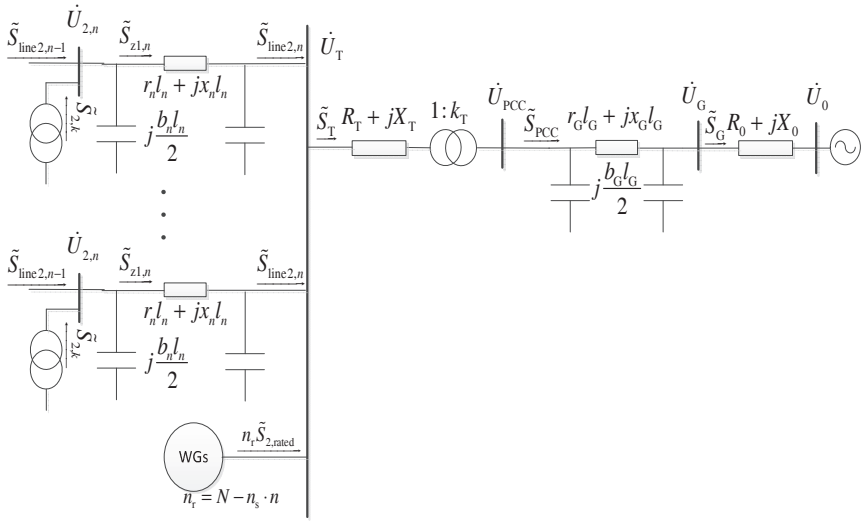


Fig. 4. Schematic of n_{s} collector lines converge into the equivalent power system by transformer and transmission line

4. Simulation and Analysis

The proposed method is calculated and verified by the example of an actual mountain wind farm in Hunan China. The wind farm consists of N=25 WGs whose rated power is 2MW. The WGs are connected by 3 collector lines, and the collector line A, B, C has 8, 8, 9 WGs respectively. The collector lines of the wind farm are cable, and the connection of WGs in each collector line is different.

The example considers 15 conditions of different lengths of transmission line and varying system equivalent reactance of the wind farm respectively. The calculation result of the proposed method, the engineering method and the actual wind farm are shown respectively. Because the wind farm has 3 collector lines, there are 3 maximum lengths of collector lines in each condition and the average value, the maximum value and the minimum value are given. When calculating by

the proposed method, the number of WGs connected to each collector line set to be n=8; the number of collector lines which connect WGs and booster transformer of the equivalent wind farm set to be n_s=3; the distance between adjacent WGs connecting to the same collector line of the equivalent wind farm set to be the actual average value, i.e. l_k=l_{ave}=0.8km (k=1, 2, …, 7). With the two-point secant method to solve Eq. 25, the ε=10^{-6}. In the engineering method, the voltage of the booster transformer low voltage bus is the average value of 15 cases, i.e. 0.9924p.u. and the rest of the parameters are the same as the calculation parameters of the proposed method.

Table 1. Calculation results of wind farm collector lines maximum length

Calculation parameters		Results of calculation L (km)		Results of actual maximum length (km)			Error of the proposed method (km) *			Error of the engineering methods (km) *		
l_G[km]	X_0[p.u.]	proposed	engineering	ave	max	min	ave	max	min	ave	max	min
0	0.001	11.68	9.8	12.32	12.63	11.78	-0.64	-0.95	-0.10	-2.52	-2.83	-1.98
0	0.01	11.97	9.8	12.60	12.92	12.04	-0.63	-0.96	-0.08	-2.80	-3.12	-2.24
0	0.1	15.18	9.8	15.70	16.24	15.03	-0.51	-1.06	0.15	-5.90	-6.45	-5.23
5	0.001	10.63	9.8	11.22	11.50	10.71	-0.58	-0.87	-0.08	-1.42	-1.70	-0.91
5	0.01	10.93	9.8	11.50	11.77	10.99	-0.57	-0.84	-0.06	-1.70	-1.97	-1.19
5	0.1	14.26	9.8	14.72	15.19	14.08	-0.46	-0.94	0.17	-4.92	-5.39	-4.28
10	0.001	9.62	9.8	10.15	10.47	9.68	-0.53	-0.85	-0.06	-0.35	-0.67	0.13
10	0.01	9.93	9.8	10.44	10.75	9.96	-0.52	-0.82	-0.03	-0.64	-0.95	-0.16
10	0.1	13.36	9.8	13.76	14.17	13.17	-0.41	-0.82	0.19	-3.96	-4.37	-3.37
15	0.001	8.64	9.8	9.11	9.46	8.67	-0.47	-0.83	-0.04	0.70	0.34	1.13
15	0.01	8.96	9.8	9.42	9.76	8.97	-0.46	-0.81	-0.02	0.39	0.04	0.83
15	0.1	12.48	9.8	12.84	13.18	12.27	-0.36	-0.70	0.21	-3.04	-3.38	-2.47
20	0.001	7.68	9.8	8.10	8.49	7.70	-0.41	-0.81	-0.02	1.70	1.31	2.10
20	0.01	8.01	9.8	8.42	8.80	8.01	-0.40	-0.79	0.01	1.38	1.00	1.79
20	0.1	11.63	9.8	11.94	12.22	11.41	-0.31	-0.59	0.23	-2.14	-2.42	-1.61

* Error = Results of calculation L - Results of actual maximum length.

5. Conclusion

This paper presents a method for rapid calculation of the maximum length of wind farm collector lines. The method accurately takes power loss of the wind farm collector system and transmission system, which have impact on wind farm voltage distribution, into account, to make up the defect of excessive error of usual engineering method; it represents external power system with simple transmission system to avoid large power flow calculation and reduce the calculation complex degree greatly.

The proposed method is calculated and verified by the example of an actual wind farm in Hunan China. The results show that the maximum error is less than 1km in each case and the proposed method can calculate the maximum length of wind farm collector lines accurately. Compared with the engineering method, the proposed method has higher precision and wider adaptability, which can be used for wind farm planning and design, especially in projects like wind farm booster substation locating and rapid determination that whether adjacent wind farms could share the same booster substation to send out wind power.

References

1. State Grid. Depth provisions of large-scale power transmission system planning and design content (draft), Beijing: State Grid, 2014.
2. Z.-J. Sun, J. An, S. Li, et al, The temporal and spatial characteristics analysis of voltage in wind farm considering wind power fluctuation, *Journal of north-east dianli university*, Vol. 33, NO. 1/2, 2013, pp. 115-119.
3. X.-H. Yang, Simulation analysis of low voltage through characteristic for Ningxia Jiaze wind farm, *Ningxia Electric power*, No. 3, 2014, pp. 20-26.
4. D.-H. Li, C.-G. Tian, X.-F. Chang, Low Voltage Ride Through Characteristic Evaluation of wind farm based on improved wind turbine transient model, *Jilin Electric Power*, Vol. 41, NO. 1, 2013, pp. 18-20.
5. X.-L. Jiang, Z. Xiang, Z.-J. Zhang, et al, Predictive Model for Equivalent Ice Thickness Load on Overhead Transmission Lines Based on Measured Insulator String Deviations, *IEEE Transactions on Power Delivery*, Vol. 29, NO. 4, 2014, pp. 1659-1665.
6. L. Yang, Y.-P. Hao, W.-G. Li, et al, Relationships among transmission line icing, conductor temperature and local meteorology using grey relational analysis, *High Voltage Engineering*, Vol. 36, NO.3, 2010, pp. 775-781.
7. X.-B. Huang, L.-S. Ouyang, Y.-N. Wang, et al, Analysis on Key influence factor of transmission Line Icing, *High Voltage Engineering*, Vol. 37, NO.7, 2011, pp. 1677-1682.
8. J. Gao, X. Cai, Y.-F. Cao, Analysis and Compari-son of wind farm models taking account of Feeder cable and internal loss, *Power System and Clean Energy*, Vol. 27, NO. 3, 2011, pp. 60-63.
9. L. Xu, I. Syed, Reliability Issues of Offshore Wind Farm Topology, Proceedings of the 10th International Conference on *Probabilistic Methods Applied to Power Systems* (PMAPS 2008), 25-29, May. 2008.
10. L. Zhang, C. Zhe, Efficiency Evaluation for Off-shore Wind Farms, International Conference on *Power System Technology* (PowerCon 2006), 22-26 Oct. 2006.

11. S. Dutta, T. J. Overbye, A Clustering based Wind Farm Collector System Cable Layout Design, 2011 *IEEE Power and Energy Conference* at Illinois (PECI), 25-26, Feb. 2011.
12. S. Dutta, T. J. Overbye, Optimal Wind Farm Collector System Topology Design Considering Total Trenching Length, *IEEE Transaction on sustainable energy*, Vol. 3, NO.3, 2012, pp. 339-348.
13. Ichiro Kousaka, Daisuke Eguchi, DaikiYamashita, et al. Cost-Minimum Network Planning in Large Wind Farm using Revised Prim's Algorithm, 2014 *IEEE PES Innovative Smart Grid Technologies Conference* (ISGT), 19-22 Feb. 2014.
14. Ala A Tamimi, Anil Pahwa, Shelli Starrett. Method for Assessing System Impact of Increasing Wind Farm Sizes Above Their Maximum Limits 2011 *IEEE Power and Energy Society General Meeting*, 24-29 July 2011.
15. Jenkins, M. Scutariu, K. S. Smith, Offshore Wind Farm Inter-Array Cable Layout, 2013 *IEEE Grenoble PowerTech* (POWERTECH), 16-20 June 2013.
16. C. Shadi, T. Ahmadreza, M.-S. Zahra, et al. Selection of HV Equipment for Large Wind Parks Connections with Power System as Stability Parameter and Direction for Network Planning, 2011 10th International Conference on *Environment and Electrical Engineering* (EEEIC), 8-11 May 2011.

Study on Anti-Clogging Performance of Large Diameter Fluidized Bed Sewage Heat Exchanger

Hai Yang Bi†

Geotechnical & Structural Engineering Institute, Dalian University, Dalian, 116622, China
†E-mail: ocean19@126.com,

Yong Mao Shang

Capital Construction, Dalian University, Dalian, 116622, China
E-mail: dldx_sym@163.com,

Xiang Hong Gu

Geotechnical & Structural Engineering Institute, Dalian University, Dalian, 116622, China
E-mail: zhzhgxh@163.com

Urban sewage can be used as cool/heat source, but clogging problem and low heat-transfer coefficient resulted by fouling limit its application because water quality can't satisfy country standard. This paper proposes a high thermal efficiency and anti-clogging heat exchange device which can completely solve these problems of urban sewage utilization. In this paper, an experimental system of large diameter fluidized bed sewage heat exchanger was built, and the anti-clogging performance was tested by this system. The result shows that it can solve the clogging problem of sewage side. This research can improve the efficiency of energy utilization system, for sewage source heat pump system (or cooling system) to provide technical guarantee for reliable operation.

Keywords: sewage source heat pump; anti-clogging; large diameter fluidized bed sewage heat exchanger.

1. Introduction

With increasing crisis of energy and water resource, people pay more attention to the utilization of low temperature energy resource[1, 2]. Sewage-source heat pump technology is a way of HVAC energy saving the most practical. Utilizing urban sewage as cooling and heat sources may decrease amount of heat which is put into the air, ease the high temperature warm-hearted island appearance of town and

have a great effect on the atmospheric pollution and the environmental protection[3,4].

2. Problems and Solution

Its unstable water quality can not meet the requirement of the heat exchange equipment operation, urban sewage contains a variety of large and small scale dirt suspended solid and soluble compounds, the former is caused by blocked heat exchange area, the latter forms a high thermal resistance and seriously affects the normal operation of heat pump system. For economically feasible utilization of sewage cooling and heat sources, we can only make on sewage pretreatment with physical filtration, filtering surface hydraulic continuous regeneration of filter effectively solved the problems of contamination jams heat exchange equipment, but still the sewage-source heat pump system for water heat transfer in the sewage contains a lot of small scale sewage sundry, leading to the build-up of hair kind of dirt in the heat exchanger, and large equipment of heat transfer equipment because of low heat exchange performance, as shown in Fig. 1. Currently the main difficulties of utilization of sewage water heat energy mainly result from two aspects: hair dirt clog sewage heat exchanger; fouling in heat surface reduces the heat transfer performance, and results in large heat-transfer equipment in the practical application.



Fig. 1 Polluted heat-exchange unit

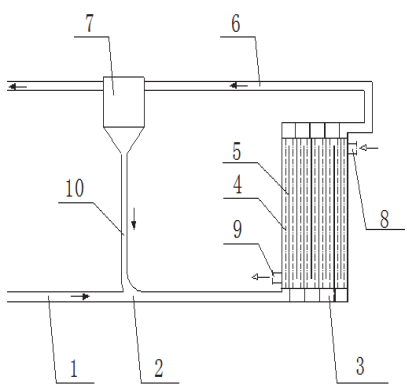


Fig. 2 Schematic of fluidized bed sewage heat exchanger of large diameter shell and tube

Large diameter heat exchanger can prevent hair clogged, and solid-liquid fluidized bed technique can be used not only to increase convection coefficient, but also to restrict fouling growing, it has prospect of wide application in sewage source heat pump[5,6,7]. This paper proposes a high thermal efficiency,

anti-clogging, and easy cleaning heat exchange device which is shown in Fig. 2 and Fig. 3.



Fig. 3 Sewage heat exchanger of large diameter shell and tube

3. Experimental Research of Anti-Clogging Performance

Anti-clogging performance of the device is unknown. In this paper, an experimental system of large diameter fluidized bed sewage heat exchanger which is shown in Fig. was built, mainly includes sewage reservoir (1), pump (2), rotameter (3), liquid–solid separator (4), solid-return pipe (5), mercury manometer of U type (6), heat exchanger (7) .The sewage pumped from sewage reservoir, entered into the heat exchanger through the bottom of downward-flowing pipe; according to gravity sedimentation and jet action of muzzle, solid particles were separated from liquid–solid separator through downward-flowing pipe into the heat exchanger and realized cycling use. Liquid and particles moved concurrently upwards into the heat exchanger and were separated in the liquid– solid separator, and then sewage was returned to sewage reservoir.

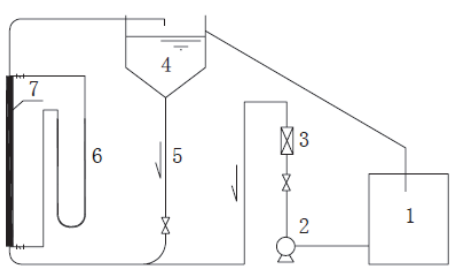


Fig. 4 Schematic of an experimental system of large diameter fluidized bed sewage heat exchanger

The anti-clogging performance was tested by this system. The experiment includes two kinds of working conditions: 1. anti-clogging performance test of heat exchanger of large diameter; 2. anti-clogging performance test of fluidized

bed heat exchanger of large diameter. Experimental sewage adds a certain amount of hair. A continuous cycle of 30 minutes, open the heat exchanger clogged sewage side, and view the blocking situation.

4. Results and Discussion

Results of two kinds of working conditions show that hair does not stay in the sewage pipe, no wall phenomenon. That is, hair can pass through the sewage pipe smoothly, and no obvious blocking phenomenon occurs. So the results prove that large diameter heat exchanger can prevent hair clogged

5. Summary

According to key problems of the sewage side in sewage source heat pump system, this paper proposes a high thermal efficiency, anti-clogging, and easy cleaning heat exchange device, and an experimental system of large diameter fluidized bed sewage heat exchanger was built. The anti-clogging performance was tested by this system. The experimental results that the device can completely solve the problem of hair clogged with large diameter heat exchanger. The heat transfer performance of the device is in need of further study. This research can improve the efficiency of energy utilization system, for sewage source heat pump system (or cooling system) to provide technical guarantee for reliable operation.

Acknowledgements

This work was financially supported by the National Youth Fund Project (NO.51108051) and the Project of Housing and Urban-rural Development (K1201392).

References

1. Jun Yin, Lei Chen, Heli Wang. *Resource regeneration of city sewage and utilization of sewage heat energy*. Beijing: Chemical industry press, 2003.
2. Bi Haiyang, Duanmu Lin, Li Zhen, *2004, SET2005-4th International Conference on Sustainable Energy Technologies*, The Key-question Analysis on Reclamation and Utilization of Non-cycle Water Heat Energy and Its Recent Developments, shandong jinan, 407-410.
3. Bi Haiyang, Duanmu Lin, Zhu Yingxin. Testing and analyzing on once-through water performance of single pipe solid-liquid fluidized bed heat exchanger. *The 7th International Symposium on Test and Measurement*. Beijing: 2007. 3161~3164.

4. YOSHII T., 2001, Technology for Utilizing Unused Low Temperature Difference Energy, *Journal of the Japan Institute of Energy*, 8, P696-706.
5. Zheng Ying, Zhu Jingxu, 2000, Overall pressure balance and system stability in a liquid-solid circulating fluidized bed, *Chemical Engineering Journal*, 79, 2, P145-153.
6. Bi Haiyang, Shang Yongmao, Gu Xianghong, *2014, the 4th International Conference Energy, Environment and Sustainable Development (EESD 2014),* Key Problem Analysis and Solution on Intake Water and Heat Transfer of Sewage-source Heat Pump System, Nanjing.
7. Feng Xiaogui, Jing Shan, Wu Qiulin, 2003, The hydrodynamic behavior of the liquid-solid circulating fluidized bed ion exchange system for cesium removal, *Powder Technology*, 134, 3, P235-242.

A Discussion on the Feasibility of Large Consumers Direct Power Purchasing

Yang Gao, Aoran Xu, Liu Zhang, Xiuping Wang, Chunyu Qu

School of Electrical Engineering, Shenyang Institute of Engineering, Shenyang, Liaoning, 110136 China
E-mail: 657080195@qq.com, 656085652@qq.com, 451932741@qq.com, 309904066@qq.com, 927309041@qq.com

Hongyu Zhong†

Graduate Department, Shenyang Institute of Engineering, Shenyang, Liaoning, 110136, China
†E-mail: 313440302@qq.com

Taking domestic a city of Liaoning called high tech Development Zone (hereinafter referred to as "high tech Zone") as an example, based on the large consumers direct power purchase access conditions, discussing the feasibility of "high tech Zone" to carry out large consumers direct power purchase, combined with the actual situation of a power plant in the area(hereinafter referred to as the "H power plant"), studying access conditions of generation companies and power consumption companies, analyzing of generation, supply and consumption power three party benefit pattern. According to the data of the power system, to carry out pilot projects possess good economy and practicality in "high tech Zone".

Keywords: High Tech Zone; Large Customers; Direct Power Purchase; Power Marketing.

1. Introduction

Power reform in ten years, large consumers direct power purchasing has become an important content of power system reform of China, which showed better economy and practicality than traditional sale/purchase power, breaking the traditional monopoly mode of Power Grid Corp management, simplify the intermediate links of the transport, distribution and supply, reducing the cost of generation, supply and consumption power three party, updating the market competition mechanism, reducing the standard of power requirements of Power Grid Corp at the same time[1]. Since April 2004, the State Electricity Regulatory Commission and National Development and Reform Commission issued

〈〈"Interim Measures" pilot power Customers purchase power from generation enterprises directly〉〉, in March 8, 2005, pilot direct power purchase in Jilin Longhua power Limited by Share Ltd pilot to Jilin Carbon Co. Ltd. opened the prelude for the first time, then the pilot in Guangdong, Sichuan, Shanxi and Gansu were launched one after another respectively, and achieved some good results. Not but issued in Liaoning, because the pilot to carry out need to satisfy the access conditions [2] the of large consumers direct power purchasing and the advantages and disadvantages of equilibrium. This paper is based on the access conditions, taking the introduction of pilot policy as conditions in Liaoning, considering the gains and losses of generation, supply and consumption power three party, discussing the feasibility of "high tech Zone" to carry out the large consumers direct power purchasing, and to carry out pilot projects will acquire reform progress in the field of the future Liaoning power marketing.

2. The Definition and the Transaction Mode of Large Customers Direct Power Purchase

Large consumers direct power purchasing refers to meet the access conditions for generation companies and power consumption companies, with separation of power plants from the power grids and competitive bidding as the prerequisite, in accordance with principle of the voluntary participation and independent consultation, to carry out sale/purchase power transactions directly. Power Grid Corp provides transmission services in accordance with the regulations, this is a new power transactions mode of national policy to encourage and support. The mode includes passing grid direct power purchase and special line direct power purchase [3]. As shown in Fig. 1.

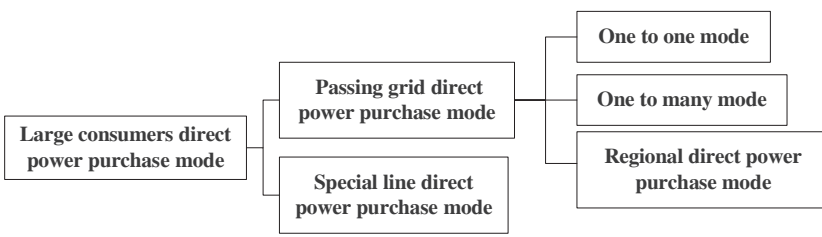


Fig. 1 Large consumers direct power purchase transactions mode

3. Feasibility Analysis of "High Tech Zone" to Carry out the Large Consumers Direct Power Purchase

Ten years has passed, the large consumers direct power purchasing has been a domestic strategic route in china’s power reform, which has been launched in

Guangdong, Sichuan, Shanxi, Gansu. In fact, Liaoning is also in the wait-and-see, because once Liaoning introduces to carry out pilot projects must joint with many uncertain relations, such as conditions, social responsibility, benefit and risk of generation, supply and consumption power three party etc. If Liaoning carry out a pilot policy, the following will combine the pilot policy and the basic situation of "high tech Zone" and "H power plant", in-depth analyzing pilot launch in "high tech Zone" will bring what benefit the pros and cons is?

3.1. *The basic situation of the "high-tech Zone"*

"High tech Zone" is a provincial level development zone approved by the provincial government in 2007, is one of the key support of the city government industrial parks, the planning area of 15.7 square kilometers. South Park is the service management area, central to Huajin Industrial Zone, and north is the chemical industrial Zone. High tech Zone has 13 key enterprises, details is as shown in Table 1.

"High tech Zone" has the following conditions:

a) Have the qualifications of a legal person, financial independent accounting, can undertake economic entity of civil liability independently.

b) Electricity load is relatively stable, the energy consumption per unit output value is low, low emission.

c) Key enterprises of high tech Zone 2013 annual power consumption was 571204700 KW•h (as shown in Table 1).

From the above information can be seen, "high tech Zone" power consumption enterprise has a certain scale of production, larger development potential, the approved annual power consumption being in more than 60000000 KW•h, as power consumption large Customers may be trying to implement the pilot.

3.2. *The basic situation of "H power plant"*

"H power plant" is located in "high tech Zone", is by the power of holding the establishment of investment limited company of large state-owned enterprises. The planning installed capacity of the project is 4 * 350MW supercritical unit construction by stages, the project construction is to meet the needs of heat load of the heating transformation and growing, and meet industrial heat load growth of the petroleum chemical industry park.

"H power plant" has the following conditions:

a) Have the qualifications of a legal person, financial independent accounting, can undertake generation companies of civil liability independently.

b) Belonging to the Liaoning Province Public thermal power enterprises.

c) The single machine capacity of 350000 KW, the total installed capacity of 1400000 KW, a phase of the project construction scale is 2 * 350000 KW supercritical coal-fired heating unit project.

From the above information can be seen, "H power plant" in line with national industrial policy, generation enterprises conditions of grid connected operation, and power supply capacity is loose relatively. "H power plant" makes full preparations as generation companies for the strategic needs of large consumers direct power purchasing.

3.3. *Economic benefit analysis of "high tech Zone" to carry out large consumers direct power purchasing*

From the analysis of 2.1, 2.2 section, regional direct power purchase in the way of passing grid direct power purchase is more suitable for "high tech Zone" to carry out large consumers direct power purchasing. So to carry out pilot projects will involve three parties' benefits inevitably: generation companies, power consumption companies and Power Grid Corp.

Concreting to analyze this three party benefit is following:

(1) Generation companies (i.e. "H power plant") benefit analysis focus on the direct power purchase mode benefits of "H power plant", we make the following assumptions:

1) Considering only one year "H power plant" with fixed quantity Q (KW•h) for large consumers transaction.

2) Passing grid costs by "H power plant" and large consumers average allocation, so "H power plant" accounted for only 1/2, its costs charge by T yuan /KW•h.

3) P1 is the contract price of "H power plant" and Power Grid Corp of "high tech Zone" in a year; P2 is the contract price of "H power plant" and large consumers direct power purchase in a year. Through the data logic assumption, income L [4] mathematical model that we derive is as follows:

$$L = (P_2 - P_1 - T/2) \times Q$$

From the mathematical model of L can be seen, "H power plant" to carry out the pilot, when the approved contract price electricity price is lower than the direct power purchase, namely P2> P1+T/2, "H power plant" will choose direct

supply and increase capacity, improve resource utilization, improve the efficiency of power generation, so as to increase the total revenue.

(2) Power consumption companies (i.e. "high tech Zone") benefit analysis

"High tech Zone", as a regional large consumers, through the direct power purchasing can be obtained thinner price than traditional, thus benefit will show the ripple growth. Passing grid cost analysis of comprehensive Guangdong, Sichuan, Shanxi, Gansu pilot, can make that the Power Grid Corp of "high tech Zone" charge $0.151 yuan/kW \cdot h$ as passing grid cost, "H power plant" ex factory price is $0.3 yuan/kW \cdot h$, could be launched sale of power price of "H power plant" is:

$$0.3 yuan/kW \cdot h + 0.151 yuan/kW \cdot h = 0.451 yuan/kW \cdot h$$

13 key power consumption enterprises traditional sale price of "high tech Zone" and direct power purchase price make the comparative form, as shown in table 1:

From the data in the table can be seen, power consumption of "high tech Zone" 13 power consumption enterprises in the years will be up to 571204700 KW•h, in which condition, the whole "high tech Zone" increasing the total profit reached 131062251 yuan for a year.

(3) Benefit analysis of "high tech Zone" Power Grid Corp

"High tech Zone" to carry out large consumers direct power purchasing is change the mode of transaction of from the view of surface, is that "H power plant" and "high tech Zone" get rid of the original part of the economic costs, including the construction funds and cross subsidies, while transferred to the Power Grid Corp of "high tech Zone" in essence[5]. So that Power Grid Corp of "high tech Zone" not only hold top this gains and losses but wear a lot of social responsibility pressure, so the grid "efficiency bottleneck" comes ripple effect, is extremely unfavorable with the Power Grid Corp of "high tech Zone". But Power Grid Corp of "high tech Zone" only bear the transmission task, with its flexible transmission price signals will determine the position signal of the power market, and promote the guiding role of the price lever in the power market supply and demand, not only the use of power market has become better flexibility, but also conform to the power system reform direction of our country.

Table 1 The contrast table of 13 key power consumption enterprises "high tech Zone" economic benefits improvement in 2013

Serial numbe	Name of the enterprise	Traditional power sale price (yuan)	Direct power purchase price (yuan)	Benefit improvement for consumers (yuan / kw·h)	Annual power consumption (ten thousand kw·h)	Increase total profit a year (ten thousand yuan)
1	"High tech Zone" northern asphalt Limited by Share Ltd	0.70	0.451	0.249	4348.44	1082.7616
2	"High tech Zone" Liaohe heavy industry equipmen Co. Ltd.	0.80	0.451	0.349	2029.77	708.3897
3	"High tech Zone" jump photoelectric science and Technology Co Ltd	0.70	0.451	0.249	64.95	16.1726
4	Liaoning Shanqi Jinxi Equipment Manufacturing Co Ltd	0.70	0.451	0.249	107.37	26.7351
5	Liaoning Xintian Pipe Industry Co., Ltd.	0.80	0.451	0.349	322.1	112.4129
6	"High tech Zone" Liaohe Oilfield vigorously Grou Co. Ltd.	0.60	0.451	0.149	1050.84	156.5752
7	"High tech Zone" Oder Petroleum Technology Service Co Ltd	0.80	0.451	0.349	60	20.94
8	"High tech Zone" Dongyue steel color plate Co., Ltd.	0.80	0.451	0.349	393	137.157
9	"High tech Zone" in the run Chemical Co., Ltd.	0.50	0.451	0.049	9729	476.721
10	"High tech Zone"Yuwang waterproof building material group(old factory)	0.70	0.451	0.249	255	717.12
11	"High tech Zone" Liaohe Oilfield pipe drilling tool manufacturing Co., Ltd.	0.70	0.451	0.249	575	143.175
12	Liaoning Tianyi Industry Limited by Share Ltd	0.70	0.451	0.249	185	46.065
13	Chinese Petro China Liaohe Petrochemical Company	0.70	0.451	0.249	38000	9462
Total					57120.47	13106.2251

4. Conclusion

Large consumers direct power purchase has become a fresh way of separation of power plants from the power grids and competitive bidding. If Liaoning province introduce pilot related policy, then the "high tech Zone" and "H power plant" can try carrying out pilot as generation companies and power consumption companies respectively, although Power Grid Corp of "high tech Zone" benefits dropped, but activating the power market marketing physique, conform with international direction of power marketing reform, it is in favor with the general public. If the "high tech Zone" carry out large consumers direct power purchase, it not only update benefit pattern of local power market "high tech Zone" three party, but also plays an important guiding significance for the city and the whole province's power reform development marketing.

Reference

1. Wen F S, David A K. Optimal Bidding Strategies for Competitive Generators and Large Consumers. *International Journal of Electrical Power and Energy Systems.* 2001.
2. *State Electricity Regulatory Commission.* Power users to buy electricity directly to the power generation enterprises Interim Measures for trial[R]. Electricity regulatory power. Transmission [2004] Document No. 17. 2004.
3. Senlin Zhang, Yao Zhang, Haoyong Chen. Large consumers direct power purchasing transaction research on several key problems[*J*]. *East China Electric Power*. 2009, 37(4): 24-25.
4. Binghong Chen. Study on the direct power supply for large consumers mode[D]. Tianjin, Tianjin University. 2009, 8: 24-25.
5. Yijun Jiang, Xuehong Li. Direct electricity purchasing mode effects on Power Grid Enterprise[c]. *Chinese society of Electrical Engineering*, Shaanxi xi'an: 2008.1-2.

Research on Distributed Generation and Its Application in Oil Field Distribution Power Network

Xu Jin*, Li hong-wei, Fang Wei

Southwest Petroleum University/School of Electrical Engineering and Information Chengdu, China
E-mail: 1lemonjin@126.com;
E-mail: lhwmail@163; villa1006@163

Integrated with the characteristics of oil field distribution power network and its renewable energy power generation conditions, this paper presents the foundation of distributed generation and its application in oil filed distribution power network. Combined with the standard distribution network modal, the improved back/forward sweep is applied to research the influence law of distributed generation on the power losses and voltage profile of oil filed distribution network which is based on associated gas power generation. The results shows that DGs could effectively reduce power losses and provide valuable voltage support only if they are rationally allocated according to their capacity, location, combining form and operation mode.

Keywords: Distributed Generation; Oil Field Distribution Power Network; Associated Gas Power Generation; Power Losses; Voltage Profile.

1. Introduction

Distributed generation (DG) is an electric power source: the power source in a few kilowatts to megawatts range which is connected directly to the customer side of the meter, that can be independent of the public power network to supply for a small amount of customers, and also can be connected to the power distribution network to provide electricity together with the public power network[1]. The operation mode and the capacity of the power source is determined by resources, environment benefit maximization and energy efficiency optimization. In recent years, with the continuous development of new energy, distributed generation technology is more and more widely applied in the small and medium-sized distribution network.

Different from other kinds of power distribution network, oil field distribution network directly geared to the needs of oilfield production, powered for the equipment of well lifting, oil field water injection, oil and gas water treatment and transportation, and it is the important guarantee system of oil field production, which gradually developed with the rolling development of oil field.

Oil field distribution network generally contains feeders of 6 kV, 10kV and 35kV, and 380/220 kV power transformer low voltage circuit, the main load is the pumping unit load, the load is fragmented, and has too many nodes, power supply area is large, and it is the multiple branch radial and long distance power supply mode, this operation mode is not flexible, the network loss is on the high side. The beam pumping unit is widely used in oil field, this kind of pumping unit has poor balance, the load fluctuation is large, the corresponding configuration of the motor rated capacity is large, and the actual operation of load under low load condition for a long time, that cause the overall distribution network run inefficiently for a long time, the grid power factor is low.

Because oil is the foundation of the national economy, the requirement on power supply reliability is higher. Combining with the characteristics of oil field distribution network, fully exploiting energy condition of oil field, it has a broad development potential to apply the distributed power generation technology to oil field power grid for establishing efficient energy utilization system and improving the overall level of oil field power grid[2].

On the one hand, oil field has rich resources of distributed generation. In the process of oilfield production of crude oil, are generally at the same time to obtain large amounts of associated gas, associated gas as a clean energy is converted to the distributed power supply to generate electricity by the micro gas turbine which has small volume, high efficiency and high power generation efficiency, and the output power is relatively stable[3]. According to the survey that by the end of 2012, Chang Qing oil field production area has constructed 133 associated gas power stations, 241 associated gas generator set, with a total installed capacity of 82.36 MW. Among them, with oil field distribution network parallel operation of the associated gas generator set, a total of 149 units, the total installed capacity is 62.89 MW[4].

On the other hand，Oil field is often in the vast rural areas, it has the rich renewable sources such as wind power and solar energy, although influenced by the weather obviously, it can used to supplement the associated gas power generation to provide oil field of crude oil heating, as well as daily life, through the technical means such as fan design, equipped with energy storage devices, etc.

2. Power Flow Calculation

2.1. *Modeling of DG*

Distributed generation can improve the reliability and economical efficiency of distribution network. But it will change the tidal current and voltage distribution

of the feeder, and will affect the trend of the distribution network, the network loss, and power quality, when the DG is access to distribution network. Power flow calculation is the main method for the quantitative analysis of the impact [5].

From the perspective of the access way of distributed power distribution network, the main flow calculation model of DG is divided into three categories: PQ node, PV node and PQ (V) node. It needs to analyze different forms of DG operation mode and control characteristic to decide how to choose the model of DG in the power flow calculation. Comprehensive analysis of various literature, in combination with the actual situation of oilfield distribution network, the oilfield associated gas resources is the priority choice of the distributed power supply selection, it realize the micro gas turbine to produce electricity,with photovoltaic and wind power to supplement[6].

The electricity from the micro gas turbine is high frequency alternating current (AC), which needs frequency conversion through the AC/AC or AC/DC/AC inverter to complete the grid-connected, the micro gas turbine has excitation and speed control system, the output energy and the voltage is a constant value that can be processed as PV node.

Most wind turbines in our country are asynchronous generator , when they produce active power at the same time also need to absorb a certain amount of reactive power on the grid, and reactive power that generators absorbed will be affected and limited by the node voltage, it usually be used as a PQ (V) node.

Photovoltaic power generation system connected to the electricity grid needs the inverter to convert direct current into alternating current that has the same phase and frequency with the power network, through controlling the maximum power point to control its active output, and through the automatic cutting capacitor to keep the photovoltaic power factor constant, thus it is used as PQ node in flow calculation.

2.2. *Basic principles and steps*

Traditional power flow calculation method can't meet the requirement of the distributed power generation system, and so far a large number of related research has been conducted, many algorithms have been proposed. Combining the distributed power characteristics of oil field distribution network, based on the traditional power generation algorithm, the reactive power correction method based on the node impedance matrix and voltage deviation is adopted in this paper to analyze the oilfield power flow which contain distributed power supply[7]. The power flow calculation method is briefly as follows:

When the distributed power is regarded as PQ node to be processed, constant power load model is adopted to simplify the process, the generator grid-connected node is used as negative power load node to be involved in the power flow calculation.

PQ (V) node processing methods are similar to PQ node, PQ (V) node is regarded as a negative power node to be involved in the calculation, it needs to note that the reactive power regulation in iterative process requires the combination with the type and parameters of DG, and through the last iteration of the voltage difference to calculate.

When process the PV node, the PV node can be regarded as PQ node to conduct the power flow calculation, after waiting for the results convergence, according to the results of power flow calculation to calculate the difference of given voltage value and the calculated value of the PV node. Then the difference as the voltage unbalance value is multiplied by the inverse matrix of node reactance matrix to calculate the reactive power correction of PV node. And stack the reactive power correction to the corresponding node, judge whether the revised reactive power output is beyond the normal range, choose reasonable reactive power values, then calculated again, judge whether it is convergent according to each node voltage difference.

Combined with the oilfield power grid, distributed generation is based on the associated gas generator set. At present, the single capacity of associated gas generator set is about 500kW, when the small-capacity distributed generation is connected to the power grid, it is rarely directly involved to adjust voltage. Furthermore, the exploration of associated gas is synchronized with the production of crude oil, and the generator output is relatively stable compared with wind energy and solar energy, and the load change is small, so the associated gas distributed generation can be simplified as PQ node for processing.

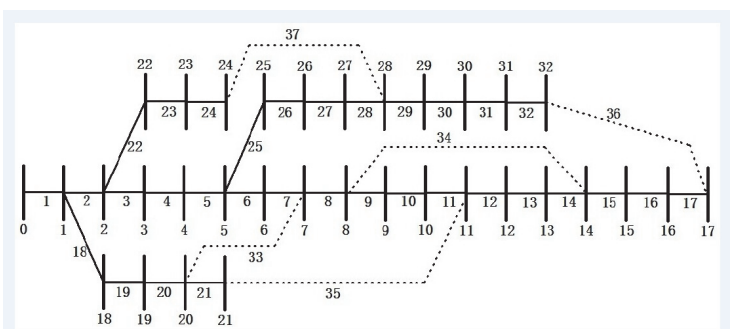


Fig.1 The topolgical structure for test system

3. Numerical Results

One radial distribution test system[8] with DG is shown in Fig. 1. The total active load is 3715kW, the total reactive load is 2300kvar. The total active load of test system is 3715kW, and the total reactive load is 2300kvar. The reference power is 10000kVA, the reference line voltage is 12.66kV, and convergence accuracy is $\varepsilon = 10^{-5}$.

The influences law of distributed generation on the power losses and voltage profile for oil filed distribution network is discussed in this section.

3.1. *Impact on voltage with different DG capacity*

Consider the simple condition that the location and operating mode of DG under certain circumstance. Two DGs were connected to grid at node 12, 29 with the same output, and were operating at lagging power factor 0.85. The total capacity of DGs were selected to be 30%, 40%, 50%, 60% of the total system loading, respectively.

Figure 2 shows that some node voltage deviation between the actual value and rating value has been exceed 7% without DG connected. While, each node voltage has significantly improved when DG are put into the system. The higher capacity ration between DG total output and the total system load, the higher voltage amplitude of each node. Of course, the DG output must be controlled within a reasonable range, many experiments show that when the DG output is too high, the voltage support will be high, and that may lead to some nodes voltage exceed the limit.

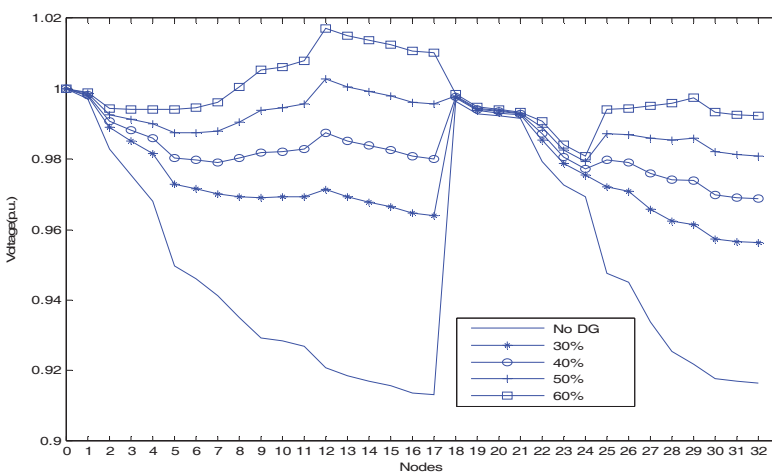


Fig. 2 Voltage profile with different DG capacity

Consider the installed capacity of associated gas generator in oil filed is small, it's a small percentage of the system load. So, the total capacity of DGs were selected to be 40% to analyze influence of DG location and operation mode on the system voltage.

3.2. *Impact on voltage with different DG location*

The simulation mainly focus on 1-17 feeder, a program on the feeder nodes were selected 5,10,12,14,17 DG placed as concentrated point. 5-32 feeders select 29 node as DG connected. The DG total output is 40% of the total system load.

The results show that the same output of DG placed at different positions, the difference of voltage distributions is mainly reflected in the area after access point node. Local maximum values are present in the vicinity of the line DG access point. Closer to the power source, the influence to power distribution on the line voltage is smaller. Instead, closer the end of the line, the greater the scope and the more obvious effect of improving voltage, but if the node and the capacity options discomfort, it will cause the node voltage exceeds the rated voltage, such as 17 nodes, and if the node is out of operation, it also will bring excessive voltage variations. Therefore, it should select a node location for distributed generation in the middle of the power line rearward.

3.3. *Impact on voltage with different running status*

In this section, the experiment simulation DG access in node 12 and node 28. The output power of DG accounted for 40% of the total load. Through changing the DG operation mode, to make it work in power factor 1, lagging and leading power factor 0.8, 0.85, 09.

Simulation results show that DG running with the lagging power factor can improve the feeder voltage, and the smaller lagging power factor, the greater the voltage amplitude. When DG working in the state of leading power, feeder voltage continues to reduce, and the smaller the lagging power factor, the faster voltage amplitude decrease. The power factor depends on the DG adopted by the technology, For example when DG interconnecting grid by inverter form, it can run under the unit power factor. When interconnection by synchronous motor, it can control power factor through the excitation regulator.

3.4. *Impact on power losses with different DG location*

In this section, 1-17 feeder was chosen as the major object. DG is connected to the grid in different node, running with the lagging power factor 0.85. The DG capacity is 743 + j460kVA.

Table 1 shows that with the DG interconnection location varying from the mains side to the line-terminal, system power losses decrease first and then increase. When DG is connected in 12 node, the system power losses is the lowest. This further proved that DG should be assembled in the middle-rearward position node of the line.

Table 1. System power losses with different DG location

Node number	System losses /kW	Node number	System losses /kW	Node number	System losses /kW
No DG	207.7	6	132.5	12	117.6
1	200.6	7	127.5	13	117.7
2	179.4	8	123.2	14	118.8
3	168.4	9	119.9	15	120.6
4	157.6	10	119.4	16	124.8
5	134.6	11	118.8	17	127.5

Table 2. System losses with different DG capacity

capacity ratio	No DG	15%	20%	25%	30%	40%	50%
System losses /kW	207.7	130.4	117.6	109.9	106.9	113.2	133.9

3.5. *Impact on power losses with different DG capacity and association form*

Table 2 lists the system power losses when DGs are concentrated in 12 node with different capacity.

The data shows that, when the DG capacity is from 25 to 30 percent of total load capacity, the loss of the system network is the lowest. Based on this, two experiments were carried out.

In the first experiment, DG total capacity accounts for 30 percent of the total load capacity. As already experiment stated, the 2, 5, 12 branch loss is bigger than others branch, and can get more effect on DG. So the scheme design is to choose the DG access the node which near the branch of the largest loss. The impact on system losses with DGs different association forms is studied. The simulation result is shown in Table 3.

Table 3 shows that the various association forms of DG can decrease system losses. Within reasonable limits, when the more decentralized the DG is, the heavier effect to decrease system losses it can give when concentrated on the same position.

The second test, respectively, for two association forms of DG, is designed to observe the influence law of system losses with different capacity. The simulation result is shown in Table 4. The DG combinations of 5, 10, 15 have

more obvious consumption effect than 10, 12, 15 combination. And when DG is running as 5, 10, 15 combination mode, the larger the DG total capacity is, the smaller system network loss is. But when DG total capacity reached 50%, for the 10, 12, 15 combination, the system losses increase instead, this phenomenon shows that the excessive increase of DG active power change the direction of the original active power, make the system losses increase, and also the node voltage is affected to certain extent.

Table 3. System power losses according to the different association of DG interconnection location

Compound mode	Node position	System losses /kW
Single DG	5	112.44
	12	106.93
	15	117.38
Two DG association	5+12	91.95
	5+15	92.38
	10+15	97.41
	12+15	104.65
Three DG association	5+10+15	86.98
	5+10+12	87.76
	5+12+15	89.05
	10+12+15	95.925
	10+14+16	98.67
	12+14+16	105.47

Table 4. System power losses according to the different association of DG location and capacity

Three DG Compound mode	5+10+15	10+12+15
capacity ratio	System losses /kW	System losses /kW
25%DG	100.6	95.925
30%DG	86.98	95.925
40%DG	75.37	95.41
50%DG	71.27	107.65

In order to further research the comprehensive influence of the DG capacity and position distribution for branch loss and voltage, the 30%, 40% and 50% were selected for the third experiment. The results show that numerous node voltage exceed the rated voltage when DG capacity equal to 50% on two kinds of association forms. When reduced to 40%, for 10, 12, 15 association, some nodes voltage is also exceed the limit, when reached 30%, the system losses of 5, 10, 15 association is lower than 10, 12, 15, but the voltage support effect is also inferior. Under the comprehensive comparison, 5, 10, 15 association form with 40% capacity and 10, 12, 15 combination with 30% is the best operation mode to reduce losses and improve the voltage level.

4. Conclusions

The results show that DGs have a greater effect on the voltage and losses of distribution network. The level of the effect depends on its capacity, operation mode, location and association forms. The simulations all consider the situation that DGs are running with lagged power-factor, providing active power and reactive power to the system at the same time, which effectively improve the voltage profile. However, in order to pursuit better economical revenues, the actual grid associated gas of oil field production units, may reduce exciting current, make the DG under the leading power factor, and absorb reactive power from the grid. Thus, reactive-load compensation equipment should be allocated with DG, and could achieve real-time reactive power adjustable. When DG won't have insufficient reactive power, it can compensate reactive power to improve the voltage profile. And it also can absorb reactive power when DG exit operating to avoid too much power losses and voltage out of limits caused by the system reactive power surplus.

Acknowledgment

The authors would like to acknowledge the financial support of the nature science foundation of Sichuan educational commission (12ZB161).

References

1. Ackermann T, Knyazkin V. "Interaction Between Distributed Generation and the Distribution Network: Operation Aspects. "In: Proceedings of IEEE//PES Transmission and Distribution Conference and Exhibition 2002: *Asia Pacific*, Vol2. Yokohama. 2002:1357-1363.
2. Pan Yi. "Present Utilization Status and Prospect of oilfield Associated Gas." *Special Oil & Gas Reservoirs* 2013.01
3. Bian Dongkui. "Research of Distributed Generation Associated Gas Technology and Its Impacts on Oilfield Distributed Power System". *Electric Engineering*, 2013.05
4. Hu Shinan." A Study on the Application of Solar Energy Technology in Xinjiang Oilfield." Environmental Protection of Oil & Gas Fields 2010, S1
5. Wang Zhi-qun."Impacts of Distributed Generation on Distribution System Voltage Profile." *Automation of Electric Power Systems*, 2004, 28(16):56-60.
6. Chen Hai-yan. "Study on Power Flow Calculation of Distribution System with DGs."*Automation of electric Power System*, 2006, 30(1)

7. Zhang Limei, Tang Wei. Back/Forward Sweep Power Flow Calculation Method of Distribution Networks With DGs[J]. *Transactions of China Electro technical Society*, 2010, 25(8):123-130.
8. Wang Shouxiang, Wang Chengshan. ”Modern distribution system analysis”. Beijing: Higer Education Press, 2007

Graphene Decorated TiO_2 Nanorods Photo-Anode for Solar Hydrogen Production

Hyun Kim[a], Sung Jin An[b] and Bee Lyong Yang[c*]

School of Advanced Materials and System Engineering, Kumoh National Institute of Technology, Yangho-dong, Gumi-si, Gyeongsangbuk-do, South Korea

E-mail: [a]hyun.k@kumoh.ac.kr; [b]sungjinan@kumoh.ac.kr; [c]blyang@kumoh.ac.kr

The solar hydrogen production process via water splitting is a carbon free technology for next generation. Many researchers and energy departments are expecting that the minimum efficiency for commercialization is about 10% of solar to hydrogen conversion efficiency (STH). However the world best STH efficiency doesn't reach yet. Among the reasons, one of the effective factors is an inefficient charge carrier transfer. In this work, we demonstrated the improved charge transfer and collection in PEC system by using a graphene decorated TiO_2 nanorods photo-anode. TiO_2 nanorods were directly grown on graphene/FTO glass by hydrothermal method. Their morphologies of surface and cross-sectional view as well as elemental analysis were examined by FESEM, FETEM, Raman spectroscopy, and XRD. Photo-catalytic properties of bare TiO_2 nanorod/FTO and TiO_2 nanorod/graphene/FTO were examined by measuring photocurrent density under white light illumination. Furthermore solar hydrogen production was carried out by gas chromatography. Consequently graphene decorated TiO_2 nanorods were revealed superior photocatalytic activity because the graphene sheets led to increase the mobility of charge carriers and recombination time.

Keywords: Graphene; Titanium Dioxide (TiO_2) Nanorod; Transient time Constant; Solar to Hydrogen (STH) Conversion Efficiency.

1. Introduction

There has been a rising demand for energy obtained from renewable energy sources. One of the renewable energy sources, hydrogen energy has been attracted as alternatives of the fossil fuels. A hydrogen fuel cell, which converts chemical energy into electricity by chemical reaction between hydrogen and oxygen, has been recently applied to various systems. However, while demand of hydrogen shall be tremendously increased in the hydrogen era, an effective technology for ecological hydrogen generation has not been developed yet. Current technologies for hydrogen production include the chemical extraction

* Corresponding author.

from fossil fuels such as natural gas and coal or electrolysis of water using electric power. By products such as CO or CO_2 resulting from the processes in these methods causes environment pollution and the shortage of the fossil fuels limit our usage in future. Ecological and low cost technologies for hydrogen mass production can be found in a photocatalytic water splitting method. Since a report for photocatalytic hydrolysis reaction in TiO_2 films, a lot of research on TiO_2 has been performed using several semiconductors. Selection of materials is important to obtain effective hydrogen generation in photoelectrochemical (PEC) cell. The requirements for PEC cell include chemical and optical stability, and photocatalytic ability to absorb broad light spectrum. Titania materials has been significantly researched due to its chemical stability and abundant resource, compared to other semiconductors such as SiC, ZnO, ZnS, and CdS. However, serious issues on titania materials have been on its band gap energy of 3.0 to 3.2 eV. Thus, UV light, which consists of only ~4% in light spectrum, can be easily absorbed, but visible light not, which consists of ~45% in light spectrum. Therefore, the photocatalytic efficiency of titania PEC cell is low. Several research results have been reported to address this issue, including the method of narrowing energy band gap of titania by doping several elements such as anion and cation. However, significant improvement in photocatalytic efficiency for water splitting has been required to commercialize the technology. The nanostructural titania showed that the photocatalytic reaction surface per unit area was increased compared to thin film and bulk titania. Titanium dioxide (TiO_2) is the popular transition metal oxide used as a photo-catalyst for solar energy conversion in PEC system because of its chemical stability, high photo-activity and low cost. However the intrinsic low electrical conductivity of TiO_2 (~1 x 10^{-12} to ~1 x 10^{-7} S/cm) led to short mean free time of photo-generated charge carriers. To overcome this problem, high conducting materials such a carbon are used with TiO_2 to improve charge transfer. Among the carbon allotropy, sp^2 hybridized graphene sheets have been much attention due to its high electrical conductivity (10^6 S/cm) and carrier mobility (200,000 $cm^2/V{\cdot}s$). In this work, we demonstrated that the improved charge transfer and collection in PEC system by using graphene decorated TiO_2 nanorods photo-anode [1-3].

2. Experimental Details

FTO glass substrates (2 x 2 cm^2) were ultrasonically cleaned for 15 minutes with TCE (Trichloroethylene), Acetone, Methanol, and finally dried under N_2 stream, and then sufficiently dried them on a hot plate in the constant temperature of ~80 ^oC. Graphene sheets were synthesized on Cu foil by a chemical vapor deposition

technique at 1,000 °C for 5~10 min. After that it was transferred on the FTO substrates. Vertically oriented TiO_2 NRs on FTO glass substrates or on graphene/FTO were fabricated by using hydrothermal method. The graphene/FTO substrates were placed into the autoclave containing solutions completely mixed with 30 mL HCl (Hydrochloric acid), 30 mL DI (Deionized) water and 1 mL Titanium-butoxide solutions (mixed synthetic solution must be transparent and pH was about 1~2). The hydrothermal reaction was conducted at 150 °C for 6 h. After the reaction, the samples were thoroughly washed in DI water, dried and subsequently annealed in air at 450 °C for 4 hr. Morphology and microstructural characterizations of the nanostructured samples were performed by using FE-SEM (Field Emission Scanning Electron Microscope, JSM-6500 F), FE-TEM (Field Emission Transmission Electron Microscope, 200kV/JEM-2100F HR) and XRD (X-ray Diffraction, Rigaku/SWXD). Uv-Vis absorbance spectra of the samples were obtained by UV-VIS-NIR (Ultraviolet-Visible-Near Infrared) spectrophotometer Cary 500 scan (Varian). Electrochemical measurements were performed using a potentiostat (AMT VERSASTAT 3) using three electrode configuration system consisting of a Pt (Platinum) wire counter electrode and a saturated Ag/AgCl reference electrode in 0.1 M Na_2SO_4 (pH = 7.15) electrolyte. Working electrode with 1 cm^2 area was illuminated using a 1 kW xenon lamp (Newport) from which infrared wavelengths were filtered by water, and wavelength below 420 nm was cut off by an optical filter for measurements under visible light. Measured light irradiance by a thermopile detector was 100 mW/cm^2. A monochromator (Newport/74000) was used for investigation of monochromatic responses (for IPCE, ABPE, and band gap energy measurements) of samples in the wavelength ranges from 300 nm to 700 nm with 0.5 V external bias. Pulsed light (on and off states) was used for measurements of transient time under 0.5 V bias. Quantitative measurements for solar hydrogen generation were performed in photoelectrochemical cell, where TiO_2 NR as a photoanode and Pt cathode were separated by Nafion membrane. In the photoelectrochemical cell, the hydrogen gas was generated on the Pt electrode. Generated gas was sampled using glass microsyringes in every 20 min and analyzed using a GC (Gas Chromatograph).

3. Results and Discussions

To demonstrate the advantages of graphene in photo-electrochemical system for hydrogen production via water splitting, we compared TiO_2 nanorod/ graphene/FTO and TiO_2 nanorod/FTO photo-anode. Schematic hybrid hetero-structured photo-electrodes and energy band diagrams are shown in Fig. 1(a) and

(b). One of the best configurations for efficient photo-electrochemical electrode system is double photo-electrodes system as shown in Fig. 1(c) because of substantial potential such as high efficiency, low running cost and easy to understand a catalytic reaction mechanisms on interface. The G/2D (= 0.34) Raman peaks ratios indicate that the graphene grown on Cu is single layer. The Raman spectra of graphene on SiO_2/Si is shown in Fig. 2. The degree of disorder in carbonaceous materials is indicated by the intensity of D peak, which can be seen to increase with the number of transferred graphene layers. Further evidence for uniformity of the as-grown graphene film can be obtained from the intensity of the G peak. Typically the G-peak intensity of graphene on copper is uniform except in regions corresponding to wrinkles or graphene grain boundaries [4]. Photocurrent densities of the TiO_2 nanorod/graphene/FTO and TiO_2 nanorod/FTO were measured to compare the photo-responses under irradiation of white light. The nanorods on graphene showed lower anodic photocurrent density as shown in Fig. 3(a). However these dynamic photocurrent measurement doesn't reflect a lifetime of photo-generated electrons and holes exactly. Thus transient times for the nanorods were measured to investigate comparatively the recombination rates. In these measurements (see in Fig. 3(b)), pulsed lights (on and off) were irradiated, and measured transient changes of photocurrents as a function of elapsed time, in which the photocurrent I(i) corresponding to on-state light at initial time t(i) is continuously decreased down to the I(f) corresponding to off-state light at finished time t(f). The times elapsed to recombine the excited electrons and holes are calculated using the relationship in equation (1) and (2) as follows [5]:

$$D = \frac{I(t) - I(f)}{I(i) - I(f)} \tag{1}$$

$$D = \exp\left(-\frac{t}{\tau}\right) \tag{2}$$

where t is a time and τ is the recombination time. The inverse slopes on the linear plots of ln (D) vs. time as shown in Fig. 3(c) means the transient time constant (τ). The analysis results for the recombination times were summarized in Table 1. The transient times of the TiO_2 nanorod/FTO were relatively faster than the TiO_2 nanorod/graphene/FTO. Consequently, while measured photocurrents of the TiO_2 nanorod/FTO were larger, compared to the TiO_2 nanorod/graphene/FTO, but the recombination times were faster as much as 20% of TiO_2 nanorod/FTO.

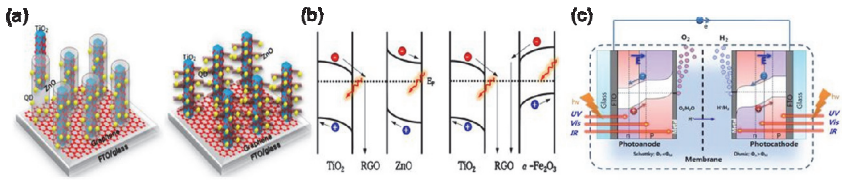


Fig. 1. Schematic (a) hybrid hetero-structures, (b) energy band diagrams and (c) solar water splitting system with double photo-electrodes and water redox reaction.

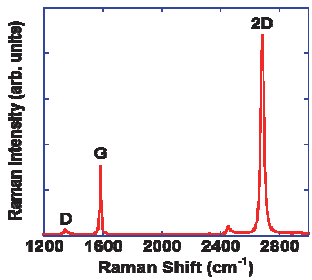


Fig. 2. Raman spectra taken from a graphene/SiO_2/Si.

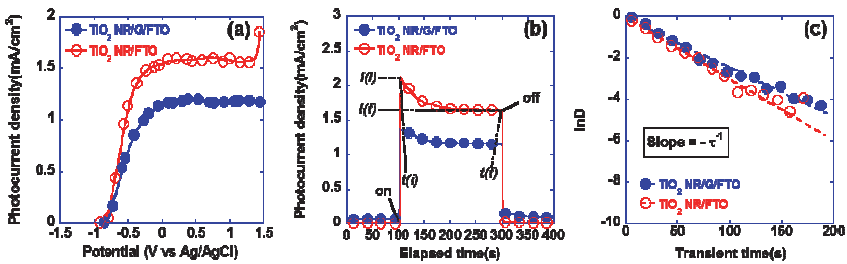


Fig. 3. (a) Photocurrent density versus applied potential plots of TiO_2 nanorods are grown by hydrothermal synthesis measured under the white light illuminations in 0.1 M Na_2SO_4 (pH =7.15). (b) Kinetics of photocurrent density and (c) Normalized photocurrent density-time dependence plots for 0.5 V (vs Ag/AgCl).

Table. 1. Calculated transient time(τ) of TiO_2 nanorods.

Samples	Transient time [s]
TiO_2 NR/G/FTO	42.3
TiO_2 NR/FTO	33.9

4. Summary

Graphene-decorated TiO_2 nanorods showed superior photocatalytic activity. The graphene sheets led to increase the mobility and recombination time of charge carriers.

Acknowledgement

This research was supported by Basic Science Research Program through the National Research Foundation of Korea (NRF) funded by the Ministry of Science, ICT and future Planning (NRF-2014R1A2A2A01005324).

References

1. Y. Dai, Y. Sun, J. Yao, D. Ling, Y. Wang, H. Long, X. Wang, B. Lin, T. H. Zeng, Y. Sun, *J. Mater. Chem*. A. 2 (2014) 1060-1067.
2. A. Yamakata, T. Ishibashi, H. Kato, A. Kudo, H. Onishi, *J. Phys. Chem*. B. 51 (2003) 14383.
3. T. Ikeda, T. Nomoto, K. Eda, H. Kato, A. Kudo, H. Onishi, *J. Phys. Chem.* C. 112 (2008) 1167.
4. C. Mattevi, H. Kim, M. Chhowalla, *J. Mater. Chem.* 21 (2011) 3324-3334.
5. M. Radecka, M. Wierzbicka, S. Komornicki and M. Rekas, *Physica B*. 348 (2004) 160-168.

Failure Analysis of a Pipeline in Sour Gas Field

Tan Gu, Honggang Chang, Qiang Zhang, Nange Zhang, Zhide Liu,
Hua Wu, Guiyang Wu, Mengwei Yang, Lin Mo

Research Institute of Natural Gas Technology,
PetroChina Southwest Oil & Gasfield Co,
Chengdu, P. R. China 610213

Jing Yan*

School of Manufacturing Science and Engineering,
Sichuan University, Chengdu, 610065, PR China

The main reasons for corrosion failure of pipeline in sour gas field have been proposed based on the analysis techniques of Optical Microscopy (OM), Scanning Electron Microscope (SEM), Energy Dispersive Spectrometer (EDS) and X-ray Diffraction (XRD). The results show that the leakage happened caused by pit corrosion in the test samples. Pit corrosion occurs under the condition of wet H_2S corrosion, while fouling and Cl^- do promotion. Test pipe material properties meet the conditions requirements of China. According to the condition of pipeline corrosion, it is suggested that the raw gas should process gas-water separation before transportation, and the filter unit should be added to reduce the sand and gravel content.

Keywords: Failure Analysis; Corrosion; XRD; Pipeline; Sour Gas Field.

1. Introduction

1.1. *Accident description*

The corroded steel pipe is found located 50m away from well site, the pipeline is L360NCS, Φ168×7mm. The leakage was coursed on a section of bent pipe. The leaking point formed in the middle of bend where fluid scouring happened, about 220 mm away from the upstream weld at 6 o 'clock direction. Corrosion zones exist in bend and downstream straight pipe at 6 o 'clock direction, stretched from upper bend upstream weld at a distance of 250 mm to lower straight upstream weld at a distance of 250 mm, consisting a large number of corrosion pit and visible mud. Bend and straight pipe connected by welding, without grinding.

1.2. *Working condition summary*

The gas was transported without water-gas separate. Corrosion inhibitor has been injecting. It is investigated that, the gas transported through the leaking pipeline contains high CO2 / H2S, with high salinity weak acid base field fluid containing Ca2 + and Cl-. In a humidity environment containing corrosive gas, corrosion is about to occur due to CaCO3 precipitation on the inner surface, moreover, Cl – promotes the occurrence and spread of local corrosion.

2. Experimental materials and methods

Leaking pipe was used for experiment. Sampling on the slightly corrosion area at 12 o 'clock direction of bent pipe for chemical analysis and mechanical properties test. Samples were first distributed into several specimen, and analysis the corrosion morphology through metallograph and SEM observation. XRD analysis is used to determine corrosion products. Tensile test was at room temperature, using (12.7 × 50) mm wall thickness longitudinal plate tensile sample. Impact test temperature was at 10ºC using (10 × 10 × 55) mm transverse specimens, three specimens were a set. Specimen for hardness test was 1/6 circle transverse wall thickness.

3. Results

3.1. *Microstructure analysis*

Figure 1 shows the appearance of the leaking bend pipe. It can be seen that the corrosion is serious. Though there is no obvious corrosion damage, a width of (40 ~ 50) mm corrosion zone exists at 6 o 'clock direction, which is 140 mm away from the upstream weld and stretch along the direction of flow downstream straight pipe.

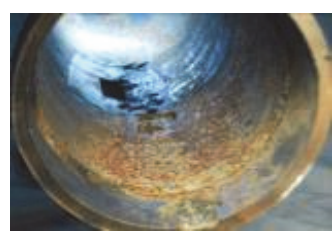


Figure 1 The internal morphology of the 1# sample

By means of observation, various sizes of pit corrosion covered black corrosion products exist on the interface of the pipe. Five corrosion pits were

selected randomly and then measured. The maximum corrosion pit is at depth of 23.88 mm, diameter of 5.31mm, and the minimum is at diameter of 0.80 mm, depth of 0.66 mm.

Outside diameter and wall thickness of samples were measured twice with a interval of 100 mm in the vertical direction. Choose 10 points in the slightly corroded area to measure the thickness.

1 # sample outside diameter and wall thickness shall in accordance with GB 9711.3 2005 < Petroleum and natural gas industries Steel pipe for pipelines Technical delivery conditions - Part 3: C grade steel> requirements.

1 # sample were no obvious local corrosion on the outer wall, bend and straight inner pipe corrosion mainly concentrated at six o'clock direction points within the corrosion zone. At 12 o 'clock direction chipped samples from the bent pipe slight area for metallographic microstructure observation.

Figure 2 shows 1 # sample's microstructure, bend material metallographic microstructure of the ferrite + pearlite + P (F) banded structure.

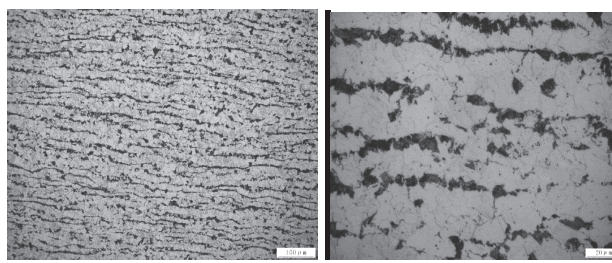


Figure 2 The microstructure of 1# sample elbow (F+P)

3.2. *Mechanical properties*

Table 1 shows the mechanical properties. 1 # sample bend material mechanics performance shall in accordance with a standard to ask. 1 # sample pipe bending various performance indicators shall in accordance with the GB/9711.3 2005 < Petroleum and natural gas industries Steel pipe for pipelines Technical delivery conditions - Part 3: C grade steel> standard requirements.

Table 1 The results of mechanical test

Sample number	Tensile strengh Rm[Mpa]	Yield strength $Rt_{0.5}$[Mpa]	Elongation A[%]	Impct resistance (Lateral, -10° C)		Hardness HV10
				Akv[J]	SA[%]	
Sample 1# elbow	530	384	26.5	103.5	100	164
GB/T 9711.3-2005	≥460	360~510	≥20	average value≥40J, single value≥30J		≤220

3.3. *Microscopic analysis of corroded areas*

Figure 3 shows 1 # sample cross-section morphology close to leaking bend pipe. A thick layer corrosion products cover the bottom, the structure is loose. The cross- section of the sample is full of holes and analysis by EDS. The results is shown in Table 2.

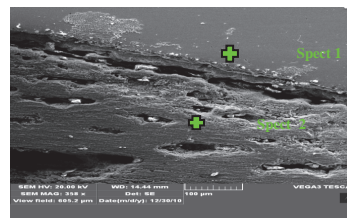


Figure 3 The 1# sample cross-section morphology of corrosion pits

Table 2 The 1# sample EDS analysis results

element	C	O	S	Fe	Mn	Si	Al	total
spectrogram 1	43.39	18.88	8.82	27.54	/	0.25	1.12	100
spectrogram 2	22.38	11.36	32.93	33.11	0.23	/	/	100

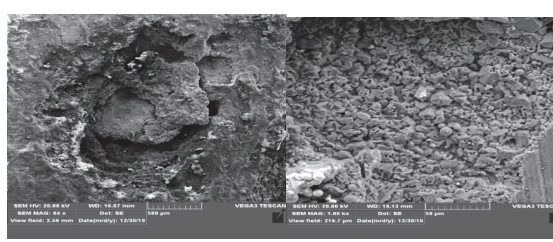
Corrosion products mainly consist of Fe, C, O, S, with slightly Mn, Si and Al.

Figure 4 shows corrosion pit morphology of 1 # sample. Corrosion pit covered with thick loose corrosion products, which is the same as cross section microscopic morphology observation. As shown in Figure 4 (a), the magnification of the product, it can be observed that the crystallization of scaly.

Figure 5 shows 1 # sample inter-wall morphology, it can be seen that local corrosion is very serious.

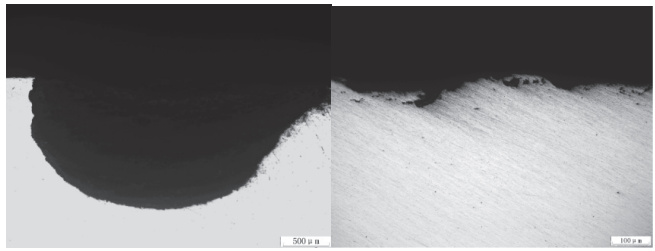
1 # sample characteristics are as following:

(1) Corrosion pit is covered with thick porous corrosion products;
(2) Corrosion products mainly consist of Fe, C, O, S, close to the base metal of the corrosion products containing Cl.
(3) Corrosion bottom is densely covered corrosion holes.



(a) (b)

Figure 4 The corrosion morphology of the 1# sample



（a）50×　　（b）200×

Figure 5 The inter wall morphology of 1#

Scrape around 1 # sample leaking point corrosion products, respectively, scrape the outer bottom corrosion products, to do component analysis. Table 3 shows EDS analysis results.

Table 3 The EDS analysis results of the corrosion product

Samplling postion	C	O	Fe	S	Si	Na	Al	Cl	K	Ca	Ti	Cu	Total
Outer layer	36.83	27.01	19.33	13.30	2.11	0.40	0.55	0.34	/	0.14	/	/	100
Bottom of corrosion pit	24.38	31.34	22.83	15.98	2.56	0.59	0.67	0.40	0.36	0.18	0.32	0.38	100

Outer corrosion products and corrosion products of corrosion pit mainly consist of C, O, Fe, S, Si, the former also contains a small amount of Na, Al, Cl, Ca, and the later contains Na, Al and Cl, K, Ca, Ti and Cu.

Outer corrosion products are mainly composed of FeS, among sand and gravel, with SiO_2, Al_2O_3 and $Ca_3Si_2O_7$ total accounted to 83.71%, and contains a small amount of CaCO3 deposition. The pit corrosion products are composed of several kinds of Fe sulfides, FeS, Fe1-xS and FeS_2, amounted to 56.79%, where its bottom contains a small amount of SiO_2 and Fe_3O_4. Considered comprehensively of EDS and XRD analysis and its working conditions of gas extraction pipeline, the corrosion products mainly consist of FeS, which indicates the H2S corrosion has occurred in wet environment, and corrosion products were mixed with sand and salt deposition.

4. Analysis and discussion

Based on the above analysis, process of pipeline leakage is as follows:

(1) Sand and gravel deposits in the pipeline at 6 o 'clock direction, where field fluid then accumulated with dissolved corrosive gas. [1]

(2) Wet H_2S corrosion damage pipeline inner face, where corrosion pits form at 6 o 'clock direction; [2]

(3) Corrosion products, sand and carbonate deposition, together with Cl – dissolved in the field fluid do credits to deepen the corrosion pit, so that accelerated the corrosion rate. [3]

Raw gas contains field water (0.441 MPa), CO2（0.441MPa）and H2S (0.435 MPa), metal materials in this environment is easy to react with corrosive gas [4]. Corrosion product composition analysis results show it's mainly consist of FeS, $Fe_{1-x}S$, FeS_2 Fe sulfides. Due to changeable environment, a series of Fe sulfides may generate Electrochemical growth of iron sulfide films in H_2S-saturated chloride media, such as $Fe_{(1-x)}S$ and FeS_2. The density of field fluid is greater than natural gas, so that the fluid accumulated in the pipe at 6 o 'clock direction during transportation, therefore, corrosion normally concentrated at this area both in direct and bend pipeline. Macro and micro analysis can be observed corrosion pit covered with thick loose corrosion products. Corrosion products are based on Fe sulfides, mixed with deposits of sand and small amounts of $CaCO_3$. The field fluid contains high content of Cl -. Fouling makes the spread of the media in the flow on the metal surface and the electrolyte is restricted, caused by blocking the medium inside the cavity of chemical composition so that the overall media have very big difference, the cavity within the medium pH and certain ions concentration, great changes have taken place for the corrosion of metals, this process is known as acid autocatalytic.

When corrosion pit occurs, the cation increases in the pit, the hydrolysis result in hydrogen ion activity increased, namely acidification, lower pH. In order to maintain the corrosion pit solution stays at electrically neutral, the outside anion move into pit, especially Cl- in the corrosive medium gives priority to spread in, that caused the difference of chemical and electrochemical states between inside and outside of the pit. Here, the low pH and high chlorine ion concentration, making the electrode potential of its contact metal is lower than that of the outside metal, which causes acceleration of corrosion pits, while the reaction ongoing, results in several sized corrosion pit patterns. In addition, corrosion is mainly concentrated in the bend and the downstream straight pipe, the upstream straight pipe has no obvious corrosion damage, which may be due to the fouling affected by the fluid and the pipe structure. The existence of weld burr

also play a role in accumulation of fouling. The causes for the leakage of pipelines is compressed:

(1) Wet H_2S environment corrosion is the main reason cause the perforation leakage.
(2) Corrosion products, sand and carbonate deposition on the pipe surface form fouling and promote pit corrosion, and Cl- are also one of the important factors.

5. Conclusions and suggestions

(1) Leakage happened caused by pit corrosion in the test samples.
(2) Pit corrosion occurs under the condition of wet H_2S corrosion, while fouling and Cl^- do promotion.
(3) Test pipe material properties are in accordance with GB 9711.3 2005 < Petroleum and natural gas industries Steel pipe for pipelines Technical delivery conditions - Part 3: C grade steel> requirements.
(4) According to the condition of pipeline corrosion, it is suggested that the raw gas should process gas-water separation before transportation, and the filter unit should be added to reduce the sand and gravel content.

Reference

1. Kentish P J. Gas pipeline failures: Australian experience[J]. *British Corrosion Journal*, 1985, 20(3): 139-146.
2. Parkins R N, Blanchard Jr W K, Delanty B S. Transgranular stress corrosion cracking of high-pressure pipelines in contact with solutions of near neutral pH[J]. *Corrosion*, 1994, 50(5): 394-408.
3. Koch G H, Barlo T J, Berry W E. Effect of grit blasting on the stress corrosion cracking behavior of line pipe steel[J]. *Mater. Performance*; (United States), 1984, 23(9).
4. Kermani M B, Morshed A. Carbon dioxide corrosion in oil and gas production-A compendium[J]. *Corrosion*, 2003, 59(8): 659-683.
5. Lucio-Garcia M A, Gonzalez-Rodriguez J G, Casales M, et al. Effect of heat treatment on H_2S corrosion of a micro-alloyed C–Mn steel[J]. *Corrosion Science*, 2009, 51(10): 2380-2386.

The Diurnal Change Model of the Instantaneous Amount of Solar Radiation Incident on the Horizontal Surface Near the Ground

Zhongsheng Guo*

State Key Laboratory of Soil Erosion and Dryland Farming on the Loess Plateau, Institute of Soil and Water Conservation, Northwest A and F University, Academy of Science, Yangling, Shaanxi, 712100, P.R. China
*E-mail: *zhongshenguo@sohu.com*

Xiaoping Zhang

College of Science, Northwest A and FUniversity, Yangling, Shaanxi, 712100, P.R. China
E-mail: zxp853418327@163.com

Solar energy is one of the cleanest forms of energy sources and considered as a green source of energy. The amount of the instantaneous global solar flux incident on the horizontal surface directly or indirectly comes from the sun. It is composed of three parts, direct radiation, scattered radiation, and thermal radiation streaming down through the atmosphere, and the dynamics of the solar radiation flux near the ground influence all life processes. In this study the daily change of solar radiation flux density was measured in order to study the quantitative characteristics of the daily change in the solar radiation near the ground. The results showed that under stable sky conditions the diurnal change in the solar radiation flux incident to the horizontal surface of the ground is only a function of time and can be describe by a simple mathematical model. The main parameters change with time (hour) and climate in a day.

Keywords: Horizontal Surface; Solar Radiation Flux; Diurnal Change; Daily Amount of Solar Energy.

1. Introduction

Solar energy is one of the cleanest forms of energy sources and considered as a green source of energy. Solar energy benefit ranges from low carbon emission, no fossil fuel requirement, long term solar resources, and other (Aman et al., 2015). Solar energy is the main energy resource for all of the life processes, and the basic condition causing varied physical phenomenon and processes in the atmosphere. The reciprocity between solar energy and life system were generalized by photosynthesis, thermal effect, and photo-morphogenesic effects (Ross, 1975; Zu ,1990). Solar radiation incident to the horizontal surface comes

either directly or indirectly from sun. It is this energy that makes photosynthesis possible. It provides the heat to warm the air and the soil to the levels that promote the life processes which in turn influence the soil energy status and water evaporation (Spurr and Barnes, 1980).

Solar energy is the main energy resource used for plant transpiration and soil evaporation. For this reason, a crops growth rate, under conditions where nutrients and water are not limited, can largely be explained by the ability of the crop to intercept and utilize radiation (Goss et al., 1986; Arkebauer et al., 1994; Olesen, 1997), and biomass production of forest stands is correlated with the capacity of stands to intercept light (Linder 1987; Cannell, 1989; Albaugh, 1998). Hence studies of the diurnal change in solar radiation is very important for explaining the dynamic mechanism of environmental factors, plant life processes, and soil physical properties.

When the solar radiation passes through the earth's atmosphere, the solar energy is dramatically reduced and dissipated in many ways. Part of the energy is reflected and part absorbed by the atmosphere, by clouds and other masses of solid particles in the atmosphere, then by the vegetation, and finally by the earth itself. The greater the amount of atmosphere through which the sun's radiation must pass, the higher the percentage of the solar radiation that is absorbed or scattered and not received on the Earth's surface. As the solar energy is dissipated, the radiation wavelengths are changed. The shorter ultraviolet rays are almost completely absorbed by the atmosphere. The radiation with wavelengths ranging from approximately 0.4-0.7 μ(photosynthetic active radiation) is visible to the unaided human eye and is termed light and accounts for approximately one-half of the total solar energy reaching the Earth's surface. When the sun is low on the horizon, therefore, very little ultraviolet radiation reaches the surface, and more infrared radiation reaches the earth than light. The solar radiation reaching the horizontal surface is composed of three terms, direct radiation, scattered radiation, and infrared radiation or long-wave radiation. The direct radiation and scattered radiation only exist in the day, and the long-wave radiation exists 24 hours period of a day (Lee 1978)

Solar radiation influences air, leaf, and soil temperature, therefore affect the life processes of plants and animals. Recently many daily changes in solar radiation reaching horizontal surfaces of the earth have been measured (Bryam and Jemison, 1943; Gates, 1980; Zu, 1990; Hong et al., 1963). Many resources indicated that the diurnal changing curve of solar radiation with time is a single peaked curve with symmetry about solar noon. However, few models have been put forward to describe quantitatively the change in diurnal solar radiation. The objective of this study is to continuously measure the total solar radiation

incident on the ground with high-preciouse equaipment to obtain the quantitative characteristics of the diurnal distribution and to establish an equation to estimate the total solar energy.

2. Materials and methods

2.1. *Study area and station*

The current study site is located on Hilly and gully region of Loess Plateau in the north region of China. It is an important area of Western Development in China. There are fragile environment and long-term drought on the Loess Plateau.

The data used in this work was measured at ChangWu experimental station under the China Academy of Sciences and Ministry of water Resources. It located at the juncture of Shaanxi Province and Gansu Province in the south part of Loess Plateau and founded in 1984. The geographic coordinate is N35° 12′, E107° 40′, with 1200 m height above sea level. The soil is Helou soil and the parent material for the soil is deep mediumloam Malan Loess.The weather is warm temperate semi humid continental monsoon climate with an altitude of about 1200 m，an average air temperature of 9.1°C and an annual rainfall of 584 mm，60 % of which is from Jul to Sep.. frost- free season is 171 days, and the water table is 50-80 maters. The station is an open management system.

2.2. *Data collection*

Solar radiation data came from ground measurements fixed in the plateau. The software of MiLOS520 automatic weather station was installed at the Changwu eco-experimental station on Loess Plateau. The data was measured and collected in 2013. Daily instantaneous solar irradiances (W/ m^2), the stability of the daily cloud cover (daily variation in cloud cover), the actual measured total solar radiation are used in this study. Instantaneous solar irradiances automatically was recorded once an hour from 0:00, the beginning of a day to 24 hour. The condition of the daily cloudy cover is observed.

2.3. *Mathematical model*

In this study, the Gaussian curve is utilized for simulating the curve of dynamic changes of daily hourly instantaneous solar irradiances (W/m^2) over time (24 hours a day). General model Gauss is:

$$f(t) = ae^{-(\frac{t-d}{c})^2} = ae^{-b(t-t_0)^2} \quad (1)$$

Here d= t_0 , b= $\frac{1}{c}$

3. Result

3.1. *The diurnal change of the solar radiation*

As the earth moves in its orbit, the total solar radiation incident on the ground surface takes on the daily change phenomenon, consisting of a symmetrical shape. The cosine equations (Lee, 1978; Gates, 1980) can be used to describe this situation, but the normal distribution equation has a higher value of R than that of the cosine equation. Because the cosine equation can only express the solar radiation from sunrise to sunset, it was omitted and the normal distribution equation selected.

The amount of sunlight incident upon the Earth's surface at any point in space and time is a function of many variables. Those factors can be divided into two groups, one function is based on the sky conditions, including the atmospheric and meteorological factors, while another function is based on the geometric relationship between the fixed horizontal forest canopy or the ground surface and the sun. The factors are functions of time, t. When the sky conditions are constant, the solar radiation reaching a horizontal surface is the function of the geometric position between the fixed level plane and the sun, and solar radiation flux is the only function of time, t. The solar radiation flux increases nonlinearly with time t ($0 \le t < t_0$).When time, t, is equal to time, t_0 , solar radiation flux reaches its peak. When time, t, exceeds time, t_0, ($24 \ge t > t_0$), the solar radiation flux decreases nonlinearly with time, t. See Figure 1.

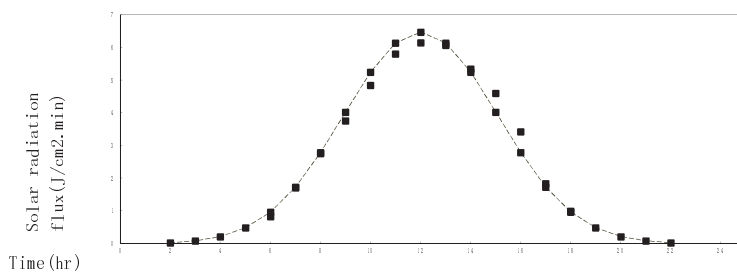


Figure 1 Diurnal change of the solar radiation incident on the canopy of massion pine forest in Nanjing, China (fine)

The relationship between solar radiation flux, $\frac{dw}{dt}$, and time, t, then be expressed as following

$$\frac{dw}{dt} = ae^{-bt^2}$$
$$t = t_i - t_0 \quad (2)$$

The value of main parameters a, b, t_0 and R^2 changed with time in a day in Changwu is shown in Table 1 on 1-20，July, 2013.

3.2. *The equation of the daily solar energy*

Because the instantaneous solar flux received on the horizontal surface is a successive function of time, t, throughout the day, equation 2 is integrated over a 24-hour period. The daily total solar energy therefore can be obtained by

$$dw = ae^{-bt^2}dt$$
$$w = \int ae^{-bt^2}dt \quad (3)$$
$$w = \int_{-12}^{12} a.e^{-bt^2}dt$$

Table 1 The change of main parameters with time in equation 2

Item	a	t_0	b	R^2
1	682.6	11.02	3.627	0.798
2	566.5	11.89	4.637	0.8674
3	393.7	10.42	3.506	0.873
4	707.8	14.16	2.849	0.8361
5	1074	12.31	4.317	0.9837
6	686.8	11.4	5.102	0.7051
7	806.5	11.81	4.731	0.8411
8	105.1	11.51	5.315	0.4676
9	181.8	11.45	3.601	0.9284
10	160.6	9.977	4.166	0.7148
11	341.2	12.9	2.171	0.8535
12	178.3	12.33	5.022	0.9157
13	509	14.19	3.784	0.8761
14	730.6	13.34	3.362	0.8477
15	371.3	14.29	3.342	0.9328
16	944.2	12.47	3.982	0.9428
17	423	8.777	2.278	0.8444
18	527.9	11.97	3.721	0.9443
19	661	11.53	4.133	0.7733
20	1018	11.18	4.142	0.943

The equation is evaluated from –12 to 12 to account for the 24 hours in a day with the average t_0 =12 because the value of t_0 varies from 10. 30 a.m. to 14.30 p.m, see table 1 apart from some special day in which the sky condition change dramatically. The units of a and t in the right side of equation are not unite, so a constant K is needed to unite the unit of a and t. When the unit of a is w/m^2 or J/cm^2.min, and the unit of t is hour, then K is equal to 60, so equation 3 can be rewritten as following:

$$W = \int_{-12}^{12} ae^{-bt^2} dt = ak \int_{-12}^{12} e^{-bt^2} dt \tag{4}$$

Let bt^2 equal ξ^2. When the time, t, tends to $\pm\infty$, ξ tends to $\pm\infty$ respectively. Then

When time t is equal to 12 or -12, the value of solar radiation, dw/dt, is so small that it can be neglected.

Let bt^2 equal ξ^2. When the time, t, tends to $\pm\infty$, ξ tends to $\pm\infty$ respectively. Then

$$\begin{aligned} d\xi &= \sqrt{b}dt \\ W &= \frac{aK}{\sqrt{b}} \int_{-12}^{12} e^{-\xi^2} d\xi \end{aligned} \tag{5}$$

Generally, on calculating the daily solar energy, we consider the value of dw/dt to be zero when time, t, is less than -12 or greater than 12.

$$W = \frac{2aK}{\sqrt{b}} \int_{0}^{12} e^{-\xi^2} d\xi = \frac{2aK}{\sqrt{b}} \int_{0}^{\infty} e^{-\xi^2} d\xi \tag{6}$$

Let ξ^2 equal x,

$$d\xi = \frac{1}{2\sqrt{x}} dx$$

Because

$$\int_{0}^{\infty} e^{-\xi^2} d\xi = \int_{0}^{\infty} e^{-x} x^{-\frac{1}{2}} dx = \int_{0}^{\infty} e^{-x} x^{-\frac{1}{2}} dx = \frac{1}{2}\Gamma(\frac{1}{2}) = \frac{\sqrt{\pi}}{2} \tag{7}$$

Inserting the equation (7) into the equation (6) yields

$$W = \frac{2aK}{\sqrt{b}} \int_{0}^{\infty} e^{-\xi^2} d\xi = \frac{2aK}{\sqrt{b}} \times \frac{\sqrt{\pi}}{2} = aK\sqrt{\frac{\pi}{b}} \tag{8}$$

Here W is the total solar energy incident on the horizontal surface per square meter (J/m^2), a and b are the same as equation 4, π is the ratio of the circumference of a circle to its diameter and K is the unit's conversion coefficient.When time t expressed in hour, K is 60.

It can be seen from Table 1 that the smaller the change of weather conditions in a day, the larger is the value of R. In a fixed position at the three scale levels of a year, a month, and a day, the shorter the period of time is, the more stable the sky conditions are, this is the reason why the diurnal solar radiation change with time t in most of days investigated in the growing seasons can be described by equation 2.

4. Discussion

The luminometer has a higher value response to the solar radiation, it therefore can not be used to measure the smaller solar radiation fluxes throughout the day. Total solar radiation and illuminance are related, however, approximate conversions are possible (Spurr and Barnes, 1980) and equation 2 can be used to describe data from different places with different radiometer. In order to prove this, the data of the diurnal change of the solar radiation was measured from 5 a.m. to 18 p.m. once every hour on 18,August 1983, a fine day in Changling (44°20′N, 123°50′E), Jilin province of China (Zu, 1990). The data had an R value of -0.966966 (n=14). The solar radiation was again measured from 6 a.m. to 18 p.m. once every hour on 11 July 1959, this time on a cloudy day. The daily total solar energy is 2249.7 (J/cm^2) and on 12 July, 1959, a fine day, the daily total energy is 2892.4 (J/cm^2) in Zijin mountain, Nanjing city of China (32°05'N,118°52'E) (Hong et al., 1963)and so on in different location in China, the expected results were obtained, and the values of R were -0.986369 on a cloudy day and -0.990669 on a fine day(n=13).

Through analysis, the amount of the instantaneous global solar flux incident on the horizontal surface, coming directly or indirectly from the sun, is composed of three parts, direct radiation, scattered radiation, and thermal radiation streaming downward from the atmospheric hemisphere. The former two terms exist in the daytime, but thermal radiation exists throughout a day, so the amount of the instantaneous global solar flux always is bigger than zero in a 24-hour period. When the sky conditions are stable, the global solar radiation received on the horizontal surface is only a function of time t of a day (Guo, 1998，2014) and equation 3 can be formally described.

$$\frac{dw}{dt} = 6.476026e^{-0.052586t^2}$$

$$W = aK\sqrt{\frac{\pi}{b}} = 6.476026 \times 60 \times \sqrt{\frac{\pi}{0.052586}} = 3003.3$$

According to Hong et al.'s report, on a fine day, the relative error is 3.8%. On a cloudy day, the relative error is 4.1%

$$\frac{dw}{dt} = 5.332115e^{-0.058574t^2}$$

$$W = 5.332115 \times 60 \times \sqrt{\frac{\pi}{0.058574}} = 2343$$

This showed that the equation 3 can be used to describe the daily change of the amount of the instantaneous global solar flux incident on the horizontal surface and the equation 10 can be used to evalue the the daily solar energy.

5. Conclusion

When the sky conditions are stable throughout a day, the solar radiation is the function of time t, and the relationship between solar radiation flux and time t can be described with Eq. 2 and the total solar energy per square centimeter is equation 8.

In fact, the sky conditions vary with time, t in a day because of atmospheric motion, and does not completely satisfy the stable sky conditions. For this reason, the value of R always approaches to 1.0, but it is not equal to 1.0. With three types of weather change processes with different time scale in a fixed level position, the shorter the time period, the more stable the sky conditions, so diurnal solar radiation change in most of the days in growing season can be described by equation 2.

Acknowledgement

The authors thank Professor Horton for their helps to revise the paper. This study was supported by the National Science Fund of China (Project No. 41271539, 41071193).

References

1. Arkebauer, T. J, Weiss A, Sinclair, Blum A., Shah et al. In defense of radiation use efficiency: a response to demetriades. *Agricultural and Meteorology*. 68, 221-7, 1994.
2. Albaugh, T.J., Allen, H.L., Dougherty, P. M., Kress, L.W. and King, J.S. Leaf Area and Above- and Belowground Growth Responses of Loblolly Pine to Nutrient and water additions. *Forest Science 2*, 317-328, 1998.
3. Aman M.M., K.H., M.S Solangi,. Hossain, A. Badarudin, G.B. Jasmon, H. Mokhlis, A.H.A. Bakar, S.N Kazi. A review of Safety, Health and Environmental (SHE) issues of solar energy system. *Renewable and Sustainable Energy Reviews*, 41:1190-1204, 2015.

4. Cannell, M.J.R. Physiological basis of wood production: A review. *Scand. J. For. Res. 4*:459-490, 1989.
5. Gates. Biophysical Ecology. Springer-Verlag, New York. Heidelberg, Berlin, 1980.
6. Hong Q. F., Q. F. and Yizhou Wang, Y. ZH. et. al., 1963, Microclimate of Masson Pine young Forest, *SCIENTIA SILVAE* (in Chinese), 283-288.
7. Goss, G., Verlet-Grancher, C., Bonhomme R., Chartier M Allirand J-M., Lemaire G. Production maximalen de matière Sèche et rayonnement solaire interceptè par un couvert vegetal. *Agoronomie 6*:47-56, 1986.
8. Guo, Z.S., Si L.M.et al., A preliminary study on microclimate in littleleaf pea shrub shrubbery. Memoir of NISWC, *Academia Sinica & Ministry of water Conservation*. Volume 14 (in Chinese with English abstract): 84-95, 1991.
9. Guo, Z. S. Research of the effects of Seabuchthorn shrubbery on its Microclimate Material of
10. International Symposium on Seabuckthorn, Russia, 1998.
11. Lee. R.. Forest microclimatology. Columbia University press, 1978.
12. Linder, S.. Responses to Water and nutrients in coniferous ecosystems. P.180-202 in Potentials and limitations of ecosystems analysis. Ecol. Studies 61. Schulze, E. D., and H.Z. Wolfer (eds.).
13. Springer-Verlage, New York, 1987.
14. Olesen. J.E. and K. Grevsen, 1997. Effects of temperature and irradiance on vegetative growth of cauliflower (Brassica oleracea L.Botrytis) and broccoli (Brassica oleracea L.italica) *Journal of Experimental Botany*. 313:1591-1598.
15. Spurr.S.H. and B.V.Barnes. Forest Ecology John Wiley & Sons, 1980.
16. Zu Y.G., Introduce of Energy Ecology. *Jilin Science and Technology Publishing House*. Changchun, China (in Chinese), 1990.

Synthesis Preparation and Properties Study on Phase Change Material of $Na_2SO_4 \cdot 10H_2O@SiO_2$

Hongmei Wang[a], Zhufeng Lu[b*]

College of Biological and Chemical Engineering, Jiaxing University, Jiaxing 314001, China
E-mail: [a]hongmei256@sohu.com; [b]luzhufeng@mail.zjxu.edu.cn

Dianwu Huang[c]

College of Engineering and Architecture, Jiaxing University, Jiaxing 314001, China
E-mail: [c]dwhuang@mail.zjxu.edu.cn

Composite phase change material of hydrated sodium sulfate and porous silica was synthesized using reverse microemulsion method. The properties of the composite material were characterized by SEM，XRD and DSC. The results indicate that the metarial can relieve the undercooling effectively, the crystallizing point under cooling can increase about 16ºC.

Keywords: Reverse Microemulsion; Phase Change Material; Sodium Sulfate.

1. Introduction

There were many kinds of phase change energy storage materials, which can be divided into inorganic, organic and mixed phase change materials by the view of chemical composition; can be divided into high temperature, middle temperature and low temperature type by the view of the temperature range from energy point; can be divided into four kinds of phase transition like solid-solid, solid-liquid, solid-gas and liquid-gas according to the phase state change[1-3]. However, the application of low temperature solid-liquid phase change energy storage materials is extensive among all these materials.

Hydrated sodium sulfate is a typical inorganic hydrous salt phase change material, commonly known as Glauber's salt. Hydrated sodium sulfate belongs to the low temperature phase change heat storage materials, has high latent heat and good thermal conductivity properties. Study on phase transformation system performance based on $Na_2SO_4 \cdot 10H_2O$ as the main phase change material has

* Corresponding author.

been paid much attention by many researchers, but its application was hindered because of the serious supercooling and phase separation. How to reduce the degree of supercooling, will greatly expand the application of phase change materials, adding nucleating agent and thickening agent is the better way[4-6]. In this experiment, $Na_2SO_4 \cdot 10H_2O@SiO_2$ core-shell structure composite material was prepared by using reverse microemulsion method, and the supercooling degree was found reduced greatly than the conventional ten aqueous sodium sulfate after the test.

2. Experimental

2.1. *Materials*

$NH_3 \cdot H_2O$, cyclohexane, Triton X-100, amyl alcohol, sodium sulfate, 3-aminopropyl triethoxysilane, tetraethyl orthosilicate ethyl ester four, deionized water.

2.2. *Preparation*

A certain three-necked flask containing 50ml cyclohexane, 10ml TritonX-100 and 10ml amyl alcohol were mixed with sodium sulfate solution after sonication 15min. Then after 30min stirring 150μl $NH_3 \cdot H_2O$ was added to the system. Continue stirring for 5min, 500μl TEOS was added. The product was obtained after 12h stirring at room temperature, and the product was washed finally.

2.3. *Characterization*

The crystal structure was checked by XRD analysis using DX-2600 with Cu target tube at 30 kV and 20 mA. The HITACH S-4800 and JEM2010 electronicmicroscope were used to observe the morphologies. Calorimetry and thermal performance were analysed using DSC-200PC.

3. Results and Discussion

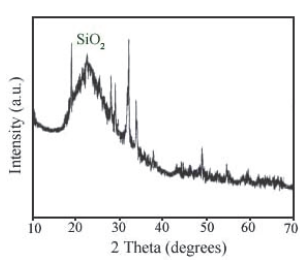


Fig. 1 The XRD pattern of $Na_2SO_4 \cdot 10H_2O@SiO_2$ composites

Fig. 1 represented the XRD pattern of $Na_2SO_4 \cdot 10H_2O@SiO_2$ composites. As shown in Fig. 1, the material showed three peaks at 2θ=19°, 32° and 34°. The peaks represented sodium sulfate (100), (200) and (130) crystal planes respectively. X-ray diffraction curve also showed there was a peak on behalf of SiO_2, which indicated that composite material is formed.

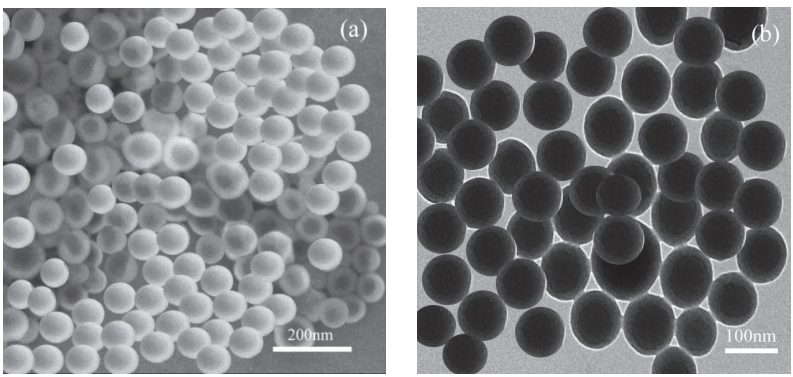


Fig. 2 The SEM and TEM images of core-shell structure of phase change material

Fig. 2(a) and 2(b) showed the SEM and TEM images of core-shell structure of phase change material. As shown in Fig. 2, the spherical morphology of the material has a regular, smooth and compact surface, preferably coated, size about 100nm, dispersed evenly. The results indicated that the composite phase change material with core-shell structure was prepared successfully through reverse microemulsion method.

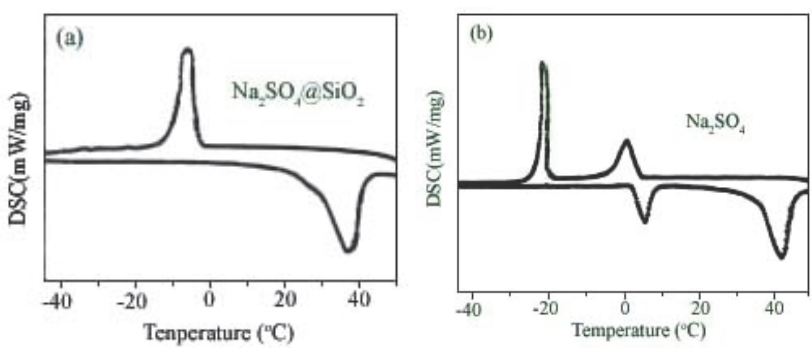


Fig. 3 DSC curves of composite materials (a); DSC curves of conventional sodium sulfate materials

As shown in Fig. 3, composite materials have great changes on thermal properties compared with the conventional sodium sulfate, crystallization temperature increased nearly 16°C under supercooling degree is far less than the

conventional phase change material. The results indicated that the material can relieve the undercooling effectively.

4. Conclusions

In this paper, composite phase change material of $Na_2SO_4 \cdot 10H_2O@SiO_2$ was synthesized using reverse microemulsion method. The spherical morphology of the material observed by using SEM and TEM has a regular, smooth and compact surface, preferably coated, size about 100nm. Composite material of hydrated sodium sulfate and porous silica has great changes on thermal properties compared with the conventional sodium sulfate according to the diagram. Supercooling degree increased 16ºC.

Acknowledgements

The authors acknowledge Jiaxing Science and Technology Projects (No. 2013AY11012), the fund of Zhejiang Province Application Research of Public Technology Project (No. 2014C33005) and Scientific Research Fund of Zhejiang Provincial Education Department (No. Y201330035).

References

1. Mohammed M F, Amar M K, Siddique A K R, et a1, A review on phase change energy storage: materials and applications, *Energy Conversion and Management*, 45 (2004) 1597-1615.
2. Sharma A, Tyagi V V, Chen C R, et a1, Review on Thermal Energy Storage with Phase Change Materials and Applications, *Renewable and Sustainable Energy Reviews*, 13 (2009) 318-345.
3. Younsi Z, Zalewski L, Lassue S, et a1, A novel technique for experimental thermophysical characterization of phase-change materials, *Int J Thermophys*, 32 (2011) 674-692.
4. Marliacy P, Solimando R, Bouroukba M, et a1, Thermodynamics of crystallization of sodium sulfate decahydrate in H_2O-NaCl-Na_2SO_4: application to $Na_2SO_4 \cdot 10H_2O$-based latent heat storage materials, *Thermochi-mica Acta*, 233 (2000) 85-94.
5. Alvarado J L, Marsh C, Sohn C, et a1, Characterization of supercooling suppression of microencapsulated phase change material by using DSC, *Journal of Thermal Analysis and Calorimetry*, 86 (2006) 505-509.
6. Hasnain S M, Review on sustainable thermal energy storage technologies, Part 1: Heat storage materials and techniques, *Energy Conversion*, 39 (2008) 1127-1138.

Study of Pore Sites Introduced by Mechanochemical Milling in Saponite Nanoparticles by Positronium Spectroscopy

K. Numata and K. Sato*

Department of Environmental Sciences, Tokyo Gakugei University, 4-1-1 Koganei, Tokyo 184-8501, Japan
E-mail: sato-k@gakugei.ac.jp

Mechanochemical decomposition was conducted for saponite nanoparticles for the purpose of introducing photocatalytically-active molecular sites. Positronium lifetime spectroscopy revealed two kinds of open spaces with sizes of ~ 0.3 nm and ~ 0.9 nm for unmilled saponite before self-assembly. The fractional intensity of the larger open space decreased from ~ 9 % to ~ 5 % with increasing time up to ~ 100 h and correspondingly the fraction of the smaller open space increased from ~ 5 % to ~ 9 % due to long-term rheological self-assembly. The larger open space disappeared and a single open space, with the size slightly larger than the original smaller one, was formed for mechanochemically decomposed saponite. Preliminary results of thermogravimetry and differential thermal analysis (TG-DTA) suggest that the local molecular structures introduced by decomposition act as photocatalytically active sites.

Keywords: Chemically Active Site; Mechanochemical Decomposition; Saponite Nanoparticles.

1. Introduction

Layered nanoparticles known as clay minerals are inorganic compounds consisting of two-dimensional (2D) nanosheets with angstrom-scale interlayer spaces as shown in Fig. 1. The 2D nanosheets are negatively charged due to the compositional and structural fluctuation. The negative layer charge is compensated by interlayer cations such as Na+ which attract to polarized H_2O molecules. Layered nanoparticles can thus contain a large amount of H_2O molecule in the angstrom-scale interlayer spaces, which is characteristic for the swelling property [1]. In addition, there exists a large surface area exceeding ~ 800 m2/g owing to highly porous structure with interlayer spaces [2]. Layered nanoparticles are thus promising materials for supporting TiO_2 particles with a high photocatalytic performance for the degradation of organics.

A uniform dispersion of TiO_2 particles on the matrix of layered nanoparticles as clay-TiO_2 composite and the resulting improvement of

photocatalytic performance has been practiced [3-4]. The photocatalytic reaction is associated with the intrinsic molecular structures of clay minerals as e.g., the surface of 2D nanosheet and open space created by 2D nanosheets called as a clay pore. In the present study, mechanochemical decomposition was conducted for saponite layered nanoparticles for the purpose of introducing photocatalytically active molecular sites.

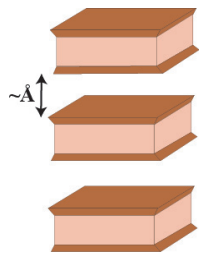


Fig. 1. Schematic illustration of layered structure with 2D nanosheets.

2. Experiments

Synthetic Na-type saponite nanoparticles (54.71 % SO_2, 5.02 % Al_2O_3, 0.03 % Fe_2O_3, 30.74 % MgO, 2. 15 % Na_2O, 0. 07 % CaO, 0. 67 % SO_3, 6. 64 % H_2O) produced by Kunimine Industries Co. Ltd., Japan were employed in this study. The sample was mechanochemically milled with tungsten carbide balls for 3 h and 9 h under dry atmosphere at ambient temperature. All the samples were dehydrated at 423 K for 12 h under a vacuum of ~ 10^{-3} Pa, and then exposed to the humidity of ~ 35 % at the temperature of ~ 300 K so that 2D nanosheets can be well self-assembled[5].

The sizes of open spaces and their fractions were investigated by Ps lifetime spectroscopy, which is described elsewhere[6].

3. Results and discussions

Ps lifetime spectroscopy for saponite milled for 0 h and 3 h revealed two kinds of open spaces, a smaller one labeled A and a larger one labeled B, whereas only a small open space was observed for saponite milled for 9 h. For unmilled saponite, the smaller open space A had a radius of ~ 0.3 nm which was unchanged with exposure time. For 3 h-milled saponite, the smaller open space A had a radius slightly larger than ~ 0.3 nm prior to self-assembly and the radius decreases down to ~ 0.3 nm, similar to that of unmilled saponite, with increasing exposure time. The radius of the larger open space B for unmilled saponite

decreased significantly from ~ 0.9 nm to ~ 0.6 nm with increasing exposure time, whereas the open space size of B for 3 h-milled saponite was unchanged with ~ 0.6 nm with exposure time.

Fig. 2 shows the measured fractional intensity of each open space obtained for saponite milled for 0 h, 3 h, and 9 h as a function of exposure time. The fraction of the smaller open space A for unmilled saponite slowly increases from ~ 5 % to ~ 9 % with increasing exposure time together with a decrease of the larger open space from ~ 9 % to ~ 5 %. The change takes place on a time scale of ~ 100 h, much longer than that of thermogravimetry and differential thermal analysis (TG-DTA) with a time scale of ~ 8 h [4] It is thus concluded that the long-term molecular dynamics probed by Ps lifetime spectroscopy originates from the self-assembly of 2D nanosheets rheologically caused by H_2O molecules. Saponite milled for 3 h indicates a completely different time variation for the fractions of the smaller and larger open spaces A and B. The fraction of the smaller open space A is ~ 14 % before hydration, which is significantly higher than for unmilled saponite. It decreases from ~ 14 % to ~ 8 % with a time scale of ~ 100 h. The fraction of the larger open space B is ~ 4 % before hydration, which is significantly lower than for unmilled saponite. It decreases from ~ 4 % to ~ 2 % with time scale of ~ 100 h. The decrease in the fraction of the smaller open space A is accelerated for saponite milled for 9 h and the larger open space B disappears.

Previously, we conducted molecular dynamics (MD) calculations to figure out the location of the two kinds of open spaces for unmilled saponite [5]. One of the simulated molecular structures is called type A, in which one 2D nanosheet is inserted into the interlayer spaces forming a open space with a size of ~ 0.3 nm. Another is type B, in which two 2D nanosheets are inserted into the interlayer spaces forming a large open space with a size of ~ 0.9 nm. The sizes of open spaces simulated by MD calculations are in agreement with those observed by Ps annihilation spectroscopy. The results of Ps lifetime spectroscopy thus demonstrate that the local molecular structure denoted as type A with the smaller open space increases maintaining its size along with self-assembly. On the other hand, the local structure of type B disappears with self-assembly shrinking this larger open space. Type A could be an intrinsic local molecular structure of unmilled saponite, whereas the type B could be a metastable structure present dominantly prior to self-assembly. It is reasonably inferred for unmilled saponite that the metastable structure of type B is gradually altered to the intrinsic structure of type A together with self-assembly.

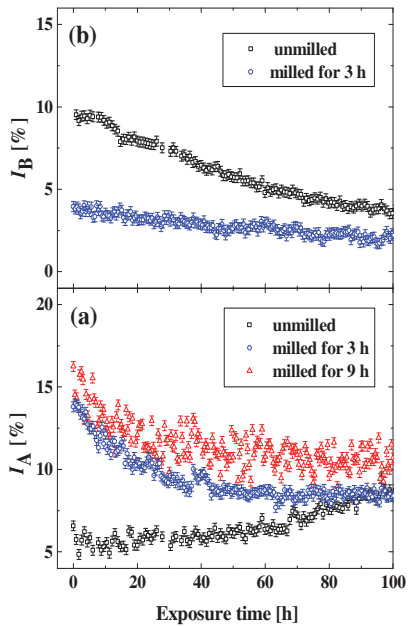


Fig. 2. The fractional intensity of small and large open spaces (IA and IB) obtained for saponite milled for 0 h (black squares), 3 h (blue circles), and 9 h (red triangles) as a function of exposure time.

It is of interest that the large open space B decreases upon mechanochemical decomposition and finally disappears. Furthermore, a open space is introduced as a result of decomposition, as deduced from the increase of the fraction of the smaller open space A (see Fig. 2). As mentioned above, the positron lifetime corresponding to the open space A is slightly longer for milled saponite prior to self-assembly. It is thus expected that the size of the open space introduced upon decomposition is slightly larger than that of the smaller open space A. Our next interest is that the above-mentioned local molecular structures introduced upon mechanochemical decomposition act as chemically active sites for photocatalytic reactions. For testing it, the photocatalytic degradation of methylene blue with ultraviolet rays (UV) was conducted for TiO_2 supported both by saponite milled for 0 h and 9 h. The relative weight decrease obtained by TG-DTA is ~ 1 % for milled-saponite-supported TiO_2 at the UV-irradiated time of 300 h, whereas the weight decrease is hardly observed for unmilled-saponite-supported one. The decrease of relative weight is expected to be caused by the decomposition of methylene blue due to the photocatalytic degradation. The photocatalytic performance could be enhanced by the chemically active sites introduced upon mechanochemical decomposition. The

results of TG-DTA mentioned here are preliminary and further investigations are now in progress.

4. Summary

Mechanochemical milling with tungsten carbide balls under dry atmosphere at ambient temperature was conducted for saponite layered nanoparticles. This treatment efficiently decomposes the local structure of 2D nanosheets yielding new kinds of molecular sites. It is found that positronium annihilation spectroscopy is powerful tool to characterize these molecular sites. Preliminary results of TG-DTA suggest that the local molecular structures introduced by mechanochemical decomposition act as photocatalytically active sites.

Acknowledgment

The authors are indebted to K. Fujimoto (Tokyo Gakugei University) and K. Kawamura (Okayama University) for fruitful discussion. This work was partially supported by a Grant-in-Aid of the Japanese Ministry of Education, Science, Sports and Culture (Grant Nos. 25400318 and 25400319).

References

1. P. Porion, L.J. Michot, A.M. Faugère and A. Delville, Structural and Dynamical Properties of the Water Molecules Confined in Dense Clay Sediments: a Study Combining 2H NMR Spectroscopy and Multiscale Numerical Modeling, *J. Phys. Chem*. C 111 (2007) 5441-5453.
2. Jean Marc Douillard, Fabrice Salles, Phenomenology of water adsorption at clay surfaces, *Interface Science and Technology* 1 (2004) 118–152.
3. Daria Kibanova, Javiera Cervini-Silva, Hugo Destaillats, Efficiency of Clay-TiO2 Nanocomposites on the Photocatalytic Elimination of a Model Hydrophobic Air Pollutant, *Environ. Sci. Technol*. 43 (2009) 1500–1506.
4. R. Kim, K. Mogyorosi, I. Dekany, Synthesis and structural and photocatalytic properties of TiO2/montmorillonite nanocomposites, *Appl. Catal*. A 32 (2006) 99-110.
5. K. Sato, K. Fujimoto, K. Kawamura, W. Dai, M. Hunger, Rheological mechanism of long-term Self-Assembly in Saponite Nanoparticles, *J. Phys. Chem.* C 116 (2012) 22954-22959.
6. K. Sato, W. Sprengel, Element-specific study of local segmental dynamics of polyethylene terephthalate upon physical aging, *J. Chem. Phys.* 137 (2012) 1049061-1049067.

The Study on Photocatalytic Degradation Performance to Musk Ketone with TiO_2/C Hybrid Aerogel in Aqueous Solution

Pan Feng, Chen Dong-hui†, Zhu Lin-lin

School of Chemical and Environmental Engineering, Shanghai Institute of Technology, Shanghai 201418, China
†E-mail: chendh@dhu.edu.cn, pffreedom@163.com

Shao Xia, Zhang Rui

School of Materials Science and Engineering, Shanghai Institute of Technology, Shanghai 201418, China
E-mail: Shaoxia@sit.edu.cn, Zhangrui@sit.edu.cn

Musk ketone was degraded with a TiO_2/C hybrid aerogel under a simulated solar light, and the effects of the mixing content of the catalyst, the pH and the concentration of hydrogen peroxide on the photo-catalytic performance were studied as well. The result shows that the TiO_2/C produced a red-shift. The removal efficiency of musk ketone by photocatalytic degradation was appreciably affected by PH, the mixing content of TiO_2/C and the concentration of H_2O_2. To better explain the experiment phenomenon, we studied reaction kinetics in light process. The result showed the reaction kinetics was first-order kinetics. Furthermore the final degradation products became some small molecules or ions, reduced the musk ketone harmfulness to the environment.

Keywords: TiO_2/C Aero-Gel; Photocatalytic; Musk Ketone; Simulation Sunlight; Kinetic Parameter.

1. Introduction

Since humans discovered that synthetic musks possessed similar performance to natural musk fragrance, it gradually dominated because of their low production and easy preparation. Musk ketone was used widely [1] and discharged by the municipal sewage treatment and domestic waste water. Due to the widespread use of MK and its potential hazard for ecotope, there is promoting concern about the harm of MK to ecotope. Therefore, musk ketone has been listed as a potential organic pollutant and controlled by multiple agencies [2,4]. Related literatures [5,6] showed that contaminant MK cannot be completely effective removal by the conventional wastewater treatment technology.

Therefore, there is an urgent for advanced technologies that can remove the amount of MK in the aqueous environment completely and no secondary pollution. In recent years, many advanced technologies and methods for removing organic pollutant in aqueous environment have been developed [7]. Although methods had been used to degrade synthetic musk, but usually the degradation efficiency are unsatisfactory and demanding conditions. However, photocatalytic degradation had proven to be an effective method for nitro musk under TiO_2.

Since then Frank and Bard [8] first discovered TiO_2 can degradation of cyanide in waste water, its application was more and more attracted people's interest in the environment. From then on, TiO_2 had been widely researched and application in wastewater treatment. While it has the following defects: 1) with wider band gap of 3.2 eV, only in ultraviolet light response; 2) the photogenic charge carrier (electronic-hole) easy to composite. So how to overcome or reduce the defects will be able to greatly improve the practicability of TiO_2. In recent years, carrying on the modification research to TiO_2 had been proven to be an effective way.

Research on photocatalytic degradation of musk ketone in water limited reported in literatures at home and abroad. And the degradation of musk ketone research rarely reported using TiO_2/C as a catalyst in the simulation sunlight and the degradation mechanism almost no available data. In conclusion, we expect to solve the following problems in this paper: 1) Preparing a efficient TiO_2/C hybrid airogel under suitable conditions, so that it cans response in visible light; 2) effects of the mixing content of the catalyst, the pH, the concentration of H_2O_2 on the photo-catalytic performance; 3) Studying the adsorption reaction in dark and the light reaction in illuminate for recognizing the whole process better. The information of degradation of MK provides some theoretical support for environment protection and a method under visible light.

2. Experiment Methods

2.1. *Chemicals and reagents*

Resorcinol(R) and furfuraldehyde(F) (AR) were purchased from Shanghai LingFeng chemical reagent Co., LTD.; Ethyl acetoacetate (AR) was supplied by Shanghai Zhanyun chemical Co., LTD.; Titanium tetrachloride, epoxy propane, anhydrous ethanol, orthophosphoric acid and H_2O_2 (30%) (AR) were purchased from Sinopharm Chemical Reagent Co., LTD.; Standard musk ketone(purity≧99.8%) was supplied by Dr. Ehrenstorfer - Schafers laboratory, Germany; Pure acetonitrile purchased from Adamas-beta; Photochemical

reaction instrument was given by Shanghai BinLon instruments Co., LTD; All the water was deionized water.

2.2. *Preparation of TiO_2 hybrid aero-gel photocatalyst*

In a typical synthesis, the mixture solution containing ethanol, furfural and resorcinol was added into the mixed solution of ethanol, ethyl acetoacetate(EA), propylene oxide and $TiCl_4$ under an ice-water bath. After placed for 5 min, the second mixed solution was transferred into small ampoules. The sealed ampoules were placed 1-2 days under ambient, and then moved in a water bath at 70 ºC for 5 days to form the TiO_2/RF wet gels. The TiO_2/RF wet gels were exchanged in the solution of propylene oxide for another 7 days, and then the unwrapped ampoules were treated for supercritical drying in an n-hexane-filled autoclave at 240 ºC and 6 MPa for 1 hour, afterwards the autoclave was depressurized at a rate of 0.1 MPa/min and cooled to ambient. The remaining solid in autoclave was so-called TiO_2/RF aerogels. After carbonizing TiO_2/RF aerogels in a vertical tube furnace at 800 ºC for 3 hours under the protection of nitrogen with a heating rate of 2 ºC/min, the expected TiO_2/C hybrid aerogels were obtained.

2.3. *Irradiation procedures*

An illumination experiment was carried out in a magnetic stirring device. Degradations were performed on 50 ml glass tubes at varying initial concentrations TiO_2 /C. Before the irradiation, the system was placed in the dark for 30 min to ensure adsorption equilibrium. At given time intervals, about 3 ml of MK solution were sampled and filtered by organic filter (13 mm * 0.22 μm) and ultrasonic. Then the clear solution was analyzed and recorded vibrations by HPLC.

2.4. *Analytical methods*

Musk ketone was degraded by a simulation sunlight by a medium pressure Xenon lamp 1000W, under cooling water. The analyses of MK samples were carried out by a HPLC (Agilent1100series, Agilent Technologies Co., LTD, American), the analytical column was Kromasil C18 (5mm, 250*4.6 mm i.d., stainless steel), A mobile phase is acetonitrile: water (80:20), the peaks were monitored at 235nm and the sample rate was 1.1ml/min, the volume is 20μl, and the experiments were conducted at room temperature.

3. Results and discussion

3.1. *Effects of operational parameters*

3.1.1. *Effect of pH*

Fig.1 presents the effect of pH on the removal of MK during dark and light on process. The pH value gradually increased from 2.0 to 12.0, conversion decrease from 95.6% to 44.9% during 120mins, respectively. The variations of pH induce modification in the charge state of TiO_2/C surface due to the following establishment of acid-base equation:[9]

$$Ti\text{-}OH + H^+ \leftrightarrow Ti\text{-}OH_2^+. \qquad pKa1 \qquad (1)$$

$$Ti\text{-}OH + OH^- \leftrightarrow Ti\text{-}O^- + H_2O. \qquad pKa2 \qquad (2)$$

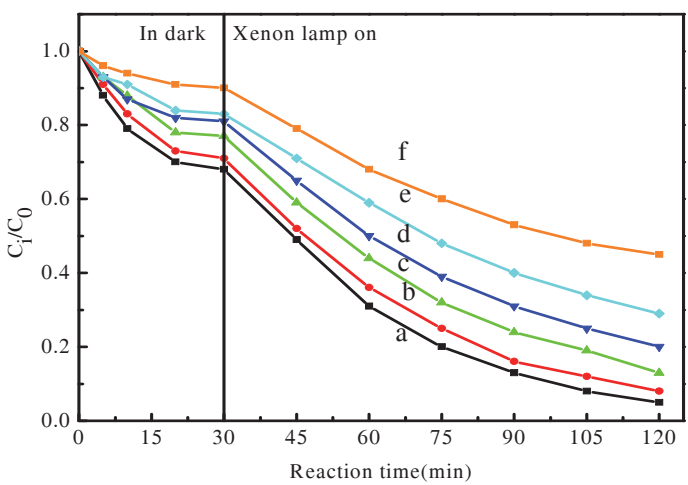


Fig.1 Degradation date variety of PH. Line (a) pH 2.0 (black), (b) pH4.0 (red), (c) pH 6.0 (light green), (d) pH 8.0 (blue), (e) pH 10 (sky blue) and (f) pH 12 (orange).

So, when we can use Eq.1 and Eq.2 explain this phenomenon through a simple electrostatic reasoning. Accordingly, with the increase of acidic PH value, making the surface TiO_2/C groups showed positive, and it would absorb more MK (mainly -NO_2) on catalyst surface. In contrast, at the alkaline aqueous solution (pH>7), TiO_2/C would inhibition MK molecular close to its surface.

3.1.2. *Effect of TiO_2/C hybrid airogel doping*

Fig.2 showed the degradation rate displayed 97.8% and 75.3% in 2h at sample concentration 250mg/l and 50mg/l, respectively. And degradation rate was 97.2% at 150mg/l.

It suggested that TiO_2/C concentration increased under the stirring will make the pollutants adsorbed onto its surface more fully. While, continuing to increase more than a certain extent the light would become difficult to reach the surface of the catalyst, and the utilization rate of light is decrease. Meanwhile, it was obtained that the adsorption quantity increased with the increase of the concentration, and that to promote the reaction to a certain extent. So, considering time and the cost savings the addition of TiO_2/C optimization mixing content should be around 150mg/l.

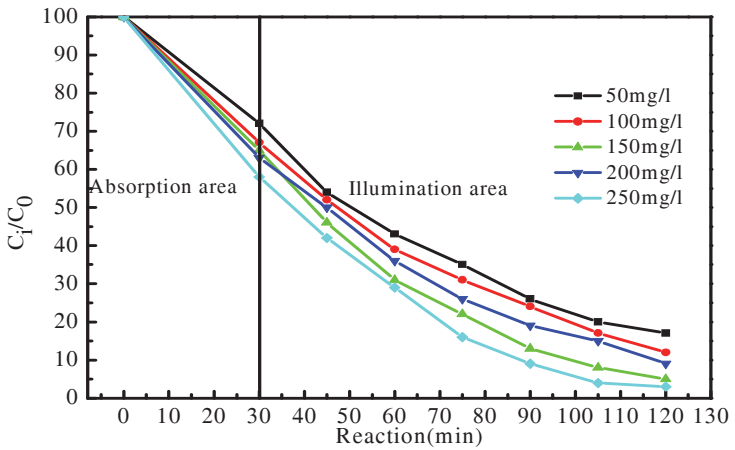


Fig.2 Effect of different TiO_2/C hybrid airogel doping. Operations were carried on the conditions pH2.0,[MK]=1.0mg/l, xenon lamp (1000W).

3.1.3. *The concentration of H_2O_2*

We can obtain that from Fig.3, the reaction was higher efficiency than without adding H_2O_2, and also reduced the degradation time. Conversion rate can reach 97.3% and 99.5% in 105 min and 120 min respectively. In addition, the efficiency decreases with the concentration of H_2O_2 more than 5mmol/l.

Studies show that [10,11] adding suitable amount of H_2O_2 can inhibit the electrons (e-) with holes (h+) compound in TiO_2 photocatalytic reaction. On the one hand, H_2O_2 can be consumed by direct photolysis or reacting with other intermediate species produced the •OH [12], thus be good for the reaction. On the other hand, the concentration achieve some extend H_2O_2 become scavenger of •OH, and inhabit the reaction. So the adding H_2O_2 should be 5mmol/l.

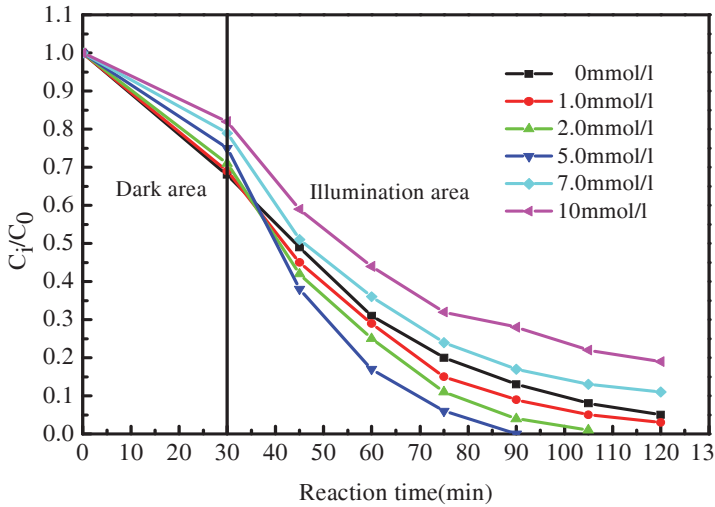


Fig.3 The influence of different H_2O_2 adding on the reaction process Ci/C0.

3.2. *Kinetics of MK degradation by simulated sunlight*

Kinetics of photocatalytic degradation musk ketone by TiO_2/C hybrid airogel can be expressed as:

$$-\frac{d_c}{d_t} = kC^m C^n_{TiO_2/C} \cdot \tag{3}$$

Assuming that the concentration of TiO_2/C remained constant in aqueous solution, the equation can be simplified to:

$$-\frac{d_c}{d_t} = k_{obs} C^m \tag{4}$$

where kobs related to the •OH generation rate, and the generation of the intermediate products and other factors. In this paper, the experimental data were fitted by liner, musk ketone showed that photocatalytic degradation process accord with pseudo-first-order kinetics, reaction order m = 1, and the kobs was obtained such as shown Fig.4.

4. Conclusions

TiO_2/C hybrid aerogel was prepared by a one-pot sol-gel method prepared occurred red shift and improved the utilization of visible light, can removal musk ketone efficient. Solutions PH, TiO_2/C dosage, the amount of H_2O_2 adding

were an important impact on the degradation effect. The increasing of pH will reduce the degradation efficiency and benefit for the degradation of pollutants at lower PH; TiO_2/C dosage from less to more, the degradation effect revealed appropriate dosage should be 150mg / l, 5mml / l in the amount of reaction was optimal in degradation process; but excessive of H_2O_2 would become scavenger of effective active group hydroxyl radical, thereby reducing the degradation efficiency. Through kinetic studies shown light reaction kinetics obeyed a pseudo-first-order kinetics. The final products mainly were formic acid, oxalic acid and other small molecule compounds. These products improved the rate of mineralization and reduced the harm to the environment, and no secondary pollution.

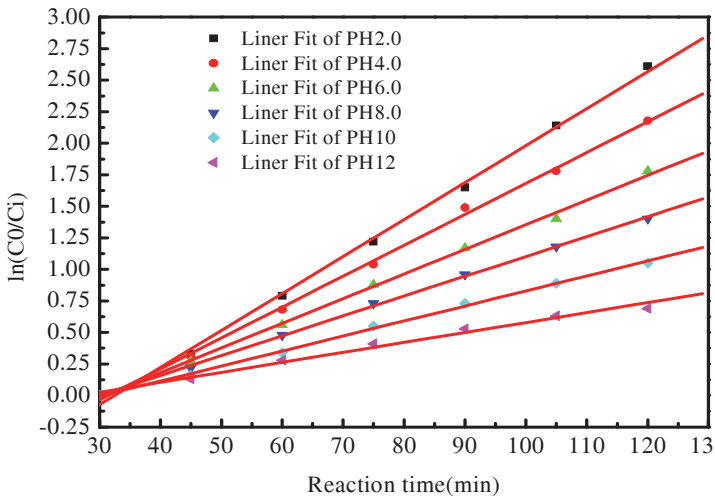


Fig.4 ln(C0/Ct)to time fitted curve at varying pH.

Acknowledgements

This work was supported by the Capacity Building Program of Shanghai Local Universities (No. 12160503600), the First-Class Discipline Construction Fund of Shanghai Municipal Education Commission (No. J201212), Nature Science Foundation of China (U1332107) and Key Discipline Construction Fund of Composite Materials of Shanghai Institute of Technology (No. 10210Q140001).

References

1. J. Reiner, K. Kannan, A survey of polycyclic musks in selected household commodities from the United States, J. Chemosphere. 62(2006)867–873.

2. Scientific Committee on Health and Environmental Risks, *Domestic-Overseas Flavor Fragrance Cosmetic Information*. 22(2006).
3. Department For Business Enterprise & Regulatory Reform, URN 08/689 Consultation on the consolidation of the existing regulations and implementation of 3 technical directives amending directive 76/768/EEC on the safety of cosmetic products, S. London: *Consumer and Competition Policy Directorate*, 2008.
4. Ministry of Health of the People's Republic of China, *Hygienic standard for cosmetics*, Beijing: Military Medical Science Press, 2007.
5. T. Ternes, J. Stuber, N. Herrmann, D. McDowell, A. Ried, M. Kampmann, B. Teiser. Ozonation, a tool for removal of pharmaceuticals, contrast media and musk fragrances from wastewater?, *J. Water Res*. 37(2003)1976-1982.
6. E. Felis, A. C. Alder, J. Surmacz-Gorska, K. Miksch: 'Advanced oxidation of the polycyclic musk fragrances with using UV and UV/H_2O_2 processes', *Arch. Environ. Protect*. 2008,34,13-23.
7. R. Guo, I. S. Lee, U. J. Kim, J. E. Oh., Occurrence of synthetic musks in Korean sewage sludge, *J. Sci. Total Environ.* 408(2010)1634-1639.
8. Frank S N, Bard A J, Heterogeneous photocatalytic oxidation of cyanide ion in aqueous solutions at titanium dioxide powder, *J. Am. Chem. Soc.* 99(1977)303-304.
9. A. Galenda, L. Crociani, N. El Habra, M. Favaro, M. M. Natile, G. Rossetto, Effect of reaction conditions on methyl red degradation mediated by boron and nitrogen doped, *J. Applied Surface Science*. 314(2014)919-930.
10. Benjamin J C, Linda A L, Peter K R, Hydrogen peroxide enhanced photocatalytic oxidation of microystin-LR using titanium dioxide, *J. Applied Catalysis B: Environmental*, 25(2000) 59–67.
11. M. Pera-Titus, V. Garcia-Molina, M. A. Banos, J. Gimenez, S. Esplugas, Degradation of chlorophenols by means of advanced oxidation processes, J. a general review', *Appl. Catal. B: Environ*. 17(2004) 219-256.
12. Glaze W. H., Kang J. W., Chanpin D. H., The chemistry of water treatment processes involving ozone, hydrogen peroxide and ultraviolet irradiation, *J. Ozanation Science& Engineering*. 9(1987)335-352.

Study on Excess Sludge Disintegration by Fenton Oxidation

Yin Jun, Wang Wanyao†, Hu Ying

Jilin Provincial Laboratory of Urban Water Resource and Environmental Remediation Engineering, Jilin Jianzhu University, China
†E-mail: wanyao8909@163.com
E-mail: hitjunyin@163.com, 89704410@qq.com

The disruption of excess sludge by Fenton oxidation is studied, and the soluble parameters of soluble chemical oxygen demand(SCOD), ammonia nitrogen(NH3-N), total phosphorus(TP), the ratio of volatile suspended solid(VSS) and total suspended solid(TSS) are selected to characterize the disruption effect. After the disruption of excess sludge by Fenton oxidation, SCOD and NH3-N increased and VSS / TSS decrease significantly. The reduction of the organic content of the sludge makes sludge stabilization degree increase. TP is significantly reduced due to the role of $FeSO_4$, but with the disruption of sludge, a part of the TP redissolves into supernatant. The experimental results show that the operation conditions were optimized with pH of 3.0, H_2O_2 dosage of 10g/L, Fe^{2+} dosage of 0.8g/L, reaction time of 1h, 70ºC between 20ºC and 70ºC reaction temperature, respectively.

Keywords: Fenton oxidation; excess sludge; soluble substances; VSS/TSS.

1. Introduction

Currently the vast majority of the sewage plants are using activated sludge process. This process is the most commonly used and sophisticated sewage treatment technology, but it produces a very large number of excess sludge. So, how to make a large number and complex composition sludge reduction, innocuousness, reclamation, stabilization through scientific treatment is an indispensable part [1,2,3].

Fenton oxidation technology has been studied in depth in domestic sewage and industrial wastewater treatment, and its mechanism is mainly Fe^{2+} catalytic decomposition of H_2O_2, generating strong oxidizing HO • radicals. It cracks extracellular polymeric of sludge surface to improve flocculation and dewatering[4] In addition, Fenton oxidation removes some organic matter in sludge, kills pathogens and improves the stability of sludge [12].

2. Materials and methods

2.1. *Characteristics of sludge*

The sludge is taken from the excess sludge after concentrate in the southeast sewage treatment plant of Changchun. Measuring the basic parameters (SCOD, NH_3-N, TP are soluble) are as follows:

Table 1

Parameters	pH	Water content (%)	SCOD (mg/L)	NH_3-N (mg/L)	TP (mg/L)	TSS (g/L)	VSS (g/L)	VSS/TSS
Value	6.6	97.72%	22.517	0.772	0.320	22.517	9.717	0.43

2.2. *Experimental methods*

Take 300mL sludge to 500mL conical flask and adjust the pH with concentrated sulfuric acid. Add a certain amount of 30% H_2O_2 and $FeSO_4 \cdot 7\ H_2O$, shake well, and then place in a thermostat water bath oscillator to shock [5]. Take out after a certain reaction time and callback to pH 7 with NaOH. After centrifuging, suction filtration with 0.45 μ m membrane, then measuring the soluble parameters.

2.3. *Analytical method*

Measure SCOD with fast COD detection instrument type 5B-1. First, find out the amount of water samples containing H_2O_2 by iodometric titration after suction filtration. Then shield the interference of H_2O_2 on SCOD measurement by calculating to add $NaSO_3$ [6]. TP use ammonium molybdate spectrophotometry. NH_3-N use Nessler's reagent spectrophotometry. TSS and VSS are meaured with standard methods.

3. Results and discussion

3.1. *Effect of pH on sludge disintegration*

Adjust pH to 2.0, 3.0, 4.0, 5.0, 6.6(raw sludge is not adjusted) with concentrated sulfuric acid, respectively. Add Fe^{2+} and H_2O_2 5g/L and 0.5g/L respectively and react for an hour at room temperature. Callback pH to 7. As shown in Fig. 1, the concentration of SCOD, NH_3-N, TP increase with the pH decreasing. The increasing soluble substances show that Fenton enhances the effect of sludge disintegration with the pH decreasing. VSS/TSS reflects the content of organic substances accounting for the total solid substances. Its curve decreases with pH

decreased, indicating that acidic condition is in favor of the decomposition of organic substances and convert into soluble substances in the sludge. From the reaction mechanism, excessive OH- is produced in high pH that would inhibit the generation of • OH, and Fe^{3+} and Fe^{2+} are precipitated as hydroxides to reduce or loss of catalytic action. Figure 1 shows that the sludge cracks best in pH 2~3. The optimum pH value is 3 taking into account that the economic factors and the gap of the cracked effect is not obvious in pH 2~3.

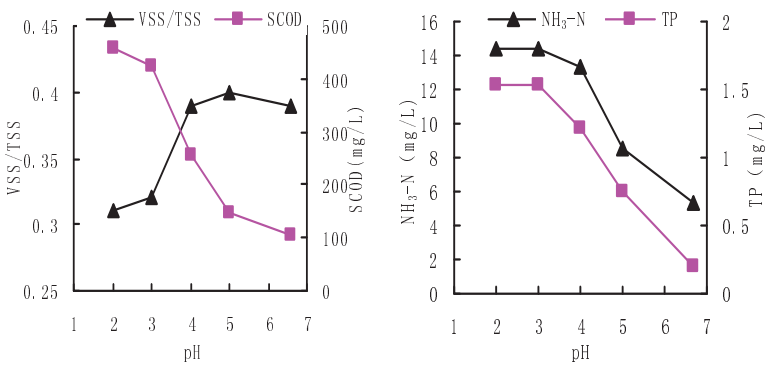


Fig. 1 Effect of pH on sludge disintegration

3.2. *Effect of Fe^{2+} dosage on sludge disintegration*

Fe^{2+} dosages are 0, 0.2, 0.4, 0.6, 0.8, 1.0g/L, respectively. H_2O_2 is 5g/L, pH=3, and react for an hour at room temperature. Callback pH to 7. Figure 2 shows the results, SCOD reflects that effect of sludge disintegration is best as Fe^{2+} is 0.8g/L. NH_3-N and VSS/TSS curves are to flatten when Fe^{2+} is 0.8. TP decreases with the Fe^{2+} increasing. Although Fenton oxidation crack sludge make the concentration of soluble TP, FeSO4 removes soluble phosphorus to solid phase of excess sludge[7]. It just make phosphorus is rich extremely as fertilizer and reduce the difficultly of treating the phosphorus in excess sludge supernatant. Fe^{2+} is as the catalyst of Fenton reaction, which can not reach the optimal response effect if the catalytic reaction produces too less • OH due to insufficient dosage. Excess dosage of Fe^{2+} would transform to Fe^{3+} with the oxidability of • OH, which making Fe^{2+} lose the original role and consuming the oxidability of • OH [9,10].

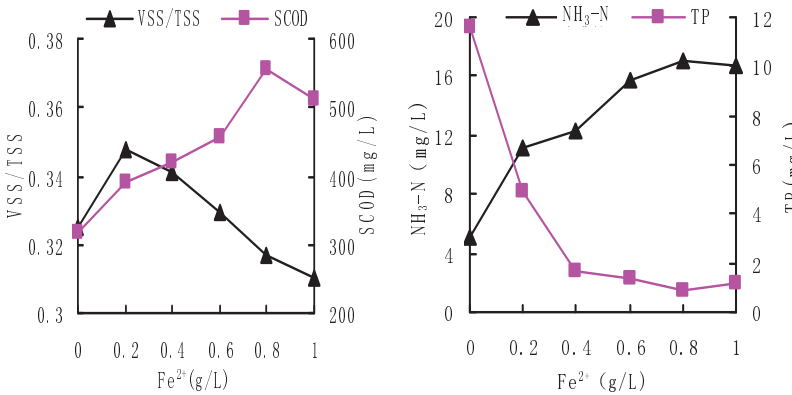


Fig. 2 Effect of Fe^{2+} dosage on sludge disintegration

3.3. *Effect of H_2O_2 dosage on sludge disintegration*

Experiment selects H_2O_2 dosages are 0, 2.0, 4.0, 6.0, 8.0, 10.0, 12.0, 14.0g/L, respectively, Fe^{2+} is 0.8g/L, pH=3, and react for an hour at room temperature. Callback pH to 7. Figure 3 shows the reaction results. The trends of SCOD, NH_3-N and TP become higher with the increasing dosage. After the H_2O_2 dosage of 10g / L, the increasing trend slows. On the contrary, VSS / TSS decreases. Overall consideration, select the H2O2 dosage of 10g/L for the best value. When H_2O_2 dosage is too high, H_2O_2 will rapidly oxidize Fe^{2+} to Fe^{3+}, make the reaction carry out with the catalyze of Fe^{3+}. The reaction efficiency decreases obviously [8]. Excess H_2O_2 generates bubbles and floats sludge.

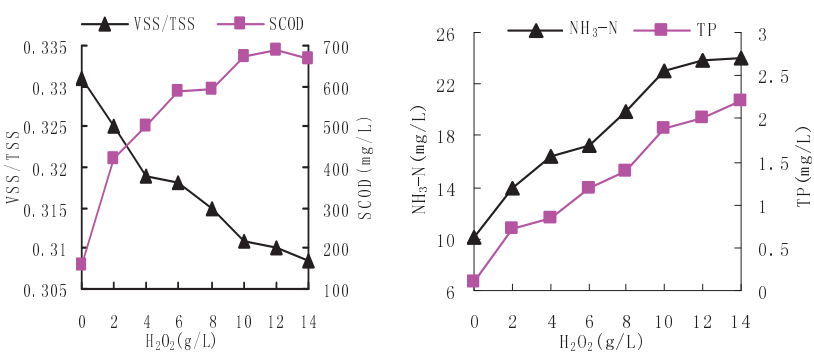


Fig. 3 Effect of H_2O_2 dosage on sludge disintegration

3.4. *Effect of reaction time on sludge disintegration*

Select the reaction times of Fenton oxidation are 20, 40, 60, 80, 100, 120min, respectively, the dosage of Fe^{2+} and H_2O_2 are 0.8g/L and 10g/L severally, pH=3, react at room temperature. Callback pH to 7. Callback pH to 7. Figure 4 expresses that the parameters' curve trend to flatten after 60 min, it can be concluded that the response essentially complete within an hour.

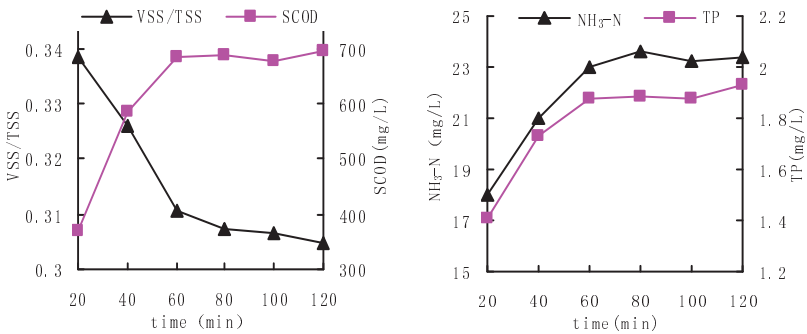


Fig. 4 Effect of reaction time on sludge disintegration

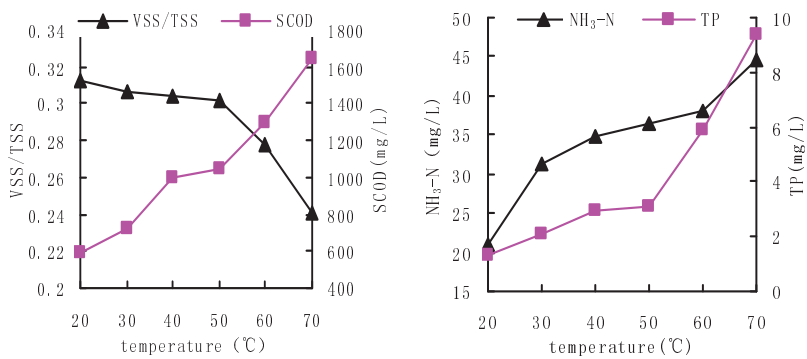


Fig. 5 Effect of reaction temperature on sludge disintegration

3.5. *Effect of reaction temperature on sludge disintegration*

Select the reaction temperatures are 20, 30, 40, 50, 60, 70ºC, the dosages of Fe^{2+} and H_2O_2 are 0.8g/L and 10g/L, respectively, pH=3, react for an hour. Callback pH to 7. Figure 5 is the effect of reaction temperature on sludge disintegration. The trends of SCOD, NH_3-N and TP become higher and VSS/TSS becomes lower with the increasing dosage. And the trends are more obvious after 50ºC than

before. Because the effect of Fenton crack sludge enhances with the increasing temperature. The best result is 70ºC between 20ºC and 70ºC. But the heat treatment causes the cell membrance rupture [11] between 45ºC and 60ºC, the effect of sludge disintegration is more obviously.

4. Conclusions

After Fenton oxidating and disrupting the excess sludge, SCOD, NH_3-N in the supernatant increase significantly, on the contrary, VSS/TSS values decrease. VSS/TSS is 44.19% of the original sludge in the optimal operation condition. It can be known that the organic content of the sludge is reduced and sludge stabilization degree is improved [13]. Because of the role of $FeSO_4$, TP in the liquid phase is transferred to the solid phase of the sludge leaving the TP of solubility decrease significantly. With the degree of the sludge disintegration enhancing, the TP of redissolved in the supernatant also increases. But it's not obviously that relative to the effects of that $FeSO_4$ remove the TP. These have positive impact on the sludge as fertilizer subsequently and also reduce the difficulty of dealing with TP in the supernatant.

According to the solubility index SCOD, NH_3-N, TP and VSS/TSS, analyze with the economic factors to determine that the operation conditions are optimized with pH of 3.0, H_2O_2 dosage of 10g/L, Fe^{2+} dosage of 0.8g/L, reaction time of 1h, 70ºC between 20ºC and 70ºC reaction temperature, respectively.

Acknowledgement

The authors gratefully acknowledge the financial support of the National Water Pollution Control and Management Technology Major Project of China (Grant Number: 2012ZX07201-001).

References

1. Yin Jun, Xuejun Tan, Sewage and sludge disposal and resource utilization[M]. Beijing: Chemical Industry Press, 2005
2. Liu Y., Tay J. H. Strategy for minimization of excess sludge production from the activated sludge process*[J]. Biotechnology Advances*, 2001, 19(2): 97-107
3. Zhong Hengwen, Kana Ninomiya. Processing of raw sludge by Fenton oxidation*[J]. ChinaWater & Wastewater*, 2003, 19(8): 46-47
4. Lu M. C., Lin C. J., Liao C. H., et al. Dewatering of activated sludge by Fenton's reagent*[J]. Advances in Environmental Research*, 2003, 7(3): 677-670

5. Li Juan, Zhang Panyue, et al. Extracellular polymeric substances disintegration by Fenton oxidation of excess sludge*[J]*. *Environmental Science*, 2009, 30(2): 475-479
6. Deng Xiaohui, Zhang Haitao, et al. Study of the interference from hydrogen peroxide on determination of chemical oxygen demand*[J]*. *Shanghai Chemical Industry*, 2008, 33(4): 11-13
7. Lin Jinnan. Phosphate removal by ferrous sulfate from wastewater[D]. Shenzhen: Harbin Institute of Technology Shenzhen Graduate School, 2012
8. Chen Yingwen, Liu Mingqing, et al. Experimental study on excess sludge disintegration by Fenton oxidation*[J]*. *Chinese Journal of Environmental*, 2011, 5(2): 409-413
9. Buyukkamaci N. Biological sludge conditioning by Fenton's reagent[*J]*. *Process Biochemistry*, 2004, 39(11): 1503-1506
10. Chen Chuanhao, Xie Bo, et al. Mechanism of municipal sludge disposal by Fenton oxidation*[J]*. *Environmental Science*, 2000, 21(5): 93-96
11. Wang Xiaoxia. Studies of the cellular materials released from waste activated sludge and phosphorus recovery during sludge reduction process[D]. Shanghai: Resource and Environmental Engineering school, East China University of Science and Technology, 2010
12. Zhou Yu, Zhang Aiju, et al. Sewage sludge disintegration and dewaterability improvement by photo-Fenton oxidation[*J]*. *Chinese Journal of Environmental*, 2011, 5(11): 2600-2604
13. Song Xiangguo, Zhang Panyue, et al. Mechanism of municipal sludge disposal by Fenton oxidation*[J]*. *Environmental Science & Technology*, 2009, 32(7): 64-67

Investigation on Environment Benefit and Problem of Solar Power Generation Technology

Qi Liqiang †, Li Zhixin and Zhang Yajuan
North China Electric Power University, Baoding, 071003, China
†E-mail: qi_liqiang@163.com,
E-mail: 5985254910@163.com, 55523603@qq.com

Solar energy technologies offer a clean, renewable, and domestic energy source, and are essential components of a sustainable energy future. The effects of solar power technology on the environment are both positive and negative. The solar power generation technology to the environment loss is lower than the coal-fired power generation technology. However, solar power system generate many environment problems include waste water and waste gas pollution such as the representative of which is containing fluorine, chromium containing wastewater and hydrogen fluoride, silicon tetrachloride gas. Moreover solar panel is a kind of light pollution, and unsuccessful dispose of solar cells that reach working life will make the stench in the air and destroy soil.

Keywords: solar power; fossil fuel; environment.

1. Introduction

At present the proportion of solar energy in energy structure is still very low [1], but future trend is that renewable energy represented by solar energy is gradually replacing traditional fossil fuel energy's dominant position [2]. Governments have set up a series of laws and regulations to support the solar industry, and scientific workers are attempting to seek more efficient and economically solar power generation technology. There is no doubt that solar power system and its installed capacity in the energy structure of share will increase [3].

However, the negative effects of solar power generation technology exist and most of people ignore this issue [4]. The process of production of solar power generation system will produce waste gas which is difficult to clean, and waste water pollution. Solar power system reaching useful life for waste will pollute the environment. Pollution source in the coal-fired power plant is mainly from the process of power generation, and in the solar power generation technology is mainly the process of preparation of photovoltaic modules.

2. The environmental benefits of solar power generation technology

Coal-fired power generation will produce large amounts of ash, dust, sulfur dioxide, nitrogen oxides, carbon dioxide and other pollutants, and waste gas must be processed before emission. In the process of power generation with solar power technology, water and fossil fuels are not consumed, and pollution is not produced. Thus it saves a lot of capital for environmental protection. It also has the advantages of no mechanical rotating without auxiliary power and no noise pollution. In addition, the solar power technology can be used independently and not into the grid. So wires, telephone poles, and transmission facilities are not needed, and it can reduce cost and can be applied to the scenic spot. Solar power components installed on the roof of metope can be used as building materials which means that it will save construction materials, reduce the construction cost, and indirectly contribute to environmental protection.

Solar power equipment can be installed on the roof, desert, and remote areas, and is not subject to regional restriction. A lot of good land will be saved and high quality land resources can be used for more meaningful projects. Thermal power plant is usually built near downtown in order to save the cost of electricity transmission, but it would have been more adverse effects on the environment.

Table 1 Solar power technology damage to the environment

Types of pollution	Pollutants equivalent charge standard (RMB)	Pollutants equivalent value (kg)	Charge standard (RMB/kg)	Environmental value(RMB/kg)	Emissions (g/kWh)	Environmental damage (10^{-3}RMB/kWh)
CO_2	--	--	--	0.023	78.62	1.81
SO_2	0.60	0.95	0.632	6.320	0.82	5.18
NO_X	0.60	0.95	0.632	6.320	0.36	2.28
CO	0.60	16.70	0.036	0.360	0.01	0.004
TSP	0.60	4.00	0.150	1.500	0.02	0.03
Ash	--	--	0.030	0.300	5.00	1.50
Residue	--	--	0.025	0.250	1.36	0.34
Total						11.14

Comparing with traditional power generation technology represented by coal-fired power generation technology, the solar power generation technology is a real green pollution-free renewable energy and conforms to the concept of sustainable development [5]. Table 1 shows the calculations of environmental loss under solar power generation and coal power generation technologies, respectively.

3. The environmental problems in the process of solar power generation

Currently solar cells include monocrystalline silicon solar cells, polycrystalline silicon solar cells, and amorphous silicon solar cells and so on. Considering the photoelectric conversion efficiency and cost factors, polycrystalline silicon solar cells are widely used. Solar cells include monocrystalline silicon, polycrystalline silicon, and amorphous silicon solar cells. A comparison of these materials is shown in Table 2. This article mainly discusses the environmental impact of polycrystalline silicon solar cells.

Table 2 Comprehensive comparison of several kinds of solar cells

Battery types	Silicon dosage	Photoelectric efficiency	Useful life	Cost of production
Single crystalline silicon solar cell	more	superior	longer	more
Polycrystalline silicon solar cell	much	high	long	much
Amorphous silicon solar cell	less	low	short	less

4. The environment impact in the production process of solar power equipments

Production process includes manufacturing crystalline silicon, producing solar battery, and assembling solar photovoltaic power generation system. Crystalline silicon enterprises as upstream of photovoltaic industry make serious environment problems. There are high energy consumption, high pollution and low level repeated construction in the enterprise. In addition, the process of solar power equipment production will produce waste water pollution and environmental problems such as air pollution. Due to the processing cost and technological level restrictions many photovoltaic enterprises just adopted a simple pollution treatment technology, and some small businesses even discharged pollutants directly without treatment.

4.1. *Wastewater*

The process of Crystalline silicon solar cells production will use chemicals such as acid and alkali, phosphoric acid, hydrofluoric acid, sodium hydroxide and these will be used for silicon wafer surface corrosion, velvet and processes to remove phosphorus silicon glass. The use of chemicals will inevitably produce alkali wastewater, organic wastewater, containing fluorine wastewater, and wastewater containing chromium containing silicon. The wastewater contains high concentration of suspended solids. Although pollutant concentration rate in the

processed sewage is very low, pollution not allow to ignore due to the crystalline silicon solar cell industry booming. Among them, the pollution in the wastewater containing chromium and fluoride respectively is as follows. Wastewater containing chromium is mainly hexavalent chromium compounds and trivalent chromium compounds, and toxic of hexavalent chromium is 100 times higher than that of trivalent chromium [6]. Wastewater with Fluoride mainly comes from the cleaning silicon process and silicon battery production process. Some enterprises in pursuit of economic benefits will discharge directly ignoring national integrated wastewater discharge standard (primary and secondary fluorine concentration emissions cap of 10 mg/L) of fluoride wastewater. Wastewater from Amorphous silicon thin film solar cell production process is lower than that from the production of small crystalline silicon solar cell industry, and its pollutant composition is simple.

4.2. *Waste gas*

System of pile and the process of phosphorus silicon glass will produce the acid gas such as hydrogen and nitrogen oxides. Phosphorus diffusion process will produce diffusion waste gas represented by chlorine gas, including hydrogen chloride gas. Plasma etching process produces etching waste gas including hydrogen, carbon dioxide, and silica etc. PECVD process will produce PECVD waste gas which is mainly composed of hydrogen and nitrogen, and no reaction borane and silane fetor. Silk screen printing and sintering process will produce printing waste gas and sintering waste gas. Waste gas from production process of solar cell needs purification treatment to reach standard of emission. Acid gas, diffusion gas, and etching waste gas can be processed by acid mist purification tower (lye spraying exhaust). Silane burn tower is available to PECVD waste gas such as silane and borane and after burning, boron trioxide, water vapor, and silica will be made. Post-combustion matter need to use filter processing. Printing and sintering waste gas can be treated by activated carbon adsorption and by adsorption processing using silica gel or molecular sieve etc [7].

4.3. *Other pollutions*

Production of Photovoltaic solar panels need to use a lot of solar PV glass, and the significant characteristic of glass industry is high energy consumption and high pollution. Glass made by heating, melting, and cooling raw materials such as quartz sand, soda ash, feldspar and limestone. The production of glass will produce harmful gases such as sulfur dioxide, nitrogen oxide and hydrogen fluoride and several kinds of waste water such as acidic waste water, wastewater

containing phenol, tar waste water, fluoride wastewater, and heavy metal wastewater etc. At the same time, the glass production process will also inevitable produce noise pollution and solid waste pollution.

5. The problems in the solar power generation process

The solar power generation process causes other forms of pollution.

5.1. *The light pollution*

Most people ignore light pollution caused by solar power equipment. In order to improve the strength of the photovoltaic device, protect the photoelectric conversion element, and meet good pervious to light performance at the same time, the surface of the photovoltaic modules need a thickness of 3.2 mm or 4 mm super white glass. Photovoltaic glass has reflection effect with light reflectivity of about 4% and reflectance is maximum for infrared with wavelength that is greater than 1200 nm. Reflected light on the surface of the glass forms a light pollution.

5.2. *The high power generation cost*

Although running cost in the process of solar power technology is extremely low, the degree of electric power generation cost is higher and several times higher than the cost of coal-fired power due to large initial investment [8], and low power generation efficiency. Solar power cost declines year by year [9], however, photovoltaic power generation has disadvantage of price compared to conventional energy or other clean energy power generation technology.

6. The problems about waste solar batteries

Use fixed number of year of Solar power generation equipment is about 20 years, and solar component reaching the year is a solid waste. Some part is dangerous solid waste and has a potential danger to the environment, and the impact is difficult to measure. If silicon, lead, cadmium, phosphorus, and flame retardants etc. are not reasonable treatment or recycling, they will have adverse impact on water, soil, air and human health. Currently handling of waste solar power equipment has no special perfect system and traditional processing methods such as electronic products burning and extraction process may cause severe secondary pollution.

Most photovoltaic devices need to use storage battery whose life is short [10]. Battery pollution to the environment problem in the production process has been basically solved, and the biggest problem of environment is reasonable recycling

of waste batteries. The participants in recycling of waste batteries are mainly self-employed individuals and small factories that have less environmental protection consciousness. Only a quarter of the lead is recycling, and most of the rest spreading through the air, water, soil and food will pollute environmental and harm human health. Lead, a kind of high toxic substances, can enter into human body through the respiratory system, digestive system, and the skin, and excessive amounts of lead can reduce the body immunity and affect intelligence, particularly serious for children. Therefore, we should take the advanced technology and equipment to improve battery production and recycling process, and the government should make strict policy of battery industry to protect environment.

7. Conclusions and suggestions

For solar power technology emerges as a new technology, we should from two aspects of positive and negative view in an all-round way. Solar energy is abundant, and there will be no energy depletion. The generating process of solar power generation system is no pollution and no energy consumption and does not produce secondary pollution. Solar power is not subject to regional restriction and can save land. However, non-green issues also exist behind the green solar energy technology. The production process of solar power generation equipment produces waste water, waste gas and solid waste. Solar electricity reaching to use fixed number of year does not have reasonable waste recycling mechanism, and unreasonable disposition can seriously pollute the environment.

Acknowledgements

This work was supported by the National Natural Science Foundation of China (Grant No. 21376072 and 51376063), the Natural Science Foundation of Hebei province (Grant No. E2012502011) and the Fundamental Research Funds for the Central Universities (Grant No. 13ZD17).

References

1. Rath Bhakta B, Marder James M. Powering the future: does the fuel gage read empty?*[J]. Advanced Materials Progresses*, 2007, 165(1)28-29.
2. Simone Espey. Renewables portfolio standard: a means for trade with electricity from renewable energy sources*[J]. Energy policy*, 2001, 29(7)557-566.

3. Elizabeth Harder, Jacqueline MacDonald Gibson. The costs and benefits of large-scale solar photovoltaic power production in Abu Dhabi, United Arab Emirates*[J]. Renewable Energy*, 2011 (36)789-796.
4. Kaygusuz, K. Environmental impacts of the solar energy systems*[J]. Energy sources*, 2009, 31(15)1376-1386.
5. Y.W. Sun, R. Wang, L.S Xiao, Economical and Environmental Analysis of Grid-connected Photovoltaic Systems in China. *China Population, Resources and Environment*, 21(2011), pp. 88-94.
6. Jin Chunhua. The harm of Cr and the treatment of wastewater containing Cr (VI). *Technical exchange of experience*, 10-13.
7. H.B. Chen, Y.L. Li, Y.X. Yin, Experiments for trichlorosilane production from silicon tetrachloride by plasma reduction. Chlor-alkali industry, 46(2010), pp. 30-33.
8. Yahyavi, M.,Vaziri, M.,Vadhva, S. Solar energy in a volume and efficiency in solar power generation [A]. IEEE computer society, *2010 IEEE international conference on information reuse and integration*[C], 2010, 394-399.
9. Esram, T., Krein, P.T., Kuhn, B.T., et al. Power electronics needs for achieving grid-parity solar energy costs[A]. 2*008 IEEE Energy 2030 Conference*[C], 2008.
10. Glavin, M.E., Hurley, W.G.. Ultracapacitor/battery hybrid for solar energy storage [A]. *2007 42nd International Universities Power Engineering Conference*[C],2007.791-795.

Qualitative and Quantitative Analysis of Bu-Gong Saponin

Cui shuling
Hebei University of Science and Technology,
Shijiazhuang 050018, China
E-mail: cuishulingling@126.com

It is tested by qualitative and quantitative analysis to Bu-gong tea saponin that the oxidative substance contained in Bu-gong tea saponin is sodium percarbonate with content of 45%. There are two kinds of alkalis in Bu-gong tea saponin by qualitative analysis: sodium hydroxide and sodium carbonate, and the content of them is respectively 29% and 4.5%.

Keywords: Bu-gong tea saponin; qualitative analysis; quantitative analysis; alkali; oxidant.

1. Introduction

In recent years, Bu-gong tea saponin as a new type of scouring and bleaching pre-treatment agent has attracted prevalent attention of the industry. It is gradually expanding its scope of application in dyeing and finishing field for textiles. But the published literatures are mostly limited to its application process [1-3] instead of its action mechanism. This paper aims at the component analysis of Bu-gong tea saponin by means of chemically qualitative or quantitative analysis so that it might provide some theoretical guidance to the practical application of Bu-gong tea saponin.

2. Experimental

2.1. *Materials*

Bu-gong tea saponin (Shanghai Jintang Textile Material Technology Co., Ltd.); hydrogen peroxide (30%, Tianjin HENGXING Chemical Reagents Manufacturing Co., Ltd.); Ceric sulfate (A.P, Tianjin Fucheng chemical reagent);

Catalase (Shanghai Daidi Industrial Development Co., Ltd.); Curcumin(Tianjin Zhiyuan Chemical Reagent Co., Ltd.); Bromocresol green (Tianjin Yongtai Chemical Reagent Development Center); 1,10-phenanthroline-ferrous indicator (Tianjin Bodi Chemical Co., Ltd.); Chloramine T (Tianjin Bodi Chemical Co., Ltd.); Sodium hypochlorite; Sodium perborate, Sodium percarbonate, Hydrochloric acid.

2.2. *Instruments*

MP200A electronic balance (Shanghai Jingke Balance Factory); 50mL burette; Transfer pipette; 250 volumetric flask.

3. Results and discussion

3.1. *Qualitative analysis of the alkali in Bu-gong tea saponin*

It was found that the pH value of Bu-gong tea saponin aqueous solution is much larger than 14. If the Bu-gong tea saponin alkaline agent is only sodium carbonate as pronounced in their patent [4], the alkalinity should not be so strong. So it may be initially deduced that there is also a strong base sodium hydroxide in the Bu-gong tea saponin besides sodium carbonate.

If excess barium chloride solution is added in the mixed solution of sodium hydroxide and sodium carbonate, the reaction is as follows: $Na_2CO_3+BaCl_2=BaCO_3\downarrow+2NaCl$. Using phenolphthalein as the indicator in the titration with hydrochloric acid standard solution, the reaction of the first stoichiometric point is $NaOH+HCl=NaCl+H_2O$. It would be tested no existence of sodium hydroxide if phenolphthalein doesn't turn red when adding excess barium chloride solution to pure sodium percarbonate[5]. But practical experiments showed that the solution turned red, explaining the presence of sodium hydroxide in Bu-gong tea saponin.

As this article discusses below, the oxidizing substances in Bu-gong tea saponin is sodium percarbonate which will decompose into sodium carbonate in water. Therefore, Bu-gong tea saponin contains sodium carbonate as can be verified by the patent declared. Both phenolphthalein-methyl orange two-step-titration and phenolphthalein-bromocresol green-methyl red two-step-titration consumed hydrochloric acid (shown in Table 1) in the second stoichiometric point, as can confirm the existence of sodium carbonate in Bu-gong tea saponin.

3.2. *Quantitative analysis of the alkali in Bu-gong tea saponin*

Add an excess of barium chloride solution into Bu-gong tea saponin solution, then titrate the mixed solution with 6.2500 mol/L hydrochloric acid standard solution using phenolphthalein-bromocresol green-methyl red as indicator[6]. The titration data is shown in Table 1.

Table 1 The consumed amount of hydrochloric acid in Phenolphthalein-bromocresol green-methyl red two-step titration

Titration number	1	2	3	4	Average value
Amount of hydrochloric acid at the first stoichiometric point with phenolphthalein as indicator (mL)	0.90	0.95	0.92	0.91	0.9200
Amount of hydrochloric acid at the end point with bromocresol green - methyl red as indicator (mL)	0.80	0.82	0.83	0.90	0.8375

According to the formula $CNaOHVNaOH=CHClVHCl$ and the data listed in the first line of Table 1, the concentration of sodium hydroxide in Bu-gong tea saponin is calculated as 0.2875 mol/L, or 11.5 g/L, or 28.75%. According to the formula $2CNa_2CO_3VNa_2CO_3=CHClVHCl$ and the data listed in the second line of Table 1, the concentration of sodium carbonate in Bu-gong tea saponin is 0.1309 mol/L, or 13.87g/L, or 34.68%.

3.3. *Qualitative analysis of the oxidizing substances in Bu-gong tea saponin*

Common oxidizing substances having bleaching function mainly include sodium peroxide, hydrogen peroxide, bleaching powder, sodium hypochlorite, sodium chlorite, chloramine T, sodium perborate, sodium percarbonate. Among them, sodium peroxide is extremely unstable, and can release fierce exothermic heat in water. What is more, it can not exist for a long time in Bu-gong tea saponin storage conditions. Therefore, oxidizing substances in Bu-gong tea saponin can't be sodium peroxide. Hydrogen peroxide is generally existed in the form of aqueous solution, and does not exist in powder state, so hydrogen peroxide can be excluded from the list. Bleaching powder is a mixture mainly consisting of calcium hypochlorite. If the oxidizing substances was bleaching powder, Bu-gong tea saponin solution would appear white precipitation when titrated with hydrochloric acid, but no sign of precipitation appeared instead of transparent solution from the experiments, showing that the oxidizing substance is not bleaching powder

neither. Sodium chlorite is also excluded by considering that it will produce chlorine dioxide gas which is toxic and corrosive to equipment in the process of the sodium chlorite bleaching, causing serious environmental pollution. Next the rest possible oxidation substances will be discussed by way of elimination one by one.

3.4. *Exclusion of sodium perborate with curcumin method*

Compounds containing boron such as boronic acid, borax, borate and sodium perborate turn red color when meet curcumin in acidic condition, and blue-green color on ammonia. Even 0.1 micrograms borate can be detected with the curcumin method[7], so this method can be used to determine whether or not sodium perborate exist in Bu-gong tea saponin. The experiment phenomena are showed in Fig.1-Fig.3.

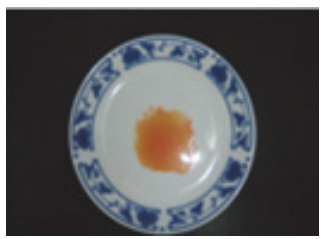


Fig.1 Sodium perborate

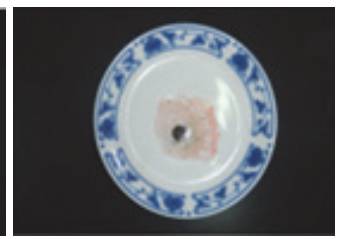


Fig.2 after dropping ammonia

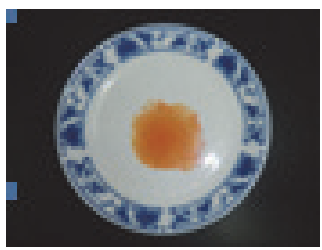


Fig.3 Bu-gang tea saponin plus curcumin

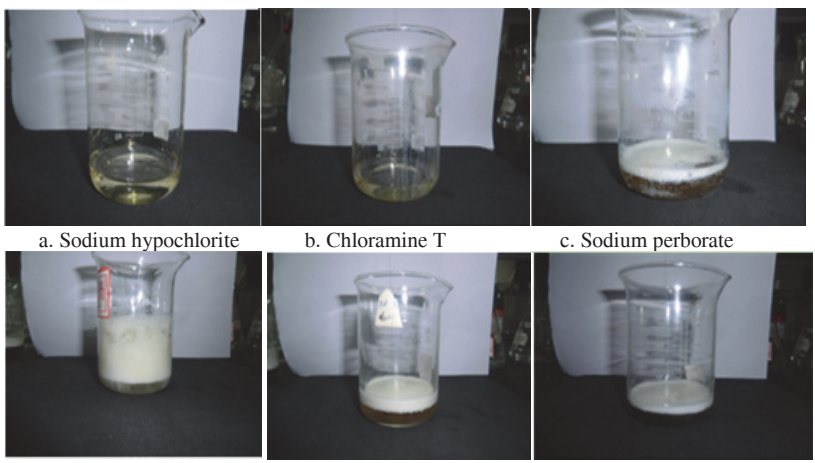


Fig.4 after dropping ammonia plus curcumin

It can be seen from Fig.1 and Fig.2 that there is a cholor change after dropwise adding ammonia to curcumin + sodium perborate solution, but no the case in Fig.3 and Fig.4, showing that there is no boron compound in Bu-gong tea saponin. Therfore, it can be concluded that Bu-gong tea saponin doesn't contain sodium perborate.

3.5. *Exclusion of sodium hypochlorite and chloramine-T with catalase*

Catalase is characterized in high catalytic specificity. It only reacts with hydrogen peroxide or substances that can produce hydrogen peroxide. Now respectively add a little catalase to the solution of sodium hypochlorite, chloramine T, hydrogen peroxide, sodium perborate, sodium percarbonate, Bu-gong tea saponin. The phenomena after adding catalase are shown in Fig.5.



a. Sodium hypochlorite b. Chloramine T c. Sodium perborate

d. Hydrogen peroxide e. Sodium percarbonate f. Bu-gong tea saponin

Fig.5 Phenomena after adding catalase into 6 substances sulution

Fig.5 shows that there is no reaction both in sodium hypochlorite solution (a) and chloramine T solution (b) after adding catalase, however, solutions of sodium perborate, hydrogen peroxide, sodium percarbonate and Bu-gong tea saponin appeared a large number of bubbles, suggeting the existence of hydrogen peroxide in those sulutions. In terms of the experimental results sodium hypochlorite or chloramine T can be ruled out from the possible oxidizing substances in Bu-gong tea saponin listed above. The presence of hydrogen peroxide and sodium perborate had been excluded by the previous experiments, therefor, only sodium percarbonate is left. Moreover, the phenomena of sodium percarbonate and Bu-gong tea saponin to catalase are extremely similar to each other, so it can be concluded that the oxidizing substances in Bu-gong tea saponin is sodium percarbonate.

3.6. *Quantitative analysis of sodium percarbonate in Bu-gong tea saponin*

The cerium sulfate titration method was used to analyze the content of sodium percarbonage in Bu-gong tea saponin. The content of hydrogen peroxide derived from Bu-gong tea saponin can be calculated by the equation of $2C_e^{4+}+H_2O_2 \rightarrow 2Ce^{3+}+2H^{+}+O_2$ when useing 1,10 - phenanthroline-ferrous as indicator [8].

Prepare 250 ml 40g/L Bu-gong tea saponin solution, dilute it for10 times and pick up 25 ml, then titrate it with a standard solution of cerium sulfate (0.1006mol/L). The titration data are shown in Table 2.

Table 2 The amount of cerium sulfate solution in titration of Bu-gong tea saponin

Titration number	1	2	3	4	5	6	Average value
Amount of cerium sulfate solution (ml)	8.45	8.56	8.55	8.43	8.50	8.48	8.495

According to $C_{Ce(SO4)2}V_{(CeSO4))}=2C_{H2O}2V_{H2O2}$, the molar concentration of hydrogen peroxide in Bu-gong tea saponin is 0.1709 mol/L, meanwhile the mass concentration is 5.8113 g/L.

According to the decomposition equation of sodium percarbonate, the mass content of sodium percarbonate is $m2Na_2CO_3 \cdot 3H_2O_2=C_{H2O2}\div 3\times 314.02l=17.89$ g/L. Then the percentage concentration of sodium percarbonate in Bu-gong tea saponin: W%=17.89÷40×100%=44.72%.

As mentioned above, the sodium carbonate content in Bu-gong tea saponin is 34.68%. This value includes both the sodium carbonate hydrolyzed from sodium percarbonate and that deliberately added for the preparation of Bu-gong tea saponin. The content of hydrolyzed sodium carbonate from sodium percarbonate is $W\%=2/3C_{H2O2}\ M_{Na2CO3}\div 40\times 100\%=30.19\%$, so the content of sodium carbonate added during the preparation of Bu-gong tea saponin is W%=34.68% − 30.19%=4.49%.

4. Conclusions

The oxidizing substance in Bu-gong tea saponin is sodium percarbonate with content of 44.72%. The alkali agent contained in Bu-gong tea saponin are mixture of sodium hydroxide and sodium carbonate with content of 29% and 4.49% respectively.

References

1. Wang GF, Bu ZQ, Zhang ZJ. Application of Bu-gong tea saponin in the cotton and blended fabric, *Dyeing and Finishing Technology*, 38 (2) (2012) 223-225.
2. Cai SY, Yu Q. Application of tea saponin in cotton and tencel/cotton interwoven fabric pre-treatment, *Printing And Dyeing Auxiliaries*, (12) (2012)115-119.
3. Li JH, Pure cotton satin fabric with the Blake tea saponin one-step pre-treatment, *Dyeing and Finishing*, 38(24) (2012) 15-17.
4. Bu Zhuqi. *China Patent*. CN101736574A (2010).
5. Du J. Double indicator method for the determination of the content of mixed alkali sample, *Liaoning Chemical Industry*, 39(8) (2010) 888-890.
6. Yao XH, Zhang D. Potentiometric titration method for the determination of the content of sodium hydroxideand sodium carbonate contained in industrial sodium hydroxide. *Modern Scientific Instruments*, (4) (2006) 96-97.
7. Hong XQ. Qualitative analysis methods of borax in food, *Modern Preventive Medicine*, 34(15) (2007) 29-39.
8. Chen Y, Wei JL. Improvement on the the ceric sulfate solution and iodine titration calibration method in the "Chinese Pharmacopoeia", *Drug Standards of China*, 11(2) (2010) 143-144.

Compressive Strength of Paper Fruit-Shipping Box and its Optimization

E Yu Ping[a*], Zhang Liang Hua[b], Zhu Tong Tong[c]

College of Materials and Textiles, Zhejiang Sci-Tech University, Hangzhou 310018, China
E-mail: [a.] packeyp@126.com, [b.] lldrwin@163.com, [c.] toy.z@foxmail.com,

Li Long Ping[d]

Zhejiang Salfo Package Co., Ltd. Shaoxing Zhejiang 311815, P. R. China
E-mail: [d.] llongping@163.com

Compressive strength of paper fruit-shipping box (PFB) was investigated in this paper by experiments. Influences of reinforcing corner, positioning notch and environmental humidity on compressive strength of PFB were obtained as follows: compressive strength of PFB having reinforcing corner increased at least 16% compare to that of PFB without reinforcing corner; while compressive strength of PFB equipped with rectangular-shaped-corners is slightly higher than that of the box with triangular-shaped-corners; further, compression strength of PFB with isosceles triangle reinforcing corners increased about 8% compared to that of PFB with scalene triangle reinforcing corners; compressive strength of PFB decreased with the increasing of the number of positioning notch, two positioning notches on each long-side of PFB were recommended from the standpoint of stacking; compressive strength of PFB declined with the increasing of environmental humidities, compressive strength of PFB under an experimental atmosphere of 23 ℃, 80% RH (relative humidity) is about half of that for PFB under the atmosphere of 23 ℃, 50% RH.

Keywords: Fruit-Shipping Box; Compressive Strength; Optimization Design.

1. Introduction

Paper fruit-shipping box (PFB) is newly developed container made of corrugated paper which has already widely used in transport packaging and supermarket sales of fruit (Fig.1a). Structure characteristics of PFB are different from the regular slotted container (RSC), that is, positioning notches located on

Contract/grant sponsor: Project 51303160 supported by the National Natural Science Foundation of China, Project 1101712-N supported by the Key Laboratory of Product Packaging and Logistics of Guangdong Higher Education Institutes and Project 2014YXQN04 supported by the Open Fund of the Top Priority Discipline of Zhejiang Provincial High Schools.

the bottom were designed to facilitate fruit paper boxes stacked align center and to guarantee the stability of stacking; double-wall structure on the long-side edge and triangular reinforcing corners can enhance the compressive strength and stacking performance of box; windows designed on the main body can facilitate customers to see the products in the cabinet, and unique breathing holes were designed for air circulation (Fig.1b).

Paper fruit-shipping box stacked in the process of transportation, storage and display, therefore, its stacking capacity is an important indicator. Although studies exploring the effects of raw material [1], aspect ratio [2], box construction [3], hand hole [4], display window [5] and humidity [6] on stacking capacity of RSC have already existed, the striking structural differences between PFB and RSC make researches on the compressive strength of PFB and its influencing factors became very necessary. However, relative research is still lacking.



(a)



(b)

Fig.1 Fruit-Shipping Box

2. Materials and Methods

Single-wall corrugated boards were supplied by Hangzhou Bingxin Papers Co. Ltd. (Hangzhou, China). They were formed by gluing a corrugated medium between two thin liners. The basis weight of upper liner was 140 g/m^2, that of lower liner was 120 g/m^2, and 100 g/m^2 for corrugated medium. The corrugated flute was C-flute. PFB was a structure fabricated by a designated single-wall corrugated paperboard and then folded and glued together. Bottom area of tested boxes was 500 mm×300 mm and height was 150 mm.

PFB must be pretreatment under condition of 23 ℃, 50% RH for 48h in accordance with the GB/T 4857.2-2008. For determination of the influence of environmental humidity on stacking performance of PFB, samples were preconditioned in the same temperature of 23 ℃, and relative humidity 50%, 65% and 80% respectively for 48 h.

Static compression was conducted on a universal testing machine (U-25, Gotech Testing Machines INC., Taiwan, China) with cross-head speeds of 12

mm/min. Every compression test was effectively conducted in five repeats, and each measurement was completed within 5 min after specimen being removed from the conditioning chamber.

3. Results and Discussion

3.1 *The effect of reinforcing corner on compressive strength of paper fruit-shipping box*

Stacking capacities of PFB equipped with the isosceles triangle shaped corner, rectangle shaped corner and without reinforcing corner respectively were examined, experimental results are shown in Fig.2.

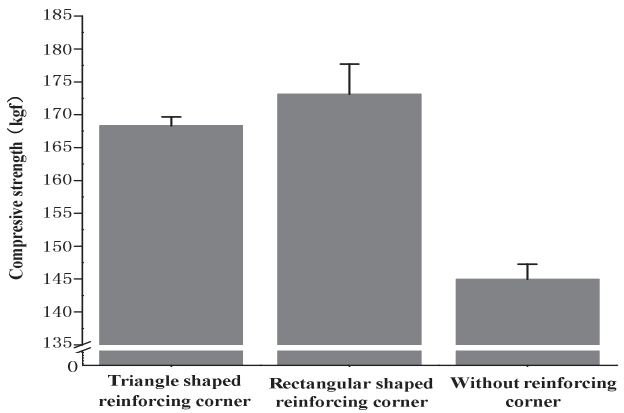


Fig.2 Compressive strength of paper fruit-shipping box equipped with different shape of strengthened corner

As can be seen from Fig.2, compression strength of PFB having reinforcing corner higher than that of PFB without the reinforcing corner, for example, the compressive strength of PFB equipped with rectangular-shaped-reinforcing corner was 173.1 kgf, while that of the box without reinforcing corner was 144.9 kgf, there is an increment of 16.2%; similarly, the compressive strength of PFB equipped with isosceles triangle shaped reinforcing corner was 168.3 kgf, there is an increment of 16% compared with that of the box without reinforcing corner. From these data we can concluded that reinforcing corner can improve the stacking capacity of PFB, its cause maybe that the load can be dissipated partly by the corrugated board of each reinforcing corner.

It can also be seen from Fig.2 that the compressive strength of PFB equipped with rectangular shaped reinforcing corners is slightly higher than that

of PFB with triangular shaped reinforcing corners, but the difference is relative small.

In order to examine the effect of corner size on the bearing performance of PFB, this paper investigated the compressive strength of PFB with isosceles triangle corner (40 mm length for each right-angle side) and scalene triangle corner (length of two right-angle sides are 40 mm and 60 mm, respectively) as shown in Fig.3.

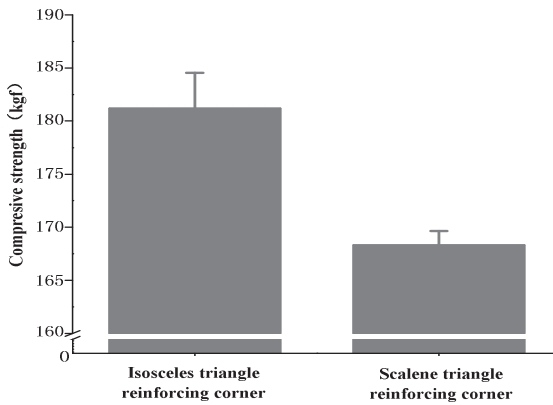


Fig.3 Compressive strength of paper fruit-shipping box equipped with different size of strengthened corner

We can see that even for PFB with triangular-shaped reinforcing corners, its compression strength changed with the side-length of the triangular, specifically, compression strength of PFB with isosceles triangle reinforcing corners increased about 8% compared to that of PFB with scalene triangle reinforcing corners. Therefore, in actual design application, PFB with isosceles triangle corner is recommended.

3.2 *The effect of positioning notch on compressive strength of paper fruit-shipping box*

Stacking capacities of PFB with zero, two and four positioning notches, respectively located on each long-side edge were examined, and the experimental results are shown in Fig.4.

Above data shows that the number of positioning notch was closely related to the compressive strength of PFB. The compressive strength declined with the increase of the poisoning notch number. The compressive strength of PFB without positioning notch was 150.4 kgf, while that of the box with four poisoning notches was 131.5 kgf, with a reduction of 12.5%.

Establishment of poisoning notch can facilitate the stacking performance, but decrease the compressive strength at the same time. However, in order to save transportation, storage and display space, paper fruit-shipping boxes are usually stacked, thus locating notch is essential. Comprehensive consideration, two positioning notches on each long-side of PFB were recommended.

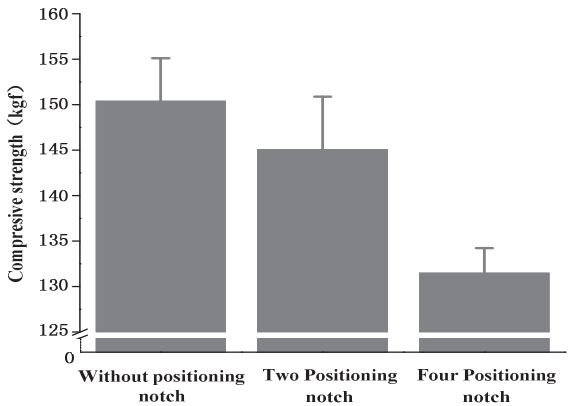


Fig.4 The effect of number of notch on compressive strength of fruit-shipping box

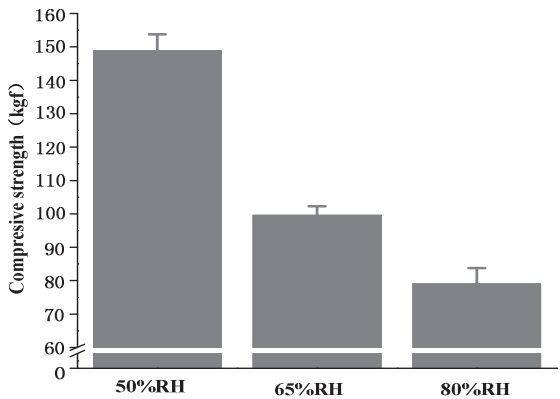


Fig.5 The effect of environmental humidities on compressive strength of fruit-shipping box

3.3 *The effect of environmental humidity on compressive strength of paper fruit-shipping box*

Compressive strength of standard PFB (bottom area is 500×300 mm, height is 150 mm, two long side each have two positioning notch, isosceles triangle strengthen corner with the side length of 40 mm) at 23 ℃, relative humidity 50%, 65% and 80% respectively are shown in Fig. 5.

In Fig.5, compressive strength of PFB showed a trend of decline with the increasing of environmental humidity. Compressive strength of PFB under the atmosphere of 23 ºC, 80% RH was 148.9 kgf, while that for PFB under 23 ºC, 50% RH was 79.1 kgf, there was a decrement of 47%.

Because of the hygroscopic nature of paper and hydrolysis of starch, water-absorbing capacity of PFB increase with the increasing of environmental humididites, then corrugated structure softened and compressive strength deteriorated. Therefore, humidity of transporting environment should be controlled during logistical process.

4. Conclusions

The influence of reinforcing corner, positioning notch and environmental humidities on the compressive strength of PFB was experimentally investigated and elucidated in this paper. The results of this research can be expected to provide useful information for optimizing design and the selection of PFB.

Reference

1. Tang Shaoyan, Wei Xing, Li Ting, et.al. Analysis of influence of raw material on compressive strength uniformity of corrugated box [J]. *Packaging Engineering*. 2012, 33(7):48-51.
2. Hua Guangjun, Zhao Dejian, Wei Zhuan. Research and analysis of influence of big aspect ratio on the compression strength of corrugated box[J]. *Packaging Engineering*. 2010, 31(2):45-47.
3. Hua Guangjun, Xiao Yingzhe. Experimental analysis of the influence of box-type on compression capacity of corrugated box for air-conditioner [J]. *Packaging Engineering*. 2010, 31(3):55-57.
4. Li Chunwei, Wang Guiying, Chen Chunsheng. Effects of handing hole on compressive strength of corrugated box [J]. *Journal of Northeast Forestry University*. 2008, 36(6):34-36.
5. He Miao Xin. Analysis on load capacity of corrugated boxes with show windows [D]. Wuxi: Jiang Nan University, 2010.
6. Duong Van Hung, Yusuke Nakano, Fumihiko Tanaka, et.al. Preserving the strength of corrugated cardboard under high humidity condition using nano-sized mists [J]. *Composites Science and Technology*. 2010 (70): 2123-2127.

Production of Low Carbon Dioxide Emission Geopolymer Green Cement

Ta-Wui Cheng [a*], Yung-Chin Ding[b] and Cing-Wun Jhong[c]

Institute of Mineral Resources Engineering, National Taipei University of Technology, Taiwan

[a] E-mail: twheng@ntut.edu.tw, [b] E-mail: ycding@ntut.edu.tw, [c] E-mail: b78116b@hotmail.com

Cement industry is one of the major CO_2 production industries. Production of one ton cement will cause 0.88 ton CO_2 emission. In order to solve this problem, geopolymeric green cement could be a potential material which may reduce the CO_2 emission problem in the cement industry. The aim of this work is to fabricate low CO_2 emission green cement at room temperatures using ground granulated blast furnace slag and coal fly ash powder reacted with alkaline solution to form geopolymeric green cement, and hope it can reduce CO_2 emission in Taiwan. Experimental results show that the properties of geopolymeric green cement are good related Portland cement. The best compressive strength can be reached 54 MPa and the maximum setting time after adding 3wt% borax retarding reagent can be reached 3h. For each ton of Portland cement replaced by geopolymeric green cement, the CO_2 emission reduction can be reached 81%.

Keywords: Carbon dioxide, Emission, Geopolymeric green cement.

1. Introduction

Cement is an important binder applied in making concrete. However, cement production causes large amounts of carbon dioxide emission[1], therefore, it needs to develop a new material to solve the carbon dioxide emission problem. Geopolymer is a three-dimensional framework aluminosilicate material[2]. It can be formed by mixing aluminosilicate materials, sodium hydroxide and sodium silicates[3]. The main raw materials are including metakaolin, ground granulated blast furnace slag (GGBFS), coal fly ash (FA) or waste glass powers. Geopolymers have the advantages of high compressive strength, and good fire/acid resistance[4]. Because of its low carbon dioxide emission, this new material can be called: “geopolymeric green cement” which can partly replace ordinary

* Corresponding author.

portland cement for construction applications. In this work, low carbon dioxide emission geopolymeric green cement was prepared by mixing GGBFS, FA and alkali solution. The physical/mechanical properties and microstructure properties of the green cement synthesized with different amounts of GGBFS were investigated.

Table 1. The molar ratios of the alkali solution and GGBFS, FA addition percentages.

Solid (wt%)		Liquid / Solid
GGBFS	FA	
30	70	0.78
50	50	
70	30	

2. Experimental

The alkali solution prepared in this study contains sodium hydroxide, sodium silicate, and sodium aluminate solutions. The molar ratios of the alkali solution used in this study are SiO_2/Na_2O =1.5 and SiO_2/Al_2O_3=20. The mixing ratio of GGBFS and FA are shown in Table 1. Geopolymeric green cement samples were synthesized by adding different amounts of GGBFS and FA to sodium silicate solution and sodium hydroxide solution that forms a liquid/solid ratio of 0.78. After mixing together for 15 minutes, the pastes were casted into a cylindrical acrylic molds with diameter of 50 mm and 100 mm height. The samples were then de-molded after 24 hours. The mechanical property test results are averaged from at least five samples for every test.

3. Results and Discussion

Figure 1 shows the compressive strength test results of the geopolymeric green cement samples prepared with different GGBFS contents and 7 days of curing time. The best compressive strength of the tested samples is 54 MPa obtained from 70wt% of GGBFS and 30% FA. From Figure 1, it can be found that the compressive strength of green cement samples increase with increasing GGBFS content. The compressive strength increased is due to the formation of C-S-H gel. The main role of GGBFS could because of it contribute dissolved calcium species. These kinds of calcium species can then react with silicate and aluminate to form various forms of calcium silicate hydrates and calcium aluminum hydrates. Alternatively, because of the GGBFS has high glassy phase causing high reactivity, it can increase the strength of the geopolymeric green cement.

Vicat Needle was used to measure setting time of the geopolymeric green cement as shown in Figure 2. The initial setting times were between 21 and 43 min;

the final setting times were between 35 and 63 min. As shown in Figure 2, the setting time is directly related to the GGBFS content. It is clearly noticed that the setting time decreases as the GGBFS content in the paste increases. It also can be found that the additional 1-3 wt% borax retarding reagent mixed in geopolymeric green cement would increase the setting time. The more the additional retarding reagent added, the more the setting time increased.



Figure 1 Compressive strength test results of geopolymeric green cement after curing 7 days

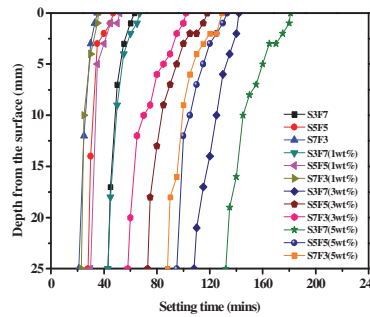


Figure 2 Setting time of geopolymeric green cement with and without retarding reagent of borax

Vicat Needle was used to measure setting time of the geopolymeric green cement as shown in Figure 2. The initial setting times were between 21 and 43 min; the final setting times were between 35 and 63 min. As shown in Figure 2, the setting time is directly related to the GGBFS content. It is clearly noticed that the setting time decreases as the GGBFS content in the paste increases. It also can be found that the additional 1-3 wt% borax retarding reagent mixed in geopolymeric green cement would increase the setting time. The more the additional retarding reagent added, the more the setting time increased.

The microstructures of green cement were tested by NMR. The ^{29}Si MAS NMR spectra of geopolymeric green cement after curve fitting area percentage are shown in Figure 3. It can be found that the percentage of curve fitting area of Q^4(4Al) was in the order of S3F7, S5F5, S7F3, and the curve fitting area percentage of Q^1 and Q^2 is opposite to Q^4(4Al), and in the order of S7F3, S5F5, S3F7. These results mean that the S3F7 sample has an aluminosilicate 3D structure, while the S7F3 sample reflects a linear structure. Because the S3F7 sample contains higher amount of fly ash, the high Si and Al in the coal fly ash could formation of extra Si-O-Al framework. On the other hand, the higher calcium content of GGBFS could promote the formation of the linear structures

because of the C-S-H gel. The needle-like structure of C-S-H gel with dense arrangement can increase the strength. The curve fitting area percentage of Q^4(0Al) is in the order of S3F7, S5F5, S7F3. It shows that the incomplete framework structure of the S3F7 sample, this may cause decreasing strength.

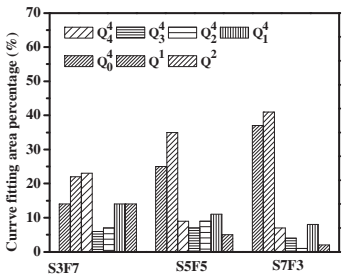


Figure 3 Curve fitting area percentage of geopolymeric green cement

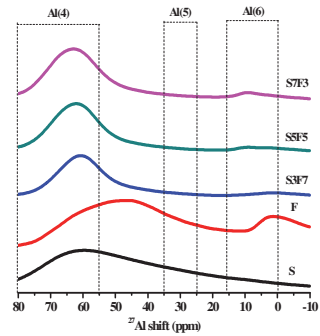


Figure 4 27Al MAS-NMR spectra of geopolymeric green cement

The ^{27}Al MAS NMR test results of geopolymeric green cement are shown in Figure 4. There are 4-coordinated Al, 5-coordinated Al and 6-coordinated Al, can be formed, due to correspond chemical shift peaks of 0-16, 25-35 and 55-80 ppm, respectively[5]. The major content geopolymeric green cements prepared in this research work have tetrahedrally coordinated Al. While the GGBFS content

Table 2 Estimation of CO2 emission

CO_2 source	OPC	Geopolymeric Green Cement for S3F7					
		GGBFS[a]	FA[b]	$NaSiO_3$[7]	NaOH[7]	Value Difference (ton)	Value Difference (%)
quantity (kg)	1000	223.4	521.4	216.3	38.9	-	-
Amount of CO_2 emission (ton)/ kg	$8.8*10^{-4}$	$5.8*10^{-5}$	0	$5*10^{-4}$	$1.1*10^{-3}$	-	-
Total (ton)	0.880	0.013	0	0.108	0.043	0.716	81.4

[a] Information source from The CHC Resource Corporation which include transportation, drying, milling, and maintenance.

[b] Coal fly ash is a by-product from thermal power plant, the CO_2 generation is zero.

increased, the chemical shift higher. It can be found the structure of green cement converts from aluminosilicate framework (AlQ4(4Si)) to chain group (AlQ2(2Si))[6]. Al (VI) found in the S7F3 sample is probably derived from the hydration product.

Generally, production of one ton OPC will produce 0.88 ton carbon dioxide. For the materials of making green cement, grinding 1 ton of GGBFS equivalent produces 58 Kg of CO_2 and FA did not generate any CO_2. As shown in Table 2, the amount of CO_2 emission for making geopolymeric green cement was estimated. Obviously, the total amount of CO_2 emission for making one ton S3F7 geopolymeric green cement was only 0.164 ton CO_2. That means compared with OPC, the green cement can be saved 81.4% CO_2 emission.

4. Summary

This present study deals with the use of ground granulated blast furnace slag and coal fly ash to fabrication geopolymeric green cement at ambient temperature by geopolymerization process. Experiment results shown that the geopolymeric green cement has good mechanical properties. The microstructure was identified by NMR to have a linear structur formed by Q^1 and Q^2 units. S3F7 is characterized to have highly polymerisd aluminosilicate structure that compose mainly three-dimensional network units, Q^4(4Al) and Q^4(3Al). Compared with OPC, produced the green cement can be saved 81.4% carbon dioxide emission. This technology has great potential for engineering application.

Acknowledgment

Ministry of Science and Technology supported this study under contracts NSC98-3114-E-027-001 and MOST 103-2221-E-027 -001 -MY2, which was gratefully acknowledged.

References

1. D. L.Y. Kong, J. G. Sanjayan**,** Damage behavior of geopolymer composites exposed to elevated temperatures, *Cement Concrete Comp.* 30 (2008) 986-991.
2. I. Lecomte, C. Henrist, M. Li´egeois, F. Maseri, A. Rulmont, R. Cloots, (Micro)-structural comparison between geopolymers, *Alkali-activated slag cement and Portland cement*, J. Eur. Ceram. Soc. 26 (2006) 3789-3797.
3. A. Hajimohammadi, J.L. Provis, J.S.J. Van Deventer, *One-Part geopolymer mixes from geothermal silica and sodium aluminate*, Ind. Eng. Chem. Res. 47 (2008) 9396-9405.

4. P. Duxson, A. Fernandez Jimenez, J.L. Provis, G.C. Lukey, A. Palomo, J.S.J. Van Deventer, *Geopolymer technology : the current state of the art*, J. Mater. Sci. 42 (2006) 2917-2933.
5. P. S. Singh, M. Trigg, I. Burgar, T. Bastow, *Geopolymer formation processes at room temperature studied by 29Si and 27Al MAS-NMR*, Mater. Sci. Eng. A 396 (2005) 392-402.
6. J. Davidovits, Geopolymer chemistry and applications, *France: Geopolymer Institute*, (2008) 61-76.
7. C.M. Benjamin, P.W. Ross, L. Janine, V.R. Arie, D.C. Glen, *Costs and carbon emissions for geopolymer pastes in comparison to ordinary portland cement*, J. Clean Prod. 19 (2011) 1080-1090.

Study on the Efficiency of Microbial Mutagenesis Experiments and Degradation of Methane

Wenjie Nie*, Shengquan Wang, Chentao Hou

College of Geology and Environment, Xi'an University of Science and Technology, Xi'an 710054, China

*E-mail: *76977485@qq.com*

This paper introduces the common methods of breeding, the mutation breeding is the most effective method, study the efficiency of different induction method for degradation of methane. In order to get the efficient degradation of methanotrophic bacteria, the experiment study on screening out the atrophy of bacillus. This experiment adopts the 10W ultraviolet irradiation of Bacillus vallismortis, make its mutation. And carries on the induction of the mutation get these mutated bacteria were cultured with lithium chloride, and then used to determine the gas degradation, degradation rate. The experimental results show that: the UV + degradation of lithium chloride induced strain rate, strain induced by UV degradation rate of lithium chloride induced bacteria, degradation rate.

Keyword: Mutation Breeding; Ultraviolet Mutagenesis; LiCl Mutagenesis; Methane Decomposition.

1. Introduction

With the development of science and technology, China's national economy is developing rapidly. However, at the present stage, as a result of the problem of management level of security and the lack of advanced technology for treatment of coal gas, it has become the biggest hidden trouble of safety in production of coal mine and gas is known as "the first killer" of china's coal mine safety [1].

Microbiological method to control gas is a kind of method that emerged in recent years [2-5]. Microbial screening, domestication and cultivation of microorganisms which can degrade methane efficiently is the key to control gas.

This experiment uses 10W UV lamp to irradiate of the atrophy of bacillus to make them mutant. And they will be induced by lithium chloride, the method is to make the mixture of lithium chloride and culture medium into slab and guarantee the mass concentration of LiCl to be 10 g/mL. Then we culture the mutant bacteria and use them to degrade methane, determining the degradation rate.

2. Experimental part

2.1. *UV + LiCl composite mutagenesis*

Lithium chloride is a kind of alkali metal halide. It itself doesn't have a significant effect on the mutagenesis, but it is shown that LiCl can have an effect by cooperating with some mutation factors in the mutation breeding of bacteria. Therefore, we added LiCL solution of 10 mg/L into the screened petridish so that methanotrophic bacteria can achieve a good effect of mutagenesis.

2.2. *Comparison of microbial growth curve before and after mutation*

As you can see from Fig. 1. The mutant strain need 55 h to reach the stable growth phase, but the strain without mutagenesis need 65 h. Therefore, mutant strain was earlier than the strain without mutagenesis 10 hours to enter the stable growth phase, which suggested that the growth rate of mutant strain has been improved. That will have directive significance to the application of the strain in reality [8].

The measured growth curve as shown in Fig. 1:

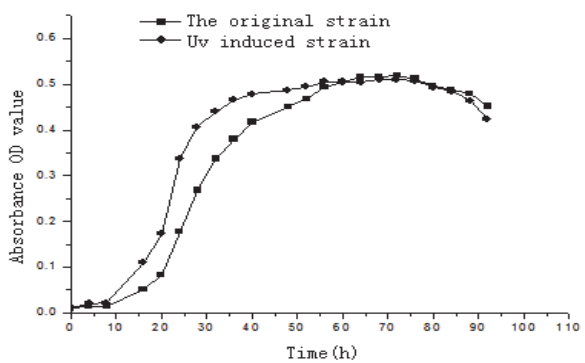


Fig. 1 Biological growth comparison before and after mutation

2.3. *The Preparation of Microbial Agents after Mutation*

The preparation method is: inoculating the purified yellow bacterium to the liquid medium of pH 6.5, then according to the volume ratio of O2:CH4=1:2 adding methane and oxygen and culturing under 32ºC for 48 h. Finally we obtained the yellow methanotrophic bacteria agents and preserved them in a refrigerator under 4ºC.

Table 1. The number of prepared inoculum

Medium	Methane	Oxygen	Strain sources
Inorganic salt liquid 20 mL	30 mL	20 mL	The yellow original strain
Inorganic salt liquid 20 mL	30 mL	20 mL	
Inorganic salt liquid 20 mL	30 mL	20 mL	Induced by Lithium chloride
Inorganic salt iquid 20 mL	30 mL	20 mL	
Inorganic salt liquid 20 mL	30 mL	20 mL	Induced by UV
Inorganic salt liquid 20mL	30 mL	20 mL	
Inorganic salt liquid 20mL	30 mL	20 mL	Induced by Lithium chloride and UV
Inorganic salt liquid 20mL	30 mL	20 mL	

3. Results and discussion

3.1. *The degradation effect of strain whose irradiation time is different*

In the condition of 32ºC and pH 6.5, we researched the degradation effect of methanotrophic bacteria under different irradiation time. So we set the UV irradiation time to 10s, 20s, 30s, 40s and studied the degradation effect of methanotrophic bacteria which was cultured under four different conditions. We set the initial concentration of methane gas to 40% and determined the concentration of methane gas every 24 h.

The concentration of methane changed with time under different irradiation time, as shown in Fig. 2:

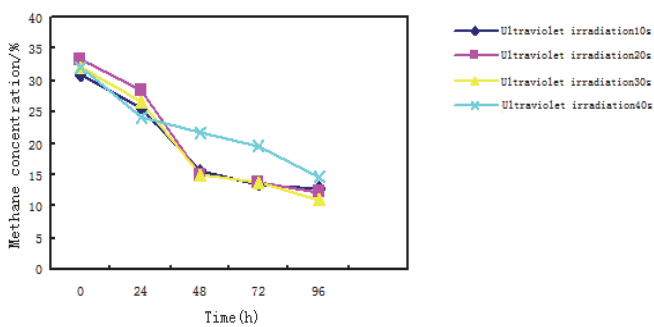


Fig. 2 The degradation effect of mutant strain under different UV irradiation time

As can be seen from the Fig. 2, with the increase of time, the concentration of methane decreases. And it is obvious that the UV mutagenesis method has an optimal irradiation time. As for the methanotrophic bacteria, mutagenic effect is better than the others when the UV irradiation time is equal to 30s. The methanotrophic bacteria whose UV irradiation time is 30s can make the removal

rate of methane reach 66% after 96h and its degradation effect is significantly better than the others.

3.2. *Studies on the degradation effect of different mutant methanotrophic bacteria under the condition of the same concentration of methane*

We took four sterilized jars, added solid medium of 1 cm thickness and 1mL methanotrophic bacteria which was induced under different condition into them separately, and filled the four jars with 125 mL oxygen and 250 mL methane gas. Then we sealed them with vaseline and shook gently so that it distributed on the medium evenly. We inverted them in the biochemical incubator and cultured them under constant temperature of 32ºC, and determined the concentration of methane in four jars every 24 h. The larger the concentration of methane is, the smaller the error is. So we set the initial concentration of methane to 50%.

The experimental result which the concentration of methane changes with time as shown in Fig. 3:

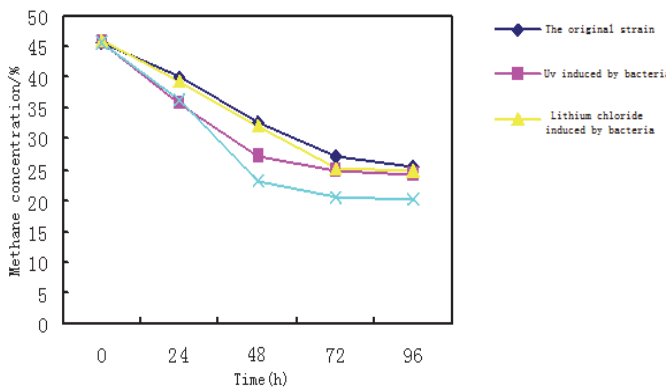


Fig. 3 The degradation effect on methane of different mutant strain

As can be seen from Fig. 3, four kinds of mutant strain has a certain degradation effect on methane. After 96h, arranged by concentration in a descending order: the original strain >strain induced by lithium chloride > strain induced by UV > strain induced by UV+LiCL. And the degradation rate from high to low were: strain induced by UV + lithium chloride > strain induced by UV > strain induced by lithium chloride > the original strain. Meanwhile, the degradation rate of strain which induced by UV and lithium chloride reached 55.7%, the highest in all mutant strain.

4. Conclusion

(1) The degradation rate of methanotrophic bacteria whose UV irradiation time is equal to 30 s can reach 66% after 96 h. The degradation effect is significantly higher than the others.

(2) The degradation effect of strain which is induced by only using lithium chloride is not obvious. However, the degradation rate of strain which is induced by UV and lithium chloride can reach 55.7%, the highest in all induced strain. Therefore, the degradation effect of strain which induce by UV and lithium chloride is remarkable.

References

1. Zhang Tiegang. Mine gas comprehensive control technology *[M]. Beijing: coal industry publishing house*, 2001
2. Yong-ping Deng. The effective ways to curb [2] coal mine gas accident. Proceedings of the third session of the national coal safety production BBS. 2009 - ZK. 91-92.
3. Wen Yongsheng. The new development of mine ventilation technology *[J]. World nonferrous metals*, 2008, 12:32-34.
4. Zhu Shishan. Of coal mine gas drainage technology *[J]. Coal technology*, 2009, 06, 102-103.
5. Ke Wei. Management of coal mine gas explosion of microbial biotechnology *[J].Journal of biological engineering*, 2005, 21 (3): 460-460.
6. Liang Shi Yi, Yue Jin. Methane oxidative bacteria research progress *[J]. Journal of combat readiness, Ecology*, 2004, 3 (5): 198-205.
7. Roslev P, Iversen N. Oxidation and assimilation of atmospheric methane by soilmethane oxidizers*[J]. Appl. Environ. Microbiol,* 1997.63: 874-880.
8. Gilbert B, Frenzel P. Rice roots and CH_4 oxidation the activity of bacteria, their distribution and the micro-environment[J]. *Soil. Biol. Bioch em,* 1998.30:1903-1916.

The Influence of Ammonia Regeneration for $CuO/\gamma\text{-}Al_2O_3$ Catalyst of Desulfurization Performance

Nie Wenjie*[1a], Zhang Lei[1, 2], Zhang Nian[1]

[1]*College of Geology and Environment, Xi'an University of Science and Technology, Xi'an 710054, China*

[2]*Environmental Protection and Energy-Saving Equipment Research Institute, China National Heavy Machinery Research Institute Co., Ltd, Xi'an 710032, China*

**E-mail: 76977485@qq.com*

In order to investigate the effects of performance of catalyst desulfurization on the different regeneration conditions, different ammonia flow, reduction temperature, and reduction time were selected for catalyst regeneration by using ammonia as a reducing gas. The results of experiment displayed: With the increase of ammonia flow, reduction temperature and reduction time, the desulfurization performance of catalyst regeneration showed increasing trend, and the optimum reduction conditions of $CuO/\gamma\text{-}A1_2O_3$ catalysts were that ammonia flow rate was 200 ml/min, the reduction temperature was 400ºC, the reduction time was 1 h.

Keywords: ammonia regeneration; catalyst; the desulfurization performance.

1. Introduction

With the development of industry, the coal consumption and SO_2 emissions will further increase, acid rain and acid fog of SO_2 do harm to environment greatly[1], thus the control of coal-combustion flue gas and SO_2 emission is the urgent problems of our country ecological environment and the healthy development of the national economy[2].

At present, the flue gas desulfurization technology in accordance with the morphology of adsorbent can be divided into dry process and semi-dry method and wet method at home and abroad[3]. In the field of atmosphere pollution prevention the technology of metal oxide supported sorbents for desulfurization of dry flue gas because of its simplification equipment, convenience of operation and management and low production costs has become an essential aspect in the frontier research[4]. But supported metal oxide catalysts are particularly susceptible to poisoning and need frequent regeneration and adverse influence for the life of the catalysts and the follow-up of the desulfurization performance may be generated by frequent warming and cooling[5].

H_2 and CH_4 are often used as a reducing agent for the regeneration of the catalyst by reduction method, strong reducibility of H_2 is more likely to cause excessive load on the oxide reduction in the regeneration process and generate some metal simple substance attached to the catalyst to reduce efficiency in the regenerated catalyst desulfurization and increase consumption of H_2[6]. The catalyst after regeneration can maintain the stability of the physical structure, the high and stability efficiency of desulfurization, and NH_3 and SO_2 generated within the reactor generate directly sulfur amine salt solid, the realization of utilization of sulfur, the lowering of the operating costs and improvement the economic benefits is impossible.

2. Experiment Part

2.1. *Experimental design*

Load copper oxide bore on the carrier of γ-$A1_2O_3$ is crystallized as the active ingredient, and the catalyst after poisoning desulfurization experiments are completed. Then poisoned catalyst after desulfurization is restored by using ammonia to study the impact on the activity of catalyst regeneration with different ammonia flow, reduction temperature and reduction time. In the experiment, load was 7%, the calcinations temperature is 350ºC, roasting time is 3h and the reaction temperature is 180ºC. By using a single variable method and flue gas analyzer, the change of SO_2 in flue gas desulfurization experiment is compared with the former content that is the comparison of desulfurization rate. The tube furnace is used to restored poisoning catalyst, then the effect of the different reduction factors of catalyst and the optimum reduction conditions is concluded by using the flue gas analyzer for testing.

2.2. *Evaluation device of catalyst activity*

Catalyst performance testing is carried out in constant temperature in the fixed bed adsorption column. Adsorption column is a quartz tube for inside diameters of 20mm and length of 50 cm. Performance testing device of catalyst is shown as in Fig.1.

2.3. *Deactivation and regeneration of catalyst*

CuO loaded on the γ-Al_2O_3 catalysis with SO_3 generated by react of O_2 and SO_2 to achieve desulfurization purpose. When the active components absorb SO_2 to reach saturation, the active component of the deactivation can use NH_3 to reinstate the regeneration and once again get copper oxide or elemental copper,

and Cu meets free of O_2 in flue gas and generates CuO. The deactivation of the catalyst is included in the tube furnace, and different ammonia flow rate (100 ml/min, 200 ml/min and 300 ml/min), reduction temperature (300ºC, 400ºC, 500ºC), the reduction time (0.5 h,1 h, 1.5 h), are selected to investigate influence of different reduction conditions on the desulfurization performance.

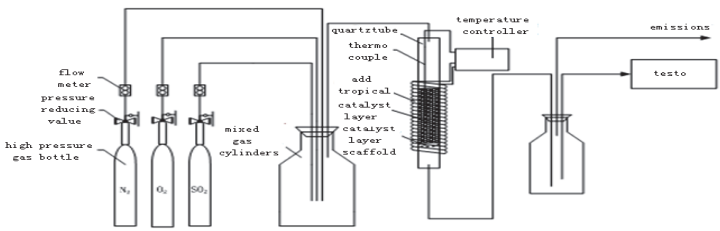


Fig.1 Performance testing device of catalyst

3. Results and Discussion

3.1. *Research on the influence of desulfurization performance on different ammonia flow rate*

As can be seen from the Fig.2, previously the effect of reduction is poor when the ammonia flow rate is 300ml/min, the effect of flow rate of 300ml/min is more than 100ml/min in the middle period, and in the whole process better effect of reduction is achieved on 200ml/min of flow rate. The conclusion is that the high ammonia reduction degree of 300ml/min leads to generate the Cu, and this is due to early oxygen content reduces quickly in the desulfurization process. Due to the copper oxide generated in the reaction, the effect of flow rate of 300ml/min is more than 100ml/min in the middle period. From the whole curves ammonia flow of 200ml/min should be choose d as the best flow to the reduction of the next step.

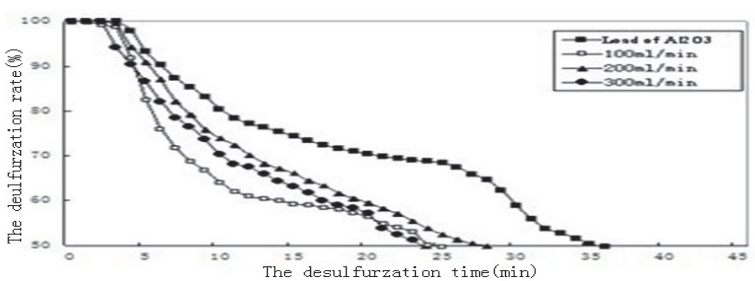


Fig.2 Desulfurization rate under different ammonia flow

3.2. *Research on the influence of desulfurization performance on different reduction temperature*

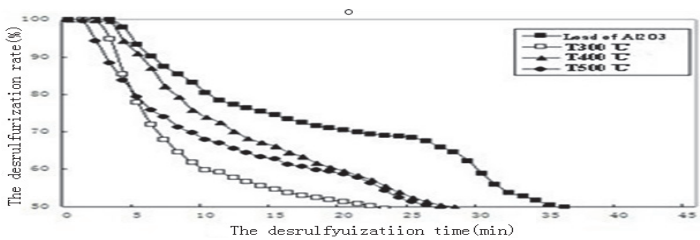


Fig.3 desulfurization rate under different reduction temperature

As can be seen from the Fig.3, in the early period of the desulfurization process, the desulfurization effect under the condition of the reduction temperature of 500ºC is the worst, in the mid period effect of 500ºC is better than that of other temperature, and effect of 400ºC is in a leading position in the process of desulfurization.

3.3. *Research on the influence of desulfurization performance on different reduction time*

At the optimum flow rate of 200ml/min and the temperature of 400ºC the reduction time is respectively 0.5hours, 1hour, 1.5hours, and three reduction curves of different temperatures are shown in Fig.4.

Early the desulfurization effect of reduction time of 1.5hours is the worst, the curve of 1.5hours later has a clear warming trend, in the whole process the reduction time of the best desulfurization effect should be 1hour. In the early period reduction time is long , and reduction product copper oxide is excessively restored into copper. Copper has not a catalytic effect in the process of desulfurization thus of desulfurization effect of reducing time of 1.5hours is the worst. Copper oxide continues to serve as a catalyst in desulfurization due to

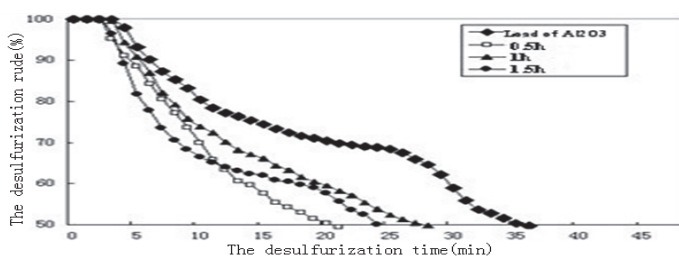


Fig.4 desulfurization rate under different reduction time

that copper is oxidized to copper oxide in the late desulfurization process, so the curve of 1.5hours has obvious warming trend and the better effect than 0.5hours. Reduction effect of 1hour should be the best one in the entire process.

4. Conclusion

Desulfurization efficiency of CuO/gamma $A1_2O_3$ after regeneration with ammonia can maintain high and stable. With the increase of ammonia flow desulfurization performance of catalyst showed a trend of increasing and optimal ammonia flow of CuO/γ-$A1_2O_3$ is 200 ml/min; With the increase of temperature, catalyst regeneration effect is also increasing and the best temperature is 400ºC; with the increase of reduction time the catalyst regeneration effect is also increasing, reduction time of the best effect is 1hour. The optimal condition of ammonia reduction screened from experiment is the flow rate of 200ml/min, temperature of 400ºC and reduction time of 1hour.

Acknowledgements

The financial support of this research by Scientific Research Program Funded by Shaanxi Provincial Education Department (Program No. 2013JK0869) in P.R. China is gratefully acknowledged.

References

1. Li Yuan, Zhang Xianglan, Xu Deping. Research on the mechanism of SO2 removal by activated carbon [J]. Coal *Processing and Comprehensive Utilization*, 2007, 12:46-49.
2. Guo Dong ming. Technology and engineering application of sulfur nitrogen pollution prevention [M]. Beijing: *Chemical Industry Publishing House*, 2001, 4.
3. Zeng Ting hua, Yang Hua. The safety and optimization of the system of wet flue gas desulfurization [M]. Beijing: *China Electric Power Press*, 2004.
4. Qian Yi, Hao Ji ming. Prevention and control of industrial pollution [M]. Beijing: *China Science and Technology Press*. 2002, 126.
5. Yin Hua qiang, Hu Yu ying. Technological advances of flue gas desulfurization in China [J]. *Sichuan Environment*, 1999, 18(4).
6. Xiang De hui, Weng Yu pan. Solid catalyst [J]. *Chemistry Industry Press*, 2003, 451.

Author Index

Ai, P., 561
An, S.J., 595
Andrea, C., 534

Bai, Q., 464
Ban, Y.Q., 53
Bi, H.Y., 573
Bi, Z.Y., 419

Cahill, D., 413
Cao, F., 370
Cen, K.F., 524
Chai, S.X., 179
Chang, H.G., 601
Chen, B., 444
Chen, C.S., 338
Chen, D.H., 626
Chen, D.J., 34
Chen, H., 179, 392
Chen, J., 345
Chen, K.X., 357
Chen, L., 281, 338
Chen, S.O., 53
Chen, T., 308
Chen, X.H., 357
Chen, Y., 135
Cheng, H.C., 247
Cheng, T.W., 661
Cui, P.C., 232
Cui, S.L., 648

Dai, H.X., 154
Dai, M.Y., 338
Dai, X.D., 338
Deng, J.G., 154
Deng, T.Q., 179
Ding, D., 357
Ding, Y.C., 661
Dmitriev, A.I., 21
Dong, X., 351
Du, X.R., 142
Dubinets, A., 215

E, Y.P., 655

Fan, Q., 40
Fang, W., 585
Fedorets, A., 215
Feng, C.F., 47, 413
Feng, C.G., 71
Filippo, C., 534

Gan, Q., 71
Gao, J.G., 232
Gao, Y., 585
Giuseppina, M., 534
Gong, Y.Y., 488
Gu, Q., 427
Gu, T., 601
Gu, X.H., 16, 573
Guan, S.J., 314
Guan, X.J., 384
Guo, H.Y., 238
Guo, X.J., 53, 226
Guo, Z.S., 608

Hao, L., 314
He, B., 380

He, C.J., 296
He, X.D., 261
Hong, B., 59, 65
Hou, C.T., 667
Hu, L., 120, 380
Hu, Y., 634
Hu, Y.X., 524
Huang, B.F., 8
Huang, D.W., 617
Huang, T., 107, 113
Huo, X.D., 220

Jhong, C.W., 661
Jiang, W.X., 269
Jiang, Y., 154
Jiang, Z.L., 513
Jin, F.M., 289
Jing, B., 464
Jing, L.Y., 53
Ju, J.T., 135

Kazuomi, N., 621
Ke, D.Q., 59, 65
Kim, H., 595
Kiminori, S., 621
Kirillov, A., 215
Kong, L.X., 47, 413
Kuo, D.H., 407
Kuznetsov, V.P., 21

Lai, C., 107, 113, 128
Lai, X., 40
Li, C., 79, 86
Li, D.G., 380
Li, H.L., 53
Li, H.W., 585
Li, J.C., 93
Li, K., 478
Li, L., 247
Li, L.J., 220
Li, L.P., 655
Li, L.Y., 561
Li, M.J., 561
Li, M.Q., 226
Li, M.Y., 269
Li, N., 444
Li, Q.X., 464
Li, S., 553
Li, X.L., 302, 434
Li, X.S., 99
Li, Y., 261, 302
Li, Z.X., 641
Liao, G.D., 561
Lin, J.Y., 524
Lin, M., 488
Liu, F.J., 27
Liu, H.F., 338
Liu, J., 544
Liu, J.Q., 275
Liu, J.Z., 524
Liu, L., 202, 351, 440
Liu, L.P., 392
Liu, M.R., 247
Liu, N.F., 220
Liu, X.B., 238
Liu, X.H., 195
Liu, X.Q., 434
Liu, X.X., 40
Liu, Y.C., 464
Liu, Y.L., 302
Liu, Z.D., 601
Lu, F.X., 120
Lu, H., 174
Lu, M.Q., 99
Lu, P., 148
Lu, X.F., 59, 65
Lu, Y., 314, 561
Lu, Z.F., 617
Luo, W.H., 553
Lv, Z.B., 506

Ma, C., 226
Ma, J.J., 255
Meng, L.M., 208

Miao, J.B., 120
Mo, L., 601
Modin, E., 215

Nie, S.B., 351
Nie, W.J., 667, 672
Niu, Y.W., 357

Pan, F., 626
Pan, Y.F., 148
Pan, Y.J., 59, 65
Pan, Z.B., 384
Peng, C., 351
Peng, X.F., 168
Peng, Z., 47
Plotnikov, V., 215
Pustovalov, E., 215

Qi, L.Q., 641
Qian, J.S., 120
Qian, J.X., 71
Qiao, H.Y., 40
Qin, C.S., 380
Qin, M., 380
Qin, X.X., 269
Qin, Z.Y., 281
Qiu, M., 296
Qu, C.Y., 578
Qu, J.H., 275

Rao, C.D., 142
Ren, J.W., 269
Ren, L.N., 338

Shang, G.Q., 544
Shang, X.B., 86
Shang, Y.M., 573
Shao, W.Q., 53
Shao, X., 626
Shao, Y.B., 506
Shen, J.J., 208
Shen, R., 202
Sheng, L.Y., 107, 113, 128
Shi, G.B., 513
Shi, J.M., 488
Shi, Z., 8
Song, G.L., 506
Song, X., 16
Song, X.F., 142
Sun, C.H., 544
Sun, C.J., 456
Sun, Y.C., 142
Sun, Y.Y., 456

Tang, H.L., 238
Tang, J.T., 135
Tao, J.Q., 99
Tao, X.X., 498
Tian, X.S., 202, 208
Tian, Z.Z., 220

Vincenzo, S., 534

Wan, Y.Y., 99, 179
Wang, B.F., 93
Wang, C., 195, 345
Wang, D., 174
Wang, D.Y., 351
Wang, F., 187
Wang, H., 142, 187
Wang, H.B., 544
Wang, H.L., 488
Wang, H.M., 617
Wang, J., 384
Wang, J.Z., 302
Wang, K.Y., 232, 255
Wang, L.Y., 392
Wang, Q.L., 128
Wang, R.Q., 472
Wang, S., 498
Wang, S.Q., 667
Wang, S.Y., 107, 113
Wang, W.Y., 634
Wang, X.B., 365

Wang, X.H., 320
Wang, X.P., 585
Wang, Y., 269
Wang, Y.B., 99
Wang, Y.P., 345
Wang, Y.W., 449
Wang, Y.X., 308
Wang, Z., 53
Wang, Z.D., 357
Wang, Z.M., 553
Wei, F.H., 226
Wu, G.Y., 601
Wu, H., 601
Wu, R.H., 456
Wu, W.P., 1
Wubet, W., 407

Xi, T.F., 107, 113, 128
Xi, X.P., 488
Xia, H.F., 40
Xia, R., 120
Xia, T.S., 365
Xiao, C.H., 400
Xiao, H.N., 148
Xiao, W., 434
Xiao, Z.Q., 472
Xie, K., 506
Xie, S.H., 154
Xie, X.T., 561
Xie, Y.S., 488
Xing, W.G., 202
Xu, A.R., 585
Xu, C.H., 302
Xu, H.R., 434
Xu, J., 585
Xu, Y.H., 478

Yan, C.J., 308
Yan, J., 601
Yan, L., 174
Yan, P.Z., 232, 255
Yang, B., 120
Yang, B.L., 595
Yang, F., 128
Yang, H.G., 154
Yang, M.W., 601
Yang, R., 427
Yang, W., 1, 506
Yang, X., 195, 370
Yao, G.D., 289
Yao, J.M., 498
Ye, Q., 174
Yeow, J.T.W., 27
Yi, Y.H., 332
Yi, Z.F., 47, 413
Yin, J., 634
Yu, B.S., 392
Yu, H.X., 327
Yuan, Z.C., 34

Zeng, P., 16
Zeng, Q.K., 384
Zeng, Z.X., 478
Zhang, B., 449
Zhang, G., 320
Zhang, G.F., 8
Zhang, H., 59, 65
Zhang, L., 154, 585, 672
Zhang, L.H., 655
Zhang, N., 672
Zhang, N.G., 601
Zhang, Q., 601
Zhang, Q.M., 261
Zhang, R., 626
Zhang, S., 449
Zhang, T., 338
Zhang, W.H., 498
Zhang, X.P., 608
Zhang, X.Q., 142
Zhang, X.W., 16
Zhang, X.Y., 232, 255, 384
Zhang, Y.H., 308
Zhang, Y.J., 154, 641
Zhang, Z.S., 289

Zhao, H.X., 174
Zheng, T.T., 71
Zheng, W.L., 281
Zhong, H.Y., 585
Zhou, C.C., 440
Zhou, J.H., 524
Zhou, L.P., 434
Zhou, N.Q., 168
Zhou, X., 320
Zhou, X.L., 8
Zhu, L.L., 626
Zhu, T.T., 655
Zhu, W.L., 168
Zhu, X.H., 464